Department of Astrophysics, Geophysics and Oceanography
*College of Space sciences*

# Search for habitable planets eclipsing ultra-cool stars

A dissertation presented by

**Elsa Ducrot**

on August 30, 2021

**Thesis supervisor:** Dr. Michaël Gillon (University of Liège)

**Jury members:** Dr. Michaël Gillon, Supervisor (University of Liège)
Prof. Denis Grodent, President (University of Liège)
Dr. Francisco J. Pozuelos, Secretary (University of Liège)
Prof. Eric Agol (Univeristy of Washington)
Prof. Brice-Olivier Demory (University of Bern)
Prof. Didier Queloz (Univeristy of Cambridge)

This dissertation is submitted for the degree of
*Doctor of Philosophy in Sciences*

I would like to dedicate this thesis to my parents Guy Ducrot and Anissa Kabbage-Ducrot.

# Acknowledgements

A PhD thesis is like a long-distance run and I would never have gotten through it if it was not for the support of my colleagues, friend and family. I therefore want to dedicate the next few lines to all the people that supported me during the last four years.

First of all, my greatest thanks go to Michaël, for his kindness, his trust and amazing support all along my PhD. Thank you also for all the wonderful opportunities, either to be part of the SPECULOOS team or to led certain studies or to allow me to attend various exciting conferences all over the world. Thank you for everything you taught me, for always being there to answer my questions (even the most silly ones) and for always finding time to carefully read and correct my reports, abstracts, papers and now thesis (two times! that's impressive!). I could not have hoped for a better supervisor!

I also want to thank my "unofficial supervisor", Didier, for his gentleness and motivation. I am very grateful for all the time you spent giving me guidance and ideas on my projects. Thanks also for always welcoming me to Cambridge and including me in the group while letting me keep my independence.

More generally, I want to warmly thank Michaël and Didier for giving me the privileged opportunity to frequently travel between Liège and Cambridge, this eased my personal life so much and allowed me to interact more closely with both parts of the SPECULOOS team.

Next, I want to thank Michaël, Didier and Brice for always being available for a chat, for all the insightful advise and for taking the time to write me tens of recommendation letters. Once again, I am sorry I applied to so many positions... But I am convinced I would not have had these offers without your help. Actually, I heard that one recruiter said my CV was fine but the really impressive part was my recommendation letters !! So for that, thank you deeply.

I would also like to thank again Michaël, Didier, Brice as well as Fran Pozuelos, Eric Agol and Denis Grodent for agreeing to be part of my jury. I must say I feel extremely glad and honoured and I hope you will appreciate reading this manuscript.

Working on an exciting project such as SPECULOOS was thrilling however it would have never been so nice without the amazing SPECULOOS team. I am so glad I've got to work in this nice dynamic and meet such great people. So, thanks to all the team members (who I did not mention yet) that were always available for advises, discussions, questions or just to chat: Amaury, Daniel, Artem, Catriona, Peter, Georgina, Julien, Max, Ben, Prajwal, Sam, Nicole, Robert, Yilen and particularly Laetitia who even turned out to become my housemate! Any way I'll keep being part of the SPECULOOS team so I am certain we will continue seeing each other a lot.

Thanks as well to the wonderful TRAPPIST team. Khalid I'll never forget our trip de Chile and I hope I'll see you at Oukaimeden soon. Thanks Manu for several late skypes during my first year that helped me master the art of telescope operation.

A special thanks to my partner in crime, Lionel. If somebody had told me seven years ago that I would end up sharing an office with you I am not sure I would have believed it. I cannot count how many times we have called each other to discuss work or just have fun. Thanks for being there frate, this was a fun ride.

Of course a huge thank to all the other PhD/Post-doc or +1: my PhD twin Martin, Charly, Clem, Marilyn, Lorenzo, Lyne, Angelo, Antoine, Mathilde, Sylvain x2 and Judith for thousands of coffee breaks, esquisse games, every nice lunches, and some memorable evenings. Way more than co-workers you all have been amazing friends during those four years. I'll deeply miss bouldering at l'Éléphant, beers for the electrolytes and our excursions at the Shamrock. Don't worry guys I'll come back to see you. How we say in Liège: Tantôt hein!

More generally, thanks to the whole B5c staff for their warm welcome. For all the birthdays, thesis or accepted paper celebrations that were all good excuses to meet and share a good Belgian beer.

I would never have been here if it wasn't for my family and friends back in France and Morocco. Please allow me to switch to French to address them a direct message.

Maman, papa je vous dédis cette thèse. C'est la moindre des chose que je puisse faire pour vous exprimer ma reconnaissance. Je parle d'astronomie depuis que j'ai 6 ans et vous m'avez toujours aidé à entretenir ce rêve, d'une part en m'offrant une enfance merveilleuse et d'autre part et étant toujours là pour me soutenir et me motiver par votre amour. Merci à mes frères Nico, Bastien, et ma sœur Sonia, les meilleurs grand frères et sœur qui puissent exister et sur qui je peux toujours compter. Une grosse pensée également pour mes +1 préférés : Achouak, Anne-Sophie et Edouard ainsi que mes neveux et nièce adorés : Titouan, Leïla et Tigrane.

Merci à mon grand-père Gérard pour sa tendresse et sa curiosité scientifique qu'il nous a bien transmis. Merci à ma tante Anne de nous avoir si bien reçus Benjamin et moi en Californie, c'était une parenthèse magique pendant la thèse. Merci évidement à Karim, Kenza, Dalil, Inji, Yezza et Myriam qui font toujours preuve d'un amour et d'une bienveillance inconditionnels à mon égard. Un merci particulier à Yezza pour être toujours venue me rendre visite où que je sois et m'avoir toujours encouragée dans mes choix, je t'attends à Paris ! Merci à ma grand-mère de cœur Renée avec qui j'aime tant partager mon amour pour les sciences et la recherche et que je me réjouis de voir plus régulièrement l'année prochaine. Merci à toute la Kabbagerie pour être des Kabbages, tout simplement. J'ai évidemment des milliers de pensées pour mon Padriss, ma Manou et ma Manette qui me manquent tellement mais qui j'en suis certaine seraient plus fiers que jamais et qui continuent de me soutenir sans relâche de là où ils sont.

Je souhaite également adresser un petit mot à ma famille d'adoption : les Béringue et + 1 (Anne, Jef, Jules, Katia, Math, Cha, Raymonde, Cathie, Christophe, Elli et Mar). Merci à tous de m'avoir aussi bien intégrée dans votre famille et de m'avoir si souvent accueillie dans la maison magique de Guenviller pendant cette thèse. Je n'aurais pas pu rêver meilleures conditions pour commencer à écrire mon manuscrit que l'ambiance « hotel california » offerte par Anne et Jef. Math et Cha merci pour toutes ces soirées/week-end entre Lille, Liège et Paris, la vie est toujours si douce avec vous. Enfin, merci à Tommie pour tous ses câlins réconfortants.

Je pense également à toute la bande de Bandol & Co que je considère comme une extension de ma famille : ma deuxième maman Juliette, ma marraine Jos, mon Parrain Jean-Marie, Pascaline et Barsou, ma "parraine" Michelle, Alix et Alex, Camille, Chacha, ma Babeth, Giles, Jean-Paul et Françoise, Cathie et Christian, Fred et Philipe, et tous les autres, qui ont participé, peu importe à quelle période de ma vie, à m'amener jusqu'ici.

Je voudrais maintenant faire un triomphe pour "tous mes meilleurs amis", qui font de moi ce que je suis. De tout mon cœur, merci aux Fondus (Lucile, Mélanie, Carola, Emma, Fanny, Raph et Boubou) qui me connaissent si bien et me soutiennent quoi qu'il arrive. Les coups de fils et milliers de messages réguliers à chacun d'entre vous ont rythmé ma thèse et m'ont permis de vous garder près de moi, même si vous êtes venus beaucoup beaucoup de fois à Liège hein ! Des amis comme vous c'est juste le rêve.

Merci aux Supopopop (Élo, Agathe, Mathieu, Pablo, Bouyss, Karen, Juliette, Rémi, Olivier, Grégoire, Pyv et tous les autres) pour les soirées et les week-end comme au bon vieux temps, qui m'ont fait l'effet grisant d'une capsule temporelle. Un mot tout particulier pour Agathe, qui a toujours été prête à me retrouver n'importe où en Belgique ou aux Pays-Bas même

juste pour quelques heures; et pour Élo que j'ai eu si souvent au téléphone, avec qui j'ai pu partager l'expérience de la thèse et surtout beaucoup rigoler.

Un mot également pour les Chaptal (Jean-Loup, Augustin, Manu, Agathe, Bart, François et tous les autres) qui sont les tout premiers à être venus me rendre visite à Liège, merci les gars grâce à vous la thèse a commencé sous les meilleurs auspices.

Enfin, un mot pour des amis qui sont à moitié de la famille: Chloé, Inès, Théo, Baptiste et Jules. Le simple fait de vous voir ou de vous avoir au téléphone me rappelle à quel point je suis bien entourée. Merci Inès et Théo d'être venus de multiples fois me voir à Liège et merci Chloé pour le soutien entre thésardes et pour avoir même pris le temps de relire mon introduction de thèse! Et puis il y a les copains liégeois! Valentina, Joé et Ariel, se fut un plaisir de créer le « Cinéma Club de Liège » avec vous, merci pour tous ces bons moments passés ensemble (là plus part au Shamrock). Et heureusement qu'il y avait Ouftimate pour faire un peu de sport. Même si j'ai passé beaucoup de temps en vadrouille, j'ai toujours tellement apprécié vous retrouver pour l'entrainement le mercredi soir, sous la pluie, la neige et la tempête, et de temps en temps pour les tournois tous aussi chouettes les uns que les autres, merci pour tous ces moments les ouftis. On se reverra lors des tournois internationaux!

Bon, maintenant il ne me reste qu'une personne à remercier, Benjamin. Je ne sais même pas par où commencer. Merci de m'avoir écouté tous les soirs te raconter ma journée au téléphone dans un bus qui roule à 120km/h sur une route défoncée et où l'on n'entend rien du tout. Merci pour toutes nos discussions sur la thèse, les exoplanètes et la cosmologie qui me permettent à chaque fois de réaliser à quel point nous sommes chanceux de faire ce métier. Merci d'avoir relu des milliers de mails, de papiers, de candidatures et même ma thèse! Merci d'avoir toujours été motivé pour se retrouver les week-end avec des programmes surchargés que ça soit en Belgique, en Angleterre, en France ou même en Californie! Plus simplement, merci pour ton amour sans failles, ton optimiste, ta motivation, ta générosité et tellement plus encore. La vie est tellement facile avec toi.

# Abstract

As the technology behind instrumentation in astronomy improves, so does our ability to detect and characterise planets outside our solar system. With missions such as the James Webb Space Telescope (JWST), the field of exoplanetology is about to enter a new era where the characterisation of earth-sized temperate planets will become feasible. Expected to be launched later this year, JWST will be able to identify rocky planets' atmospheres and search for molecular signatures of habitability and life. While more and more potentially habitable exoplanets are being discovered, knowing which targets to prioritise is of paramount importance. In that respect, planets orbiting ultra-cool stars have been identified as the most amenable ones for the first atmospheric exploration of potentially habitable terrestrial worlds in the next decade.

In this dissertation, I focus on the detection and characterisation of planets in the habitable zones of ultra-cool stars. In my first Chapter, I introduce the concepts and notions necessary for the reader to understand the context, content, and challenges of this thesis. Using astrobiology as the guiding theme, I briefly expose some basic notions on the definitions of life, discuss its detectability on exoplanets and justify the opportunity offered by planets orbiting ultra-cool stars in the search for life elsewhere in the Universe.

In the second Chapter, I present my contribution to the SPECULOOS project (Search for habitable Planets EClipsing ULtra-cOOl Stars) which aims to search for terrestrial planets orbiting the smallest stars and substellar objects (<0.15 $R_{\odot}$) of the solar neighbourhood, using the transit method. I explain my implication in various aspects of SPECULOOS: from technical monitoring to data management and analysis, to the identification of new planetary candidates. I also present a versatile tool that I have developed to manage and optimise the observations of SPECULOOS targets by the different telescopes. Finally, I expose the performances of the survey and discus some specific discoveries.

In the third chapter, I explain the methods used to turn astronomical images into light curves. Then, I introduce different algorithms that I relied on during my PhD to analyse those light

curves and deduce meaningful information on exoplanets and their host star.

The first exoplanetary system revealed by SPECULOOS is the TRAPPIST-1 system, which is composed of a nearby ultra-cool star orbited by seven transiting planets, three of which lie within the star's habitable zone. This system represents a truly unique opportunity for a detailed study of potentially rocky, temperate, Earth-sized exoplanets, and has therefore galvanised the exoplanet community to study it in details, both observationally and theoretically. During my thesis, I had the chance to be strongly involved in these studies.

In Chapter 4, I present the outcomes from the analysis I led of an intensive follow-up campaign carried out with the Spitzer space telescope. Through those analyses and thanks to the transit method, I was able to significantly improve the precision on several key parameters of the planets and star, and even to set upper constraints on the dayside temperature of the two inner planets. Such results will reveal particularly interesting to prepare the follow-up of the system with the JWST. In parallel, I discuss the impact of flares on the habitability of TRAPPIST-1 habitable zone planets, and notably infer where the planets stand with regards to the abiogenesis zone. Finally, I derive precise timings for all transits of the seven planets and explain how those were used to refine the planet masses using in a subsequent dynamical analysis.

I also had the opportunity to be involved in the follow-up of the TRAPPIST-1 system from the ground. In Chapter 5, I explain how I used a multitude of observations in various bandpasses to construct the broadband transmission spectra of the seven planets. From these spectra, I managed to set the first empirical constraints on the impact of stellar contamination (resulting from the presence of heterogeneities of the stellar's photosphere), and compare it to predictions from existing models. I then propose alternative morphologies (sizes and temperatures) for those photospheric heterogeneties and discuss their relevance. Ultimately, I present some on-going work that I am carrying out to unveil the nature of the stellar phostosphere using the star's multi-bandpasses photometric variability.

Finally, in my last Chapter, I summarise the main results presented in this thesis and raise some perspectives for the study of the TRAPPIST-1 system and the future of the SPECULOOS project, as well as some prospects for the work I will be undertaking after my PhD.

# Résumé

À mesure que les performances technologiques en astronomie progressent, notre capacité à détecter des planètes en dehors de notre système solaire, et à les caractériser, s'améliore. Avec des missions telles que le James Webb Space Telescope (JWST), le domaine de l'exoplanétologie est à l'aube d'une nouvelle ère où la caractérisation de planètes tempérées de la taille de la Terre devient possible. Avec un lancement prévu en fin d'année 2021, le JWST devrait être capable d'identifier pour la toute première fois la présence d'atmosphère sur des exoplanètes rocheuses et tempérées, et même d'y chercher des signatures moléculaires d'habitabilité et potentiellement de vie. Alors que de plus en plus de planètes potentiellement habitables sont découvertes chaque mois, un des grands enjeux pour préparer cette mission réside dans la priorisation des cibles, à savoir, quelles planètes sont les plus adaptées pour une future caractérisation atmosphérique. Depuis une dizaine d'années, il est reconnu que les planètes orbitant des étoiles ultra-froides sont les plus à même de remplir ce rôle.

Mon travail de thèse est consacré à la recherche et la caractérisation de planètes situées dans la zone habitable d'étoiles ultra-froides. Pour décrire les différents aspects de mon travail ce manuscrit est décomposé en 6 chapitres. Mon premier chapitre entend donner au lecteur les éléments nécessaires pour pouvoir comprendre le contenu, le contexte et les enjeux de cette thèse. La question des exoplanètes potentiellement habitable y est abordée du point de vue de l'astrobiologie. Après une courte introduction sur la définition de « vie », j'y discute sa détectabilité (biosignatures) sur les exoplanètes et explique l'intérêt d'étudier les planètes orbitant des étoiles ultra-froides.

Dans le second chapitre, je décris ma contribution au projet SPECULOOS (Search for habitable Planets EClipsing ULtra-cOOl Stars) qui a pour but de détecter des planètes telluriques en orbite autour des plus petites étoiles et objets substellaires situés dans le voisinage du système solaire. J'y présente l'organisation et le fonctionnement de SPECULOOS, ainsi que le rôle que j'y occupe. J'ai en effet eu la chance d'être impliquée dans divers aspects du projet, allant du suivi technique des télescopes à l'identification de nouvelles planètes, en passant par la planification des observations ainsi que la réduction et l'analyse des données. En particulier, j'explique le fonctionnement d'un outil que j'ai développé dans le but de gérer,

d'optimiser et de programmer automatiquement les observations des cibles SPECULOOS sur les différents télescopes.

Dans mon troisième chapitre, j'explique les méthodes utilisées pour traiter les images et obtenir une courbe de lumière pour chaque cible observée pendant la nuit. J'y détaille ensuite le fonctionnement des algorithmes que j'ai utilisé pour analyser les données et en déduire les paramètres physiques des planètes et de leur hôte.

Le tout premier système planétaire découvert par le projet SPECULOOS est le système TRAPPIST-1, composé de sept planètes rocheuses en transit autour d'une étoile ultra-froide proche, dont trois sont situées en zone habitable. Ce système représente une opportunité unique pour l'étude détaillée de planète telluriques tempérées et de la taille de la Terre. Pour cette raison, depuis sa découverte, il galvanise toute la communauté exoplanète et a été au cœur de nombreux travaux, à la fois observationnels et théoriques. Tout au long de mon doctorat, j'ai été fortement impliquée dans certains de ces travaux.

Dans mon chapitre 4, je présente les conclusions que j'ai tirée de l'analyse de plus de 1000 heures d'observations de TRAPPIST-1 avec le télescope spatial Spitzer. En utilisant la méthode des transits j'ai pu parfaire l'exactitude des paramètres des différents objets constituant le système, tels que le rayon de chaque planètes, ou encore la densité de leur étoile hôte. Par la tentative d'observation d'occultations (configuration lors de laquelle l'étoile est située entre la planète et l'observateur) des planètes b et c, j'ai pu contraindre la température de leur face jour. Mes analyses ont également permis de rapporter les temps exacts de passage de chaque planète (à quelques secondes près) afin que ceux-ci soient utilisés dans une analyse dynamique qui a mené à une amélioration significative de la précision sur les masses des planètes. Avec ces nouvelles valeurs de rayons et de masses, la densité et même la composition interne de chaque planète peut être discutée. Pour finir, je détaille le travail que j'ai mené sur l'impact des éruptions solaires sur l'habitabilité des planètes TRAPPIST-1 situées en zone habitable. Ce dernier a notamment permis de situer ces planètes par rapport à leur zones d'abiogenèse actuelles, que j'ai estimé à partir de la fréquence et l'énergie des éruptions solaires observées par Spitzer.

Le système TRAPPIST-1 n'a pas été observé que depuis l'espace, il a aussi été largement suivi par des télescopes au sol. Pendant ma thèse, j'ai eu la chance de gérer le suivi régulier de TRAPPIST-1 avec les télescopes SPECULOOS. Dans mon cinquième chapitre, je présente les résultats découlant de l'analyse de ces centaines d'heures d'observation. En combinant une multitudes d'observations à différentes longueurs d'onde j'ai pu construire de manière empirique le spectre en transmission des sept planètes. Ces spectres m'ont permis d'apporter les premières contraintes observationnelles de l'effet de la contamination stellaire (qui trouve son origine dans l'hétérogénéité de la photosphère de l'étoile) sur les spectres des planètes.

J'ai ainsi prouvé que certains modèles avaient surestimé l'impact de cette contamination. Cependant, il est très important que cet effet soit correctement modélisé pour optimiser de futures potentielles caractérisations atmosphériques avec le JWST. C'est pourquoi dans ce chapitre, je propose également des scénarios alternatifs pour décrire le type d'hétérogénéités (température et taille) attendues à la surface de TRAPPIST-1. Enfin, j'expose le statut d'une nouvelle étude que je dirige actuellement et qui vise à contraindre la nature de ces hétérogénéités en utilisant la variabilité photométrique de l'étoile dans différentes bandes passantes.

Pour conclure, le chapitre 6 rassemble les principaux résultats de cette thèse, les perspectives attendues pour SPECULOOS et TRAPPIST-1, ainsi que mes perspectives personnelles.

# Table of contents

# Chapter 1

# Introduction

The conclusive discovery of a planet around the main-sequence star 51-Pegasi was announced the year I was born. This seminal discovery initiated a brand new field of astronomy: exoplanetology, the detection and study of planets in orbit around other stars than the Sun. Since then, this nascent field has developed exponentially. The detection of new planets has almost become trivial, and we can read on NASA website that "since the first exoplanets were discovered in the early 1990s, the number of known exoplanets has doubled approximately every 27 months". In parallel, the tree of exoplanetology has grown a large diversity of branches. For a few years now, the field has not only focused on the detection of these new worlds but on their characterisation. As we can read in E. W. Schwieterman et al. (2018) "we are poised at the transition between exoplanet detection and demographic studies and the detailed characterisation of exoplanet atmospheres and surfaces". In Dec 2019, the launch of the CHaracterising ExOPlanets Satellite (CHEOPS) opened the era of space missions only dedicated to the characterisation of Exoplanets. It will soon be followed by the launch of the James Webb Space Telescope (JWST) in Oct 2021, which will dedicate almost 25% of its time to exoplanets.

Through my thesis, my aim was to detect and characterise potentially habitable terrestrial planets orbiting ultra-cool stars. Although I am an astronomer by training, in this thesis introduction I have decided to approach the research I have been carrying out from an astrobiology point of view. Astrobiology falls down into two simple questions: "What is the history and future of terrestrial life?" and "Is there life elsewhere?" (D. Catling 2013). Before we can detect life on other planets, we need to have a proper idea of what we are looking for. In my first chapter, I will therefore recall some basis about the building blocks of life on Earth, the possible pathways for its origin on Earth, and what kind of biological traces or biosignatures we could be looking for on exoplanets. Then, I will present how astronomers

detect these new planets and what methods are used to characterise them and to assess their potential habitability. Finally, I will explain why I particularly focused on planets orbiting ultra-cool stars to search for potentially habitable worlds during my PhD.

## 1.1 Search for life

Astrobiology raises the difficult question of how to define life. What is it exactly that we are looking for beyond Earth? In this first section, I will undertake to broadly define what is meant by life in order to contextualise the search for signs of life on other planets. I will first give a broad overview of the building blocks of life on Earth and a few avenues for its origin. Then, I will discuss the different types of biosignatures we should be looking for on exoplanets and I will introduce the notion of habitability and habitable zone.

### 1.1.1 Defining life

#### Building blocks of life on Earth

One of the fundamental questions raised by astrobiology is "What is Life?". Unfortunately, it seems extremely complicated to settle on one unique definition of life. To begin with, it seems essential to highlight that all livings organisms on Earth share a couple of properties in their structure and mode of operation. As a matter of fact, the matter from which life is made of is surprisingly based on only six common "building blocks" elements of the Periodic Table: carbon $C$, hydrogen $H$, nitrogen $N$, oxygen $O$, phosphorus $P$ and sulphur $S$ (also referred as CHNOPS). In particular, carbon is used as the backbone of the complex biomolecules such that life on Earth is frequently referred to as "carbon-based". The great biological advantage of carbon is its versatility in breaking down and forming new molecules. More precisely, it can form stable bonds with several others compounds (and itself) without requiring and releasing too much energy, which results in the possibility to create a large diversity of molecules. Carbon can associate with hydrogen to build alkanes [$C_nH_{2n+2}$] as well as with other functional groups such as amino groups [-$NH_2$], carboxyl group [-$COOH$], phosphate group [-$PO_4$], alcohols [-$OH$], another alkyl group [-$R$] etc. The nearly infinite collection of complex carbo-based molecules has even led to the emergence of a dedicated sub-field of chemistry: "organic chemistry'.

Another feature that is really representative of life on Earth is its propensity to form chains (Cockell 2015) composed of the same kind of molecular building blocks. Four types of chain

in particular: proteins, carbohydrates, lipids and nucleic acids, which I briefly present in the following.

1. Proteins are chains of amino acids which are defined by the following chemical formula:

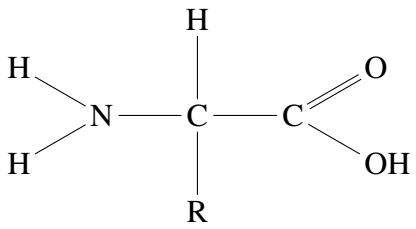


Amino acid

where -*R* is a side group that gives the amino acid its property (some are polar, some are charged, some are hydrophobic) and name. More than 500 amino acids are known so far, yet life on Earth only uses a subset of 20 of them. To form proteins, amino acids assemble through peptidic bonds: the -*OH* of the carboxyl group is replaced by a bond with the nitrogen atom of another amino acid's amino group taking the place of one hydrogen and releasing a molecule of $H_2O$. This reaction therefore is a dehydration reaction. Chiral molecules are molecules that are mirror images of each other and are non-superimposable. Chiral molecules have a tendency to polarise light in particular directions, if it rotates to the left we say the molecule is levorotatory (or "L") whereas if it rotates to the right we say the molecule is dextrorotatory (or "D"). Remarkably, all amino acids used in life are chiral (except glycine) and all of them are in the levorotatory form. Although there are no clear explanation why life on Earth developed a biochemistry based on the L form it is believed to be linked to molecular recognition (Cockell 2015). Molecular recognition is based on the observation that some proteins have active sites that recognise only a certain chiral form, "L" or "D". Once a given biochemical architecture emerged with a prevalence for "L" forms for instance, molecular recognition theory assumes this choice perpetuated via natural selection up to the point where all life on Earth was "L"-based.

2. Carbohydrates, or commonly called sugars, are abundant and versatile biomolecules consisting of hydrogens, oxygen and carbon atoms with the generic molecular formula $C_n{\leftharpoondown}H_2O{\leftharpoondown}_n$ (where n is at least 3). They assemble together through glycosidic bonds, however they also can bind to other molecules than sugars through nitrogen (N-glycosidic) and sulfur (S-glycosidic) bonds, which allow for the creation of a great diversity of molecules. Similarly to amino acids, sugars are chiral and remarkably life on Earth uses primarily D-sugars (dextrorotatory).

3. Lipids are long-chained carboxilic acids with many single bound carbon chains. They are also referred to as fatty acids. Side groups can be attached at their end and many are charged such as phospholipids for instance (that habour a hydrophilic phosphate group at one end). This induces that one side of the phospholipid (the charged one) tends to be attracted to water (hydrophilic) while the other end of the lipid is repulsed by water (hydrophobic) due to its non-polarity. Such molecules are said to be amphiphilic, and they tend to form lipidic bilayers in water. In particular, phospholipids are building blocks of cell membranes. Fatty acids are also useful for energy storage as they can store a lot of energy in their many bonds.

4. Finally, nucleic acids are complex molecules whose main biological function is to store information. The most famous one is the deoxyribonucleic acid or DNA. DNA is a double chain of units called nucleotides. Each nucleotide is composed of a sugar (desoxyrobise), a phosphotate group, and a nucleobase. In each chain, the nucleotides are connected by a bond between their sugar and their phosphate group. Four nucleobases exist in DNA: thymine (T), adenine (A), guanine (G) and cytosine (C). Each DNA chain is linked to the other by weak and selective bonds between the nucleobases: adenine bonds only to thymine, and guanine only to cytosine. This double chain coils on itself to form the famous DNA double helix strand. The genetic code is a set of three-letter combinations of nucleotides called codons, each of which corresponds to a specific amino acid or stop signal. The latter are associated by ribosomes to form proteins used by living organisms for their biological functions. Another well-know nucleic acid is the ribonucleic acid or RNA. RNA has a similar structure as DNA except for two important differences: the base Thymine is replaced with Uracil (U) and the ribose sugar in RNA has an hydroxyl (–OH) group on the carbon 2 position unlike the sugar in DNA (which is why it is called deoxyribose). It must be mentioned that, protein synthesis from amino acids relies on RNA and consists in two processes: transcription and translation. During transcription, DNA is used as a template to make a molecule of messenger RNA (mRNA). The molecule of mRNA then leaves the nucleus (for eukaryotic cells) and goes to a ribosome in the cytoplasm, where translation occurs. During translation, the genetic code in mRNA (expressed as codons which are triplets of nucleotides) is read and used link amino-acids together through peptidic bonds (each codon correspond to one amino acid). Finally, chains of amino acids (polypeptide) make proteins. This process is illustrated on Figure 1.1

In addition to CHNOPS and chains, a common feature of every forms of life is the need for a solvent to mediate the biochemical reactions. As a matter of fact, reactants must be able to

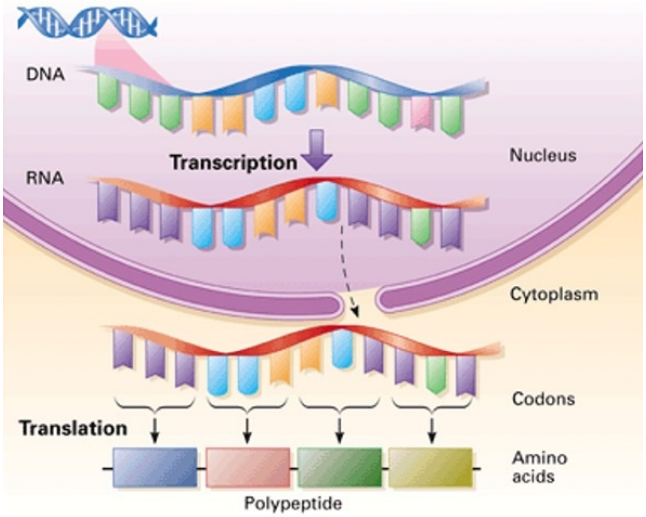


**Fig. 1.1** Schematic of the protein synthesis process with the two distinct phases: transcription in the nucleus of the cell and translation in its cytoplasm. Source: https://www.earthslab.com

move and interact freely for a chemical reaction to happen. Furthermore, this solvent must possess a number of properties such as a proper viscosity to enable the reactions. On Earth this solvent is liquid water, $H_2O$, which presents a variety of characteristics that make it particularly suitable for life. Without getting into too much details, I will briefly present those characteristics. First, liquid water has a significant polarity (or dipole moment) that allows it to dissolve salts (which are a source of cations and anions) and small hydrophilic organic molecules such as amino acids. It plays therefore a major role in organic polymerization (creation of chains). $H_2O$'s polarity also enables interactions with anions via H-bonds and with many cations via coordination between the lone pairs of electrons on the oxygen atom and the empty orbitals of the cations (Cottin et al. 2017). Besides, water's polarity forces also the gathering of hydrophobic molecules into layers, which is important for the lipidic membranes of cells and cellular organs. Its relatively weak hydrogen bond also provides complex organic molecules with the plasticity required for their functions, e.g. the enzymes' active sites whose function requires a change of configuration. In addition, liquid water has a high heat of vaporisation which promotes a stable liquid phase inside organisms and stabilises its temperature (Cockell 2015). Finally, liquid water has the property of being denser than its solid form, ice. Although, it is not really clear how such a property would be essential to life as it is known that many microorganisms can resist freezing, astrobiologists believe it must have favoured life as it prevented lakes and oceans from freezing completely and maintained water in a liquid state under a ice layer over long periods of time.

Finally, life requires a source of energy in its environment to drive metabolic reactions and to maintain the functions carried out by a cell (Cottin et al. 2017). On Earth, life uses either

solar energy (phototrophs organisms) or chemical energy sources that include both organic compounds, inorganic elements and molecules (chemotrophs organisms). We can split those two groups in two new categories depending on how they build their organic compounds: autotrophs if they can build them from simple inorganic molecules, and heterotrophs if they transform or use directly other organic compounds. Then, energy is transferred within the cell thanks to a universal molecule (in all known Earth life forms) called adenosine triphosphate (ATP) which can be seen as the energetic building block of life. Without getting into details, ATP is synthesised from adenosine diphosphate (ADP) and inorganic phosphate (Pi) by a complex protein lodged in the membrane called *ATP synthase* that uses existing pH gradients on each side of a cell membrane to work (with the outside usually more acidic than the inside). Because ATP is generally unstable in water, it is an ideal molecule to release free energy quickly when needed.

Now that I have presented some key properties and characteristics that are shared by all living organisms on Earth, I can start questioning its apparition.

### Origin of Life of Earth

According to sedimentary rocks dating from within the Archaean Eon, life has emerged around 3.8 billions years ago shortly after the Late Heavy Bombardment (LHB) (although life might have occurred long before we found evidence of it). The LHB is the name given to a cataclysmic spike in the cratering rate that occurred in the late Hadean age about 4 to 3.8 Ga ago ($\simeq$700 million years after the planets formed). The *Nice model* (Gomes et al. 2005) is the leading hypothesis to explain the LHB and relies on planetary dynamics modeling, suggesting a 2:1 resonant configuration between Saturn and Jupiter (Saturn orbited the Sun once for every two Jupiter orbits). Such a configuration would have induced strong gravitational interactions that would have modified the orbits of the two giant planets, pushing Uranus and Neptune outwards. In addition, it is hypothesised that a large population of icy objects were located beyond the two ice giants such that the outer planets would have scattered those planetesimals towards the inner Solar System. As a consequence the Earth must have suffered many impacts, even more than the Moon because of its greater size and gravity. Traces of the LHB were also identified on the Moon, Mars, and Mercury. Whether the apparition of life happened immediately after the LHB or life managed to survive it, is still not clear (D. Catling 2013).

Regardless, there is wide agreement that the origin of life would have been preceded by a period of chemical evolution, or prebiotic chemistry, during which more complex organic molecules were produced from simpler ones. The transition from abiotic chemistry to life is

called abiogenis. It is the process by which simple molecules came together to form more complex ones and ultimately a self-replicating organism (Cockell 2015). Over the centuries many different theories were given to explain the apparition of life. Notably the spontaneous generation theory whereby abiotic material could be transformed into living matter, which persisted for centuries before being finally discarded by Louis Pasteur in 1859. Another scenario is panspermia whereby life came from somewhere else in the Universe, brought either by comets, asteroids, space dust, or even transferred from other planets. However, it still does not solve the question of how and where life first occurred. Therefore, the most common approach is to assume that life appeared on Earth and then use our knowledge of the early Earth and organic chemistry in the Universe to explain its origin (Cockell 2015).

One crucial point is to understand from where organic compounds on Earth originated. In the early twentieth century, scientists proposed that gases in Earth's early atmosphere would have been converted by ultraviolet sunlight or lightning into organics. In that regard, it is interesting to mention the most famous experience that was designed by the scientists Stanley Miller (1930–2007) and Harold Urey (1893–1981) to confirm this hypothesis. Their objective was to simulate the chemistry of an hypothetical primitive-Earth environment and atmosphere in the presence of an electrical discharge to see if it can produce some of the building blocks of life (the experimental setup of the experience is shown on Figure 1.2). Water was poured in a balloon to simulate the ocean and heated up to mimic evaporation processes. Water vapour then entered the "primitive atmosphere", assumed to be composed of methane, ammonia, and hydrogen and subjected to electrical discharges. Finally, the resulting vapour was condensed and collected in a trap at the bottom of the set up. In the condensed water, Miller and Urey successfully observed the formation of a diversity of molecules including amides, carboxylic acids, and most importantly amino acids. Yet, no aromatic acids were synthesised, and several scientists criticised the fact that the atmosphere used in the experiment was highly reducing while the early Earth's atmosphere was probably slightly oxidizing (Trail et al. 2011). Furthermore, the Miller-Urey experiment used only electric discharges as the energy source whereas other sources of energy such as UV light, geothermal sources, impact shocks, or cosmic rays were available on Earth (Cockell 2015).

It is thought that the atmosphere in the Hadean was mostly maintained from gases released through outgasing (volcanism), so the air should have consisted predominantly of $CO_2$ and $N_2$. However, there are some uncertainties about the exact composition of the primitive Earth, such that astrobiologists have considered several avenues for the origin of organic molecules. As mentioned before, with panspermia, meteorites have been considered as a possible origin for organic carbon. Alternatively, deep-sea alkaline hydrothermal vents have also been considered (Sojo et al. 2016). Indeed, hydrogen released in hydrothermal vents

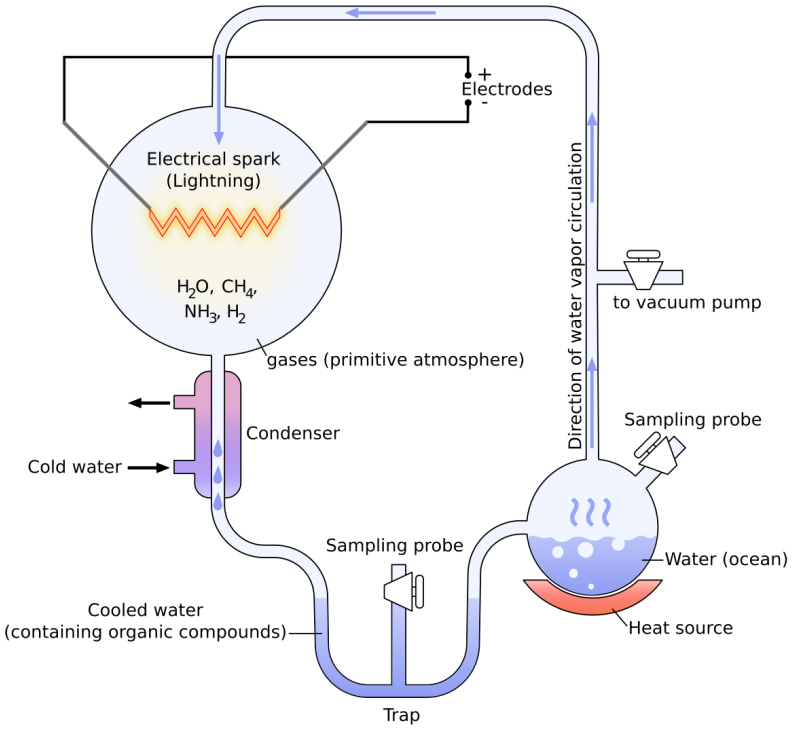


**Fig. 1.2** Set up of the Miller-Urey experiment. The putative primitive Earth atmosphere is embodied by the upper left bulb and the oceans by the lower right bulb. Source: wikicommons

from reactions between water and rocks can combine with carbon dioxide to make methane and larger organic molecules. According to D. Catling (2013), it is believed that during the Hadean, tiny pores in the mineral structures of hydrothermal vents could have contained and concentrated simple molecules and serve as nurseries for them to react and make more complex prebiotic molecules. In addition, because the fluid emerging from hydrothermal vents is more concentrated in alkanes (simple hydrocarbon chains with one single bonds between carbon atoms) than the sea, a natural gradient in pH appears, and this gradient turns out to be similar to the one observed in organic cells. Therefore, if life originated in such an environment, it might explain why energy production is so intimately tied to pH gradients (notably to synthesise ATP, see section 1.1.1) . Nevertheless, these are just assumptions, and in the end the precise origin of the organic compounds that led to the origin of life - whether is it the atmosphere, space, hydrothermal vents or all of the above combined - is unresolved. Now, assuming the molecular building blocks of life were created, the next step is to understand what were the reaction pathways that led to the formations of larger blocks such as amino acids, sugars, lipids and nucleic acids. In the next paragraph, I briefly mention some of the most famous pathways for their synthesis while by no mean being exhaustive.

- One commonly considered path for the synthesis of amino acids is called the Strecker synthesis, named after the German chemist Adolph Strecker (1822–1871). He demonstrated that the reaction of hydrogen cyanide, $HCN$, with ammonia and an aldehyde (a compound containing a functional group with the structure $CHO$), followed by hydrolysis, leads to the formation of an amino acid. Yet, this reaction is highly dependent on the environment (temperature, pH, $HCN$, $NH_3$, and aldehyde concentrations) such that it has yet to be shown that it can occur under natural environmental conditions at significant yields. Interestingly, $HCN$ could either have been brought from comets or synthesised in the primitive Earth atmosphere from electric discharges in a reducing atmosphere (Cockell 2020).

- Then, among the chemical reactions that have been proposed as able to synthesise early sugars the most important one is the formose reaction. The formose reaction is based on the autocatalytic polymerisation of formaldehyde, $HCHO$, which requires high concentrations of formaldehyde and alkaline conditions (pH > 10). However, some problems with the formose reaction as a source of sugars on the primitive Earth have been noted (Cleaves 2012). Notably, in such conditions the sugars formed are expected to undergo various reactions on short geological time scales which can turn out to be counterproductive to their accumulation in the environment. Alternatively, some sugars have also been found in meteorites, such as the Murchison meteorite (Callahan et al. 2011).

- Several pathways have been considered to form nucleobases (which compose nucleic acids, see Section 1.1.1). Although different processes have been discussed to form the different nucleobases, it is interesting to note that $HCN$ is involved in the formation of purines (nucleobases $A$ and $G$) and cyanoacetylene $HCCCN$ in the formation of pyrimidines (nucleobases $C$, $T$ and $U$). Because of the importance of $HCN$ concentration in both the synthesis of sugars and purines, some scientists have made the hypothesis that the formation of their prebiotic ancestors could have been correlated (Arrhenius et al. 1994).

- Finally, a prebiotic synthesis of lipids has been suggested based on the acid-catalyzed reaction of formaldehyde $HCNO$ with isobutene $C_4H_8$ (Ourisson et al. 1994).

In a nut shell, it seems that given adequate experimental conditions, it is possible to synthesise many organic molecules in the laboratory under simulated prebiotic conditions. However, the fact that they formed in the laboratory does not necessarily mean that they were essential for the origin of life, or that they were likely prebiotically available.

Besides, I evoked already the importance of the environment in prebiotic chemistry. To this extent, we could ask ourselves what the Earth's early climate was like before life. Astrobiologists believe that the carbonate–silicate cycle probably regulated climate before life even originated. This carbonate–silicate cycle can be summarised as follow: first, the atmospheric $CO_2$ is dissolved in rainwater and reacts with silicate rocks on the continents (this process is also called chemical weathering). When dissolved, $CO_2$ reacts with water to form carbonic acid, a weak acid able to dissolve rocks over long timescales (weathering). These reactions yield ions that are carried away by water into the ocean. One of these ions is the bicarbonate ion that enrich the ocean in carbon. The net effect of this part of the cycle is thus the removal of $CO_2$ from the atmosphere and the increase in carbon in the ocean. In the ocean, the bicarbonate ion reacts with some other ions to form solid compounds that eventually sink down to the ocean floor. It is interesting to notice that life plays a key role here, as most bicarbonate ions will end up as calcium carbonate in the shells and skeletons of marine organisms. Then, carbonated seafloors are transported on the slowly moving oceanic plates until it dives beneath a continental plate (because it is denser) and sinks into the mantle, this process being called subduction. During subduction, the carbonates are squeezed and heated under strong pressures, causing them to decompose back into $CO2$. Finally, $CO_2$ returns to the atmosphere through volcanism or metamorphism. The whole cycle of $CO_2$ loss and replenishment is what we call the carbonate–silicate cycle (D. Catling 2013). Figure 1.3 illustrates the mechanism of the carbon–silicate cycle. This

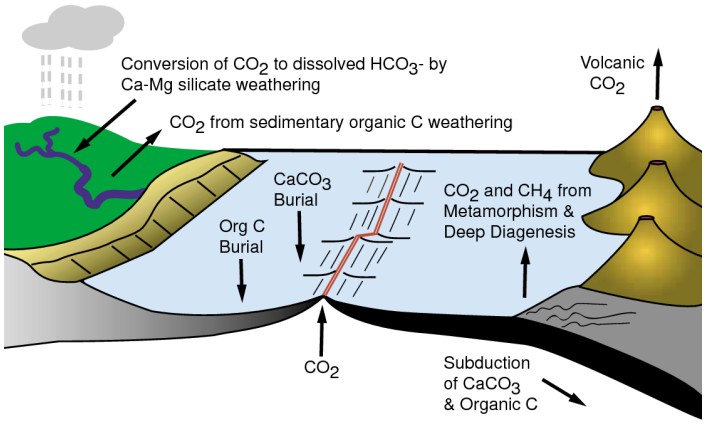


**Fig. 1.3** Illustration of the mechanism of the carbonate-silicate cycle. Figure from Berner (1999).

carbon–silicate cycle acts as a thermosat, which must have been essential to the development of life. If the climate gets warmer, there will be more rainfall and faster weathering in order to consume $CO_2$ (which is a greenhouse gas) and consequently cool the Earth's atmosphere. Similarly, if the Earth gets colder, $CO_2$ removal from the dry air will be slower, such that $CO_2$ will accumulate from geological emissions, in order to increase the greenhouse effect

and therefore warm the atmosphere. However, they are great chances that the cycle may have operated differently in the Hadean. The internal heat of the Earth mantle takes its origin in the decay of radioactive elements. Yet, radioactive decay decreases exponentially with time such that there should have been more heat released by the planet's interior in the past. Consequently, the mantle should have been hotter which could have allowed oceanic crust to sink more quickly. However, knowing exactly how tectonics operated on the early Earth remains an open question (D. Catling 2013).

Finally, apart from prebiotic chemistry, another crucial question in the origin of life remains: How did early molecules come together into a self-replicating organism? More specifically, how was DNA formed? It is not the objective of this thesis to discuss this question, however I would like to very briefly mention one of the most studied hypothesis: the RNA world hypothesis Gilbert (1986). This theory assumes that RNA preceded DNA as the genetic material. As DNA is similar to RNA but more complicated, it seems intuitive that RNA appeared first. The pivotal moment happened when (Gilbert 1986) discovered that some RNA molecules (called ribosomes, used by cells to form their proteins from DNA instructions) can act as catalysts. From this discovery, we can imagine that RNA once catalysed its self-replication and assembled from smaller molecules. Then, RNA would begin to make proteins (see Figure 1.1), some of which would be better catalysts than RNA itself. Eventually, DNA would replace RNA because it is more stable and can be larger which provide more advantage for reproduction (natural selection).

Although some pathways are being explored by scientists, the origin of life on Earth remains a mystery. In this paragraph, I mentioned some of these pathways as well as some basic notions of prebiotic chemistry and the hypothetical primitive Earth environment. My aim was to present the main avenues of reflection on the origin of life in order to set some benchmarks before I carry on discussing its definition.

### Definitions and their limitations

Now that I have briefly introduced the building blocks of life and its origin on Earth, I can start discussing some of its proposed definitions. A common approach to define life is to list several traits that are common to life on Earth: reproduction, growth, energy utilisation through metabolism, response to the environment, evolutionary adaptation and the ordered structure of cells and anatomy (Domagal-Goldman et al. 2016). Yet, this list describes what life does rather than what life is (D. Catling 2013), and several of those characteristics are not unique to life. For instance, crystals, fires, and hurricanes are all able to grow, reproduce, and utilise forms of potential energy (Domagal-Goldman et al. 2016).

Alternatively, astrobiologists frequently use NASA's current working definition of life: "*Life is a self-sustain chemical system capable of Darwinian evolution*". In this synthetic definition each word is of importance. The word "system" refers to an ensemble of components that are in interaction. The system is qualified of "chemical" which is a broad term to avoid assuming a prominent role of carbon or liquid water for instance. The word "self-sustained" translates the idea that this system is able to draw from its environment the necessary resources to maintain his structure. Finally, "Darwinian evolution" embodies the process of evolution through natural selection as theorised by Darwin and enabled by the existence of DNA (discovered later) which carries information in modular units called "genes". The term "Darwinian evolution" is voluntarily vague to allow for the existence of other molecules than DNA to store genetic information. An alternative molecule will nevertheless need to possess two essential properties: replication (meaning information can be copied) and errors (because without errors there would be no evolution).

Although this definition seems sufficient to describe life as we know it, some astrobiologists are worried that it may be to Earthly-centric and may blind future research of life in the universe. A recent study by Bartlett et al. (2020) shed light on the need to paint a more general picture of life that is less restricted to its Earthly form. The authors suggested that the term ***life*** should be restricted to life on Earth as we know it (as described in section 1.1.1), and that we should use the term ***lyfe*** (pronounced "loif") to designate life more broadly and that could exist elsewhere in the Universe. They define lyfe as a dissipative structure capable of autocatalysis, homeostasis, and learning, each of these terms being defined as follow:

1. A dissipative structure could be seen as a far-from-thermodynamic-equilibrium system that maintains its local level of organisation (low-entropy) at the expense of producing environmental entropy. Indeed, every living cell or animal feeds itself with extremely well-ordered state of matter with high energy quality (low entropy) food and turns it into high-entropy waste (heat) (Lovelock 1965). In the past, several scientists, such as Erwin Schrodïnger in the processes *What is life?* or James Lovelock, have resorted to the use of thermodynamic to define life. Yet, while all known life is made of dissipative structures not all dissipative structures are alive. For instance, a tornado, fire, or just a convective cell (as observed at the surface of boiling water in a pot) are dissipative structures but are not alive.

2. Autocatalysis is the ability of a system to exhibit exponential growth. The property of autocatalysis can appear in different forms including self-catalysis, cross-catalysis, and network autocatalysis, as long as the effect leads to exponential growth (Bartlett et al. 2020). On Earth, autocatalysis is embodied by cell division and reproduction.

Similarly to dissipative structures, autocatalysis does not necessarily involve life. For example, forest fires or viruses show autocatalysis but are not life (a discussion about whether viruses should be considered alive is out of the scope of this thesis).

3. Homeostasis is the capacity shown by life to stabilise or self-regulate itself. A “lyving” system has means to limit the variation of its internal systems when external conditions change (Bartlett et al. 2020). For instance, humans shake when it gets cold and sweat when it gets hot. However, an ideal gas at equilibrium also shows homeostasis.

4. Learning is a generalisation of Darwinian Evolution. More precisely, Bartlett et al. (2020) defines it as the "ability of a system to record information about its external and internal environment, process that information, and carry out actions that feed back positively on its probability of surviving/proliferating". For instance, a neural network can perform learning.

According to Bartlett et al. (2020), if a system possesses all four pillars it can be considered alyve and consequently alive (as lyfe includes life). Figure 1.4, from Bartlett et al. (2020), shows a Venn diagram of how several systems can perform one or more pillars but only lyfe can perform all four.

I believe this new conceptual framework is particularly relevant in the context of astrobiology, and therefore helps to clarify the objectives and discussions surrounding origins and biosignature research. Nevertheless, the definition of lyfe is still extremely recent and does not really apply to the researches I have been carrying out on exoplanets for now, as such specific properties will very likely not be observable before several decades or even centuries on extra-solar planets. For these reasons, I will focus the rest of this introduction chapter on the specific matter that interests me: the search for life (not lyfe) on extra-solar planets.

### 1.1.2 Detecting life

Now that I have broadly defined the characteristics and properties of life and even open the search to lyfe (life elsewhere in the universe) I will discuss how we can detect signatures of life. A full thesis could be dedicated to the search for life in the solar system (either on others rocky planets or icy moons), however as this PhD thesis deals with the study of habitable planets outside of the solar system, I will only discuss the case of exoplanets here. Exoplanets are planets orbiting other stars than the sun, and a detailed introduction to the search for exoplanets will be given in section 1.2.

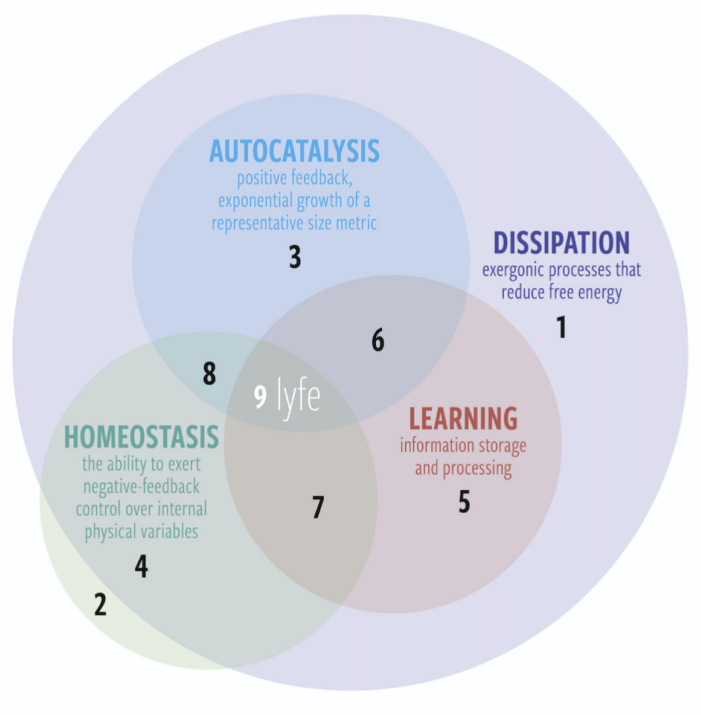


**Fig. 1.4** A Venn diagram of the four pillars of lyfe. Sublyfe (regions 1–8) are any system that performs some but not all of the pillars, while lyfe (region 9) is any system that performs all four. The fact that autocatalysis and learning require a continuous supply of free energy implies that they must be part of a dissipative structure; however, homeostasis can occur even in systems which are in thermodynamic equilibrium and therefore does not always require dissipation. Figure from Bartlett et al. (2020)

### Biosignatures

Life alters the chemistry of a planet (atmosphere, surface etc), therefore to find life we must look for traces of its presence, also referred to as biosignatures. A biosignature is defined as "object, substance, and/or pattern whose origin specifically requires a biological agent" (Des Marais et al. 2008; Marais et al. 1999) or as "any phenomenon, substance, or group of substances that provides evidence of the presence of life" (D. C. Catling et al. 2018). In this thesis I focus on the search for life on extra-solar planets. Considering *in situ* sampling of exoplanets is not possible, astrobiologists must identify signatures of life (biosignatures) that are remotely observable. In that regard, biosignatures can be grouped into three categories according to Meadows (2008): gaseous biosignatures, surface biosignatures, and temporal biosignatures as shown on Figure 1.5 from E. W. Schwieterman et al. (2018). In the following paragraphs, I will detail each of these categories.

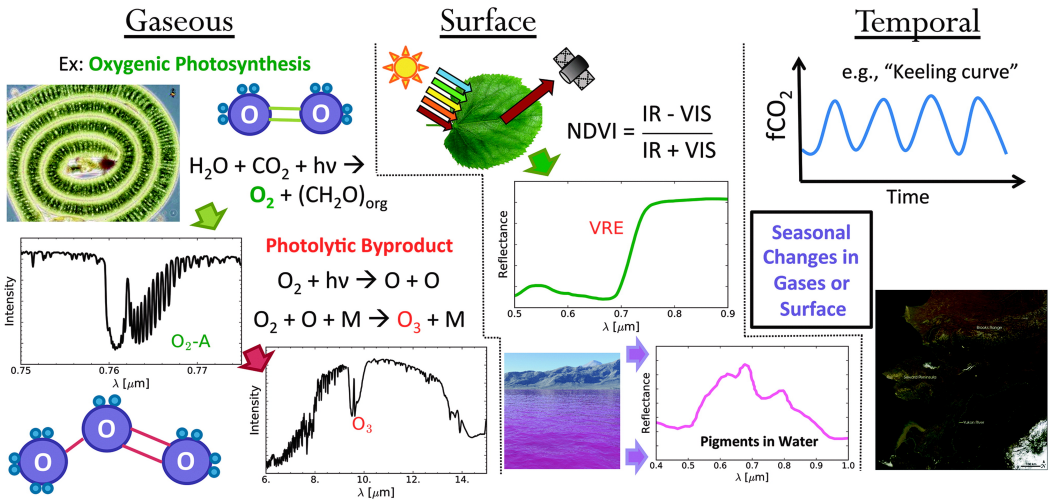


**Fig. 1.5** Summarising figure of the three different types of biosignatures. *Left panel*: gaseous biosignatures which can be direct or indirect products of biological processes. For example, molecular $O_2$ generated from photosynthesis (direct gaseous biosignature) that is then photochemically processed into $O_3$ in the stratosphere (indirect gaseous biosignature). *Middle panel*: surface biosignatures are the spectral signatures incited by reflected light that interacts directly with living organisms. For example, the vegetation red edge (VRE) produced by plants and the associated Normalized Difference Vegetation Index (NDVI) used for mapping surface vegetation. *Right panel*: time-dependent changes in observable quantities, including gas concentrations or surface albedo features, may be used as temporal biosignatures if they can be linked to the response of a biosphere to a seasonal or diurnal change. For example, the seasonal oscillation of $CO_2$ as a response to the seasonal growth and decay of vegetation. Figure from E. W. Schwieterman et al. (2018) adapted from E. Schwieterman (2016).

**Gaseous biosignatures:** This category includes all direct and indirect (secondary compounds resulting from environmental processing of biogenic products) products of metabolism. The hunt for biosignatures is driven by our knowledge of terrestrial life such that probing the Earth atmosphere is essential to get insights on the kind of biasignature gases we should look for. In this context, the spectrum of Earth reveals some major absorption features attributable to components of the atmosphere, as shown on Figure 1.6. In 1990, the near infra-red spectrometer on-board the Galileo spacecraft observed the spectrum of the Earth during its journey to Jupiter and successfully detected the presence of ozone, $O_3$. Ozone is an indirect product of metabolism as it is formed from the photolysis of $O_2$ (produced from photosynthesis) in the stratosphere by UV radiation. Oxygen possesses strong absorption bands in the visible and near-infrared (as shown in Figure 1.6) and it is thought that photosynthesis is the only mechanism able to product such high oxygenic concentrations in a terrestrial-like atmosphere. Oxygen is therefore a strong biosignature that has been extensively studied (Meadows et al. 2018a). Two distinct issues arise with oxygen: creating false negative/positive situations. First, it is known that oxygen was not present right at the

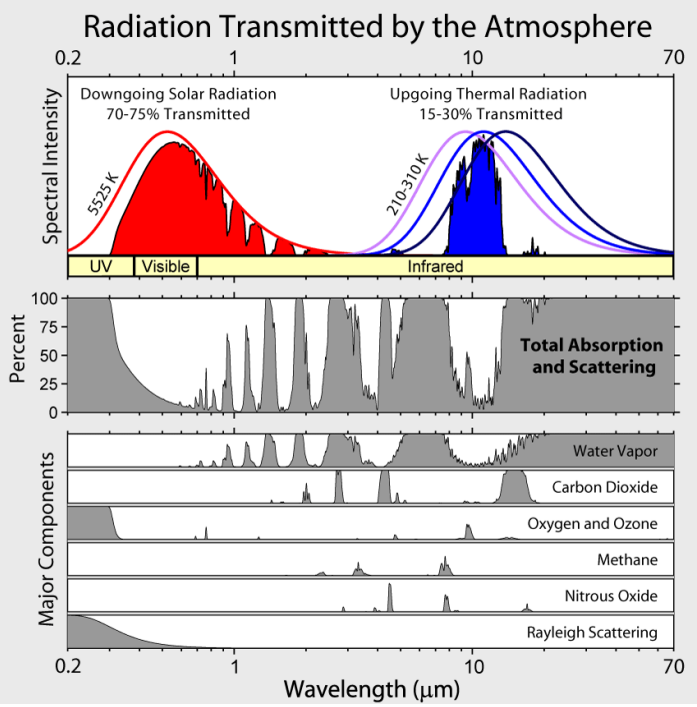


**Fig. 1.6** *Top panel*: the radiation received by the Earth from the Sun filled in red (downgoing solar radiation) while the solid red curve is the radiation from a blackbody radiator at 5525 K superimposed; the radiation emitted by the planet is filled in blue (upgoing thermal radiation) and the solid purple, blue and black curves are equivalent black bodies temperature at 210K, 260K and 310K. *Middle panel*: Total absorption (including scattering) spectrum of the Earth from 0 to 70 $\mu m$. *Lower panel*: Decomposition of the Earth's absorption spectrum into the individual contributions of its major atmospheric components and Rayleigh scattering due to atmospheric aerosols, to highlight their spectral signatures. Source: Wikipedia Commons

apparition of life, its detectability evolved through time. All through the Archean age of Earth, prior to the Great Oxydation Event (GOE), the atmosphere should have been very poor in oxygen and enriched in $CH_4$ despite the existence of life (see Figure 1.7). If exo-planetologists were to characterise a Archean Earth-like planet and use oxygen as the only biosignature they would wrongly conclude that an Archean Earth is deprived of life. This would be a false negative situation. Secondly, oxygen could be produced in large quantities by abiotic processes such that the detection of oxygen would be wrongly associated to the presence of life, a false positive situation. Such scenario could happen for instance for planets around M stars, subjected to intense, extremely short wavelength UV radiation (more details in section 1.3.2) such that they could undergo a runaway greenhouse effect where large quantities of water vapour are subject to photolysis because of high-energy irradiation by the star, leading to high concentration of $O_2$ in the atmosphere while having a very hostile and

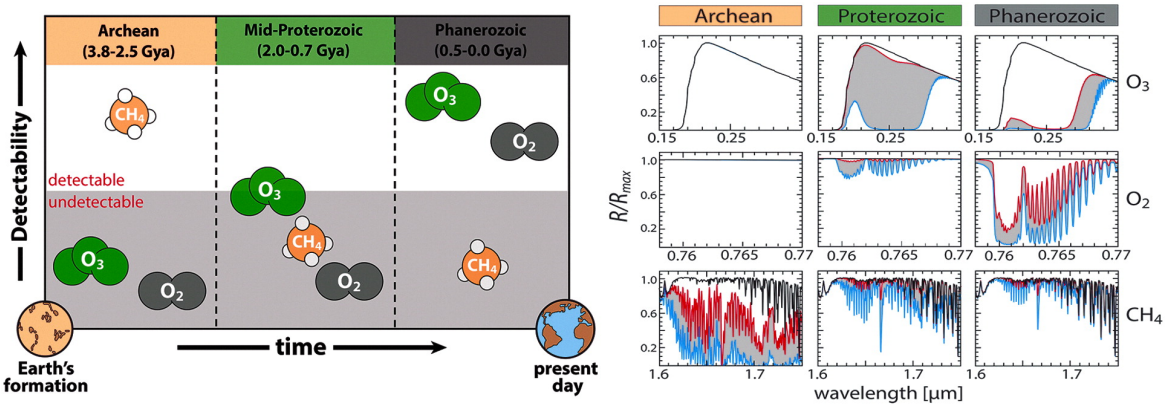


**Fig. 1.7** *Left figure*: Conceptual figure illustrating the difficulty of detecting oxygen and methane through Earth history. *Right figure*: Synthetic reflectance spectra of selected $O_2$, $O_3$, and $CH_4$ bands as a function of geologic epoch assuming gas abundances consistent with geochemical fossils and/or biogeochemical modeling constraints. The black line represents the case with no absorption. Lower abundance limits are given in red, upper limits are given in blue, and the region between these limits is shaded grey. Figure from E. W. Schwieterman et al. (2018) partly adapted from Reinhard et al. (2017)

sterile environment.

Other gaseous signatures have been considered including:

1. Methane, $CH_4$, (Krasnopolsky et al. 2004; Sagan et al. 1993), as methanogenesis (a form of anaerobic microbial metabolism that produces $CH_4$ as a waste product, most commonly by consuming $CO_2$ (E. W. Schwieterman et al. 2018)) is the dominant source of non-anthropogenic $CH_4$ in the modern Earth atmosphere. However, it has been shown that there exist many different sources of abiotic methane on Earth (Etiope et al. 2013) which does not make it a reliable biosignature. Furthermore, $CH_4$'s strongest bands in the infrared overlap with $H_2O$ bands which complicates its detection at low resolution (see Figure 1.6).

2. Nitrous oxide, $N_2O$, which is produced by Earth's biosphere via the denitrification of nitrate ($NO_3^-$) to $N_2$ gas (Cockell 2020). $N_2O$ has a short life time in the atmosphere ($\simeq$110 years), meaning its significant presence in an atmosphere would suggest a biological mechanism for its production. Furthermore, current studies indicate that only a small amount of $N_2O$ is produced by abiotic sources (E. W. Schwieterman et al. 2018). Nevertheless, detection of $N_2O$ on another planet will likely be challenging as it will require very high spectral resolution power and sensitivity. Indeed, most of its absorption bands are weak at Earth-like abundances or/and overlap with other potentially abundant gases such as $H_2O$, $CO_2$, or $CH4$ (see Figure 1.6).

3. Complex sulfur gases such as dimethyl sulphide, $DMS$, or dimethyl disulphide, $DMDS$, are produced by bacteria and higher order life-forms in wetlands, inland soils, coastal ecosystems, and oceanic environments (Rasmussen 1974; Saltzman et al. 1989). They have the advantage not to be produced by any known abiotic sources on modern Earth. Unfortunately, in modern-Earth atmosphere they are rapidly destroyed and their low abundances make them spectrally undetectable. However, Domagal-Goldman et al. (2011) showed that for planets receiving extremely low UV fluxes, which may exist in the habitable zone of an inactive M dwarf, the concentrations of biogenic sulphur gases could increase up to remotely detectable levels. Interestingly, the most detectable feature would actually be an indirect product of organic sulphur gases, ethane $C_2H_6$ (Domagal-Goldman et al. 2011). The inconvenience with ethane being that it would be an ambiguous signature, since it can be generated abiotically (E. W. Schwieterman et al. 2018).

Besides, as first introduced by James Lovelock (Lovelock 1965), it must be highlighted that chemical disequilibria could also be strong indications of biological activity in exoplanet atmospheres. Krissansen-Totton et al. (2016) quantified the thermodynamic disequilibrium in the atmospheres of Solar system planets and showed that the biosphere of the Earth makes its thermodynamic chemical disequilibrium $\simeq$20 times stronger than the other planets'. For instance the presence of $O_2$ and $CH_4$ at significant concentrations in the atmosphere of the Earth is only made possible by a continuous resupply of both gases from biological sources. In the absence of life, these two gases should rapidly ($\simeq$10 years) oxidise to $CO_2$ and $H_2O$. Yet, some scientists argue that such a biosignature would actually not be adapted to detect life on Archean Earth-like planet as it is linked to the abundance of oxygen which is expected to be low during the Archean (E. W. Schwieterman et al. 2018). In that regard, some recent studies have discussed other kinds of thermodynamic disequilibria that occurred over Earth history (Krissansen-Totton et al. 2018b) because of the presence of life. Krissansen-Totton et al. (2018a)'s models indicate that a $CH_4 - N_2 - H_2O - CO_2$ disequilibrium should have existed in the Archean biosphere as well as a $O_2 - N_2$ disequilibrium during the Proterozoic. In principle such disequilibria should be detectable on exoplanets, although great challenges will have to be overcome in the quantification of gaseous abundances. For a comprehensive summary of potential biosignature gases and their associated properties I refer the reader to Table 3 & 4 from D. C. Catling et al. (2018).

Finally, it is interesting to mention that some work has been dedicated to the identification of gaseous anti-biosignatures (a gas that provides evidence against the presence of life). One antibiosignature candidate is carbon monoxide (present in Mars's atmosphere) as several chemical studies predicted it would be rapidly consumed by life if present (notably

by microbes in the presence of water). Accordingly, Walker et al. (2018) suggest that future missions aiming at characterisation of exoplanetary atmospheres use $CO$ as an anti-biosignature. Another possible anti-biosignature is the coexistence of abundant $H_2$ and $CO_2$ (D. C. Catling et al. 2018).

**Surface biosignatures:** In addition to detecting absorption features from gases present in the atmospheres of exoplanets, astrobiologists can look for spectral signatures originating from pigments in living organisms, from light scattered by the physical structures of organisms, from fluorescence of pigments, and even from bioluminescence. The most discussed surface biosignature in the literature is the vegetation red edge (VRE) (Seager et al. 2005) as it is the only one known to produce a unique biological fingerprint on the disk-averaged spectrum of our own planet (E. W. Schwieterman et al. 2018). The VRE results from the absorption by the photosynthetic chlorophyll molecule in red region of the spectrum contrasted with a strong reflectance signature in the infrared region (change happens around $0.67 - 0.76 \mu m$ (Cockell 2020; Sagan et al. 1993; Seager et al. 2005)) as shown on Figure 1.8. According to Cockell (2020) this property of high reflectivity in the infrared could

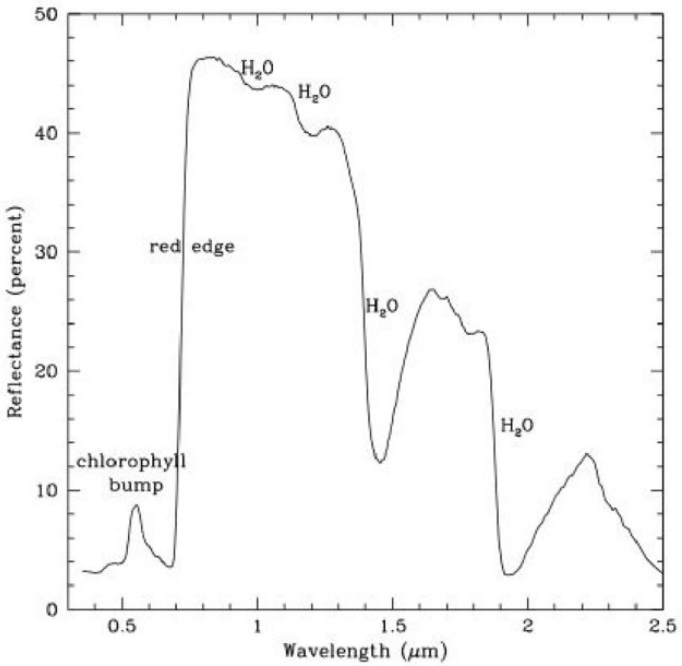


**Fig. 1.8** Reflection spectrum of a deciduous leaf with indications of the main absorbers and their bands. Notably, the vegetational red edge is the most important rise (between 700 and 800 *nm*) and is a consequence of the existing contrast between the strong absorption of chlorophyll in red and the otherwise reflective leaf in near-IR. Figure from (Seager et al. 2005), data from (Clark 1993).

be the result of an evolved mechanism to protect the plants from metabolically dangerous overheating. The VRE on Earth is well visible from space, to the point where it can be used to map the vegetation on the surface of the Earth. To measure the strength of the VRE and produce such maps, common practice is to use the Normalized Difference Vegetation Index (NDVI) defined as:

$$NDVI = \frac{r_{NIR} - r_{red}}{r_{NIR} + r_{red}}, \tag{1.1}$$

where $r_{NIR}$ and $r_{red}$ are reflectance in the near infrared and red, respectively. It must be specified that the exact wavelength and strength of the red edge varies with the type of vegetation and the spectral type of the host star. In that regards, on an habitable planet in orbit around an M-dwarfs, i.e. a star much cooler than the Sun (spectra shifted to the red and lower in intensity, see section 1.3.1), vegetation could be craving for energy and therefore be black instead of green (Cockell 2020). Besides the red edge, life produces a great diversity of pigments. For instance, O'Malley-James et al. (2018) studied the absorption and emission characteristics of common coral fluorescent pigments and proteins as a potential biosignature. Alternatively, DasSarma et al. (2021) proposed to use bacteriorhodopsin (which is a protein found in some archaea) as a surface biosignature of Archean-Earth life, based on the purple Earth hypothesis. The latter states that there was a rise of retinal pigment-based phototrophic life forms (including bacteriorhodopsin) on Earth's surface in the Archean before the apparition of anoxygenic and oxygenic photosynthesis pigments (such as chlorophyll), which made the Earth appear purple rather than green. However, most of these biological surface features are only detectable in local remote sensing data, and it is not clear whether any of these features could dominate on a global scale on an exoplanet (D. C. Catling et al. 2018). Furthermore, the detectability of all surface biosignatures is strongly dependent on the land covering fraction of the planet.

**Temporal biosignatures:** Another interesting kind of potential biosignature arises from the different cycles we observe in the life processes on our planet, either diurnal or seasonal cycles of sunlight (Meadows 2008). In this case, we would be looking for photometric brightness or spectral features that are varying with time. For instance, on Earth we observe a seasonal cycle in the concentration of $CO_2$ and $CH_4$ in the atmosphere as a response to the changing productivity of the land biosphere as a function of temperature and insolation (Keeling et al. 1976; Meadows 2008), as shown on Figure 1.9. In addition, the amplitude of the change is dependent on hemisphere and latitude, for instance in the northern hemisphere the amplitude of the concentration of $CO_2$ varies from $\simeq$3ppm near the equator to $\simeq$10–20 ppm at high latitudes (Keeling et al. 1976). The amplitude is lower in the southern hemisphere due to a smaller continental coverage fraction. Seasonal variability in $CH_4$ is more complicated as it

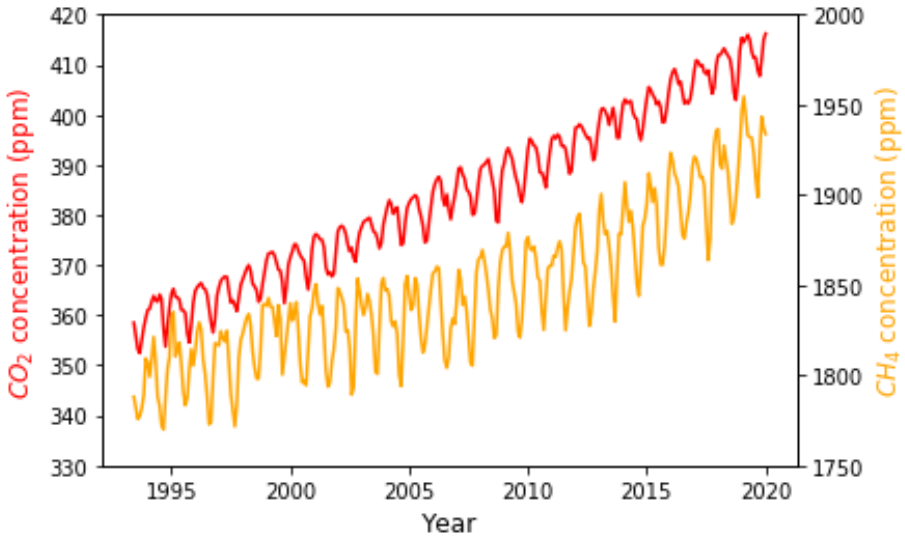


**Fig. 1.9** Evolution of the concentration of $CO_2$ and $CH_4$ in the Earth atmosphere from 1994 to the present date (April 2021) recorded in UTAH, USA. Gas concentration seasonal oscillations of both gases are partly reflective of the seasonal change in the productivity of the biosphere in the northern hemisphere and could be used as a temporal biosignature. However, the secular increase in both gases is attributable to industrial emissions. This figure was reproduced using the most recent data from the NOAA's Earth System Research Laboratory (www.esrl.noaa.gov)

is only partly biogenic and has a more complex modulation. Unfortunately, these seasonal variations are very small, and their detection is beyond the capabilities of next-generation observatories (Meadows 2008). Furthermore, it is highly possible that the absorption band chosen for $CO_2$ or $CH_4$ will be saturated, such that it would be impossible to observe variation in abundances.

### Detectability

As I mentioned in the previous section, the existence of false positives and false negatives could make the detection of biosignatures difficult to interpret. Indeed, one big concern of astrobiologists is to quantify the level of certainty required to designate features as biosignatures (E. W. Schwieterman et al. 2018). In that regard, it is worth mentioning that recent studies (D. C. Catling et al. 2018; Walker et al. 2018) have addressed this issue by deriving an expression for the Bayesian posterior probability of life existing on a given exoplanet. As an illustration, Walker et al. (2018) drew a conceptual diagram of such Bayesian framework that is shown on Figure 1.10. For instance, in Bayesian terms a biosignature is defined as an object, substance, and/or pattern of biological origin, such that $P(data \mid life) > 0$. This conditioned probability is the likelihood, e.g. the probability to have gathered the

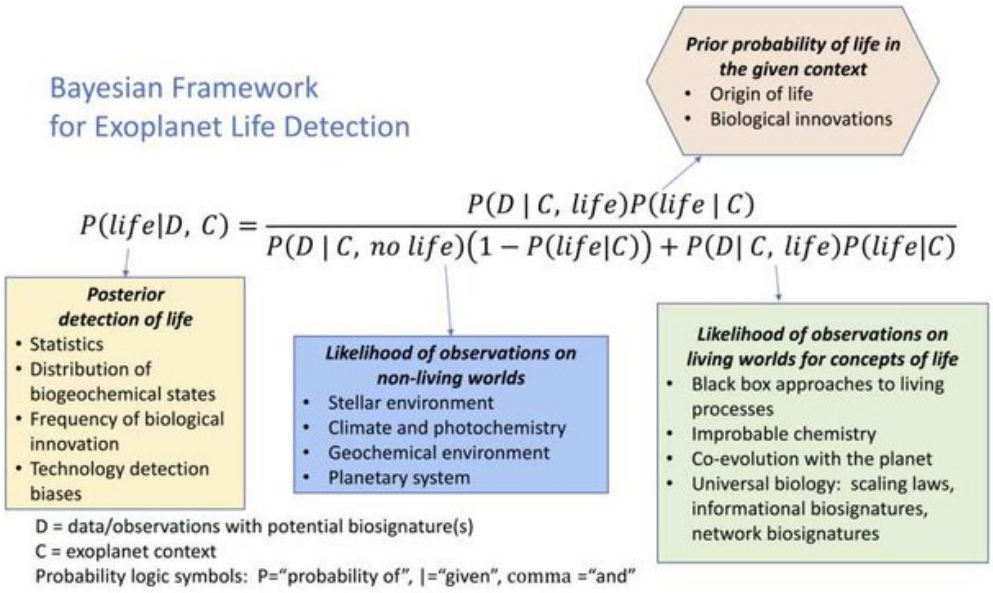


**Fig. 1.10** Conceptual diagram of a Bayesian framework for detection of exoplanet biosignatures. Figure from Walker et al. (2018).

data given that life exists on the planet. Similarly, false positive biosignatures (abiotic observables that mimic biologically produced observables) are defined by $P(data \mid life) > 0$ and $P(data \mid abiotic) > 0$. False negative biosignatures are defined by $P(data \mid life) \approx 0$, even if life is present. Anti-biosignatures are expressed as: $P(data \mid life) = 0$. And finally the detectability (likeness for a biosignature to be of biological origin) is defined (in the absence of noise) as: $D_{bio} = \frac{P(data|life)}{P(data|abiotic)}$. For instance, on modern Earth $O_2$ is a good biosignature because $P(O_2 \mid oxygenic\ photosynthesis) \gg P(O_2 \mid abiotic)$, such that $D \gg 1$.

Back to the expression of the posterior probability of life existing on a given exoplanet shown on Figure 1.10, it must be underlined that this is the product of a prior probability and a likelihood function. In this case, the prior probability is the a priori probability of life to exist given the context, embodied by the term $P(life \mid C)$. And the likelihood function is the likelihood of the signal arising due to living processes, embodied by the term $P(D \mid C, life)$. The denominator term in Figure 1.10 is a normalisation term that considers all possible hypotheses. In the previous paragraph about biosignatures, I have already discussed $P(data \mid C, abiotic)$ and $P(data \mid C, life)$. However, the most complicated term to quantify in this expression is $P(life \mid C)$. Indeed, to asses this prior of life in given context, one need to know the prior probability for life to exist in the first place, $P(life)$, however it is very challenging to constrain. As we saw in section 1.1.1, life is a path-dependent process, such that any new biological innovation is dependent on the previous one, which implies

that $P(life)$ takes the form of conditional probabilities for each evolutionary step, including $P(emerge)$, the probability for the emergence of life. Then it gets even more challenging as we currently have no constraints at all on $P(emerge)$, except from the fact that it cannot be equal to zero as life on Earth has emerged at some point. The only statement we can draw is that we must better understand the mechanisms underlying the origins of life to make a case for $P(emerge)$. The only simplification we can make is to decompose $P(life)$ into a sum of probabilities of all living processes (such as oxygenic photosynthesis for instance) for which we expect to have a nonzero prior on the planet of interest. In the end, the quantification of $P(life)$ is fundamentally interdisciplinary. Astronomers must therefore interface with scientists studying evolutionary biology, the co-evolution of Earth and life, and the origins of life if they ever hope to compute the posterior probability of life existing on a given exoplanet one day. Such a multidisciplinary approach is at the core of astrobiology.

Although detectability is distinct from habitability (a world might be habitable, but could host life that is not detectable), habitability can provide guidelines for detectability (Walker et al. 2018). In exoplanetology we frequently approximate habitability using the intuitive concept of habitable zone. In Bayesian terms the habitable zone is such that: $P(life)_{Earth\ like}$ and $P(data \mid life)_{Earth\ like} > 0$ within the habitable zone. Here $P(life)_{Earth\ like}$ and $P(data \mid life)_{Earth\ like}$ are the prior probability for Earth-like life and the likelihood of observing the data given Earth-like life conditions, respectively. In the next section I will provide more details about how exoplanetologists set the boundaries of the habitable zone and on which physical parameters they depend.

### Habitable zone

The term habitable zone (HZ) refers to the circumstellar region around a star in which an Earth-like planet (terrestrial radius and mass with an $N_2 - CO_2 - H_2O$ dominated atmosphere) could maintain liquid water on its surface at some instant in time (D. Catling 2013; Kasting et al. 1993). Because it is based solely on the surface, this definition does not consider sub-surface and buoyant forms of life. The concept of habitable zone has the advantage of being a quantifiable metric that can act as a proxy for the habitability of a planet orbiting another star than the Sun, which by itself is extremely complicated to characterise rigorously. In Bayesian terms, the habitable zone is the region around a star where an orbiting planet has the highest probability of being detectably habitable for present and near-future remote-sensing studies (R. k. Kopparapu et al. 2019). The habitable zone is delimited by an inner and an outer boundary. The inner boundary is set to be the place where a planet's surface temperature become high enough to initiate the runaway evaporation of a planet's oceans,

consequently increasing the infrared opacity of the atmosphere and reducing the ability of the surface to cool. Such a process is called the runaway greenhouse effect and is thought to have affected Venus in its early history (Rasool et al. 1970). In this situation, once the water content of the planet is boiled away in its atmosphere, $H_2O$ molecules suffer photolysis in $H$ and $O$, the former being loss to space and the latter recombining with rocks (Cockell 2020), removing water from the environment. If the stratospheric water vapour volume mixing ratio becomes greater than $10^3$, we observe a "moist" greenhouse effect where the photolysis of water molecules happens on timescales of $\simeq$10 to $\simeq$100 million years, long before the runaway greenhouse sets in (Cockell 2020; R. K. Kopparapu 2018). Notably, moist greenhouse effect occurs at lower insolation levels than the runaway greenhouse limit (R. K. Kopparapu 2018) (see Figure 1.11). The outer boundary of the habitable zone, called the maximum greenhouse limit, corresponds to the distance from which greenhouse gases (such as $H_2O$ or $CO_2$) are unable to maintain surface temperatures above the freezing point, regardless of their abundances. Generally, the outer edge of the HZ is referred to as the place where the $CO_2$ in the atmosphere starts to condense, marking the end of greenhouse warming combined with an increase in albedo that results in the further cooling of the planet's surface, and ultimately in a runaway glaciation (Kaltenegger et al. 2010). In the solar system, Mars is representative of the outer edge of the HZ as it currently has insufficient greenhouse effect and atmospheric pressure to sustain bodies of liquid water on its surface (Cockell 2020). Frequently, the region between the runaway greenhouse and maximum greenhouse limits is called the conservative HZ (CHZ) and the region between a "recent Venus" limit and an "early Mars" limit indicates the optimistic estimate of the HZ (OHZ) as shown on Figure 1.11. "Recent Venus" is an empirical estimate based on the inference that Venus has not had liquid water on its surface for at least the past 1 billion years, and "early Mars" stands for Mars as it was 3.8 billions years ago, assuming it was warm enough for liquid water to flow on its surface as evidenced by remote and in-situ observations (Salese et al. 2020).

It is important to mention that several additional external effects can affect the definition of the habitable zone. Notably, several studies have discussed the impact of clouds on the location of the HZ boundaries, showing that clouds can either push away the outer edge of the HZ from the host star through greenhouse effects, or push closer the inner edge of the HZ by scattering stellar radiations back to space through albedo effects (Kitzmann 2017; Pierrehumbert et al. 2011; Seager 2013; Selsis et al. 2007). For instance, dihydrogen clouds have an important greenhouse effect as $H_2$ molecules can absorb radiation over a wide wavelength range and do not condense until a few kelvins at 1- to 100-bar (Seager 2013). In that regard, Pierrehumbert et al. (2011) first pointed out that the presence of primordial $H_2 - He$ mixtures on a planet can maintain surface temperatures above the freezing point of water well beyond the traditional

habitable zone defined for $CO_2$-rich greenhouse atmospheres. Similarly, the planetary surface conditions such as land/ocean fractions or the presence of ice can have an albedo feedback effect that directly impacts the position of the HZ's inner edge (Shields et al. 2013; Zsom et al. 2013). To address these specific cases, astronomers have developed one-dimensional (1D) radiative–convective models and more recently sophisticated 3D general circulation models (GCMs) to simulate as faithfully as possible different atmospheric conditions (composition, pressure, profile) and therefore reliably define the HZ boundaries in a variety of scenarios.

Another aspect that should be taken into account is the fact that the inner and outer edges of the HZ are a function of time as the host star's luminosity evolves with time (Domagal-Goldman et al. 2016). Indeed, nascent stars' luminosity first decreases as they collapse down to their main-sequence size. Once they have reached the main-sequence, they experience gradual brightening on longer timescales as they fuse hydrogen into helium in their cores, increasing the core temperature and accelerating fusion (Meadows et al. 2018b). For this reason, the literature sometime refers to the continuously habitable zone as the zone where liquid water could have been present over geological timescales (Domagal-Goldman et al. 2016). For instance, in the case of the solar system the continuously habitable zone has been estimated to extend from 0.95 to 1.15 AU (Kasting et al. 1993). Indeed, as a comparison, four billion years ago the Sun's luminosity was only about 75% of what it is at the present time.

More generally, the spectrum of the host star has a strong influence on the HZ. The spectral energy distribution (SED) of the star is the amount of radiation as a function of wavelength that the star emits and it is a strong function of the temperature of the stellar photosphere which emits the radiations. Stars hotter than the Sun will have their HZ further away, while stars cooler than the Sun will have their HZ closer in. Figure 1.11 shows the theoretical evolution of the HZ distances with the temperature of the host star. The host star can impact the planetary environment through two main means: radiation and gravitation (Meadows et al. 2018b). First, the stellar evolution and activity can severely affect the climate and atmospheric composition of HZ planets either through escape processes or photochemistry. Second, gravitational interaction with the star and/or others planets can modify insolation levels of HZ planets and consequently their climate. We will specifically detail those processes for planets in the HZ of M dwarfs in section 1.3.2.

Similarly, orbital evolution should have a direct impact on a planet's habitability. For instance, planets on eccentric orbits could move in and out of the habitable zone over a full orbital period. Bolmont et al. (2016) showed that depending on the eccentricity of the planet and luminosity of the star, planets can or cannot sustain surface liquid water during the whole orbital period. In such a situation, we would expect the planet to have a surface water

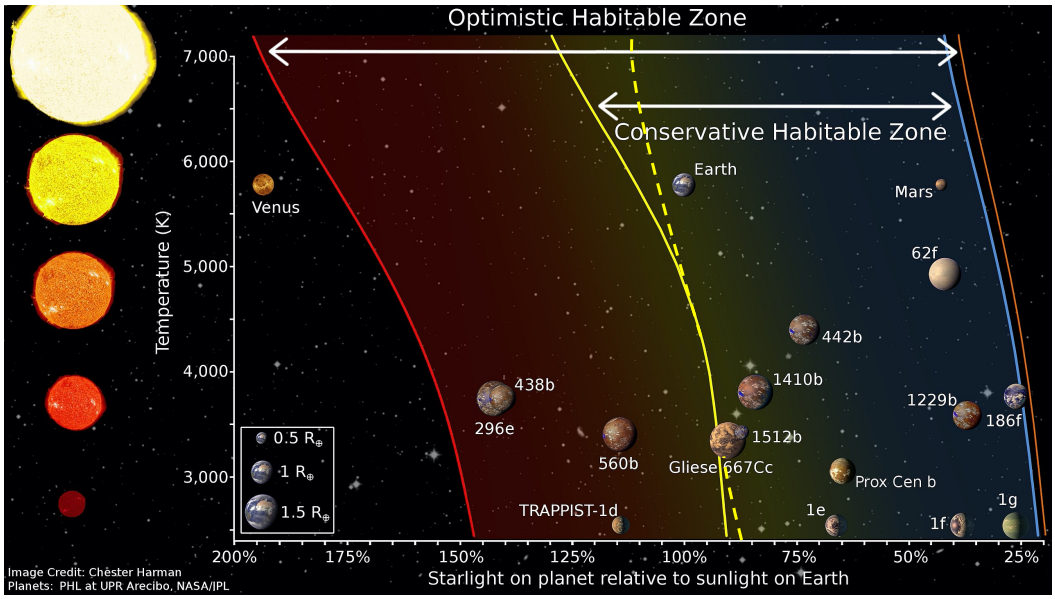


**Fig. 1.11** Habitable zone boundaries around stars, and how the boundaries are affected by the spectral type of the host star. The vertical axis shows stellar effective temperatures ($T_{eff}$). The solid red line indicates the recent Venus stage, the solid yellow line indicates the runwaway green house limit, the dotted yellow line indicates the moist greenhouse limit, the solid blue line indicates the maximum greenhouse limit and the solid red line indicates the early Mars limit. Credit: Chester Harman - Wikisource

ocean around periastron that would gradually froze as the planet goes towards apoastron. Then, additional effects would have to be considered such as orbital variations of albedo, greenhouse, and heat redistribution (Méndez et al. 2017) as they might strengthen or invert this trend. Interestingly, Williams et al. (2002) demonstrated that the habitability of planets on highly elliptical orbits near the HZ depends on the average stellar flux received over an entire orbit and not on the amount of time spent within the HZ. Similarly, some studies discussed the effect of obliquity variations on the habitability of an habitable zone planet and showed that the habitable fraction of the planet's surface should increase for large obliquities (Dobrovolskis 2013). And planets that experience high-frequency oscillations in obliquity may avoid global glaciation (as neither pole of the planet faces away from the star long enough for a thick ice sheet to develop) which would suppress the ice-albedo feedback and increase the outer edge of the habitable zone (Armstrong et al. 2014). Yet, it is extremely challenging to constrain exoplanets obliquities from observations. Finally, in multiple-planet systems, habitable zone planets around low mass stars can be subject to strong tidal forces that can deform the planets and affect its atmospheric dynamics (R. k. Kopparapu et al. 2017; 2019), particularly if there are tidally-locked to their stars. In some cases, tidal deformation can be important enough to heat the planetary interior, drive off a planetary ocean, enhance

tectonic activity, and shut down the magnetic dynamo on the planet. The potential habitality of M dwarf planets is discussed in more details in Section 1.3.2.

As I mentioned before, the habitable zone is an essential concept as it allows us to identify planets that are most likely to be habitable. Still, we showed that multiple factors, characteristics, and processes can affect planet's habitability and, by extension, challenge the simplicity of the HZ concept. Figure 1.12 from Meadows et al. (2018b) summarises all these external influences gathered in three intertwined groups: stellar effects, planetary systems or dynamical effects, and planetary properties. In this Figure, the factors written in blue are the

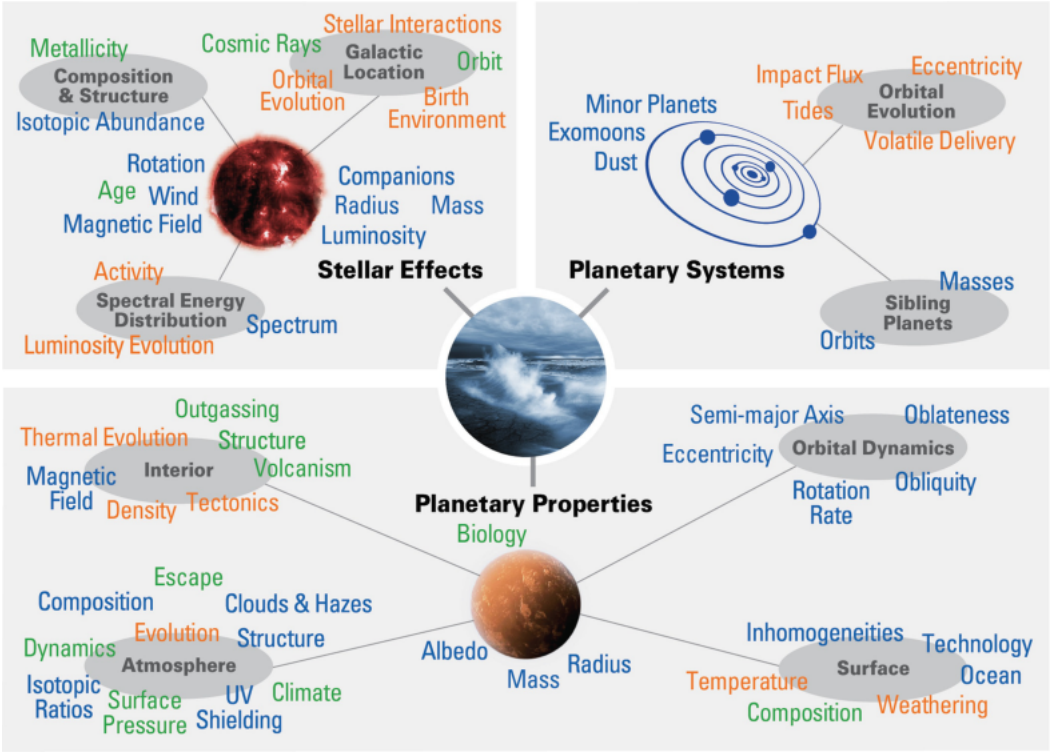


**Fig. 1.12** Diagram showing all the different factors that can impact planetary habitability identified so far. Text colours denote whether the indicated property/characteristic could be observed directly with sufficiently powerful telescopes (blue), those that require modelling interpretation (green), and those that are accessible mainly through theoretical modelling (orange). Figure from Meadows et al. (2018b).

ones that are potentially observable, while those in green are the ones that require modelling interpretation (possibly constrained by observations), and finally those in orange are the properties or processes that are accessible mainly through theoretical modelling (Meadows et al. 2018b). While many characteristics and processes that inform planetary habitability will have to be explored via modelling, or a combination of modelling and observations (at least for the next decades), it is exciting to notice all the properties that can be constrained from

observations of an exoplanet. In that regard, the next section is dedicated to the detection of new exoplanets and their characterisation.

## 1.2 Exoplanets

In 2019 the whole field of exoplanetology was on the front stage as the Swiss scientists Didier Queloz and Michel Mayor received the Nobel Prize of Physics for their seminal discovery of an exoplanet orbiting a solar-type star in 1995. Although the first detection of an exoplanet was announced three year earlier around the millisecond pulsar PSR1257+12 (Wolszczan et al. 1992), it was Mayor and Queloz's discovery of a planet around a main-sequence star (Mayor et al. 1995) that literally revolutionised the field of astronomy and initiated exoplanetology. Only twenty-six years later, almost 4500 exoplanets have been confirmed with another 2600 candidates waiting to be confirmed (source NASA Exoplanet Archive).

To detect new planets, several methods exist. Some are qualified as direct methods as they allow to get an image or a spectrum of the planet's light, while others are qualified as indirect as they look for stellar properties, such as position or brightness, which are affected by the presence of unseen planets. From an astrobiological point of view, direct detection techniques are particularly interesting as they enable to capture light from a planet (D. Catling 2013). Unfortunately, the detection capabilities of direct imaging techniques are currently limited to massive giant planets (or brown dwarfs) in very wide orbits around nearby stars, and many technological developments are still required to bring this potential into the temperate Earth-sized regime. This limited detection potential comes from the extremely high contrast and resolution required to detect a dim planet in the glare of its bright host star (Trauger et al. 2007). Although direct imaging is evolving extremely fast, the most successful methods to detect exoplanets so far have been the two indirect detection methods: stellar Doppler shift (radial velocity), and transits. Figure 1.13 shows the population of confirmed exoplanets as a function of their masses (or minimum mass in the case of RV detections) and their orbital periods, as well as the methods by which the planets were detected.

In particular, the transit and the radial velocity (RV) methods represent 76% and 19% of the discoveries respectively. The RV method relies on the Doppler shift of electromagnetic waves. In a planetary system, the planet is gravitationally attracted by the star and so is the star by the planet, and both of them revolve around their common centre of mass. The electromagnetic waves emitted by the star are therefore compressed when the star moves towards us (consequently the star's light shifts towards the blue) and stretched when the star moves away from us (the star's light shifts towards the red). The observation of the displacements of known spectral-lines in the star's spectrum are therefore used to reveal

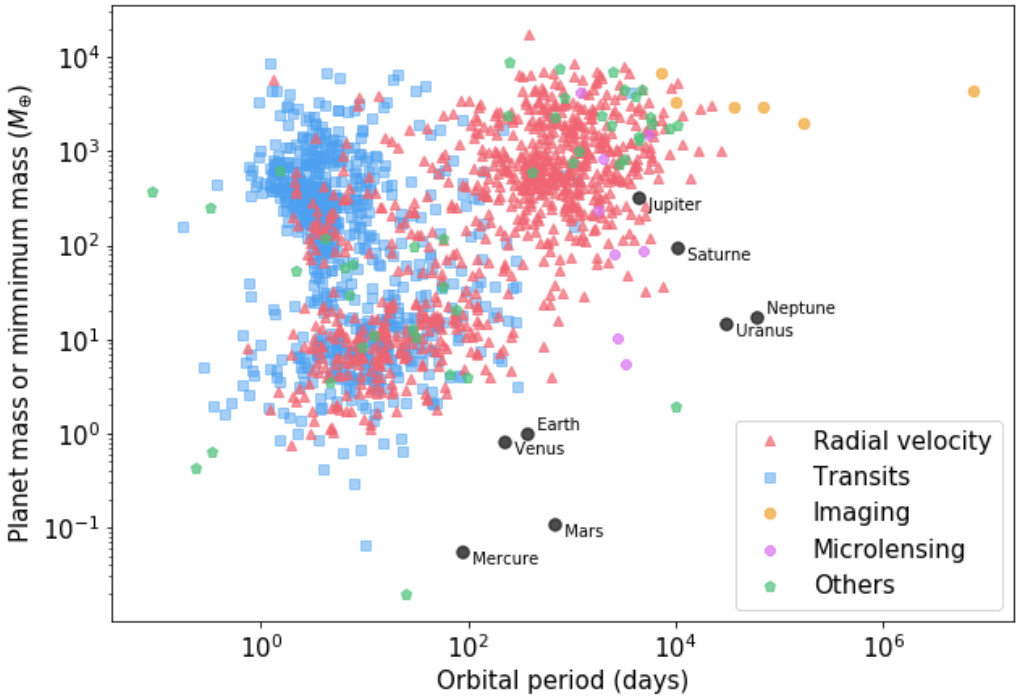


**Fig. 1.13** Distribution of the 4375 confirmed low mass companions to stars (at the time this thesis is being written, April 2021) as a function of their mass ($M_\oplus$) and period (days) in log scale. The colour code indicates which method was used to confirm the detection of the companion. The eight know planets of the solar system are shown as black dots for comparison. This figure was produced using data from the NASA Exoplanet Archive.

the presence of an exoplanet around it. The RV method can offer a measurement of the quantity $M_p \sin i$, where $M_p$ is the mass of the planet and $i$ is the inclination of its orbit, but not the value of $M_p$ or $\sin i$ individually. This method has the great advantage of being less dependent on the position of the planet relative to the observer compared to the transit method. However, its sensitivity can be limited by stellar activity. Indeed, as the star rotates, potential spots and faculae present on the star's photosphere come in and out of view, inducing RV variations that can look similar to radial-velocity signals from small, close-in planets. In addition, stellar granulation and pulsations can also impact high-cadence RV time-series. Besides, the faintness of the stars in the optical and the flurry of blended molecular lines present in late M-dwarfs spectra limit the study of planetary systems around such stars with the RV method. Nonetheless, this might be about to change with the recent development of NIR spectrographs such as SPIROU (Donati et al. 2018) or NIRSP (Wildi et al. 2017).

The transit method relies on the fact that, given a suitable alignment, a planet passes in front of its star once per orbit (transit), blocking a fraction of the starlight and causes a small dip in the star's brightness as seen by the observer. This dip (called a transit) corresponds to the area of the stellar disk that the planet obscures from our view, and is thus proportional to the square of the planet-to-star radius ratio. Assuming that an estimate of the size of the star is at hand, the measured amplitude of this dip can thus provide us directly with an estimate of the size of the planet. The first conclusively observed exoplanetary transit was announced in 1999 by Charbonneau et al. (1999) and G. W. Henry et al. (1999) for the sun-like type star (HD-209458), known from radial velocity measurements to have a planetary-mass companion in a very-short orbit. Although the transits method is limited by the probability of transit of a planet (the probability that the Earth lies in the shadow of the planet, which requires the orbital inclination to be very close to 90°), it has been the most prolific one to find extra-solar planets for the last 21 years, and it offers great possibilities in terms of characterisation (atmospheres, dynamics, interiors). In that regard, the following section will be dedicated to provide the reader with a detailed presentation of the method, including the fundamental equations behind transits and the ways they are used to characterise exoplanets.

### 1.2.1 Detection of transiting planets

#### Planetary orbit geometry and eclipse probability

As stated by Kepler's first law, in all planetary systems stars and planets move in closed elliptical orbits in inertial space, with the centre of mass at one focus, as shown in Figure 1.14 from Perryman (2018). In this figure, $\nu$ is the angle between the direction of pericentre and the current position of the body measured from the barycentric focus of the ellipse ($F_1$). $E(t)$ is the eccentric anomaly and is the corresponding angle of the current position of the body on the auxiliary circle of the ellipse. $a$, $b$ and $e$ are, respectively, the semi-major axis, semi-minor axis and eccentricity of the ellipse. The elliptical orbit of the planet around the star is defined as follow in polar coordinates:

$$r = \frac{a(1-e^2)}{1+e\cos\nu}, \tag{1.2}$$

where $r$ is the star-planet distance, $\nu$ is the true anomaly which is the angle between the direction of pericentre and the current position of the body measured from the barycentric focus of the ellipse (as shown on Figure 1.14). Then, a Keplerian orbit of a planet is defined in three dimensions with the following seven parameters (see Figure 1.15 from Perryman (2018)):

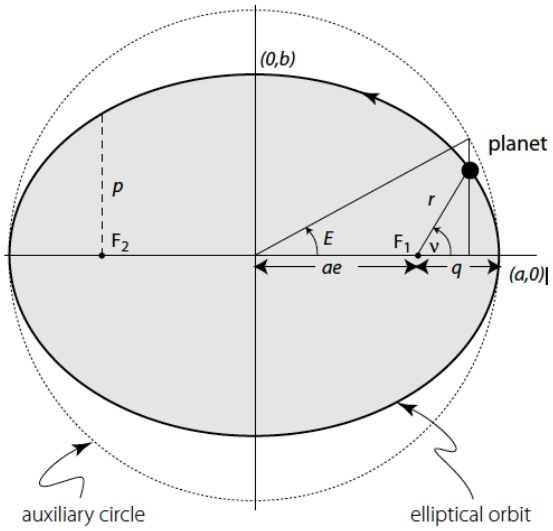


**Fig. 1.14** Geometry of an elliptical orbit. Points on the orbit can be described in terms of the true anomaly $\nu$ (with respect to the ellipse) or the eccentric anomaly $E$ (with respect to an auxiliary circle of radius equal to the semi-major axis a). Focus $F_1$ is the barycentre of the star-planet system while $F_2$ is the empty focus. Figure from Perryman (2018).

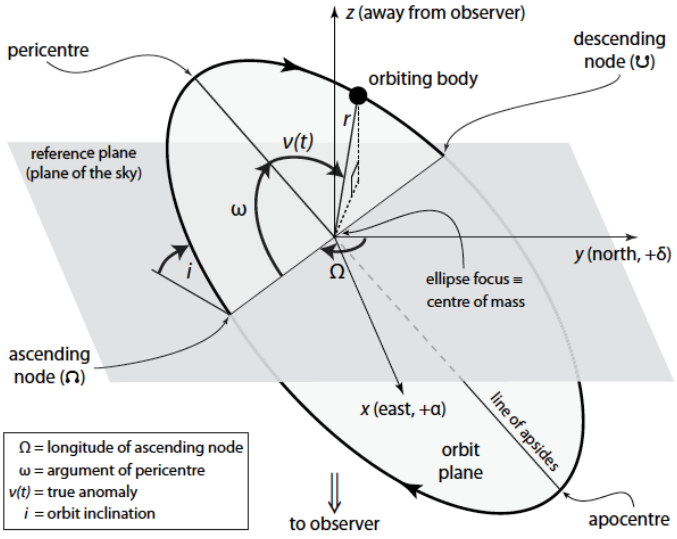


**Fig. 1.15** Geometry of an elliptical orbit in three dimensions. The reference plane is tangent to the celestial sphere, $i$ is the inclination of the orbital plane, and the nodes define the intersection of the orbit and reference planes. $\Omega$ is the longitude of the ascending node, measured in the reference plane. $\omega$ is the fixed angle defining the object's argument of pericentre relative to the ascending node. Figure from Perryman (2018).

- $a$, the semi-major axis,

- $e$, the eccentricity, if $e = 0$ the orbit is circular,
- $P$, the orbital period of the planet which is linked to the semi-major axis through the third Kepler's law:

$$P^2 = \frac{4\pi^2}{GM} a^3, \tag{1.3}$$

- $t_P$, the position of the object along its orbit at a particular reference time, generally with respect to the pericentre passage,
- $i$, the orbit inclination with respect to the reference plane (taken to be the plane of the sky for exoplanets),
- $\Omega$, the longitude of the ascending node, i.e the point where the orbit crosses the reference plane with the planet moving in the -$z$ direction (toward the observer) on Figure 1.15,
- $\omega$, the argument of periastron, i.e the angular coordinate of the object's pericentre relative to its ascending node $\Omega$.

$a$ and $e$ give the size and shape of the elliptical orbit where as $i$, $\Omega$, and $\omega$ depend solely on the orientation of the observer with respect to the orbit. If we chose to align the line of node with the X-axis such that $\Omega = \pi$, the position of the object at all time can be defined as follow in Cartesian coordinates:

$$\begin{aligned} X &= -r\cos(\omega + \nu), \\ Y &= -r\sin(\omega + \nu)\cos i, \\ Z &= r\sin(\omega + \nu)\sin i, \end{aligned} \tag{1.4}$$

such that the position of the object projected in the reference plan can be expressed as (Winn 2014):

$$\begin{aligned} r_{ref\,plan} &= \sqrt{X^2 + Y^2}, \\ r_{ref\,plan} &= \sqrt{r^2(\cos^2(\omega + \nu) + \sin^2(\omega + \nu)\cos^2 i)}, \\ r_{ref\,plan} &= \frac{a(1-e^2)}{1 + e\cos\nu}\sqrt{1 - \sin^2(\omega + \nu)\sin^2 i}. \end{aligned} \tag{1.5}$$

We then consider that the conjunction between the exoplanet and its host star (when two objects are most closely aligned, as viewed by the observer) happen when $r_{ref\,plan}$ is minimal. The conjunction when $X = 0$ and $Z > 0$ and the planet is behind the star (as viewed from the observer) on Figure 1.15 is called the secondary eclipse or occultation. On the opposite, the conjunction that happens when $X = 0$ and $Z < 0$ and the planet is in front of the host star as viewed from the observer is called the primary eclipse or transit. For the most general

case of an elliptical orbit, transit occurs when $\nu+\omega=\pi/2$ (and when $\nu+\omega=-\pi/2$ for the occultation). The transit impact parameter $b$, defined geometrically as the projected distance between the planet and star centres during mid-transit in units of $R_\star$, can be expressed as follow:

$$\begin{aligned} b &= \frac{a(1-e^2)}{R_\star(1+e\sin\omega)}\sqrt{1-\sin^2 i}, \\ b &= \frac{a\cos i}{R_\star}\Big(\frac{1-e^2}{1+e\sin\omega}\Big). \end{aligned} \tag{1.6}$$

For more clarity, we can visualise the transit as viewed from the observer's point of view (see schematic on Figure 1.16) such that geometrically, a planet of radius $R_p$ will transit its host star (from the observer's point of view) only if:

$$|b| < 1+\frac{R_p}{R_\star}. \tag{1.7}$$

Then, if $1-\frac{R_p}{R_\star} < |b| < 1+\frac{R_p}{R_\star}$ the transit is grazing (only a fraction of the planet's disk will pass in front of the star) and if $|b| < 1-\frac{R_p}{R_\star}$ the transit is full. In that regard, the probability for a randomly oriented planet on a elliptical orbit to be favourably aligned for a transit, also called transit probability, is defined as:

$$p_{transit} = \frac{R\star \pm R_p}{r} = \Big(\frac{R\star \pm R_p}{a}\Big)\Big(\frac{1+e\sin\omega}{1-e^2}\Big), \tag{1.8}$$

where the $\pm R_p$ acts as a way to exclude or include grazing transits in the transit probability estimation (Perryman 2018). For a circular orbit, equation (1.8) becomes:

$$p_{transit} = \frac{R\star \pm R_p}{a}, \tag{1.9}$$

and assuming $R_p \ll R\star$, it can be further simplified as $p_{transit} \simeq \frac{R_\star}{a}$. The probability of transit logically increases for planets orbiting close to their host star. As a comparison the probability that an Earth-like planet transit a Sun-like star is $\simeq 0.5\%$ whereas it is $2\%$ for a planet receiving the same irradiation as the Earth in close orbit around an ultra-cool star (see Section 1.3.1) such as TRAPPIST-1d. Similarly, the probability for a randomly oriented planet on a elliptical orbit to be favourably aligned for secondary eclipse is defined as:

$$p_{occ} = \frac{R\star \pm R_p}{r} = \Big(\frac{R\star \pm R_p}{a}\Big)\Big(\frac{1-e\sin\omega}{1-e^2}\Big). \tag{1.10}$$

### Transit parameters

A transit is usually defined by five main observables: the orbital period $P$, the transit depth $\Delta F$, the interval between the first and fourth contacts $t_T$, the interval between the second and third contacts $t_F$, and the mid-transit time $t_0$ (Figure 1.16). Indeed, when a transit is not grazing we can specify four distinct contact points, referred to as 1, 2, 3 and 4 on Figure 1.16. $t_1$ is the time when the leading edge of the planetary disc is in contact with the stellar disc from the observer's point of view. $t_2$ and $t_3$ are respectively the times when the entire disc of the planet starts (stops) being in front of the stellar disc. Finally, $t_4$ is the time when the trailing edge of the planetary disc is last in contact with the stellar disc. For a grazing transit there are no $t_2$ nor $t_3$. For a given planet on an elliptical orbit, $t_T$ and $t_F$ can be derived by

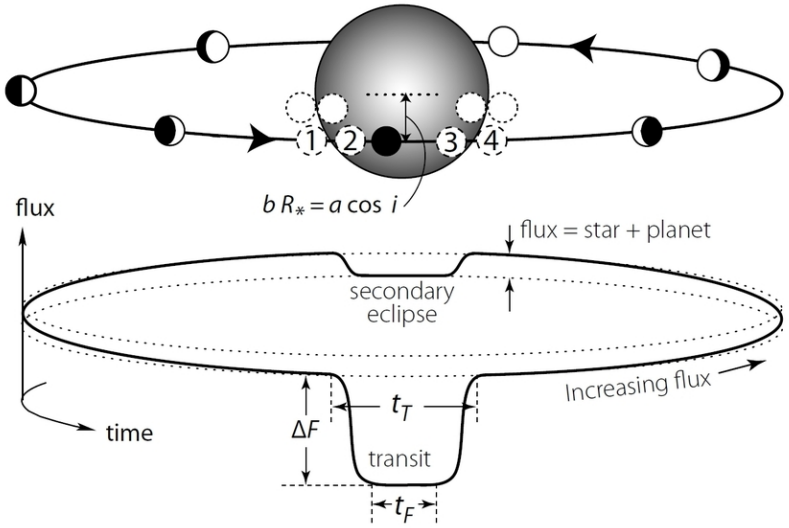


**Fig. 1.16** Schematic of a transit showing the evolution of the combined flux of the star and planet over the whole orbital period of a planet. During the transit, the planet blocks a fraction of the starlight. Dashed circles show first to fourth contact points; dotted ones for a smaller impact parameter. The total transit duration $t_T$ is between first and fourth contact, while $t_F$ is timed between second and third contact. Figure from Winn (2014).

setting equation (1.5) equals to $R\star \pm R_p$ to find $\nu$ at the times of contact and then integrating equation (44) of C. D. Murray et al. (2011) to obtain:

$$
\begin{aligned}
t_T &= t_4 - t_1, \\
t_T &= \frac{P}{\pi}\sin^{-1}\left[\frac{\sqrt{(1+R_p/R_\star)^2 - b^2}}{1-\cos^2 i}\right]\frac{\sqrt{1-e^2}}{1 \pm e\,sin\omega}.
\end{aligned}
\tag{1.11}
$$

$$
\begin{aligned}
t_F &= t_3 - t_2, \\
t_F &= \frac{P}{\pi}\sin^{-1}\left[\frac{\sqrt{(1-R_p/R_\star)^2 - b^2}}{1-\cos^2 i}\right]\frac{\sqrt{1-e^2}}{1 \pm e sin\omega}.
\end{aligned}
\tag{1.12}
$$

The ± sign refers to transits when set to + and occultations when set to − (Winn 2014). Besides, equations (1.12) and (1.11) show that $t_T$ and $t_F$ depend on the impact parameter $b$. As a matter of fact, we can invert equations (1.12) and (1.11) such that we have $b$ as a function of $t_F$, $t_T$, $P$ $R_p$ and $R\star$:

$$
b = \left[\frac{(1-R_p/R_\star)^2 - [\sin^2(t_F\pi/P)/\sin^2(t_T\pi/P)](1+Rp/R\star)^2}{1-[\sin^2(t_F\pi/P)/\sin^2(t_T\pi/P)]}\right]^{1/2}. \tag{1.13}
$$

The larger the impact parameter the longer the "ingress" and "egress" of the transit. The ingress of the transit is the time difference between $t_1$ and $t_2$, while the egress is the time difference between $t_3$ and $t_4$. As an order magnitude, the duration of the transit for an Earth-like planet around a Sun-like star is $\simeq$ 13 hours, against $\simeq$ 25 hours for a Jupiter-like planet, for orbital period of 1 and 11 years respectively. Then, as I mentioned before, the orbital period $P$ can be derived from Kepler's third law, equation (1.3). Finally, the transit depth $\Delta F$ which corresponds to the fraction of light blocked when the planet is eclipsing the host star is defined as:

$$
\begin{aligned}
\Delta F &= \frac{F_{out\ of\ transit} - F_{in\ transit}}{F_{out\ of\ transit}}, \\
\Delta F &= \frac{[S_\star \pi R_\star^2 + S_p \pi R_p^2] - [S_\star \pi (R\star^2 - R_p^2) - S_p \pi R_p^2]}{S_\star \pi R_\star^2 + S_p \pi R_p^2}, \\
\Delta F &= \frac{S_\star \pi R_p^2}{S_\star \pi R_\star^2 + S_p \pi R_p^2},
\end{aligned}
\tag{1.14}
$$

where $S_\star$ and $S_p$ are the surface brightness of the star and the exoplanet respectively. An usual assumption in the exoplanet community is to neglect $S_p \pi R_p^2$ against $S_\star \pi R_\star^2$ (as planets are much cooler and smaller than stars) such that:

$$
\Delta F \approx \left(\frac{R_p}{R\star}\right)^2. \tag{1.15}
$$

A second drop of brightness happens during the secondary eclipse (see Figure 1.16) and is defined as:

$$\begin{aligned} \Delta F_{occ} &= \frac{F_{out\ of\ occ} - F_{in\ occ}}{F_{out\ of\ occ}}, \\ \Delta F_{occ} &= \frac{[S_\star \pi R_\star^2 + S_p \pi R_p^2] - S_\star \pi (R\star^2)}{S_\star \pi R_\star^2 + S_p \pi R_p^2}, \\ \Delta F_{occ} &= \frac{S_p \pi R_p^2}{S_\star \pi R_\star^2 + S_p \pi R_p^2}. \end{aligned} \tag{1.16}$$

It can be approximated as:

$$\Delta F_{occ} \approx \left(\frac{R_p}{R\star}\right)^2 \frac{S_p}{S_\star}. \tag{1.17}$$

The elegance of the transit method resides in the fact that many physical parameters of the planet or its host star can be extracted from a single transit light curve. This is the subject of the next paragraph.

### Physical parameters

As presented by Seager et al. (2003), five distinct physical parameters can be derived directly from the observables $\Delta F$, $t_F$, $t_T$, and $P$. Firstly, the value of the semi-major axis can be easily derived from Kepler's third law, see equation (1.3). In that equation $M$ is equal to $M\star + M_p$ but assuming $M_p \ll M\star$ we obtain:

$$a = \left(\frac{P^2 G M\star}{4\pi^2}\right)^{1/3}. \tag{1.18}$$

Secondly, in the particular case where the planet has a circular orbit ($e = 0$), we can rearrange equation (1.12) to express the ratio $a/R_\star$ as a function of $P$, $t_T$ and $\Delta F$. Similarly, we can invert Kepler's third law to express $M_\star$ as function of $a$ and $P$. Then, remarkably, we can derive the stellar density $\rho_\star$ as a function of the observables:

$$\begin{aligned} \rho_\star &\equiv \frac{M_\star}{R\star^3} = \frac{4\pi^2}{P^2 G}\frac{a^3}{R_\star^3}, \\ \rho_\star &\equiv \frac{4\pi^2}{P^2 G}\left[\frac{(1-\sqrt{\Delta F})^2 - b^2[1-\sin^2(t_T\pi/P)]}{\sin^2(t_T\pi/P)}\right]^{3/2}, \end{aligned} \tag{1.19}$$

where $b$ can be expressed from observables as well as shown in equation (1.13). In parallel, we can invoke the stellar mass-radius relation:

$$R_\star = kM_\star^x, \tag{1.20}$$

where $k$ is a constant, distinct for main sequence or giants, and $x$ is the corresponding power law of the sequence ($x \simeq 0.8$ for F-K main-sequence stars, (Cox 2000)), in order to express $M_\star$ and $R_\star$ as a function of $\rho_\star$ and consequently $\Delta F$, $t_T$, and $P$:

$$\frac{M_\star}{M_\odot} = \left(k^3 \frac{\rho_\star}{\rho_\odot}\right)^{1/(1-3x)} \tag{1.21}$$

$$\frac{R_\star}{R_\odot} = \left(k^{1/x} \frac{\rho_\star}{\rho_\odot}\right)^{x/(1-3x)}, \tag{1.22}$$

where $\rho_\odot$ is the density of the Sun.

Thirdly, still in the case of circular orbit, we can derive the inclination of the orbit from the impact parameter as $b = a\cos i/R_\star$ when the orbit is circular, such that:

$$i = cos^{-1}\left(b\frac{R_\star}{a}\right), i \quad = cos^{-1}\left(b\frac{R_\star(4\pi^2)^{1/3}}{(P^2 G M_\star)^{1/3}}\right). \tag{1.23}$$

Finally, from the observation of a transit, we can easily derive the radius of the planet with $R_p = \sqrt{\Delta F} R_\star$ (from equation (1.15)).

I should also mention that several of these expressions can be simplified with further approximations such as $R_\star \ll a$ and $t_T \pi / P \ll 1$ (Perryman 2018).

Interestingly, there is a unique solution for the planet and star parameters from a planet transit light curve with two or more transits if the planet has a circular orbit and the light curve is observed in a bandpass where limb darkening is negligible (e.g if we assume that the stellar disk has uniform brightness) (Seager et al. 2003). The uniqueness of this solution allows for the derivation of physical parameters from the transit photometry alone. Furthermore, if $M_\star$ and $R_\star$ are known from the spectral type, then the problem is over-constrained and we can derive the orbital period even if only a single transit is observed, using equation (1.24):

$$P = \frac{M_\star}{R_\star} \frac{G\pi}{32} \frac{(t_T^2 - t_F^2)^{3/2}}{\Delta F^{3/4}}. \tag{1.24}$$

Nevertheless, in practice, the uncertainties on the transit parameters, even when observing in the IR and with high Signal to Noise Ratio (SNR), leaves only possible a rough estimate

of $P$ from a single transit light curve. Besides, one of our hypothesis was to neglect limb-darkening. In the next paragraph I explain what is limb-darkening and describe its effect on the transit light curve and the derived parameters.

### Limb darkening

The effect of limb darkening refers to the gradual decrease of intensity in a star's disk moving from its centre to its limb. It originates from the spherical shape of the star combined with the increase of the temperature towards the deeper layers of its atmosphere. Because transit light curves are constructed from the evolution of the observed stellar flux when a planet passes in front of the star, the limb-darkening effect has a direct impact of the shape of the transit.

The limb darkening originates from the fact that: (1) the temperature decreases with altitude in the stellar atmosphere; (2) at a given wavelength, the emission in a given direction of a column of material parallel to this direction originates mostly from the layer corresponding to an optical depth of 1, this optical depth being the integration over the column, from its surface to its deeper layers, of the absorption coefficient and the density, defined as:

$$\tau_\nu(x) = \int_x^\infty k_\nu(s)\rho(s)ds. \tag{1.25}$$

For a given observer, given the thermal structure of the stellar atmosphere and the spherical shape of the star, the "columns" are more and more inclined relative to the normal of the stellar surface as we move from the centre to the disk, resulting in $\tau = 1$ corresponding to cooler/higher altitude layers. As a hotter layer will emit more flux than a cooler one, the centre of the stellar disk appears brighter than its edges, this is the limb darkening effect. As shown on the right panel of Figure 1.17, for $\tau_\nu = 1$ we don't expect the photons to be emitted from the same atmospheric layer depending on their latitude on the star. Indeed, from the observer's point of view the photons comings from A (centre of the star) on the figure belongs to a hotter and denser layer than those coming from B (limb of the star). Furthermore, the limb-darkening effect is wavelength dependent and especially pronounced for the shorter wavelengths (larger frequencies). The stronger extinction in short wavelengths together with the lower temperature at higher photospheric layers is the reason for the colour dependence of the limb darkening, as the energy of a black body at a given temperature is ruled by Planck law and therefore function of $\nu^4$.

The limb-darkening effect is generally modelled by an analytical function relating the intensity at a given angle $\theta$ (between the light ray and the normal to the stellar surface) to the intensity at the centre of the disk. The most frequently used law is the quadratic law which is express

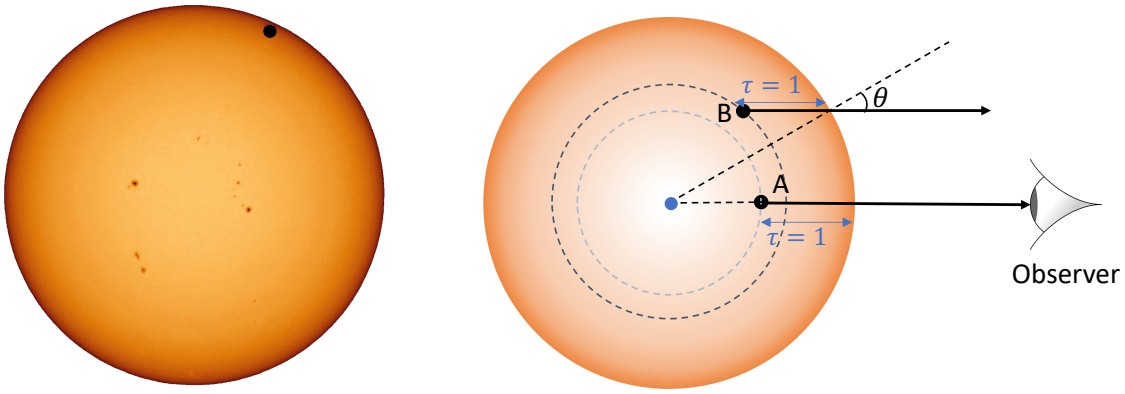


**Fig. 1.17** *Left figure*: Transit of Venus in 2012 seen from San Francisco, USA. The limb darkening is clearly visible (The limb appears also more red compared to the centre) as well as prominent spot groups. Source: Wikipedia. *Right figure*: Illustration of the reason for limb darkening. Coloured annuls represent the photosphere with hotter layers as the colour get brighter and cooler layers as the colour get darker. Credit: Elsa Ducrot.

as follow:

$$\frac{I(\mu)}{I(1)} = 1 - u_1(1-\mu) - u_2(1-\mu)^2, \tag{1.26}$$

where $\mu = \cos\theta$, $I(1)$ is the intensity at the centre of the stellar disk (as seen from the observer), $I(\mu)$ is the intensity at $\theta$ from the centre of the disk, and $u_1$, $u_2$ are the quadratic limb-darkening coefficients (LDCs). The value of $u_1$ and $u_2$ are generally derived from a stellar atmospheric model. Still, in case of high signal-to-noise transit light curve, they can be constrained from the light curve itself.

Figure 1.18 shows how the transit shape is massively influenced by the limb darkening. In particular, the depth of the transit is highly dependent on the strength of the limb darkening effect. Consequently, it is crucial to account for limb darkening when modelling a transit light curve. In that regard, Mandel et al. (2002) derived analytic expressions to model the eclipse light curve of a star described by quadratic or nonlinear limb darkening laws, that is still extensively used. Applications of Mandel et al. (2002) methods will be presented in Chapter 3. Finally, it is interesting to observe that while we usually use stellar characteristics (mass, radius, limb darkening laws) to derive the transit parameters the other way around is practicable. Indeed, the planet can act as a probe and transit light curves can be used to study the photospheric structure of the star, including its limb darkening.

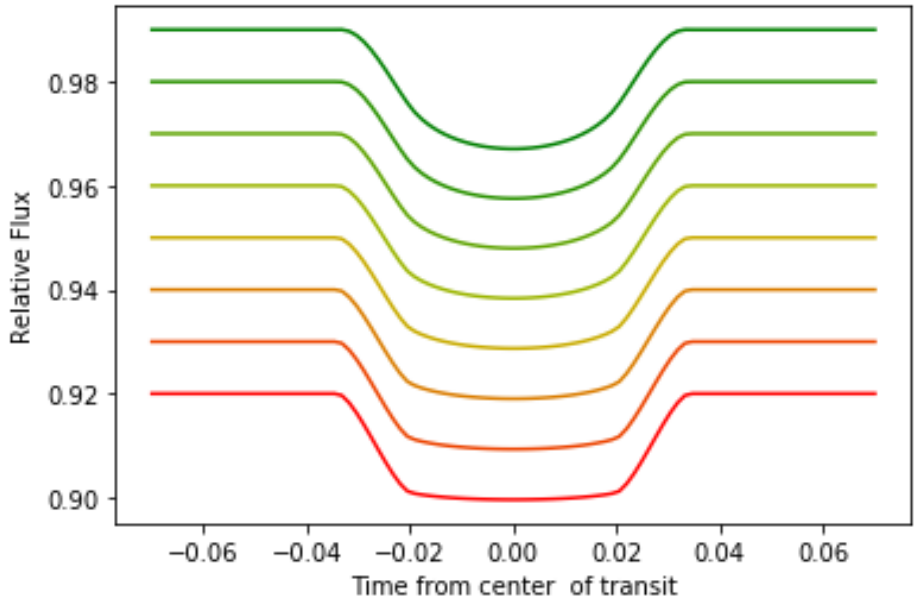


**Fig. 1.18** Evolution of the shape of the transit with the wavelength for WASP-19b. The colours of the line go from green (visible) to red (near-IR). The transit light curves have been offset for more clarity. Figure produced with `Batman` (Kreidberg 2015).

### 1.2.2 Characterisation of exoplanets

In the previous section, I have detailed how to detect an exoplanet using the transit method. In this section, I will show that both transits and occultations can play a key role in the further characterisation of a planet. Indeed, eclipses (transit or occultation) provide particularly important probes of an exoplanet's atmospheric composition and structure. As I mentioned in section 1.1.2, one of the long-term objectives of exoplanetology is to measure the spectrum of habitable exoplanets. One way to do that is to analyse the evolution of the combined light of the star–planet system. Along the planet's orbit, the integrated flux will vary either due to the star light being blocked by the planet or attenuated by its atmosphere during transit, or due to reflection or emission of light from the planet itself. From the analysis of the combined star + planet flux measured by spectroscopy (and even by broad-band photometry to some extent), the chemical composition of the planet's atmosphere, its structural profile, its energy transport properties and its thermal profile can be derived.

#### Transit spectroscopy

During a transit, a small fraction of the light emitted from the star passes through the narrow layer of atmosphere surrounding the planet (assuming the planet has an atmosphere), as shown on Figure 1.19. As they pass through the planet atmosphere, photons will be absorbed

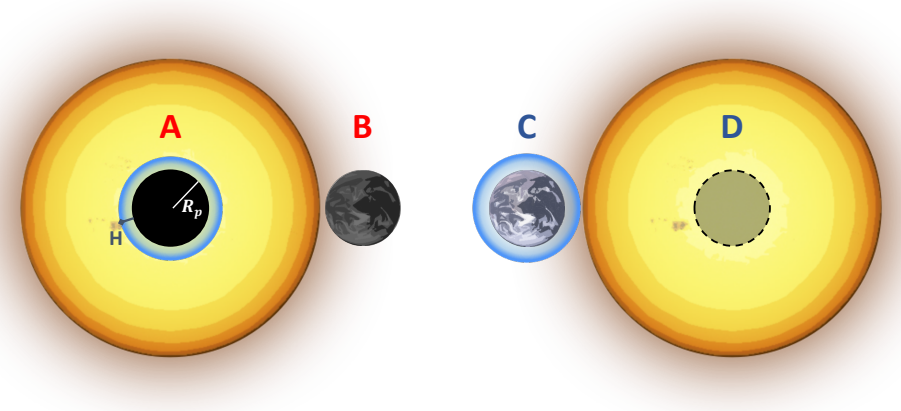


**Fig. 1.19** Geometry of transmission (left) and emission spectroscopy (right). During the transit, part of the star light passes through the (annular) atmosphere of the planet (situation A). Transit transmission = *A* - *B*. During the secondary eclipse, there is a switching off of the light reflected or emitted from the day-side surface of the planet (situation D). Secondary eclipse emission = *C* - *D*. *H* stands for the scale height and $R_p$ for the radius of the planet. Credit: Elsa Ducrot, adapted from Perryman (2018).

at specific wavelengths depending on the molecules and atoms present in the atmosphere, or scattered by aerosols. The transit is directly impacted by those spectral signatures as its depth will vary as more or less light is being blocked, or scattered by the atmosphere of the planet. The wavelength-dependence of the transit depth, and hence the apparent planet radius, effectively provides what is called a "transit transmission spectrum". As an order of magnitude, the change in eclipse depth $\Delta D$ across spectral lines in transmission can be approximated as (Miller-Ricci et al. 2009b):

$$\Delta D \simeq \frac{2HR_p}{R_\star^2}, \tag{1.27}$$

where $R_p$ is the radius of the planet, $R_\star$ the radius of the star and $H$ the atmospheric scale height (the height above which the pressure decreases by a factor exp) which can be defined as:

$$H = \frac{k_B T}{\mu_m g_p}, \tag{1.28}$$

assuming hydrostatic equilibrium and using the ideal gas law. In this equation, $k_B$ is the Boltzmann constant, $T$ the atmospheric temperature, $\mu_m$ the mean molecular weight, and $g_p$ the planet's surface gravity. We note that since $H$ depends on $g$ it also implicitly depends on the radius and the density of the planet. Equations (1.27) and (1.28) reveal that atmospheric signatures are especially strong for large planets that have hot, extended (H-dominated) atmosphere and low-gravity, such as Hot Jupiters. For an Earth-like planet orbiting a Sun-like

star, $\Delta D$ is of the order of $\simeq 0.2$ ppm while it is $\simeq 200$ ppm for a Hot Jupiter like WASP-19b (using scale height value derived by Espinoza et al. (2019)).

Yet, to fully interpret transit spectra, models must include temperature, pressure, and composition as a function of the altitude, and integrate the radiative transfer equations to obtain a theoretical spectrum to compare to the observations. From these considerations Brown (2001) showed that $\Delta D$ takes the form:

$$\Delta D = \frac{2}{\pi R_\star^2} \int_0^{z_{max}} (R_p + z)(1 - \exp^{-\tau(z,k)}) \mathrm{d}z, \tag{1.29}$$

where $k = 2\pi/\lambda$ is the wavenumber, $z$ is the height of the transiting ray above the planet's (reference) surface, and $\tau$ is the tangential optical depth, itself a function of the species' opacity and wavenumber. Alternatively, studies such as those of Lecavelier Des Etangs et al. (2008) and Howe et al. (2012), developed analytic models of molecular absorption and Rayleigh scattering that allow to derive estimates of the atmosphere's temperature, pressure, and mean molecular weight, providing the opacity is independent of temperature and pressure (Howe et al. 2012).

Over the last 20 years, transit spectroscopy of exoplanets has developed exponentially. Notably, thanks to the Hubble Space Telescope (HST), dozens of spectra have been acquired from Hot Jupiters like WASP-19b (Anderson et al. 2010) to Sub-Neptunes like K2-18b (Benneke et al. 2017) and even terrestrial planets such as TRAPPIST-1e (Gillon et al. 2017b), with a large majority of Hot Jupiters. Figure 1.20 shows the spectra of ten distinct Hot Jupiters obtained from the combination of observations with the HST Space Telescope Imaging Spectrograph (STIS) instrument, the HST Wide Field Camera 3 (WFC3) instrument, and the Spitzer space telescope Infrared Array Camera (IRAC). These spectra show a variety of spectral absorption features due to the presence of $Na$, $K$ and $H_2O$, as well as strong optical scattering slopes suggestive of the presence of high-altitude aerosols.

The limitations in the interpretation of transit spectra are two-fold: (1) while the detection of some molecules can be unambiguous, the accurate measurement of their abundances, inferences on the thermal profile, surface conditions, etc, is very model-dependent. This is why most spectroscopic analyses are now following the 'retrieval' approach, which is based on the exploration of a broad range of models to derive accurate inferences by marginalising over all models consistent with the data; and (2) the limitations of the photometric/spectroscopic performances of our instruments.

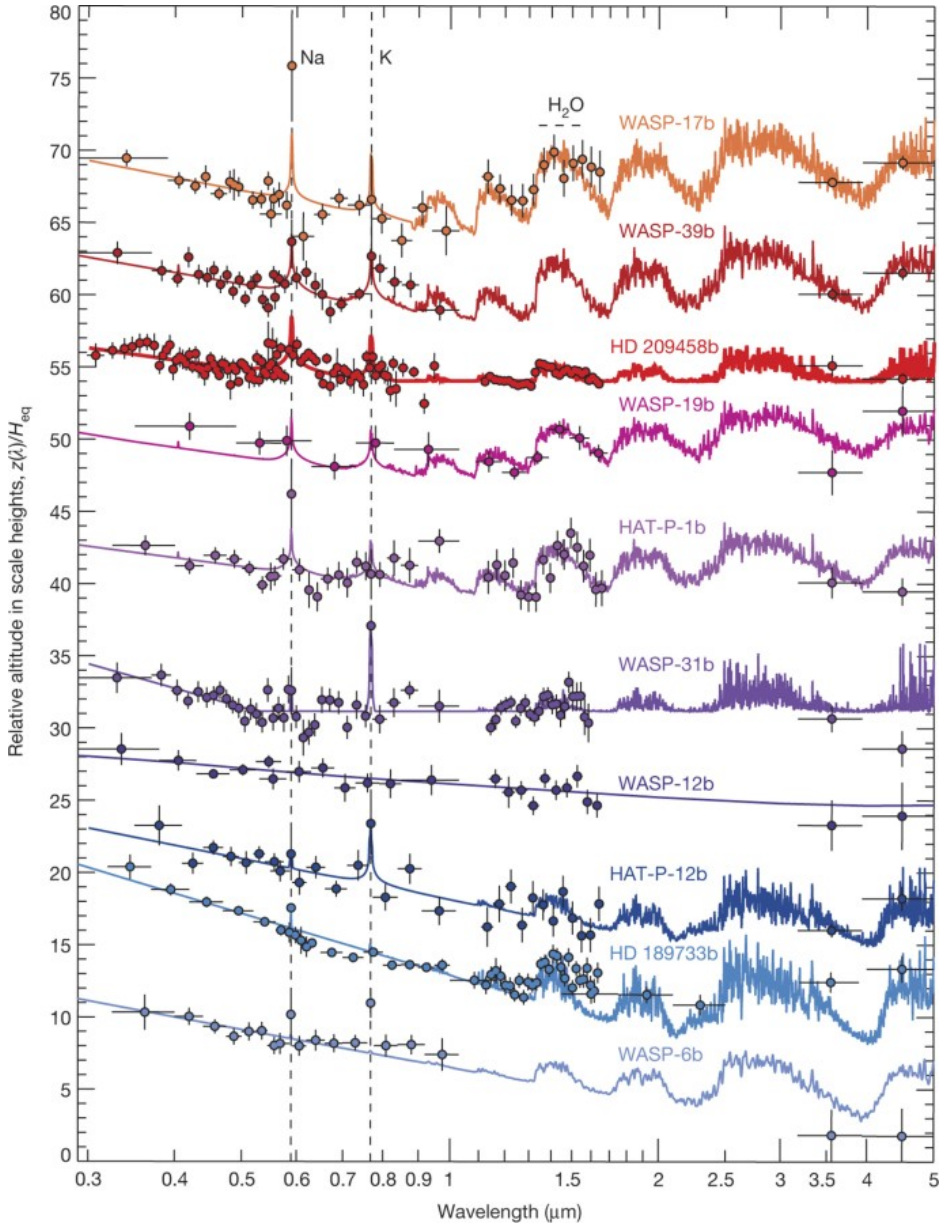


**Fig. 1.20** HST/Spitzer transmission spectral sequence of hot-Jupiter survey targets. Solid coloured lines show fitted transmission models with prominent spectral features indicated. The spectra have been offset for clarity. Horizontal and vertical error bars indicate the wavelength spectral bins and $1\sigma$ measurement uncertainties, respectively. Planets with predominantly clear atmospheres (top) show prominent alkali ($Na$, $K$) and $H_2O$ absorption, with infrared radii values commensurate with or higher than the optical altitudes. Very hazy and cloudy planets (bottom) have strong optical scattering slopes, narrow alkali lines and $H_2O$ absorption that is partially or completely hidden by clouds. Figure from Sing et al. (2016).

### Occultation spectroscopy

Similarly to transit (transmission) spectroscopy, occultation (emission) spectroscopy aims at measuring the secondary eclipse depth in different wavelengths to probe the emission (or

reflection) spectrum of the planet's dayside. As a reminder, the depth of the occultation can be expressed as equation (1.17). In the most general case, the surface brightness that we measure for the planet's dayside is a combination of thermal emission and reflected light. However, whether we assume reflected light is dominant or thermal emission is dominant, equation (1.17) takes another form. If we assume only reflected light we can write:

$$\Delta F_{occ} = A_g\Big(\frac{R_p}{a}\Big)^2 \Phi(\alpha), \tag{1.30}$$

where $A_g$ is the geometric albedo, $R_p$ is the planetary radius, $a$ the semi-major axis, and $\Phi(a)$ is the phase function ranging between 0 and 1, which for the case of a secondary eclipse can be approximated to 1 (and to 0 for the transit).

Alternatively, if we assume only thermal emission, either reprocessed from stellar irradiation or from purely internal origin, we can assume black-body emission for the star and planet's day-side and write:

$$\Delta F_{occ} = \frac{B(\lambda, T_\star)}{B(\lambda, T_{p,d})}\Big(\frac{R_p}{R_\star}\Big)^2, \tag{1.31}$$

where $B(\lambda, T_\star)$ is a blackbody at the effective temperature of the star $T_\star$ and $B(\lambda, T_{p,d})$ at the temperature of the planet day-side $T_{p,d}$. This assumes that the emission of the dayside is isothermal, which is not the case, meaning this emission is not representative of the whole planet's sphere (Schwartz et al. 2015). To get around this issue we can use the formalism of Cowan et al. (2011) to estimate the day-side and night-side temperature of the planet while quantifying the efficiency of the transport of the incident flux from the sub-stellar point (where the rays from the star reach the planet perpendicularly to its surface) to the night-side:

$$\begin{aligned} T_{p,d} &= T_0(1-A_B)^{1/4}\Big(\frac{2}{3} - \frac{5}{12}\epsilon\Big)^{1/4}, \\ T_{p,n} &= T_0(1-A_B)^{1/4}\Big(\frac{\epsilon}{4}\Big)^{1/4}, \end{aligned} \tag{1.32}$$

where $T_0$ is the equilibrium temperature of the sub-stellar point of the planet defined as $T_0 = T_{eff}\sqrt{R_\star/a}$, $A_B$ is the Bond albedo defined as the capacity of the planet to reflect light from the star and comprised between 0 and 1, and $\epsilon$ is the redistribution efficiency also comprised between 0 and 1. We notice that if the redistribution is perfectly effective, $\epsilon = 1$, the temperature of the planet is homogenised and $T_{p,d} = T_{p,n}$. On the contrary, if the day–night re-circulation efficiency is null $T_{p,d} = T_0(1-A_B)^{1/4}(2/3)^{1/4}$ while $T_{p,n}$ is null. Alternatively, even if we cannot describe the planetary radiation by a block-body, a common practice is to define a brightness temperature $T_b$ which we consider to be the blackbody temperature that would lead to the observed value of $\Delta F_{occ}$. Yet, difficulties remain to

quantify the contribution from reflected light and that from thermal emission of the planet in the measured $\Delta F_{occ}$. To work around this, we can carry out observations in different regions of the spectrum. As a matter of fact, at short wavelengths (in the visible) the signal will be dominated by reflected light whereas at longer wavelengths (in the near-IR) most of the signal will be from thermal emission.

To this date, emission spectra have been obtained for almost a dozen of exoplanets. The majority of observations of secondary eclipse were made from space, either with HST or Spitzer. Figure 1.21 from Sheppard et al. (2017) shows the emission spectra of planet WASP-18b constructed from observation with HST and Spitzer. Remarkably, this emission

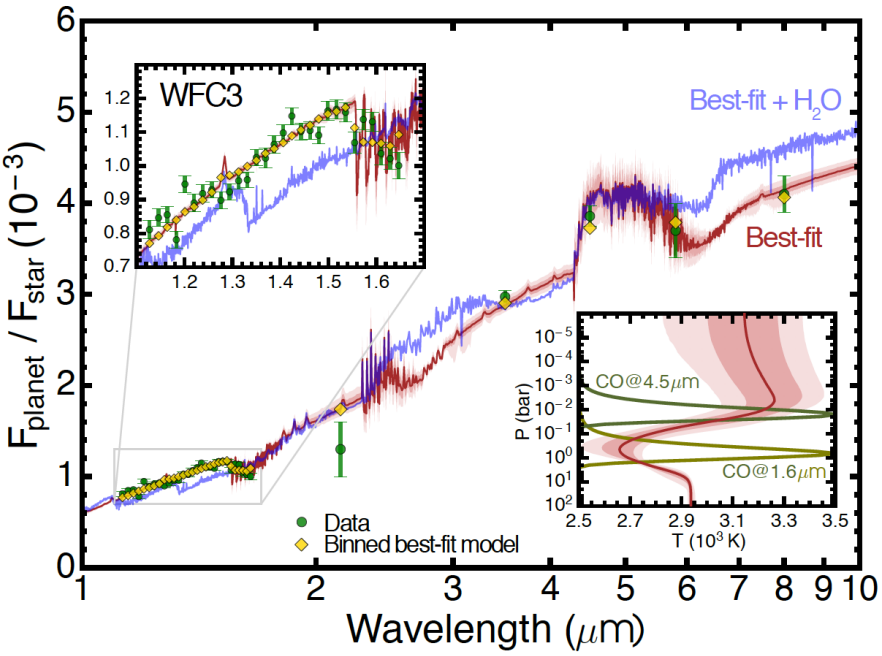


**Fig. 1.21** Observed emission spectrum and retrieved solutions of the hot Jupiter WASP-18b, the most populated one published to this date. WFC3 and Spitzer data are shown in green. The median retrieved spectrum, with the uncertainity envelopes, is shown in red. A model with solar-abundance $H_2O$ absorption is shown in blue to demonstrate the lack of an $H_2O$ feature in the data. Figure from Sheppard et al. 2017.

spectrum contains 34 observational points which were sufficient to reveal a thermal inversion (or stratosphere) in the day-side atmosphere, the presence of either $CO$ or $CO_2$, and to measure the planet's metallicity from an atmospheric retrieval analysis (not detailed here). Yet, Burrows (2014) warns us on the fact that interpretation of an emission spectra is extremely model-dependent and include several degeneracies such as the one between albedo and redistribution factor. Interestingly, some degeneracies can be broken when combining

emission spectrum, accurate transit parameters, and a complete phase curve of the planet (Alonso 2018). For that reason, phase curves are the subject on the next paragraph.

Finally, I must underline that transit and emission spectra are complementary. The former is directly sensitive to molecular composition and atmospheric scale height whereas the latter is sensitive to temperature structure in addition to atmospheric composition. This synergy can prove particularly useful to derive the temperature-pressure profile of the atmosphere, as shown by Kreidberg et al. (2014a) and Sheppard et al. (2017). Indeed, if the temperature increases with altitude (meaning a stratosphere is present), we could either see spectral features in emission that are not present in absorption or the opposite, depending on whether the molecules responsible for these spectral signatures exist above or below the tropopause (the atmospheric boundary layer between the troposphere and the stratosphere).

### Phase curve

The phase curve is the evolution of the measured flux of the star–planet system over the full orbital period including outside of the transit and eclipse phases. Variations in a phase curve are due to inhomogeneous illumination of the planet, as over the course of one orbit, we see different hemispheres of the planet, ranging from its day-side (before and after the eclipse of the planet by the star) to its night-side (Parmentier et al. 2018). Hence, a phase curve is sensitive to the day–night contrast and is a useful probe of planetary atmospheres. Figure 1.22 from Snellen et al. (2009) shows the phase curve of the exoplanet CoRoT-1b. Similarly to the secondary eclipse case, the flux from the planet has reflective and thermal components intertwined. Consequently, phase curves are wavelength-dependent. At shorter wavelengths (UV or visible), when the brightness of the planet is dominated by reflected light, the phase curve can be used to reveal longitudinal variation of the planet's albedo. On the contrary, at longer wavelengths (infrared), when the brightness is mostly thermal emission, the phase curve provides information on the longitudinal variation of the planet's temperature and chemical composition (Parmentier et al. 2018). Depending on whether the wavelength at which the phase curve is obtained corresponds to the absorption structure of a species present in the atmosphere or not, upper or deeper layers of the planet's atmosphere are probed (Kataria et al. 2016; Showman et al. 2009), which *in fine* can provide a two dimensional (longitude, depth) mapping of the atmosphere's structure (Cowan et al. 2018)

Three observables are important for phase curve analysis:

1. The depth of the secondary eclipse $\Delta F_{occ}$. I showed in the previous paragraph that $\Delta F_{occ}$ gives access to the day-side brightness.

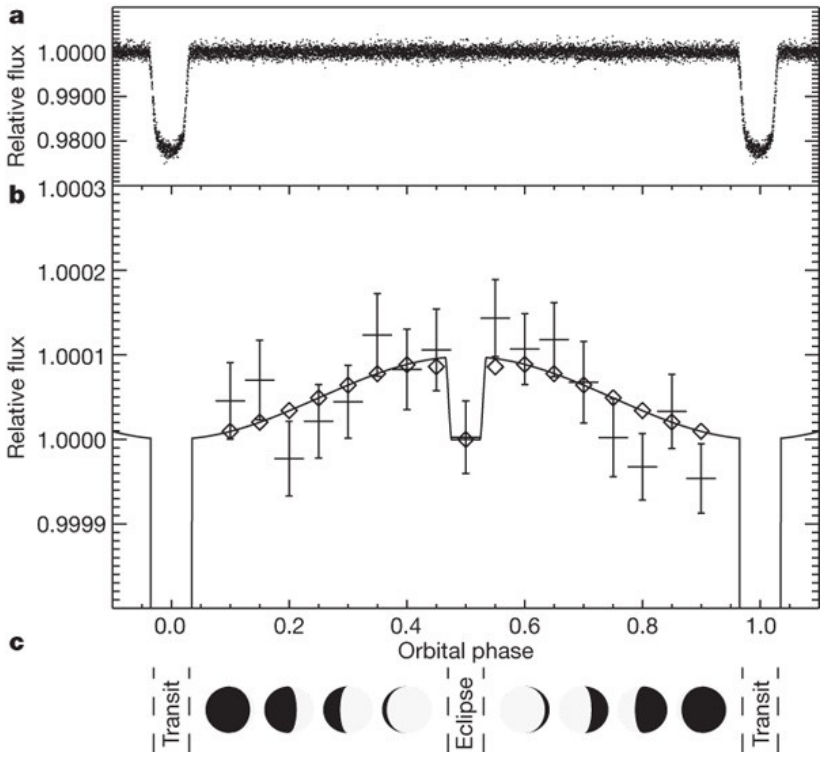


**Fig. 1.22** Optical phase variation for CoRoT-1b centred on the planetary eclipse observed over 55 days (36 orbits), and phase-folded at the orbital period P = 1.5089557 days. *Top panel*: unbinned data. *Middle panel*: data binned in phase intervals of 0.05. The solid curve is the best fit model to the unbinned data assuming uniform (but distinct) surface brightness for the day-side and night-side hemispheres. *Bottom panel*: schematic of the day-side hemisphere rotating into view, being eclipsed by the star, and rotating out of view again. Figure from Snellen et al. (2009).

2. The phase offset, which is the difference between the phase of the maximum of the phase curve to the phase of the secondary eclipse. It gives information on the localisation of the brightest spot on the planet compared to the sub-stellar point. Planets with a high equilibrium temperature, dominated by thermal emission, have a positive phase offset (meaning the hottest spot of the atmosphere lays eastward of the sub-stellar point) whereas planets with a low equilibrium temperature, dominated by reflected light, have a negative offset (indicating the presence of reflective material such as clouds on the western part of the day-side). Phase offsets are indicative of the existence of atmospheric dynamics happening on the planet such as circulation processes. Such effects are particularly strong for tidally-locked planets that show always the same side to their host star.

3. The phase curve relative amplitude, $A = (F_{p,max} - F_{p,min})/F_{p,max}$. It informs us on the day-night temperature contrast. As we have seen above, the amplitude of the phase

curve is wavelength-dependent, it is larger if the atmospheric layer probed is shallower (inside molecular bands) and smaller if the atmospheric layer probed is deeper (outside molecular bands).

Now that I have given a comprehensive description of the detection and characterisation of transiting planets, I will approach the specific case of planets orbiting M-dwarfs stars.

## 1.3 Planets orbiting M dwarfs stars

Over the past decade, more and more interest has been given to terrestrial planets orbiting M-dwarf stars. While increasing detections and follow up observations of planet around M stars have been performed with ground- and space-based facilities, several theoretical studies have also been carried out to further constrain their climate and potential habitability, as well as the importance of their interactions with their host star. In this section, I first introduce M-dwarfs stars and explain the opportunity they represent for the search for potentially habitable planets. Then, I discuss their specific dynamic, climate, and environment, including star-planet interactions.

### 1.3.1 The M dwarfs opportunity

#### Spectral type

M-dwarfs are the faintest, coolest, and smallest kind of main-sequence stars, and are therefore located in the bottom right corner of the Hertzsprung-Russell (HR) diagram (Figure 1.23). The main sequence is the region of the diagram in which stars are carrying out stable hydrogen fusion in their core. M dwarfs have small masses and radii, between 0.6 to 0.08 $M_{\odot}$, and 0.6 to 0.1 $R_{\odot}$. They form similarly to every other stars: first a cloud of dust and gas gravitationally collapses due to an external force (supernovae shock-wave, stellar winds for O, B stars, etc). By conversation of the angular momentum, the cloud rotates faster as it collapses. It also flattens and starts to form an accretion disk with a protostar embedded at the centre. The protostar gets more and more luminous as matter (gas and dust) falls down towards the centre of the disk. Then once the core of the protostar reaches critical temperature and pressure, hydrogen fusion begins. The energy released by fusion opposes the gravitational contraction of the star on itself (creating an hydrostatic equilibrium). At that stage, the star has reached the main-sequence. The end of the main sequence occurs when the star has depleted all the hydrogen in its core.

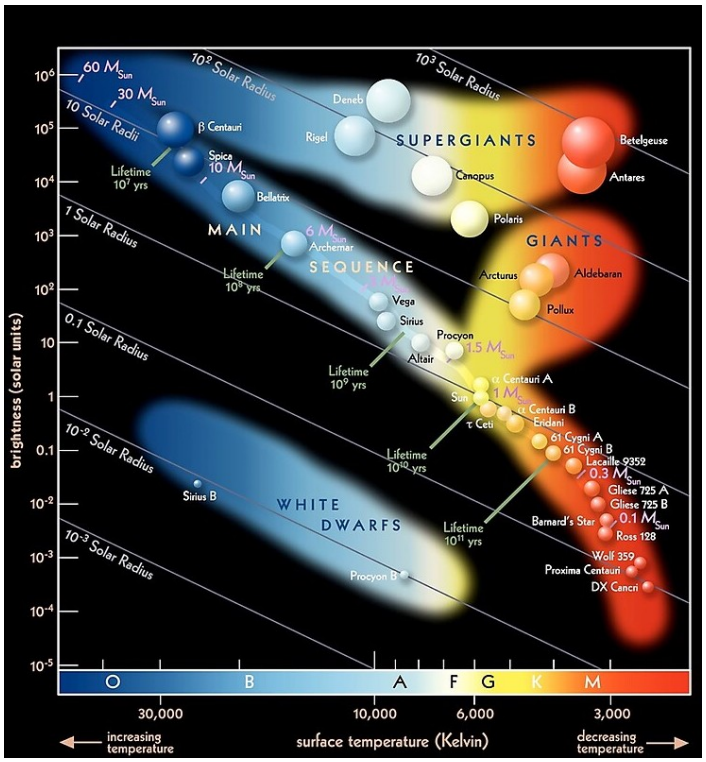


**Fig. 1.23** Hertzprung-Russell diagram. The temperature of stars are plotted against their luminosity. The position of a star in the diagram provides information about its present stage and its mass. Stars that burn hydrogen into helium in their core lie on the diagonal branch, the so-called main sequence. Red dwarfs like Proxima Centauri lie in the cool and faint corner (bottom-right). When a star exhausts all the hydrogen, it leaves the main sequence and becomes a red giant or a supergiant, depending on its mass. Stars with the mass of the Sun which have burnt all their fuel evolve finally into a white dwarf (bottom-left corner). Credit: ESO.

M dwarfs have lifetimes (much) longer than the Sun's. The lowest-mass specimens could burn for trillion of years (Cockell 2015). As a comparison, an M3V type star lives ≃15 times longer than the Sun (which is an G2V type star). This value goes up to ≃650 times for an M9V star. We note that spectral types are defined by the absorption lines seen in the star's spectra, and can roughly be seen as another way to define the effective temperature of stars. The number "2" in G2V is the sub-type which is also dependent on the temperature (the smaller the sub-type, the hotter the star). Then the "V" from G2V indicates that the star is on the main sequence phase.

M-dwarfs' spectra show specific spectral features. Indeed, their spectra get more and more complex as the stellar sub-type increases, because of the increasing presence of billions of weak molecular lines (titanium oxide $TiO$, vanadium oxide $VO$, water $H_2O$, carbon monoxide $CO$, iron $FeH$, etc), that blend with other atomic lines and "pollute" the continuum of the spectra. Figure 1.24 shows the difference between the spectrum of a G2V star's (like the

Sun) and those of an early (M3V) and a late M-dwarf star (M8V). Constructing theoretical

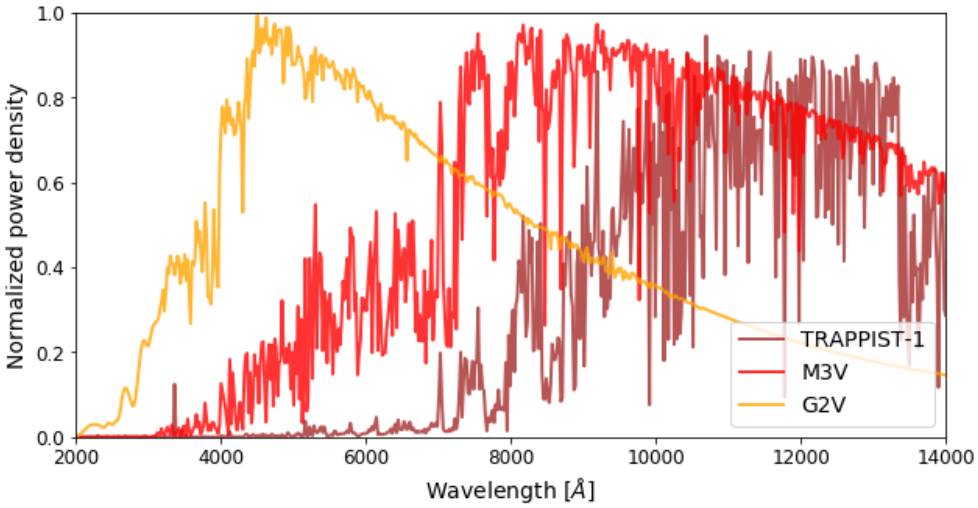


**Fig. 1.24** Normalised spectra of a G2V, a M3V, and TRAPPIST-1 (M8V) stars. The spectral resolution is 20 Å for each spectrum. This figure was produced using the STSCI HAZMAT Archival data.

spectra for M-dwarfs is particularly complicated as computationally intensive modelling of convection in low-mass stellar interiors and molecular composition are required (Allard et al. 2000; Browning 2008). Consequently, estimation of physical parameters from spectroscopic modeling, as is done for solar-type stars, is challenging for M-dwarfs. Several studies have developed empirical methods to derive their stellar properties. For instance, M-dwarfs in wide binaries with FGK dwarfs (whose metallicities can be measured via comparison of observed spectra to theoretical models) have been used to provide benchmarks for measuring M-dwarfs metallicities (Bonfils et al. 2005; Mann et al. 2014; Neves et al. 2014). Similarly, mass, radius, and effective temperature have been derived for M dwarfs in eclipsing geometries with other stars (Carter et al. 2011; Chew et al. 2014; R. J. Jackson et al. 2009). Alternatively, for M-dwarfs close enough to have their diameters directly measured via interferometry, radius and temperature can be directly inferred (Braun et al. 2011; 2012). Recently, thanks to the Gaia mission (Collaboration et al. 2016), very precise parallax measurements of nearby M dwarfs has drastically reduced systematic error on their radii and refine their uncertainties (and correspondingly, the radii of their planets) (Dittmann et al. 2014). Indeed, precise knowledge of stellar parameters of M-dwarfs are all the more important that they are essential to reliably characterise potential planets orbiting these stars as they can profoundly affect the interpretation of the planet's composition (Shields et al. 2017).

Besides, it is important to highlight that M dwarfs can have observable signatures of activity that include: significant X-ray emission, $H_\alpha$ in emission (as well as spectral features), high rotation rates, and spot coverage. All these phenomena are associated with the strength of the

star's magnetic field. These signatures of magnetic activity in their atmospheres are linked to their age and physical properties (Shields et al. 2017). For instance, there are clear evidences of the existence of rotation-age and mass-period relations in M-dwarfs populations, as shown by E. R. Newton et al. (2016). Furthermore, magnetic activity of M-dwarfs (traced by the presence of $H_\alpha$ in emission) appears to decrease with age (A. A. West et al. 2006; 2008) and seems to have finite lifetimes from $\simeq$ 1-2 Gyr for early-type M dwarfs (M0-M3) to $\simeq$ 7-8 Gyr for later type stars (M5-M7) (A. A. West et al. 2011). In addition, $H_\alpha$ emissions have been found to correlate with X-ray emission (Covey et al. 2008; Reid et al. 1995) which could also jeopardise the habitability of extra-solar planets orbiting M-dwarfs as I will discuss in the next paragraph.

Finally, M dwarfs are the largest population of main sequence stars, representing $\simeq$ 70% of the stars in our galaxy (Bochanski et al. 2010). This, combined with their exceptionally long lifetime suggest that, from a purely statistical consideration, they may be the best places to look for life elsewhere in the universe (Shields et al. 2017). A comprehensive description of the opportunity in studying planets around M-dwarfs is given in the next paragraph.

#### Planets around M-dwarfs

Several factors conspire to make M-dwarfs ideal laboratories for exoplanet search, in particular for the study of potentially habitable terrestrial planets:

- First, because of the small size of the host star, transits of planets (notably terrestrial) are easier to detect. An Earth-sized planet induces transit depths of 1.3 mmag for an M4V type host star and 8.4 mmag for an M8V type star, as opposed to 0.084 mmag for a Sun-like star (Charbonneau et al. 2007).

- Second, the lower luminosity of M-dwarfs translates into shorter orbits for planets in their habitable zone. For instance, an Earth-like-irradiation around an M4V type star would be located at 0.077 AU, and at 0.017 AU for an M8V type star. As a direct consequence of equations (1.8) and (1.10), the primary and secondary eclipse probabilities of planets in the habitable zone of M-dwarfs are therefore increased. As a comparison, the probability of a transit for a planet residing at the inner edge of the habitable zone is 1.5% for an M4V dwarf, 2.7% for an M8V dwarf where as it is only 0.47% for the Earth-Sun system (Charbonneau et al. 2007).

- Third, because HZ planets orbit closer to their stars, transits are more frequent. Indeed, we expect orbital periods of 15 days and 2.5 days at the inner edge of habitable zone

of M4V and M8V type stars, respectively. This factor turns out to be essential for improving the photometric precision on transit light curve observations.

- Fourth, the occurrence rate of small planet around M-dwarfs is larger than for FGK stars. Indeed, Mulders et al. (2015) demonstrate that small (between 1 and 4 $R_\oplus$) planets around M stars occur twice as frequently as around G stars, and thrice as frequently as around F stars.

For all these reasons, more and more surveys have been fully or partially dedicated to the detection and characterisation of planets orbiting M-dwarfs stars such as: the M-Earth project (Nutzman et al. 2008), project EDEN (Gibbs et al. 2020), the SPECULOOS project (Burdanov et al. 2017; Delrez et al. 2018b; Sebastian et al. 2020), the SPIROU instrument (Donati et al. 2018), the TESS survey (Ricker et al. 2014), the CARMENES instrument (Quirrenbach et al. 2014). So far $\simeq$ 250 planets have been found orbiting M-dwarfs (including all sub-types) according to the NASA Exoplanet Archive, as show on Figure 1.25. In this

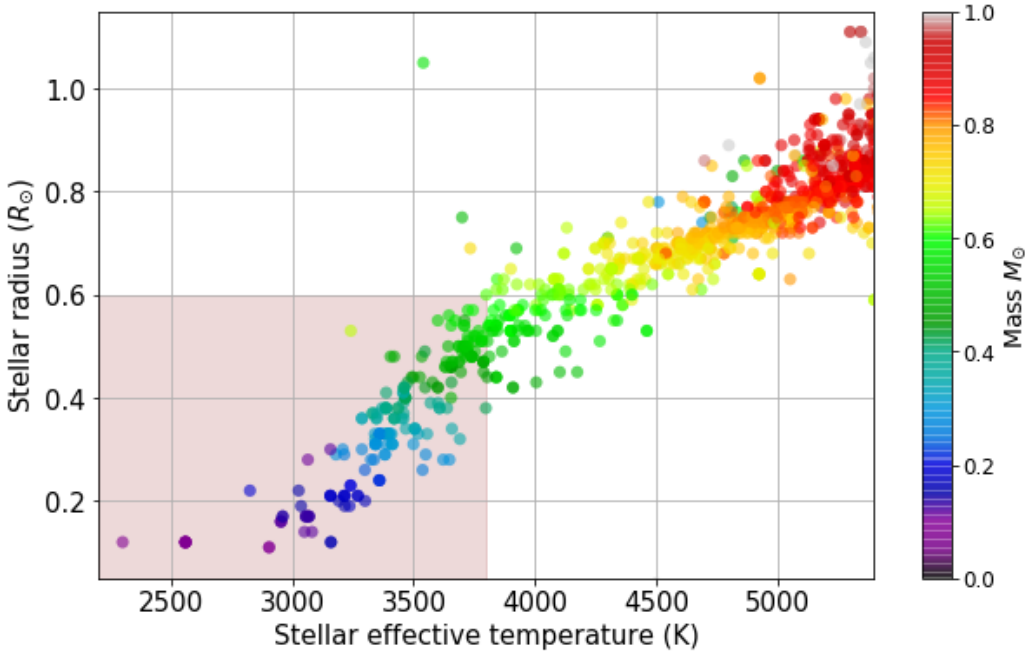


**Fig. 1.25** Population of planets detected around stars with effective temperature lower that 5400K and radii smaller that 1.1 $R_\odot$ at the time this thesis is written (April 2021). Planets around M dwarfs stars are the ones within the red rectangle. The colour bar indicates the mass of the stars. Figure produced using data from the NASA Exoplanet Archive data.

section, I explained that M stars are very different from our Sun and showed that their planetary population present many advantages for detection and characterisation, notably with the transit method. Yet, in such particular environment, we expect those planetary

systems to be drastically different from our own solar system. In the next section, I give an overview of the environment and properties of these planets.

### 1.3.2 Environment of planets orbiting M dwarfs

#### Dynamics

The climate of exoplanets orbiting M-dwarfs should be extremely dependent on the dynamical interactions with their host star and potentially with other planets in the system. The short orbits of planets around M-dwarfs imply that they can experience tidal forces orders of magnitude larger than the Earth, which can cause deformations of the solid body (in the case of a terrestrial planet) or the envelope (in the case of a gaseous planet) able to impact their energy budget, surface conditions, and atmospheric properties. Indeed, such deformations can induce the dissipation of a large quantity of energy through a process called tidal heating. Tidal heating can be quantified with the tidal heating rate $H_r$ (B. Jackson et al. 2008):

$$H_r = \frac{63}{4} \frac{(GM_\star)^{3/2} M_\star R_p^5}{3Q_p/2k} a^{-15/2} e^2, \tag{1.33}$$

where $Q_p$ and $k$ are the tidal dissipation parameter and Love number, respectively. More precisely, $Q_p$ represents the planet's response to tidal processes and combines a myriad of internal properties, such as density, equation of state, etc (R. Barnes et al. 2009b). We note that the tidal heating rate increases as the planet gets closer to its star (the semi-major axis $a$ decreases) but decreases as its orbit circularises (the eccentricity $e$ decreases).

Planets in the habitable zones of M dwarfs are so close to their host that tidal evolution can lead to major orbital effects such as orbit "shrinking", orbit circularisation, evolution toward zero obliquity, and planet spins-orbit periods resonances[1] or even synchronisation. In particular, planets around very-late M dwarfs are very likely to be circularised within 1 Gyr only (R. Barnes 2017). When planets are synchronous rotators, we say they are tidally locked, their rotation is synchronous with the star such that the same face always faces the star meaning the planet would have one side in eternal sunlight and the other in perpetual darkness. Such a configuration has been a source of concern for planet habitability (Meadows et al. 2018b). However, over the past decade great improvements in modelling has caused opinion on the effect of this spin state on planetary habitability to shift. It has indeed been shown that if a planet is synchronously rotating and has a dense enough atmosphere

[1] Spin-orbit resonances happen when the orbital period of the planet and its rotation period are commensurable. We say it is synchronous in the specific case of 1:1 spin-orbit resonance, e.g the orbital period is exactly equal to the rotation period, as it is the case for Moon and the Earth.

(containing greenhouse gases such as $CO_2$) it should distribute efficiently enough its heat to the night side so to prevent a catastrophic collapse (freeze-out) of the atmosphere (Joshi 2003; Wordsworth 2015). Moreover, Yang et al. (2014) showed that, for planets with slow rotation rate and an ocean, synchronous rotation could even improve habitable surface conditions on planets orbiting at the inner edge of their stars' habitable zones, and extend the habitable zone for M-dwarf stars (Shields et al. 2017). This is explained by the fact that a slow rotating rate induces a weak Coriolis force which, combined to a long day time illumination (because they are synchronous), promotes strong convergence and convection in the sub-stellar region and results in the formation of optically thick clouds that eventually increase the planetary albedo.

Alternatively, some studies have considered the counter-balance effect of thermal atmospheric tides in comparison with the usual gravitational tides (Leconte et al. 2015). Thermal atmospheric tides or thermal tides are large-scale mass redistribution inside the atmosphere. We experience thermal tides every day on Earth as the atmospheric temperature oscillate between night and day. In addition, we observe a delay in the thermal response between solar heating and thermal inertia of the ground and atmosphere, which translates into the fact that the hottest moment of day happens a few hours after the moment when the Sun is directly overhead, as explained by Leconte et al. (2015). Interestingly, because the atmosphere and the surface are coupled by friction in the atmospheric boundary layer, the angular momentum transferred from the orbit to the atmosphere is then transferred to the bulk of the planet, and eventually modify its spin. This effect is negligible on Earth but is very strong on Venus for instance, where thermal tides fight against the state of synchronous rotation and are responsible for its slow retrograde rotation (Leconte et al. 2015). Back to planets orbiting M-dwarfs, it is believed that because they receive high stellar insolation, the resulting thermal tides could be large enough to act as an atmospheric torque that opposes tidally-induced spin synchronisation and consequently drives planets out of synchronous rotation (Correia et al. 2010; Cunha et al. 2015; Leconte et al. 2015).

In section 1.1.1, I highlighted the crucial role of plate tectonics for the carbon cycle and consequently for the development of life on Earth. The Universe is only 13.8 Gyr old, and M-dwarfs are not much older than G dwarfs from a statistical point of view, such that we can expect the planet orbiting them to have cooled down to the point where plate tectonics does not exist anymore, greatly jeopardising their habitability.

Interestingly, the effect of tidal heating could boost plate tectonics, favouring the replenishment of the atmosphere and planet's habitability in the process (R. Barnes et al. 2009a). Nevertheless, if tidal heating gets too strong it could result in intense global volcanism, as currently observed on Jupiter's moon Io, and rapid resurfacing that will affect the de-

velopment of a biosphere and ultimately render the surface uninhabitable. In that regard, R. Barnes et al. (2009a) defined the tidal habitable zone (THZ) as the region around a star where $h_{min} < h < h_{max}$ with $h$ being the heating flux defined as $h = H_r/(4\pi R_p^2)$, $h_{min}$ being the minimum internal heating flux required to drive plate tectonics and $h_{max}$ being the maximum heating flux the planet could have before undergoing intense global volcanism and rapid lithosphere recycling (R. Barnes et al. 2009a). Figure 1.26 shows the inner and outer edges of the THZ compared to the CHZ (conservative habitable zone) (defined in Section 1.1.2). Be-

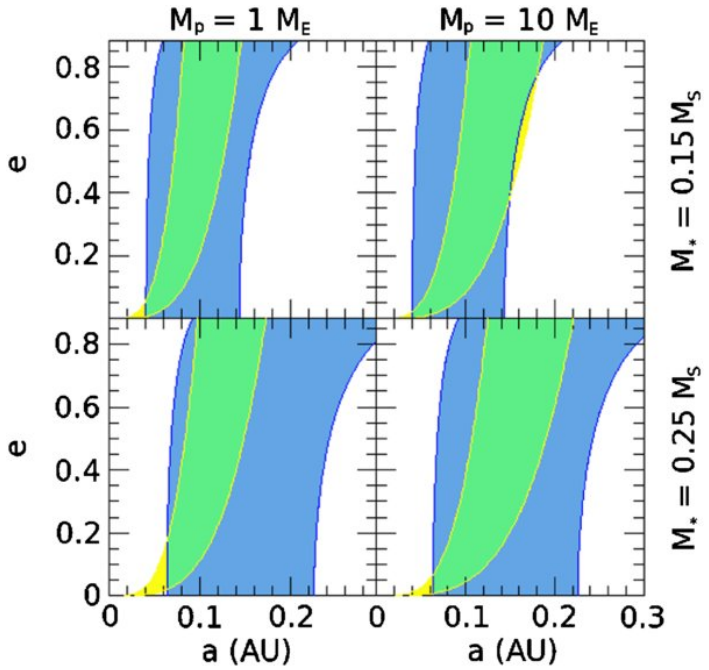


**Fig. 1.26** Comparison of the tidal HZ with the conservative HZ. *Upper-left panel*: Yellow regions represent regions in which tidal heating of a planet with a mass of $M_p = M_\oplus$ is favourable for habitability for a late M star with $M_\star = 0.15 M_\odot$. The blue region is the conservative habitable zone derived from estimates of stellar flux and assuming an Earth-like atmosphere (Selsis et al. 2007). The green region represents the overlap of the two types of habitability. *Upper-right panel*: Similar to upper-right with $M_p = 10 M_\oplus$. *Lower-right panel*: Similar to upper-right with $M_\star = 0.25 M_\odot$. *Lower-left panel*: Similar to upper-right, with $M_p = 10 M_\oplus$ and $M_\star = 0.25 M_\odot$. Figure from R. Barnes et al. (2009a).

sides, we note that, according to equation (1.33) if the planet has a circular orbit there should be no heat flux from tidal heating, such that without any radiogenic heating (from radioactive decay, as it happens on Earth), the planet would become uninhabitable (R. Barnes et al. 2009b). Nevertheless, this situation can be avoided if there exist other planets in the system that perturb the orbit and prevent the eccentricity from being exactly null. Fortunately, recent theoretical works and observations suggest that not only the occurrence rate of small planets is higher around M-dwarfs stars, but they are also more likely to reside in multiple-planet

systems (Lissauer et al. 2012). In addition, as shown by Fang et al. (2013), the large majority of multiple-planet systems around M-dwarfs stars exist in close, dynamically packed orbits creating stronger gravitational effects. This could result in significant effects on dynamical stability, the evolution of the planets' orbital parameters (such as eccentricity and semi-major axis) and even on the climate of the planets. Interestingly, such gravitational effects are observable for transiting planets in multiple-planet system around M dwarfs though transiting timing and duration variations Agol et al. 2018.

Planets in such systems gravitationally interact with each other so that their orbits slightly deviate from strict Keplerian ones over time. In the case of a transiting exoplanet, a non-Keplerian orbit implies that the planet's transits are no longer exactly periodic, creating transit timing variations (TTVs) and transit duration variations (TDV). TTVs depend sensitively on the masses and orbital configuration of the planets in the system (Agol et al. 2018). The monitoring and analyses of TTVs can therefore provide a powerful method to solve the inverse problem of determining planets' masses and orbits from their transits (providing TTVs are detectable). Similarly, the observations of TDVs can have several origins (Agol et al. 2018): the existence of a torque due to the rotational oblateness of the star that modifies the transit shape, the result of eccentricity variations due to a resonant interaction with the other planets that consequently modify the speed at which the planet moves along the transit chord, or even the precession of the orbital plane of the planet due to the torques from other planets that induce inclination variations which directly affect the duration of the transit (as shown by equation (1.11)).

In particular, if the planets are in (or near) mean motion resonance, the exchange of energy and angular momentum at each planet conjunction adds coherently and results in larger TTVs/TDVs that are easier to detect. We say that planets are in mean motion resonance (MMR) when their mean motions are related by commensurabilities of the form $\frac{n_2}{n_1} \simeq \frac{p}{p+q}$, where p and q are integers and q gives the order of the resonance. In that regard, transiting systems in MMR are particularly interesting targets for in-depth characterisation as this configuration allows us to infer several physical parameters of the systems/planets from TTV/TDV analysis.

Since the Kepler mission, several TTV or/and TDV studies of resonant systems have been carried out such as Almenara et al. (2015), Becker et al. (2015), Dawson et al. (2014), Fabrycky et al. (2012), Hinse et al. (2015), Mills et al. (2016), 2017, Nesvorny et al. (2013), Nesvorný et al. (2016), Sanchis-Ojeda et al. (2012), Steffen et al. (2012), and Szabó et al. (2012) among many others. Through TTV and TDV analyses, dynamical diagnostics of the planets were drawn, revealing their orbital configuration, their masses and - in combination with their transit-derived radii - their densities, an essential parameter to constrain the

potential habitability of a temperate rocky planet. We will discuss TTV analysis in more details in Chapter 4.

### Radiations and habitability

Climate and dynamics are completely intertwined. As we saw in the previous paragraph, almost all dynamical effects have consequences on the planet's atmosphere. For instance, for a tidally locked planet, atmospheric circulation can appear to decrease contrasts of temperature between day and night sides. In this paragraph, I will specially focus on the atmospheric structure of planets orbiting M dwarfs, and the impact of their interactions with their host stars on their potential habitability. Over the past decade, thanks to the development of 3-dimensional global climate models (GCMs), the theoretical surface and atmospheric properties of planet orbiting M dwarfs stars have been extensively explored.

First, Hu et al. (2014) underlined the crucial role of ocean heat transport in the climate state of tidally locked planets. They used fully coupled atmosphere–ocean general circulation models to conclude that ocean heat transport should substantially extend the area of open water along the equator that is expected for a tidally locked planet in orbit around an M-dwarf, showing a lobster-like spatial pattern of open water, instead of an "eyeball". For sufficiently high greenhouse-gases concentrations or strong stellar radiation, ocean heat transport is more efficient than atmospheric heat transport and can induce deglaciation on the night-side, greatly enlarging the habitable surface area of tidally-locked planets. They also investigated the effect of the deepness of the ocean as they expect strong equatorial currents. Their conclusion is that ocean heat transport should be enhanced with ocean deepness (providing continents don't block such circulation).

Then, concerning the composition of atmospheres, it is important to notice that gases that strongly absorb in the mid-IR and near-IR are of particular interest for planet around M dwarfs. Indeed, works such as Selsis et al. (2007) showed that the larger absorption cross sections of $CO_2$ and $H_2O$ in the near-IR should result in a smaller broadband planetary albedo for planet orbiting M dwarfs compared to those around Sun-like stars. Furthermore, the same spectral dependence explain why the strength of the ice-albedo feedback is expected to be less important for planet around M stars (as they primarily emit in the near IR, where the snow and ice albedo is low) (Joshi 2003; Paris et al. 2013). Remarkably, a decreased albedo could allow such planets to reside further away from their host than expected while still being in the HZ (Kasting et al. 1993; Paris et al. 2013; Selsis et al. 2007).

In addition, in terms of detectability of molecular spectral features in planetary atmospheres, Wunderlich et al. (2019) predicts an increased detectability of $CH_4$, $H_2O$, and $CO_2$ in the

middle atmosphere (stratosphere and mesosphere) of Earth-like planets around M-dwarfs compared to the Earth around the Sun. In particular, Rugheimer et al. (2015) highlighted that the activity and sub-type of an M star has a further impact on this detectability. The abundances of $O_3$ increases for planets around active M dwarfs and decreases for planets around inactive M dwarfs. On the opposite, low levels of UV flux around inactive M dwarfs could lead to a build-up of molecules such as $CH_4$ and $N_2O$ in the atmosphere of an Earth-like planet (Rugheimer et al. 2015).

More specifically, M-dwarfs intense magnetic activity is characterised by the presence of spots, faculae, stellar cosmic rays, coranal mass ejection (CME) and flares (from "microflares" $\simeq 10^{29}$ ergs in the U band, to high energy flares with total energies as large as $10^{34}$ ergs (Hawley et al. 2014)). Such activity originates from the interaction of the star's atmosphere with its magnetic field driven by their mostly (early M) or totally (late M) convective interiors (Tilley et al. 2019). Since the habitable zone of M stars is located at only a fraction of an AU, the energy flux from these events can be at least an order of magnitude stronger compared to Earth. The most active stars have been observed to produce dozens of flares per day (with total energies $\simeq 10^{30}$ erg) and super flare events ($\simeq 10^{34}$ erg) every month. Worryingly, flares can lead to atmospheric erosion and destroy ozone layers on oxic planets (Tilley et al. 2019; Valio et al. 2018). While, some studies (Kiang et al. 2007) predict that underwater organisms would still be able to survive UV flares from young M stars, others (O'Malley-James et al. 2017) suggest that an eroded or anoxic atmosphere would allow more UV to reach the surface, making environments hostile even to highly UV tolerant terrestrial extremophiles. According to Segura et al. (2010), the UV radiations of a single high energy flare (such as the 1985 April 12 flare from the M dwarf AD Leonis (Hawley et al. 1991)) on the atmospheric chemistry of an habitable planet (assuming similar composition to that of present Earth) does not produce a significant change in the ozone column depth of the planet. However, the additive effects of repeated flares observed on certain M stars may drive extreme losses of oxygen for an Earth-like planet within a short period of time (Tilley et al. 2019) as the planet may not return to equilibrium before another flare occurs.

On the other hand, several studies revealed that flares on M dwarfs could have positive and even essential effects for the apparition and development of life:

- For instance, it has been demonstrated that for late M dwarfs, the UV flux brought by flares could be essential to drive UV-sensitive prebiotic chemistry that may have been important to abiogenesis, notably for the synthesis of pyrimidine ribonucleotide, as the UV flux from the star alone would be insufficient (Ranjan et al. 2016). Pyrimidine ribonucleotide is essential as it may allow RNA synthesis (see Section 1.1.1) and eventually help initiating prebiotic chemistry (Rimmer et al. 2018). However, the main

path to synthesise pyrimidine ribonucleotide is from hydrogen cyanide and bisulfite in liquid water, and is likely driven by photochemical processes in the presence of ultraviolet (UV) light. In that regard, Rimmer et al. (2018) defined the "abiogenesis zones" around stars of different stellar types depending on whether their UV fluxes provide sufficient energy to build a sufficiently large prebiotic inventory, as shown on Figure. 1.27. I will discuss the abiogenesis zone in further details in Chapter 4.

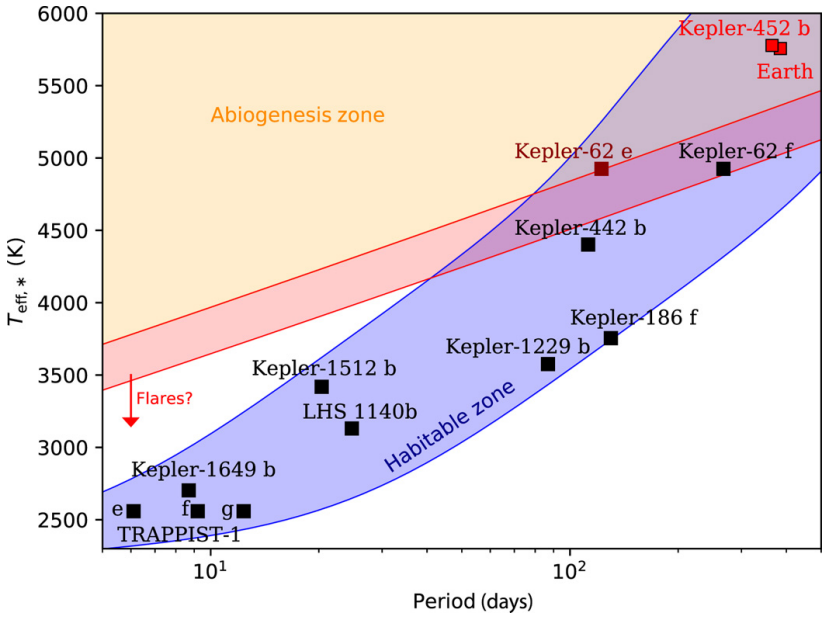


**Fig. 1.27** The abiogenesis zone. This plot shows the stellar host effective temperature versus planet orbital period of confirmed exoplanets within the liquid water habitable zone (and Earth), taken from a catalogue (Angelo et al. 2017; Kane et al. 2016; Morton et al. 2016), along with the TRAPPIST-1 planets (Gillon et al. 2017b) and LHS 1140b (Dittmann et al. 2017). The "abiogenesis zone" indicates where the stellar UV flux is large enough to result in a significant yield of photochemical product (threshold set to 50%). The red region shows the propagated experimental error. The liquid water habitable zone as defined by R. K. Kopparapu et al. (2013) is also displayed. Figure from Rimmer et al. (2018).

- Besides, Mullan et al. (2018) showed that flares would be the only way to bring oxygenic photosynthesis' effectiveness on planets in the HZ of M dwarfs up to values comparable to those on Earth (in particular for late M dwarfs). This is explained by the fact that the quiescent (non-flaring) state of the star would not supply enough visible photons (with wavelengths between 400 and 700 *nm*) required for oxygenic photosynthesis. In addition, Mullan et al. (2018) suggested that the "yearly" cycle of growth and dormancy characteristic of many plants on Earth might be replaced by the activity cycle of the star for M dwarfs planets as photosynthesis would be enhanced by radiation from flares.

Finally, intense XUV radiation from M dwarfs has been considered as a possible path to turn small planets with large $H/He$ gas envelopes into habitable planets. As a matter of fact, statistical studies of Kepler planets found that a significant fraction of close-in, small planets have large $H/He$ gas envelopes (Shields et al. 2017; Wolfgang et al. 2015). Owen et al. (2016) looked at the impact of the strong stellar activity of M stars on such hydrogen-rich envelops and showed that their intense XUV radiations can lead to photo-evaporation of these gas envelopes through hydrodynamic escape and ultimately to more habitable environments. They note that this process is dependent on the mass of the core of the planet, possible only for low mass cores $\simeq 1 M_{\oplus}$, as above this value the planet retains most of its initial voluminous $H/He$ envelope. With similar processes Luger et al. (2015) showed that the extended pre-main sequence contraction phase of M dwarfs may cause the habitable zones of these stars to move inwards by up to an order of magnitude in semi-major axis over the course of the first several hundreds Myr. Indeed, M dwarfs take up to 1 Gyr to reach the main sequence because of their extended Kelvin-Helmholtz contraction timescales (Baraffe et al. 1998), a period during which their luminosity can be two orders of magnitude larger (Luger et al. 2015). Since terrestrial planets are expected to be formed in 10 to 100 Myr (Raymond et al. 2007), they should thus endure a long period of high stellar irradiation before eventually reaching the habitable zone. Luger et al. (2015) predicts that such a configuration could result in planets around M dwarfs undergoing a runaway greenhouse state for several millions years. Over this period, planets will be bombarded with XUV radiation that will induce photolysis of water vapour in the stratosphere followed by the hydrodynamic escape of the upper atmosphere (Luger et al. 2015), as predicted by Owen et al. (2016). From this observation, it is possible that the only way to form volatile-rich Earth-sized planets around M-dwarf stars may be through the evaporation of the $H/He$ envelopes of mini-Neptunes by XUV radiation followed by inward migration toward the parent star (Luger et al. 2015). However, in the situation where the planet becomes totally desiccated and inhabitable, a large amount of oxygen (resulting from the photolysis of water) will build up in the atmosphere (if no efficient oxygen sinks are present) to the point where these planets will become oxygen-rich. Such a scenario where large amounts of abiotic oxygen accumulate in the atmosphere is a typical false-positive scenario biosignature (see Section 1.1.2).

Similarly, Gao et al. (2015) studied the impact of the long pre-main sequence of M dwarfs on a desiccated (poor in $H_2O$) $CO_2$-rich atmosphere. They conclude that depending on its initial atmospheric hydrogen content, the atmosphere could turn out to be depleted in $CO_2$ while producing abundances of abiotic $O_2$ and $O_3$, posing here again as false positive in the search for biosignatures.

Aside from radiations, CMEs, which are large expulsions of plasma from the star's corona with strong magnetic field, are also expected to impact planet orbiting in the HZ of M dwarfs. Kay et al. (2016) predicts that the frequency of CME impacts for planets around M star should be 2 to 20 times the average at Earth during solar maximum (Kay et al. 2016), such that the planetary magnetic field needed to shield efficiently those planets from CME impacts (and maintain an atmosphere) would have to be tens to hundreds of Gauss, which seems very strong for such rocky planets (but not impossible) (Kay et al. 2016; Lammer et al. 2007). Moreover, studies such as Lammer et al. (2007) suggested that the magnetic moments of tidally locked planets around M dwarfs may be weakened, further hindering their ability to protect their atmospheres against CMEs. Fortunately, Driscoll et al. (2015) remarkably demonstrated that tidal heating can counter these pessimistic prospects. Indeed, the more tidal heating a planetary mantle experiences, the better it is at dissipating its heat, thereby cooling the core, which in turn helps creating the magnetic field and ultimately increases the chances for habitability. This is all the more verified (tidal heating process is more extreme) for late types M dwarfs(Driscoll et al. 2015).

Now that we have extensively discussed the environment of planets in the habitable zone of M dwarfs, it is important to quantify the detectability of spectral/photometric signatures with current and near-future instruments/observatories.

### 1.3.3 Detectability, the ultra-cool dwarf stars opportunity

Although all previous discussions on habitability and environment are fascinating, as an astronomers what interests me the most is to know whether we can confirm or discard any of these scenarios with data. Indeed, while simulations are essential, data are the key that orients research and drives the models.

So far a couple of hundreds of planets orbiting M dwarfs have been discovered. However, we noticed on several occasion already, in the previous sections, that all M dwarfs sub-types are not equivalent. In particular, the latest M-dwarfs - i.e. the lowest-mass main-sequence stars- stand out. They are also called ultracool dwarf stars (UCDS). In fact, the spectral type range of these stars extend beyond M, down to the L2 spectral type. It is also worth mentioning that UCDS are the stellar component of the "ultracool dwarfs" class which also encompasses brown dwarfs. These UCDS present several important features for the search and study of potentially habitable planets.

First, in terms of detection, they show the great advantage of being even smaller, cooler, and fainter than early- and mid-type M-dwarfs. Consequently, transits are deeper, more frequent, and more likely to happen. Figure 1.28 shows the number of eclipses (transits or occultations)

per year, the transit depth $\Delta F$, and the probability of transit $p_{transit}$ as a function of the stellar mass. Figure 1.28 makes it very clear that M dwarfs with masses $< 0.1 M_{\oplus}$ (.e.g UCDS) show

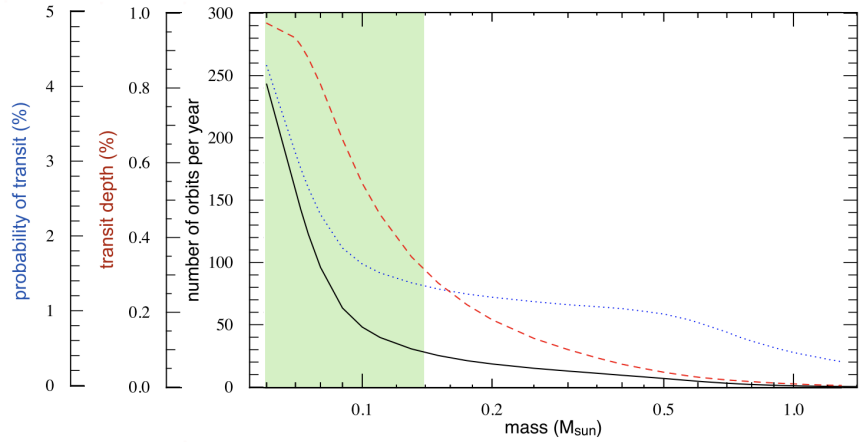


**Fig. 1.28** Evolution of the number of orbits per year, transit depth, and probability of transit as a function of the mass of the star. The green area is approximately where a $5\sigma$ detection of spectral signatures can be reached with the mission lifetime of JWST. Figure adapted from He et al. (2017) and Triaud et al. (2013).

great potential to detect more planets. For a given light curve, according to Pont et al. (2006), the signal to noise ratio (SNR) for a transiting planet is defined as follow:

$$SNR = \sqrt{\frac{\Delta F^2}{\sqrt{\frac{\sigma_w^2}{n} + \frac{\sigma_r^2}{N_{tr}}}}}, \tag{1.34}$$

where $N_{tr}$ is the total number of data points per star, $n$ is the number of points during the transit, $\sigma_w$ is the uncertainty of the white noise (uncorrelated noise), and $\sigma_r$ is the uncertainty of the red noise (due to the presence of systematics). For a given instrumental precision and a given Earth-like transiting exoplanet, the SNR will be higher for a UCD host star than for an early- or mid-type M-dwarf as $N_{tr}$, $n$ (which is inversely proportional to the semi-major axis $a$) and $\Delta F$ will increase. Similar conclusions can be derived for occultations.

Furthermore, the detectability of spectral features in transmission spectra and emission are also enhanced for UCDS. Wunderlich et al. (2019) studied the detectability of the most important features from 0 to 10 $\mu m$ in the transmission spectra of an Earth-like planet orbiting host star with spectral type from M1.5V to M8V using a coupled 1D climate-chemistry-model and assuming each of them are located at $10 pc$. Their results show that for all features, SNRs are greater for late-type M-dwarf planets than for early- to mid-type, almost twice as large for certain molecular species such as $CH_4$, $H_2O$ and $N_2O$. Figure 1.29 from Wunderlich et al.

(2019) illustrates these conclusions. In addition to enhanced spectral features detectability,

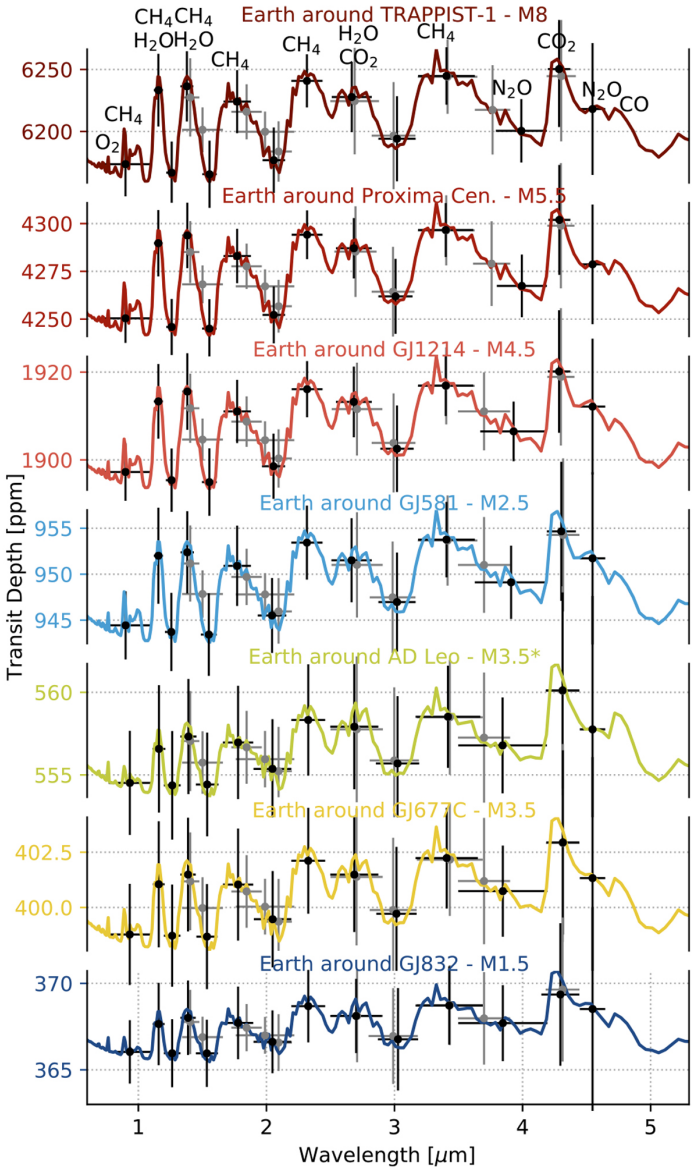


**Fig. 1.29** Transmission spectra for an hypothetical Earth-like planet orbiting in the habitable zone (HZ) of different types of M stars placed at 10pc. Coloured lines show the simulated transit depth of all hypothetical Earth-like planets around their M-host stars for a fixed resolving power of 100. Black dots show the simulated measurements that would be obtained using the JWST NIRSpec instrument in BOTS mode[2], with their error bars. Gray dots show the simulated measurements using JWST NIRCam instrument. Figure from Wunderlich et al. (2019)

Earth-like planet around late M stars are expected to have increased abundance of certain biosignature compounds such as $CH_4$ or $H_2O$. Indeed, Wunderlich et al. 2019 show that the type of the host star can has a direct effect on the abundance molecular species in the atmosphere of Earth-like planets around M-dwarfs. This is due to the fact that, as we move to

later types, the spectra are shifted to the near-IR, which lead to the built up of species such as $H_2O$, $NO_2$ or $CH_4$ and the decreased production of $O_3$ in the planetary atmosphere (because of weaker UV emission). This was also demonstrated by Rugheimer et al. 2015. As a results of lower $O_3$ abundance, the temperature profile of an Earth-like planet around a late M dwarf is expected not to show a temperature inversion (like we see in the Earth atmosphere). And enhanced $CH_4$ abundances is expected to lead to additional heating that can increase the temperature in the middle atmosphere of Earth-like planets around late-type M-dwarfs by up to 60 K (consequently slightly influencing on the edges of their HZ).

In parallel, as shown on Figure 1.29, the detection of spectral features on Earth-like planets around UCDS is feasible with telescope such as the JWST, where as it is challenging for early- and even for mid-type M-dwarfs. The JWST is a 6.5 m diameter space-based telescope - to be launched at the end of the year 2021 - that will be dedicating about 25% of its observing time to exoplanets and is equipped with a set of four instruments (NIRCam, NIRISS, MIRI, NIRSpec) capable of spanning a broad wavelength range (0.6-28$\mu m$), adapted to perform spectroscopy of exoplanets. Remarkably, because of its wide near-IR band pass, the JWST is particularly well suited to study transiting planets around late-type M-dwarfs, either in transmission or in emission.

## 1.4 Dissertation overview

In this first Chapter, I have showed that the search for life elsewhere in the universe is an extremely vast topic that requires very diverse knowledge. In the particular case of the search for life on exoplanets, I have presented the essential proxies that we rely on to orient our search: the habitable zone and the biosignatures. I have explained how some planets, and more generally systems, are more suitable than other. Notably, I have highlighted that UCDS are currently our best opportunity to detect and characterise potentially habitable planets in the next decade. In the rest of this thesis, I will describe my implication in the search for and study of potentially habitable planet eclipsing UCDS.

In chapter 2, I describe what is the SPECULOOS project, its objectives, the facilities, the instruments, the data, their analysis and its discoveries. In chapter 3, I particularly focus of the methods that I have used during my PhD, notably to analyse transit photometry. The first system discovered by SPECULOOS is the TRAPPIST-1 system. In only a few years, this system has imposed itself as the most amenable one for in-depth characterisation of HZ Earth-sized planets. For this reason, it was monitored extensively from space and ground. In Chapter 4, I present the work I have been leading on the analysis of the Spitzer space telescope *Red World* campaign and how it significantly improved our knowledge of the

TRAPPIST-1 planets. In Chapter 5, I describe the additional intense ground-based follow-up observations and how they helped deriving empirical constraints on the effect of stellar contamination on the transmission spectra of the planets. Finally in Chapter 6, I summarise my work and discuss some prospects for SPECULOOS and TRAPPIST-1 as well as my contribution to them.

# Chapter 2

# The SPECULOOS project

## 2.1 SPECULOOS

As we saw in Chapter 1, the most amenable target for biosignatures detection with up-coming observatories would be an habitable terrestrial planet transiting one of the nearest ultra-cool dwarf stars, i.e. a very-low-mass star with spectral type M7 or later. We defined ultra cool dwarfs (UCDS) as late M stars with spectral type M7V and later including brown dwarfs (BDs) (Kirkpatrick et al. 1995; 1997). The long-awaited James Webb space telescope (JWST) is expected to be particularly well suited for probing the atmospheric composition of such potentially habitable Earth-sized planet (Barstow et al. 2016; Morley et al. 2017).

I already mentioned a few transit surveys dedicated to the detection of planets around M dwarfs such as TESS (Ricker et al. 2014) or M-Earth (Nutzman et al. 2008). However, those surveys have a sweet-spot detection potential for mid-type M-dwarfs (M3-M5) and lack photometric precision to detect planetary candidates around UCDS. The latest type planet-host identified by TESS is LP 791-18, an M5±1 V star orbited by one super-Earth (1.1 $R_\oplus$), one sub-Neptune (2.3 $R_\oplus$) (Crossfield et al. 2019) and a temperate Earth-sized planet (Peterson et al. 2021). While the latest type planet-host identified by M-Earth is an M4.5 V type star, LHS 1140, which turns out to be orbited by two rocky planets with size 1.727 $R_\oplus$ and 1.282 $R_\oplus$ respectively (Dittmann et al. 2017; Ment et al. 2019). To fill the gap of knowledge on UCDS planetary population, a prototype search for habitable planets transiting ultra-cool stars was initiated in 2011 (Gillon et al. 2013) on the 60cm robotic telescope TRAPPIST (TRAnsiting Planets and PlanetesImals Small Telescope) located at La Silla Observatory (Chile) (Gillon et al. 2011). This prototype search consisted in the monitoring of 50 UCDS among the nearest and brightest in the southern hemisphere, for about 50 hours using a wide very-near-IR filter. The objective was to demonstrate the potential of this

concept by quantifying the photometric precision that could be reached on such stars, the impact of stellar activity in transit search (as M-dwarfs are considered active) and finally the incidence of the terrestrial atmosphere on very-near-IR ground-based observations. The results were extremely encouraging as they concluded that, when present, the variability of the UCDS (flares + rotation) does not limit the ability to detect transits, that no hint of significant extra-amount of correlated noise was noted compared to earlier-type targets, and that the photometric precision was sufficient for a $5\sigma$ detection of Earth-sized planets around UCDS (Gillon et al. 2013). These conclusions were strengthened by the detection of an amazing planetary system around one of the TRAPPIST-South UCDS target, an M8V type star renamed TRAPPIST-1 that we will discuss extensively in Chapter 4.

As we showed in section 1.3.3 the search for planet orbiting UCDS presents a unique opportunity for the search of life and is feasible from the ground with 60cm size telescopes according to the TRAPPIST-UCDTS mini-survey. In this context, the project SPECULOOS (Search for habitable Planets EClipsing ULtra-cOOl Stars) was created as an extension of the TRAPPIST-UCDTS mini-survey to thousands of UCDS by the University of Liège (Belgium) in collaboration with the Cavendish Laboratory at the University of Cambridge (UK), the University of Birmingham (UK), the Center for Space and Habitability of the University of Bern (Switzerland) and the Massachusetts Institute of Technology (MA, USA).

### 2.1.1 Facilities

The basic concept of the SPECULOOS project is to explore all UCDS within 40pc for transits, with a special focus on those that are bright enough in the near-infrared to make the atmospheric characterisation of Earth-sized planets with the JWST feasible. Before discussing the target selection and strategy of the survey (see section 2.1.2) I will present the different facilities and their technical characteristics. The SPECULOOS project relies on four different observatories spread at different locations in the world.

#### SPECULOOS-South Observatory

The SPECULOOS-South Observatory (SSO) is the core facility of the SPECULOOS project. It is located at the exceptional site of Cerro Paranal (Chile) which benefits from exquisite astronomical conditions. The facility is composed of four identical telescopes built by the German company ASTELCO [1], named after Jupiter's moons Io, Europa, Ganymede and Callisto because of the expected similarity of UCDS planetary systems with the Galilean

[1] http://www.astelco.com/

moons system. The four telescopes are shown on Figure 2.1. Each telescope is a Ritchey-

**Fig. 2.1** Photo of the four SPECULOOS-South telescopes at dusk. From left to right: Callisto, Ganymede, Europa, Io. Credit: Peter Aniol

Chretien, which is a specialised variant of the Cassegrain telescope that has an hyperbolic primary mirror and an hyperbolic secondary mirror, especially designed to eliminate coma (an off-axis aberration which results in stellar images being distorted, appearing to have a tail). The primary mirror is 1-m diameter and has an $f/2.3$ focal ratio coupled with a 28-cm diameter secondary mirror located at a relative distance of 1.6 m resulting in a system with a combined $f/8$ focal ratio. Both mirrors are covered with a raw aluminium coating (resulting combined reflectance curve is shown in Figure 2.2). The telescopes have a compact and open design with a lightweight optical tube assembly made of steel, aluminium and carbon fibre components (Jehin et al. 2018). This design provides high wind resistance, enabling observations in wind speeds reaching 50 km $h^{-1}$. The focusing of each telescope is achieved through motorised axial movement of the secondary mirror to an accuracy of $5\mu m$.

Each telescope is enclosed in a 6.25m-diameter circular building surmounted by an automated hemispheric wide-slit dome with sliding doors (visible on Figure 2.1), constructed and equipped with an automation system from ASTELCO (named AstelOS). The domes are made of aluminium painted in white to minimise internal heating during the day, and dark inside to minimise reflections during the night. The dome is slaved to the telescope and a complete azimuth rotation takes less than one minute. Each building also includes a small control room used from commissioning activities, equipment storage, and telescope control cabinets and computers. The distance between the domes is optimised to prevent vignetting of any telescope by another, down to 21° above the horizon.

Each telescope is associated with a robotic equatorial New Technology Mount NTM-1000 from ASTELCO. This mount uses direct drive torque motors, which allows very fast slewing

($8°/sec$, up to $20°/sec$ possible), accurate pointing (pointing accuracy better than $5''$) and tracking (tracking accuracy without auto-guider better than $1''$ over 10 min), without periodic errors. Such a good tracking accuracy can be achieved thanks to the high encoder resolution ($0.0029''$/increment) that allows to minimise jitter effects (Delrez et al. 2018b).

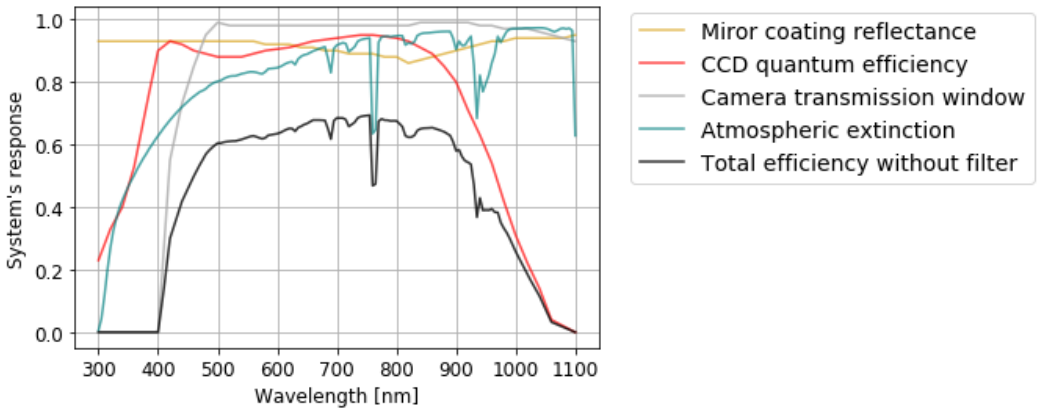


**Fig. 2.2** Overall system efficiency (black curve) taking into account the CCD quantum efficiency (red curve), the CCD window transmission (grey curve), the combined reflectance curve of the primary+secondary mirrors (shown here for one mirror, yellow line), and atmospheric extinction (for an airmass of 1.5, green line), but assuming no filter. Figure adapted from Delrez et al. (2018a).

Behind each telescope, an Andor iKon-L[2] thermoelectrically-cooled camera is mounted. This camera is equipped with a near-IR-optimised deeply depleted 2Kx2K e2v[3] CCD detector with 13.5 $\mu m$ pixel size. The field of view on sky is $12' \times 12'$, yielding a pixel scale of $0.35''$/pixel. The camera can be cooled down to -100°C (via five-stage Peltier cooling). We usually operate at -60°C with a dark current of $\simeq 0.1\ e.s^{-1}.pixel^{-1}$. The detector provides a good sensitivity from $\simeq 350\ nm$ (near-UV) to $\simeq 950\ nm$ (near-IR), with a maximum quantum efficiency of $\simeq$94% at both 420 and 740 $nm$, as shown on Figure 2.2 (red solid curve). However, the window of the camera is optimised for the visible/near-IR and blocks all wavelengths below $\simeq 400\ nm$, as shown on Figure 2.2 (grey solid curve). The camera also has a very low fringing in the near-IR (<1%) thanks to both the wedge-design of the window and e2v proprietary fringe suppression technology applied to the detector. There are 4 readout speeds available, up to 5 MHz. SPECULOOS observations are usually performed using the 1MHz readout mode, no binning and a gain of about 1.1 electrons $ADU^{-1}$, which provides a low readout noise of about 6.0 electrons.

In order to achieve high photometric precision the targeted star must be observed on the same few pixels of the CCD for a whole exposure sequence. This is done using an updated version

[2] http://www.andor.com/
[3] https://www.e2v.com/

of the DONUTS autoguiding system, described by McCormac et al. (2013). DONUTS is designed to fix stellar positions at the sub-pixel level (⩽0.2 pixel) for high-cadence time-series photometry, and also capable of autoguiding on defocused stars. The algorithm behind DONUTS works as follow: (1) when the first science image on a target has been acquired it becomes the reference image to which subsequent images of this field will be compared to determine guide corrections (2) when a second science image is acquired the corresponding pixel shifts in the X and Y directions from the reference image are calculated. These pixel shifts are then converted to telescope coordinates (e.g., right ascension and declination), sent to the mount, and the process is repeated for each image acquired (McCormac et al. 2013).

Each camera of each telescope has its own filter wheel from Finger Lakes Instrumentation[4] (model CFW3-10), which can host 10 different 5x5 cm filters. A selected set of broad-band filters, all manufactured by Astrodon company[5], is available on each telescope: notably the Sloan g', r', i', z' filters and two special exoplanet filters; the near-infrared luminance I+z filter (transmittance > 90% from 750 to beyond 1000 nm); and a blue-blocking filter called Exo (transmittance > 90% from 500 to beyond 1000 nm), both shown on Figure 2.3. Some

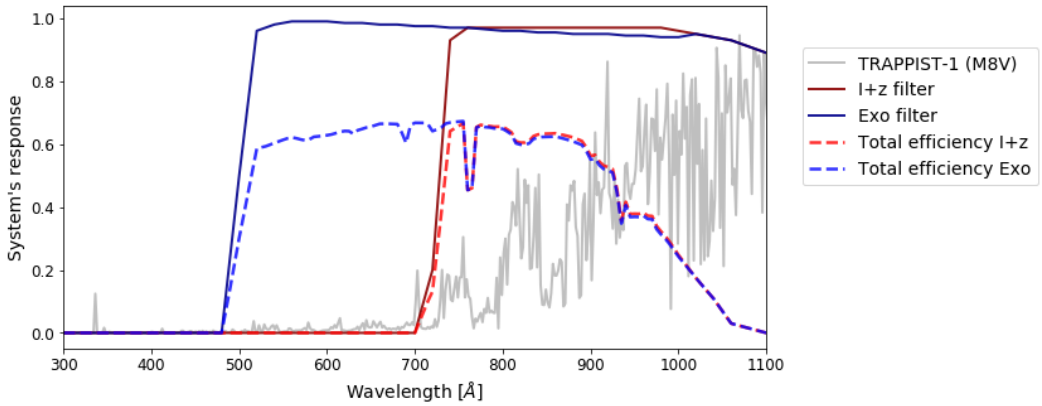


**Fig. 2.3** Transmittance of the two special exoplanet filters of the SSO telescopes compared to the spectrum of a well know ultra-cool dwarf star: TRAPPIST-1. The solid blue line shows the Exo filter bandpass and the solid red line shows the I+z filter bandpass. The blue and red doted line show the system efficiency through the Exo and I+z filters respectively. Finally the grey line shows the spectrum of an M8V type star (TRAPPIST-1) from the STSCI HAZMAT Archival data.

of the telescopes also provide broad-band Johnson-Cousins B, RC and V filters, the Sloan u' filter, and the Ha, S II and O III narrow-band filters, see table 2.1. The most frequently used filter for the observation of UCDS is the I+z filter.

[4] http://www.flicamera.com/
[5] http://www.astrodon.com/

The SSO observatory is nearly fully robotic and can be controlled remotely via a secure Virtual Private Network (VPN) connection between Paranal and the University of Liège. The telescopes are then controlled trough the ACP Expert Observatory Control Software4, installed on the control computer of each telescope unit. ACP interacts with other software to control the telescope mounts, CCD imagers, guiding sensors, filter selectors, focusers, instrument-package rotators, weather sensors, and dome control systems. In particular, if the weather conditions are bad ACP, can trigger an automatic closure of the dome via interactions with the weather sensors. Each telescope is equipped with a Boltwood Cloud Sensor II weather station from the Diffraction Limited company[6], which monitors the cloud cover, wind speed, humidity, dew point, and amount of daylight. Each dome is also equipped with additional rain and light sensors, working independently from the telescope control computer for extra safety. Several IP-power sockets are connected to the electrical devices inside the domes, to allow remotely rebooting the systems if necessary. Finally, each telescope is also equipped with an uninterruptible power supply (UPS), as well as several webcams (inside and outside the domes) and microphones.

After a commissioning phase of two years during which the Astelco, Gambato, and SPECULOOS teams built, installed and tested the telescopes, the SPECULOOS-South observatory officially started its operation in January 2019. Although, informal operations on the first SSO telescopes started as early as June 2018.

### SPECULOOS-North Observatory

The SPECULOOS-North observatory (SNO) is the northern counterpart of SPECULOOS-South observatory. It is located at Teide Observatory on the island of Tenerife, Canaries (Spain). So far, SNO is composed of one robotic telescope, named Artemis, which is a perfect twin of the SPECULOOS-South telescopes. An image of SNO and Artemis is shown on Figure 2.4. The only small difference between the SSO telescopes and Artemis are the filters it is equipped with, as shown in Table 2.1. The Teide Observatory is an astronomical observatory by the Teide Volcano, 2,400 meters above sea level and operated by the Insituto de Astrofisica de Canarias. Although not as exquisite as Paranal, the site offers very good observing conditions and allows the SPECULOOS project to hunt for exoplanets in the northern hemisphere.

SNO was inaugurated in June 2019 and is operated by a consortium including the Massachusetts Institute of Technology (MIT), the University of Liège, and the Institute of Astrophysics of the Canaries (IAC).

[6] http://diffractionlimited.com/

**Fig. 2.4** Photo of the SPECULOOS-North observatory. At the forefront the Artemis telescope, on the right a platform ready to host a potential second telescope and in the background the Teide volcano. Credit: EAPS.

### SAINT-EX

The SAINT-EX observatory, located at the National Astronomical Observatory of Mexico in San Pedro Mártir (Mexico), is the youngest of the SPECULOOS family. A photo of SAINT-EX is shown on Figure 2.5. SAINT-EX is almost an identical twin of the SSO and

**Fig. 2.5** Photo of the SAINT-EX telescope. Credit: University of Bern.

SNO telescopes but distinguishes itself by a few differences. First, SAINT-EX is not only

dedicated to the SPECULOOS survey but also plays a major role as a ground-based support for the ESA CHEOPS space mission. Then, the camera is operated a bit differently than on the other SPECULOOS, notably with a gain of 3.6 electrons $ADU^{-1}$ allowing to observe brighter stars like the CHEOPS follow-up targets, and is operated at -70°C instead of -60°C for others SPECULOOS telescopes. The filters available for observations with SAINT-EX are presented in Table 2.1.

| Telescope | Available filters |
|---|---|
| Io | u', Ha, Rc, z', r', i', g', I+z, Exo |
| Europa | Rc, B, z', V, r', i', g', I+z, Exo |
| Ganymede | OIII, Ha, SII, z', r', i', g', I+z, Exo |
| Callisto | u', B, z', V, r', i', g', I+z, Exo |
| Artemis | u', z', r', i', g', I+z, Exo |
| Saint-Ex | u', z', r', i', g', I+z, Exo |

**Table 2.1** Filters available on each one of the SSO/SNO/SAINT-EX telescope's filter wheels.

SAINT-EX started operations in January 2019 and is run by the SAINT-EX Consortium and the National Autonomous University of Mexico (UNAM). The SAINT-EX Consortium is composed of the Center for Space and Habitability at the University of Bern (CH), the NCCR PlanetS (CH), the University of Liège (Belgium), the University of Cambridge (UK) and the University of Geneva (CH).

### The TRAPPISTs

Finally, the SPECULOOS project was greatly supported by the TRAnsiting Planets and PlanetesImals Small Telescope (TRAPPIST) (Gillon et al. 2011) telescopes, both in the North and in the South, see Figure 2.6. As we previously mentioned, the proof of concept of the project was carried out with TRAPPIST. At this time only one TRAPPIST telescope was built, TRAPPIST South, at La Silla, Chile. La Silla observatory offers excellent observing conditions (comparable to Paranal) with a very good stability of the atmosphere (low turbulence) and a low humidity level. TRAPPIST South started his operations in June 2010 and has been devoted to the detection and characterisation of exoplanets around other stars as well as the study of comets orbiting around the Sun since then. TRAPPIST-South is a 60-cm (F/8) Ritchey-Chretien telescope, equipped with a near-IR optimised 2Kx2K CCD camera with a pixel scale of $0.64''$/pixel and field of view of $22' x 22'$ (like the SPECULOOS telescopes), offering excellent quantum efficiencies from 300 to >900 *nm*. TRAPPIST-North is an identical twin of TRAPPIST-South built in 2016 which greatly supported the TRAPPIST project

**Fig. 2.6** Photo of the TRAPPISTs telescopes. On the left is TRAPPIST-South located at La Silla (Chile), on the right TRAPPIST-North located at Oukaimeden (Morocco).

in the discovery of new planets (Gillon et al. 2017b), comets (Moulane et al. 2020), and follow-up of TESS or WASP candidates (Barkaoui et al. 2019; Demory et al. 2020). At the present time, TRAPPIST telescopes do not observe SPECULOOS targets on a daily basis but can still play a key role in the confirmation/discarding of potential SPECULOOS candidates (when there are not too faint) and are highly involved in TESS follow-up observations.

### 2.1.2 Target selection

In this section, I will detail how we build the SPECULOOS target list. This presentation will be based on a publication I significantly participated to, led by my collaborator Daniel Sebastian entitled: *"SPECULOOS - Ultracool Dwarf Transit Survey"* (Sebastian et al. 2020).

#### Selection

To build our target list, we first developed a catalogue of M- and L-dwarfs within 40 pc, starting with the 35781 objects in the Gaia DR2 catalogue with a trigonometric parallax $d \geq 25$ mas. For each of them, we (1) applied the correction to the Gaia DR2 parallax recommended by Stassun et al. (2018); (2) computed the J2000 equatorial coordinates considering only the proper motion as measured by Gaia (the epoch of Gaia DR2 coordinates is J2015.5); (3) computed the absolute magnitude $M_G$ from the apparent $G$-band magnitude and the Gaia distance modulus measured; (4) computed an estimate of the effective temperature $T_{\rm eff}$ based on the empirical law $T_{\rm eff}(M_G)$ of Pecaut et al. (2013) and assuming a systematic error of 150 K added quadratically to the error propagated from the error on $M_G$. From the resulting list we discarded all objects with $M_G < 6.5$ or a colour $G_{BP} - G_{RP} < 1.5$ to keep only dwarf stars later than ~K9-type. We also discarded objects missing a $G_{BP} - G_{RP}$ colour in Gaia DR2 and ended up with 21137 potential nearby M- and L-dwarfs. Afterwards, we cross-matched each of these objects with the 2MASS point sources within $2'/d$ (= $3''$ at

40 pc). This $1/d$ dependency of the search radius aimed to take into account that, for the nearest stars, the astrometric position at a given time can differ significantly from the one computed by correcting the J2015.5 position from the proper motion. This is due to the significant amplitude of their 3D motion, meaning that their radial velocity should also be considered. For instance, there is an astrometric difference $> 30''$ between the J2000 position of Proxima Centauri as measured by 2MASS and the one computed from its Gaia DR2 J2015.5 coordinates and proper motion.

For each 2MASS object falling within $2''/d$ of a selected Gaia DR2 object, we computed two estimates of $T_{\rm eff}$, one based on the $T_{\rm eff}(G-H)$ empirical relationship of Pecaut et al. (2013) assuming a systematic error of 150K, and one based on the $T_{\rm eff}(M_H)$ empirical relationship of Filippazzo et al. (2015), assuming a systematic error of 100K, and with the absolute magnitude $M_H$ computed from the apparent $H$-band magnitude measured by 2MASS and from the distance modulus measured by Gaia. To extend the empirical relationship of Filippazzo et al. (2015) for late-type M-dwarfs to earlier-type stars, we derive $T_{\rm eff}(M_H)$ for targets with $M_H < 7.83$ using the empirical relationship of Pecaut et al. (2013). This value of 7.83 was found to ensure the continuity of the two laws. We then computed for each Gaia - 2MASS couple the following metric:

$$\left(\frac{T_{\rm eff}(M_G)-<T_{\rm eff}>}{\sigma_{T_{\rm eff}(M_G)}}\right)^2+\left(\frac{T_{\rm eff}(G-H)-<T_{\rm eff}>}{\sigma_{T_{\rm eff}(G-H)}}\right)^2+\left(\frac{T_{\rm eff}(M_H)-<T_{\rm eff}>}{\sigma_{T_{\rm eff}(M_H)}}\right)^2+\left(\frac{\delta_{position}}{\sigma_{\delta_{position}}}\right)^2 \quad (2.1)$$

where $< T_{\rm eff} >$ is the mean of the three temperature estimates and where

$$\delta_{position} = \arccos(\sin\delta_1 \sin\delta_2 \quad (2.2)$$

$$+ \cos\delta_1 \cos\delta_2 \cos(\alpha_1-\alpha_2)), \quad (2.3)$$

$\alpha_i$ and $\delta_i$ being the right ascension and declination of the star $i$, and where $\sigma_{\delta_{position}}$ is the error on the position difference between the two objects computed from propagation of the errors on $\alpha$ and $\delta$ quadratically (assuming a measurement error of $1.21''$ for 2MASS, (Stassun et al. 2018)), summed quadratically to an error of $85''/d$ to take into account the significant 3D motion of the nearest stars. This value of $85''$ is the Gaia-vs-2MASS position difference of SCR1845-6357, the very nearby (4 pc) star with the highest $\delta_{position}$ / distance ratio.

Each Gaia DR2 object was cross-matched with the 2MASS object within $2''/d$ that minimised its metric function, i.e. with the nearest position and the best match in terms of $T_{\rm eff}$ as derived from $M_G$, $M_H$ and $G-H$. For 3660 objects, no cross-match was found, i.e. no 2MASS object was found within 2'/$d$. For the remaining 17477 objects (21137 - 3660), the three

temperature estimates $T_{\rm eff}(M_G)$, $T_{\rm eff}(G-H)$, and $T_{\rm eff}(M_H)$ were compared between each other. In case of discrepancy at more than $2\sigma$, the object was discarded. 2848 objects were rejected through this comparison, leaving 14629 objects.

For these objects, we (1) derived an estimate of the spectral type (SpT) by inverting the empirical relationship $T_{\rm eff}(M_H)$ of Filippazzo et al. (2015), assuming an internal error of 113K for it; (2) computed an estimate of the $I_c$-band magnitude from the 2MASS $J$-band magnitude and the spectral type estimate using online tables with empirical colours as a function of spectral type[7]; (3) computed a $J$-band bolometric correction $BC_J$[8]; (4) computed an estimate of the bolometric luminosity $L_{\rm bol}$ (+ error) from $M_J$ and $BC_J$; (5) computed an estimate of the radius $R_\star$ (+ error) from $L_{\rm bol}$, $T_{\rm eff}$, and the relationship $L_{\rm bol} = \sigma 4\pi R_\star^2 T_{\rm eff}^4$, where $\sigma$ is the Stefan-Boltzmann constant; (6) computed an estimate of the mass $M_\star$ (+ error) from the empirical relationship of Mann et al. (2019) (assumed internal error = 3%) for objects earlier than L2.5, assuming them to be low-mass stars (Dieterich et al. 2014).

For later objects (i.e. brown dwarfs), we assumed the following relationship to derive a crude estimate of the mass: $M_\star = 0.075 - ({\rm SpT} - 12) \times 0.0005 {\rm M}_\odot$. As the spectral type of a brown dwarf is not only correlated with its mass but also its age, this relationship has no ambition to be accurate at all and should not be used as scientific reference for these targets. It simply aims to represent that, statistically speaking, a hotter brown dwarf tends to be more massive than a colder one. We assign an error of 80% to the mass as these brown dwarfs cannot have masses substantially larger than 0.075 $M_\odot$ but could be as low as a few ten Jupiter masses.

At that stage, we rejected another batch of 520 objects for which at least one of the following conditions was met:

- The computed radius was smaller than 0.07 $R_\odot$, i.e. too small for an ultra-cool dwarf (Dieterich et al. 2014).
- The number of 2MASS objects within $2'$ was over 250 and the $K$ magnitude larger than 12.5, making a confusion case likely (galactic disk + bulge).
- The inferred spectral type was later than M5.5 [M9], $K$ was larger than 8 (so no saturation in 2MASS images), and still the $J-K$ colour was smaller than 0.6 [1.0], suggesting a wrong cross-match or a confusion case.
- The inferred mass was smaller than 0.2 $M_\odot$ while the inferred radius was larger than 0.4 $R_\odot$, i.e. too large for a low-mass M-dwarf.

[7] http://www.stsci.edu/~inr/intrins.html

[8] We used the $BC_J$(SpT) relationship of Filippazzo et al. (2015) (assumed internal error = 0.163), and for stars earlier than SpT M6.64 (selected so to ensure the continuity of the two laws), we used the $BC_J(T_{\rm eff})$ relationship of Pecaut et al. (2013) assuming an internal error of 0.2.

We ended up with a 40 pc M+L dwarfs catalogue containing 14109 objects. Still, we noticed that some well-known nearby late-M and L-dwarfs were missing from the catalogue because they had no parallax in Gaia DR2, including very nearby objects like Scholz's star (M9.5+T5.5 at 6.7 pc, (Burgasser et al. 2015)), Luhman-16 (L7.5+T0.5 at 2.0 pc, (Luhman 2013)), or Wolf 359 (M6.0 at 2.4 pc, (T. J. Henry et al. 2004)). To account for this, we cross-matched our catalogue with the spectroscopically verified sample of M7-L5 classical ultra-cool dwarfs within 25 pc of Gagliuffi et al. (2019). For each object within this sample and not present in our catalogue, we (1) used the $T_{\rm eff}$(SpT) empirical relationship of Filippazzo et al. (2015) to estimate the effective temperature, (2) used the same procedure than for the Gaia DR2 objects to estimate the bolometric correction, the luminosity, the radius, and the mass. We discarded objects flagged as close binary in the catalogue of Gagliuffi et al. (2019), objects with an inferred size smaller than 0.07 $R_\odot$, objects with an inferred mass greater than 0.125 $M_\odot$ (too massive for an ultra-cool dwarf, suggesting a blend or a close binary case), and objects later than M9.0 with a $J-K$ colour index smaller than 1.0 and a $K$ magnitude larger than 8. This procedure added 59 objects to our catalogue, for a total of 14168. Except for one target, 2MASS J21321145+1341584 which does not have a corresponding source in Gaia DR2, we cross-matched all added objects with the Gaia DR2 catalogue. Figure 2.7 shows the spectral type distribution and the mass-radius diagram of the 14168 objects. One

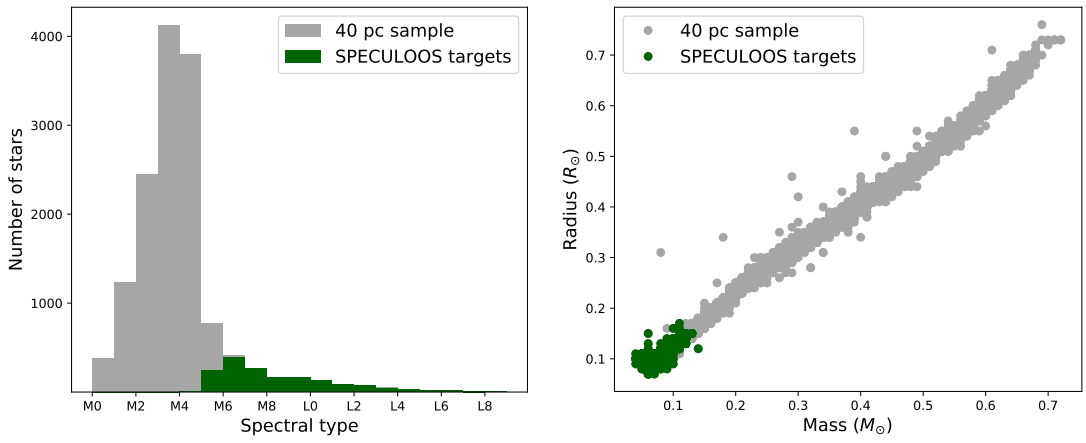


**Fig. 2.7** Spectral type distribution (*left*) and mass-radius diagram (*right*) for our 40pc ML-dwarfs catalogue. Gray: The Gaia-2MASS 40 pc sample for late-type stars, Green: The SPECULOOS targets.

can notice that our catalogue of 40 pc M + L dwarfs[9] is dominated by ~M4-type objects, in line with earlier results (e.g. (T. J. Henry et al. 2018)).

[9]The full catalogue is only available as 40pc_list in electronic form at the CDS via anonymous ftp to cdsarc.u-strasbg.fr (130.79.128.5) or via http://cdsweb.u-strasbg.fr/cgi-bin/qcat?J/A+A

Our final goal was to build the target list of SPECULOOS, using a consistent target selection method, rather than presenting a complete sample of late type stars. Therefore, we did not try to recover stars earlier than M6 absent from our catalogue because they do not have a Gaia DR2 parallax. Extrapolating our results for ultra-cool dwarfs to earlier M-dwarfs, we estimate that there must be at most a few hundreds of them. To estimate the number of stars that were still missed by our selection process, we derived the number density of stars per cubic parsec. For the early M-dwarf sample (M0 to M5), we derive a distance independent number density of $(46.6\pm0.8)\,\mathrm{x}\,10^{-3}\,\mathrm{pc}^{-3}$. Figure 2.8 shows the number density for the late M-dwarfs and BDs of our 40 pc sample. We observe a lower density for targets closer than 15 pc. This is mainly due to a few nearby stars that are not covered by the Gagliuffi et al. (2019) survey and have missing parallaxes in Gaia DR2. For M6 to M7 stars, we derive a distant independent number density between 10 and 40 pc of $(3.4\pm0.2)\,\mathrm{x}\,10^{-3}\,\mathrm{pc}^{-3}$. Assuming a homogeneous distribution, we conclude that this sample, as well as our early M-dwarf sample are distance limited with no or negligible brightness selection. For late UCDS with spectral types M8 to L2, we see a drop for targets between 30 and 40 pc, which can be explained by a selection effect that leads to a lack of stars in the order of $10^2$, mostly due to their faintness or crowding in the galactic plane. Finally for BDs with spectral types later than L2, we see a steep drop with distance. The number density of BDs in our sample decreases by 50% between 10 and 15 pc. This lack of BDs is expected due to the intrinsic faintness of those objects and the limiting magnitude of Gaia (Reylé 2018; Smart et al. 2019).

Within 25 pc, we find 214 targets with a photometric spectral type between M6.5 to L0, corresponding to a mean number density of $(3.2\pm0.3)\mathrm{x}10^{-3}\ \mathrm{pc}^{-3}$. This value is about 25% lower than the raw volume-corrected value derived by Gagliuffi et al. (2019) ($(4.1\pm0.3)\mathrm{x}10^{-3}\ \mathrm{pc}^{-3}$). This absolute difference can be explained by our selection method, which excludes (i) most close binaries and (ii) blended stars.

### Programs

The core science cases of the SPECULOOS survey can be broken down into (1) the search for transiting, rocky planets well-suited for atmospheric characterisation with future facilities, and (2) a statistical census of temperate planets around UCDS. To optimise these goals, we divide the survey into three non-overlapping programs.

Anticipating the launch of JWST[10], we focus in our first program on a census of targets for which the atmospheric properties of an "Earth-like" planet could be studied in some details by an ambitious JWST transit spectroscopy observation (Gillon et al. 2020). As "Earth-like",

[10] https://www.jwst.nasa.gov/content/about/faqs/facts.html

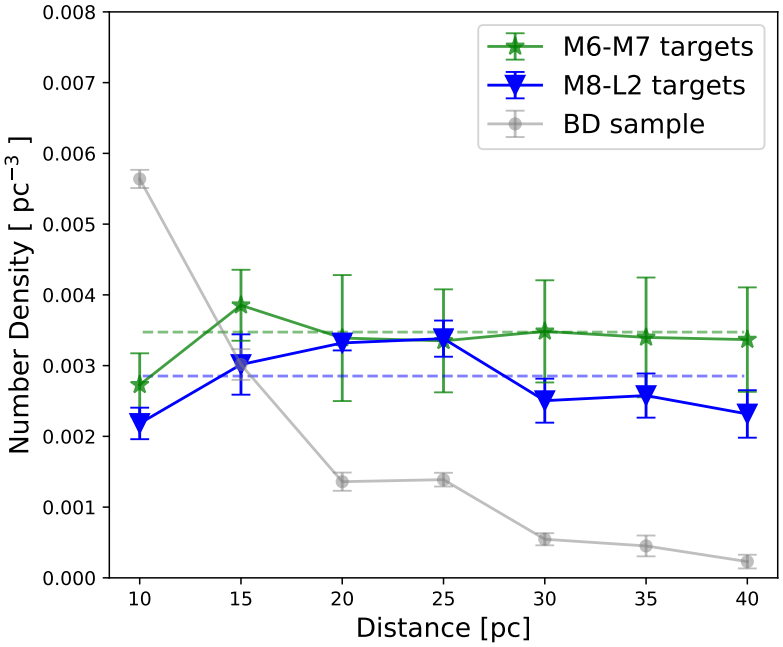


**Fig. 2.8** Number densities per distance for different spectral types: green stars for sub-types M6 and M7; blue triangles for sub-types M8 to L2; and grey dots for BDs with types later than L2. The horizontal lines mark the average densities for the three populations.

we denote a planet with the same mass, same size, same atmospheric composition and same irradiation from the host star than the Earth.

Our second program focuses on a census of temperate rocky planets in the overlapping region between SPECULOOS and TESS, in the M5-M6 type range. As temperate, we denote a planet that receives at most four times the irradiation the Earth receives from the Sun. Indeed, in this spectral type range, TESS has a declining sensitivity to Earth-sized planets due to a lack of photons, while SPECULOOS detection efficiency is decreased by the larger periods of temperate planets (relative to later M-dwarfs) that extend the telescope time required per target. A synergetic approach combining the long and continuous observations of TESS and the higher photometric precision of SPECULOOS could thus make easier detections that would be difficult to achieve individually for both surveys.

Our third program focuses on a statistical search for transiting exoplanets within all remaining targets. The criteria to select the targets of the three programs from our 40 pc list are presented in the following paragraphs.

**Program 1: "Earth-like" planets for JWST** To set up the target list of our first program, we computed the typical signal-to-noise ratio (SNR) achievable in transit transmission

spectroscopy by a 200 hr observation with JWST/NIRSPEC for all 14,168 objects within our 40 pc sample. Our aim here is to efficiently probe the atmospheric properties of an "Earth-like" planet. For the typical amplitude of the transmission signals, we used the following equation (Winn et al. 2010):

$$\Delta\delta = 2N_H\delta\left(\frac{H}{R_\oplus}\right), \tag{2.4}$$

where $H$ is the atmospheric scale height and $N_H$ the number of scale heights. To derive a value for $H$, we assume an "Earth-like" planet with the same atmospheric composition as the Earth, an isothermal atmosphere with a mean molecular mass of 29 amu, and a temperature equal to the equilibrium temperature of the planet (with an Bond albedo of 0.3 and irradiation of $1\,S_\oplus$). $\delta$ is the transit depth, and $R_\oplus$ is the Earth's radius. We assumed a value of 5 for $N_H$, the number of scale heights corresponding to a strong molecular transition. For the assumed planets, the orbital distance corresponding to an "Earth-like" irradiation was computed based on the stellar luminosity, the corresponding orbital period was computed using Kepler's third law combined with the stellar mass estimate, and the duration of a central transit was computed using equation 15 from Winn (2014).

Then, we computed the JWST/NIRSPEC (Prism mode) noise at 2.2 $\mu$m for a spectral bin of 100 nm and for an exposure sequence with the same duration as the transit using the online tool PandExo (Batalha et al. 2017). We assumed a red noise over a transit timescale of 30 ppm that we added quadratically to the white noise estimate of PandExo. We computed the number of transits observed within the 200 hr JWST program, assuming for each transit observation a duration equal to the transit duration plus 2.5 hr (for pointing, acquisition, plus out-of-transit observations). The noise per transit was then divided by the square root of the number of observed transits, and we added quadratically to the result an absolute floor noise of 10 ppm. At the end, we obtained for each target a transmission signal-to-noise (SNR) by dividing the transmission amplitude by the global noise. Figure 2.9 (left) shows the resulting SpT – SNR distribution. In this figure, we drew a line at SNR = 4, assuming this value to be an absolute minimum for deriving meaningful constraints on the atmospheric composition of our assumed "Earth-like" planets. TRAPPIST-1 is shown as a magenta star symbol in this figure. For the majority of the targets in the whole 40 pc sample, the achievable SNR is $\sim 1$.

We found that 366 objects – including TRAPPIST-1 – have a SNR $\geq 4$, and only 44 of them have a SNR larger than TRAPPIST-1. These 366 objects constitute the target list of SPECULOOS Program 1. Of the 366, 92 have a spectral type earlier than M6 (and none of them is earlier than M4). We chose to also include these earlier targets in our target list even if they are not *bona fide* UCDS.

**Program 2: Temperate, Rocky Planets from TESS** We set up the targets for our second program identifying the synergetic region between SPECULOOS and TESS within our 40 pc sample. For this, we derived first the detection threshold for a temperate, Earth-sized planet for both surveys.

First, we estimated the photometric precision that should be achieved by TESS within 30 min for each object. For this, we adopted the moving 10th percentile of the TESS RMS in one hour, as a function of the T magnitude, published in Figure 6 of the TESS Data Release Notes NASA/TM-2018-000000[11], assuming the T magnitude to be similar to the $I_c$ magnitude, derived earlier. This RMS was multiplied by $\sqrt{2}$ to get the RMS in 30 min. Then, we assumed for each target an Earth-sized planet on a close-in orbit (receiving an irradiation of four times that of Earth), and computed the detection SNR expected from two 27 d observations with TESS. For the noise of the TESS observations, we took into account the mean number of observed transits during the observation, their depths, durations (assuming a central transit), as well as our estimate for the TESS photometric precision for the star. Furthermore, we assumed a floor noise of 50 ppm per transit, and no noise for the phase-folded photometry. If the computed SNR was ≥5, a detection within the reach of TESS was inferred.

We applied the same procedure for SPECULOOS. First, we used the SPECULOOS Exposure Time Calculator (ETC) to compute the typical photometric precision for each target that should be achieved by a SPECULOOS 1m-telescope in the I+z filter (Delrez et al. 2018b) as a function of the apparent $J$-band magnitude and the spectral type of the target. We assumed a 100 hr-long photometric monitoring and a floor noise of 500 ppm per transit (which is a realistic floor noise for high-precision ground-based photometry from a good astronomical site and state-of-the-art equipment). Here too, a detection was deemed possible when the computed SNR was ≥5.

Figure 2.9 (right) shows a summary of our results. For our 40 pc sample the detection SNR with TESS for temperate, rocky planets increases for earlier M-dwarfs due to its excellent time coverage and the decreasing orbital periods for temperate planets with increasing spectral type. Nevertheless, it greatly decreases at spectral type ~ M5 due to the faintness of these objects, which is in line with Sullivan et al. (2015). The colour coding shows the SNR, achieved by SPECULOOS for the same temperate planets. The SNR starts to increase at spectral type ~ M5 towards later spectral types, due to its shorter monitoring strategy (for most earlier-type objects only one transit can be observed in 100 hr), but its smaller photon noise compared to TESS.

In this context, for the second program (hereafter Program 2), we selected stars with photometric spectral types M5 and later, for which Earth-sized planets with an irradiation four

[11] https://tasoc.dk/docs/release_notes/tess_sector_04_drn05_v03.pdf

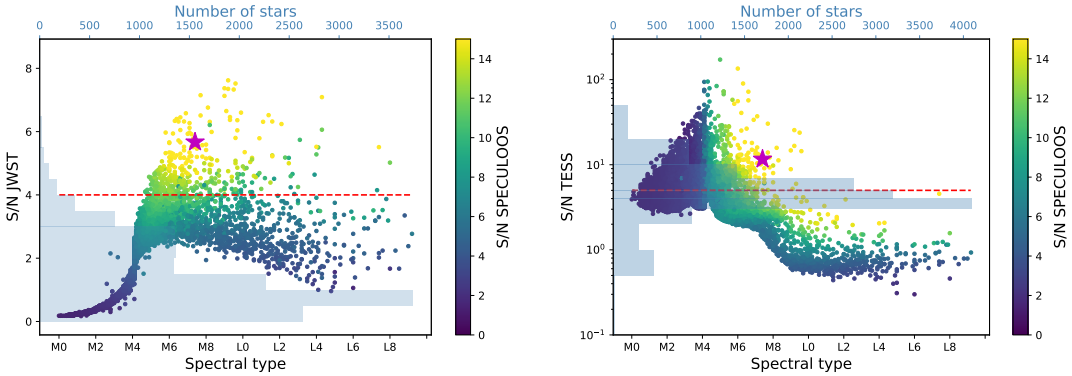


**Fig. 2.9** SPECULOOS program selection: *Left*: Estimated signal-to-noise ratio (SNR) in transmission spectroscopy with JWST/NIRSPEC (assuming an 'Earth-like' planet, 200 hr of JWST/NIRSPEC time, and a spectral sampling of 100 nm) as a function of spectral type for the 14,164 M- and L-dwarfs within 40 pc. TRAPPIST-1 is shown as a magenta star. Red dashed line: SNR = 4, used to select Program 1 targets. Colour coding: estimated SNR for a single transit of an Earth-sized planet with one telescope of the SPECULOOS network, with yellow points representing a SNR ≥ 15. Light-blue histogram: distribution of all objects and their corresponding SNRs.
*Right*: Estimated signal-to-noise for TESS to detect an Earth-sized planet with an irradiation four times larger than Earth. Colour coding: estimated SNR for the transit of an Earth-sized planet with the SPECULOOS network, with yellow points representing a SNR ≥ 15. Red dashed line: SNR = 5, used to select Program 2 targets. Light-blue histogram: distribution of all objects and their corresponding SNRs.

times that of Earth can be detected by TESS with a SNR ≥5. These criteria were met for some targets previously selected in our Program 1. We thus applied those criteria to select stars from our 40 pc sample that are not in Program 1.

The target list of Program 2 finally contains 171 objects that have spectral types mainly between M5V and M6.5V. For these targets we aim to identify low-significance (5 to 8 sigma) transit signals of Earth-sized planets in TESS photometry first, which are then observed with SPECULOOS to confirm or discard their planetary nature.

**Program 3: The SPECULOOS Statistical Survey** The third program (hereafter Program 3) is the SPECULOOS statistical survey. It focuses on all objects from our target list not covered by the two first programs, including all UCDS (later than M6) from our 40 pc sample. Given the uncertainty of our classification, we select all objects with photometric classifications of M6 and later to ensure the inclusion of all UCDS. This program contains 1121 targets.

**SPECULOOS input catalogue** The full SPECULOOS input catalogue is composed of all targets from the three programs described above. As a final step, we cross-matched this catalogue with known objects in the literature. As there is no complete database for all UCDS available so far, we cross-checked with several catalogs and databases. The most comprehensive database so far is SIMBAD (Wenger et al. 2000). It lists spectroscopic classifications for 44% of our targets. Further catalogues, which we used for the cross-check were: DwarfAchives.org[12], the compilation by J. Gagné[13], the list published by Kiman et al. (2019) and compiled from the BOSS ultracool dwarf survey, the compilation from Gagliuffi et al. (2019), as well as the compilations from Smart et al. (2019), Reylé (2018), and Scholz (2020) based on Gaia DR2. If spectral types from optical and infrared spectra were given, we adopted the spectral type derived from the optical spectrum first and only adopted the infrared spectral type if no optical spectrum was obtained. If a spectral type or catalogue entry was derived from photometry only, we denoted this entry as a photometric spectral type. If the origin of a spectral classification cannot be verified (for example a reference is missing in SIMBAD), we denoted this entry as a photometric spectral type too. We rejected the object 2MASS J10280776-6327128 from our catalog, as it is a known white dwarf (Kirkpatrick et al. 2016). Another three targets were rejected, as they are classified as subdwarfs, namely 2MASS J02302486+1648262 (Cruz et al. 2002), 2MASS J14390030+1839385 (Gizis et al. 2017), and 2MASS J17125121-0507249 (Aganze et al. 2016). Finally, we ended up with a catalogue of 1657 SPECULOOS targets. Due to its size the total list is only available in the online version [14]. Table 2.2 shows the list descriptions for the online table.

It contains all SPECULOOS targets, their derived parameters as well as well as the spectral types available in the literature. We find that 50% have spectral types in literature, 28.1% have photometric spectral type only, and 21.9% (363 targets) have been classified in this work for the first time. The majority of the latter (260 targets) are classified as M6 and later. Including the uncertainties from our photometric classification, we refer to those targets as potential "new" UCDS, see Figure 2.10. The spectral type distribution of the SPECULOOS catalogue peaks at M6V with about 400 targets and decreases with later spectral types. As shown in Figure 2.7, the catalogue is incomplete for targets earlier than M6V because of the varying spectral type cut of the different programs. Nevertheless, no cuts were introduced for later-type stars. In Figure 2.10 we show the distribution of UCDS within catalogue (photometric spectral type M6V or later) and the corresponding coverage with literature spectral types. We note an apparent lack of spectral classifications for earlier-type objects, while the sample is almost complete for BDs. This bias is in line with the findings by Reylé

[12] http://spider.ipac.caltech.edu/staff/davy/ARCHIVE/index.shtml
[13] https://jgagneastro.com
[14] https://vizier.u-strasbg.fr/viz-bin/VizieR-2

**Table 2.2** Column description of the SPECULOOS target list. The complete tables are available for download in the online archive. In all tables, the photometric spectral type derived in this work is given as floating point number, starting at 0 for M0. For example 6.5 and 12.0 denote spectral type M6.5 and L2, respectively.

| Column name | Unit | Description |
|---|---|---|
| spc | | SPECULOOS ID |
| twomass | | 2MASS designation |
| gaia | | Gaia DR2 source_id |
| Simbad_main_id | | Main identifier for the object |
| Ra | deg | Right ascension J2000 |
| Dec | deg | Declination J2000 |
| dist | pc | Distance |
| dist_err | pc | Distance error |
| G | mag | Gaia DR2 G magnitude |
| G_err | mag | Gaia DR2 G magnitude error |
| I | mag | Ic magnitude |
| I_err | mag | Ic magnitude error |
| J | mag | 2MASS J magnitude |
| J_err | mag | 2MASS J magnitude Error |
| H | mag | 2MASS H magnitude |
| H_err | mag | 2MASS H magnitude Error |
| K | mag | 2MASS Ks magnitude |
| K_err | mag | 2MASS Ks magnitude Error |
| bp_rp | mag | Gaia DR2 Colour index |
| spt | | Photometric spectral type |
| spt_err | | Photometric spectral type error |
| teff | K | Effective temperature |
| teff_err | K | Effective temperature error |
| mass | $M_\odot$ | Stellar mass |
| mass_err | $M_\odot$ | Stellar mass error |
| radius | $R_\odot$ | Stellar radius |
| radius_err | $R_\odot$ | Stellar radius error |
| BCj | mag | Bolometric correction in J |
| BCj_err | mag | Bolometric correction error in J |
| L_bol | $L_\odot$ | Stellar Luminosity |
| L_bol_err | $L_\odot$ | Stellar Luminosity error |
| spec_spt | | spectroscopic Spectral type |
| spec_spt_ref | | Reference for spectroscopic type |
| phot_spt | | photometric Spectral type |
| phot_spt_ref | | Reference for photometric type |
| Known_Binary | | Object is a known binary |
| program | | The SPECULOOS observing program |

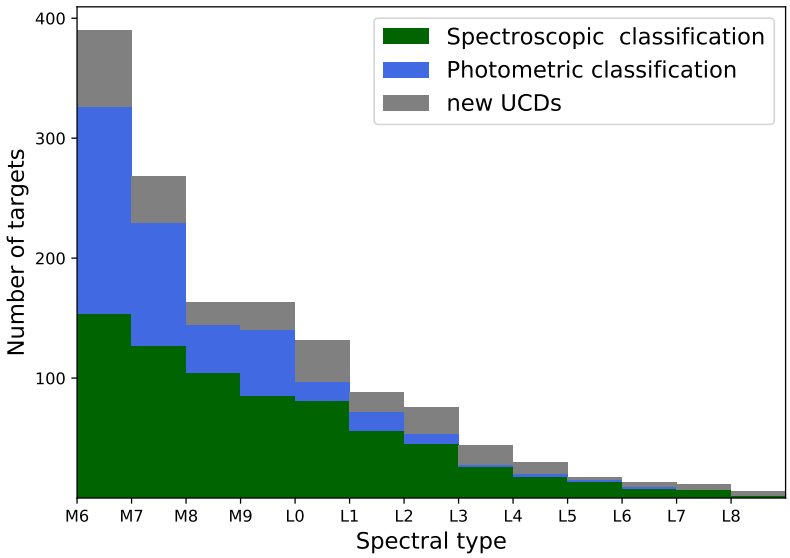


**Fig. 2.10** Distribution of photometric spectral types for UCDS within 40 pc from the SPECULOOS input catalogue. Colour coding: Targets with spectroscopic classification (green), with photometric classification (blue); and "new" UCDS without spectral type in the literature (gray).

(2018). It originates mostly from intensive spectral typing of the BD sample in the past decade.

### 2.1.3 Strategy and scheduling

One of my objectives as a PhD student was to work on the selection and implementation of the observational strategy of the SPECULOOS survey. In that regard I developed a python package to help the planification of all observations on the SPECULOOS telescopes, either core or external programs (presented in section 2.1.4). In the following paragraph I present the strategy in place for our three core programs.

First, the basic observational strategy of SPECULOOS is to observe each target continuously with one telescope for a duration long enough to make likely the observation of at least one transit of a temperate planet. Therefore, we observe with each telescope one or two targets per night. Other surveys have chosen to proceed differently using a dithering strategy (Nutzman et al. 2008; Tamburo et al. 2019), but considering our requirement for very-high photometric precision and the expected short transit duration (down to 15 min) for very-short-period ($\leq$ 1 d) planets orbiting UCDS, we estimated that a continuous observation approach is more appropriate ((Delrez et al. 2018b; Gibbs et al. 2020)).

Considering that we have divided our target list in three distinct programs, SPECULOOS's observing strategy is also divided in three. For instance, Program 1 aims to perform a more completed coverage of the habitable zone of its targets than Program 2 and 3, and so its monitoring duration per target has to be larger than for the two other programs. Until Nov. 2019, our strategy was the same for all programs, with a monitoring duration of 100 hr for any target no matter which program it belonged to (that is to say stars were observed until 100 hr of photometric data were gathered). Furthermore, we used to split the observation for each target into two observation blocks of each 50 hr per year. Our intention back then was to survey many targets to quickly detect very-short-period planets, in order to trigger intensive follow-up and ultimately detect additional planets with larger periods (if present) in the system. However, we have now settled on a different strategy: a monitoring duration of 200 hr in one block for Program 1's target, and a monitoring duration of 100 hr in one block for Program 2 and 3's targets.

To ensure we picked the most appropriate strategy for the three SPECULOOS observation programs, we used a metric, that we call the effective phase coverage, to quantify the efficiency of our planet search. This metric gives an estimation of how the phase of an hypothetical planet would be covered for a range of periods, using existing observations from the SPECULOOS network. More precisely, we computed the percentage of phase covered for each orbital period from $P = 0.1$ d to $P = P_{max}$ and took the effective phase coverage for periods $\leq P_{max}$ to be the integral over the period range. Figure 2.11 shows the phase coverage for each possible orbital period for an arbitrary target observed for 134.3 hours with SPECULOOS. The effective phase coverage is depicted by the blue area, for $P_{max} = 6$ d.

### Strategy for Program 2 and 3

Programs 2 and 3 focus on the detection of planets with irradiations similar to TRAPPIST-1b ($4\ S_\oplus$) and thus with short orbital periods. To ensure that we cover all short-period planets, we set $P_{max} = 6$ d and calculated the effective phase coverage for all targets for which observations with the SPECULOOS network have been started. Additionally we performed simulations of SPECULOOS observations, assuming 4 hours of observations per night per target and losses (bad weather or full moon too close) of 30%.

Figure 2.12 shows the evolution of the effective coverage as a function of the number of hours surveyed for all periods $\leq P_{max} = 6$ days. We observe that for 50 hours of observations the expected phase coverage is 60%, whereas for 100 hours of observations it increases to 80%. The SPECULOOS data agree well with our simulations and show that for our targets in Programs 2 and 3, a monitoring duration of 100 hr will allow us to detect close-in planets

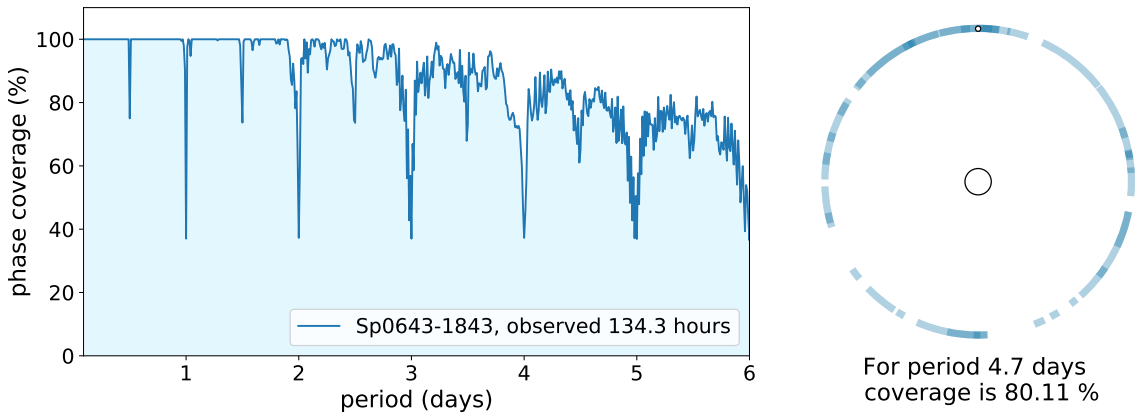


**Fig. 2.11** *Left:* Phase coverage as a function of the orbital period of an hypothetical planet around the target `Sp0643-1843` (chosen arbitrarily), observed for 134.3 hours in total by SPECULOOS. *Right:* Graphical visualisation of the coverage of target `Sp0643-1843` for an orbital period of 4.7 days. Each blue circular arc represents one night of observation; its size is proportional to the number of hours observed each night and the full circle depicts a duration of 4.7 days.

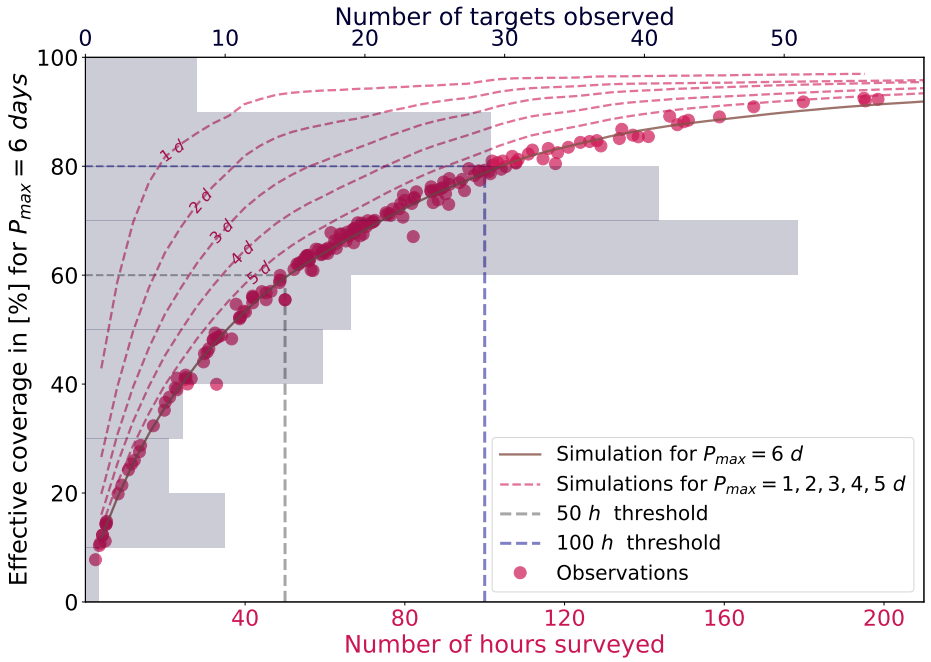


**Fig. 2.12** Effective coverage as a function of the number of hours surveyed for all targets observed by the SPECULOOS telescopes so far. Coloured dots show the coverage calculated from existing observation for periods going from 0.1 to 6 days, and the solid red line is the corresponding simulation. Dashed red lines are simulations for various values of $P_{max}$ ranging from 1 to 5 days. Gray histogram: Number of targets in each slice of coverage.

with an effective phase coverage of more than 80%. Figure 2.12 also shows the number of targets for which observations have started as a function of the coverage. We see that the

majority of these targets have been covered at 60-70% for periods going from 0.1 to 6 days. This is explained by the fact that for many targets we already gathered more than 50 hours during the first year of observations.

To analyse the effect of splitting the 100 hr observations into two blocks of 50 hr per year, we compared the effective phase coverage for two SPECULOOS targets that have both been monitored with SPECULOOS for 100 hr, but with the two different strategies. Figure 2.13 shows the phase coverage for each possible orbital period for both targets. Also shown are simulated SPECULOOS observations, for comparison. In the first scenario, the target was

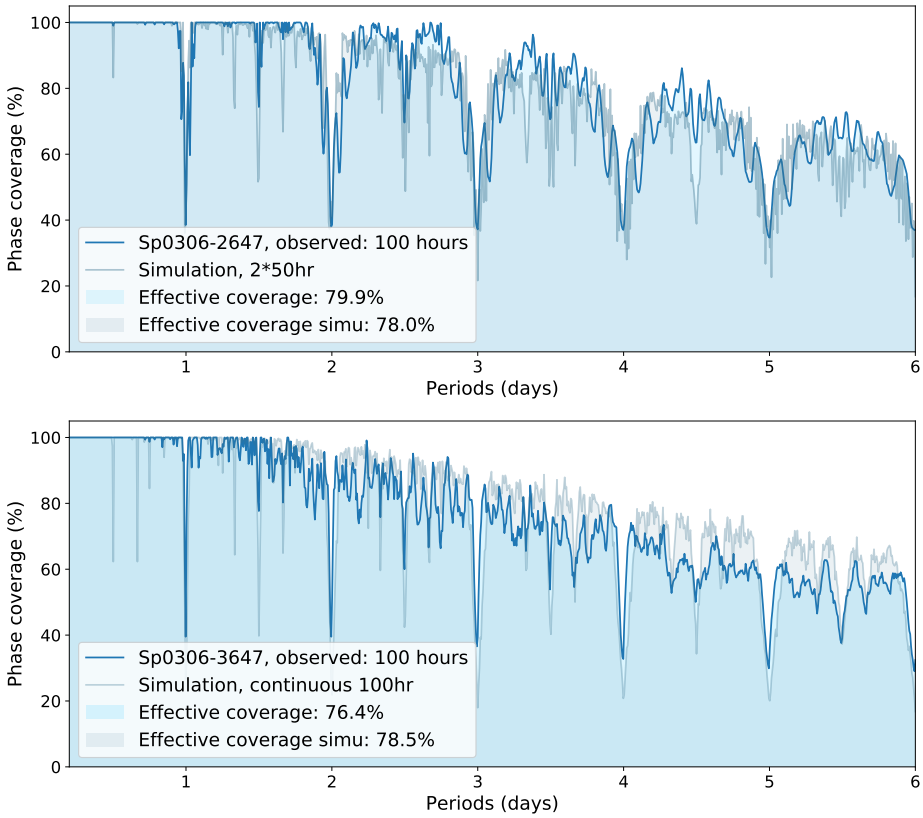


**Fig. 2.13** *Top:* Evolution of the phase coverage as a function of the period for one SPECULOOS target (`Sp0306-2647`) observed for 100 hr with SSO in two blocks of 50hr several months apart. The solid blue line shows the evolution of the coverage calculated from existing observations whereas the gray line is the result of simulations. *Bottom:* Same for another SPECULOOS target (`Sp0306-3647`) observed 100 hr with SSO but on consecutive days. Again the solid blue line shows the evolution of the coverage from existing observations, and the gray line from simulations.

observed for 50 hr on consecutive days, and again 50 hr one year later (top panel of Figure 2.13), whereas in the second scenario the target was observed day after day until 100hr of observations were reached (bottom panel of Figure 2.13). We found that splitting the observations better shuffles the phases but also introduces aliases that result in a slightly

decreased coverage for orbital periods close to multiples of sidereal days. As a whole, observations and simulations indicate that the effective coverage is within $-0.7 \pm 1.4\%$ similar for both scenarios.

More generally, in our simulations we used a period grid of 15 min in line with the the minimum expected transit duration. We find that between 0.1 and 6 days, about 40% of all possible orbital periods gain phase coverage from continuous observations, compared to 20.0% that loose coverage. Despite similar effective phase coverage, for about 20% (30% for planets with 8-12 d period) of all possible orbital periods we find a better phase coverage for continuous observations with SPECULOOS. Besides, as the continuous observations strategy is also more straightforward from a scheduling point of view, we opted to observe each target without additional splitting until its program-specific monitoring duration is reached. In the same way, we expect a slight increase of effective phase coverage of $1.2 \pm 0.7\%$ for observations in the case that we can observe a target all night long. We also find an increased phase coverage for about 7% of all possible orbital periods. We thus opted to observe each target the whole night, if possible.

#### Strategy of Program 1

The objective of our Program 1 is to detect putative transiting "Earth-like" planets with irradiations similar to Earth ($1\ S_\oplus$) and thus with orbital periods in or close to the habitable zone (HZ) of its host. Figure 2.14 shows the effective coverage of program 1 targets already started with SPECULOOS as a function of the number of hours surveyed. In here, we use as $P_{max}$ the middle of the HZ, which has been calculated for each target following R. K. Kopparapu et al. (2013). For most of the observed Program 1 targets, a hypothetical planet in the HZ would have a period of 8 to 10 days and would require $\simeq 200$ hr of observation to reach an effective phase coverage $\geq 80\%$. Thus, for our targets in program 1 a monitoring duration of 200 hr will effectively allow us to detect planets in the habitable zone. Besides, the conclusion derived for program 2 & 3 targets are still true for 200 hr, such that we decided to monitor each target on consecutive days if possible, until the monitoring duration has been reached, without splitting the observations in different years.

### 2.1.4 spock

Now that I have explained the selection of targets and the strategy adopted for the SPECULOOS survey, I can detail the scheduling procedure that I developed for the SPECULOOS targets. During the first year of my PhD, I worked on developing an open source python

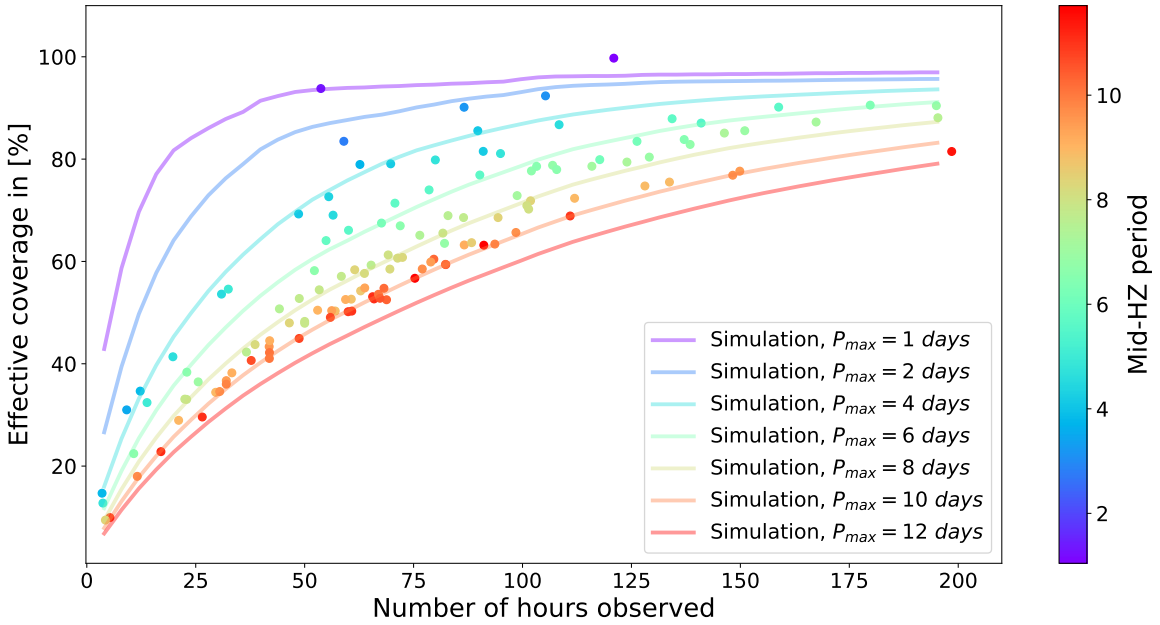


**Fig. 2.14** Coverage of the middle of the HZ for Program 1's targets observed so far by the SPECULOOS survey. Solid lines: theoretical simulations. Coloured dots: actual SPECULOOS observations. Colour coding: The expected maximum orbital periods associated with the middle of the HZ of each target.

package to handle the planification of observation on the SPECULOOS telescopes. This tool was named `spock` (SPeculoos Observatory sChedule maKer) and is accessible on Github. `spock`'s utilisation falls down in two main modes that are associated with two different python classes: the `long_term_scheduler` class for the planification of core programs observations, and the `short_term_scheduler` for external programs. I will detail these two modes in the following and then present some additional functionalities offered by `spock`.

### Core programs

As mentioned in section 2.1.1, all SPECULOOS observatories are controlled using the commercial software ACP. ACP drives the telescopes by reading a series of plans consisting of very simple text files chained to each other and written in an intuitive programming language. An example of startup plan is presented on Listing 1. Therefore, the final product delivered by `spock` will be daily observing scripts (ACP plans) for the SSO, SNO and SAINT-EX observatories. Before producing such files, `spock` identifies which targets are the most interesting to observe at a given time, for how long and with which telescope while

```
; == Startup ==
;
#waituntil 1, 2021/05/29 21:56:55
#domeopen
;
#chill -60
;
#waituntil 1, 2021/05/29 22:06:55
#duskflats Cal_flatexo.txt
;
#quitat 2021/05/29 22:39:40
;
#chain Obj_Sp1546-5534.txt
;
```

**Listing 1** - Example of a ACP plan. The `#waituntil` command asks ACP to wait until a given time before executing the following commands. The `#domeopen` command opens the dome. The `#duskflats` command launches the acquisition of flats (calibration images, see Chapter 3 for details). Finally, the command `#chain` allows ACP to chain this script to the next one that will drive the observation of the object `Sp1546-5534`.

respecting the strategy agreed for each observation program. To do so, `spock` relies on several criteria:

- The planet detectability of a target. For program 1 targets, this is quantified with $SNR_{JWST}$ which essentially is the estimated SNR in transmission spectroscopy that we would theoretically obtain from 200 hr of observation with JWST/NIRSPEC of an "Earth-like" planet orbiting a given target. For program 2 targets we rather use the TESS detection SNR for a temperate planet, while for program 3 targets, the selection criterion is the SPECULOOS detection SNR for a temperate planet.

- The target's observability $obs_{cov}$ which indicates the most appropriate time to observe a given target. To do so, `spock` computes the best visibility window of the year for each target. Every time a schedule is made, `spock` selects new targets that are at their optimum visibility at this time of the year. The selected targets are then ranked and the one with the highest priority is scheduled (providing it respects constraints imposed by the facility like moon distance and minimum elevation). If observable all night, the target is simply scheduled all night, but if some gaps remain an additional target is added to complement the schedule and avoid losing observing time. Furthermore, to prevent having too short observation blocks (1 h or less) the duration of the two targets are set to be comparable. For instance, if one night is $\simeq$8 h long and target 1 is

observable for the first 7 h only, target 2 is not going to be scheduled for the last hour only but rather the night will be split in half such that target 1 and 2 are observed for approximately the same amount of time. We say approximately because we do not exactly split the night in half, instead we adapt nightly the duration to each target's visibility (which shifts from night to night as the target visibility shifts from sunrise to sunset). This situation of observing two targets per night rather than one can happen frequently since many targets have latitudes that do not allow to fill up all the night time available for a given site, and this even at their peak visibility. As a whole, we can make the assumption that a night lasts ≃8 h, and approximate that the duration of the observation for each target is ≃4 h, which justifies why we used observation blocks of 4 h in the simulations we carried out in Section 2.1.3.To implement those constraints, `spock` makes use of the `astroplan` package (Morris et al. 2018a), a flexible python toolbox for astronomical observation planning and scheduling. `spock` also optimises on the period of the year for which the target is the most visible at a relatively low airmass.

- The target's completion ratio, $r_{comp} = \frac{hours_{observed}}{hours_{threshold}}$, which embodies the fraction of hours of observation completed versus the number of hours required for each target. Note that the value of $hours_{threshold}$ depends on the program to which the target belongs, 200 hr for Program 1 and 100 hr for Program 2 and 3. Using this completion ratio to rank targets is useful to favour the quick completion of on-going targets rather than starting new ones continually.

- The program to which the target belongs, $p$. This criteria is useful if the user wants to favour a program more than the others. For instance, our current strategy is to complete observations of program 1 targets, such that $p = 1$ for program 1 targets, $p = 0$ for program 3 targets, $p = 0.3$ for TESS targets (program 2) to have back up targets in case no program 1 targets are observable.

- The *coordination* potential of observations with multiple sites. Indeed, as SPECULOOS uses a multi-site telescope network, one of the main roles of `spock` is to handle the coordination of multi-site observations. For instance, between two targets with similar priority but one observable only from one site and the other from several sites, `spock` will choose the target that yields the best coverage. Besides, when possible, 1 hour overlap between observations from two different sites is scheduled to help the recombination of the light curves.

`spock` ranks all targets by multiplying these four criteria to compute the target's priority, which is simply defined as:

$$priority = (SNR_{JWST})^a * (obs_{cov})^b * (r_{comp})^c * p + coordination, \tag{2.5}$$

where $a, b, c$ are specific orders that we apply to each criteria based on their importance (higher order for *planet detectability* than *completion ratio* for instance) such that $a > b > c$. We note that *coordination* is the only additive criterion as coordination of observations between observatories has no incidence on our ability to observe a target nor on its interest for exoplanet search, such that a target with lack of coordination potential should not be discarded.

Once the priority of each target for a given day is computed `spock` picks the one with the highest score as the first target. Then, a function checks the observability window of the target, that is to say if it is observable all night, from sun set to mid-night, from mid-night to sun rise or from after sun set to before sun rise. In the latter scenario the target is discarded and the first target becomes the one with the second highest priority score (and so on) in order to avoid having short observations sequences of a second and third targets before and after the rise and set times of the first target. Then, another `spock` function checks that the selected first target respects the moon distance and elevation constraint, and if not, this target is discarded and `spock` picks the next target in descending order of priority as the first target. For all telescopes the moon distance constraint is set to a minimum of 30° and the elevation constraint is set to a minimum of 25° for SSO, SNO, TS/TN but a minimum of 28° for Saint-Ex (decided by the consortium). We note that AstelOS also has an intrinsic elevation lower limit of 21°. Finally, if the selected target fulfils all these conditions it is scheduled and if not observable all night a second target is picked via the same selection process. As I mentioned in the description of the observability criterion, we avoid to observe more than two SPECULOOS targets per night to maximise on-target time and phase coverage. The exposure time for each target is computed using the SPECULOOS exposure time calculator (ETC) which is integrated in `spock` in the form of a python class. The SPECULOOS ETC allows to compute the exposure time that will enable to reach a certain level of flux in a certain filter on a target, given its spectral type and magnitude (in either J or V), given the technical characteristics of the SPECULOOS telescopes (mirror size, focal ratio and coating) and cameras (quantum efficiency, temperature, gain, pixel scale, dark current, binning, read out noise) and given a set of conditions (seeing, airmass, moon phase, observatory altitude).

In Listing 2 I show how to make the schedule from 2021-05-01 to 2021-05-06 for the telescope "Io" of the observatory "SSO" in a few lines of code.

```
import SPOCK.long_term_scheduler as SPOCKLT
from astropy.time import Time

schedule = SPOCKLT.Schedules()  # define the schedule class
schedule.observatory_name = 'SSO'
schedule.telescope = 'Io'
schedule.load_parameters(date_range=['2021-05-01 15:00:00',
                                     '2021-06-01 15:00:00'])
schedule.make_schedule(Altitude_constraint=25, Moon_constraint=30)
```

**Listing 2** - Example of `long_term_scheduler` on SSO/Io telescope with `spock`

When the `.make_schedule()` function is executed `spock` reads the SPECULOOS targets list from our own private database called STARGATE, then targets are ranked and chosen as detailed above, eventually for each target a `night block` is created, which essentially is an `astropy.table` object with the following columns: target name, start time, end time, the duration in min, right ascension of the target, declination of the target, configuration (essentially the filter used for the observation and the exposure time computed by the ETC), see Figure 2.15. A full night of observations therefore simply is a sequence of `night blocks`

| target | start time (UTC) | end time (UTC) | duration (minutes) | ra (h) | ra (m) | ra (s) | dec (d) | dec (m) | dec (s) | configuration |
|---|---|---|---|---|---|---|---|---|---|---|
| Sp1524+2925 | 2021-05-12 03:06:20.026 | 2021-05-12 12:10:40.026 | 544.333333 | 15.0 | 24.0 | 24.7506 | 29.0 | 25.0 | 31.54152 | {'filt': 'I+z', 'texp': '66'} |

**Fig. 2.15** Example of a night block used for Saint-Ex observation on the night of the 2021-05-11.

as shown on the Gantt chart produced with `spock` on Figure 2.16. Ultimately, sequences of `night blocks` are turned into ACP scripts and uploaded to the control computer of each SPECULOOS telescope. Every day a `crontab` on the control computer updates the plan for the night (as some files need to be over-written from one night to another). In addition, plans for each telescope and each date are stored on the Cambridge Archive in the form of ACP plans and sequences of `night block` (`astropy.table` object). We also note than the number of hours observed per target is updated everyday as the pipeline processes the data (see section 2.2.1) such that the completion ratio is always recalculated for each target when `spock` is run.

Figure 2.17 shows the targets scheduled so far by `spock`. As explained in Section 2.1.3, the former strategy of dividing the observations in blocks of 50hr was prevailing until recently (Nov 2019). Therefore many targets are currently observed between 50 and 100 hours. We note that, logically, the targets with the highest $SNR_{JWST}$ metric have been preferably scheduled by `spock` until 200 hours of observation were reached. Notably the 43 targets

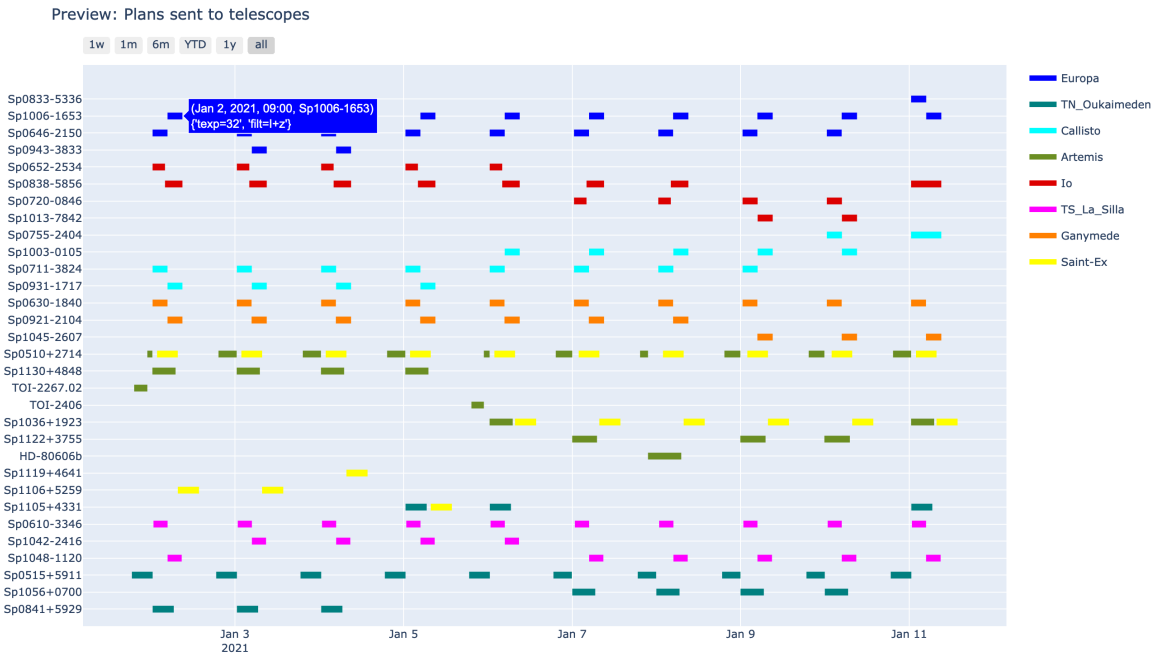


**Fig. 2.16** Gantt chart of the schedules created with `spock` for each SPECULOOS telescope from January the 1st 2021 to January 15th 2021. When created with `spock` this graph is interactive as it is produced using through `plotly`[15].

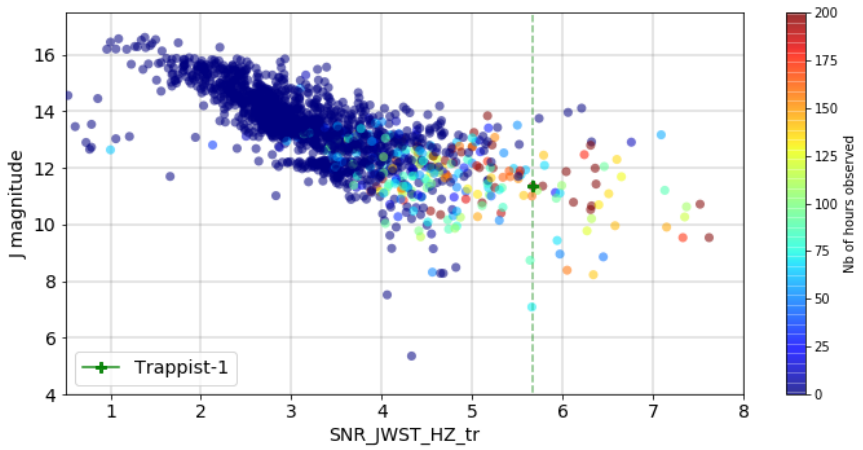


**Fig. 2.17** Magnitude in J band as a function of the estimated $SNR_{JWST}$ for all SPECULOOS targets. The colour bar indicates the number of hours observed for each target. This figure illustrates how `spock` operates, from high priority targets to lower priority targets.

with larger $SNR_{JWST}$ than TRAPPIST-1, that we mentioned in section 2.1.2, have all been observed extensively. Unfortunately, no clear candidates have been identified around these targets for the moment.

### External programs

Besides the three core programs detailed above, SPECULOOS dedicates 20% of its observing time to external programs (and even up to 50% in the special case of SAINT-EX with CHEOPS follow-up). For this reason, I developed another mode on `spock` that allows to schedule the observation of external targets either for a defined period of time, with a given ephemeris or as long as physically possible. In that regard, `spock` distinguishes four distinct cases of external programs:

1. Monitoring of a target for a given duration and in specific conditions (fixed airmass for instance). An example of the piece of code necessary to schedule such monitoring observations is given on Listing 3.

```
import SPOCK.short_term_scheduler as SPOCKST
from astropy.time import Time

schedule = SPOCKST.Schedules()
schedule.load_parameters()
schedule.observatory_name = 'SSO'
schedule.telescope = 'Europa'
schedule.day_of_night = Time('2020-12-12 15:00:00')
schedule.start_end_range = Time(['2020-12-12 23:00:00',
'2020-12-13 01:00:00'])
schedule.monitoring(input_name='Trappist-1', airmass_max=1.5,
time_monitoring=10) # time_monitoring in minutes
```

**Listing 3** - Example of creation of a monitoring `night block` for the target TRAPPIST-1 for 10min at a maximum airmass of 1.5 on SSO/Europa using `short_term_scheduler` class.

2. Observation of a target as long as possible given the site constraints (moon distance, elevation, twilight limits). An example of the piece of code necessary to schedule such an observation is given on Listing 4.

3. Observation of a target given specific start/ end times for the observations. If the input times do not respect the intrinsic constraints of the observatory a warning is triggered and the start/end times are automatically adapted. An example of the piece of code necessary to schedule such an observation is given on Listing 5.

4. Follow-up observation of an up-coming transit or occultation event given a set of ephemeris. An example of the piece of code necessary to schedule such an observation is given on Listing 6.

```
import SPOCK.short_term_scheduler as SPOCKST
from astropy.time import Time

schedule = SPOCKST.Schedules()
schedule.load_parameters()
schedule.observatory_name = 'SSO'
schedule.telescope = 'Europa'
schedule.day_of_night = Time('2021-05-21 15:00:00')
schedule.special_target(input_name='TOI-2096')
```

**Listing 4** - Example of creation of a `night block` lasting for as long as possible on the night of the 2021-05-21 for the target TOI-2096 on SSO/Europa telescope using `short_term_scheduler` class.

```
import SPOCK.short_term_scheduler as SPOCKST
from astropy.time import Time

schedule = SPOCKST.Schedules()
schedule.load_parameters()
schedule.observatory_name = 'Saint-Ex'
schedule.telescope = 'Saint-Ex'
schedule.day_of_night = Time('2020-12-12 15:00:00')
schedule.start_end_range = Time(['2020-12-12 23:00:00',
'2020-12-13 01:00:00'])
schedule.special_target_with_start_end(input_name='NGTS-11')
```

**Listing 5** - Example of creation of a `night block` with given start/end limits for the target NGTS-11 on Saint-Ex telescope using `short_term_scheduler` class.

```
import SPOCK.short_term_scheduler as SPOCKST
from astropy.time import Time

schedule = SPOCKST.Schedules()
schedule.load_parameters()
schedule.observatory_name = 'SSO'
schedule.telescope = 'Europa'
schedule.day_of_night = Time('2021-05-21 15:00:00')
schedule.transit_follow_up(input_name='Trappist-1c')
```

**Listing 6** - Example of `short_term_scheduler` on SNO/Artemis telescope with `spock`

In each case the `short_term_scheduler` class creates a `night block` that is either inserted in the existing sequence for the night (in the case a schedule already exists), or saved

as a "locked" `night block` that will be automatically included when the schedule will be made for this day through the `long_term_scheduler` class. When a `night block` is inserted in an existing sequence different scenarios are possible, they are summarised on Figure 2.18.

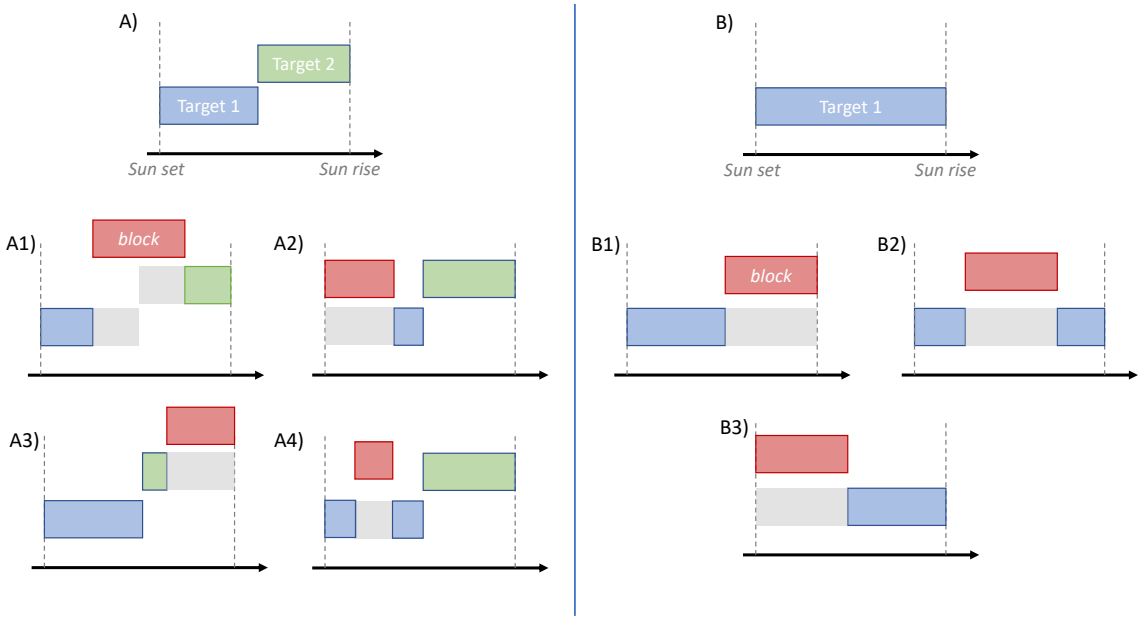


**Fig. 2.18** Illustration of the different cases for the insertion of a external program `night block` in an existing sequence. These cases are separated in the two most common scenarios (A) one target is already scheduled all night long (B) two targets are scheduled. The new block can either split an existing night block in two, change the start time of an existing block or change the end time of an existing block. The process is identical when more than two targets are already scheduled.

### Additional functionalities

In addition to its scheduling features, `spock` offers easy access to several specific plots and tables that are particularly insightful for strategy and scheduling. Some of these functionalities and associated code are exposed on Figure 2.19.

Now that I have explained the SPECULOOS project's strategy and how observations are scheduled, I will explain what happens once the data have been acquired.

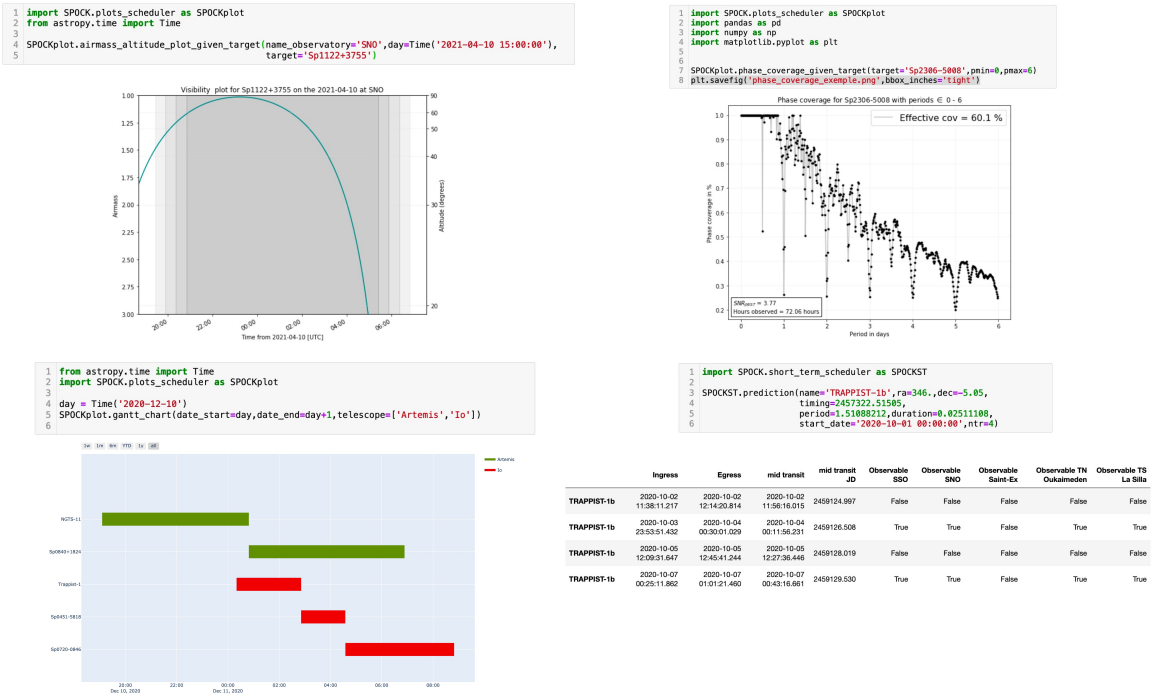


| | Ingress | Egress | mid transit | mid transit JD | Observable SSO | Observable SNO | Observable Saint-Ex | Observable TN Oukaimeden | Observable TS La Silla |
|---|---|---|---|---|---|---|---|---|---|
| TRAPPIST-1b | 2020-10-02 11:38:11.217 | 2020-10-02 12:14:20.814 | 2020-10-02 11:56:16.015 | 2459124.997 | False | False | False | False | False |
| TRAPPIST-1b | 2020-10-03 23:53:51.432 | 2020-10-04 00:30:01.029 | 2020-10-04 00:11:56.231 | 2459126.508 | True | True | False | True | True |
| TRAPPIST-1b | 2020-10-05 12:09:31.647 | 2020-10-05 12:45:41.244 | 2020-10-05 12:27:36.446 | 2459128.019 | False | False | False | False | False |
| TRAPPIST-1b | 2020-10-07 00:25:11.862 | 2020-10-07 01:01:21.460 | 2020-10-07 00:43:16.661 | 2459129.530 | True | True | False | True | True |

**Fig. 2.19** *Top left:* Visibility plot produced with `spock`. *Top right:* Evolution of the phase coverage for a given SPECULOOS target as a function of the period of an hypothetical planet. *Bottom left:* Gantt chart for a given date of all night blocks scheduled on a chosen set of SPECULOOS telescopes (here Artemis and Io). *Bottom right:* Table with the *ntr* upcoming transits event for a given candidate and set of ephemeris from a start date.

## 2.2 Data processing and analysis

Every night, operators (which are members of the SPECULOOS consortium) connect to the control computer of each telescope, check the weather status, the smooth running of the softwares, and launch ACP plans to start the observations. This can be done hours before the night actually starts, and it is the only manual manipulation that the operators need to do. From then, all actions are automatised (update of the ACP observation plans, telescope guiding, calibration images acquisition, data acquisition, interruption due to bad weather etc). In this section, I will detail how SPECULOOS data are reduced and how light curves are produced on a daily basis. This presentation will be based on a publication I significantly participated to, again led by my collaborator Daniel Sebastian and entitled: *Development of the SPECULOOS exoplanet search project*.

### 2.2.1 SPECULOOS data reduction pipelines

The raw images from the SSO observatory are automatically transferred at the end of each night to the online ESO archive[16]. These images are then downloaded to a server at the University of Cambridge (UK) the next day. In parallel, the raw images from the SNO observatory are directly transferred each day to the same Cambridge server.

#### SSO & SNO

Images from the SSO and SNO observatories are then processed daily by the automatic SSO Pipeline (C. A. Murray et al. 2020). The SSO Pipeline is custom-built for the calibration and photometry requirements of the SPECULOOS survey, following a modular architecture similar to the Next-Generation Transit Survey (NGTS) pipeline (Wheatley et al. 2018), and utilising the `CASUTOOLS` (Irwin et al. 2004) package of image processing tools (namely `IMCORE, WCSFIT, IMSTACK` and `IMCORE_LIST`). The science images are reduced using standard methods of bias and dark subtraction and flat-field correction (detailed in Chapter 3). We then use a local version of `ASTROMETRY.NET` code (Lang et al. 2010) to cross-match our science images with reference catalogues built from the 2MASS catalogue to generate initial World Coordinate System (WCS) solutions. To refine these WCS solutions, we perform source detection on our images and then, using the initial WCS solutions, cross-match these sources with the Gaia DR1 catalogue (Prusti et al. 2016), to further correct each image for translations, skews, scales, and rotations. For each field that is observed the pipeline requires an input catalogue, containing the positions of every source from which to extract aperture photometry data. We choose to have one, unique catalogue for every observed field for all nights that field is observed. This allows us to monitor the photometry of all sources in this field consistently over long periods of time. To create this catalogue, we perform source detection on a stacked image, generated from 50 images taken in the middle of the first night of observation of a field. We also cross-match this catalogue with Gaia DR2 (Gaia Collaboration et al. 2018) to apply proper motion corrections on a nightly basis. There is also the facility to cross-match with other catalogues, such as 2MASS (Skrutskie et al. 2006). This catalogue then defines the central positions of apertures from which we measure raw photometry for each object in the field, for 13 different aperture radii. The 13 apertures used are multiples ($1/2$, $1/\sqrt{2}$, 1, $\sqrt{2}$, 2, $2\sqrt{2}$, 4, 5, 6, 7, 8, 10, 12) of $r_{core}$, with $r_{core} = 4px = 1.4$" by default.

Once the raw, aperture photometry has been extracted, the SSO Pipeline corrects for ground-based systematics shared by other objects in the field by using an automated differential

[16] http://archive.eso.org/eso/eso_archive_main.html

photometry algorithm. This iterative algorithm calculates an "artificial" comparison light curve by weighting the sufficiently bright comparison stars according to their variability and distance to the target. Due to the survey's design, the redder comparison stars in the field are significantly fainter than the target, therefore we do not input any colour information into the weightings, to avoid introducing noise into the target's light curve. This mismatch in spectral type between the target and comparison stars leads to second-order differential extinction residuals imprinted on the target's light curve. To mitigate these residuals we implement a correction for precipitable water vapour from first principles, detailed in section 2.2.2.

### SAINT-EX

SAINT-EX uses a different reduction process than SSO and SNO. The data are reduced by a custom pipeline, PRINCE (Photometric Reduction and In-depth Nightly Curve Exploration), that ingests the raw science and calibration frames and produces clean light curves. The PRINCE pipeline performs standard image reduction steps, applying bias, dark, and flat-field corrections (detailed in Chapter 3). Astrometric calibration is conducted using Astrometry.net (Lang et al. 2010) to derive correct World Coordinate System (WCS) information for each exposure. Photutils star detection algotithm (Bradley et al. 2019) is run on a median image of the whole exposure stack to create a pool of candidate stars in the field of view. Stars whose peak value in the largest aperture is above the background by a certain threshold, defined by an empirical factor times the median background noise of the night, are kept as reference stars for the differential photometric analysis. From the WCS information and the detected stars' coordinates, the pipeline runs centroiding, aperture and annulus photometry on each detected star from the common pool, using LMFit (Newville et al. 2021) and Astropy (Price-Whelan et al. 2018; Robitaille et al. 2013), and repeats this for each exposure to obtain the measured light curves for a list of apertures.

PRINCE then corrects for systematics in these light curves via two separate methods. The first is a simple differential photometry approach that corrects a star's light curve by the median light curve of all stars in the pool except for the target star. The second method is a weighted Principal Component Analysis (PCA) approach (Bailey 2012)[17] with some added features. Outlying data points are removed by an iterative sigma-clipping procedure. Stars for which a large fraction of the light curve are outliers are flagged. Stars which appear blended or have close neighbours are also flagged. In the PCA, data points of each star are weighted by the SNR, with flagged stars, the target and outliers having their weight set to zero. The PCA is then run a second time, with uncertainties scaled such that a reduced $\chi^2$ for each

[17] https://github.com/jakevdp/wpca

star's light curve equals unity. This has the effect of increasing the weight of well-behaved stars.

### 2.2.2 The effect of precipitable water vapour

Observing in the NIR, necessary due to the faintness of very red targets in the optical, provides additional photometric challenges to those usually faced by ground-based observatories. For the SPECULOOS core program, we use the $I+z$ photometric filter for the majority of observations. This wavelength range is strongly affected by telluric lines, most notably by atmospheric water absorption lines. As redder wavelengths are more readily absorbed by water than bluer wavelengths, the photometric impact will depend on the spectral energy distribution, and therefore increases for later spectral types. When we perform differential photometry we then introduce differential residuals due to the difference in spectral types between the red target and bluer comparison stars. The amount of water in the atmosphere can change rapidly and the resulting photometric residuals can be significant, of the order of $\sim$1%. Mitigating this water vapour effect is therefore essential as it can mimic transit features in our light curves and complicate the long term variability studies of our targets.

Where they are available, we can use measurements of the precipitable water vapour (PWV) to directly probe the level of water absorption in the atmosphere, allowing us to model the Earth's atmospheric transmission. For the SNO observatory, 30 minute cadence PWV measurements are already available from a GPS based system (Castro-Almazán et al. 2016). It is planned to install and test a tau-monitor (Furuno) in 2021, which should provide more precise and accurate PWV measurements and with a higher cadence. For the SSO observatory we have access to high cadence zenith PWV measurements from the LHATPRO (Low Humidity And Temperature PROfiling radiometer) instrument at the Very Large Telescope in Cerro Paranal, situated approximately 150 m in altitude difference and 1.8 km in lateral distance from the SSO observatory (Kerber et al. 2012). To model the atmospheric conditions at the SSO observatory we use the Sky-Calc Sky Model Calculator, a tool developed by ESO which is based on the Cerro Paranal Advanced Sky Model (Jones et al. 2013; Noll et al. 2012). This tool uses PWV and airmass values to provide a corresponding atmospheric transmission model. By taking into account the instrument response through the $I+z$ filter, and using synthetic stellar spectra from PHOENIX (Husser et al. 2013), we can predict the photometric impact for objects of different spectral types, for a given PWV value and airmass. We then correct the differential light curves by dividing by the predicted PWV effect. This process (Pedersen et al. 2021a) is intrinsic of the SSO Pipeline differential photometry algorithm. Unfortunately, no PWV measurement are available for the moment for SAINT-EX

observatory, although an alternative method using satellite images is under study and foresee promising results.

### 2.2.3 SPECULOOS portal

To enable easy access to the SPECULOOS pipelines's output, a web-based service and interface was designed, called PORTAL (Pipeline Output inteRacTion Analysis Layer). It was built using a common backend stack – LAMP (Linux, Apache, MySQL, PHP/Python), with the JavaScript framework `Vue.js`[18], the Python framework `Plotly`[19], and the JavaScript library `D3.js`[20]. Its main operation permits quick and interactive visualisation of nightly light curves from the SSO, SNO and SAINT-EX observatories. It also serves as a `RESTful`[21] application program interface (API) that uses HTTP requests to access and use data, which allows members of the SPECULOOS consortium to download and analyse any of the pipeline's outputs and connected metadata.

#### Backend

The backend bridges the link between SSO Pipeline/PRINCE data products and the user-friendly frontend interface, by behaving as a `RESTful` API. The pipeline's output directories are navigated by the backend, using Gaia DR2 source IDs as the main search parameter, with the option to further refine by specifying date, telescope, and filter – with arrays of values and wildcards permitted in a search query. To retrieve nightly observation data, the backend processes multiple text files (one per aperture) containing nightly differential light curves (PWV and non-PWV corrected) and metadata (relative RA and DEC movement, FWHM, PSF, sky level, and airmass), and formats them into a single JSON structure.

For larger queries, a SQL (Structured Query Language) database was implemented. It contains all the nightly observation data, as well as environment/telescope specific metadata (technical logs). The tables are updated whenever a directory is updated by the pipeline. The database also stores SPECULOOS' observation history (based on the pipeline's output directories) and the observation schedule (provided by `spock`'s output files). The SQL database also stores user submitted flags and comments on nightly data provided by the frontend. The total number of hours a target has been observed for, as processed by the pipeline, can be also queried. The backend also produces low resolution videos from the

[18] https://vuejs.org/
[19] https://plotly.com/
[20] https://d3js.org/
[21] https://restfulapi.net/

raw 2K × 2K images acquired during an observation, which forms part of a target's detailed observation view produced by the frontend.

### Frontend

The frontend is a user-centred designed interface for displaying differential photometry data. It allows navigation and interaction with observations made by all of SPECULOOS' facilities, on a target and nightly basis. The user-friendly interface, as shown in Figure 2.20, has a vertical menu panel and an interchanging main panel.

The navigation panel contains a search function with autocomplete capabilities. A user can search based on either a target's Gaia DR2 source ID or the shorter SPECULOOS target ID. By default, the search function will return all the light curves for a particular target, ordered by latest dates first. Nightly light curves are presented within interactive scatter plots, with raw and binned data. In its default view, the scatter plots are displayed with PWV corrected light curves (if available) using an aperture value pre-determined by the pipeline, within the differential flux range of [0.98,1.02], and a binned period of 0.005≃JD. A user can quickly interact with the data by zooming in/out and toggling between apertures, binned periods, and the PWV applied correction. If a user spots an interesting feature, such as a flare, a transit feature, a type of variability, or an issue with the data, they can tag the data, as well as submit a comment to be connected with the observation. On hover, one can view previous submissions, or one can view all submissions for a target on a separate tab.

To vet the data further, one can access a target's detailed observation view for a night, as exemplified in the bottom of Figure 2.20. Here, one can explore metadata, such as relative RA and DEC movements, FWHM, sky level, airmass and comparison stars light curves. Some of the extended metadata are quality-checked for anomalies, which are used to inform the user. A video of the observation is also present, which allows one to navigate though the images of the night, triggered by hovering over different parts of the light curve. Lastly, one can automatically open a Slack channel to allow for further discussions of the target with the rest of the SPECULOOS consortium. To promote further vetting of data, a user can view the latest light curves, a random target's light curves, or a detailed observation view for a random target and night. The schedule can also be navigated by date, and if the target has been observed, it links to its respective detailed observation view. The final links on the navigation panel are to the telescopes' status pages, and a timelapse view of SSO's widefield night-sensitive webcam.

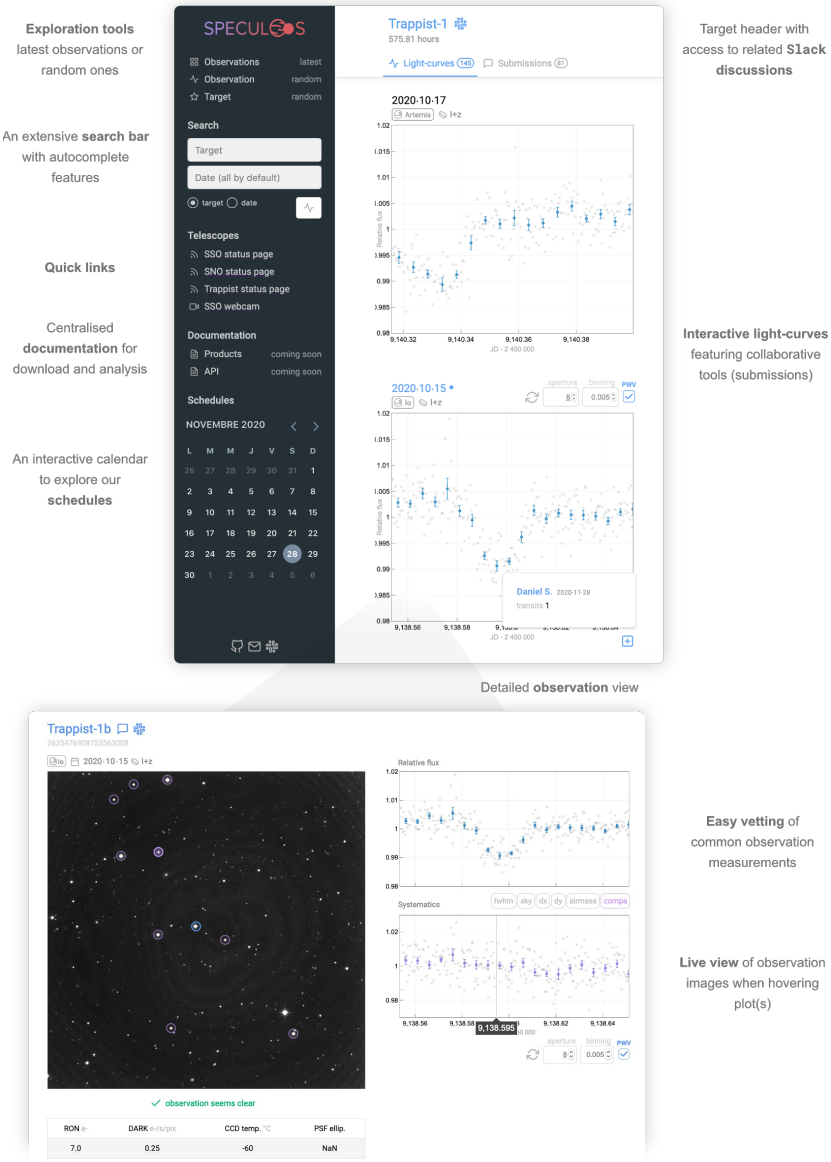


**Fig. 2.20** A descriptive view of PORTAL's web interface. *Top:* a target specific view for Trappist-1, with an example set of interactive light curves and a flag submitted by an user. *Bottom:* a detailed observation view for a particular night for TRAPPIST-1. The collection of tools offered by PORTAL allows for an intuitive and collaborative exploration of differential photometry data, which can be downloaded for extensive offline analysis via the backend's RESTful API. Figure from Sebastian et al. (2020).

## 2.3 Results

Now that I have exposed SPECULOOS operations, strategy, scheduling, data acquisition, reduction andorganistion I will discuss several scientific cases that were revealed or studied with SPECULOOS.

### 2.3.1 Core programs

While the official inauguration of the SSO observatory was the 1st of January 2019, informal operations on the first SSO telescopes started as early as June 2018. This combined with the plurality of telescopes at the SSO observatory justifies why the majority of SPECULOOS core program observations (to this date) were performed with SSO telescopes. Consequently, the first study on the photometric performance of the SPECULOOS telescopes was carried out on SSO observations. In this section, I succinctly present the photometric quality reached with the SSO pipeline and shortly discuss the photometry variability and activity of the sample of UCDS observed so far with SSO. This presentation is based on the results from two distinct publications, both led by my collaborator Catriona Murray, that I was involved in. For more details I refer the reader to C. A. Murray et al. (2020) and C. Murray et al. (2021).

#### Photometric quality of SSO observations

To assess the photometric quality of the SSO observatory, the fractional RMS of each target light curves was measured for 30 minute bins, from January 1st (start of official scientific operations) to September 18th, 2019 (C. A. Murray et al. 2020). This data sample contained 98 targets observed over 179 nights of observation with the SSO telescopes. No detrending, no correction for intrinsic variability nor removal of sub-optimal observing conditions was performed. All data were processed with the SSO pipeline and the resulting light curves showed a photometric precision that is reaching sub-millimag performances for ~30% of the light curves (with a median precision of 1.5 mmag), and up to 0.26 mmag for the brightest objects.

As a comparison with TESS performances, Figure 2.21 shows the light curves obtained from simultaneous observations of a variable M6V object with a single SSO telescope and TESS 2 minute and 30 minute cadence.

We note that, there is excellent agreement between the three datasets, with the SSO light curve exhibiting the least white noise. As TESS is not optimised for UCDS, we expect that the quality of the SSO light curves will exceed TESS for cooler and redder objects, however for the bright M5V and M6V objects the quality of the photometry will be comparable. This demonstrates how we can utilise the synergy between SPECULOOS and TESS to optimise the detection of Earth-sized planets, as in Programme 2.

In addition, to illustrate the typical capability to detect single transits of Earth-size planets, Figure 2.22 displays the measured fractional RMS (for 30-min bins) for the SSO target lightcurves, for each night of observation. To ensure there was at least 5 bins for each lightcurve, only lightcurves where there was more than 150 minutes of total exposure were

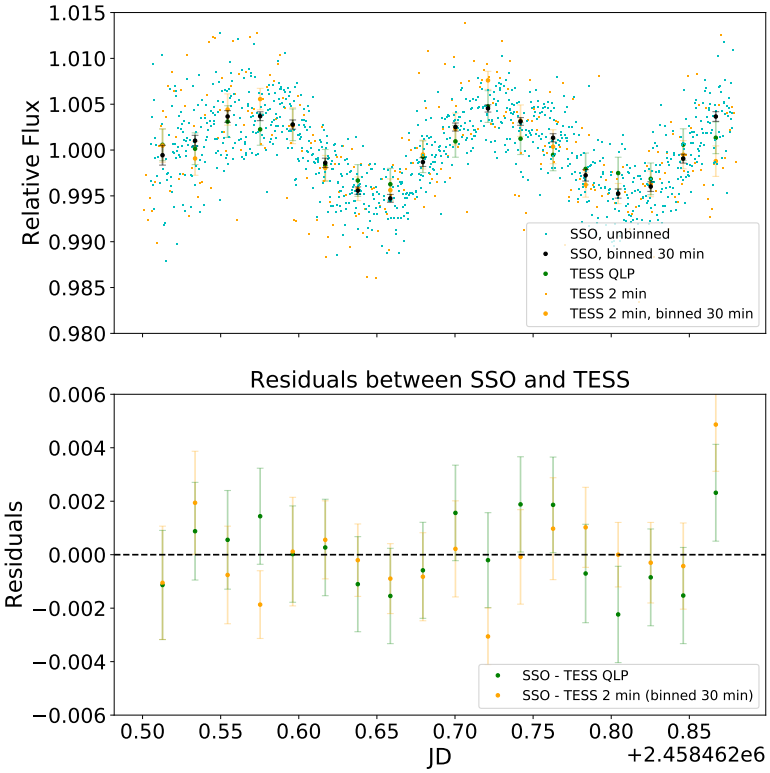


**Fig. 2.21** *Top*: Comparison of light curves from the SSO observatory and TESS for an M6V object (J = 10.3mag) on 2018 December 10. The differential light curve from a single SSO telescope is in cyan, with 30 minute binned data in black, the light curve from TESS 2 minute cadence data is in orange and MIT Quick Look Pipeline 30 minute cadence data is in green. *Bottom*: The residuals between the SSO light curve and the two TESS light curves. Figure from C. A. Murray et al. (2020).

included. This accounts for 106 targets and 184 combined nights of observations with multiple telescopes from January to September 2019. The binning time-scale adopted to compute the RMS was set to match the typical transit duration of a short-period planet orbiting an UCDS. This figure demonstrates that for quiet targets on nights with good observing conditions, we are reaching the best possible precision, as determined by the noise model. This noise model (Merline et al. 1995) accounts for several different contributions: Poisson noise from the star, read noise from the detector, noise from background light, noise from dark current, and atmospheric scintillation. For the atmospheric scintillation, a modified form of Young's approximation, specific to Paranal (Osborn et al. 2015) was used. The targets observed have exposure times from 10–60 s, therefore the noise model for 60 s exposure was assumed, with an overhead of 10.5 s, which gives 25 data-points in each 30-min bin. The noise model illustrated in Figure 2.22 is also assumed for an aperture of 11.3 pixels on the

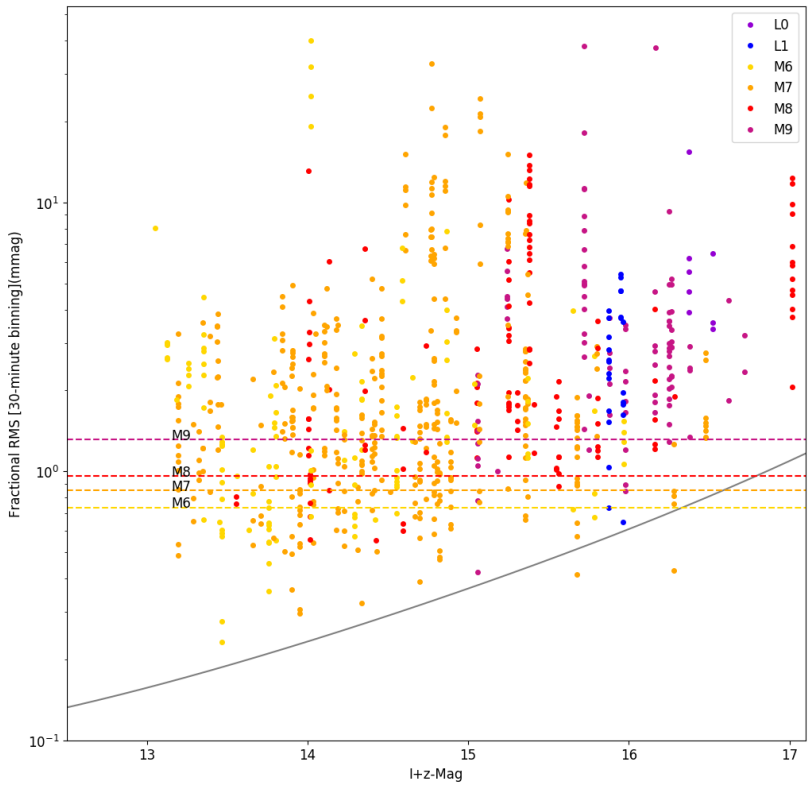


**Fig. 2.22** Fractional RMS (for 30-min binning) of all the SSO's UCDS target lightcurves carried out with $I+z'$ filter from 2019 January 1 to 2019 September 18. There is a data-point for each target on each night of observation - the vertical lines correspond to different fractional RMS on different nights of observation for the same target. The noise model for the best possible observing conditions is shown in grey. The dashed lines show the minimal level of precision needed to detect a single transit of a TRAPPIST-1b-sized planet (1.127 $R_\oplus$) around stars of different spectral types at 9-sigma. These statistics were computed on the raw light curves (no detrending, expect PWV). This means that fast rotators (which display very short timescale photometric variability) can have high 30-min RMS value despite very good photometric measurement's precision. Figure from C. A. Murray et al. (2020).

best possible night, with an airmass of 1 and a background sky level of 37.8 ADU pixel$^{-1}$ (the lowest recorded sky background since January 2019).

There is no correction for photometric variability or selection of the nights with the best observing conditions in this Figure. This results in the vertical stripes for each target corresponding to large spreads in RMS in the lightcurves for different nights, related to the wide range of observing conditions and potentially target's intrinsic variability. This spread can be seen as a limitation to single transit detection efficiency, which outlines the fact that we need to include or remove photometric variability in our transit search.

As a whole, the photometric precision reached by the least active SPECULOOS targets in this diagram show that SSO is reaching sub-millimag precisions for approximately 25% of

lightcurves, and up to ~0.23 mmag for the brightest objects. In Figure 2.22, we superimposed an approximation of the minimum photometric precision required to measure a single transit by a TRAPPIST-1b size planet (1.127 $R_\oplus$) with a signal-to-noise ratio of 9 for different spectral types. This demonstrates SSO's exceptional quality and detection capability, especially for quiet targets observed on nights with good observing conditions. We also note that, although no statistical study was carried out (like on SSO) due to the more recent start of operation, SNO and SAINT-EX show comparable photometric performances before PWV corrections.

### Flares

As I mentioned in Chapter 1, stellar flares on UCDS can be both a source of concern and hope for exoplanets' habitability. In Chapter 4, I will discuss this aspect extensively for the TRAPPIST-1 system. However, first, I would like to highlight some results from a recent study, also led by my collaborator Catriona Murray, on the population of flaring UCDS in the observed SPECULOOS targets.

For this work, over the 661 nights of observations (from 1st June 2018 to 23rd March 2020) were used. This corresponds to 182 unique photometric targets observed for at least one night. These observations had typical exposure times of 20–60 seconds. Any objects that were not part of SPECULOOS's core program (external programs, see sections 2.1.4) were removed. Only the objects which have been observed more than 20 hours with one telescope were considered, resulting in 158 targets. The observation time was defined as the sum of the span of all observation nights (end of night to start of night), where any gap longer than 15 minutes was excluded. These objects covered a spectral type range extending from M4 into the early L dwarf regime (with masses of 0.07–0.2$M_\odot$). All objects in this sample are therefore expected to be fully convective, as the convection limit occurs around 0.35$M_\odot$ (Chabrier et al. 1997). While M4 and M5 objects are not considered ultra-cool dwarfs, they were included in this sample to explore any differences between mid-M, late-M, and L dwarfs.

Among those targets, my collaborators looked for flares following a three steps approach: (1) carry out an automatic search for flares using lightcurve gradients, (2) separate flare candidates from flare-like signals replicated by noise, (3) manually inspect these candidates to confirm those which can be clearly identified as matching the standard flare shape of a sharp flux increase followed by a slower, exponential flux decay, in order to obtain the final flare sample.

As a result of this procedure, 232 flares were identified. Of the 158 unique targets, 85 were found to be flaring (54 %). These flaring stars span spectral type range from M4 ($T_{\rm eff}$ = 3160K) to L0 ($T_{\rm eff}$ = 2313K).

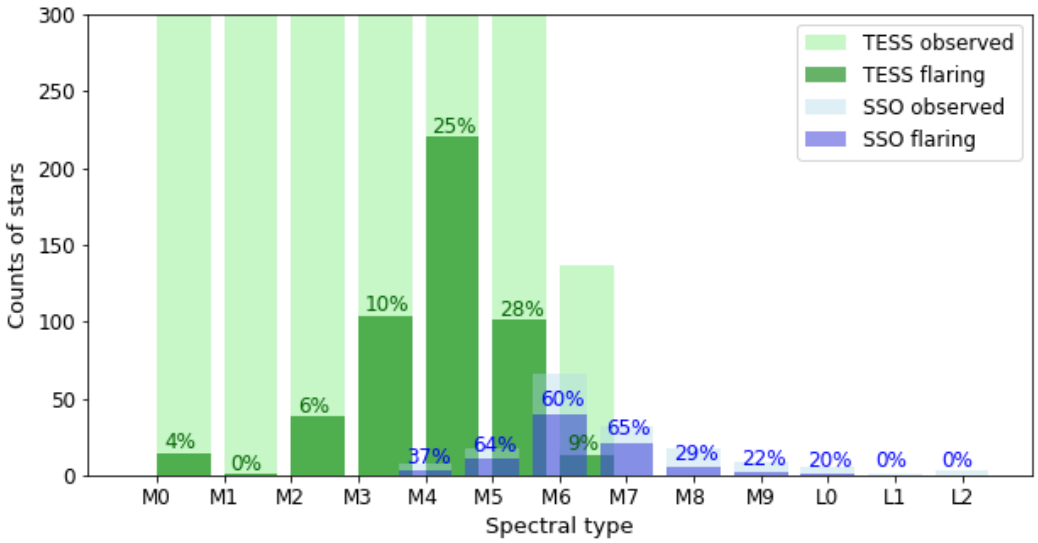


**Fig. 2.23** Histogram comparing the fractions of flaring stars as function of the spectral type from the M dwarf and ultra cool dwarf stars samples used by Günther et al. (2020b) based on TESS observations (in green) and by C. Murray et al. (2021) based on SPECULOOS observations (in blue). For the sake of clarify, the bars are centred on the x-ticks for SPECULOOS and offset to the right edge for TESS.

Figure 2.23 shows the spectral type distribution and proportions of the flaring objects identified in the SSO sample. From this Figure we see that the proportion of flaring stars stays consistently above 60 % for objects of spectral type M5–M7. We also see that the rate of flaring stars begins to decline around M8 ($\simeq$ 30 %), with no detected flares for any object beyond L0. The coolest flaring star detected is a 2313K, M9.6V object (which is rounded to L0 in Figure 2.23). However, for the L dwarfs we are limited by the small sample size, and therefore cannot draw any conclusions about whether the fraction of flaring objects continues to decrease beyond late M dwarfs.

This sample slightly overlaps with the TESS flares survey presented by Günther et al. (2020b) therefore we tried to compare the results. However, we noticed that the populations are unfortunately not very comparable as the number of M type stars (+ UCDS) analysed in Günther et al. (2020b) is greater the 3000 whereas it is only 158 for SSO and only M4V, M5V, M6V type stars were observed with both TESS and SSO. If we gloss over this, in terms of proportions, the fraction of stars flaring in the SSO sample is significantly higher than in the TESS sample. This could stem from: (1) disparities in the flare detection algorithms used on each sample, (2) difference in cadence (higher for SSO than TESS) that could result in

flares rates being underestimated in TESS, (3) lack of photometric precision in TESS light curves of late M stars (4) exceptionally "flary" sample of SPECULOOS targets observed with SSO.

A similar classification system as in E. R. Newton et al. (2016) to the rotating objects. Classifying rotators helps account for the difficulties in deriving a unique non-ambiguous value for the rotation period from sparse ground-based data.When examining each lightcurve, the following questions were asked:

1. Can the candidate periodic rotation signal be seen by eye in the binned, phase-folded data?
2. Was the object observed for long enough to span multiple periods?
3. Is the frequency an alias of the “day signal”, seen as integer multiples in frequency space (periods of 1, 0.5, 0.33 d )?
4. Is there a correlation with systematics (notably in airmass or FWHM periodograms)?
5. Can the rotational modulation be seen by eye in the un-phased lightcurve?
6. If this object was observed with more than one telescope, do the concurrent data agree?
7. Can the “real” period be easily disentangle from its one day aliases?
8. Is the amplitude of the periodic signal above the level of noise in the lightcurve?

If a rotator passed all the above criteria, it was classified as ‘A’. If it failed any of the above, but the rotation still seems likely, it was classified as a ‘B’ grade rotator. Most commonly, the ‘B’ rotators were convincing, but not observe multiple cycles, or it was not esay to choose between the period and its one-day aliases. Any lightcurves for which some periodic structures was spotted, but for which the period was not easily determined, was classified as ‘U’. This can result from broad peaks in the Lomb-Scargle periodogram[22], or multiple possible periods due to lack of observations, or a very low amplitude periodic signal that is comparable to the noise level. Because of these ambiguities in the period measurements, no errors were placed on the period estimates. If not any periodic signal was detected or correlations with systematics existed (such as for very crowded fields), the object classed as ‘N’. Finally, in addition to the classes defined in E. R. Newton et al. (2016), an extra ‘L’

[22]The Lomb-Scargle algorithm (Scargle 1982) is a variation of the Discrete Fourier Transform (DFT), in which a time series is decomposed into a linear combination of sinusoidal functions. The Lomb-Scargle periodogram is optimised to identify sinusoidal-shaped periodic signals in time-series data.

grade was added. 'L' stands for the lightcurves where a long-period rotation was observed, but the period is similar to or longer than the time window observed. In a nut shell the stars that were qualified of "rotators" are those classified as 'A', 'B' or 'L' whereas those classified as 'U' or 'N' are "non-rotators". 69 (24 'A', 22 'B', and 23 'L') rotators were identified, with periods ranging from 2.2 hours to 65 days. 29 objects were identified as 'U' and 60 as 'N' class objects.

For 42 targets, both flares and rotation were detected. Therefore, of the 85 flaring objects, described above, 49% have clear rotation. Alternatively, 61% of the rotators show flares. It appears that while the fraction of rotators across all spectral types stays consistently between 20-50%, there are increasing proportions of slow rotators for the later M9 and L0 stars, which is very surprising as their loss of angular momentum should be lower compared to more massive stars, except if their photosphere is more homogeneous than earlier stars. On Figure

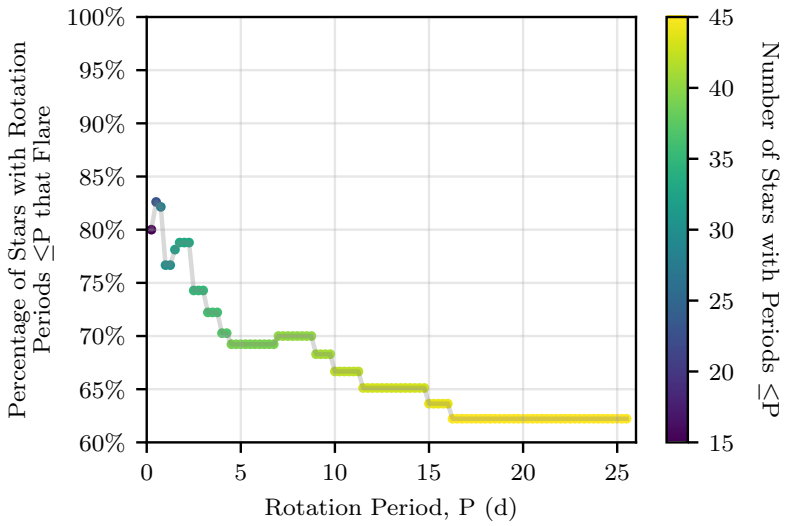


**Fig. 2.24** The proportion of stars with rotation periods ≤ $P$ that have detected flares, against rotation period $P$. Only 'A' and 'B' rotators are included, which range in period from the fastest rotator at 0.09 d to 25.7 d. The colour scale shows the number of stars with rotation period ≤ $P$. Figure from C. Murray et al. (2021).

2.24 we see clearly that the very fast rotators are much more likely to flare than slow rotators. By comparing the rotation period, $P$, with the proportion of stars with rotation periods ≤ $P$ that flare (see Figure 2.24),this demonstrates that the likelihood of flaring decreases as the rotation slows. For this plot only 'A' and 'B' rotators are included, as the uncertainties on the 'L' (long period) rotators are too large. In the sample at least 75% of fast-rotating stars, which rotate with periods less than two days, flare. A slight correlation between the rotation period and flare rate exist, implying that the fastest rotators are more likely to have high flaring rates,

independent of mass. This work therefore confirms the trend of a decrease in the observed flare frequency as a function of rotation period pointed out by Davenport et al. (2019).

Although it is out of the scope of this thesis, studies of the rotation-activity relation of M-type stars are essential to enhance our understanding of stellar dynamos and angular momentum evolution. In particular, the behaviour in the fully convective regime (UCDS) is especially interesting as it has been poorly sampled so far. To that extend, futures population studies of SPECULOOS targets with an even larger sample will be essential.

### 2.3.2 Follow-up

To this date the SPECULOOS telescopes have already enabled the detection, validation and/or characterisation of 22 planetary candidates: EPIC 249631677 b (Niraula et al. 2020), HIP-41378 f (Bryant et al. 2021), TOI-178 b, c, d, e, f (Leleu et al. 2021), TOI-1266 b, c (Demory et al. 2020), TOI-2096 b, c (Pozuelos 2021), TOI-2406 b (Wells et al. 2018), WASP-150 b, WASP-176 b (Cooke et al. 2020), WASP-161 b, WASP-163 b & WASP-170 b (Barkaoui et al. 2019), WASP-190 b (Temple et al. 2019b), WASP-169 b, WASP-171 b, WASP-175b b, WASP-182 b (Nielsen et al. 2019). In addition, SPECULOOS telescopes have driven the discovery of a nearby eclipsing double-line brown dwarf binary (Triaud et al. 2020), as well as the characterisation of a set of M-dwarf stars with complex, sharp-peaked, and strictly periodic photometric modulations (Günther et al. 2020a). In the rest of this section, I have decided to provide the reader with a bit more details on two discoveries I was particularly involved in during my PhD, led by my collaborators Dr. Maximilian Günther and Prajwal Niraula.

#### Complex Modulation of Rapidly Rotating Young M Dwarfs

*Context*

Young M dwarf stars are often fast rotators, with rotational periods ranging from hours to one or two days. In turn, their large rotational energies drive their magnetic dynamos and thus stellar activity (Browning 2008; Moffatt 1978; Parker 1979). This can be observed in terms of activity indicators, such as hydrogen and calcium H & K emission lines, frequent and strong flaring activity, and significant star spot coverage (Benz et al. 2010; Günther et al. 2020b; E. Newton et al. 2017; A. A. West et al. 2015; Wright et al. 2018). In photometric observations, young M dwarfs with spots often show smooth, semi-sinusoidal rotational modulation with amplitudes of a few percents. Their patterns are rather "simple", manifesting only a few peaks in a Fourier transform, even in the presence of multiple spots and differential rotation.

However, some phenomena clearly stood out from this norm such as the so-called *dipper* and *burster* stars, which show abrupt dips or bursts of light in a quasi-periodic or stochastic manner (Alencar et al. 2010; Ansdell et al. 2016; Cody et al. 2014; Morales-Calderón et al. 2011), and were grouped by their photometric morphology into seven distinct classes[23](Cody et al. 2014). In addition, (Stauffer et al. 2017; 2018) discovered three additional morphology classes in Kepler/K2 data[24]. These three new morphologies share common features, such that we refer to them collectively as *scallop shells*. These *scallop shells* differ from the *dippers/bursters* in two substantial ways: (1) the objects discussed by Stauffer et al. (2018) are strictly periodic; and (2) they rotate much more rapidly, typically on timescales of $\lesssim$2 days, compared to the timescales of multiple days to weeks for the *dippers/bursters*. Zhan et al. (2019) discovered very similar objects in TESS data, dubbed *complex rotators*, which are most likely from the same morphology class as the *scallop shell* variables. In total, they discovered 10 targets among all of TESS Sectors 1 & 2, all of which showed dozens of peaks in fast Fourier transform. In comparison, "normal" rotators show only one or two peaks.

It must be noted that all of the *dipper* and *burster* classes were linked to the presence of dusty disks and a viewing-angle dependency, suggested by observations of strong infrared excess, see top panel of Figure 2.25. In parallel, the *scallop shells* were suggested to arise from a patchy torus of clouds of material at the Keplerian co-rotation radius periodically transiting the star, middle panel of Figure 2.25 (Stassun et al. 2018; Stauffer et al. 2017). Considering the similarity between those three morphology classes and *complex rotators* we could wonder whether the latter originate from one of these scenarios. However, while trying to find an explanation for the *complex rotators*, Zhan et al. (2019) presented the following counterarguments to the following hypotheses:

- *Spots only*: even the superposition of up to eight cold and hot stellar spots would only lead to smooth variations and can at most explain one or two peaks in the frequency spectrum (Kovari et al. 1997; Stauffer et al. 2017) but not all of them.

- *Accreting dust disk*: (i) the stable periodicity for *complex rotators*' modulation is very different from the semi-periodic and stochastic nature of the variable classes stemming from accreting disks; (ii) the absence of significant infrared excess in the spectral energy distributions (SEDs) of *complex rotators* contradicts the presence of accreting disks; (iii) the rotation periods of *complex rotators* are much shorter than those of *dippers* (Stauffer et al. 2017).

[23] *periodic dippers*, *aperiodic dippers*, *stochastic variables*, *periodic variables*, *quasi-periodic variables*, *bursters*, and *long-timescale variables*.

[24] *scallop shell*, *persistent flux-dip*, and *narrow flux-dip variables*

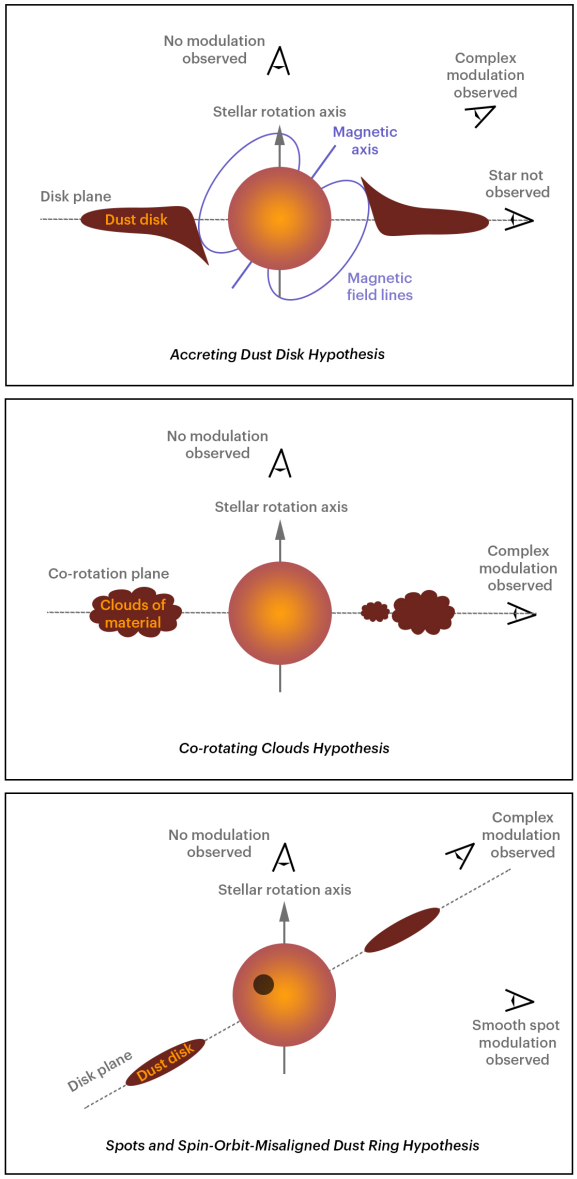


**Fig. 2.25** Three hypotheses to explain complex morphologies of young M dwarfs. *Top panel*: accreting dust disk hypothesis (Bodman et al. 2017). An accreting dust disk seen from different observing angles could explain dipper and burster stars. *Middle panel:* co-rotating clouds hypothesis (Stauffer et al. 2017; 2018). A patchy toroid of gas clouds co-rotating with the star would periodically block out stellar light and cause scallop shell modulation. *Bottom panel:* spots and misaligned disk hypothesis (Zhan et al. 2019). A fast rotating star with spots and a spin-orbit misaligned dust disk might explain the complex rotators. Figure from Günther et al. (2020a).

- *Co-rotating clouds*: (i) if the material is gas, it is challenging to explain the large amplitude of the modulation; (ii) the material cannot be dust, as it cannot be stably confined at the required distances of several stellar radii because the magnetic field at those large distances from the surface would be too weak; (iii) any material (either gas

or dust) trapped in the magnetic field closer to the stellar surface could not reproduce the observations of sharp features with amplitudes of several percents.

Therefore, in this study led by collaborator Dr. Maximillian Günther, we aimed to unveil the nature and origin of these intriguing *complex rotators* following a three-folded approach:

1. investigate the occurrence rates and following plausibility of several hypotheses,
2. study the photometric morphologies' stability and longevity with TESS and SPECULOOS Southern Observatory (SSO) over one (non-continuous) year, and
3. probe colour dependencies with simultaneous SSO photometric monitoring.

*The role of SPECULOOS*

With SSO we observed four targets, TIC 201789285, TIC 206544316, TIC 332517282, and TIC 425933644, each simultaneously in at least two wavelength bands (g', r', i', and z' band filters) for an entire observing night. Light curves were extracted using the SSO pipeline (C. A. Murray et al. 2020). As explained in detail in Section 2.2.1, for each observing night, the SSO pipeline uses the `casutools` software (Irwin et al. 2004) to perform automated differential photometry, and, when possible, detrends for systematics caused by time-varying telluric water vapour. These photometric observations were completed with TESS short-cadence data from Sector 1 (2018-07-25 to 2018-08-22) and Sector 2 (2018-08-22 to 2018-09-10) and part of the cool dwarf catalogue (Muirhead et al. 2018; Stassun et al. 2018) prepared with the Science Processing Operations Center (SPOC) pipeline (Jenkins et al. 2016).

We gathered a total of nine telescope nights of SSO observations to monitor four of the *complex rotators* in simultaneous multi-color bandpasses. All light curves are shown and compared with phase-folded TESS observations (taken one year prior to SSO observations) in Figure 2.26. Evidently, the sharp-peaked features are more prominent in bluer bandpasses, and less expressed in the reddest bandpasses. This can match the expectations from both the *co-rotating clouds* and *spots and misaligned disk* hypotheses: (i) for the *co-rotating clouds* hypothesis, the material's extinction would have to be stronger in the blue, leading to deeper features. (ii) for the *spots and misaligned disk* hypothesis, the contrast between the stellar surface ($\simeq$3000K) and a cool spot is stronger in blue wavelengths than it is in red / infrared wavelengths. The disk material could be a gray absorber or could have a colour dependency, which would add a secondary effect. Combining TESS data with SSO r', i' and g' band observations, our total data span more than one year. We found that the same features were still present in the data at the predicted phases meaning these features remain remarkably stable over the time spanned. While the main features of the *complex rotators* remained

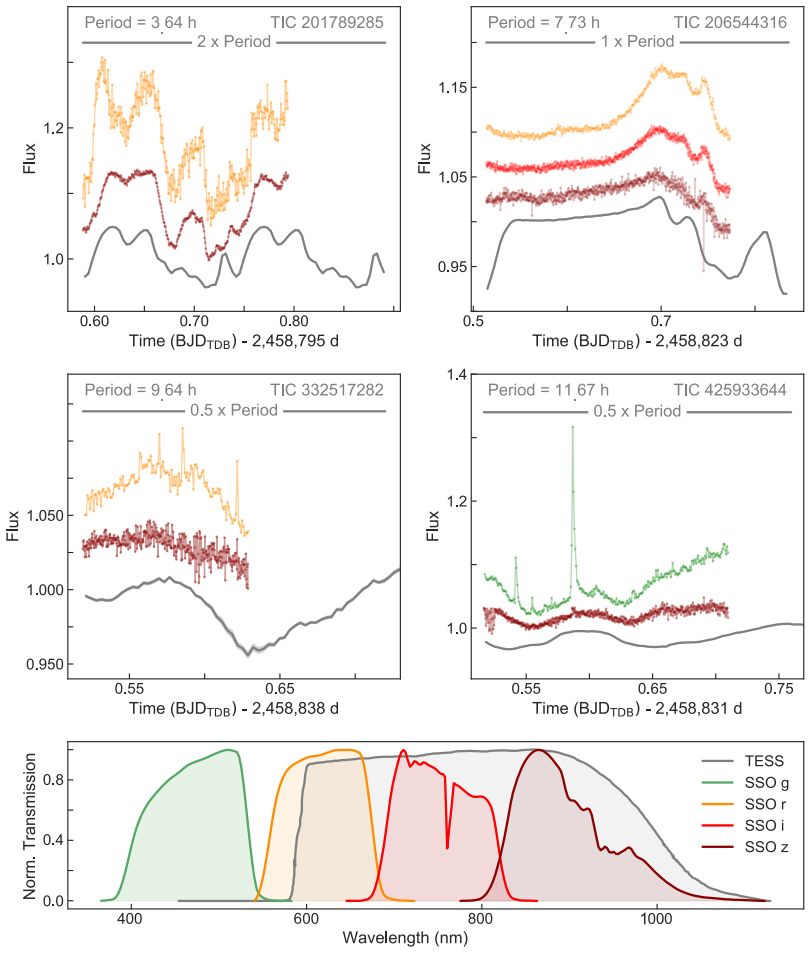


**Fig. 2.26** Comparison of multi-color light curves of four of the ten complex rotators: TIC 201789285, TIC 206544316, TIC 332517282, and TIC 425933644. For each target, SSO observations were taken simultaneously in at least two of the g', r', i', and z' bandpasses (shown as green, orange, red and dark-red curves, respectively). For TESS observations, flares have been removed, and light curves are averaged over all available Sectors, binned in 5 min intervals, and slightly shifted in phase to correct for imprecision in the period measurement (shown as dark-grey curves). The lower panel compares the normalised transmission functions of all respective bandpasses. There is a clear color dependency of the light curve features visible in the simultaneous SSO observations, with features being much more prominent in bluer bandpasses. Additionally, the general shape and largest features in the SSO light curves are still comparable to the TESS light curve, even though the SSO data were taken about 1 year later. This suggests that the overall mechanism causing these patterns also causes a colour-dependency (e.g., spots, non-grey dust, or pulsations), and that it is stable over long times. Fiugre from Günther et al. (2020a).

unchanged, we found evidence for additional small features building up and decaying over a few weeks. In the *Co-rotating Clouds hypothesis*, this would imply subtle changes in the dust/gas cloud structures. In the *Spots and Misaligned Disks hypothesis*, this can very likely

be caused by smaller spots appearing and disappearing, major spots changing size, or spots wandering along the surface.

*Results*

Using these photometric measurements (for colour and time dependency) combined with the computation of occurrence rate, we build a list of pros and cons of the various hypotheses for the origin of this *complex rotators* morphology:

- Spots only; *Pro:* spot modulations can be strictly periodic and stable over many years, even in the presence of differential rotation (Davenport et al. 2020). The temperature difference between the surface and the spots causes a colour dependency, and spots would not cause any infrared excess. Most young stars are spotted and are often accompanied by strong signs of magnetic activity, such as flaring. *Con:* Spots alone cannot explain the sharp-peaked features (Zhan et al. 2019). Yet, spots could still play a major role in combination with other factors (e.g, pulsation or circumstellar material.

- Accreting dust disk; *Pro:* accreting dust disks can lead to the morphologies for *dipper/burster* stars and occur frequently enough. They might show colour dependency depending on the absorption and scattering properties of the material. *Con:* accretion is a rather stochastic process, and thus neither strictly periodic nor stable. The *dippers* and *bursters* also show strong infrared excess due to the large disks, which is not observed.

- *Co-rotating clouds* of material; *Pro:* clouds of material at the Keplerian co-rotation radius could qualitatively explain sharp features and strict periodicity (Stassun et al. 2018; Stauffer et al. 2017). Depending on the material, a colour dependency is possible, and small enough clouds would cause no infrared excess. As young stars are often surrounded by material, they could also occur at high enough rates. *Con:* if the material is gas, the absorption would likely not be able to explain percentage-scale amplitudes (Zhan et al. 2019). If the material is dust, these clouds are likely not stable at the required distances ($d/R_\star \gtrsim 3$; (Zhan et al. 2019)). Another challenge might be the stability and longevity of the morphology over year-long time spans, i.e., over hundreds of orbital periods. With some parts of the clouds slowly drifting away from co-rotation, the signals would be expected to blur out and evolve, which is not observed.

- Material trapped near the surface; *Pro:* material trapped in the magnetic field and bound to the stellar rotation would remain strictly periodic, and could survive over many years near the stellar surface ($d/R_\star \sim 1$; (Zhan et al. 2019)). Depending on the material's properties, a colour dependence is possible, and in small amounts it

might not cause any infrared excess. *Con:* any material that close to the star cannot explain the sharp-peaked, percentage-scale amplitudes of the modulation but would instead produce a rather smooth variation similar to spots; this can only be explained by material at larger distances ($d/R_\star \gtrsim 3$; (Zhan et al. 2019)).

- Spots and spin-orbit-misaligned dust disks; *Pro:* the patterns can be strictly periodic and stable over many years. The spots will induce a colour dependency, and the disk material might add to this effect. There are enough young and rapidly rotating M dwarfs in the sample to explain the high occurrence rates (with caveats, see below). Lastly, the spots are a sign of magnetic activity, and agree with the frequent flaring found on the *complex rotators* and *scallop shells*. *Con:* this scenario would require that a large fraction of young M dwarfs have close-in dust disks with spin-orbit misalignments. There is no obvious formation mechanism that would explain this behaviour. Also, the one M dwarf for which we have disk and rotation measurements, Au Mic, does appear co-planar. However, the misalignment does not necessarily need to be very large. A 10° obliquity between the spin and magnetic axes of T Tauri stars is reasonable, based on Zeeman studies and recent work by McGinnis et al. (2020). If the disks are confined by the magnetic field, this slight misalignment could already be enough to mitigate this caveat and cause the observed morphologies. A potential driver for such misalignment might be perturbations from nearby passing stars, either dynamically or through radiation pressure (Rosotti et al. 2014).

We concluded that all new clues to the case - including occurrence rates, longevity and colour-dependency - could in principle match any of the hypotheses shown in Figure 2.25. It is well possible that the truth lies somewhere in between all these hypotheses. Rapidly rotating young M dwarfs are known to be magnetically active, so the final answer will likely have contributions from both spots and circumstellar material, leading to their complex photometric morphologies.

### $\pi$ Earth: a 3.14-day Earth-sized Planet

Beyond the SPECULOOS Survey, the SPECULOOS telescopes have been used to study the planetary population around mid- and late-M dwarfs. In that context, SPECULOOS facilities have been involved in following up and validating several planetary candidates, notably several identified by *TESS* (Demory et al. 2020; Günther et al. 2019; Kostov et al. 2019; Leleu et al. 2021; Quinn et al. 2019; Wells 2021). Yet, my collaborator Prajwal Niraula decided to revisited *K2* data and identified a strong candidate that we then confirmed to be a

planet. In this section I briefly present this discovery leading by Prajawal, that I significantly contributed to.

*Context*

In order to investigate weaker signals, we revisited *K2* data. We reanalysed the light curves of stars with $T_{\rm eff} < 3500$ K, a Kepler magnitude < 15, and a $\log g > 4.5$. While these criteria were motivated particularly to look for planets around ultra-cool dwarfs, they were relaxed in order to allow room for errors in the stellar properties and improve completeness of the analysis. Among the 1213 stars fitting these criteria, EPIC 249631677 presented the strongest periodic transit-like signal.

EPIC 249631677 was observed by *K2* in Campaign 15 from 2017-08-23 22:18:11 UTC to 2017-11-19 22:58:27 UTC continuously for about 90 days as part of program GO 15005 (PI: I. Crossfield). For our purpose, we used the light curve from the `everest` pipeline throughout this analysis. We used a bi-weight filter with a window of 0.75 days, as implemented in the `wōtan` package[25] (Hippke et al. 2019b), to generate the flattened light curve for further analysis. The simple aperture photometric light curve had a scatter of 2527 ppm, which improved to 685 ppm after `everest` processing. We searched the detrended data for periodic transit signals using the transit least squares algorithm (`TLS`) (Hippke et al. 2019a), and found a prominent peak around 3.14 days. We assessed the presence of additional candidate signals after modelling out the 3.14-d signal by re-running TLS, but did not find any with a significant signal detection efficiency (i.e., SDE>10).

*The role of SPECULOOS*

We followed up on the planetary candidate by observing with SPECULOOS Southern Observatory (SSO) two transit windows on UT 25 February 2020 by Ganymede and on UT 18 March 2020 by Io, and one transit window with SPECULOOS Northern Observatory on UT 18 May 2020 by Artemis. To schedule these windows we used `spock`, described in section 2.1.4. Observations were made with an exposure time of 40 s in an I+z filter (see Section 2.1.1 for details). SSO data were then processed using the SSO Pipeline (Section 2.2.1). SNO data were processed using `prose`[26] (Garcia et al. 2021b). We recovered the transit events in the SPECULOOS observations, whose timings were within $1\sigma$ of the calculated ephemeris from *K2* data. Since these observations were obtained two years after *K2* Campaign 15, they improved the precision of the transit ephemeris by an order of magnitude.

*Results*

[25] https://pypi.org/project/wotan/
[26] https://github.com/lgrcia/prose

The search for transiting planets around small stars has been motivated in large part by their potential for atmospheric characterisation. Owing to the size and proximity of its host, EPIC 249631677 b is thus one of the few known terrestrial exoplanets possibly amenable for atmospheric characterisation in the next two decades. In order to quantify and contextualise its prospects for atmospheric study, we followed the same approach as for TRAPPIST-1 in De Wit et al. (2013) and Gillon et al. (2016), focusing here on all known terrestrial planets. We selected terrestrial planets as planets with a reported radius below 1.6 $R_\oplus$ in the NASA Exoplanet Archive[27] (Fulton et al. 2017; Rogers 2015).

We derived the amplitude of the planets' signals in transmission as:

$$S = \frac{2R_p h_{\rm eff}}{R_*^2}, \text{with}$$
$$h_{\rm eff} = \frac{7kT}{\mu g}, \tag{2.6}$$

where $R_p$ is the planetary radius, $R_*$ is the stellar radius, and $h_{\rm eff}$ is the effective atmospheric height, $\mu$ is the atmospheric mean molecular mass, $T$ is the atmospheric temperature and $g$ is the local gravity. We assumed $h_{\rm eff}$ to cover seven atmospheric scale heights, $\mu$ the atmospheric mean molecular mass to be 20 amu (atomic mass unit), and the atmospheric temperature to be the equilibrium temperature for a Bond albedo of 0. For the planets with missing masses, we estimated $g$ using the `Forecaster`[28] package (Chen et al. 2016) which is based on a probabilistic mass–radius relation conditioned on a sample of 316 well-constrained objects.

The signal amplitudes are reported in Figure 2.27 together with the SNR relative to TRAPPIST-1 b's, calculated by scaling the signal amplitude with the hosts' brightness in $J$ band. We found that EPIC 249631677 b fares closely to the outer planets of TRAPPIST-1 in terms of potential for atmospheric exploration with *JWST* -its warmer and thus larger atmosphere compensating for its larger star. In fact, its relative SNR for transmission spectroscopy is half those of TRAPPIST-1 f–h, meaning that assessing the presence of a $\mu \sim 20$ atmosphere around the planet would require of the order of 40 transits - four times the ~10 transits required for a similar assessment for TRAPPIST-1 f–h (Lustig-Yaeger et al. 2019). EPIC 249631677 b is thus at the very edge of *JWST*'s capability for atmospheric characterisation, mostly due to its "large" host star. With an estimated radial velocity semi-amplitude of 1.3 m $s^{-1}$ (assuming a mass comparable to that of Earth), the planet could be accessible for mass measurements using modern ultra-precise radial velocity instruments. Such possibilities combined with a

[27] https://exoplanetarchive.ipac.caltech.edu
[28] https://github.com/chenjj2/forecaster

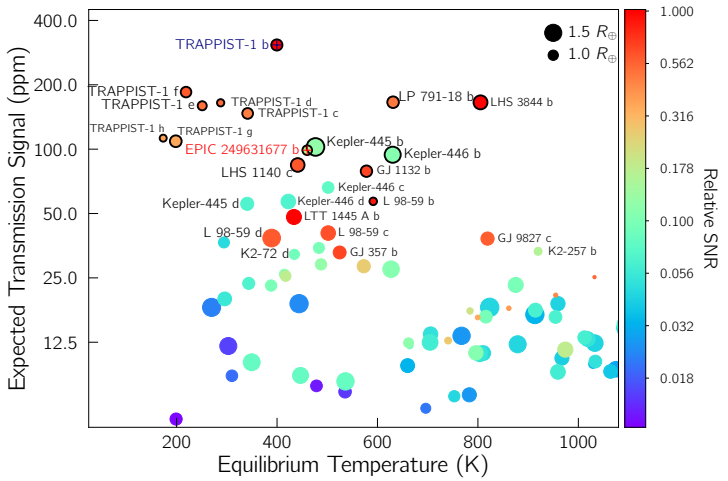


**Fig. 2.27** Most promising terrestrial planets for atmospheric characterisation at the time of publication of the paper, Aug 2020. Point colours illustrate the SNR of a *JWST/NIRSPEC* observation relative to TRAPPIST-1 b. SNR below 1/100th of TRAPPIST-1b and transmission signal less than 5 ppm have been removed to enhance readability of the figure. The planets for which the presence of an atmosphere could be assessed by *JWST* within ~ 50 transits are encircled in black, if their atmospheric signals are above *JWST*'s threshold of ~50 ppm. The rest of the uncircled pool of terrestrial planets may be accessible with the successors of *JWST* if ten times better performance can be achieved. The size of the circle is proportional to the size of the planet. Circles for 1.5 $R_\oplus$ and 1.0 $R_\oplus$ are drawn in the upper right corner for reference. Figure from Niraula et al. (2020).

ranking amongst the 10 best-suited Earth-sized planets for atmospheric study, make EPIC 249631677 b an interesting planet for comparative exoplanetology of terrestrial worlds.

In this second Chapter, I provided an overview of the SPECULOOS project. I detailed its operation, organisation and general functioning. In particular, I presented the different tools/codes that have been developed to facilitate the exploitation of the SPECULOOS data on a daily basis, such as: the automatic SSO pipeline, the PRINCE pipeline, `spock` or the PORTAL. Finally, I introduced some relevant studies that demonstrate the potential of SPECULOOS to discover new planets orbiting UCDS or to successfully assist the detection and/or characterisation of new astronomical objects (planets, *complex rotators* or binaries). In the next Chapter, I will focus on the methods I have been using during my PhD to analyse these data (SPECULOOS, or others) in order to draw scientific inferences on exoplanets.

# Chapter 3

# Methods

In this chapter I detail the methods and tools that were used in my PhD, (1) to produce lightcurves from observations, and (2) to analyse those light curves in order to constrain the parameters of planetary systems (planets + host star).

## 3.1 Data reduction and photometry

In this section, I describe the standard reduction procedure used to extract high-precision light curves from SPECULOOS images. Every night one or two SPECULOOS targets are observed on each telescope (see Section 2.1.3) which represents an average of $\simeq$ 500 images per target per night (of 8.2 MB per image). The reduction of those data is performed as the first step of the pipelines (SSO pipeline or PRINCE) as mentioned in Section 2.2.1. In the following, after a short introduction on CCD imaging, I detail the steps necessary to obtain light curves from raw images.

### 3.1.1 CCD imaging and noises

To estimate the goodness of observations performed using a CCD detector one must estimate the signal-to-noise (S/N) ratio of the observation. This S/N is defined by the "CCD Equation" (Mortara et al. 1981):

$$S/N = \frac{N_\star}{\sqrt{N_\star + n_{pix}(N_B + N_D + N_R + N_S)}}, \tag{3.1}$$

where $N_\star$ stands for the total number of photons (signal) collected from the object of interest. $N_\star$ is generally extracted from several pixels (all of those contained within a stellar profile).

The denominator is the “noise” terms with $n_{pix}$ the number of pixels under consideration for the S/N calculation, $N_B$ the total number of photons per pixel from the background or sky, $N_D$ the total number of dark current electrons per pixel, $N_R$ the total number of electrons per pixel resulting from the read noise, and $N_S$ the noise from scintillation (which is particularly important for ground-based photometry (Mann et al. 2011)).

### 3.1.2 Reduction

The reduction of CCD images makes use of a basic set of images that form the core of the calibration and reduction process, namely: flat field, dark, bias and obviously the data frames of the object(s) of interest (i.e. the scientific images). The calibration/reduction process is the combination of a series of steps:

1. Around nautical twilight (the exact time depends on which SPECULOOS telescope is being used), once the dome is opened and the camera is cooled, flat field images are taken in all the filters that will be used for the scientific observations of the night. The main role of a flat field image is to correct the scientific images from pixel-to-pixel sensitivity variations within the CCD, but also to compensate for any image vignetting and for time-varying dust accumulation, which may occur on the camera window and/or filters within the optical path. Flat field calibration frames are needed for each colour, wavelength region, or different instrumental setup used. A good flat should remain constant to about 1%. At least 5 or more flat fields should be taken and averaged to produce the final "master" flat used for image calibration. On SPECULOOS telescopes, in each filter used for scientific observations, we usually take 7 flats at the evening twilight and an additional 7 at the morning twilight (before the dome closes). All flats are then sigma-clipped to remove outlying pixels (notably stars) and median combined to create a master flat image.

2. After flat field images are acquired in the morning, the dome and camera shutter are closed. Then begins the acquisition of dark frames images with a series of different exposure times. CCD dark frames are images taken with the shutter closed with non-null integration times, usually equal to that of the exposure time of the scientific images. Once corrected for the bias (see below), the dark frames will inform us on the number of photo-electrons thermally generated within an exposure for each pixel of the chip. They also provide information about bad or “hot” pixels that may exist as well as an estimate of the rate of cosmic ray strikes at a given observing site. Dark images are then median-combined to obtain a master dark image.

3. Once dark images acquisition is completed in the morning, bias frame images are taken. Bias frames essentially are images that have an exposure time of zero second. The shutter remains closed and the CCD is simply read out. The purpose of a bias or zero frame is to allow the user to determine the "zero" level of each pixel, whose positive value originates from the CCD on-chip amplifiers. This zero level is set to a positive value to ensure that an analog-to-digital converter will never have to deal with negative values for the charge. A bias frame informs us both on the DC (direct current) offset level (overscan) and the variations of that level (the read). A single bias frame will not sample these variations well enough, so an average of ≃10 frames are taken. Then, they are median-combined to create a master bias image.

4. Once all master calibration images are obtained the science images are corrected. First, the master bias is subtracted from the master dark to create a bias-corrected master dark. Then, this bias-corrected master dark and the master bias are subtracted from the master flat, which is normalised to create a corrected master flat. Finally, the bias-corrected master dark and master bias are subtracted from the raw science frames and divided by the corrected master flat to obtain the calibrated science images (see equation (3.2)).

$$\text{corrected data} = \frac{data - m_b - m_{d,b}}{m_{f,c}}, \tag{3.2}$$

   Where $m_{f,c}$ is the corrected master flat with $m_{f,c} = \frac{m_f - m_{d,b} - m_b}{m_f}$, $m_b$ is the master bias, $m_d$ is the master dark and $m_{d,b}$ is the bias-corrected master dark with $m_{d,b} = m_d - m_b$.

5. The calibrated images are then aligned. Indeed, despite good performance of the telescope tracking with DONUTS, there remain very small drifts in object positions during the night, of the order of ≃0.1 arcsec (≃0.3 pixels). First, stars are detected in each frame following the procedure detailed in section 2.2.1 with the `IMCORE` program. Stars are identified when their peak value is higher than a certain sigma threshold above the local background (dependent on the pipeline used). Their $x, y$ positions with respect to the first images are estimated. The images are then aligned based on these mean $x$ and $y$ shift values, and combined by averaging to produce a stacked image. Outlier pixels are then rejected by using a sigma clipping algorithm.

### 3.1.3 Photometry

Once the scientific images have been calibrated, the stellar fluxes are measured in each of them. To do so, we generally use the aperture photometry technique. In the following, I detail this process:

1. Aperture photometry makes no assumption about the shape of point spread function (PSF) of the source but simply collects and sums up the observed counts within a circular aperture (of radius $r$) centred on the source. By summing the counts collected by the CCD for all the pixels within the area $A = \pi r^2$, and removing the estimated background sky contribution within $A$, we can derive an estimated value of the intensity of each object for each frame. The optimum aperture radius should be the one that maximises the S/N. According to equation (3.1) the S/N increases as more flux is collected (larger aperture) but decreases as the number of pixels within the aperture increases, such that a balance must be found to compute the optimum aperture. To this extend, we take photometric measurements of each source on every image for a multitude of aperture sizes. The flux of each star $i$ (in ADUs) is calculated as $F_i = N_\star - n_{pix} N_B$. We note that $N_B$ is measured in an annulus around the star's aperture.

2. For the detection and characterisation of transits from the ground, we are mainly interested in the relative variability of the stellar flux and not particularly in its absolute value. We therefore rely on what is called "differential photometry". Differential photometry is a technique based on the assumption that stars of similar brightness and colour in a field of view will experience a common photometric pattern, due to shared atmospheric and instrumental effects. Differential photometry measures the flux of a target star relative to the combined flux of one or more comparison stars. First, single aperture photometry is performed on one or more target stars and one or more comparison stars. Then a target star's differential flux is calculated by dividing the target star's net integrated counts, $F_i$ , by the sum of the net integrated counts of all comparison stars (i.e. the sum of $FC_i$, where $i$ ranges from 1 to the number of comparison stars n). For the SSO pipeline, an algorithm was developed to automatically choose and combine multiple comparison stars to ensure that the final differential lightcurves would be reproducible and to avoid the time-intensive, manual selection of stars and potential observer bias. Statistically, it is optimal to use as many stars as possible, weighted appropriately, to reduce the noise levels in the final differential lightcurves. The algorithm implemented in our pipeline is based on a concept described in Broeg et al. (2005). This iterative algorithm automatically

calculates an "artificial" comparison lightcurve (ALC) by weighting all the comparison stars accounting for their variability, and removing those which are clearly variable. These weights are computed following the procedure:

(a) Each object is assigned an initial weight, $W_{var,i}$, determined by its variability, initially defined as $W_{var,i} = 1/\sigma^2_{photon,i}$, where $\sigma_{photon,i}$ is the photon noise of star $i$. These weights are normalised such that they sum to 1.

(b) The ALC is constructed from the weighted mean of the normalised flux ($F_i$) of each of the n objects in the field, at each frame $j$:

$$ALC_j = \frac{\sum_{i=1}^{n} W_{var,i} F_{i,j}}{\sum_{i=1}^{n} W_{var,i}}. \tag{3.3}$$

(c) Every star's absolute lightcurve, $F_i$, is divided by this ALC to produce a differential lightcurve.

(d) The weight for star $i$ is updated to be $W_{var,i} = 1/\sigma_i^2$ where $\sigma_i$ is the standard deviation of the differential lightcurve for star $i$.

(e) Steps (b), (c) and (d) are repeated until the weights are constant to within a threshold of $1e^{-5}$.

(f) To produce the final weights, we multiply the ones obtained at the previous step by an additional weight based on projected distance from the target star, $W_{dist,i} = \frac{1}{\frac{a*s_i}{s_{max}}}$, where $s_i$ is the separation of the comparison star $i$ from the target star, $s_{max}$ is the maximum distance of any star from the target and $a$ is a parameter optimised for each night. The value of $a$ is chosen to minimise the "average spread" of the target's differential lightcurve.

(g) Finally, those weights are normalised.

Then, the final aperture for a given night is chosen to be the one that balance minimises the "average spread" and correlated noise in the target's final differential lightcurve. The "average spread" of the target's differential lightcurve is defined to be the average standard deviation inside 5-min bins. We chose to minimise the RMS inside the bins multiplied by the RMS of the binned lightcurve to avoid minimising genuine photometric structure in the lightcurve (e.g. stellar variability), whilst also avoiding adding correlated noise in the lightcurve, for example from the changing FWHM and airmass during the night if we choose an aperture that is too small.

3. Finally the lightcurve of the target is obtained. An example of light curve obtained with SNO/Artemis is shown on Figure 3.1. We note that the time is expressed in the

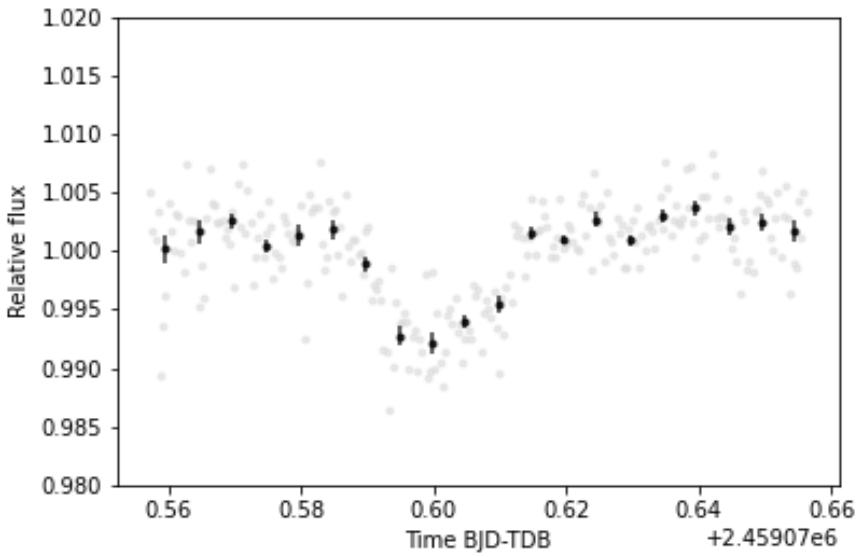


**Fig. 3.1** Example of a transit lightcurve derived from the observations of TRAPPIST-1b transit with SNO/Artemis on the 8th of August 2020.

Barycentric Dynamic Time (TDB) system (which is also the default time standard that is used by our MCMC code in all the analyses). When aperture photometry is performed, in addition to the normalised differential flux and the photometric error, several time-dependent variables specific to the night conditions and target are recorded, such as: the airmass, PSF FWHM (in both dimensions), background, target's position on the chip ($x$ and $y$), PWV (when available). All these variables are useful to model the photometric baseline in a MCMC analysis, see Section 3.2.

## 3.2 Bayesian analysis

Exoplanet research is frequently carried out at the limits of the capabilities of current telescopes and instruments, such that the planetary signals of interest are weak and embedded in complex systematics (noise) from instrumental, telluric, and astrophysical sources. The reliability of the information inferred from the observations depends on how well we understand the statistical characteristics of the observations, and on how well these characteristics are taken into account by the methods used to carry out the inference. To overcome this issue, astronomers rely on statistical inference and particularly Bayesian inference. In brief, the Bayesian approach first assigns a probability to an hypothesis, then a prior probability distribution is used to encode prior information about the hypothesis, and the product of this

prior (probability) distribution and the "likelihood" distribution (which quantifies agreement between the model and the data) will result into a posterior probability distribution. In other words, the Bayesian approach tries to find model parameters that fit well the observations, but also that are in line with the knowledge gathered prior to the observations. Bayesian inference offers several advantages compared to other statistical inference approaches: (1) a consistent approach for combining observational information from different types of observations with prior information, (2) versatile modelling of the observational uncertainties (errors), (3) robust analyses, and (4) a unified, self-consistent, approach for parameter estimation and model comparison. In particular, posterior estimation can be done using Markov Chain Monte Carlo (MCMC) sampling. During my PhD I used the adaptive MCMC code developed by my supervisor Dr. Michaël Gillon, described in Gillon et al. (2010), 2012b, 2014, to perform the combined data analyses for all the candidates, planets or systems that I have studied. In this section, I provide the reader with more details on Bayesian inference and on this particular MCMC code.

### 3.2.1 Bayesian inference

The goal of Bayesian inference is to make probability statements about unobserved quantities that are dependent on observed data. More specifically, in the case of parameter estimation (when we fit a model to data), the goal is to infer the joint probability distribution for the model parameters given some observational data and prior information on the parameter. The probability distribution is called the deduced posterior distribution (posterior), and it is obtained by updating a prior distribution (prior) with a sampling distribution also known as the likelihood or data distribution. In the following we define each of these terms.

#### Posterior distribution

The posterior distribution contains the information about the model parameters given the prior information and the likelihood from observations. We note that the (probability) distributions of individual parameters are obtained from the integration of the posterior over all other parameters than the parameter of interest, also called marginalisation. The joint posterior distribution can be derived from Bayes' theorem (Bayes et al. 1763):

$$P_r(H \mid D) = \frac{P_r(H)P_r(D \mid H)}{P_r(D)}, \tag{3.4}$$

where $P_r(H \mid D)$ is the posterior probability for an hypothesis $H$ given data $D$, $P_r(H)$ is the prior probability for the hypothesis, $P_r(D \mid H)$ is the probability for the data given the hypothesis (or likelihood, see below), and $P_r(D)$ is the probability for the data.

Now if we express equation (3.4) in terms of parameters we have:

$$P(\theta \mid \mathbf{y}) = \frac{P(\theta)P(\mathbf{y} \mid \theta)}{P(\mathbf{y})} \quad = \frac{P(\theta)P(\mathbf{y} \mid \theta)}{\int_\theta P(\theta)P(\mathbf{y})\mathrm{d}\theta}, \tag{3.5}$$

where $\theta$ is a vector containing the model parameters, $\mathbf{y}$ is a vector containing the observed data[1] (in our case photometry). We note that the denominator of equation (3.5) is the probability for the data, and acts as a normalising constant called the marginal likelihood or model evidence. For clarity, equation (3.5) can be re-written as:

$$\text{posterior} = \frac{\text{prior} * \text{likelihood}}{\text{marginal likelihood}}. \tag{3.6}$$

### Prior distribution

A prior distribution's role is to embody the information and assumptions made about a model parameter. Along a Bayesian analysis, the priors are updated by the likelihood to produce posterior distributions. Priors can be classified as either informative priors or uninformative priors, depending on how strongly they restrict the parameter space. Informative priors can be based on results from the literature or obtained theoretically. A common practice is to use a normal distribution as an informative prior with mean and standard deviation based on previously reported parameter mean and uncertainty estimates. On the other hand, uninformative priors aim to minimise the effect the prior will have on the posterior and is appropriate when little is known on the parameter. From these definitions we see that choosing whether a prior should be informative or not is a subjective decision. It is therefore important to test how sensitive the parameter estimation is on the priors and clearly report the priors used in every analysis.

### Likelihood

The likelihood represents the probability that the observations follow a model at a particular point in the model's parameters space. In other words, it quantifies the agreement between the model and the data. The model usually consists of two distinct parts: (1) a deterministic

[1] It can happen that the elements of $\mathbf{y}$ are vectors themselves, in which case we have a matrix of observations $\mathbf{Y}$. For instance, this the case for transmission spectroscopy, where the observed dataset consists of a set of narrowband light curves constructed from a spectroscopic time series

part that represents the signals that can be modelled using a parametric model (for example the model of a transit) (2) a stochastic part that stands for the noise. There are two types of noise: uncorrelated noise (also called white noise) and correlated noise (also called red noise). Depending on whether we consider only white noise or red and white noise the likelihood takes different forms.

#### Marginal likelihood

The marginal likelihood is the denominator term of equation (3.5) and is also referred to as the model evidence. For parameter estimation it can generally be ignored but it is important for model comparison.

#### Marginal posterior distribution

For parameter estimation the marginal likelihood can be ignored, such that the joint posterior density can be simplified to read:

$$P(\theta \mid \mathbf{y}) = P(\theta)P(\mathbf{y} \mid \theta). \tag{3.7}$$

And the posterior distribution for a single parameter can be expressed as the integral of the joint posterior density over all other parameters and is referred to as the marginal posterior distribution:

$$P(\theta_i \mid \mathbf{y}) = \int P(\theta \mid \mathbf{y}) \mathrm{d}\theta_{j \neq i}. \tag{3.8}$$

Ultimately, the goal of Bayesian inference is to estimate the model parameters from observations. To do so, we must obtain an estimate of the joint posterior distribution for the model parameters given the data and prior information and then derive, per parameter, marginal posteriors from the joint posterior (see equation (3.8)). To estimate the model parameters we must find a way to sample this joint posterior distribution. Markov chain Monte Carlo (MCMC) sampling is specifically designed to sample from —and thereby provide sampling approximations to— the joint posterior efficiently even in parameter spaces with large numbers of dimensions.

### 3.2.2 MCMC code

In this section, I present the MCMC code I have used extensively during my PhD.

### MCMC samplers

MCMC is a sampling method that aims at producing a set of samples drawn from the posterior distribution by constructing a Markov chain with the posterior distribution as its equilibrium distribution. The specificities of MCMC methods are (1) the randomness of the search, which is the Monte Carlo part (2) the property that a proposed solution entirely depends on the current state of the process and not at all on the previous states (the system has a memory of one step only), which is the Markov part. Then the term chain gives the indication that this is a process that is carried out in several steps. The more steps, the better the sampling of the posterior distribution. Each of these steps corresponds to a set of parameters from which we derive a model which is compared with the data. For each parameter, the final distribution of the values selected at each step will represent a sample of their actual posterior probability distribution. The transition (or jump) from one set of parameters to the next one can be expressed as:

$$\theta_{n,j} = \theta_{i-1,j} + f\sigma_{\theta_j} G(0,1), \tag{3.9}$$

where $j$ denotes each parameter in turn, $i$ is the step increment that counts the number of accepted states while $n$ counts the number of proposed states. The second term $f\sigma_{\theta_j} G(0,1)$ is refereed to as the step size and embodies how different the new state will be from the current one, with $f$ a scaling factor ensuring that a certain percentage of steps are accepted (see acceptance rate below), $\sigma_{\theta_j}$ is a standard deviation associated to each jump parameter[2] $\theta_j$ and $G(0,1)$ is a Gaussian random number of mean of 0 and standard deviation of 1.

At each step, from the output set of parameters $\theta_n$ we generate a model $\mu$ that we compare to our data $\nu$. To estimate the goodness of the fit we use the $\chi^2$ statistics defined in this case as:

$$\chi^2_n = \sum_{k=1}^{l} \frac{(\nu_k - \mu_k)^2}{\sigma^2_{\nu_k}}. \tag{3.10}$$

The sum is made over all data points (here indexed by $l$). Then we must add some Bayesian penalties to our merit function for parameters for which we have some prior knowledge. These priors are expressed as $\theta_{0,j} \pm \sigma_{\theta_{0,j}}$. If the assumed prior distributions are gaussian, the merit function $Q$ takes the form:

$$Q^2_n = \chi^2_n + \sum_j \frac{(\theta_{n,j} - \theta_{0,j})^2}{\sigma_{0,j}}. \tag{3.11}$$

[2]Jump parameters (or combinations of actual model parameters) are the model parameters that are randomly perturbed at each step of the MCMC.

The goal of the MCMC is to recreate a probability density function (PDF) for each parameter, yet in order to recreate this function, we must estimate at each step our new state $\theta_n$ as a function of our present state $\theta_{i-1}$ and know which state we decide to accept or not. To do so there exist different MCMC algorithms. In the following I present two algorithms that are implemented in the MCMC code I used during my PhD.

- *The Metropolis-Hastings algorithm:* The Metropolis-Hastings (M-H) algorithm is the most commonly used one (Hastings 1970). To know whether we should accept a new state or not, we must show that the likelihood that $\theta_n$ describes the data is larger than the likelihood $\theta_{i-1}$ describes the data. Therefore, we compute the likelihood ratio $r$:

$$r = e^{-0.5(Q_n^2 - Q_{i-1}^2)}. \tag{3.12}$$

  From the value of $r$ different scenarios can occur:

  - if $r > 1$ the new state is accepted. Then a new $n$ is proposed and $i$ is incremented such that now $Q_i^2$ is the new $Q_{i-1}^2$ and $\theta_i$ is the new $\theta_{i-1}$
  - else we draw a uniformly distributed number $u$ between 0 and 1:
    - if $u < r$ the step is rejected implying that $Q_i^2 = Q_{i-1}^2$ and $\theta_i = \theta_{i-1}$. Then a new $n$ is proposed and $i$ is incremented but $Q_{i-1}^2$ and $\theta_{i-1}$ do not change.
    - if $u > r$ the step is accepted, implying that $Q_i^2 = Q_n^2$ and $\theta_i = \theta_n$. Then a new $n$ is proposed and $i$ is incremented such that now $Q_i^2$ is the new $Q_{i-1}^2$ and $\theta_i$ is the new $\theta_{i-1}$.

    This process is then repeated until $i$ reaches the total number of steps (usually ranging from 10000 to 50000).

  Remarkably, it has been demonstrated that M-H algorithm always converges (Betancourt 2018b; Gregory 2005) to an equilibrium state no matter which step size is chosen. Yet, the number of steps to reach "equilibrium" will vary. In that regard, choosing wisely the step size is essential to avoid having all states being accepted (consequence of a step size that is too small) or all rejected (consequence of a step size that is too large). To overcome these problems, we adapt the value of $f$ (from equation (3.9)). We fix the statistical length $l_s$ (usually to 100) to be the number of steps on which we evaluate the acceptance rate, that is to say the percentage of states accepted against $l_s$ steps. According to the literature the optimal acceptance rate we should aim for is 23% (Gelman 2013). Therefore, every $l_s$ steps we adjust the value of $f$ to have an acceptance rate of $\simeq 23\%$.

Another aspect that needs to be taken into account is the fact that the starting location in parameter space might affect the chain's convergence. For instance, if we start the chain far from the posterior state, it may take time before the chain starts to sample the high-probability posterior space. A common practice is to discard a certain percentage of the early iterations in the Markov chain simulation. This process is called "burn-in" or "warm-up" (Gelman 2013). In the analysis I have carried out during my PhD I have always set the "burn-in" to be 20%. Some time during this "burn-in" phase a Gibbs sampling algorithm can be implemented. The Gibbs sampler is the simplest of the Markov chain simulation algorithms, when just a single jump parameter changes at each step. The idea behind Gibbs sampling is to assume that $P(\theta)$ is too complex to draw samples from directly, but that its conditional distributions $P(\theta_j \mid \{\theta_i\}_{i \neq j})$ are tractable to work with. Figure 3.2 illustrates how Gibbs sampling work in the simple case of two variables $\theta = (\theta_1, \theta_2)$. Gibbs sampling allows to derive an individual scaling

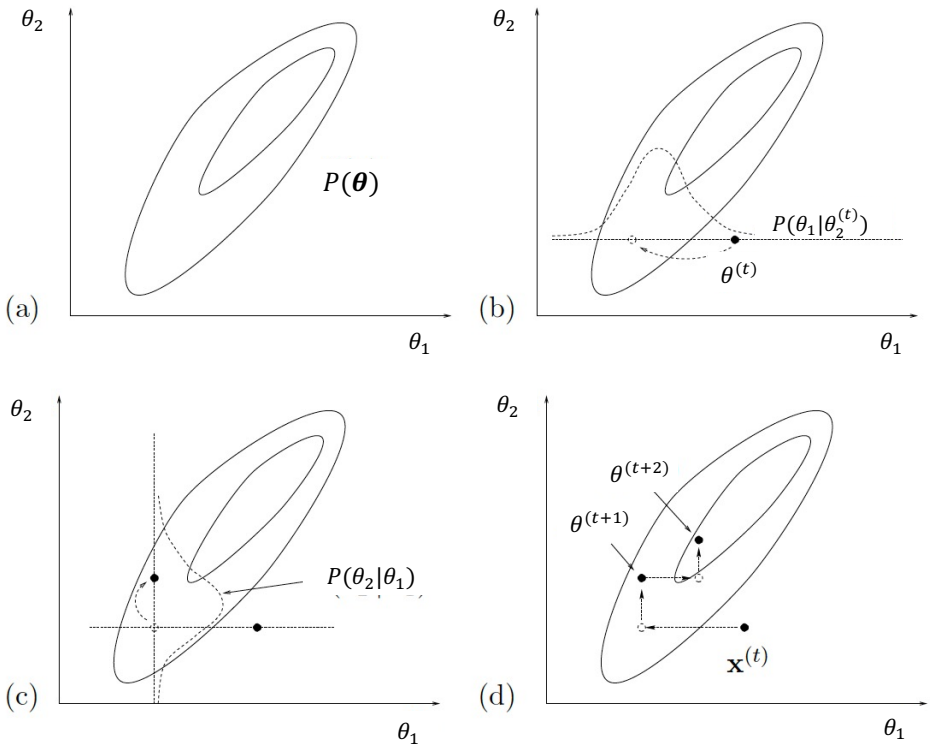


**Fig. 3.2** Gibbs sampling in the simple case of two variables. (a) The joint density $P(\theta)$ from which samples are required. (b) Starting from a state $\theta^{(t)}$, $\theta_1$ is sampled from the conditional density $P(\theta_1 \mid \theta_2^{(t)})$. (c) A sample is then made from the conditional density $P(\theta_2 \mid \theta_1)$. (d) A couple of iterations of Gibbs sampling. Figure adapted from MacKay (2003).

factor $f_j$ for each jump parameter $\theta_j$ during the "burn-in". Once the burning phase is

finished, we are back to varying all jump parameters at each step and adjusting the step size with a common factor $f$.

Usually, multiple chains are run in order to start from different locations in the parameter space. Having multiple chains also allows to test for convergence as converged chains should be statistically similar to each other. Once converged, we assume that the chains have efficiently sample the posterior and can thus be used for inference. There exist several numerical convergence tests to test for chain convergence, I present the one implemented in the MCMC code I used in section 3.2.2.

In terms of probabilities, an M-H algorithm compares $P(\theta_{i,j} \mid D, I)$ against $P(\theta_{i-1,j} \mid D, I)$ where $D$ is the data, $H$ the hypothesis and $I$ the priors, such that we can also express $r$ as:

$$r = \frac{P(\theta_i \mid D, I) q(\theta_{i-1} \mid \theta_n)}{P(\theta_{i-1} \mid D, I) q(\theta_n \mid \theta_{i-1})}, \tag{3.13}$$

Where $q$ is the proposal distribution, that encapsulates all the necessary setup to propose the next point to which the random walk might move.

- *EMCEE:* Developed by Dr. Dan-Foreman Mackey, `EMCEE`[3](Foreman-Mackey et al. 2013) is a Python implementation of the affine-invariant ensemble sampler for Markov chain Monte Carlo (MCMC) proposed by Goodman et al. (2010). `EMCEE` presents the advantages of (1) having excellent performances (2) requiring hand-tuning of 2 parameters only (the number of walkers, and the number of steps per walker) (3) being efficient in sampling correlated parameter spaces while not requiring to calculate posterior derivatives. For these reasons, `EMCEE` was implemented by my supervisor in his MCMC code. The algorithm behind `EMCEE` being quite different from M-H, I will try to describe it concisely but the interested reader should refer to Foreman-Mackey et al. (2013) and Goodman et al. (2010) for further details.

  The algorithm relies on objects called *walkers* which are affine invariant ensemble samplers constructed as follow:

  1. An ensemble of $K$ *walkers* $S = \{X_k\}$ is defined, where the proposal distribution for one walker $k$ is based on the current positions of the $K-1$ walkers in the complementary ensemble $S_{[k]} = \{X_{j,j\neq k}\}$. What we call position is actually a vector in the N-dimensional, real-valued parameter space, with $N$ the number of jump parameters.

[3] https://pypi.org/project/emcee/

2. A walker $X_k$'s position is updated by randomly drawing a walker $X_j$ from $S_{[k]}$ and a new position $Y$ is proposed such that:

$$X_k \longrightarrow Y = X_j + Z[X_k(t) - X_j], \tag{3.14}$$

where $Z$ is a random variable drawn from a distribution $g(Z = z)$ where $g$ satisfies the symmetry condition and is such that:

$$g \propto \begin{cases} \frac{1}{\sqrt{z}} \text{if z} \in [\frac{1}{a}, a] \\ 0 \text{ otherwise} \end{cases}, \tag{3.15}$$

where the parameter $a > 1$ can be adjusted to improve performance (usually set to 2 in `EMCEE`). This move from $X_k$ to $Y$ is called the stretch move and is illustrated on Figure 3.3.

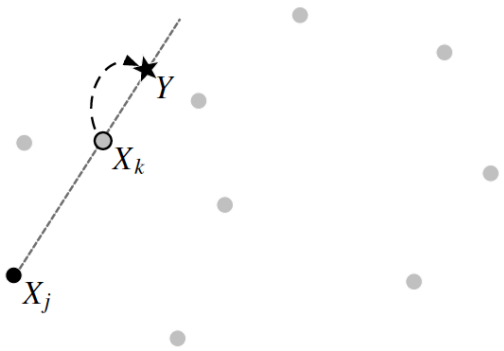


**Fig. 3.3** A stretch move. The light dots represent the walkers not participating in this move. The proposal is generated by stretching along the straight line connecting $X_j$ to $X_k$. Figure from Goodman et al. (2010)

3. A probability $q$ is assigned to the move. $q$ is defined as:

$$q = min\Big\{1, Z^{N-1} \frac{P(Y)}{P(X_k(t))}\Big\}. \tag{3.16}$$

4. As described in the M-H paragraph, a uniformly distributed number $r$ is drawn between 0 and 1:
   - if $r \leq q$ the move is accepted, meaning we set $X_k(+1) = Y$,
   - otherwise the move is rejected and we set $X_k(t+1) = X_k(t)$.

One step of the ensemble Markov chain $X(t) \longrightarrow X(t+1)$ consists in one cycle through all $L$ walkers in the ensemble.

For similar reasons than described in the M-H paragraph, it is recommended to run a few "burn-in" steps (for instance 100 steps) in the MCMC chain to let the walkers explore the parameter space and use the final state of this "burn-in" as a new starting point.

### Convergence

Whether we use M-H or `EMCEE` algorithm we must assess the convergence of our Markov chains. Several statistical tests exist to assess chains convergence but the one implemented in our MCMC code is the Gelman-Rubin (G-R) diagnostic. This diagnostic compares the estimate for the marginal posterior variance $V$ for a parameter $\theta$ to the mean within-chain variance $W$. Indeed, for a set of well-converged chains, $V$ and $W$ should be approximately equal. We therefore define the *estimated scale reduction* for $M$ chains with $N$ steps $\hat{R}$ as:

$$\begin{aligned} \sqrt{\hat{R}} &= \sqrt{\frac{\hat{V}}{W}}, \\ &= \sqrt{(\frac{N-1}{N} + \frac{M+1}{MN}\frac{B}{W})}, \end{aligned} \tag{3.17}$$

where $B$ is between-chain variance, $W$ is the within-chain variance and I have dropped the factor $\sqrt{df/(df-2)}$ compared to the original equation from Gelman et al. (1992), with $df$ the degree of freedom. $B$ and $W$ can be expressed as follow:

$$\begin{aligned} B &= \frac{N}{M-1}\sum_{m=1}^{M}(\hat{\theta}_m - \hat{\theta})^2, \\ M &= \frac{1}{M}\sum_{m=1}^{M}\hat{\sigma}_m^2, \end{aligned} \tag{3.18}$$

where $\hat{\theta}$ is the parameter mean estimated using all samples, $\hat{\theta}_m$ is the mean estimated from a single chain, and $\hat{\sigma}_m^2$ is the parameter variance estimated from a single chain. If the chains are well converged the *estimated scale reduction* should be close to unity. The Gelman-Rubin has to be calculated for each jump parameter. We note that, in the case of `EMCEE`, the computation of G–R diagnostic must use multiple chains in the same ensemble because the chains are not independent, therefore in our MCMC code the walkers are merged into five chains before we estimate the G-R statistic.

Once the chains are converged we can obtain the final joint posterior PDF. Then, we just report the values of all jump parameters (and derived system parameters) obtained at each step throughout the algorithm (either M-H or `EMCEE`) to construct their posterior PDFs. Ultimately, the values and errors for each parameters are the medians and $1\sigma$ limits of these PDFs.

### Model and input parameters

Our MCMC code is adapted for the analysis of both LC and RV time series, however as I only work with photometry during my PhD I will detail only this aspect. To model a transit our MCMC code uses the photometric model by Mandel et al. (2002) that determines the flux as a function of orbital phase. This model takes only four distinct parameters as input:

- the planet-to-star radius ratio $p = R_p/R_\star$,
- the coefficients for limb darkening $u_1$, $u_2$, assuming a quadratic law (see Chapter 1 section 1.2.1 for details),
- the centre-to-centre distance between the star and the planet $r_{ref\ plan}$, and more specifically the normalised separation of the centres $z = r_{ref\ plan}/R_\star$.

Our MCMC code also includes the implementation of the `ellc` FORTRAN subroutines, which offers a binary star model that is designed for the analysis of the light curves of detached eclipsing binary stars and transiting extra-solar planets, which can notably model the effects of star spots. In addition, our MCMC code includes a flare model represented by an instantaneous flux increase followed by an exponential flux decrease. This flare model is embodied by equation:

$$F_{\mathrm{flare},t} = \mathrm{A_{flare}} \times e^{\left(\frac{-dt}{\tau_{\mathrm{flare}}}\right)}, \tag{3.19}$$

where $dt = t - t_{f,0}$ ($t_{f,0}$ being the time of the instantaneous flux increase), $\tau_{\mathrm{flare}}$ is the flux decrease timescale, and $\mathrm{A_{flare}}$ is the flux increase amplitude. To model flares the MCMC code requires an indication on the number of flares present in the light curve and priors on the $t_{f,0}$, $\tau_{\mathrm{flare}}$ and $\mathrm{A_{flare}}$ of each flare. Finally, although not particularly adapted for UCDS, our MCMC code offers the possibility to use a version adapted by Enoch et al. (2010) of the empirical law deduced by Torres et al. (2010) from well-constrained detached binary systems. This law enables to use the mass of the star from $T_{\mathrm{eff}}$, [Fe/H] (both usually derived from spectroscopic measurements) and $\rho_\star$ (constraint by the photometry). In this case, the mass of the star is estimated at each step of the MCMC, without the need for any stellar evolution modelling.

In term of choice of jump parameters, we note that MCMC algorithms' efficiency to sample approximately multivariate normal posteriors is maximal when minimal correlation exists between parameters. And as inefficient sampling implies that a long chain is required to obtain a representative posterior sample, it is preferable to carry out the sampling with a set of parameters that minimise mutual correlations. Several studies (Carter et al. 2008; Ford 2006; Kipping 2010) have investigated how the sampling parameter set affects the efficiency of MCMC routines in the transit light curve modelling and concluded that a transit model can be generally defined using a set of 7 to 11 parameters. In our MCMC code the main jump parameters are:

- the transit depth $\Delta F$ and/or the occultation depth $\Delta F_{occ}$. If there are light curves in multiple filters, we add the transit depth difference $d\Delta F = \Delta F_B - \Delta F$ in each wavelength band $B$,
- the impact parameter in the case of circular orbit $b' = a\cos i/R_p$,
- the eclipse duration $T_{14}$, that is the time between the first and last contact (see Chapter1),
- the eclipse timing $T_0$ (time of inferior conjunction, when the true anomaly at transit is $\nu_{T_0} = \frac{\pi}{2} - \omega$ (with $\omega$ the argument of the periastron),
- the orbital period $P$,
- the quantities $q_1 = \sqrt{e}\cos\omega$ and $q_2 = \sqrt{e}\sin\omega$, where $e$ is the orbital eccentricity and $\omega$ still is the argument of the periastron,
- the stellar metallicity [Fe/H],
- The stellar effective temperature $T_{\rm eff}$,
- the combination of limb-darkening coefficients $c_{1,B}$, $c_{2,B}$ in each band B, with $c_{1,B} = 2u_{1,B} + u_{2,B}$ and $c_{2,B} = u_{1,B} - 2u_{2,B}$ where $u_1$ and $u_2$ are the quadratic limb darkening coefficients,
- the stellar radius $R_\star$,
- the stellar mass $M_\star$,

The optimal sampling parametrisation depends on the purpose of the analysis but a couple of tricks exist to minimise the correlation between jump parameters. For instance, assuming $b'$

instead of $b$ (neglecting the eccentricity-dependent term), or replacing the semi-major axis $a$ by transit duration (Kipping 2010) or stellar density $\rho_\star$ (using equations (1.18) and (1.19)), or using the parametrisation via $q_1$ and $q_2$ (as recommended by Anderson et al. (2011)) to overcome the fact that sampling in eccentricity, and argument of periastron, can be inefficient with most MCMC samplers. Indeed, such a parametrisation ensures that a uniform prior on $q_1$ and $q_2$ leads to a uniform prior on the eccentricity, and $q_1$ and $q_2$ can then be mapped to $e$ and $\omega$ via: $e = q_1^2 + q_2^2$ and $\omega = arctan(q_2, q_1)$. Besides, we must underline that the limb-darkening coefficients (LDC) are mutually correlated and degenerate with the planet-star radius ratio and impact parameter. Which means that many combinations of LDC values, radius ratios, and impact parameters can explain the observations equally well. To overcome these degeneracies several approaches can be considered: (1) using fixed LDC (2) using unconstrained LDC or (3) using LDC constrained by model-based informative priors. The third option presents the advantage of being a good compromise between the first two as it uses information from the models while reducing biases (compared to the first approach) and is less likely to underestimate the parameter uncertainties or reduce the sampling efficiency (compared to the second approach). Consequently, in my MCMC analyses I have always put informative priors on the LDC.

More generally, for each jump parameter we must decide which kind of prior we provide, either informative or non-informative. Usually, normal (informative) prior PDFs are assumed for $T_{\rm eff}$, [Fe/H], $u_{1,B}$, and $u_{2,B}$. Such priors are generally obtained from independent spectroscopic analysis for $T_{\rm eff}$ and [Fe/H] and interpolated from the literature for $u_{1,B}$ and $u_{2,B}$ (using Tables from Claret et al. (2012), 2013). For the other jump parameters, uniform (non-informative) priors are usually assumed. Along the chains, each of these parameters is then perturbed from its previous value by a small, random amount at each step of the MCMC following equation 3.9. The eclipse model is then obtained by computing the relative flux at each time $t_k$ using the analytic formulation derived by Mandel et al. (2002) that relies on $p$, $z$, $u_1$ and $u_2$, where $p$ is directly derived from $\Delta F$, $u_1$ and $u_2$ are directly derived from $c_1$ and $c_2$, and $z$ is derived from:

$$\begin{aligned} z &= \frac{r_{refplan,t_k}}{R_\star}, \\ z &= \frac{a}{R_\star}\frac{(1-e^2)}{1+e\cos\nu_{t_k}}\sqrt{1-\sin^2(\omega+\nu_{t_k})\sin^2 i}, \end{aligned} \tag{3.20}$$

in which $\nu_{t_k}$ must be computed at each $t_k$ following the next logical steps:

1. Geometrically (see Figure 1.14) $\nu_{t_k}$ can be expressed as a function of $E_{t_k}$, the eccentric anomaly at time $t_k$ by:

$$\nu_{t_k} = 2\tan^{-1}\left(\sqrt{\frac{1+e}{1-e}}\tan\left(\frac{E_{t_k}}{2}\right)\right), \tag{3.21}$$

   where $e$ is the eccentricity of the planet's orbit.

2. Then we derive $E_{t_k}$ by solving Kepler's equation which states that:

$$E_{t_k} - e * \sin(E_{t_k}) = M_{t_k}, \tag{3.22}$$

   where $M_{t_k}$ is the mean anomaly defined as $M_{t_k} = n * (t_k - t_p)$ with $n = \frac{2\pi}{P}$ the mean motion (and $P$ is the orbital period of the planet), and $t_p$ is the time of the periastron.

3. To compute $M_{t_k}$ we need $t_p$ which is obtained from:

$$\begin{aligned} t_p &= T_0 - \left(M_{T_0} * \frac{P}{2\pi}\right), \\ &= T_0 - \left(E_{T_0} - e * \sin(E_{T_0})\right) * \frac{P}{2\pi}, \\ &= T_0 - \left(2\tan^{-1}\left(\sqrt{\frac{1-e}{1+e}}\tan\left(\frac{\nu_{T_0}}{2}\right)\right) - \right. \\ &\left. e\sin\left(2\tan^{-1}\left(\sqrt{\frac{1-e}{1+e}}\tan\left(\frac{\nu_{T_0}}{2}\right)\right)\right)\right)\frac{P}{2\pi}, \end{aligned} \tag{3.23}$$

   where $T_0$ still is the time of inferior conjunction and $\nu_{T_0}$ is simply equal to $\frac{\pi}{2} - \omega$.

4. Then, once we have $t_p$, we have $M_{t_k}$, $E_{t_k}$ from equation (3.22) and finally we have $\nu_{t_k}$ from equation (3.21). Each are derived only from $\omega$, $e$, $P$, and $T_0$, which are all jump parameters.

To conclude on the computation of $z_{t_k}$ we must derive the ratio $\frac{a}{R_\star}$ and the inclination $i$. $i$ can be simply obtained via $i = \cos^{-1}(\frac{b' R_\star}{a})$. And we can express $\frac{a}{R_\star}$ by rearranging equation (1.19) as:

$$\frac{a}{R_\star} = \sqrt{\frac{(1-\sqrt{\Delta F})^2 - b^2[1-\sin^2(T_{14}\pi/P)]}{\sin^2(T_{14}\pi/P)}}, \tag{3.24}$$

where the impact parameter $b$ and transit duration $T_{14}$ can both be expressed from jump parameters only. Indeed, from $b = b'\frac{1-e^2}{1+e\sin\omega}$ and from equation(1.11).

The eclipse model is then multiplied by a trend model aimed to reproduce all the systematic effects. These systematics effects can either have astrophysical or instrumental origin, and are responsible for photometric variations that will add up to the transit itself. To do so, the code rely on polynomial functions of first to fourth order with respect to either time, airmass, PSF FWHM, sky background, stellar position on the detector, or any other external parameter. Such baseline models are unique for each light curve, their coefficients are not jump parameters but are determined at each step of the MCMC by linear least-squares minimisation, using a singular value decomposition (SVD) method.

For each photometric time series, the selection of the optimal baseline model is made by running preliminary MCMC and identifying the model that minimises the Bayesian Information Criterion (BIC) (Schwarz 1978). The optimal baseline model being the one for which the lowest level of noise in the residuals is reached with a minimum number of parameters. The BIC is defined as:

$$BIC = \hat{Q}^2 + N \ln l, \tag{3.25}$$

where $\hat{Q}$ is the smallest merit function $Q$ found in the Markov chains, $N$ is the number of free parameters of a given model, and $l$ is the number of data points.

### Posteriors

Once an MCMC analysis is over and converged (according to the G-R diagnostic) it is always recommended to inspect the chains and the posterior PDFs of the parameters visually (when practical). Figure 3.4 shows the resulting corner plot (useful to visualise multidimensional samples) of the jump parameters obtained from an analysis of a couple of light curves, derived from the observations of the TRAPPIST-1 system, with our MCMC code. On this figure we see that all posterior PDFs are well sampled and that the analysis is well converged.

### Noise and photometric error correction

In the ideal case, observations would be modelled with a parametric model and an additive uncorrelated noise component only. However observational noise is rarely white as instrumental systematics, Earth's atmosphere, and different astrophysical processes all imprint part of time-correlated (red) noise that has to be taken into account in the analysis. If not considered, red noise can lead to biased parameter estimates with underestimated uncertainties or even false detection of planetary candidates (Pont et al. 2006).

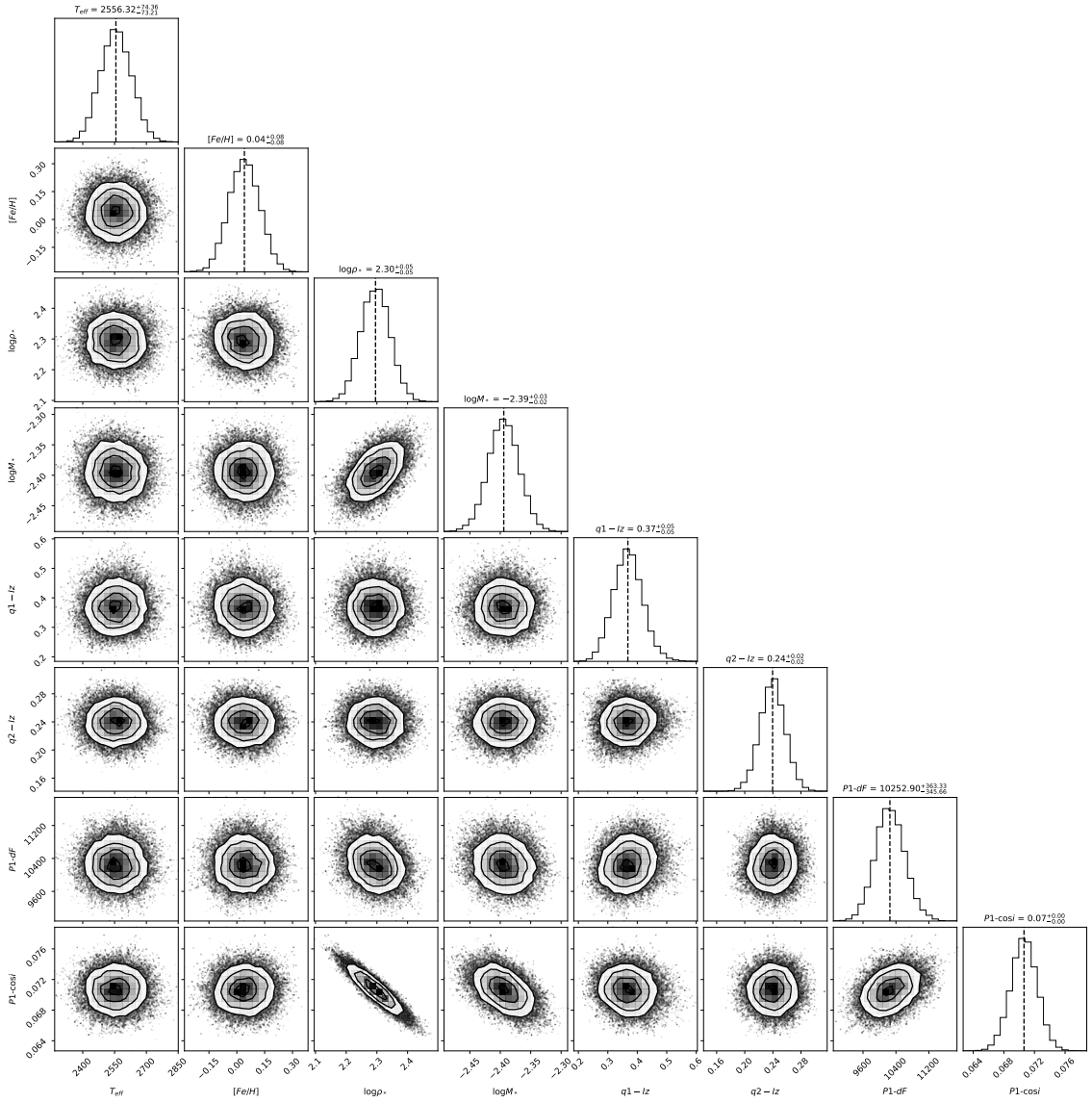


**Fig. 3.4** Example of corner plot of the resulting jump parameters from an MCMC analysis carried out with our MCMC code on a couple of light curves obtained from the observations of the TRAPPIST-1 system with SPECULOOS. Figure produced using the `corner.py`[4] Python package (Foreman-Mackey 2016).

To overcome this issue in our MCMC analyses, for each of them, we ran a preliminary analysis with one Markov chain of 50 000 steps to evaluate the need for re-scaling the photometric errors through the consideration of a potential under- or over-estimation of the white noise of each measurement and the presence of time-correlated (red) noise in the light curve. The white noise is represented by the factor $\beta_w$ issued from the comparison of the rms of the residuals and the mean photometric errors. The red noise is represented by the scaling

factor $\beta_r$ derived from the rms of the binned and unbinned residuals for different binning intervals, for each binning we compute:

$$\beta_{r,bin} = \frac{\sigma_N}{\sigma_1}\sqrt{\frac{N_{bin}(M-1)}{M}}, \tag{3.26}$$

where $N_{bin}$ is the mean number of points in each bin, $M$ the number of bins, and $\sigma_1$ and $\sigma_N$ are the standard deviations of the unbinned and binned residuals respectively. Then, the maximum value among all the available $\beta_{r,bin}$ values is set as the reference $\beta_r$. The photometric errors provided by the observations are multiplied by the correction factor $CF = \beta_w * \beta_r$ in order to re-scale them. Once the $CF$ of each light curve is reported a new MCMC run is launched with the updated (re-scaled) error bars to obtain reliable error bars on the fitted parameters.

We note that correlated noise can alternatively be represented as a stochastic (random) process in time, such that if it follows a normal distribution, it can be modelled as a Gaussian process (GP) (Gibson et al. 2012). Although I did not make use of GP in my analyses, the MCMC code I used does include the modelling of red noise with GPs as an option.

# Chapter 4

# TRAPPIST-1, the *Red World* Spitzer campaign

As mentioned in Chapter 2, the SPECULOOS project started in 2011 with a prototype survey on TRAPPIST-South (Gillon et al. 2013). The purpose of this prototype was to assess the feasibility of the SPECULOOS project, notably in terms of photometric precision and variability of ultracool dwarfs stars (UCDS). The prototype on TRAPPIST did way more than this as it provided the first signs ever of the existence of Earth-sized planets in temperate orbits around an UCDS. Indeed, it detected a transit of a first Earth-sized planet around the star 2MASS J23062928-0502285 in Sept 2015, soon followed by more transits of the same planet, but also transits of two others. This UCDS was then renamed TRAPPIST-1 because of the telescope's name. This announcement was already a major breakthrough as it presented the detection of three Earth-sized planets (at this time only the planet b, c and g as we call them today) orbiting a rather close by (40 light-years away), small star (Jupiter-sized) in the Aquarius constellation (Gillon et al. 2016). Because of the small size of the host star, the signal detection was highly significant, and the period of the planets rather short, which allowed to gather a large number of transits in a small amount of time. But this was only the beginning of the TRAPPIST-1 venture. Indeed, once the TRAPPIST team got several transits, they asked for follow up time on larger telescopes such as the Very Large Telescope (VLT) located in Paranal, Chile. A night of observation with the VLT revealed a triple transit, i.e three planets transiting at the same time. At first sight, the team thought that two of these planets (planet c and g, as we call them today) were among the three already caught in transit by TRAPPIST. Unfortunately, the star was no more visible after the VLT observations in Dec 2015. It was re-observed with Spitzer in DDT time in Feb 2016, and then from the ground again from June 2016. The new Spitzer + ground-based data convinced the team that there

were at least 5 planets in the system, but some periods remained undetermined because of the discontinuous coverage from the ground, so the TRAPPIST team asked for continuous observation with Spitzer. The *Red worlds* program was accepted (DDT ID: 13067, PI: Gillon) and an intensive follow up campaign of the TRAPPIST-1 system was initiated, first as a 20-day long (i.e., 480 hrs) near-continuous monitoring of the system at 4.5 $\mu$m in 2017, followed by an intense high-precision monitoring of the eclipses of the known planets at 3.6 $\mu$m and 4.5 $\mu$m from 2017 to 2019 (program ID: 14223 and 13175, PIs: Agol and Delrez). The 20-day long monitoring revealed that the system was hosting 7 Earth-sized planets, including 6 in mean-motion resonnance (MMR). Subsequent K2 observations allowed to determine the period of planet h, and to show that the whole system was in MMR. For the record, the mystery of the VLT triple transit was unravelled as these new observations revealed that among the three worlds caught transiting the star at the same time, only one was known at that time (planet c), the two other ones being the smaller planets e and f! In 2019, I was given the extraordinary opportunity to lead the analysis of the entire Spitzer Space Telescope's time-series photometry of the TRAPPIST-1 system. This work led to a publication in the journal Astronomy & Astrophysics. In the first part of this chapter I detail all the work I undertook in this paper. In the second part, I discuss how this work was complemented by a subsequent paper, led by my colleague Prof Eric Agol, in which the transit times that I had measured were used to refine the planets' masses, radii, densities, dynamics, and ephemerides.

## 4.1 Global Results of the Spitzer Exploration Science Program

One of the primary goals of this ambitious Spitzer program was to create a complete inventory of the transiting objects (planets, moons, Trojans) of the inner system of TRAPPIST-1, not only to constrain its dynamical properties, history, and stability, but also to identify more objects well-suited for detailed atmospheric characterisation with next-generation telescopes. It also aimed to perform a thorough assessment of the infrared variability of the star. Finally, it aimed to determine the masses and constrain the orbital parameters of the planets through the transit timing variation method (Agol et al. 2005; Holman et al. 2004). The precise and accurate determination of the masses and radii of the planets - and the resulting constraints on their bulk compositions - is indeed critical for their thorough characterisation, notably for the optimal exploitation of future atmospheric observations (Morley et al. 2017).

To this date, this system provides the best opportunity for a detailed study of potentially rocky, temperate Earth-sized exoplanets, and has therefore galvanised the exoplanet community to study it in detail, both observationally and theoretically. To illustrate this point, I should mention that, since its discovery in 2016, more than 190 publications focused on TRAPPIST-1 have been posted on NASA ADS[1], and more than 700 papers have cited the discovery paper of 2017 Gillon et al. (2017b). While a comprehensive review of all the research carried out on TRAPPIST-1 is out the scope of this thesis, in the following I briefly review some of the most interesting characteristics of the TRAPPIST-1 system.:

- First, the host star is an old M8V type star ($7.6 \pm 2.2$ Gyr, (Burgasser et al. 2017)) with a moderate flaring activity (about 1 or 2 flares per week (Gillon et al. 2017b)), and a (putative) stellar rotation period of $3.30 \pm 0.14$ days derived from K2 observations by Luger et al. (2016).

- Recent study by Gonzales et al. (2019) presented a distance-calibrated SED for the star and found, from band-by-band comparisons, that TRAPPIST-1 exhibits a blend of field star and young star spectral features.

- Its XUV luminosity is similar to the Sun's, which, when considering its past evolution - notably its ~1 Gyr-long pre-main sequence phase (Fleming et al. 2020) and the small orbital distances of the planets (between 0.01 and 0.06 AU) - potentially drove extreme atmospheric erosion and water loss (Bolmont et al. 2016; Bourrier et al. 2017; Fleming et al. 2020; Wheatley et al. 2017). In that regard, if the habitable zone planets originally had primordial H/He envelopes, XUV evaporation may have rendered the planets habitable (Luger et al. 2015; Owen et al. 2016).

- TRAPPIST-1 is orbited by seven transiting earth-sized planets. The system is extremely compact with periods ranging for 1.5 to $\simeq$ 18 days. Three planets orbit within the conservative habitable zone of the star (Gillon et al. 2017b), and planet e is the most likely to harbour liquid water on its surface (Fauchez et al. 2020b; Turbet et al. 2018; Wolf 2017; Wolf et al. 2017).

- The seven planets form the longest resonant chain known to date (Luger et al. 2017a; Papaloizou et al. 2018). This resonant configuration combined with the planets' proximity to one another, causes strong planet-planet perturbations, leading to significant TTVs (from a few to tens of minutes). Interestingly, monitoring these TTVs yielded

[1]This statistics was obtained by filtering all publications which include TRAPPIST-1 in their title on NASA ADS. This number includes refereed paper, accepted proposals (when public), and conferences.

strong constraints on the masses and orbits of the planets (Gillon et al. 2017b; Grimm et al. 2018), as we will see in more details in section 4.2.

- Given the high compactness of the system, tidal interactions (with the star and between planets) are expected to be strong and to influence the orbital and rotational dynamics of the system. It is likely that tides have spun-down the planets to the spin-orbit synchronous resonance in a relatively short time, leading the planets being in synchronous rotation (Gillon et al. 2017b; Turbet et al. 2018). In addition, tidal heating is expected to be the dominant interior heating process for the inner planets (but not for outer ones). As a consequence, we could maybe expect the inner planets to have intense volcanism. Volcanism can replenish/feed an atmosphere whose greenhouse effect could strongly impact the surface's temperature. So, indirectly, tides could be a significant source of warming of the planets' surface, but it could also counterbalance the atmospheric erosion due to the planet's proximity to the star Owen et al. 2016.

- Some works modelled the planet formation process from small dust grains to full-sized planets, while keeping track of their water content using pebble and planetesimal accretion mechanisms (Coleman et al. 2019; Ormel et al. 2017; Schoonenberg et al. 2019). Several studies agreed on a possible formation scenario via Type I migration such that the planets first formed far away from their host star and then migrated inwards (in a timescale of $10^6$ years) in resonant convoys to reach their present location, very close to their host star (Tamayo et al. 2017).

- The planets are good potential targets for atmospheric characterisation with the James Webb Space Telescope (JWST) (Barstow et al. 2016; Fauchez et al. 2019; Krissansen-Totton et al. 2018a; Lincowski et al. 2018; Lustig-Yaeger et al. 2019; Wunderlich et al. 2019). In that regard, to coordinate the programs and maximise the scientific outcomes of the observation of TRAPPIST-1 with JWST, an initiative arouse in 2020: the TRAPPIST-1 JWST community initiative (Gillon et al. 2020). Preliminary atmospheric reconnaissance was performed with HST/WFC3, and the resulting low-resolution transmission spectra acquired in the 1.1-1.7 $\mu$m spectral range made it possible to exclude clear hydrogen-dominated atmospheres for six of the seven planets (De Wit et al. 2016; 2018; Moran et al. 2018; Wakeford et al. 2018). A comprehensive review of possible planetary atmospheres in the TRAPPIST-1 system was published last year (Turbet et al. 2020a).

- Last but not least, the TRAPPIST-1 system is currently the most observationally favourable system for a detailed study of potentially rocky, Earth-sized exoplanets

with incident fluxes spanning the range of the terrestrial planets in our Solar System. According to Gillon et al. (2020), only 44 nearby UCDS could theoretically be better targets - i.e. lead to higher SNRs on atmospheric signatures with JWST (all things being equal) - than TRAPPIST-1, if transiting earth-like planets were to be found orbiting them. Considering that the statistics of the planetary population of UCDS are poorly understood (Delrez et al. 2018b; Lienhard et al. 2019) and that the transit probability for such planets would be only around 2%, the odds of finding a better target than TRAPPIST-1 for JWST are very small. Moreover, even if such a system was to be detected, it will be rather unlikely that it brings together the same extraordinary properties as the TRAPPIST-1 planets.

As a whole, the TRAPPIST-1 system offers a unique laboratory for comparative planetology of terrestrial planets, and may provide insights and constraints on the formation and evolution of terrestrial planets around the lowest-mass stars. But although it is gradually revealing itself, some big questions still remain. For instance, we still can not explain why the periodic modulation seen in K2 photometry is not detected in Spitzer light curves (Delrez et al. 2018a; Luger et al. 2017a; Morris et al. 2018c). Neither do we know if the host star's high-energy incident flux on the planets can jeopardise their habitability (Roettenbacher et al. 2017; Vida et al. 2017) or if it can alternatively drive chemical processes needed for life's origin, through, for example, CME-driven generation of prebiotically relevant molecules (Airapetian et al. 2016), and by increasing NUV flux for the production of life's building blocks (Ranjan et al. 2017; Rimmer et al. 2018). We are also uncertain about the information content that we will be able to retrieve from the planetary transmission spectra, and how significant the impact of stellar contamination may be on their interpretation. In this context, the work I conducted with my collaborator on the Spitzer dataset aimed to (1) meet the initial expectations of the *Red Worlds* program, (2) try to answer as much as possible those interrogations and enlighten the upcoming exploration of the system with the JWST.

### 4.1.1 Observations

The dataset we relied on includes all time-series observations of TRAPPIST-1 carried out by Spitzer/IRAC since the discovery of its planetary system: 45hrs of observations gathered within the DDT program 12126 in Feb and March 2016 (Delrez et al. 2018a; Gillon et al. 2017b) and all data (1080hr) taken within the Spitzer Exploration Science program Red Worlds (ID 13067) between Feb 2017 and Oct 2019 (see Figure 4.1), including data from the DDT program 13175 (PI: L. Delrez) targeting occultations of the two inner planets, and data from the DDT program 14223 (PI: E. Agol) taken in Oct 2019 to better constrain the

masses of the planets and to tighten the ephemeris forecast for observations with JWST, see Agol et al. (2020b). All these data can be accessed through the online Spitzer Heritage Archive database[2]. This extensive dataset includes 65, 47, 23, 18, 15, 13, and 7 transits of planets b, c, d, e, f, g, and h, respectively. Among these 188 transits, 88 are "new", i.e. they were observed in fall 2017 and fall 2019, and were not included in the analysis discussed in Delrez et al. (2018a) which presented data taken by Spitzer up to March 2017. As our aim is to give an overview of the exploration of TRAPPIST-1 system with the Spitzer space telescope, we therefore did not include transits observed with other telescopes, but the results of the analysis of those additional observations can be found in existing papers: (Grimm et al. 2018; Luger et al. 2017a) for K2 observations, (De Wit et al. 2016; 2018; Wakeford et al. 2018) for HST observations, (Ducrot et al. 2018) for SPECULOOS and Liverpool telescope observations, (Burdanov et al. 2019) for VLT, AAT and UKIRT observations.

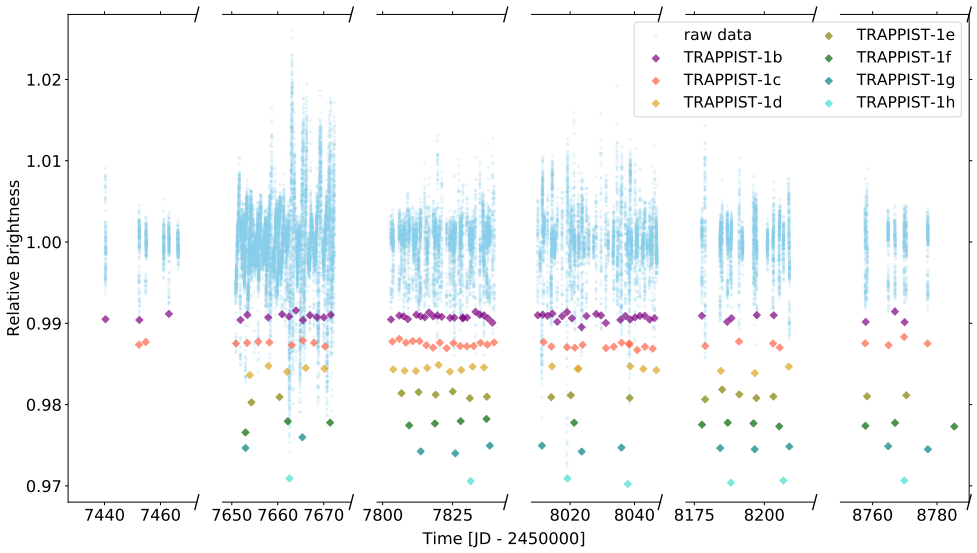


**Fig. 4.1** Spitzer photometric measurements (sky blue) resulting from observations of the star from February 2016 to Oct 2019 cleaned of data gaps between the four campaigns. Colored diamonds show the positions of the transits of the different planets with their corresponding depth + a constant offset by planet for clarity.

Back on the Spitzer dataset, we identified 29 blended transits (i.e. transits of multiple planets simultaneously) or partial transits (see Table 4.1) which were analysed individually, but not included in our global analysis presented in Section 3. Indeed, shapes of blended + partial transits are less constraining than well isolated full transits so we chose not to include them in

[2]http://sha.ipac.caltech.edu

| Planet | # Isolated transits | # Blended or partial transits | Total |
|---|---|---|---|
| TRAPPIST-1 b | 54 | 11 | 65 |
| TRAPPIST-1 c | 39 | 8 | 47 |
| TRAPPIST-1 d | 20 | 3 | 23 |
| TRAPPIST-1 e | 17 | 1 | 18 |
| TRAPPIST-1 f | 13 | 2 | 15 |
| TRAPPIST-1 g | 9 | 4 | 13 |
| TRAPPIST-1 h | 6 | 1 | 7 |

**Table 4.1** Number of transits monitored by Spitzer from early 2016 to late 2019 for each TRAPPIST-1 planet

our global analysis of all transits so to ensure a better convergence. We also did not include them in our global planet by planet analyses for similar reasons when the transit was partial, and because we wished to deal with only one planet in these analyses.

Besides, we targeted 28 occultations of TRAPPIST-1b and 9 of TRAPPIST-1c with Spitzer/IRAC channel 2 with the aim to detect a signal or at least obtain an upper bound on the occultation depth, and consequently derive the first empirical constraints on the planets' thermal emission. Indeed, as the orbits of the seven TRAPPIST-1 planets are close to be circular (Luger et al. 2017a), we expect all planets to undergo secondary eclipse. Notably the inner planets should be warmer than the other planets, and thus harbour deeper occultation depths. Furthermore, given the small size of the planets, our best chance to catch an occultation signal is to phase-fold several occultations which makes the inner planets, with the smallest periods, even more suitable. It should be mentioned here that an updated transit timing variations (TTV) analysis using all transits observed by Spitzer, HST, K2, and ground-based transits observed up to 2019 (Agol et al. 2020b), that I will present in more details in section 4.2, confirmed that the expected eccentricities are very small (eccentricity $< 0.01$ for all planets). It is also interesting to note that we did not spot any sign of planet-planet eclipses in our analyses of the blended transits, and for none of them was a planet "caught up" by a more inner one during its crossing of the stellar disk.

As described by Gillon et al. (2017b), the star was observed nearly-continuously from 19 Sep to 10 Oct 2016 within the program 13067 (480 hours). The rest of the dataset (595 hours) is composed of sequences of a few hrs corresponding to the observations of one or several transit(s) and/or occultation(s). For all observations in both bandpasses, each frame is composed of 64 subexposures each of 1.92 seconds on the target plus an additional 0.8s for read out, which gives a cadence of a point every 2.06 minutes. All these observations were obtained with the Infrared Array Camera (IRAC) (Carey et al. 2004) of the Spitzer Space telescope in subarray mode ($32 \times 32$ pixels windowing of the detector). No dithering

was used (continuous staring), and the observations were all done using the 'peak-up' mode (Ingalls et al. 2016) to maximise the accuracy in the position of the target on the detector's sweet spot (as detailed in IRAC Instrument Handbook) to minimise the so-called 'pixel phase effect' of IRAC detectors (e.g., (Knutson et al. 2009)). All the data were then calibrated with the Spitzer pipeline S19.2.0, and delivered as cubes of 64 subarray images of 32 × 32 pixels (pixel scale = 1.2 arcsec).

All 2016 and 2019 data were obtained with the 4.5 $\mu$m IRAC detector. In 2017 and 2018, additional observations were obtained at 3.6$\mu$m with the goal of further constraining the chromatic variability of the transit depths of the seven planets. The same method was used for the photometric extraction as that described by Gillon et al. (2017b) and Delrez et al. (2018a). We converted the fluxes from MJy/sr to photon counts, and then we used the IRAF/DAOPHOT[3] software (Stetson 1987) to measure the flux of TRAPPIST-1 within a circular aperture of 2.3 pixels. For each subarray image, the aperture was centred on the star's point-spread function (PSF) by fitting a 2D Gaussian profile, yielding measurements of the PSF width along the x- and y-axis in the process. We discarded subarray images corresponding to $> 10\ \sigma$ discrepant measurements for the PSF centre, target flux, and background flux, as described by Gillon et al. (2014). We then combined the measurements per cube of 64 images. The photometric error of each cube (which is the standard error on the mean) was taken as the error of its average flux measurement.

### 4.1.2 Analysis

Our data analysis was divided in three distinct steps. First, we performed individual analyses of each transit light curve to select an optimal photometric model and assess the variability of the photometry. We also carried out an analysis aiming to refine the stellar parameters of TRAPPIST-1. Then, we performed several sets of global analyses: (a) one with the entire set of transits to refine the physical parameters of the system; (b) seven others (one for each planet) for which we allowed the transit depths to vary in order to assess their stability; and (c) a repeat of the seven global analyses (planet by planet), this time to improve the errors on the timings. Finally, we carried out a global analysis of the light curves from program 13175 (PI: L. Delrez) obtained around the expected occultation times for planet b and c to search for occultation signals.

[3]IRAF is distributed by the National Optical Astronomy Observatory, which is operated by the Association of Universities for Research in Astronomy, Inc., under cooperative agreement with the National Science Foundation.

### Transit per transit

First, we used our adaptive MCMC code described in Chapter 3 to analyse each transit light curve individually. As a reminder, this code uses the eclipse model of Mandel et al. (2002) as a photometric time-series, multiplied by a baseline model to represent the other astrophysical and instrumental systematics that could produce photometric variations. We select a model to represent each light curve through the minimisation of the Bayesian Information Criteria (BIC; (Schwarz 1978)) given by equation (3.25). We tested a large range of baseline models to account for different types of external sources of flux variations/modulations (instrumental and stellar effects). This includes polynomials of variable orders in: PSF size and position on the detector (to account for the Spitzer "pixel-phase" effect and the breathing of its PSF; (Gillon et al. 2017b)); time (to correct for time dependent trends); and the logarithm of time (to represent the "ramp" effect, (Knutson et al. 2009)). For some light curves, the "pixel-phase" effect was additionally corrected by complementing the position polynomial model with the bi-linearly-interpolated subpixel sensitivity (BLISS) mapping method presented by Stevenson et al. (2012). To do so, we sampled the detector area probed by the PSF centre in several sub-pixel box such that at least five measurements fell within the same boxes. Further details of the implementation of BLISS mapping in our MCMC code can be found in Gillon et al. (2014). The details of the baseline model adopted for each transit light curve are given in Table 4.17. Once the baseline was chosen, we ran a preliminary analysis with one Markov chain of 50 000 steps to evaluate the need for re-scaling the photometric errors through the consideration of a potential under- or over-estimation of the white noise of each measurement and the presence of time-correlated (red) noise in the light curve. The white noise is represented by the factor $\beta_w$ issued from the comparison of the rms of the residuals and the mean photometric errors. The red noise is represented by the scaling factor $\beta_r$ derived from the rms of the binned and unbinned residuals for different binning intervals ranging from 5 to 120 min, following the procedure detailed in Winn et al. (2009). The values of $\beta_w$ and $\beta_r$ derived for each light curve are listed in Table 4.17.

The jump parameters that were randomly perturbed at each step of the Markov chains were:

- the mass $M_\star$, the radius $R_\star$, the effective temperature $T_{eff}$, and the metallicity [Fe/H] of the star, assuming the following prior probability distribution functions (PDFs) for these stellar parameters: $M_\star \in \mathcal{N}(0.089, 0.007^2)M_\odot$, $R_\star \in \mathcal{N}(0.121, 0.003^2)R_\odot$, $T_{eff} \in \mathcal{N}(2511, 37^2)$K and [Fe/H] $\in \mathcal{N}(0.04, 0.08^2)$dex;
- the planet/star area ratio $dF = (\frac{R_p}{R_\star})^2$, where $R_p$ and $R_\star$ are the radius of the planet and the star, respectively;

- the transit impact parameter $b$ for the case of a circular orbit, defined as $b = a\cos(i_p)/R_\star$ where $a$ and $i_p$ are, respectively, the semi-major axis and inclination of the orbit;
- the mid-transit time $t_0$ (inferior conjunction) for which we assumed a noninformative uniform prior PDF;
- the transit duration $T_{14}$, assuming a circular orbit, obtained from equation (1.11) with $e = 0$.
- the linear combinations of the quadratic limb darkening coefficients ($u_1$, $u_2$) in Spitzer's 3.6 and 4.5 $\mu$m channels, defined as $c_1 = 2 \times u_1 + u_2$ and $c_2 = u_1 - 2 \times u_2$. Values and errors for $u_1$ and $u_2$ in a given band pass were interpolated from the tables of Claret et al. (2012), 2013 basing on the stellar parameters $T_{eff}$=2511 K $\pm$ 37 K, $\log(g[\mathrm{cm\,sec^{-2}}]) = 5.18 \pm 0.06$, and [Fe/H] = $0.04 \pm 0.08$ dex, (Delrez et al. 2018a). The corresponding normal distributions were used as prior PDFs (for channel 1: $u1 \in \mathcal{N}(0.1633, 0.0364^2)$ and $u2 \in \mathcal{N}(0.2549, 0.0570^2)$, for channel 2: u1 $\in$N(0.1442 ,$0.0324^2$)) and $u2 \in \mathcal{N}(0.2173, 0.0482^2)$). In terms of combined limb darkening coefficients those value translates as: for channel 1: $c1 = \mathcal{N}(0.5815, , 0.0676^2)$ and $c2 = \mathcal{N}(-0.3465, 0.0676^2)$, for channel 2: c1 = $\mathcal{N}(0.5057, 0.0581^2)$) and $c2 = \mathcal{N}(-0.2904, 0.05801^2)$).

All of our priors come from the updated system parameters presented in Delrez et al. (2018a). We recognise that those values were derived from analyses carried out on a subset of the same data set, noting that in this section our intention is not to determine the physical parameters of the system, but rather to assess the stability (or variability) of the transits parameters.

We then re-scaled the photometric errors by multiplying the error bars by the correction factor $CF = \beta_w * \beta_r$. Once the correction factor was applied, we ran two Markov chains of 100 000 steps each to sample the PDFs of the parameters of the model and the system's physical parameters (Ford 2006), and assessed the convergence of the MCMC analysis with the Gelman & Rubin statistical test (Gelman et al. 1992). Our threshold for convergence was a Gelman-Rubin statistic lower than 1.1 for every jump parameter, measured across the two chains.

For all of the analyses, the resulting values and error bars for the jump and system parameters as well as the complete details on the assumed baseline and on the correction factor applied can be found in Table 4.17. In addition to setting the baseline to use for each light curve, proceeding to individual analyses was also a way to search for variability in the transits, notably spot/faculae crossing or flares events (see 4.1.3).

Once we selected a baseline model for each light curve, we continued to the next steps of our analysis. In the next paragraph, I present our global analysis of all the light curves together to refine the transit parameters. This is an update of the parameters presented in Table 1 of Delrez et al. (2018a) with the advantage that a global analysis with transits in both channels enables us to lift a part of the degeneracy between the transit parameters and the assumed limb-darkening coefficients.

### All transits

We actually ran two distinct global analyses of all transits. The first one aimed at deriving updated stellar parameters using 142 of the 171 TRAPPIST-1's planets transits observed with Spitzer (the transits not included were either partial or multiple). We proceeded as follows: (1) we inferred the density of the star $\rho_\star$ and its error through a global MCMC analysis of all stacked transit (detailed in the following paragraph); (2) we derived the mass of the star $M_\star$ following the empirical relationship between $M_{K_s}$ (magnitude in K band) and $M_\star$ (with $M_\star$ spanning from $0.075M_\odot < M_\star < 0.70M_\odot$) derived from 62 nearby binaries by Mann et al. (2019). The mass and its error were estimated by taking the metallicity of the star (from Van Grootel et al. (2018)) into account and through the use of the open-access code $M_- - M_K-$ provided by Mann et al. (2019), which accounts for systematic errors. With this estimate of the mass of the star and its error, we derived the radius of the star $R_\star$ from our posterior probability distribution function (PDF) on the density:

$$R_\star = \left[\frac{3M_\star}{4\pi\rho_\star}\right]^{1/3}. \tag{4.1}$$

Using the exquisite parallax value ($d = 80.4512 \pm 0.1211$ mas) from Gaia DR2 (Lindegren et al. 2018) and the integrated flux derived from Filippazzo et al. (2015), we computed the luminosity of the star, with no correction for extinction.:

$$L_\star = 4\pi d^2 \int_{0\mu\mathrm{m}}^{1000\mu\mathrm{m}} F_\lambda(t) d\lambda, \tag{4.2}$$

Finally, we derived the effective temperature of TRAPPIST-1 from its luminosity and its radius following the Stefan-Boltzmann Law:

$$T_{eff,\star} = \left(\frac{L_\star}{4\pi R_\star^2 \sigma_{SB}}\right)^{1/4}, \tag{4.3}$$

where $\sigma_{SB}$ is the Stefan-Boltzmann constant. The errors on $R_\star$, $L_\star$, and $T_{eff,\star}$ errors were then computed through error propagation on equations 4.1, 4.2 and 4.3. The stellar parameters derived from this approach are presented in Table 4.2.

| **Quantity** | **Value** |
|---|---|
| Density $\rho_\star$ ($\rho_\odot$) | $52.31 \pm 2.2$ |
| Mass $M_\star$ ($M_\odot$) | $0.0898 \pm 0.0024$ |
| Radius $R_\star$ ($R_\odot$) | $0.1197 \pm 0.0017$ |
| Luminosity $L_\star$ ($L_\odot$) | $0.000553 \pm 0.000019$ |
| Effective temperature (K) | $2557 \pm 47$ |

**Table 4.2** Updated stellar parameters of TRAPPIST-1. We note that those parameters are not the final one, the final stellar parameters from this work are given in Table 4.3.

Once the stellar parameters were derived, we ran a second global analysis. This one consisted of a preliminary run of one 50 000 steps Markov chain to estimate the correction factors $CF$ to be applied to the photometric error bars, and a second run with two Markov chains of 500 000 steps for which we used the Gelman-Rubin test to assess the convergence. The relatively large number of steps for the two chains is necessary for a dataset of this size. This analysis strategy is identical to the one conducted by Delrez et al. (2018a), but included an increased number of transits observed at 4.5 $\mu$m for all planets and newly observed transits at 3.6 $\mu$m for planets c, d ,e, f, g, and h. The jump parameters were $R_\star$, $M_*$, $T_{eff}$, [Fe/H], the linear combinations $c_1$ and $c_2$ of the quadratic limb-darkening coefficients ($u_1$, $u_2$) for each bandpass. For each planet, parameters include:

- the transit depth at 4.5$\mu$m, $dF_{4.5\mu\mathrm{m}}$
- the impact parameter, $b$ (in case of circular orbit)
- the transit depth difference between Spitzer/IRAC 3.6 $\mu$m and Spitzer/IRAC 4.5 $\mu$m channels, $ddF = dF_{3.6\mu\mathrm{m}} - dF_{4.5\mu\mathrm{m}}$
- the transit timing variation (TTV) of each transit with respect to the mean transit ephemeris derived from the individual analyses

For the mass of the star, we used a normal prior PDF based on the value given in Section 4.1.2 ($M_\star = 0.0898 \pm 0.0024\ M_\odot$). Then, for the metallicity and the limb-darkening coefficients in both channels we assumed the same normal prior PDFs as in Section 4.1.2. For the rest of the

jump parameters, we assumed uniform non-informative prior distributions. We did not set the transit duration as a jump parameter because it is defined for each planet by its orbital period, transit depth, and impact parameter, combined with the stellar mass and radius (Seager et al. 2003). Furthermore, dynamical models predict rather small amplitudes of variation for the transit durations (Luger et al. 2017b). The convergence of the chains was checked with the Gelman-Rubin statistic (Gelman et al. 1992). The value of the statistic was less than 1.1 for every jump parameter, measured across the two chains, which indicates that the chains are converged. From the jump parameters, the code deduced the physical parameters of the system at each step of the MCMC. In particular, the value of the effective temperature, $T_{eff}$, was derived at each MCMC step from the $R_\star$ and $L_\star$ values given in the stellar parameters global analysis. Then, for each planet, values for the radius of the planet $R_p$, its semi-major axis $a$, its inclination $i$, its irradiation $S_p$, and its equilibrium temperature $T_{\rm eq}$ were deduced from the values for the stellar and transit parameters. Table 4.3 presents the outputs from this analysis.

We note that prior to this study different stellar parameters for TRAPPIST-1 were published. In 2019 Gonzales et al. (2019) presented a distance-calibrated SED of TRAPPIST-1 using a new NIR FIRE spectrum and parallax from the Gaia DR2 data release from which they derived updated fundamental parameters for the star. Back in 2018, Van Grootel et al. (2018) derived stellar parameters from two distinct approaches to compute the mass of the star, first via stellar evolution modelling, and secondly through an empirical derivation from dynamical masses of equivalently classified ultracool dwarfs in astrometric binaries. The stellar parameters we derived are in agreement with those two previous studies, as shown in Table 4.4.

### Planet per planet

In the preceding paragraph, we mentioned that we derived the stellar density through a global MCMC analysis of all isolated transits. This method uses the transits shapes and Kepler third's law to constraint the stellar density (Seager et al. 2003). However, in this particular case, the TRAPPIST-1 system is composed of 7 planets, that is to say 7 different sets of transit parameters. Hence, it is legitimate to investigate whether there are noticeable differences between the stellar density values inferred from each individual planet's analysis and the one inferred from all transits together. A good level of agreement between the values would justify further the use of the globally derived stellar density. Figure 4.2 shows the stellar density value as obtained from individual planet analysis with its error bars and a

| Parameters | Value | | | | | | |
|---|---|---|---|---|---|---|---|
| **Star** | **TRAPPIST-1** | | | | | | |
| Mass [a] $M_\star$ ($M_\odot$) | $0.0898 \pm 0.0023$ | | | | | | |
| Radius $R_\star$ ($R_\odot$) | $0.1234 \pm 0.0033$ | | | | | | |
| Density $\rho_\star$ ($\rho_\odot$) | $47.98 \pm 3.90$ | | | | | | |
| Luminosity [a] $L_\star$ ($L_\odot$) | $0.000552 \pm 0.000018$ | | | | | | |
| Effective temperature (K) | $2520 \pm 39$ | | | | | | |
| Metallicity [a] [Fe/H] (dex) | $0.0535 \pm 0.088$ | | | | | | |
| LD coefficient, $u_{1,3.6\mu m}$ [a] | $0.168 \pm 0.016$ | | | | | | |
| LD coefficient, $u_{2,3.6\mu m}$ [a] | $0.245 \pm 0.019$ | | | | | | |
| LD coefficient, $u_{1,4.5\mu m}$ [a] | $0.141 \pm 0.016$ | | | | | | |
| LD coefficient, $u_{2,4.5\mu m}$ [a] | $0.198 \pm 0.018$ | | | | | | |
| Combined LD coefficient, $c_1, 3.6\mu m$ | $0.581 \pm 0.039$ | | | | | | |
| Combined LD coefficient, $c_2, 3.6\mu m$ | $-0.322 \pm 0.045$ | | | | | | |
| Combined LD coefficient, $c_1, 4.5\mu m$ | $0.482 \pm 0.031$ | | | | | | |
| Combined LD coefficient, $c_2, 4.5\mu m$ | $-0.256 \pm 0.044$ | | | | | | |
| **Planets** | **b** | **c** | **d** | **e** | **f** | **g** | **h** |
| # of transits | 54 | 39 | 20 | 17 | 13 | 9 | 6 |
| Period (days) | 1.51088432 ± 0.00000015 | 2.42179346 ± 0.00000023 | 4.04978035 ± 0.00000266 | 6.09956479 ± 0.00000178 | 9.20659399 ± 0.00000212 | 12.3535557 ± 0.00000341 | 18.7672745 ± 0.00001876 |
| Mid-transit time $t_0$ - 2450000 ($BJD_{TDB}$) | 7322.514193 ± 0.0000030 | 7282.8113871 ± 0.0000038 | 7670.1463014 ± 0.0000184 | 7660.3676621 ± 0.0000143 | 7671.3737299 ± 0.0000157 | 7665.3628439 ± 0.0000206 | 7662.5741486 ± 0.0000913 |
| Transit depth ($R_p^2/R_\star^2$) at 4.5$\mu$m(%) | $0.7236 \pm 0.0072$ | $0.7027 \pm 0.0068$ | $0.3689 \pm 0.0067$ | $0.4936 \pm 0.0081$ | $0.6313 \pm 0.0091$ | $0.745 \pm 0.011$ | $0.351 \pm 0.012$ |
| Transit depth ($R_p^2/R_\star^2$) at 3.6$\mu$m(%) | $0.7209 \pm 0.0067$ | $0.721 \pm 0.014$ | $0.351 \pm 0.016$ | $0.491 \pm 0.011$ | $0.655 \pm 0.019$ | $0.724 \pm 0.024$ | $0.313 \pm 0.027$ |
| Transit impact parameter $b$ ($R_*$) | $0.254^{+0.110}_{-0.085}$ | $0.254^{+0.110}_{-0.087}$ | $0.235^{+0.120}_{-0.094}$ | $0.299^{+0.085}_{-0.072}$ | $0.391 \pm 0.056$ | $0.430 \pm 0.049$ | $0.448 \pm 0.054$ |
| Transit duration $T_{14}$ (min) | 36.309 ± 0.093 | 42.42 ± 0.12 | 49.37 ± 0.32 | 56.31 ± 0.25 | 63.28 ± 0.31 | 69.10 ± 0.36 | 76.28 ± 0.81 |
| $R_p/R_\star$ at 4.5$\mu$m | 0.085062 ±0.00042 | 0.083827 ±0.00040 | 0.06073 ±0.00056 | 0.07025 ±0.00058 | 0.07945 ±0.00057 | 0.08632 ±0.0062 | 0.05927 ±0.0099 |
| $R_p/R_\star$ at 3.6$\mu$m | 0.084903 ±0.00040 | 0.08495 ±0.00086 | 0.0593 ±0.0013 | 0.07009 ±0.00075 | 0.0809 ±0.0013 | 0.0851 ±0.0014 | 0.0559 ±0.0025 |
| Inclination $i$ (°) | $89.28 \pm 0.32$ | $89.47 \pm 0.24$ | $89.65 \pm 0.15$ | $89.663 \pm 0.092$ | $89.666 \pm 0.059$ | $89.698 \pm 0.044$ | $89.763 \pm 0.037$ |
| Semi major axis a ($10^{-3}$AU) | $11.534^{+0.099}_{-0.092}$ | $15.79^{+0.14}_{-0.13}$ | $22.26^{+0.19}_{-0.18}$ | $29.24^{+0.25}_{-0.23}$ | $38.7740^{+0.33}_{-0.31}$ | $46.81528^{+0.40}_{-0.37}$ | $61.8656^{+0.53}_{-0.49}$ |
| Scale parameter $a/R_\star$ | $20.13^{+0.46}_{-0.55}$ | $27.57^{+0.62}_{-0.76}$ | $38.85^{+0.88}_{-1.1}$ | $51.0^{+1.2}_{-1.4}$ | $67.1^{+1.15}_{-1.9}$ | $81.7^{+1.8}_{-2.3}$ | $107.9^{+2.4}_{-3.0}$ |
| Irradiation $S_p$ ($S_\odot$) | $4.15 \pm 0.16$ | $2.211 \pm 0.085$ | $1.114 \pm 0.043$ | $0.645 \pm 0.025$ | $0.373 \pm 0.014$ | $0.252 \pm 0.0097$ | $0.144 \pm 0.0055$ |
| Equilibrium temperature $T_{eq}$ (K)[b] | $397.6 \pm 3.8$ | $339.7 \pm 3.3$ | $286.2 \pm 2.8$ | $249.7 \pm 2.4$ | $217.7 \pm 2.1$ | $197.3 \pm 1.9$ | $171.7 \pm 1.7$ |
| Radius $R_{p,3.6\mu m}$ ($R_\oplus$) | $1.1407 \pm 0.035$ | $1.141 \pm 0.037$ | $0.799 \pm 0.026$ | $0.944 \pm 0.025$ | $1.087 \pm 0.027$ | $1.147 \pm 0.041$ | $0.752 \pm 0.037$ |
| Radius $R_{p,4.5\mu m}$ ($R_\oplus$) | $1.144 \pm 0.027$ | $1.128 \pm 0.027$ | $0.817 \pm 0.022$ | $0.945 \pm 0.026$ | $1.068 \pm 0.028$ | $1.161 \pm 0.030$ | $0.797 \pm 0.025$ |

[a] Informative prior PDFs were assumed for these stellar parameters

[b] where $T_{eq}$ is computed from $T_{eq} = \left[\frac{(1-A)*S_p}{4*\sigma}\right]^{1/4}$, assuming a null Bond albedo

**Table 4.3** Updated system parameters derived for TRAPPIST-1: median values and $1\sigma$ limits of the posterior PDFs derived from our global MCMC analysis of all nonblended and partial transits of TRAPPIST-1 planets observed by Spitzer.

colour code for the number of transits used in each analysis, while Table 4.5 presents the corresponding values. We precise that in those analyses, for the star, $M_\star$, $R_\star$, $T_{eff,\star}$, [Fe/H], and the linear combinations $c_1$ and $c_2$ of the quadratic limb-darkening coefficients (u1,u2) for each bandpass were jump parameters, with informative priors on $M_\star$,$T_{eff,\star}$, [Fe/H], $u_1$ and

| Quantity | Gonzales +2019[a] | Van Grootel +2018 | This work |
|---|---|---|---|
| Mass $M_\star$ ($M_\odot$) | 0.0859 ± 0.0076 | 0.0889 ± 0.0060 | 0.0898 ± 0.0023 |
| Radius $R_\star$ ($R_\odot$) | 0.1164 ± 0.0030 | 0.1182 ± 0.0029 | 0.1234 ± 0.0033 |
| Luminosity $L_\star$ ($L_\odot$) | 0.000608 ± 0.000022 | 0.000522 ± 0.000019 | 0.000552 ± 0.000018 |
| Effective temperature (K) | 2628 ± 42 | 2516 ± 41 | 2520 ± 39 |
| Parallax (mas) | 80.45 ± 0.12 | 82.4 ± 0.8 | 80.45 ± 0.12 |

[a] Derived for age range 0.5 to 10 Gyr, the field age constraint from Filippazzo et al. (2015), see Gonzales et al. (2019).

**Table 4.4** Comparison of stellar parameters value from various studies.

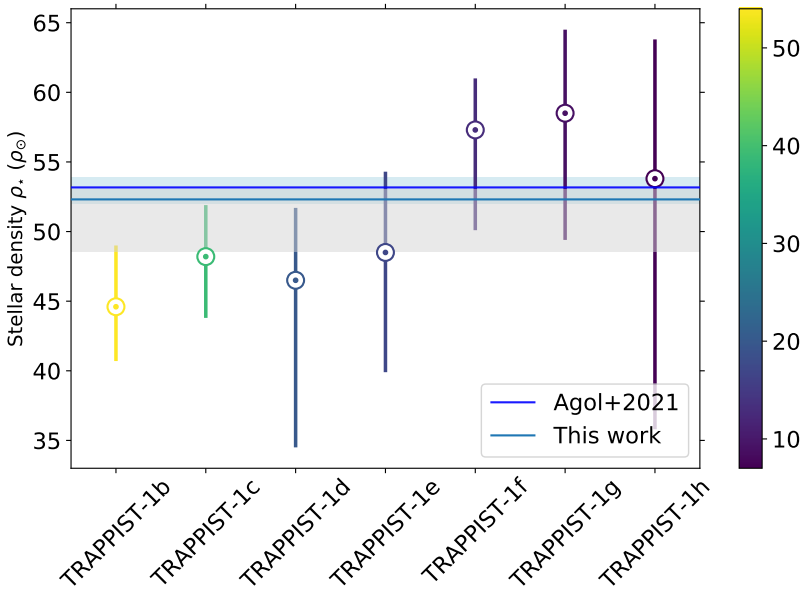


**Fig. 4.2** Coloured dots gives the stellar density derived from MCMC analyses of transits from a single planet, solid black line gives the density derived from a global analysis of all transits observed with its $1\sigma$ uncertainty in grey shades. Colorbar shows the number of transits used in each analysis. Solid blue line gives the stellar density value computed by Agol et al. (2020b) using a photodynamical model created with the mass-ratios and orbital parameters derived from a transit-timing analysis, with its $1\sigma$ uncertainty in blue shades.

$u_2$. And for each of the planets, the transit depth 4.5$\mu m$, the impact parameter and the transit depth difference between Spitzer/IRAC 3.6$\mu m$ and Spitzer/IRAC 4.5$\mu m$ channels were also jump parameters. From Figure 4.2, it appears that the inner planets favour a lower stellar density than the outer ones. This could be translated as a correlation between period $P$ and the inferred stellar density $\rho_\star$. We carried out a linear regression between $\rho_\star$ and $P$, and computed the Akaike information criterion (AIC) and Bayesian information criterion (BIC) to identify the best fit, see Figure 4.3. According to Figure 4.3, it turns out that a linear relation between the period and the stellar density is slightly preferred over a constant density

| Planet | # transits | $\rho_\star$ ($\rho\odot$) |
|---|---|---|
| TRAPPIST-1 b | 54 | $44.6^{-3.9}_{+4.4}$ |
| TRAPPIST-1 c | 39 | $48.2^{-4.4}_{+3.7}$ |
| TRAPPIST-1 d | 20 | $46.5^{-12.0}_{+5.2}$ |
| TRAPPIST-1 e | 17 | $48.5^{-8.6}_{+5.8}$ |
| TRAPPIST-1 f | 13 | $57.3^{-7.2}_{+3.7}$ |
| TRAPPIST-1 g | 9 | $58.5^{-9.1}_{+6.0}$ |
| TRAPPIST-1 h | 6 | $53.8^{-18.0}_{+10.0}$ |

**Table 4.5** Stellar density from individual planets' MCMC analyses with its $1\sigma$ uncertainty. For each planets the number of transits used in the analysis is indicated in the second columns.

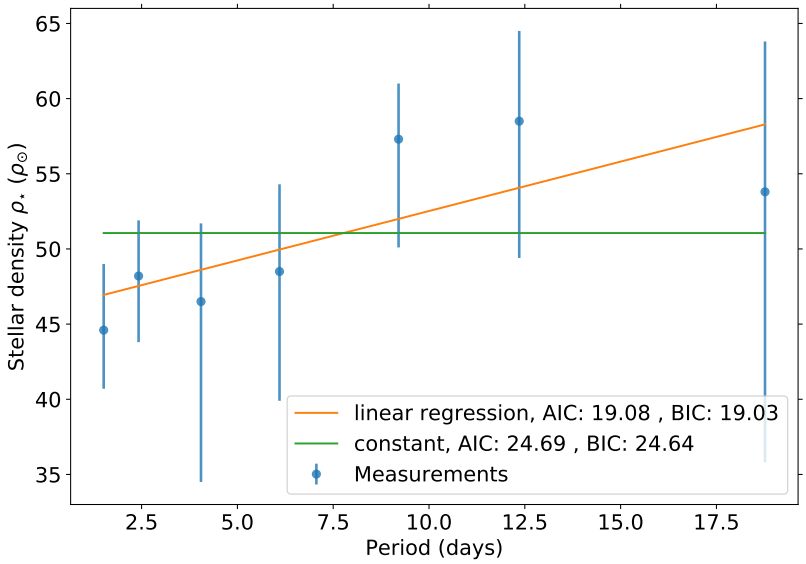


**Fig. 4.3** Stellar density inferred from individual planet's analysis versus period of the corresponding planet and its linear and constant fit with their corresponding AIC and BIC values.

(with a functional form of $\rho_\star = 0.65 * P + 45.95$). A Delta BIC of 5.61 corresponds to a Bayes Factor of 16. Based on Jeffreys' scale, the evidence for the bias is "strong" (Denison et al. 2002), but far from decisive. A correlation may thus exist between density and orbital period (and therefore b and $T_{14}$), but it is not firmly confirmed from our data. However, the amplitude of this bias is smaller than the $1\sigma$ error bars on the stellar density from the individual planet analyses, and therefore we conclude it is insignificant (at least at the current level of precision). On the origin of this weak trend in stellar density versus period, it could be the result of a trend of orbital eccentricity with orbital period. However, the eccentricities computed by Agol et al. (2020b) (see Section 4.2.1) do not seem to confirm this scenario. It could also be related to the limb-darkening. Indeed, for inner planets, we probe a larger range of $\cos\theta$ (see Section 1.2.1) than for the outer ones, as the first have smaller impact parameters

(see Table 4.3). Another explanation could be the impact of an observational bias, as we have less transits for the outer planets (details on the number of transits per planets in Table 4.1). As a whole, this comparison shows the advantage of having a multiplanetary system where the planets sample different parts of the stellar disk. We conclude that using the stellar density derived from a global analysis of all transits, as we did in the previous paragraph, is appropriate. Furthermore, in Figure 4.2 we have added the stellar density computed by Agol et al. (2020b) using a photodynamical model created with the mass-ratios and orbital parameters derived from a transit-timing analysis. We observe that the value derived from our global analysis is in excellent agreement with the one by Agol et al. (2020b), which strengthens our confidence in adopting this value.

In a second time, for each planet, we carried out two distinct global analyses: a global analysis to extract the TTV of each transit and a global analysis with an independent depth for each transit to monitor the evolution of the transit depths. In addition, we also performed an analysis of the occultation observations for planets b and c.

1. **Transit timing variations:** We used nearly the same priors and jump parameters as in the individual analyses although we fixed the time of transit for epoch zero ($t_0$) and period $P$ for each planet, and set TTV as a jump parameter for each transit. The priors value for $t_0$ and $P$ are extracted from Delrez et al. (2018a). In this analysis, the same depth was assumed for all transits observed in the same bandpass. For each transit, we assumed the same baseline as the one obtained from its individual analysis. Then, after one Markov chain of 50 000 steps, we re-scaled our photometric errors with the resulting correction factor and ran two Markov chains of 100 000 steps each. Transits timings and their corresponding TTVs are reported in Table 4.22 and displayed on Figure 4.4. From these, we performed for each planet a linear regression of the timings as a function of their epochs to derive an updated mean transit ephemeris, i.e., an updated value of the mid-transit time $t_0$ and the orbital period $P$ for each planet, see Table 4.3 (similarly to what was done in Delrez et al. (2018a)). Finally the medians of the global MCMC posterior PDF of the transit depth in both channels are given in Table 4.6. Those results are discussed and used to construct the planetary transmission spectra in Section 4.1.3.

2. **Transit depth variations:** Here, we also used similar priors as in the individual analyses except that this time we fixed the values of transit timings and periods $P$ but we set the TTV of each transit and $\delta$dF, the depth variations from one transit to another, as jump parameters. Again we ran first a 50 000 steps Markov chain to get the $CF$, and then two 100 000 steps chains. The evolution of the transit depths as a function of

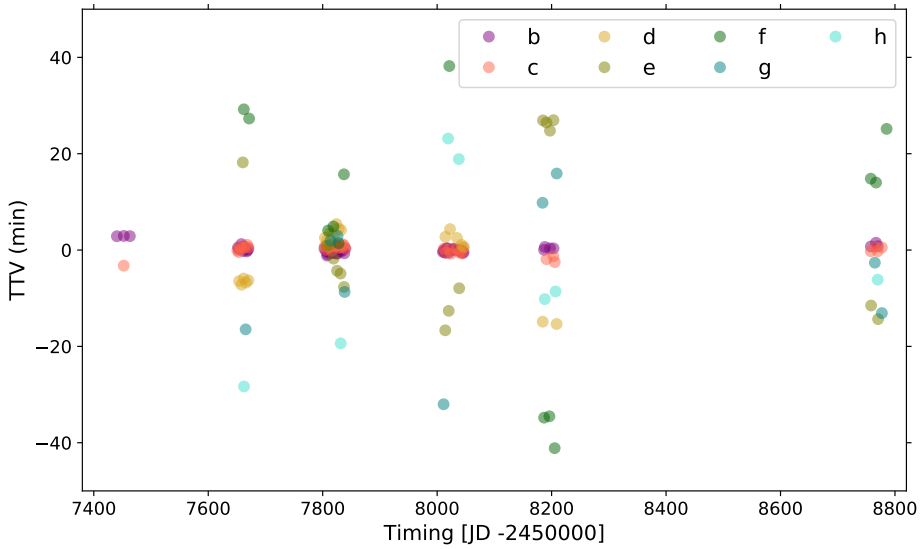


**Fig. 4.4** TTVs measured for the seven planets as obtained from our global planet by planet analyses (see Section 4.1.2) relative to the ephemeris ($t_0$ and $P$) given in Table 4.3.

| **Planet** | **Transit depth** $dF_{3.6\mu m}$ ± 1$\sigma$ - 3$\sigma$ **(%)** | | | **Transit depth** $dF_{4.5\mu m}$ ± 1$\sigma$ - 3$\sigma$ **(%)** | | |
|---|---|---|---|---|---|---|
| b | 0.7179 | 0.0058 | 0.021 | 0.7195 | 0.0069 | 0.021 |
| c | 0.7211 | 0.0130 | 0.039 | 0.6996 | 0.0058 | 0.018 |
| d | 0.3407 | 0.0150 | 0.042 | 0.3653 | 0.0070 | 0.021 |
| e | 0.4889 | 0.0010 | 0.027 | 0.4950 | 0.0075 | 0.023 |
| f | 0.6463 | 0.0175 | 0.047 | 0.6240 | 0.0093 | 0.029 |
| g | 0.7049 | 0.0330 | 0.094 | 0.7449 | 0.0110 | 0.024 |
| h | 0.3120 | 0.0210 | 0.069 | 0.3478 | 0.0130 | 0.039 |

**Table 4.6** Median of the global MCMC posterior PDF of the transit depth derived from global analyses of all transits, planet by planet, with no transit depth variations allowed. Those values are used to construct transmission spectra in Section 4.1.3.

the epochs is presented for each planet in Figure 4.5. For further comparison, these figures also display the medians of the global MCMC PDFs as obtained by the previous global analysis with TTV and no $\delta$dF variations (values from Table 4.6). We compared the results obtained from the individual and global analyses of the transits and found them to be fully consistent. In Figure 4.5, we chose to plot the depth values obtained from the global analysis with $\delta$dF variations allowed instead of those derived from the individual analyses, because the global analysis should be less impacted by systematic errors due to the red noise (i.e., the response of the pixels to time-varying illumination)

in Spitzer photometry.

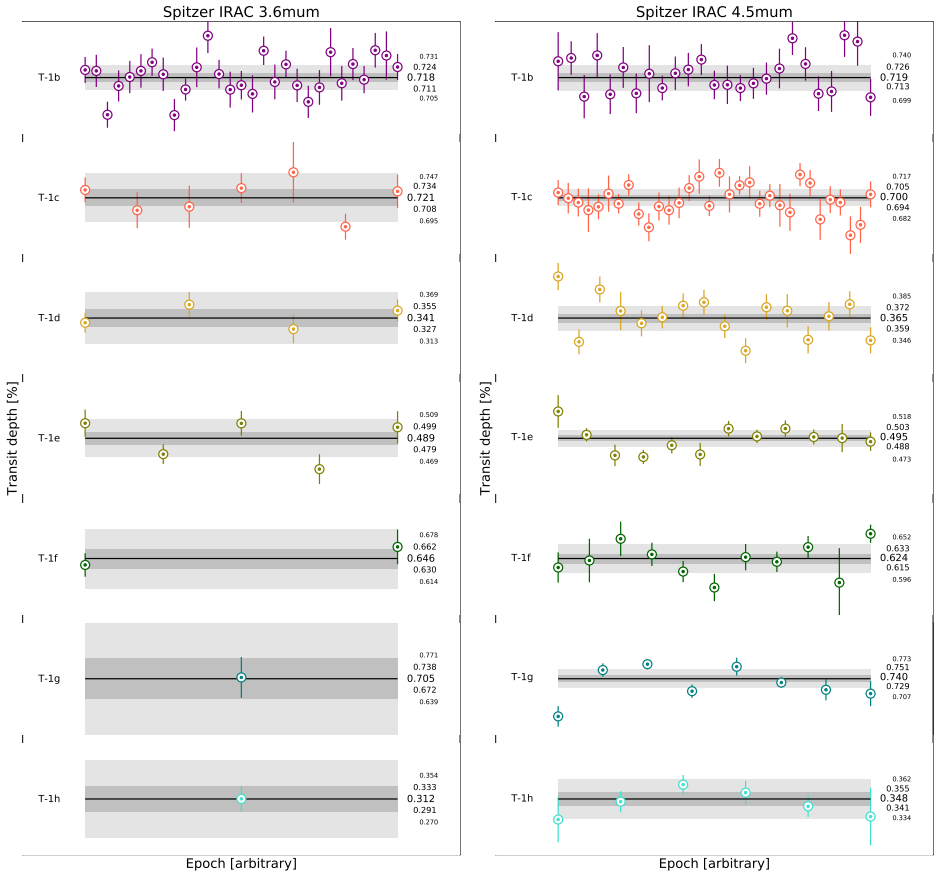


**Fig. 4.5** *Left*: evolution of the measured transit depths from the planet- per- planet global analyses of transit light curves at 3.6 $\mu$m. The horizontal black lines show the medians of the global MCMC posterior PDFs from the planet- per- planet analyses with TTV and no transit depth variations allowed (with their 1$\sigma$ and 2$\sigma$ confidence intervals (see values in Table 4.6) in shades of grey). Events are ranked in order of capture, left to right (but not linearly in time). *Right*: similarly, but for transits observed at 4.5 $\mu$m.

3. **Occultations:** Similarly than for transits, we used the eclipse model of Mandel et al. (2002) to represent occultations of TRAPPIST-1b and c as photometric time-series, multiplied by a baseline model to represent external sources of photometric variations (either from astrophysical or instrumental mechanisms). All occultation events were observed in channel 2 (4.5$\mu$m) as part of the DDT program 13175 (PI: L. Delrez). Our aim was to constrain the day-side brightness temperature of the two inner planets from the occultation depths. Ths dataset included 29 occultations of planet b and 8 occultations of planet c. For both planets, we performed a global analysis of the occultation light curves, assuming as priors the Gaussian PDFs corresponding to the

values for the stellar parameters and for the planets' transit depths, impact parameters, mid-transit-times, and orbital periods derived from our global analysis of all Spitzer transit light curves (Table 4.3). Circular orbits were assumed for both planets, and the occultation depth was the only jump parameter of the analyses for which a uniform prior PDF $[0, +\infty]$ was assumed. We justify the assumption of circular orbits from the fact that in a system with planets that have migrated by type I migration and ended in a Laplace resonance configuration, like TRAPPIST-1, eccentricities are expected to be very small. Indeed simulations carried out by Luger et al. (2017b) show that within a few Myr, eccentricities of each planet should be damped to less than 0.01. In addition, recent results by Agol et al. (2020b) from TTV and photodynamical modelling confirm that all planets eccentricities are most likely inferior to 0.01. Furthermore, when calculating the timing of secondary eclipse using the eccentricities derived by Agol et al. (2020b) (see Section 4.2.1) and their $3\sigma$ uncertainties, we compute a shift in time of 0.28 hours and 0.27 hours for planet b and c respectively. Considering that the out-of-secondary eclipse time is $\simeq$ 2 hours for each light curve of this DDT program, we can thus confidently state that we did not miss the time of secondary eclipse.

As with the transit analysis reported above, we identified the most applicable baseline for each light curve and ran a first chain of 50 000 steps to get the CF coefficients, applied these coefficients to the photometric error bars, and then ran two MCMC chains of 100 000 steps. We ascertained the convergence of our analyses with the Gelman & Rubin test (less than 1.1 for all jump parameters, as recommended by Brooks et al. (1998) and Gelman et al. (2021)). Unfortunately, no significant occultation signal was detected. Table 4.7 gives values of the occultation depths derived from the MCMC analysis with their $1\sigma$ and $3\sigma$ uncertainties. Those results are further discussed in Section 4.1.3.

| Planet | $\delta_{occ} \pm 1\sigma$ (ppm) | $\delta_{occ} \pm 3\sigma$ (ppm) |
|---|---|---|
| TRAPPIST-1 b | $90^{+5.9\times10^{1}}_{-5.3\times10^{1}}$ | $90^{+1.80\times10^{2}}_{-9.0\times10^{1}}$ |
| TRAPPIST-1 c | $74^{+8.0\times10^{1}}_{-5.2\times10^{1}}$ | $74^{+2.90\times10^{2}}_{-7.4\times10^{1}}$ |

**Table 4.7** Median of the posterior PDFs for the occultation depths of planets b and c + their $1\sigma$ and $3\sigma$ uncertainties as derived from the global analysis of 28 occultations of TRAPPIST-1b and 9 occultations of TRAPPIST-1c observed at 4.5 $\mu$m.

### 4.1.3 Results and discussion

#### Transits

*Noise floor*

From the transit depths globally derived in each band (Table 4.6), and from the mean error on the depths of each transit given in Tables 4.20 and 4.21, we can estimate the amplitude of the noise floor of Spitzer photometry of TRAPPIST-1. To do so, we compute the mean depth error $\overline{\sigma_{dF,i,c}}$ for the $i$th planet in each band, $c$, from Tables 4.20 and 4.21. Assuming a purely white noise, the expected error for $n$ transits of planet $i$ in band $c$ should be $\sigma_{global,exp} = \frac{\overline{\sigma_{dF,i,c}}}{\sqrt{n}}$. We then subtract in quadrature this expected value from the globally derived transit depth to estimate the Spitzer noise floor:

$$\sigma_{noise floor} = \sqrt{\sigma^2_{global,obs} - \sigma^2_{global,exp}}. \tag{4.4}$$

From equation 4.4, we calculate the noise floor for each planet and derive the mean noise floor in each channel. The resulting values are 36 ppm in channel 1 and 22 ppm in channel 2. These values are consistent – and even lower actually– than those derived for a sample of ~20 bright sun-like stars by Gillon et al. (2017a). Considering how small these values are, we can conclude that stacking dozens of transits of TRAPPIST-1 observed in the infrared does improve the precision nearly in a $\sqrt{n}$ manner. This agrees well with the high photometric stability of TRAPPIST-1 observed during its Spitzer 20d continuous monitoring (Delrez et al. 2018a; Gillon et al. 2017b). Furthermore, the larger value of the noise floor at 3.6 $\mu$m –as observed by Gillon et al. (2017a) for brighter Sun-like stars– suggests that this floor is mostly of instrumental origin, as the pixel-phase effect is significantly larger in IRAC channel 1 than in channel 2 and requires more complex baseline models (see Table A.1).

These results are particularly encouraging for the upcoming atmospheric characterisation of the planets by transit transmission spectroscopy with JWST (Gillon et al. 2020). Indeed, the detectors of the JWST instruments (HgCdTe for all except SiAs for MIRI) should all have a much better intrapixel homogeneity than the IRAC InSb arrays, which should result in much less severe position-dependent effects in the JWST spectrophotometric light curves. This is supported by the results obtained by Kreidberg et al. (2014b), who observed 15 transits of GJ1214b with HST/WFC3 (also an HgCdTe array, like NIRISS, NIRSPEC and NIRCAM) and obtained global transit depth errors consistent with a noise floor of ~ 10 ppm. Based on these considerations, noise floors in the 10-20ppm range can thus be expected for JWST observations of TRAPPIST-1, low enough to enable the detection and characterisation of compact atmospheres around the planets (Lustig-Yaeger et al. 2019).

*Time-dependent variations of the transit depths*

One possible way to gain insight into the host star of a planetary system is to use transits as a scan of the stellar photosphere (Espinoza et al. 2019). By comparing the transit depths at different epochs, we can identify unusual events that could inform us about the (in-)homogeneity of the star. Spot and faculae crossings are typically the kind of signatures detected with this method. For this purpose, we looked for unusually low or high depth values in the results from the global planet-by-planet analyses (Figure 4.5). We identified one clear outlier at $3\sigma$ lower than the other measurements for planet g (first point of the plot at 4.5 $\mu$m on Figure 4.5, epoch 0). The corresponding light curve and the fit for this epoch obtained from the global analysis are displayed in Figure 4.6. Yet, when we look at

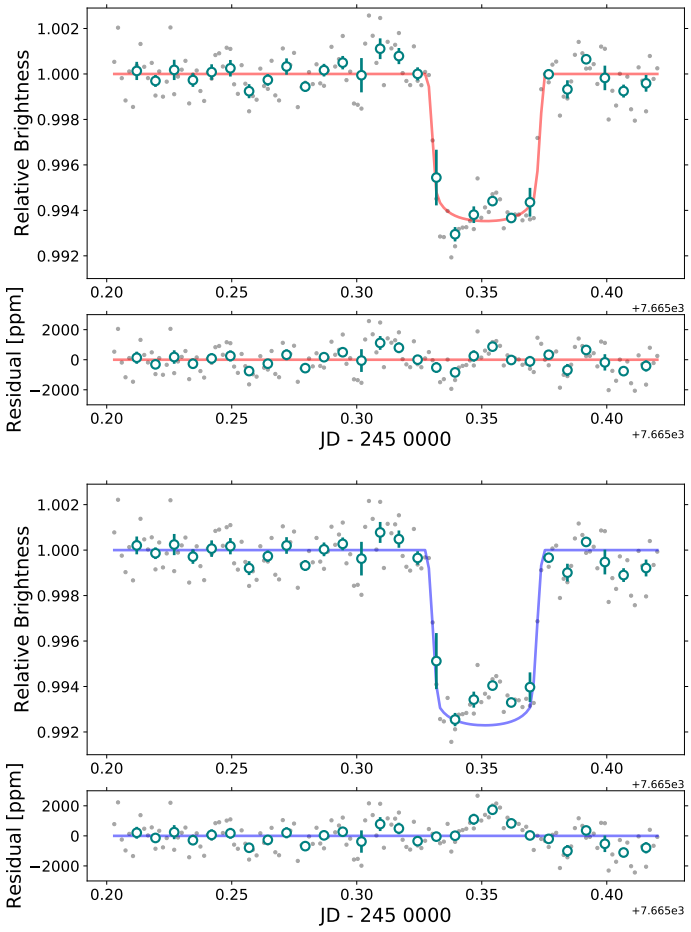


**Fig. 4.6** *Top panel:* detrended light curve of the first isolated transit of TRAPPIST-1g observed by Spitzer with, superimposed in red, the best-fit model resulting from the global per-planet analysis with variations of the transit depth allowed. *Bottom panel:* similar to top panel but with the best-fit model resulting from the individual analysis assuming a constant depth for all transits superimposed in darkblue.

the same light curve as modelled in the global planet-by-planet analysis assuming a constant transit depth (Figure 4.6 bottom panel), the first part of the transit seems to be consistent with the global model, while the rest is affected by a significant flux increase as expected for a spot-crossing event (Espinoza et al. 2019).

The discrepancy between individual and global fits is explained by the fact that in the global analyses per planet, the model tries to optimise the fit with free transit depth variations allowed, so the MCMC favours an unusually small depth for planet g to fit the unusual structure (see Figure 4.6). From the individual fit (Figure 4.6 bottom panel) we see that the structure in transit is very large (almost as long as the transit duration). If it corresponds to a spot crossing event this spot must be very large and at quite a low latitude as planet g has an impact parameter of $\simeq 0.42$ from Table 4.3. To investigate the origin of this structure, first we checked all the planetary transits happening near the outlier, meaning several days before and several days after the event, and found no evidence of a similar structure in any of those transits including transits of TRAPPIST-1f, the planet with the closest impact parameter to planet g (see Table 4.3). Nevertheless, it is worth mentioning that the closest transit of planet h to the event (happening 3 days before the event at 2457662.55449 JD precisely) is one of the outliers shown in Figure 4.8 (see below for details of this Figure), yet this light curve is particularly noisy in- and out- of transit and therefore not reliable. Secondly, as this event was captured during the continuous observation of the system by Spitzer in 2016, we looked in the photometry for evidence of important variations in the amplitude of the stellar variability around this event as a sign of a sudden appearance of a massive spot that could explain the structure in planet g's epoch 0 transit. To do so we applied a time rolling window (of fixed size equal to 20min) on the residuals of the detrended light curve corresponding to several days before and after the event, and from this rolling window we calculated the standard deviation and amplitude of the residual in order to catch any significant increase. Unfortunately, there does not seem to be any correlation between the appearance of the structure in the transit light curve of g and the variability of TRAPPIST-1, and as the Spitzer space telescope underwent some tracking problems during this campaign, our interpretation is limited. In a nutshell, this event is most probably isolated, which weakens the spot-crossing hypothesis considering that a massive photospheric heterogeneity would be needed to explain the observations. Nevertheless, as we could not correct this structure with any detrending of the systematics, one could still hypothesise that planet g transits a different stellar hemisphere than the other planets, or at least compared with f and h (as they have similar transit chords), and that the expected changes in stellar variability for such a large spot is not significant enough in the near infrared to significantly influence the stellar variability. However, this hypothesis is ruled out by the monotonic increase in the planets' transit duration and impact

parameters with orbital period, which implies an extremely coplanar planet system (Luger et al. 2017a).

Based on this experience with planet g, we visually inspected all individual light curves associated with the other outlier values in the global analysis results of Figure 4.5, but we did not find additional peculiar transits. To identify transit depth anomalies, we computed the median values and deviation of the photometric residuals in and out of transit (Table 4.23) as derived from the planet-by-planet global analyses (like in Delrez et al. (2018a)). Figure 4.7 and Table 4.23 present the standard deviations obtained for the in- and out of transit residuals. Such statistics allow us to investigate the localised spot/faculae population through the "in-transit" variations and the global stellar activity more generally through the "out-of-transit" variations. We deal specifically with stellar flares in Section 4.1.3.

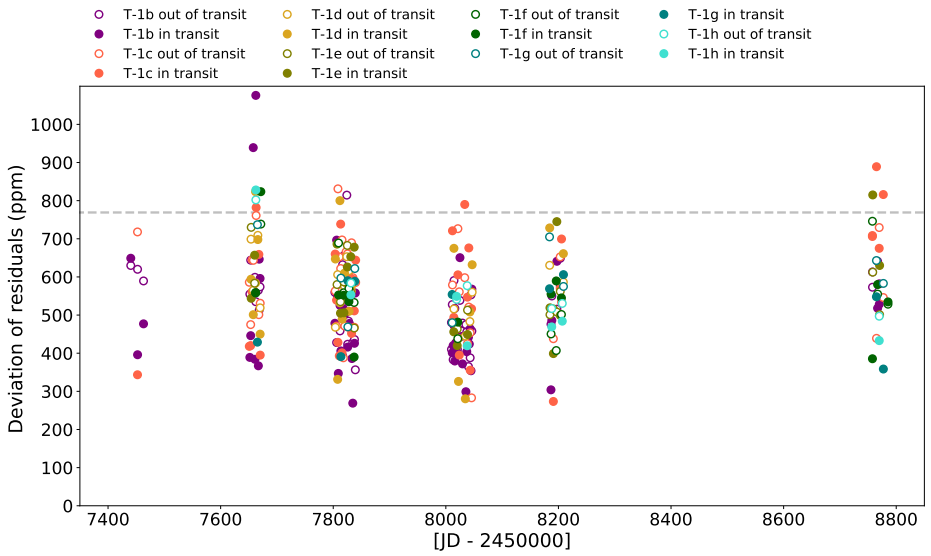


**Fig. 4.7** Standard deviation of the residuals (ppm) in- and out-of-transit for each planet (filled dots for in-transit data, empty dots for out-of-transit) such that for each transit's epoch there is one empty dot and one filled dot. Each colour is associated with a planet: purple for planet b, orange for c, yellow for d, olive for e, dark green for f, teal for g and turquoise for h. The dashed grey line shows the limit value above which we consider transits as outliers.

Considering the scatter of the measurements throughout the observations, we choose to define outliers as transit depth measurements whose standard deviations of the residuals is above 769ppm (median of deviation in- and out-of-transit + 3 $\sigma$, dashed grey line on Figure 4.7). Then, a careful look at all the light curves shed some light on the source of uncertainty of those measurements. We were particularly interested in cases where the standard deviation of the in-transit residuals is larger than the standard deviation of the out-of-transit residuals as this could correspond to spot or faculae crossing events. Yet, we kept in mind that the

standard deviation of the residuals in-transit has a lower precision because it is calculated with fewer points than the standard deviation of out-of-transit residuals as the planets spend more time out-of-transit than in-transit, limiting the amount of data that can be collected in-transit. In Figure 4.7, we identify nine outliers, notably two transits of planet b which show a standard deviation of the in-transit residual of more than 1000ppm and 900 ppm respectively. The corresponding light curves are presented in Figure 4.8.

In Figure 4.8, we observe that for some light curves the large value of the standard deviation of the in-transit residuals is explained by a structure that modifies the shapes of the transit. Such structures could indeed be due to the crossing of spots or faculae located within the transit chord of the planet at the time of transit. Light curves #1, #2, #4, #5, #6 and #9 could be interpreted as cases of bright spot crossing, while light curves #3, #7, and #8 could be interpreted as cases of dark spot crossing. The potential presence of spots could be worrisome for a precise derivation of the radius of the planets which is an essential step toward their detailed characterisation (Roettenbacher et al. 2017). To weight the relevance of those anomalies and leverage the statistical bias mentioned above, we calculated the significance of the difference between the median of the standard deviation of the residual in- and out-of-transit which we define by the following formula:

$$\text{significance} = \frac{|\text{median}_{\text{in}} - \text{median}_{\text{out}}|}{\sqrt{\sigma_{\text{in}}^2 + \sigma_{\text{out}}^2}} \tag{4.5}$$

where $\text{median}_{\text{in}}$ and $\text{median}_{\text{out}}$ are the medians of the residuals in- and out-of- transit, and $\sigma_{\text{in}}$ and $\sigma_{\text{out}}$ are the absolute deviations of the residuals in- and out-of transit, respectively. The results are presented in Table 4.23 and on Figure 4.9 for clarity.

We do not notice any significant difference between the in- and out-of-transit medians as they are comparable to within $1\sigma$ for all transits, see Figure 4.9. Those results do not favor the spot/faculae crossing hypothesis to explain the variability in transit depths that we discussed earlier, but rather systematic effects or some high-frequency stellar variability equally affecting in- and out-of-transit data to explain those anomalies. In fact, most of the outliers identified previously belong to the second of the five campaigns, during which the Spitzer telescope had some known drifting issues due to the use of inaccurate pointing coordinates (Gillon et al. 2017b). We conclude that although it is hard to firmly discard this scenario, our results do not support the presence of stellar photospheric heterogeneities (spots and faculae affecting the transit shape at 3.6 $\mu$m and 4.5 $\mu$m). However, one could argue that the lower contrast expected in the mid-IR may explain why we do not firmly detect any spot/faculae crossing event. Yet, recent results by Ducrot et al. (2018) failed to observe any spot crossing event in either the visible or the near-IR which favors a rather homogeneous

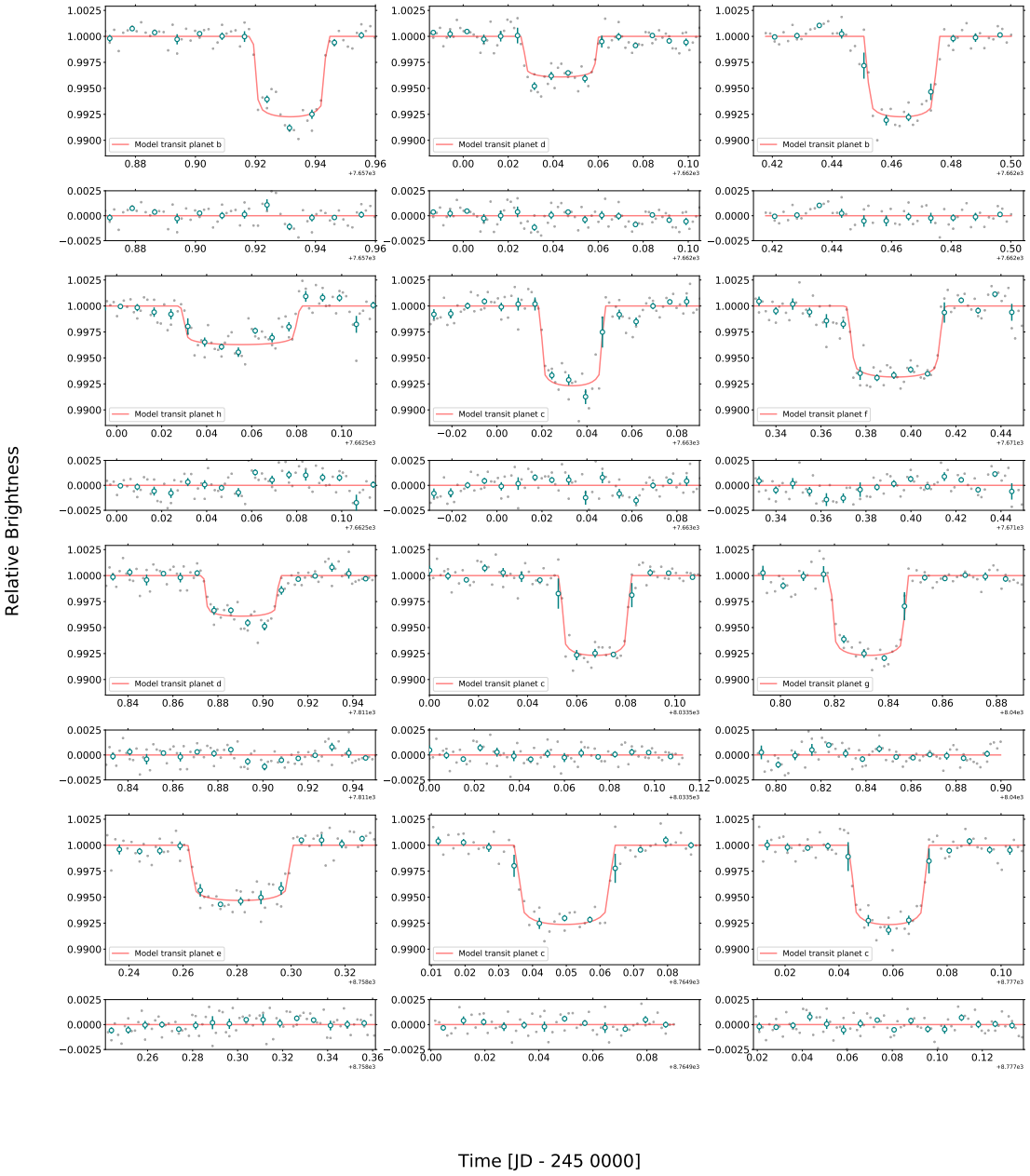


**Fig. 4.8** Transit light curves and their residuals for the 9 outliers identified on Figure 4.7. Each outlier was attributed a number in chronological order from 1 to 9. The corresponding transiting planet is indicated in each plot.

stellar photosphere, at least for the portion transited by the seven planets. If numerous, spots would be expected to be relatively cool and small or out of the transits chords to agree with the very few events observed, see Delrez et al. (2018a), Ducrot et al. (2018), and Morris et al. (2018c). Nevertheless, it is still worth mentioning that some techniques are being developed to recover the true radii of planets transiting spotted stars with axisymmetric spot

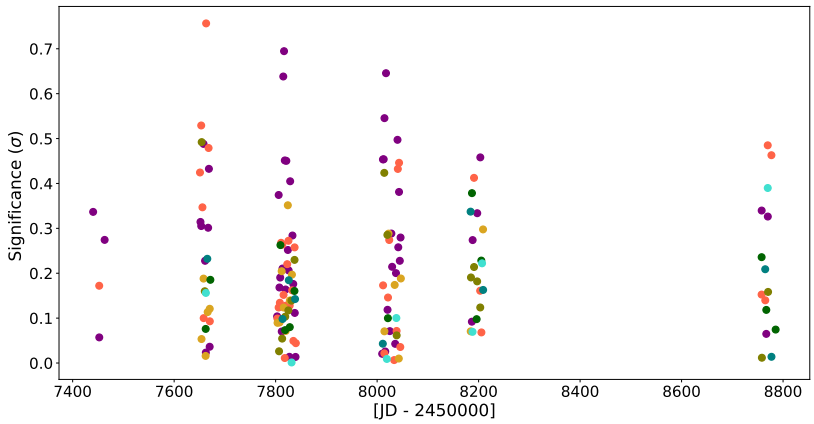


**Fig. 4.9** Significance of the difference between the median of the residuals (ppm) in and out of transit for each planet computed as: significance $= \frac{|\text{median}_{\text{in}} - \text{median}_{\text{out}}|}{\sqrt{\sigma_{\text{in}}^2 + \sigma_{\text{out}}^2}}$. Each dot stands for one unique transit. Each colour is associated to a planet: purple for planet b, orange for c, yellow for d, olive for e, dark green for f, teal for g and turquoise for h.

distributions from measurements of the ingress/egress duration, on the condition that the limb-darkening parameters are precisely known, see Morris et al. (2018c). The authors of the latter paper applied this technique to TRAPPIST-1 and concluded that active regions on the star seem small, low contrast, and/or uniformly distributed (Morris et al. 2018b). In any case, future JWST observations are expected to be more precise and therefore decisive for the confirmation of those conclusions.

Figure 4.10 shows the period-folded photometric measurements for all transits in both bands, corrected for the measured TTVs as well as the corresponding best-fit baseline models. We observe no recurrent structure for all planets. The limb darkening effect is less important at those wavelengths than in the visible or near-IR (see Ducrot et al. (2018)) and the difference between the two channels is hardly noticeable by eye in Figure 4.10.

*Transmission spectra*

On Figure 4.11, we show the updated version of the transmission spectra of the seven planets presented by Burdanov et al. (2019). This update consists of an additional point at 3.6$\mu$m for planets c-h, updated values at 4.5$\mu$m, and updated weighted mean values for all planets (continuous lines in the plot). Figure 4.11 combines results from Burdanov et al. (2019), De Wit et al. (2016), 2018, Ducrot et al. (2018), and Wakeford et al. (2018) and shows transmission spectra with the largest number of experimental measurements to date for the TRAPPIST-1 planets. We took the decision not to include HST measurements (De Wit et al. 2016; 2018; Wakeford et al. 2018) to compute the weighted mean depth for each planet (black continuous line). This choice is justified by the fact that, although the transit transmission

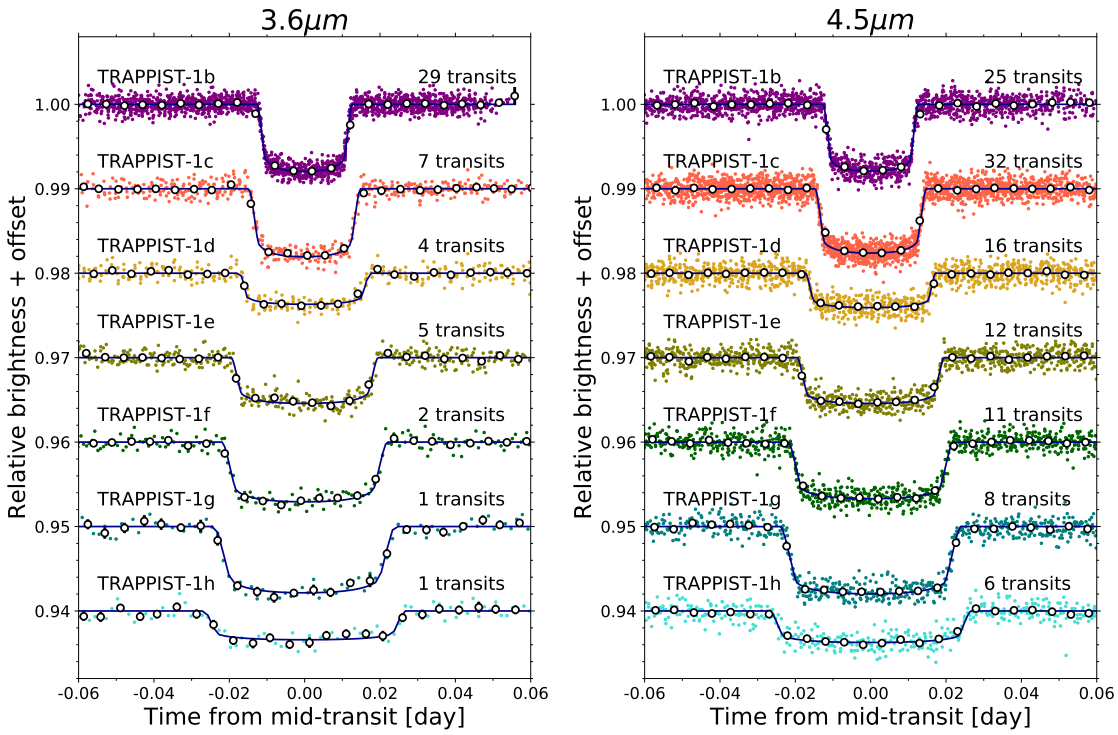


**Fig. 4.10** *Left:* period-folded photometric measurements obtained with Spitzer/IRAC channel 1 (at 3.6 $\mu$m) near the transits of the seven planets, corrected for the measured TTVs. Colored dots show the unbinned measurements; open circles depict the measurements binned over 5 minutes for visual clarity. The best-fit transit models are shown as dark blue lines. The numbers of transits that were observed to produce these combined curves are written on the plot. *Right*: similarly at 4.5 $\mu$m.

spectra measured in HST/WFC3 spectra are certainly reliable in relative terms, the derived absolute values of the transit depths themselves can be questioned because HST/WFC3 spectrophotometric observations are affected by orbit-dependent systematic effects which can result in diluted or amplified monochromatic transit depths, as implied by several previous studies (De Wit et al. 2016; Ducrot et al. 2018; Wakeford et al. 2018).

Concerning the Spitzer observations only, on Figure 4.11 we observe that for all planets there are no significant differences between the 3.6$\mu$m to 4.5$\mu$m measurements (particularly in comparison with visible and near-IR variations), both agreeing with each other better than 2-$\sigma$ for all planets (value given in Table 4.6). When we next consider all of the observational points, the depths measured at different wavelengths are all consistent with each other at better than 1-$\sigma$ for planet b, and better than 2-$\sigma$ for planets d and g. However, for planets c, e, f, and h the transmission spectra show a scatter larger than expected based on the measurement errors alone. For planet h, only one point exceeds the two sigma confidence, the one derived from the Liverpool Telescope (LT) dataset. But, it is worth mentioning that the effective wavelength for LT observations (0.9046 $\mu$m) is very close to that of SPECULOOS (0.9102

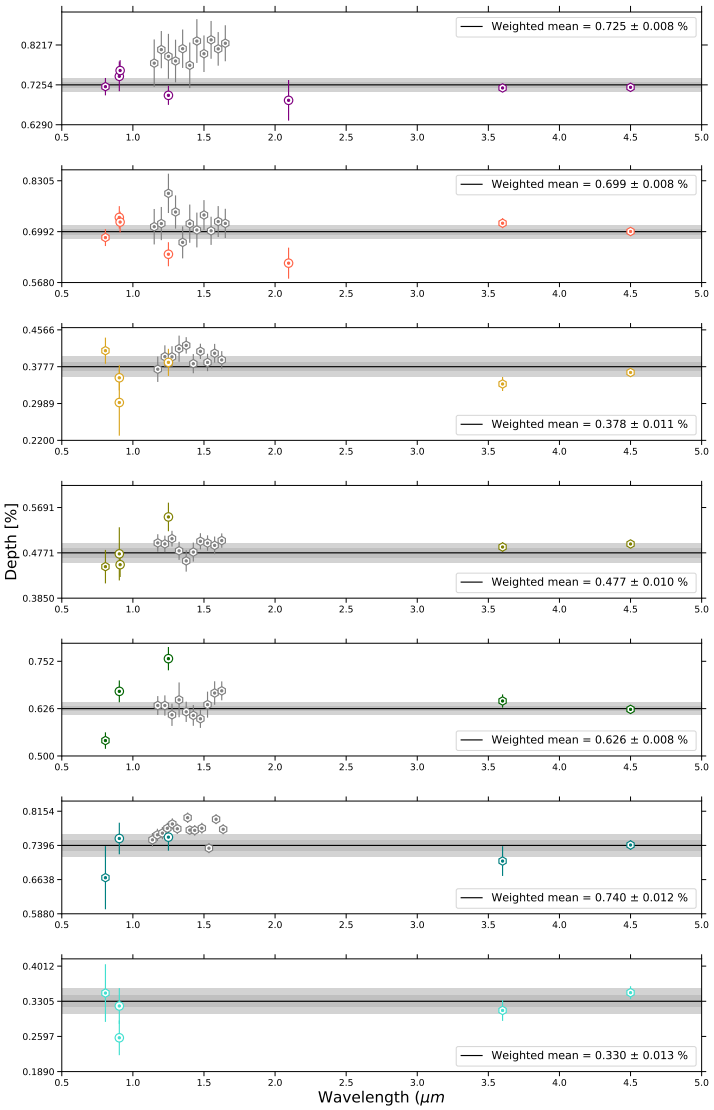


**Fig. 4.11** Updated version of the transit transmission spectra of the seven TRAPPIST-1 planets. In each subplot the continuous line is the weighted mean depth of all non-HST measurements, with its $1\sigma$ and $2\sigma$ confidence intervals in shades of grey. HST measurements are presented as grey points. Coloured dots stand for the measured transit depth at the effective wavelength of the instrument, ground based measurement are symbolised by circles and space based measurement by hexagons. Each point is associated with a particular observation, in ascending order of wavelength: one point for K2 (value from Ducrot et al. (2018)), one for SSO (value from Ducrot et al. (2018)), one for LT (value from Ducrot et al. (2018)), one in the J-band for UKIRT/WFCAM and/or AAT (value from Burdanov et al. (2019)), one for the NB-2090 filter band, one point for VLT/HAWK-I only for planet b and c (value from Burdanov et al. (2019)), in the 1.1-1.7 microns ranges 11 points for b and c, 10 for d, e, f and 13 for g taken with HST/WFC3 (values from De Wit et al. (2016) and 2018 and Wakeford et al. (2018)) and two points for Spitzer/IRAC channel 1 and 2 (values from this work, Table 4.6).

$\mu$m) and yet the SPECULOOS value is not discrepant with the others. Furthermore those data were obtained at the same period on SPECULOOS and LT. Therefore, the difference in depth measurements between those two facilities is probably more of a systematic rather than a physical origin. Yet, for planet c and e, the points that are the most inconsistent with the weighted mean value are the measurements obtained from observations carried out in the near-infrared, with either UKIRT, VLT, AAT, or HST.

One of the most ambitious results that the exoplanet community wishes to achieve with the upcoming JWST is the first detection of an atmosphere around a terrestrial exoplanet (Madhusudhan 2019). For the reasons discussed earlier, the TRAPPIST-1 system is particularly favorable for the achievement of this goal via transit transmission spectroscopy (Barstow et al. 2016; Batalha et al. 2018; Fauchez et al. 2019; Krissansen-Totton et al. 2018a; Lustig-Yaeger et al. 2019; Morley et al. 2017), and offers the opportunity to probe atmospheres not only around terrestrial planets but also around temperate terrestrial planets within the habitable-zone of their host star. In the next chapter, we will discuss the impact of stellar contamination on the planet transmission spectra, but in this section, we only discuss potential detections of atmospheric features of the transmission spectra. Here, we limit our discussion to include only the cases of TRAPPIST-1b, c, e and g because (a) b and c have the smallest periods - that is to say the most transits and therefore the greatest precision on measurements, (b) planet e is arguably the most promising candidate for habitability, for the reasons given in Wolf (2017) and Wolf et al. (2017), Turbet et al. (2018) and Fauchez et al. (2020b), and (c) planet g was the most observed with HST/WFC3 (Wakeford et al. 2018).

Combining ground and space-based observations, we could construct the broadband transmission spectra for each planet and compare them to recent atmospheric models of the TRAPPIST-1 atmospheres computed by Lincowski et al. (2018), see Figure 4.12. To construct this figure, we have added a vertical offset to Lincowski et al. (2018)'s models to optimally overlap the observations. These offsets correspond physically to the difference between the assumed radius for TRAPPIST-1b and the solid body radius assuming a model atmosphere and its associated absorbing radius above the surface (Lincowski et al. 2018). We have applied this offset such that the models crossed the measured transit depth at the value of the sum of the weighted mean depth of each planet (shown in grey solid line on Figure 4.12). For the reasons mentioned above, we also applied an offset to adjust the mean level of each HST/WFC3 spectra to the weighted mean depth for each planet. By doing this we can benefit from the trustful information given by HST/WFC3 measurements on relative depths and use it to better constrain atmospheric properties.

Those spectra illustrate our current knowledge of the transit transmission spectra gained from follow-up observations. The wavelength range that has been probed since the discovery of

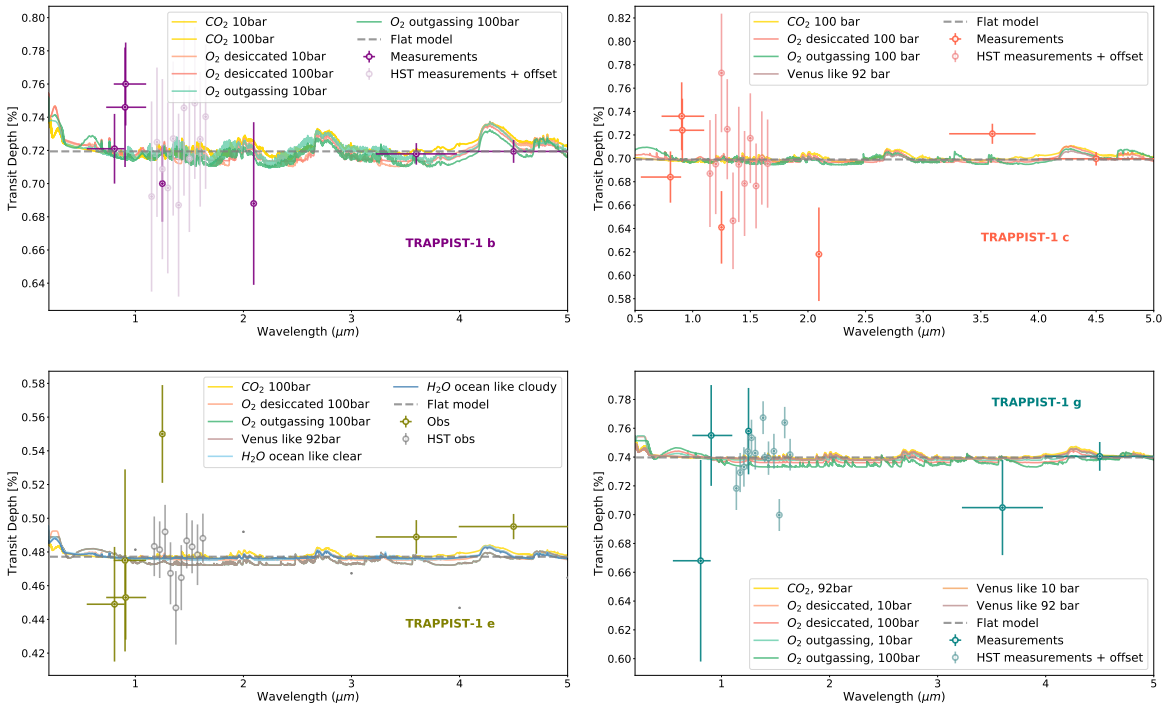


**Fig. 4.12** *Top-left:* transit transmission spectrum of TRAPPIST-1b from observations compared with simulated transit transmission spectra derived by Lincowski et al. (2018) for different terrestrial atmospheres. Each color is associated with a different scenario: - gold stands for 10 or 100 bars $CO_2$-rich atmospheres - salmon stands for 10 or 100 bars $O_2$-rich desiccated atmospheres - green stands for 10 or 100 bars $O_2$-rich outgazing atmospheres - brown stands for 10 or 92 bars Venus-like atmospheres - and blue stands for an aqua planet with either clear or cloudy sky. *Top-right:* similarly but for TRAPPIST-1c. *Bottom-left:* similarly but for TRAPPIST-1e. *Bottom-right:* similarly but for TRAPPIST-1g.

the system goes from $\simeq 0.6$ $\mu$m to $\simeq 5$ $\mu$m. In this spectral range the strongest molecular features that we could expect in the absence of clouds and haze - and in a plausible planetary environment - are $CO_2$, $CH_4$, $H_2O$ and CO (Gordon et al. 2017; Morley et al. 2017; Tennyson et al. 2012). Considering the poor sampling of the spectra we can only look for broad and strong features: - the $CO_2$ 4.3 $\mu$m spectral feature in the 4-5 $\mu$m channel of Spitzer/IRAC (width of the bandpass is 1.015 $\mu$m for that channel) - the $CO_2$ 2.1 $\mu$m spectral feature in the VLT/HAWK-I's NB-2090 filter bandpass (width of the bandpass is 0.020 $\mu$m for NB-2090 filter) - and the $CH_4$ 3.3 $\mu$m spectral feature in the 3.15-3.9 $\mu$m channel of Spitzer/IRAC (width of the bandpass is 0.750 $\mu$m for that channel).

We deliberately did not consider models of hydrogen-dominated atmospheres as there is now plenty of evidence that all TRAPPIST-1 planets are unlikely to host this kind of atmospheres. First, transmission spectroscopy with HST/WFC3 has shown that most of the planets in the system are unlikely to have cloud-free H2-rich atmospheres (De Wit et al. 2016; 2018;

Wakeford et al. 2018). Although transmission spectroscopy cannot rule out H2-dominated atmospheres containing high-altitude aerosols (Moran et al. 2018), such configuration is in fact unlikely. This stems from the fact that any small variation of hydrogen content between planets, as expected from (1) variations in the hydrogen-rich gas accretion rates during the planet formation phase (Hori et al. 2020) and from (2) variations in H2 escape rates (Bolmont et al. 2017; Bourrier et al. 2017; Owen et al. 2016), are expected to produce large variations in density between planets (Turbet et al. 2020a) that are not observed (Agol et al. 2020b; Grimm et al. 2018).

The transmission spectrum of TRAPPIST-1b - HST/WFC3 measurements excluded - can be relatively well fit by the models. It contains the observational points with the best precision with an error bar as low as 58 ppm (Table 4.6) in Spitzer/IRAC channel 2 measurement (thanks to the combination of 28 transits). Yet, even with 28 transits combined the reached precision is still of the same order than the expected amplitude of atmospheric features on TRAPPIST-1b (Lustig-Yaeger et al. 2019; Morley et al. 2017). TRAPPIST-1c's spectrum shows a greater scatter than the one of b with an apparently poor fit to the models, yet the uncertainties on the measurements are large (at least relatively to the expected atmospheric features) and those variations are not significant at more than $3\sigma$. Then, for planets e and g, the expected spectral features are even shallower than for b and c, and the observations are less precise because of the smaller number of transits analysed; thus it is impossible to speculate on the presence of any molecular species.

One possibility to gain some precision in the measured transit depths is to study the combined transit transmission spectrum of several planets. Figure 4.13 shows a transmission spectrum constructed from the combination of planets b, c, d, e, f and g's transmission spectra.

In Figure 4.13, we have applied an offset on HST-measurements to adjust the mean level to the weighted mean depth calculated from the rest of the observations, and we have over-plotted several simulated combined transmission spectra from Lincowski et al. (2018) and Morley et al. (2017). For the reasons we mentioned earlier, we have added a vertical offset to the atmospheric models to optimally overlap the observations. The offset value is such that the models crossed the value of the sum of the weighted mean depth of each planet (shown in blue dotted line on Figure 4.13). From the observations, only points derived from the Spitzer dataset analyses have a precision of comparable magnitude than the variations expected in presence of an atmosphere. Table 4.8 gives the reduced chi square $\chi^2_\nu = \chi^2/\nu$ for each model if its aim was to fit the observations, with $\nu$ the number of degrees of freedom and $\chi^2$ is defined by:

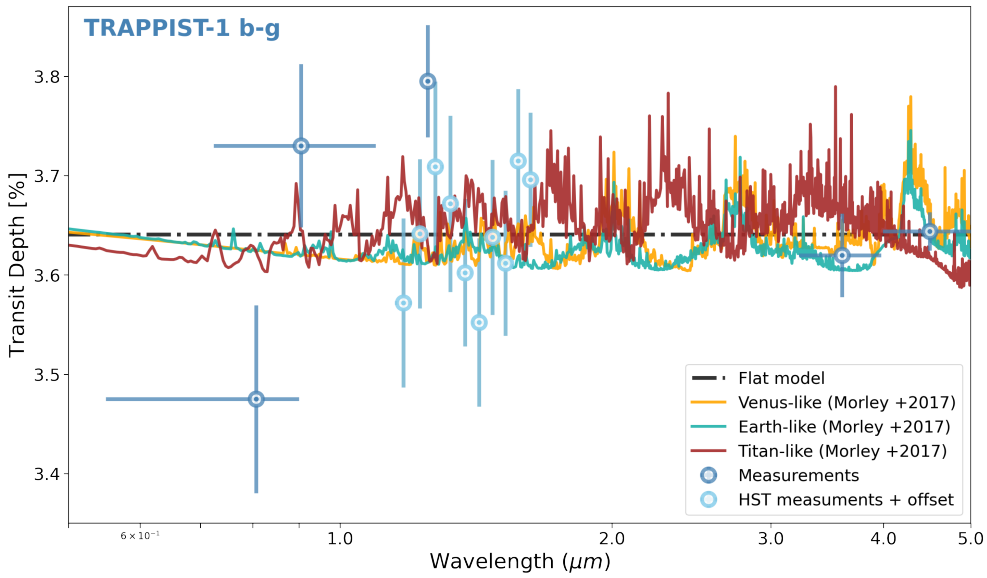


**Fig. 4.13** TRAPPIST-1 combined transmission spectra for planets b+c+d+e+f+g (blue points) constructed from individual spectra (see Figure 4.11). The blue-green curve represents the simulated combined transit transmission spectra expected for an Earth-like atmosphere, the orange curve for a Venus-like atmospheres and the brown curve for a Titan-like atmospheres. Corresponding coloured hexagons give the value expected from the models at the wavelengths of the observations. The grey dashed lines is the flat model at the weighted mean value of the transit depth. Wavelength is in log scale.

$$\chi^2 = \sum_i \frac{(pred(i) - obs(i))^2}{\sigma(i)^2} \tag{4.6}$$

where $obs(i)$ is the measured depth at wavelength i, $\sigma(i)$ its error, and $pred(i)$ is the depth predicted by the model for wavelength i.

On Figure 4.13, Earth-like (Morley et al. 2017), Venus-like (Morley et al. 2017) and $CO_2$-dominated (Lincowski et al. 2018) atmospheric scenarios seem to agree reasonably well with Spitzer experimental values, showing notably a larger depth in IRAC channel 2 than in channel 1 like the data suggest. In contrast, in a Titan-like (i.e., $CH_4$-dominated) scenario the depth measured in channel 1 is expected to be larger than the one measured in channel 2. This explains by the fact that a Titan-like atmospheres exhibit a strong, broad $CH_4$ absorption feature centered at 3.3$\mu$m that produces a deeper transit depth in the Spitzer channel 1 than in the channel 2. We note that the discrepancy between Titan-like atmospheres and the measured Spitzer channels 1-2 transit depths would be even greater if we assume that stellar contamination occurs at these wavelengths. Looking at the value reported in Table 4.8, we indeed confirm that a Titan-like atmosphere appears to be the less likely considering our

| Model fitted to the data | Reduced $\chi^2$ |
|---|---|
| No atmosphere | 1.1920 |
| Venus-like atmosphere [c] | 1.4376 |
| $CO_2$, 92bar [b] | 1.5086 |
| Earth-like atmosphere [c] | 1.5554 |
| Titan-like atmosphere [c] | 1.8542 |

[a] (Zhang et al. 2018)
[b] (Lincowski et al. 2018)
[c] (Morley et al. 2017)

**Table 4.8** Reduced $\chi^2$ values for different atmospheric models. The number of degrees of freedom used in calculating the reduced-chi-squared values listed here equal to the size of the observation sample - 1.

current observational points and their errors bars. As a very preliminary estimation, we could predict that, assuming high-mean-molecular weight atmospheres the TRAPPIST-1 planets, it is rather unlikely that most of the TRAPPIST-1 planets possess a $CH_4$-dominated atmosphere.

Yet, what we can also note from Table 4.8 is that the most likely scenario, given the current observations, is a model with no atmosphere where the transit depth is equal to the sum of the weighted mean depth at all wavelengths. However, we cannot drawn any clear conclusion because as we mention before we are extremely limited by the precision on our each measurements, even for Spitzer/IRAC channel 1 and 2.

In conclusion, from Figure 4.12 we can only lament that our current level of precision is not high enough to draw proper conclusions about the existence of compact, high mean-molecular weight atmospheres around the TRAPPIST-1 planets. Even the combination of 22 transits of planet b at 4.5 $\mu$m and 28 transits at 3.6 $\mu$m with the Spitzer space telescope cannot reduce our error bars to sufficient precision. Nevertheless, the combined transmission spectrum of planets b to g presented in Figure 4.13 tells us that the atmospheres of the TRAPPIST-1 planets are unlikely to be all methane-dominated. Yet, this interpretation is made from only two observational points (Spitzer IRAC channels 1 and 2) and requires further investigation. A more rigorous study of the planets' atmospheres will likely have to wait for JWST. In particular, the Prism mode of the NIRSPEC instrument shows a high potential to detect compact atmospheres around the planets (Batalha et al. 2018; Fauchez et al. 2019; Lincowski et al. 2018; 2019; Lustig-Yaeger et al. 2019). Several independent simulations predict that it could take less than 10 transits for the seven planets to detect the dominant absorber (Batalha et al. 2018; Krissansen-Totton et al. 2018a; Lustig-Yaeger et al. 2019; Morley et al. 2017;

Wunderlich et al. 2019). This number may increase if clouds and/or photochemical hazes are present (Fauchez et al. 2019). Besides, more and more studies focus on understanding how JWST could provide us with insight into the planets' potential habitability, either through the presence of biogenic oxygen in their atmospheres (Lincowski et al. 2018; Meadows et al. 2018a; Morley et al. 2017), or via the detection of anoxic biosignatures such as $CH_4$ + $CO_2$ minus CO (Krissansen-Totton et al. 2018a), while keeping in mind the importance of false positives/negatives (Harman et al. 2015; Reinhard et al. 2017) (refer to Chapter 1 section 1.1.2 for details).

### Occultations

We also analysed 29 predicted occultations of planet b and 8 predicted occultations of planet c, all observed in channel 2 (centred in 4.5$\mu$m), hereafter indexed as c2. Our aim was to derive the day-side brightness temperature $T_{p,c2}$ of the two inner planets from their occultation depths. Unfortunately, we did not detect the occultation signal of either planet b or planet c (see Figure 4.14), but we were able to estimate a 3$\sigma$ upper limit on their day-side brightness temperatures. No occultation observations were taken in channel 1.

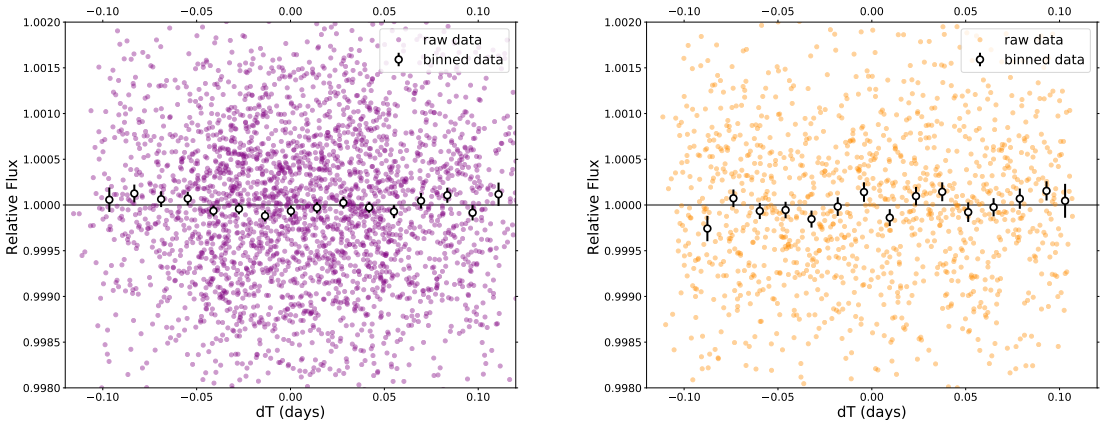


**Fig. 4.14** *Left:* period-folded photometric measurements obtained by Spitzer IRAC/channel 2 (centred in 4.5 $\mu$m) near the 28 occultations of planets TRAPPIST-1b, corrected for the measured TTVs. Coloured dots show the unbinned measurements; open circles depict 20min-binned measurements for visual clarity, and solid grey line is simply an horizontal line centred in 1. *Right:* similarly but for 9 occultations of TRAPPIST-1c.

To derive the brightness temperature $T_{p,c2}$ from the occultation depths, we used the method described in Charbonneau et al. (2005) and Deming et al. (2005). Our starting point was to define the occultation depth as the ratio of the flux of the planet and the total flux outside

of transit. This translates into equation (4.7), where $\Omega_p$ is the solid angle subtended by the planet, $\Omega_\star$ is the solid angle subtended by the star, $B_p$ is the surface brightness of the planet and $B_\star$ is the surface brightness of the star,

$$\delta_{occ} = \frac{\Omega_p B_p}{\Omega_p B_p + \Omega_\star B_\star}. \tag{4.7}$$

Then, assuming that the planet is a blackbody, its surface brightness $B_p$ can be expressed with Planck's blackbody law,

$$B_p(\nu) = \Big(\frac{2h\nu^3}{c^2}\Big)\Big(\frac{1}{e^{h\nu/k_b T_{B,p}} - 1}\Big), \tag{4.8}$$

where $\nu$ is frequency, $h$ is the Planck constant, $c$ is the speed of light in vacuum, $k_b$ is the Boltzmann constant, and $T_{B,p}$ is the brightness temperature. Equation 4.8 can be re-arranged as follows:

$$T_{B,p}(\nu) = \frac{h\nu}{k_b \ln\Big(\frac{2h\nu^3}{c^2 B_p} + 1\Big)} \tag{4.9}$$

In addition, when we develop equation (4.7) we get the ratio $\frac{\Omega_p}{\Omega_\star}$ which we approximate as the ratio of the planet area with the star area, see equation (4.10), such that equation (4.8) becomes:

$$\frac{R_\star^2}{R_p^2} \simeq \frac{\Omega_\star}{\Omega_p} \tag{4.10}$$

giving

$$B_p(\nu) = \frac{\delta_{occ} B_\star(\nu)}{1 - \delta_{occ}} \Big(\frac{R_\star}{R_p}\Big)^2. \tag{4.11}$$

Finally, substituting equation (4.11) in equation (4.9) we obtain the brightness temperature $T_{B,p}$ as a function of the occultation depth $\delta_{occ}$, the surface brightness of the star $B_\star$, and the frequency of the observations:

$$T_{B,p}(\nu) = \frac{h\nu}{k_b \ln\Big(\frac{2h\nu^3}{c^2 \frac{\delta_{occ} B_\star(\lambda)}{1-\delta_{occ}} \Big(\frac{R_\star}{R_p}\Big)^2} + 1\Big)} \tag{4.12}$$

To obtain the value of the star surface brightness $B_\star(\nu)$, we followed two different approaches. First, we approximate that the host star as a blackbody and derive $B_\star(\nu)$ from the value of the stellar temperature obtained in Table 4.3. Secondly, as TRAPPIST-1 is not an ideal blackbody, we computed $B_\star$ directly from the flux measurements in Spitzer raw images. To do so, we measured the flux of the star in the Spitzer Basic Calibrated Data (BCDs) corrected

from instrumental signatures and calibrated in physical units (MJy). We then followed the procedure described in the IRAC Instrument Handbook to obtain the absolute flux density of the star in Spitzer channel 2, such that we multiplied the measured counts by $2.3504 * 10^{-11}$ sr.arcsec$^{-2}$ x $1.22^2$ arcsec$^2$.pixel$^{-1}$, and then divided by $\left(\frac{R_\star}{d}\right)^2$ to get the flux density in W.m$^{-2}$.Hz$^{-1}$.sr$^{-1}$, $R_\star$ being the radius of TRAPPIST-1 and $d$ the distance of the system from GAIA/DR2 (Gaia Collaboration et al. 2018). Results from both approaches are presented in Table 4.9.

| Planet | # occultations | $3\sigma$ upper limit for $T_{B,p}$ from BB assumption $[K]$ | $3\sigma$ upper limit for $T_{B,p}$ from measured flux $[K]$ |
|---|---|---|---|
| b | 28 | 743 | 768 |
| c | 9 | 812 | 842 |

**Table 4.9** $3\sigma$ upper limit brightness temperatures computed from the occultation depth outputs by the MCMC analysis carried out in Section 4.1.2 (values given in Table 4.7) using equation(4.9). The brightness temperature is a function of the surface brightness of the star that was either computed using a blackbody model (BB) or derived from the fluxes measured in the Spitzer telescope raw images of TRAPPIST-1.

Even though we did not significantly detect any occultation signal, we can compare the occultation depths outputs by the MCMC analysis and its $3\sigma$ uncertainty with planetary thermal emission models. On Figure 4.15, we compare the secondary eclipse spectrum models of TRAPPIST-1b and c for different simulated atmospheric models from Lincowski et al. (2018) with the values derived from our analysis. With Figure 4.15 our intention is not to fit a model to the 3-sigma occultation depth measurement but rather to be informative on the level of precision that needs to be reached to draw conclusions from thermal occultations, and how our Spitzer occultation measurements compare to that. We observe that, for all atmospheric scenarios explored in Lincowski et al. (2018) for TRAPPIST-1b and c, the expected occultation depths are significantly smaller than the $3\sigma$ precision that can be reached with existing Spitzer IRAC channel 2 measurements.

From Table 4.9, the $3\sigma$ upper limit brightness temperatures derived from observations are $\sim$ 750 K and $\sim$ 830 K for TRAPPIST-1b and c, respectively. By comparison, the equilibrium temperatures of TRAPPIST-1b and c are $\sim$ 400 and $\sim$340K, respectively, assuming a null albedo. If we make the additional assumptions that the planets are (i) in synchronous rotation – which is one of their most likely spin state (Makarov et al. 2018; Turbet et al. 2018) – and (ii) that they are devoid of atmosphere, then we calculate that equilibrium temperatures on the dayside of TRAPPIST-1b and c are $\sim$ 510 and $\sim$430K, respectively. In a thick atmosphere,

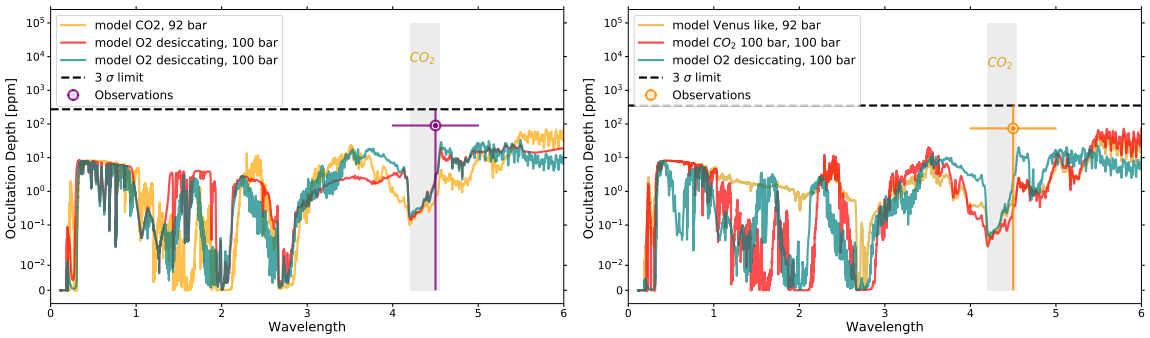


**Fig. 4.15** *Left:* occultation emission spectrum models of TRAPPIST-1b for different assumptions on its atmospheric composition, as simulated by Lincowski et al. (2018), over-plotted with our empirical value, derived from the global analysis of 28 occultations observed with Spitzer IRAC/channel 2 (centred in 4.5 $\mu$m), the error bar shown corresponds to the 3$\sigma$ confidence interval of the measurement. The y-axis has a logarithmic scale. The shade grey band stands for the zone where a spectral absorption from $CO_2$ molecule - if present in the atmosphere - is expected. *Right:* Similar but for TRAPPIST-1c.

the energy coming from the absorption of stellar radiation by the planet on a $\pi R_p^2$ area is efficiently redistributed over the surface of the planet of $4\pi R_p^2$ area, leading to a dilution factor of 4. On an airless, synchronously rotating planet, the dilution factor is 1.5 due to the absence of heat redistribution combined with geometric factors. Koll (2019) provides an analytic framework to estimate this factor.

As a result, our 3$\sigma$ upper limits on the of occultation depths of both planets are not small enough to rule out the presence or absence of an atmosphere, and cannot be used to infer the spin states of the planets. They can be used in principle to set an upper limit on the tidal heat flux of the planet, but tidal calculations have shown it should be on the order of 0.1-40 W m$^{-2}$ (Dobos et al. 2019; Papaloizou et al. 2018; Turbet et al. 2018), depending on the tidal dissipation factor assumed and eccentricity assumed and/or calculated. These tidal heat fluxes are more than two orders of magnitude lower than the irradiation received on TRAPPIST-1b and should thus not contribute in any significant way to the thermal infrared flux emitted by the planet.

From the results presented in Table 4.9, we can also speculate what kinds of atmosphere would theoretically induce brightness temperatures higher than our measured upper limit in order to eliminate those scenarios for planet b and c. To maximize thermal emission between 4 and 5 $\mu$m (i.e., in the Spitzer IRAC channel 2), we can build a virtual planet with a thick atmosphere that absorbs strongly at all wavelengths (specifically at wavelengths superior to 5 $\mu$m), except in the 4-5 $\mu$m spectral range. To be in agreement with our upper estimate measurements of occultation depths (see Table 4.9), we calculate (assuming a dilution factor of 4, because here the planet needs to have a thick atmosphere producing a strong greenhouse

effect and which is likely to redistribute heat efficiently) that ~ 76% and ~ 114% of the total flux absorbed (assuming a null albedo) by TRAPPIST-1b and c, respectively, need to be thermally emitted in the 4-5 $\mu$m spectral range. It seems very unlikely for planet b (and virtually impossible for planet c) to build an atmosphere which would emit nearly 100% of its thermal flux in the 4-5 $\mu$m spectral range. This justifies a posteriori why we did not detect any occultation signal of planet b nor planet c.

The most likely yet plausible atmosphere to maximize thermal flux in the 4-5 $\mu$m spectral range is a thick $H_2O$ dominated atmosphere, due to a gap between two infrared absorption bands of $H_2O$ near 4 $\mu$m (Hamano et al. 2015; Katyal et al. 2019; Miller-Ricci et al. 2009a). This is one of the most likely scenarios for the atmospheres of the innermost planets of the TRAPPIST-1 system if the planets formed water-rich (rich enough that they survived atmospheric erosion) as supported by some planet formation scenarios (Bitsch et al. 2019; Coleman et al. 2019; Izidoro et al. 2021; Raymond et al. 2018; Schoonenberg et al. 2019) and density measurements (Grimm et al. 2018). This stems from the fact that TRAPPIST-1b and c have incident fluxes beyond the runaway greenhouse limit for which water has been shown to be unstable in condensed form and should rather form a thick $H_2O$-dominated atmosphere (Turbet et al. 2018). Using the thermal emission spectra of Hamano et al. (2015) (e.g., their Figures 1a and 3), we calculate that 15-30% of the thermal flux is emitted in the 4-5 $\mu$m spectral range, depending on the assumption made on the total water content of the planet. For TRAPPIST-1b, this corresponds to a brightness temperature of 470-530 K. These brightness temperatures are similar in magnitude to those calculated for a synchronously rotating, airless planet (equilibrium temperature on the dayside of TRAPPIST-1b of ~ 510 K). This demonstrates how decisive JWST occultation observations of the two TRAPPIST-1 inner planets will be to constrain different realistic scenarios about the nature of these planets.

Additional gases are also likely to quantitatively change these numbers (Katyal et al. 2019; Marcq et al. 2017). Specifically, there is a very strong $CO_2$ absorption band around 4.3 $\mu$m which implies that even a small amount of $CO_2$ in the atmospheres of both planets (if any) could mitigate their 4-5 $\mu$m brightness, which would limit the ability of the Spitzer/IRAC channel 2 to detect any signal. Again, the large spectral coverage of the various instruments of JWST (NIRSpec, MIRI) combined with their expected high sensitivity will be of great use to constrain these types of atmospheres.

### Flares

The study of flares is essential to obtain insights into planetary evolution and the potential presence of life on extrasolar planets. On one hand, intense flare activity can induce strong

atmospheric erosion and make the surface of a planet uninhabitable (Lammer et al. 2007), but on the other hand flares could be a key element to the emergence of life (Airapetian et al. 2016; Ranjan et al. 2017). Indeed, a minimum flaring activity seems beneficial to the formation of the ribonucleotides that will allow ribonucleic acid (RNA) synthesis and initiate prebiotic chemistry afterwards, as presented by Rimmer et al. (2018). This latter work outlines that further analyses of the frequencies of energetic flares around stars later than M4 are necessary to assess the habitability of temperate planets around the lowest-mass stars. Rimmer et al. (2018) recommended also to focus on very energetic flares because of higher risks of uncertainties and contradictory findings with low energy flares. In this context, we looked for high energy flares in our extensive Spitzer data set and isolated the 5 largest-amplitude flares, 3 of them having been observed during the continuous period of observations in 2016. This includes flares previously discussed by Davenport (2017) (flare #1, #2, #3) and two new flares (flare # 4 and # 5). We analysed the corresponding light curves with the same MCMC code used to analyse the transits and occultations, as it also includes a flare model represented by a instantaneous flux increase followed by an exponential flux decrease. This flare model is embodied by equation 4.13:

$$F_{\text{flare},t} = \text{Amplitude}_{\text{flare}} \times e^{\left(\frac{-dt}{\tau_{\text{flare}}}\right)} \tag{4.13}$$

where $dt = t - t_0$ ($t_0$ being the time of the instantaneous flux increase), $\tau_{\text{flare}}$ is the flux decrease timescale, and $\text{Amplitude}_{\text{flare}}$ is the flux increase amplitude.

The parameters resulting from our fits are presented in Table 4.10 and the corresponding light curves are displayed in Figure 4.16. We estimated the quality of the fit through the Gelman & Rubin test, and for all light curves the Gelman & Rubin coefficient was below 1.1.

Table 4.10 gives the flare parameters obtained from those fits. From those values, we computed estimates of the bolometric luminosity of each flare. To do so, we followed the procedure described by Shibayama et al. (2013), i.e. we estimated the total energy of each flare from its amplitude and duration combined to the stellar luminosity by assuming that the spectrum of a flare can be described by a black body function with an effective temperature of $T_{flare} \simeq 9000K$. The justification for this assumption came from the observation of Kowalski et al. (2010), and was reinforced in other works like (Kretzschmar 2011).

Assuming that the star is a blackbody radiator, the bolometric flare luminosity can be defined as equation:

$$L_{\text{flare,bol}} = \sigma_{SB} T_{\text{flare}}^4 A_{\text{flare}}, \tag{4.14}$$

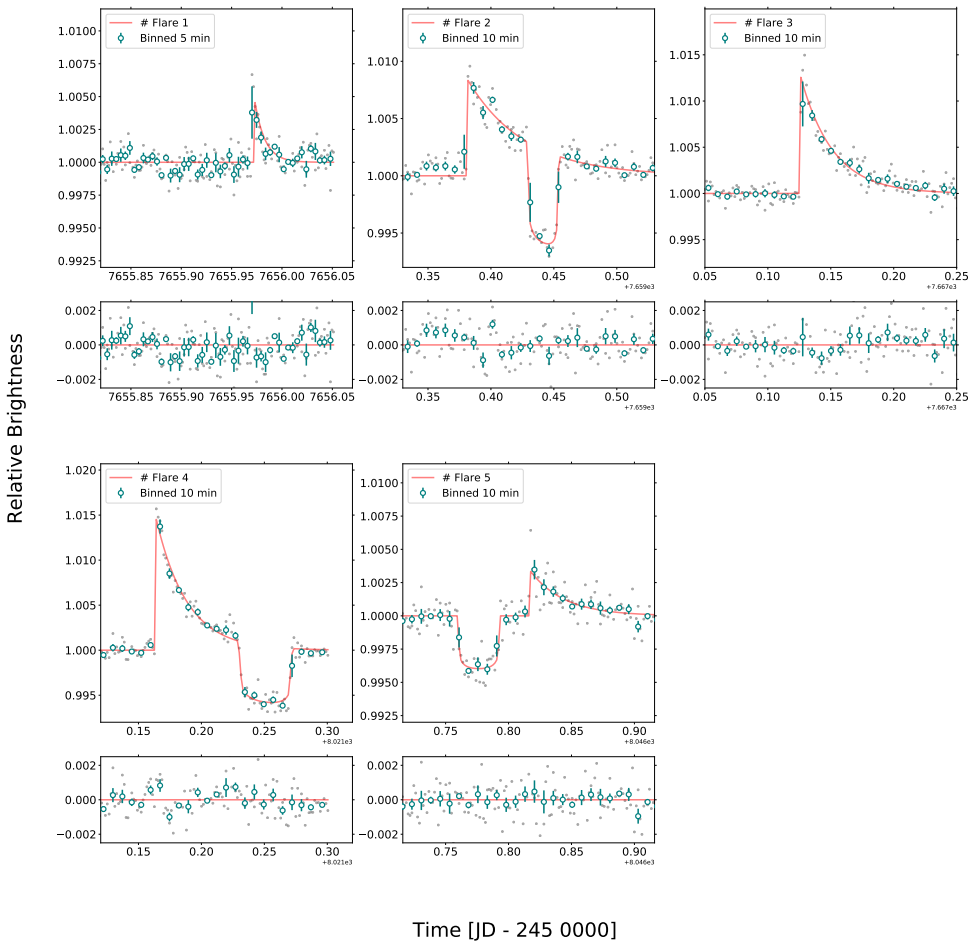


**Fig. 4.16** Light curves of the five highest amplitude flares found in our Spitzer time-series photometry. Some flares happened soon after/before a transit. The light curves are ranked in chronological order and a number is associated with each flare.

where $\sigma_{SB}$ is the Stefan-Boltzmann constant, $T_{\rm flare}$ is the black-body temperature of the flare, and $A_{\rm flare}$ is the area of the flare.

Then, to estimate $A_{\rm flare}$, we used the observed luminosity of the star ($L_\star$), the luminosity of the flare ($L_{\rm flare}$) defined by equation (4.15), where the integration is made for the 3.72 - 5.22 $\mu$m band pass (corresponding to IRAC/channel 2 spectral range in which all flares were observed) :

$$L_{\rm flare,c2}(t) = A_{\rm flare}(t) \int R_\lambda B_\lambda(T_{\rm flare}) d\lambda \tag{4.15}$$

and the flare amplitude of the light curve $\frac{\Delta_{F(t)}}{F(t)}$ defined as equation (4.16) :

$$\frac{\Delta F(t)}{F(t)} = \frac{L_{\text{flare,c2}}(t)}{L_\star}. \tag{4.16}$$

In equation (4.15), $R_\lambda$ stands for the spectral response function of Spitzer/IRAC instrument and $B_\lambda$ is the Planck function. From equations (4.15) and (4.16), we can derive $A_{\text{flare}}$:

$$A_{\text{flare}} = \frac{\Delta F(t)}{F(t)} \pi R_\star^2 \frac{\int R_\lambda B_\lambda(T_{\text{eff}}) d\lambda}{\int R_\lambda B_\lambda(T_{\text{flare}}) d\lambda} \tag{4.17}$$

Finally, the total bolometric energy of the flare ($E_{\text{flare}}$) is defined as the integral of $L_{\text{flare,bol}}$ over the flare duration, equation (4.18) :

$$E_{\text{flare}} = \int L_{\text{flare,bol}}(t) dt \tag{4.18}$$

As underlined by Shibayama et al. (2013), since the star is not a blackbody radiator, such bolometric energy estimates may have errors of a few tens of percent, too small to affect our inferences described below. The results derived from those calculations are shown in Table 4.10.

| **Flare #** | **Timing ± 1$\sigma$ [JD - 2450000]** | | **Amplitude ± 1$\sigma$ [%]** | | **Duration ± 1$\sigma$ (min)** | | **Flare energy ± error (erg)** | |
|---|---|---|---|---|---|---|---|---|
| 1 | 7655.97363 | 0.0038 | 0.635 | 0.39 | 10.92 | 0.53 | 8.41 e+31 | 5.08e+31 |
| 2 | 7659.38103 | 0.00051 | 0.846 | 0.065 | 64.91 | 10.36 | 6.64 e+32 | 4.02e+32 |
| 3 | 7667.12545 | 0.00052 | 1.276 | 0.092 | 38.01 | 4.89 | 5.79 e+32 | 3.50e+32 |
| 4 | 8021.16339 | 0.00052 | 0.148 | 0.093 | 35.71 | 4.77 | 6.41 e+31 | 3.87e+31 |
| 5 | 8046.8164 | 0.0011 | 0.346 | 0.048 | 43.19 | 23.04 | 1.81 e+32 | 1.09e+32 |

**Table 4.10** Output from the individual MCMC analyses of the light curves with the 5 highest energy flares. Timing, amplitude, and duration are measured through a MCMC analysis of the corresponding light curves, while the flare energy is computed by applying equation (4.18) and its error is estimated to be ± 60% of the flare energy following the recommendations of Shibayama et al. (2013)

The values that we obtained are consistent with flare energies amplitudes given by Paudel et al. (2018) and Vida et al. (2017) (energy range from 0.65 to 710 $\times 10^{30}$ erg). In Figure 4.17, we compare the flare frequency distribution of TRAPPIST-1 from our measurements to the frequencies reported in these studies. This figure is a log-log plot of cumulative frequency of flare energies; for instance, the cumulative frequency of flares with an energy E is the number of flares with energies superior or equal to E per day.

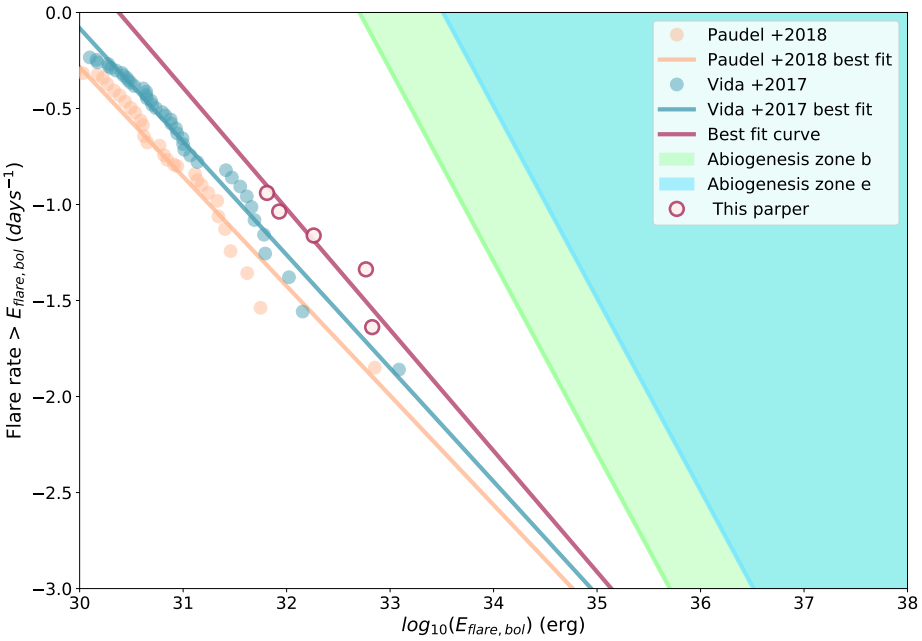


**Fig. 4.17** Flare frequency distributions (FFD) in log-log scale, x-axis is the flare energy and y-axis is the cumulative rate of flares per day, that is to say how many flares of a corresponding energy E -or higher- happen per day. Solid lines represent the linear regressions defined by equation (4.19). The red solid line stands for the result from this work while the orange line stands for results from Paudel et al. (2018) and the green one from Vida et al. (2017). The green zone denotes the abiogenesis zone for planet TRAPPIST-1b, a zone where the inequality (4.20) is satisfied, the green bold line on the edge of the zone represent the minimum flare rate and energy required to trigger prebiotic chemistry on this planet (Rimmer et al. 2018), which corresponds mathematically to equation (4.20). The blue zone is similar to the green zone but for planet TRAPPIST-1e.

We noticed that the flare energy distribution of TRAPPIST-1 follows a power law as equation (4.19):

$$log(\nu) = \beta log(E) + \alpha, \tag{4.19}$$

where $\nu$ is the frequency, and $\beta = -0.6303 \pm 0.1358$, fitted from our measurements. This value is consistent with the $\beta = -0.61 \pm 0.02$ derived by Paudel et al. (2018).

As TRAPPIST-1 is an ultracool dwarf star and its habitable zone planets are particularly close to their host, the question of whether those planets could harbour life in such radiation environments naturally arises (Glazier et al. 2020; O'Malley-James et al. 2017). Within this context, we discuss the meaning of our results in terms of habitability; notably on how flares can promote the emergence of life. To do so, we based our discussion on the work of Grimm et al. (2018), where the authors explain how the synthesis of pyrimidine ribonucleotides - part of the building blocks of RNA - from hydrogen cyanide and bisulfite in liquid water is likely driven by photochemical processes in the presence of ultraviolet (UV) light. From

experiments, the authors defined the "abiogenesis zones" around stars of different stellar types depending on whether their UV fluxes provide sufficient energy to build a sufficiently large prebiotic inventory (Rimmer et al. 2018). Using the flare estimates of Rimmer et al. (2018), modified to account for the semi-major axes of the TRAPPIST-1 planets (Günther et al. 2020b, their Eq. (10)), we derived the flare frequencies, $\nu$, for which UV flux received by each TRAPPIST-1 planets would be sufficient for the planet to lie in the abiogenesis zone. Those frequencies are defined by the equation:

$$\nu > 25.5\text{day}^{-1}\Big(\frac{10^{34}\text{erg}}{E_\text{U}}\Big)\Big(\frac{a}{1\text{AU}}\Big)^2 \tag{4.20}$$

where $\nu$ is a function of the flare's U-band energy $E_\text{U}$, the stellar radius, $R_\star$, and the stellar temperature, $T_\star$. To solve inequation (4.20), we need the U-band energy $E_\text{U}$ and the semi-major axis $a$. We took the semi-major axis from the refined parameters value (see Table 4.3) and we obtained the U-band energy from the bolometric energy through the integration of the flux density in the U-band spectral response function, like it was done by Günther et al. (2020b) (see equation 4.21). We assumed that the flux density of the flare could be expressed as a 9000 K blackbody. We estimate that 6.67% of the flare's bolometric energy belongs to the U-band, $E_\text{U} \simeq 6.7\% E_\text{flare}$.

$$E_\text{flare,U-band} = \int_t A_\text{flare} \int_{Uband} R_\lambda B_\lambda(T_\text{flare}) d\lambda dt \tag{4.21}$$

We over-plot the abiogenesis zone in terms of flare frequency and energy on Figure 4.17 for planet TRAPPIST-1e; in other words, a zone where the inequality 4.20 is satisfied. We chose planets b and e because e is the planet that is the most likely to harbour liquid water on its surface (Fauchez et al. 2020b; Turbet et al. 2018; Wolf 2017) and b is the closest to the host star. We note that a planet could lie in the abiogenesis zone while not being in the classical habitable zone (Rimmer et al. 2018), yet, by choosing to study planet e, we maximise the similarities with Earth.

In Figure 4.17, if TRAPPIST-1's power-law flare rates would have crossed the power law of inequality 4.20 - represented by the blue zone on the Figure - it would have potentially meant that TRAPPIST-1e was located within the abiogenesis zone of its host star. However, we see that TRAPPIST-1's power-law flare rates do not cross the blue zone. This means that TRAPPIST-1e currently does not receive enough UV flux to build up the prebiotic inventory photochemically. We note that the same interpretation can be made for planet b (the abiogenesis zone of b being the green patch on Figure 4.17).

Nevertheless, TRAPPIST-1 is an old M8V type star (7.6 ± 2.2 Myr old according to Burgasser et al. (2017)) and empirical observations showed a decrease of the activity of ultracool dwarfs with age. Indeed, Paudel et al. (2019) compared the flare frequency distribution of 2M0837+2050 - a young ≃ 700 Myr old M8 type star - with TRAPPIST-1 - an old 7.6 Gyr old M8 type star - and found that the highest flare energy on 2M0837+2050 are ≃3 times larger than the ones on TRAPPIST-1, and that a flare of energy E=$10^{34}$erg has 10 times more chances to happen on 2M0837+2050 than on TRAPPIST-1. Considering that those two stars have a similar spectral type (M8 type) but different ages this argument could be used to hypothesise that TRAPPIST-1 used to show more energetic and more frequent flares in its youth. Both Ranjan et al. (2017) and Rimmer et al. (2018) discuss this scenario and argue that flares may be the only means to generate the building blocks of life via the pathways of Xu et al. (2018) and Patel et al. (2015). Furthermore, contrary to the classical habitable zone, it is not required that a planet remains in the abiogenesis zone of its star to maintain the presence of life. This would imply that planet e might have received enough UV flux in its history to drive the emergence of life's building blocks.

Unfortunately, those interpretations are drawn from empirical studies and are limited by the number of flaring M8 type stars studied so far. Specifically, it remains to be seen whether there is a "golden mean" for flare rates, at which there are enough stellar energetic particles (SEP) to form feed-stock molecules needed for prebiotic chemistry, and enough NUV light to drive that prebiotic chemistry, but not so much XUV light and SEP's that the atmosphere is stripped (Dong et al. 2018; Garraffo et al. 2017), continually transformed (Tilley et al. 2019; Vida et al. 2017), or the planet desiccated (Luger et al. 2015). This 'golden mean' for flare rates only applies for host planets outside the abiogenesis zone as delineated by quiescent stellar NUV flux. For those planets outside the abiogenesis zone, stellar activity would be the only means to generate sufficient NUV for this prebiotic chemistry. The Earth has resided well within the abiogenesis zone throughout its history.

It should be emphasized that the abiogenesis zones delineated by Günther et al. (2019) and Rimmer et al. (2018) and in this work are scenario-dependent. It may be that life's building blocks can arise another way, either within hydrothermal vents (Rimmer et al. 2019), in surface scenarios without ultraviolet light (Rimmer et al. 2019), or that they may be delivered exogenously (Rimmer et al. 2019). In addition, within the scenario explored by Rimmer et al. (2018), the threshold UV flux provides a necessary but not sufficient condition for the origins of life on a rocky planet. Hydrogen cyanide, bisulfite and phosphate must be present at high concentrations within liquid water, along with other chemical constituents (Patel et al. 2015; Xu et al. 2018). Given these added conditions, it is likely that each major category of life's building blocks: amino acids, phospholipids, nucleotides, would be present in high

concentrations, along with a mechanism for joining them together to form macromolecules: proteins, phospholipid membranes, RNA and DNA (Liu et al. 2019). The problem of how life arises from this system, or any complex molecular system, remains unsolved.

### Search for additional transiting objects

One of the primary goals of the *Red Worlds* program was to search for additional transiting planets. In this context, we ran a Transit Least Square analysis (TLS) with period spanning from 0.2 to 200 days on the residuals of the full photometric dataset corrected from all known transits. The TLS algorithm, presented by Hippke et al. (2019a), aims to detect transit-like features from time-series photometry while taking the stellar limb-darkening, the planetary ingress and egress into account. The TLS algorithm is particularly relevant here as it is optimized for small planets and was found more reliable than the Box least Square (BLS) algorithm in finding any kind of planets by Hippke et al. (2019a). We combined this with a visual inspection of all the light curves. Results are shown on Figure 4.18 were obtained using the Transit Least Squared (TLS)[4] python package by Hippke et al. (2019a).

The periodogram peaks at 15.7397 days period, yet this result must be interpreted with care as the maximum value of the Signal Detection Efficiency (SDE) for this period is only 6.767 whereas (Pope et al. 2016) recommend to consider planetary candidate only for SDE > 8. This SDE is defined as SDE= $max(power)/std_{power}$. Besides, the depth of the corresponding phase folded transit signal is relatively small (1487 ppm) and of the same order of magnitude as the dispersion of out-of-transit measurements (standard deviation $\simeq$ 1987 ppm) (Figure 4.18 bottom panel). In a nutshell, those results favours a non-physical explanation (most probably systematics) for this periodic signal spotted at 15.7397 days by the TLS algorithm. We did not consider any other periods in the periodogram as their SDE were always inferior to 8 (Pope et al. 2016).

However, one thing we can do is to compute the photometric precision that can be reached as a function of period, then inject planets with signal-to-noise ratio (SNR) of 8 at each period and see if we recover them with TLS. Such results can help us define which kind of hypothetical eighth planet can be discarded from Spitzer's photometry. Figure 4.19 shows the precision that we get from the photometry for a set of periods going from 0.2 to 200 days. To construct this figure, we have folded the data on each period for a set of transit timings such that the full period is covered, binned them, and computed the standard deviation of this binned light curve. This standard deviation is what we refer to as the photometric precision reached for a given period. The minimum planet radius (hereafter $R_{p,min}$) was then derived

[4] https://github.com/hippke/tls

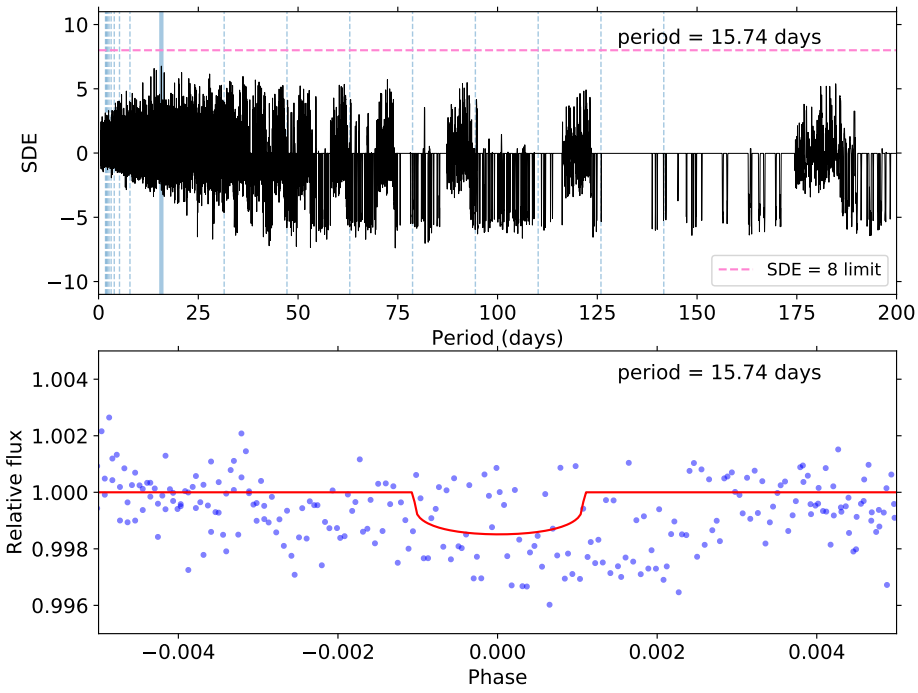


**Fig. 4.18** *Top panel:* periodogram computed with the help of the Transit Least Squared (TLS) python package (Hippke et al. 2019a) applied to the time series made by the residuals of the entire Spitzer photometric (cleaned from all known transits and flares). The x-axis is the period while the y-axis is the Signal Detection Efficiency (SDE) associated with each period. A steel-blue line indicates the harmonic for which the SDE reached is the largest, here this output period is 15.74 days. *Bottom panel:* phase-folded transit signal for the most probable period output by the periodogram (blue dots) + transit model computed from the parameters output by the TLS algorithm (red solid line).

from a depth equivalent to a SNR of 8, where the SNR is expressed as $SNR = \frac{dF}{\sigma} * \sqrt{N}$, with $\sigma$ the precision at a given period and N the number of points in transit, as defined by Pont et al. (2006).

Assuming an hypothetical planets with circular orbit and null impact parameter, we observe that our precision on the dataset is good enough to detect any Mars-sized planet with period inferior to $\simeq$ 45 days (with an SNR of 8), and good enough to detect any Earth-sized planet with a period between 0.2 and 200 days (with an SNR of 8). We observe that above P $\simeq$ 50 days the precision seems to stagnate. This is due to the fact that gaps exist in the dataset such that at some point only one event is used to construct the period-folded light curve for most of the periods. Yet, as the duration of the transit increases with the period and the precision stays more or less constant for P $\geq$ 50, the minimum planetary radius that we can detect with SNR=8 tends to decrease for P $\geq$ 50. To second those results, we performed some transits injection/recovery tests, the retrieval phase being essentially the capacity to find back the transits injected with an SDE > 8 when performing a TLS analysis on the residual + injected

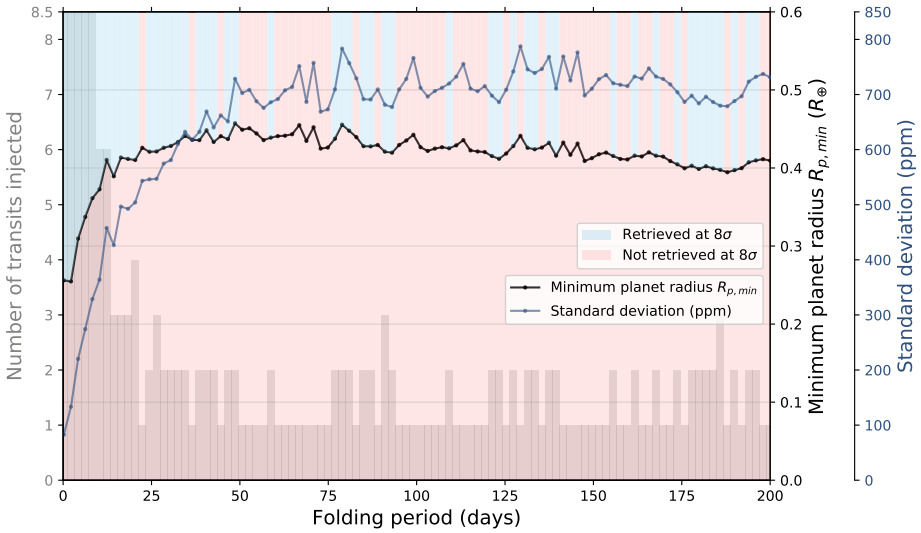


**Fig. 4.19** Evolution of the photometric precision and its corresponding planet radius for SNR = 8 as a function of the folding period. The number of injected transits for each period is given by the plot bar in grey. The blue patches show the periods for which the "injected planet" is recovered where as the red patches show the periods for which it is not.

transits. The retrieval is obviously greatly dependent on the transit timing used as reference, as a scenario where no transits fall in the observations is likely. Therefore, we imposed this reference timing to be within Spitzer's time series such that for all periods there is at least one transit in the data. The parameters of the injected transit are chosen as follow: - its period P is the main variable, - its depth $df_p$ is such that $SNR = 8$, with the SNR as defined above - its width $T_{14,p}$ is calculated analytically from $df_p$ and P assuming a circular orbit and a null impact parameter.

As a result, TLS does recover all the injected planets with an SDE > 8 as long as at least 2 transits fall in the data, see figure 4.19. Hence, if present, we should have detected any Mars-sized planet with period inferior to ≃ 50 days and all Earth sized planet with P < 200 days providing at least 2 of its transits happened during the observations.

To complement this analysis, we conducted a careful visual inspection of the light curves to catch any single occurrence event that could have been missed by the TLS. We found four orphan transit-like structures that did not correspond to any known planetary transit and that we could not model with any function of external parameters (e.g., x- and y-position of the star on the IRAC chip, fwhm variation and ramp effect). Therefore, we treated those events as possible transits of unknown transiting objects and tried to fit them with our MCMC code (see Chapter 3). We choose to freely vary the period and the impact parameter while assuming priors on the transit depth, the eclipse duration, and the transit timing with large

error bars that we estimated visually. For the stellar parameters, we used the same priors as for our individual transit analysis (see Section 4.1.2). The results from those analyses can be found in Table 4.11, and the visualisation of the fits is shown on Figure 4.20.

| **Orphan #** | **Timing ± 1$\sigma$ [JD - 2450000]** | | **Depth ± 1$\sigma$ [%]** | | **Duration ± 1$\sigma$ (days)** | | **b ± 1$\sigma$** | | **P ± 1$\sigma$ (days)** | |
|---|---|---|---|---|---|---|---|---|---|---|
| #1 | 7658.47094 | 0.00110 | 0.463 | 0.091 | 0.0287 | 0.0039 | 0.920 | 0.058 | 17 | 10 |
| #2 | 7666.28113 | 0.00058 | 0.151 | 0.068 | 0.048 | 0.012 | 0.83 | 0.36 | 59 | 42 |
| #3 | 7671.45227 | 0.00053 | 0.249 | 0.146 | 0.0185 | 0.0017 | 0.65 | 0.42 | 1 | 2 |
| #4 | 8045.11500 | 0.00230 | 0.198 | 0.091 | 0.0331 | 0.006 | 0.903 | 0.062 | 34 | 28 |

**Table 4.11** Outputs from the individual MCMC analysis of four transit-like structures found in Spitzer's photometric observations of TRAPPIST-1. Convergence of our analyses was assessed with the Gelman & Rubin test (Gelman et al. 1992) (lower that 1.1 for all jump parameters).

From Table 4.11, we note that if those events were associated with one or more transiting objects this object would be highly grazing as the impact parameters output from our fit are all larger than 0.6. Yet, we observe that the differences in duration and amplitude between events # 1, 2, 3 and # 4 tend to discard a common origin scenario. Event # 3 was caught in a particularly noisy AOR so even if the light curve structure can not be removed with any baseline detrending, we are doubtful this is a physical transit. As a general comment, event # 1, 2 and 3 were caught during the second campaigns which, as mentioned before, had some known drifting issues due to the use of inaccurate pointing coordinates, weakening our confidence in the detrending performed. Besides, none of the timings of those orphan transits are included in the transits timings associated to the TLS most favoured period of 15.74 days. Furthermore, at the time of event # 1, 2 and 3 we found out that some K2 observations were carried out simultaneously but the data do not confirm any of the structures we identified, which strongly weakens any astrophysical origin scenario. Finally, event # 4 is rather shallow $\simeq$ 0.2 % and of similar order than the out-of-transit dispersion ($\simeq$ 0.12%), the event being significant at the 1.6$\sigma$ level only. In a nut shell, none of these 4 orphan structures can be considered as a strong transit candidate.

In the first part of this chapter, I have presented the extensive analyses of Spitzer's photometric time series that I have been carrying out to derive transit and stellar parameters, retrieve transit timings, construct transmission spectra, and extract all information from out of transit structures (occultations, flares and orphan structures). In the second part, I will focus on the exploitation of the transit timings and describe how the results of their dynamical analysis

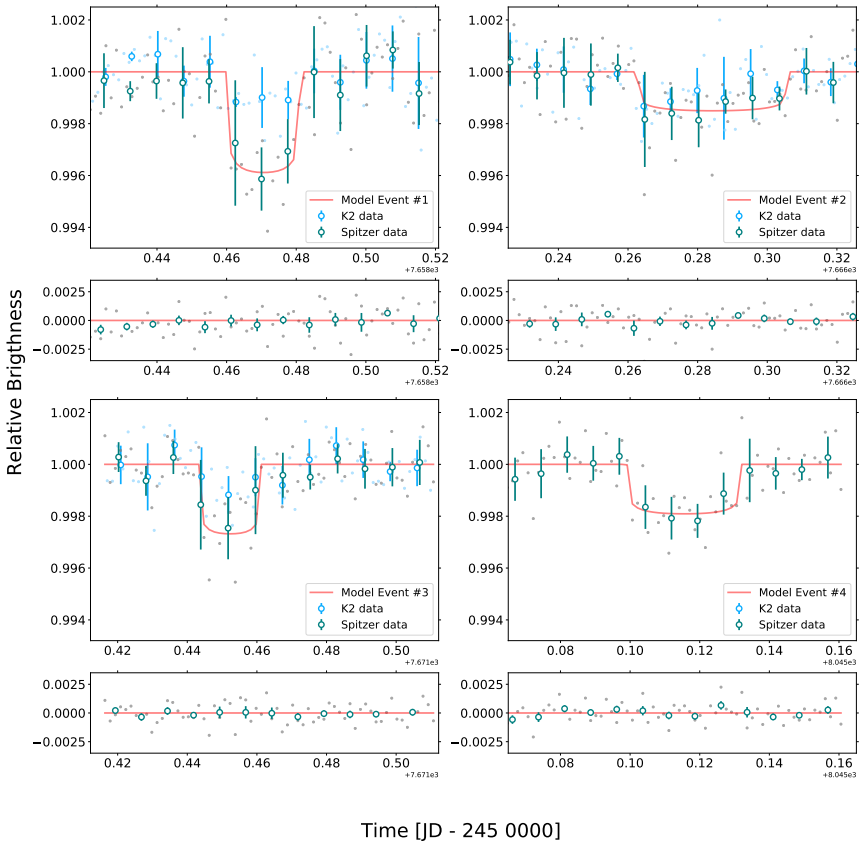


**Fig. 4.20** Visualization of the fits of the light curve of the four transit-like structures found in Spitzer photometry. Grey dots show the unbinned measurements for Spitzer; green open circles depict 10 min-binned measurements for visual clarity. The best-fit transit models are shown as red solid lines. Events are ranked and assigned a number corresponding to their chronological order: Top-left is event #1, top-right is event #2, bottom-left is event #3 and bottom-right is event #4. When available K2 simultaneous measurements are over-plotted in blue dots with 10 min-binned measurements as blue open circles.

combined to a photodynamical analysis of the Spitzer photometry enabled us to improve further the characterization of the system.

## 4.2 Refining of the physical parameters of the TRAPPIST-1 planets

In a compact system like TRAPPIST-1, the gravitational mutual interactions of the planets can constantly alter their orbits by frequent pulls and tugs. This implies that the time between transits is not exactly the same over the course of observations. Indeed, the transits of a distant star by a single planet on a Keplerian orbit occur at time intervals exactly equal to the orbital period (Agol et al. 2005), if one neglects the radial motion of the star[5]. However, if an additional planet orbits the same star, the orbits are not Keplerian anymore and the transits are no longer exactly periodic. In this situation, for a given planet, we observe the planet's transit earlier or later than predicted, depending whether it is accelerated by neighbouring planets or decelerated. Those changes in the timing of the transits of a given planet are called transit timing variations or in short TTVs. Those TTVs depend sensitively on the masses and orbital configurations of the planets in the system such that the monitoring and analyses of TTVs can provide a powerful method to solve the inverse problem of determining planets' masses and orbits from their transits. TTVs are further amplified when planets are in mean resonance motion because it dramatically increases the exchange of energy and angular momentum at each planet conjunction (when the planets are the closest to each other) (Grimm et al. 2018).

In that regard, the resonant property of the TRAPPIST-1 system is an essential asset for its characterisation, that notably led to the discovery of planet h. As a matter of fact, this complex but predictable pattern in the frequency at which each of the six innermost planets orbit their star was unravelled by Spitzer data. The relationships between the planet's periods suggested that by studying the orbital velocities of its neighbouring planets, the exact orbital velocity of planet h could be predicted, and hence its orbital period. Six possible resonant periods for planet h that would not disrupt the stability of the system were calculated, but only one was not ruled out by existing observations. Indeed, there was a lack of obvious additional transits at the expected times for five of these periods, the only remaining period that could not be ruled out was 18.766 days. K2 observations confirmed it. This new discovery of a planet from the study of the motion of other planets in the system is a great example of what happens when theory and observation matches perfectly, and on several aspects it recalls the story of the discovery of Neptune (Laskar 2017).

[5]The limited speed of light results in measured transit periods slightly smaller or larger than the true orbital period depending if the system is approaching us or receding from us, respectively. This is the same process that explains the Doppler effect.

More than just in resonance, the seven TRAPPIST-1 planets remarkably form a series of generalised three-body Laplace relations[6] between adjacent triplets of planets (Luger et al. 2017a). Such configuration cause adjacent pairs of planets to reside near mean-motion resonances, such that $jP_i^{-1} \simeq (j+k)P_{i+1}^{-1}$ for integers $j$ and $k$ for the $i$th and $i+1$th planets. This proximity causes a resonant timescale for $k = 1$ given by:

$$P_{TTV} = \frac{1}{jP_i^{-1} \simeq (j+1)P_{i+1}^{-1}} \tag{4.22}$$

$P_{TTV}$ is called the super period (Lithwick et al. 2012), which is the characteristic timescale of the TTVs of the outer five planets. The period of the resonant terms for each of these pairs of planets is $P_{TTV} = 491 \pm 5$ days (ranging from 485 to 500 days for each pair). Consequently, the transit times for each planet need to be sampled on at least this timescale, preferable covering two cycles ($t_{min} = 2 * P_{TTV}$) so that the amplitude and phase of the cycles may be distinguished from the planets' orbital periods. The first TTVs study on TRAPPIST-1 was performed by Grimm et al. (2018) and although it enabled the first density determinations of temperate, Earth-sized planets exterior to the Solar System, the timescale covered was inferior to $t_{min}$. In that context, it was necessary to revisit the TTV analysis with a more complete and extended dataset, including notably the extensive dataset of the completed Spitzer program. This endeavour was performed in a recent study led by my colleague Prof. Eric Agol, and to which I brought a significant contribution. In the following section, I briefly described the main results from this work. For the complete study, I refer the reader to the original publication by Agol et al. (2020b).

### 4.2.1 Transit timings and photodynamical analyses

In this study, I was in charge of collecting all transit timings of TRAPPIST-1 planets we had accumulated over the past 5 years. A large proportion ($\simeq 70\%$) of those transits came from my previous works (Ducrot et al. 2018; Ducrot et al. 2020), the rest came from other studies such as Burdanov et al. (2019), De Wit et al. (2016), 2018, Gillon et al. (2017b), Grimm et al. (2018), Luger et al. (2017a), and Wakeford et al. (2018). All those timings were used as inputs for the transit-timing analysis that was carried out. I also provided all detrended light curve from Spitzer photometry (obtained from Section 4.1.2), on which the photodynamical model was performed. However, I was not involved in the data analysis part, which is why in

[6] Laplace resonance is a particularly interesting case of three-body resonance which satisfies: $pP_1^{-1} - (p+q)P_2^{-1} + qP_3^{-1} \simeq 0$, where subscripts 1, 2, 3 refer to the planets. The most commonly known example of Laplace resonance being the Galilean moons Io, Europa and Ganymede (with p=2 and q=1).

the following I will give only a few details on this aspect to provide the reader with some context, and then jump to the discussion of the results.

### Dataset

The transit timing analysis that I describe in the next section used the timings derived from section 4.1.2 complemented with timings from K2, HST and some ground based observations, details can be found on Table 4.12.

| Planet | HCT | SSO/TN/TS | LT | WHT | VLT/AAT/UKIRT | HST | Spitzer | K2 | Duplicates | Total |
|---|---|---|---|---|---|---|---|---|---|---|
| b | 1 | 45 | 7 | 1 | 10 | 1 | 64 | 48 | 17 | 160 |
| c | 0 | 28 | 8 | 0 | 7 | 1 | 47 | 30 | 14 | 107 |
| d | 0 | 11 | 1 | 1 | 5 | 2 | 23 | 17 | 7 | 53 |
| e | 0 | 18 | 4 | 0 | 3 | 2 | 1 | 11 | 7 | 49 |
| f | 0 | 9 | 2 | 0 | 4 | 2 | 16 | 7 | 6 | 34 |
| g | 0 | 11 | 0 | 0 | 3 | 2 | 13 | 5 | 4 | 30 |
| h | 0 | 3 | 2 | 0 | 0 | 0 | 7 | 4 | 2 | 14 |
| Total | 1 | 125 | 24 | 2 | 32 | 10 | 188 | 122 | 57 | 447 |

**Table 4.12** Number of transits from ground-based and space-based observations. Duplicates indicates the excess planet transits observed simultaneously with two or three distinct observatories. Table adapted from Agol et al. (2020b).

The K2 mission (Howell et al. 2014) observed the TRAPPIST-1 system over campaigns 12 and 19 (Luger et al. 2016) in both long- and short-cadence imaging modes. We only used the short-cadence data from campaign 12 for this analysis, with $\simeq$ 1 minute sampling. Concerning HST observations, transit times were taken from De Wit et al. (2016) and 2018 and Wakeford et al. (2018). From the ground, 125 transits were observed by the SPECULOOS-South Observatory, TRAPPIST-South telescope, and TRAPPIST-North telescope. These observations were carried out in an I+z filter with exposure times 23s, 50s and 50s, respectively; characteristics of this filter are described in section 2.1.1. Observations were also performed with the Liverpool Telescope (LT; (Steele et al. 2004)) and the William-Herschel Telescope (WHT), both installed at the Roque de los Muchachos Observatory, La Palma. Only one transit of planet b and one of d were targeted with the WHT whereas 15 transits of several planets were targeted with LT. For LT observations, the IO:O optical wide field camera was used in Sloan z' band with 20s exposure time. One transit of b was observed with the Himalayan Chandra Telescope (HCT). Finally, a total of 26 transits were observed in the near-IR (1.2 - 2.1 m) with the WFCAM near-IR imager of the United Kingdom Infra-Red Telescope (UKIRT; (Casali et al. 2007)), the IRIS2IR-imager installed on the the Anglo-Australian Telescope (AAT; (Wittenmyer et al. 2017)), and the HAWK-I cryogenic wide-field imager installed on Unit Telescope 4 (Yepun) of the ESO Very Large Telescope (VLT; (Siebenmorgen et al.

2011)). In total, 504 transit observations were collected with 57 duplicate (or triplicate) transits which were observed by a second (or third) observatory simultaneously, for a total of 447 unique planetary transit times. Additional information may be found in Gillon et al. (2016) for WHT and TRAPPIST, in Ducrot et al. (2018) for SSO and LT, and in Gillon et al. (2017b) and Burdanov et al. (2019) for AAT, UKIRT and VLT.

### Transit timing analysis

As I mentioned above, I was not involved in the data analysis part of this work. However, I believe some outcomes of these analyses deserve to be evoked in this thesis. Thus, in the following sections, I succinctly describe the analyse conducted by my collaborators, and then discuss some interesting results that aroused from them.

To perform the transit timing analysis, a N-body integrator was used to model the dynamics of the system. More precisely, it was a novel general-purpose symplectic integrator for arbitrary orbital architectures called `NbodyGradient`[7], which is based on the algorithm originally described in Hernandez et al. (2015). This integrator is presented in detail in a recently published paper by Agol et al. (2021).

The position of each planet relative to the star was computed such that the transit times for a given planet were reported when the dot product of the relative velocity of the planet and star with their relative position equals zero. The resulting modelled transit times $t_{i,j}$ ($i$ being the planet and $j$ the number of the transit) were then compared to the observed transit times $t_{obs,i,j}$. The total log likelihood function was assumed to be a sum of the log likelihood function for each data and planet (neglecting possible correlation between timing errors). The likelihood was then multiplied with the prior function to obtain the posterior probability distribution. A uniform prior was assumed for the mass and orbital element of each planet, with smooth bounds on each, with the exception of the initial eccentricity vectors.

To sample the posterior probability, an Hamiltonian Monte Carlo (HMC) sampler (Betancourt 2018a; Duane et al. 1987; Monnahan et al. 2017; Neal 2011) was used. 112 HMC chains of 2000 steps were ran, and took nine days and four hours to complete! As shown on Figure 4.21, the resulting model agrees very well against the data.

On this Figure, the super period $P_{TTV}$ of $\simeq$ 492 days is visible for the five outer planets. We also see some smaller amplitude high frequency oscillations, referred to as “chopping" TTV, that are visible in the fit and the data for all planets except planet d. Such variations are associated to the synodic periods of pairs of adjacent planets (which is the time span between the points in time of successive identical positions of a celestial body with respect to the

[7] available on: https://github.com/ericagol/NbodyGradient.jl

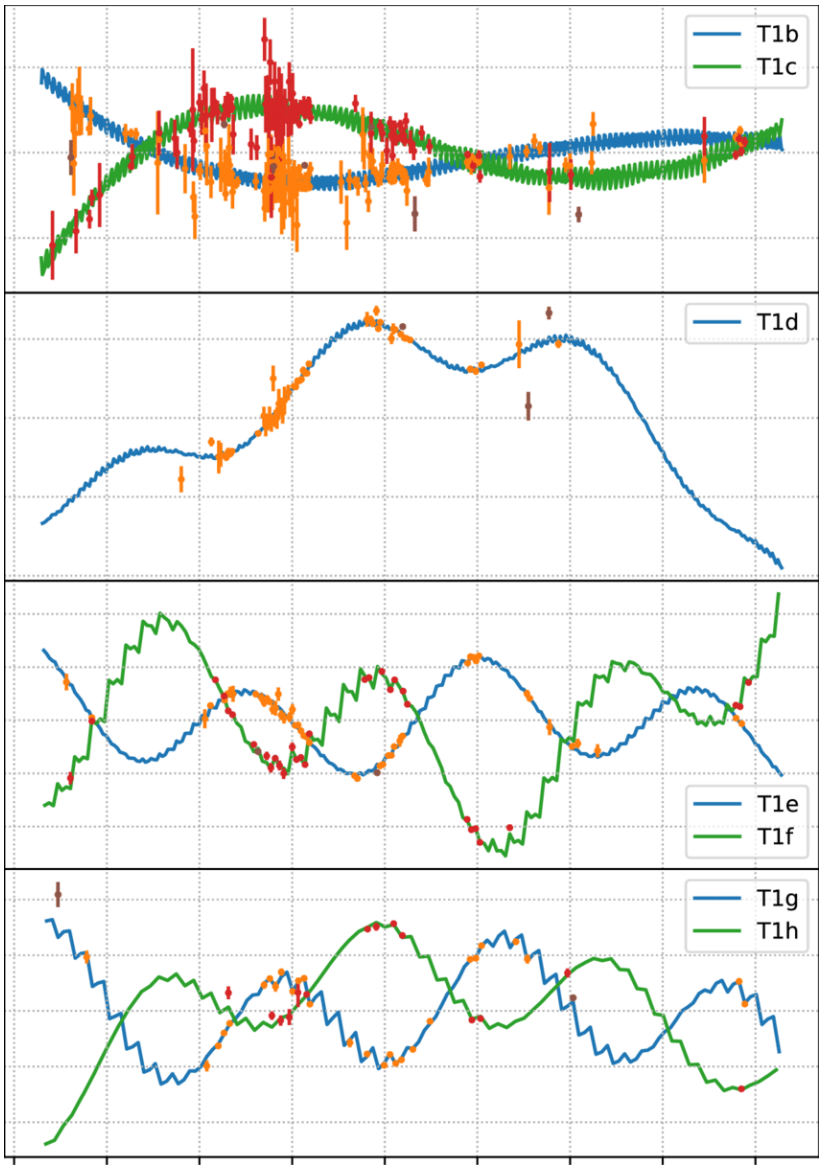


**Fig. 4.21** Transit time variation measurements (orange/red error bars) and best-fit transit-time model (blue/green lines) for a subset of our Spitzer/K2/ground-based data set. The TTVs are the transit times for each planet with a best-fit linear ephemeris removed. Brown error bars indicate $> 3\sigma$ outliers. Figure from Agol et al. (2020b).

other). Chopping TTVs turn out to be extremely useful to break existing degeneracies, as their encode the mass-ratios of the companion planets to the star without the influence of the eccentricities, which results in better constrained planet-star mass ratios. The results of the posterior distribution of this transit timing analysis are summarised in Table 4.13. We note that compared with the mass estimates from Grimm et al. (2018), the masses of each

| Planet | $\mu \left[\frac{M_p}{0.09 M_\odot}\right]$ | $\frac{\sigma_\mu}{\mu}$ | P [day] | $t_0$ [$BJD_{TDB}$ - 2450000] | $e\cos\omega$ | $e\sin\omega$ |
|---|---|---|---|---|---|---|
| b | 1.3771 ±0.0593 | 4.3 | 1.510826 ±0.000006 | 7257.55044 ±0.00015 | -0.00215 ±0.00332 | 0.00217 ±0.00244 |
| c | 1.3105 ±0.0453 | 3.5 | 2.421937 ±0.000018 | 7258.58728 ±0.00027 | 0.00055 ±0.00232 | 0.00001 ±0.00171 |
| d | 0.3885 ±0.0074 | 1.9 | 4.049219 ±0.000026 | 7257.06768 ±0 : 00067 | -0.00496 ±0.00186 | 0.00267 ±0.00112 |
| e | 0.6932 ±0.0128 | 1.8 | 6.101013 ±0.000035 | 7257.82771 ±0.00041 | 0.00433 ±0.00149 | -0.00461 ±0.00087 |
| f | 1.0411 ±0.0155 | 1.5 | 9.207540 ±0.000032 | 7257.07426 ±0.00085 | -0.00840 ±0.00130 | -0.00051 ±0.00087 |
| g | 1.3238 ±0.0171 | 1.3 | 12.352446 ±0.000054 | 7257.71462 ±0.00103 | 0.00380 ±0.00112 | 0.00128 ±0.00070 |
| h | 0.3261 ±0.0186 | 5.7 | 18.772866 ±0.000214 | 7249.60676 ±0 : 00272 | -0.00365 ±0.00077 | -0.00002 ±0.00044 |

**Table 4.13** Parameters of the TRAPPIST-1 system from transit-timing analysis and their $1\sigma$ uncertainties. Note that the mass ratios, $\mu = \frac{M_p}{M_\star}$, of the planets are computed relative to the star, which is assumed to have a mass of $0.09 M_\odot$. The parameters $P$, $t_0$, $e\cos\omega$, and $e\sin\omega$ describe the osculating Jacobi elements at the start of the simulation, on date $BJD_{TDB} - 2450000 = 7257.93115525$ days. Table adapted from Agol et al. (2020b).

planet have increased with the exception of planet e which has decreased and planet h which remains the same.

Those results were further validated by carrying out an independent analysis using the GPU hybrid symplectic N-body code GENGA (Grimm et al. 2014) with a Differential Evolution Markov Chain Monte Carlo Method (DEMCMC; (Braak 2006)) as described in Grimm et al. (2018). The derived masses from the two different analyses were consistent, with a maximal deviation of the median masses of better than 0.4%, and than 13% for mass-ratio uncertainties.

### Photodynamical model

Once the N-body transit-timing analysis was converged, the dynamical constraints from the transit-timing model were used to improve the photometric constraints upon planet and stellar parameters, notably: the transit depth, the transit duration, the ingress/egress duration, the orbital period, the impact parameters and the density of the star (Seager 2013). The process was different than in section 4.1.2, this time a photodynamical model (described in Carter et al. (2012)) was fitted to the data with the following procedure:

- To model the transit, my collaborators used the analytic model presented in Agol et al. (2020a) for which the limb-darkening profile was taken to be a polynomial function of the stellar elevation. The transit model was integrated for each Spitzer (sub)exposure with an adaptive Simpson rule[8] (which had a uniform duration binned to 2.15 minutes, consistent with the cadence given in section 4.1.1), yielding a light curve computed with a precision of better than $10^{-7}$ for all cadences.

- Quadratic limb-darkening of the star with parameters $\{q_{1,ch1}; q_{2,ch1}; q_{1,ch2}; q_{2,ch2}\}$ was taken into account in the two Spitzer channels. For each planet a planet-to-star radius ratio ($R_p/R_\star$) was specified and a mid-transit impact parameter ($b_0$) was assumed. The limb darkening parameters were a function of wavelength for the two Spitzer channels, while the planet radius ratios were assumed to be identical in both wavebands based on their consistency across all planets (see results from my global analysis of the full dataset presented in Table 4.3).

- Using light curves corrected for systematic variations from the analysis conducted in Section 4.1.2, each transit window was fitted with the transit model multiplied by a cubic polynomial whose coefficients were solved via regression at each step of the Markov chain.

- After carrying out an initial optimisation of the model, the photometric error were taken to be the scatter in each observation window to yield a reduced chi-square of unity in that window. With this photometric scatter, the $\chi^2$ of the model with respect to the Spitzer photometric data was computed. The model was then optimised using a Nelder-Mead algorithm (Nelder et al. 1965).

- Finally, the uncertainties on the parameters were derived using an affine-invariant Markov chain Monte Carlo algorithm (Goodman et al. 2010). Uniform prior were assumed on the following parameters: $b_0$, $R_p/R_\star$, $\{q_{1,ch1}; q_{2,ch1}\}$, $\{q_{1,ch2}; q_{2,ch2}\}$, $\rho_\star$.

The resulting best-fit photodynamical model is displayed on Figure 4.22. We notice that both the super period timescales of the five outer planet and chopping are visible again. The parameters derived from this photodynamic model are presented in Table 4.14. Using equations (1.19) and (1.23), the corresponding semi-major axes and inclinations were derived for all planets Those parameters are very consistent with the ones I derived from the global analysis presented in section 4.1.2.

[8] Simpson's Rule is a numerical method that approximates the value of a definite integral by using quadratic functions.

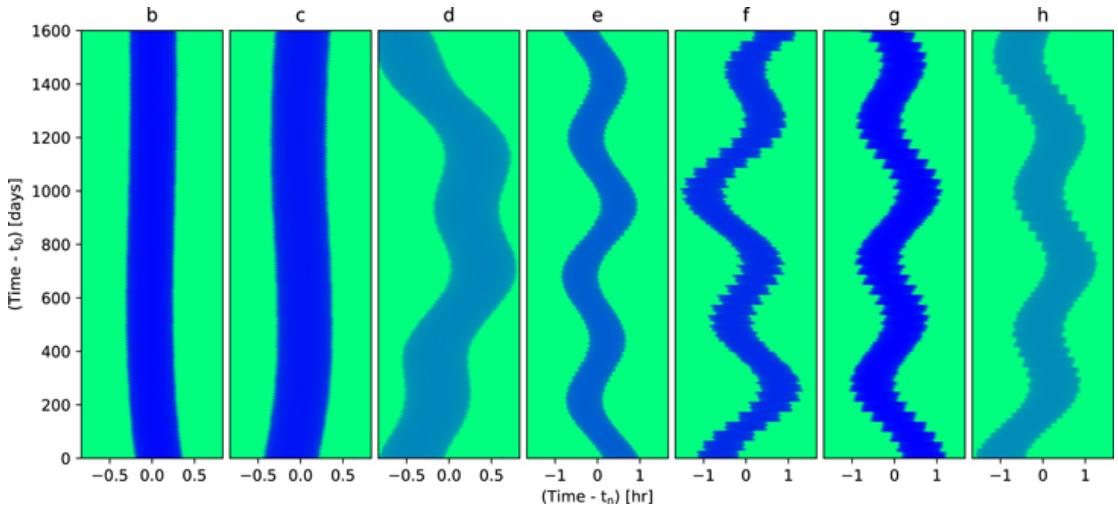


**Fig. 4.22** River plots showing every transit over 1600 days for one planet per panel (multiple transits are omitted from each panel). The x-axis ranges over $200/400 * 30$-second exposures centred on the mean ephemeris for the $n^{th}$ transit for b-d/e-h respectively (the 30 sec exposures are higher resolution than the binned Spitzer time-resolution which is 2.06min). Each row contains a transit model, with green being the out-of-transit, and blue in transit. There are 1059 of b, 661 of c, 395 of d, 262 of e, 173 of f, 129 of g, 85 of h. Planets d and h have the smallest sizes, and hence shallowest depths, causing a lighter blue colour during transit. Figure from Agol et al. (2020b).

| Planet | $R_p/R_\star$ | Depth [%] | $T_{14}$ [min] | $b/R_\star$ | $a/R_\star$ | $i$ [°] |
|---|---|---|---|---|---|---|
| b | 0.08590 ±0.00037 | 0.7378 ±0.0064 | 36.06 ±0.11 | $0.095^{+0.065}_{-0.061}$ | $20.843^{0.094}_{-0.155}$ | 89.728 ±0.165 |
| c | 0.08440 ±0.00038 | 0.7123 ±0.0064 | 42.03 ±0.13 | $0.109^{+0.059}_{-0:061}$ | $28.549^{+0.129}_{-0.212}$ | 89.778 ±0.118 |
| d | 0.06063 ±0.00052 | 0.3676 ±0.0063 | 48.87 ±0.24 | $0.063^{+0.063}_{-0.043}$ | $40.216^{+0.182}_{-0.299}$ | 89.896 ±0.077 |
| e | 0.07079 ±0.00055 | 0.5012 ±0.0078 | 55.76 ±0.26 | $0.191^{+0.041}_{-0.041}$ | $52.855^{+0.239}_{-0.392}$ | 89.793 ±0.048 |
| f | 0.08040 ±0.00047 | 0.6465 ±0.0076 | 62.85 ±0.25 | $0.312^{+0.023}_{0.018}$ | $69.543^{+0.314}_{-0.516}$ | 89.740 ±0.019 |
| g | 0.08692 ±0.00053 | 0.7555 ±0.0092 | 68.24 ±0.28 | $0.379^{+0.018}_{-0.014}$ | $84.591^{+0.382}_{-0.628}$ | 89.742 ±0.012 |
| h | 0.05809 ±0.00087 | 0.3375 ±0.0101 | 76.16 ±0.56 | $0.378^{+0.024}_{-0.023}$ | $111.817^{+0.505}_{-0.830}$ | 89.805 ±0.013 |

**Table 4.14** Parameters derived from the photodynamical model. Table adapted from Agol et al. (2020b)

Now that I have briefly explained how my collaborators processed to refine the masses of the planets from transit timing analysis, and their radii from a photodynamical method, I will discuss how the results gave us some insights on the planets' interiors.

### 4.2.2 Discussion

#### Mass-radius relation

Combining masses and radii, densities of the seven planets were derived. The resulting values revealed that the planets' densities range from 75% to 99% the density of the Earth. Each of the planets has a density intermediate between Mars ($\rho_{Mars} = 3.933\ g/cm^3 = 0.713\ \rho_\oplus$) and Earth ($\rho_\oplus = 5.514\ g/cm^3$). The surface gravities span a range from 57% of Earth (planet h) to 110% of Earth (planet b). Results are shown in Table 4.15.

| Planet | b | c | d | e | f | g | h |
|---|---|---|---|---|---|---|---|
| $\rho_p$ [$\rho_\oplus$] | $0.987^{+0.048}_{-0.050}$ | $0.991^{+0.040}_{-0.043}$ | $0.792^{+0.028}_{-0.030}$ | $0.889^{+0.030}_{-0.033}$ | $0.911^{+0.025}_{-0.029}$ | $0.917^{+0.025}_{-0.029}$ | $0.755^{+0.059}_{-0.055}$ |
| $g_p$ [$g_\oplus$] | 1.102 ±0.052 | 1.086 ±0.043 | 0.624 ±0.019 | 0.817 ±0.024 | 0.951 ±0.024 | 1.035 ±0.026 | 0.570 ±0.038 |

**Table 4.15** Densities and surface gravities of the seven planets derived from combining the transit-timing and photodynamic analysis. Table adapted from Agol et al. (2020b).

Being able to derive the densities of the planets while solely relying on transit information is a key asset of the TRAPPIST-1 system and it enables to question the planets interiors. Although we can not examine the interiors of planets directly (only possible with seismology on our own Earth), we can still construct models that compute what are the most likely interior compositions and fit them to existing data.

Relaying of the stellar mass from Mann et al. (2019) ($M_\star = 0.0898 \pm 0.0024$), the probability distribution for the masses and radii of the planets was compured from the posterior distribution of the transit-timing analysis and photodynamic analysis. The resulting probability distribution for the masses and radii of the seven planets are shown in Figure 4.23.

Figure 4.23 shows that all seven TRAPPIST-1 planets could to be consistent in composition at the $1\sigma$ level. Besides, all planets have lower uncompressed densities than Solar System terrestrial planets, implying they either have a smaller core (i.e. lower iron content) or are enriched with volatiles (e.g. water). To understand what composition can explain this observation I discuss some interior composition scenarios that are proposed in the paper (computed by Dr. Caroline Dorn and Prof. Eric Agol) in the next section.

#### Interior composition

There is significant degeneracy in the possible interior compositions of the TRAPPIST-1 planets as constrained by their mass and radius measurements alone, even if these latters are of unprecedented precision for terrestrial exoplanets. In the following, I introduce some

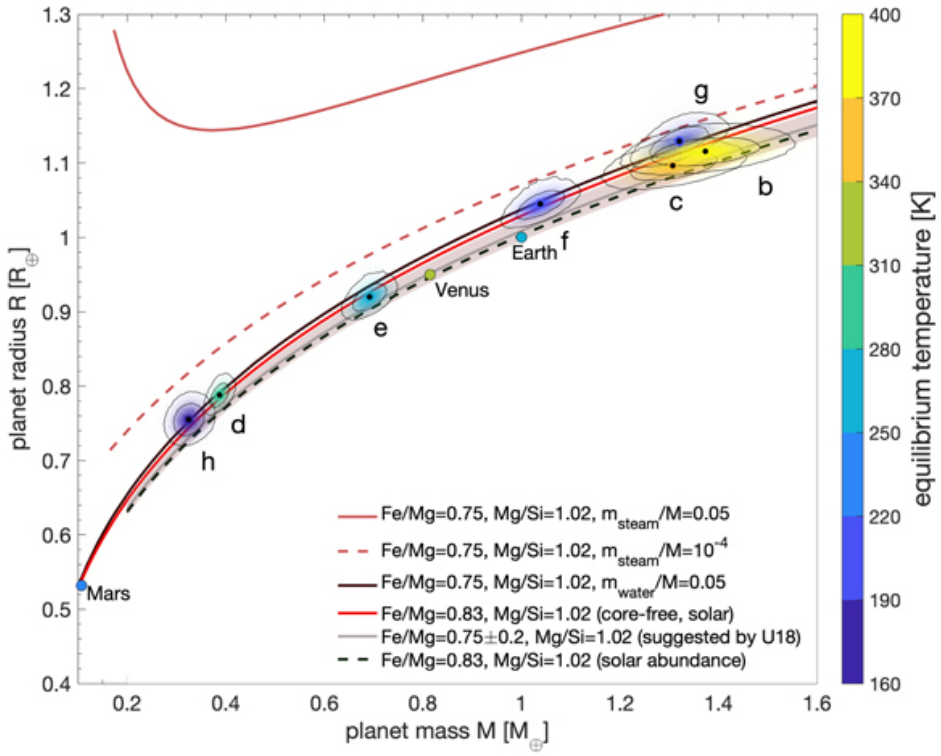


**Fig. 4.23** Mass-radius relation for the seven TRAPPIST-1 planets based on transit-timing and photodynamic analysis. Each planet's joined posterior probability distribution is coloured by the equilibrium temperature (see colourbar), with the intensity proportional to probability, while the $1\sigma$ and $2\sigma$ confidence levels from the Markov chain posterior are plotted with solid lines. Theoretical mass-radius relations are over-plotted using the model in Dorn et al. (2017) for an Earth-like molar $Fe/Mg = 0.83$ ratio with a core (black dashed line) and core-free (red solid line), and a range of cored models with molar $Fe/Mg = 0.75 \pm 0.2$ (grey). The solid grey line refers to the model from Unterborn et al. (2018), called U18. The solid black line was calculated for a 5% water composition, for irradiation low enough (i.e. for planets e, f, g and h) that water is condensed on the surface (assuming a surface pressure of 1 bar and a surface temperature of 300 K). The umber dashed and solid lines were calculated for a 0.01% and a 5% water composition, respectively, for irradiation high enough (i.e. for planets b, c and d) that water has fully evaporated in the atmosphere, with the U18 interior model with $Fe/Mg = 0.83$ and $Mg/Si = 1.02$ (Turbet et al. 2020b). The Earth, Venus and Mars are plotted as single points, also coloured by their equilibrium temperatures. Figure from Agol et al. (2020b).

plausible scenarios for their interior composition and refer the interested readers to the original paper (Agol et al. 2020b) for further information.

- First, if assumed that the planets' atmospheres contribute a negligible amount to their total radius, and that the planets are fully differentiated, composed of rocky mantles ($MgSiO_3$) and iron cores only, a core mass fraction (CMF) - i.e. the portion of the planets' mass which is contained within their cores - that is consistent with the observation can be derived for each planet. The CMF estimates of the TRAPPIST-1

planets range from $16.1^{+3:5}_{-4.2}$ wt% for planet g up to $26.6^{+4.6}_{-5.1}$ wt% for planet c. The CMF iron fraction of the planets are very consistent with one another, with the mean of all planets being 21.4 wt%. As a comparison, the Earth has a iron CMF of 32.5%. This means that the TRAPPIST-1 planets could have fully-differentiated interiors like the Earth but with cores that are depleted in iron compered to the Earth.

- Alternatively, the difference in density compared to Earth and the observed (weak) variations among all seven planets may be due to their differing volatile (e.g. water) content. If a rocky Earth-like interior (CMF=32.5%, fully-differentiated) with an additional condensed water layer that contributes to the total radius is assumed, the corresponding water mass fractions of the seven planets can be estimated. The corresponding water content are presented in Table 4.16 (for a surface temperature of 300 K at 1 bar). The lower densities of planets d, f, g, and h (see Table 4.15) can allow

| Planet | b | c | d | e | f | g | h | Earth |
|---|---|---|---|---|---|---|---|---|
| Water content [%] | $2.8^{+2.1}_{-1.9}$ | $2.3^{+1.8}_{-1.7}$ | $4.4^{+2.0}_{-1.5}$ | $2.9^{+1.7}_{-1.5}$ | $4.5^{+1.8}_{1.2}$ | $6.4^{+2.0}_{-1.6}$ | $5.5^{+4.5}_{-3.1}$ | $0.12 \pm 0.02$ |

**Table 4.16** Required water mass fractions to explain the derived densities assuming Earth-like fully-differentiated interiors for all seven planets.

for two to three times as much water than for planets b, c, and e. In parallel, as the three inner planets are expected to be more irradiated than the runaway greenhouse irradiation limit (R. K. Kopparapu et al. 2013; Turbet et al. 2018; Wolf 2017), all water on these planets should be steamed, forming a thick $H_2O$-dominated atmosphere. As a result, their water mass fractions should drop drastically to less than 0.01 wt%, more than several times lower than the water ocean mass fraction of the Earth.

- More exotic scenarios can also be considered. For instance, my collaborators proposed that the interiors of the planets are fully oxidised to $FeO$, meaning that instead of forming a core, all of the iron remains in the mantle. Elkins-Tanton et al. (2008) showed that in this configuration, the size of a planet could be amplified by a few percent. This could explain the increased radii of the TRAPPIST-1 planets when compared with our Solar system terrestrial planets. According to Elkins-Tanton et al. (2008), such planets may be more likely to form later in accretion, when temperatures in the planetary nebula have fallen, and may therefore be more likely to form farther from the star where volatile-rich material is more common. However, it is not clear for the moment which processes could lead to such extreme oxidation of iron. Besides, it is interesting to notice that such fully silicate core-less planets would not have a

liquid core and therefore would have no magnetic dynamo. Considering a planet's magnetic field is believed to be critical in shielding the atmosphere from energetic particles (see Chapter 1 section 1.1.2), this interior composition scenario could actually be challenging for a planet's habitability.

## 4.3 Prospects

The Spitzer Exploration Program *Red Worlds* is among the largest programs ever undertaken with the Spitzer Space Telescope. It gathered more than 1000 hours of observation of the touchstone TRAPPIST-1 system. This program has largely met its expectations, notably through the discovery of 4 new planets orbiting the TRAPPIST-1 star, all well-suited for detailed atmospheric characterisation with next-generation telescopes (Gillon et al. 2017b), as well as multiple global analyses that enabled us to significantly improve the stellar and planets' transit parameters (Delrez et al. 2018a; Ducrot et al. 2020), and the determination of planet masses through transit timing analysis (Agol et al. 2020b; Grimm et al. 2018). And although other observations were important, this program has been crucial in making the TRAPPIST-1 planets the best-known rocky temperate planets after the terrestrial planets of our own solar system to this date. The most recent observations of the TRAPPIST-1 system with Spitzer were performed in October 2019, and will unfortunately be the last. But on a brighter note, the James Webb Space Telescope (JWST) is on its way to take over and yield even more insight into this extraordinary system.

JWST is a 6m-aperture infrared space telescope, the largest telescope ever sent in space and it is equipped with a set of four instruments (NIRCam, NIRISS, MIRI, NIRSpec) capable of spanning a broad wavelength range, adapted to perform transmission spectroscopy of exoplanets. At the time of the writing of this manuscript, its launch is now scheduled for October 2021. It will be able to probe the planets' atmospheric compositions, to constrain their surface properties, and to assess their habitability. In the most optimistic scenarios, it could even detect molecules of possible biological origins (Fauchez et al. 2019; Lincowski et al. 2018; Lustig-Yaeger et al. 2019; Morley et al. 2017). Several simulations of the capabilities of JWST observations for TRAPPIST-1 planets show very promising results. Lustig-Yaeger et al. (2019) predict that many molecular absorption features may be detectable with JWST in ≃2-15 transits for all seven planets, as shown on Figure 4.24. For instance, we should be able to detect $CO_2$ features in the transit transmission spectrum of planet b (if present) with less then 5 transits. We further expect to be able to disentangle between different atmospheric scenarios. These predictions justify why the TRAPPIST-1 is the only planetary system targeted by four JWST Guaranteed Time of Observation (GTO) programs

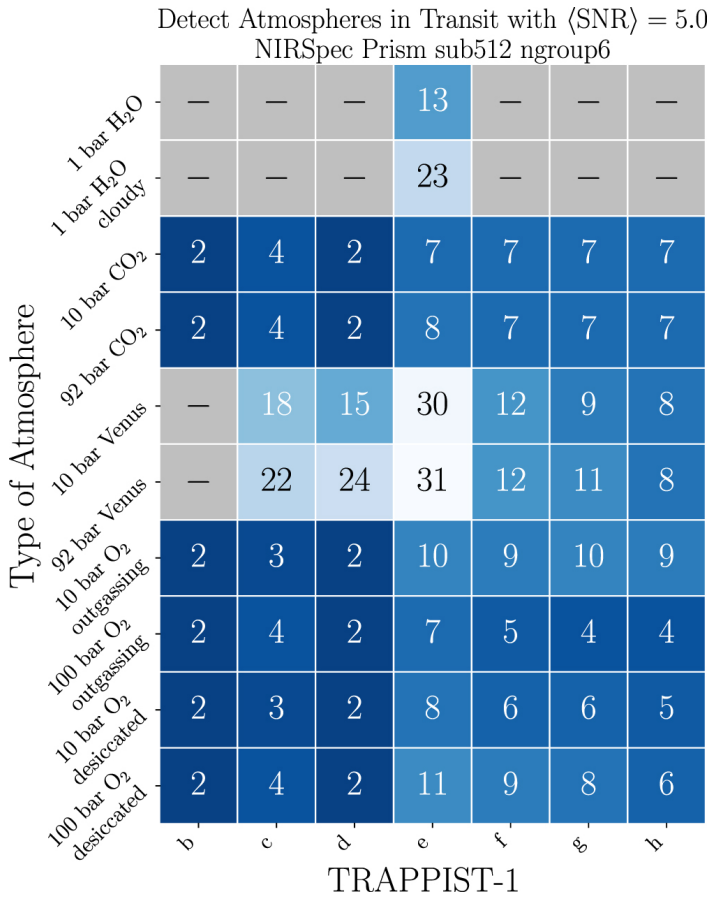


**Fig. 4.24** Number of transits for each TRAPPIST-1 planet necessary to rule out a featureless spectrum with $S\hat{N}R = 5$ for different self-consistent atmospheric compositions using JWST NIRSpec Prism with the optimised readout mode of Batalha et al. (2018). Figure from Lustig-Yaeger et al. (2019).

(GTO ID: 1177, 1279, 1201 and 1331). GTO programs provide guaranteed observing time and exclusive access to science data during an exclusive access period. Moreover, three additional Guest Observer (GO) programs have recently been accepted and will observe TRAPPIST-1 (GO ID: 2420, 2589, 2304). In total, this represent $\simeq$ 190 hours of observation already planned on this target !

Unfortunately, there is one possible limitation to these prognostics: stellar contamination. As photometric precision increases the stellar photospheric heterogeneity on star becomes a major astrophysical source of noise. Indeed, we cannot directly measure the spectrum of the spatially resolved photospheric region that illuminates an exoplanet atmosphere during a transit. As a simplification, we adopt the spectrum of the out-of-transit stellar disk as our reference and neglect differences between the disk-averaged spectrum and the spectrum of the transit chord. The consequences of this simplification are very profound as these spectral differences can be imprinted on the transmission spectrum of the exoplanet and strongly limit

the deciphering of its atmospheric properties. For this reason, stellar contamination is the subject of the first part of my next chapter.

In addition to the atmospheric aspect, observations of TRAPPIST-1 with JWST will offer precious measurements for its dynamical characterisation. As matter of fact, either to validate the current Nbody transit-timing analysis or to reveal a periodic orbit configuration, high precision timing from JWST will be essential. For instance, if we assume we can observe every single TRAPPIST-1 transit visible with JWST for the next 5 years and extract their timings (assume we know perfectly the mass of the star) we should be able to recover the planets masses to better than 0.02% for planets d-h, and to 0.1% for planets b and c. Although in practice not every transit will be scheduled, any timing of the outer planets will results in more precise masses. And while we wait for JWST, we have organised an extensive transit timing campaign from the ground with the SPECULOOS and Liverpool telescopes, that we intend to pursue in parallel to JWST observations. I present this on-going campaign in the second part of Chapter 5.

## 4.4 Appendix of Chapter 4

**Table 4.17** Adopted baseline model for the individual analysis of each transit. For each light curve, this table shows the date of acquisition, the number of data points, the epoch based on the transit ephemeris given in Table 4.3, the selected baseline function (see Section 4.1.2) and the deduced values for $\beta_w$ , $\beta_r$ , and $CF = \beta_r * \beta_w$. For the baseline function, p($\epsilon^N$ ) denotes, respectively, a N-order polynomial function of time ($\epsilon = t$), the full width at half maximum ($\epsilon = fwhm$), x and y positions ($\epsilon = xy$), the background ($\epsilon = b$), the airmass ($\epsilon = a$) and a scalar ($\epsilon = s$).

| Date | Number of Points | Epoch | Baseline | $\beta_w$ | $\beta_r$ | CF | Channel |
|---|---|---|---|---|---|---|---|
| **TRAPPIST-1b** | | | | | | | |
| 2016-02-21 | 108 | 78 | $p(t^3)+p(fwhm_x^1)+p(xy^1)$ | 1.09 | 1.0 | 1.09 | c2 |
| 2016-03-04 | 132 | 86 | $p(xy^1)$ | 0.84 | 1.12 | 1.06 | c2 |
| 2016-03-15 | 164 | 93 | $p(t^3)+p(xy^1)$ | 1.01 | 1.07 | 1.08 | c2 |
| 2016-09-20 | 114 | 218 | $p(fwhm_y^1)+p(xy^1)$ | 1.05 | 1.08 | 1.13 | c2 |
| 2016-09-21 | 665 | 219 | $p(xy^1)$ | 1.04 | 1.21 | 1.25 | c2 |
| 2016-09-26 | 132 | 222 | $p(fwhm_y^1)+p(xy^1)+p(r^1)$ | 1.03 | 1.31 | 1.35 | c2 |
| 2016-09-29 | 135 | 224 | $p(t^1)+p(xy^1)$ | 0.97 | 1.04 | 1 | c2 |
| 2016-09-30 | 56 | 225 | $p(t^1)+p(xy^1)$ | 0.75 | 1.21 | 0.9 | c2 |
| 2016-10-05 | 141 | 228 | $p(xy^1)$ | 0.87 | 1.04 | 0.91 | c2 |
| 2016-10-07 | 126 | 229 | $p(xy^1)$ | 0.99 | 1.13 | 1.12 | c2 |
| 2016-10-08 | 127 | 230 | $p(t^2)+p(xy^1)$ | 0.96 | 1.09 | 1.05 | c2 |
| 2017-02-18 | 67 | 318 | $p(xy^1)$ | 0.99 | 1.0 | 0.99 | c2 |
| 2017-02-21 | 70 | 320 | $p(xy^1)$ | 0.91 | 1.0 | 0.91 | c2 |
| 2017-02-23 | 67 | 321 | $p(t^1)+p(fwhm_y^1)+p(xy^1)+p(r^1)$ | 0.97 | 1.0 | 0.97 | c2 |
| 2017-02-24 | 67 | 322 | $p(t^1)+p(fwhm_y^1)+p(xy^1)$ | 0.86 | 1.15 | 0.93 | c1 |
| 2017-02-27 | 105 | 324 | $p(xy^1)+p(r^1)$ | 0.92 | 1.0 | 0.92 | c2 |
| 2017-03-01 | 74 | 325 | $p(fwhm_x^1)+p(xy^1)$ | 0.81 | 1.09 | 0.9 | c2 |
| 2017-03-02 | 67 | 326 | $p(fwhm_y^1)+p(xy^1)$ | 0.72 | 1.28 | 0.92 | c1 |
| 2017-03-04 | 67 | 327 | $p(fwhm_y^1)+p(xy^1)+p(r^1)$ | 0.93 | 1.0 | 0.93 | c1 |
| 2017-03-05 | 74 | 328 | $p(xy^1)$ | 1.03 | 1.0 | 1.03 | c2 |
| 2017-03-07 | 67 | 329 | $p(fwhm_y^1)+p(xy^1)$ | 0.87 | 1.18 | 1.03 | c1 |
| 2017-03-08 | 67 | 330 | $p(t^1)+p(fwhm_y^1)+p(xy^1)$ | 0.87 | 1.14 | 0.97 | c1 |
| 2017-03-11 | 68 | 332 | $p(xy^1)$ | 1.13 | 1.0 | 1.13 | c2 |
| 2017-03-13 | 67 | 333 | $p(t^2)+p(fwhm_x^1)+p(fwhm_y^1)+p(xy^1)$ | 0.84 | 1.15 | 0.96 | c1 |
| 2017-03-14 | 67 | 334 | $p(fwhm_y^1)+p(xy^1)$ | 0.79 | 1.39 | 1.11 | c1 |
| 2017-03-16 | 67 | 335 | $p(t^1)+p(fwhm_y^1)+p(xy^1)$ | 0.87 | 1.51 | 1.31 | c1 |
| 2017-03-20 | 67 | 338 | $p(t^1)+p(fwhm_y^1)+p(xy^1)$ | 0.66 | 1.07 | 0.71 | c1 |
| 2017-03-22 | 67 | 339 | $p(t^1)+p(fwhm_y^1)+p(xy^1)$ | 0.76 | 1.0 | 0.76 | c1 |
| 2017-03-25 | 67 | 341 | $p(t^2)+p(fwhm_x^2)+p(fwhm_y^1)+p(xy^1)$ | 0.96 | 1.0 | 0.96 | c1 |
| 2017-03-26 | 67 | 342 | $p(t^2)+p(fwhm_y^1)+p(xy^2)$ | 0.61 | 1.0 | 0.61 | c1 |
| 2017-09-13 | 67 | 455 | $p(t^1)+p(fwhm_y^1)+p(xy^1)+p(r^1)$ | 0.84 | 1.21 | 1.01 | c1 |
| 2017-09-14 | 118 | 456 | $p(t^1)+p(xy^1)$ | 1.14 | 1.24 | 1.42 | c1 |
| 2017-09-16 | 67 | 457 | $p(t^1)+p(fwhm_y^1)+p(xy^1)$ | 0.86 | 1.0 | 0.86 | c1 |
| 2017-09-17 | 95 | 458 | $p(t^4)+p(fwhm_y^3)+p(xy^1)+p(r^1)$ | 1.1 | 1.0 | 1.1 | c1 |
| 2017-09-19 | 67 | 459 | $p(t^1)+p(fwhm_x^1)+p(xy^1)$ | 1.06 | 1.0 | 1.06 | c1 |
| 2017-09-21 | 67 | 460 | $p(t^1)+p(fwhm_y^1)+p(xy^1)$ | 1.17 | 1.15 | 1.34 | c1 |
| 2017-09-24 | 67 | 462 | $p(fwhm_x^1)+p(fwhm_y^1)+p(xy^1)+p(r^1)$ | 0.9 | 1.17 | 1.05 | c1 |
| 2017-09-28 | 67 | 465 | $p(t^2)+p(xy^1)$ | 0.93 | 1.0 | 0.93 | c1 |
| 2017-10-01 | 67 | 467 | $p(t^1)+p(fwhm_y^1)+p(xy^1)$ | 0.84 | 1.33 | 1.12 | c1 |
| 2017-10-03 | 67 | 468 | $p(fwhm_x^1)+p(fwhm_y^1)+p(xy^1)$ | 0.85 | 1.21 | 1.03 | c1 |
| 2017-10-09 | 67 | 472 | $p(xy^1)$ | 0.88 | 1.59 | 1.4 | c1 |
| 2017-10-10 | 67 | 473 | $p(fwhm_y^1)+p(xy^1)$ | 1.01 | 1.42 | 1.44 | c1 |
| 2017-10-13 | 67 | 475 | $p(t^1)+p(fwhm_y^1)+p(xy^1)$ | 0.66 | 1.05 | 0.69 | c1 |
| 2017-10-15 | 67 | 476 | $p(xy^1)+p(r^1)$ | 0.87 | 1.0 | 0.87 | c1 |
| 2017-10-16 | 52 | 477 | $p(t^2)+p(xy^1)+p(r^1)$ | 0.9 | 1.0 | 0.9 | c1 |
| 2017-10-18 | 70 | 478 | $p(t^2)+p(fwhm_x^1)+p(fwhm_y^1)+p(xy^1)$ | 1.13 | 1.0 | 1.13 | c1 |
| 2017-10-19 | 66 | 479 | $p(t^1)+p(fwhm_x^1)+p(fwhm_y^1)+p(xy^1)$ | 0.84 | 1.0 | 0.84 | c1 |
| 2018-03-09 | 129 | 572 | $p(fwhm_y^2)+p(xy^1)$ | 0.97 | 1.17 | 1.14 | c2 |
| 2018-03-10 | 96 | 573 | $p(fwhm_x^1)+p(xy^1)$ | 0.99 | 1.0 | 0.99 | c2 |
| 2018-03-19 | 80 | 579 | $p(xy^1)$ | 0.94 | 1.22 | 1.16 | c2 |
| 2018-03-25 | 68 | 583 | $p(t^2)+p(xy^1)$ | 1.1 | 1.0 | 1.1 | c2 |

**Table 4.17** continued.

| Date | Number of Points | Epoch | Baseline | $\beta_w$ | $\beta_r$ | CF | Channel |
|---|---|---|---|---|---|---|---|
| 2019-10-01 | 182 | 950 | $p(t^1)+p(fwhm_x^1)+p(fwhm_y^1)+p(xy^1)$ | 1.06 | 1.0 | 1.06 | c2 |
| 2019-10-10 | 150 | 956 | $p(t^2)+p(fwhm_x^1)+p(fwhm_y^1)+p(xy^1)+p(r^1)$ | 0.97 | 1.0 | 0.97 | c2 |
| 2019-10-13 | 180 | 958 | $p(fwhm_x^1)+p(fwhm_y^1)+p(xy^1)$ | 1.05 | 1.0 | 1.05 | c2 |
| **TRAPPIST-1c** | | | | | | | |
| 2016-03-04 | 66.0 | 70 | $p(xy^1)$ | 1.01 | 1.0 | 1.01 | c2 |
| 2016-09-19 | 118.0 | 152 | $p(xy^1)+p(r^1)$ | 0.88 | 1.38 | 1.21 | c2 |
| 2016-09-21 | 82.0 | 153 | $p(xy^1)+p(r^1)$ | 0.83 | 1.0 | 0.83 | c2 |
| 2016-09-24 | 108.0 | 154 | $p(xy^1)$ | 1.12 | 1.58 | 1.77 | c2 |
| 2016-09-26 | 111.0 | 155 | $p(xy^1)$ | 1.0 | 1.21 | 1.22 | c2 |
| 2016-10-01 | 134.0 | 157 | $p(fwhm_x^2)+p(fwhm_y^1)+p(xy^1)+p(r^1)$ | 0.86 | 1.44 | 1.24 | c2 |
| 2016-10-06 | 156.0 | 159 | $p(xy^1)$ | 0.98 | 1.06 | 1.04 | c2 |
| 2016-10-08 | 153.0 | 160 | $p(xy^1)$ | 0.82 | 1.25 | 1.02 | c2 |
| 2017-02-18 | 67.0 | 215 | $p(xy^1)$ | 1.03 | 1.0 | 1.03 | c2 |
| 2017-02-21 | 77.0 | 216 | $p(t^2)+p(xy^1)$ | 0.84 | 1.0 | 0.84 | c2 |
| 2017-02-23 | 67.0 | 217 | $p(xy^1)$ | 1.05 | 1.26 | 1.32 | c2 |
| 2017-02-26 | 67.0 | 218 | $p(fwhm_x^1)+p(xy^1)+p(r^1)$ | 1.0 | 1.0 | 1.0 | c2 |
| 2017-02-28 | 67.0 | 219 | $p(fwhm_x^1)+p(xy^1)$ | 0.93 | 1.0 | 0.93 | c2 |
| 2017-03-03 | 67.0 | 220 | $p(t^1)+p(fwhm_x^1)+p(xy^1)$ | 0.95 | 1.0 | 0.95 | c2 |
| 2017-03-05 | 52.0 | 221 | $p(xy^1)$ | 0.95 | 1.02 | 0.97 | c2 |
| 2017-03-07 | 59.0 | 222 | $p(xy^1)$ | 0.9 | 1.0 | 0.9 | c2 |
| 2017-03-10 | 67.0 | 223 | $p(fwhm_x^1)+p(xy^1)+p(r^1)$ | 0.9 | 1.11 | 0.99 | c2 |
| 2017-03-12 | 95.0 | 224 | $p(fwhm_x^1)+p(xy^1)+p(r^1)$ | 0.99 | 1.02 | 1.01 | c2 |
| 2017-03-15 | 95.0 | 225 | $p(xy^1)+p(r^1)$ | 0.92 | 1.0 | 0.92 | c2 |
| 2017-03-20 | 67.0 | 227 | $p(t^1)+p(fwhm_x^1)+p(xy^1)$ | 0.94 | 1.0 | 0.94 | c2 |
| 2017-03-22 | 67.0 | 228 | $p(fwhm_y^1)+p(xy^1)$ | 1.01 | 1.11 | 1.12 | c2 |
| 2017-03-24 | 110.0 | 229 | $p(t^2)+p(xy^1)$ | 0.99 | 1.0 | 0.99 | c2 |
| 2017-03-27 | 67.0 | 230 | $p(fwhm_x^1)+p(fwhm_y^1)+p(xy^1)$ | 0.95 | 1.47 | 1.4 | c2 |
| 2017-09-15 | 94.0 | 301 | $p(fwhm_x^1)+p(xy^1)+p(r^1)$ | 1.04 | 1.54 | 1.6 | c2 |
| 2017-09-17 | 113.0 | 302 | $p(t^2)+p(xy^1)$ | 0.95 | 1.41 | 1.34 | c1 |
| 2017-09-24 | 105.0 | 305 | $p(xy^1)$ | 1.04 | 1.0 | 1.04 | c2 |
| 2017-09-27 | 67.0 | 306 | $p(fwhm_y^1)+p(xy^1)$ | 0.91 | 1.21 | 1.11 | c1 |
| 2017-10-07 | 108.0 | 310 | $p(t^2)+p(xy^1)$ | 1.07 | 1.0 | 1.07 | c2 |
| 2017-10-11 | 100.0 | 312 | $p(fwhm_y^1)+p(xy^1)+p(r^1)$ | 0.82 | 1.56 | 1.38 | c1 |
| 2017-10-14 | 74.0 | 313 | $p(t^3)+p(xy^1)+p(r^1)$ | 0.91 | 1.46 | 1.33 | c2 |
| 2017-10-16 | 59.0 | 314 | $p(fwhm_x^1)+p(fwhm_y^1)+p(r^1)$ | 1.09 | 1.02 | 1.11 | c1 |
| 2017-10-19 | 60 | 315 | $p(t^2)+p(fwhm_y^2)+p(xy^1)+p(r^1)$ | 0.74 | 1.07 | 0.8 | c1 |
| 2018-03-13 | 65.0 | 375 | $p(t^1)+p(fwhm_y^1)+p(xy^1)+p(r^1)$ | 0.9 | 1.03 | 0.93 | c1 |
| 2018-03-25 | 83.0 | 380 | $p(fwhm_y^1)+p(xy^1)$ | 1.07 | 1.07 | 1.15 | c2 |
| 2018-03-28 | 98.0 | 381 | $p(t^1)+p(fwhm_y^1)+p(xy^1)$ | 1.11 | 1.27 | 1.4 | c1 |
| 2019-10-01 | 182 | 609 | $p(fwhm_x^1)+p(fwhm_y^1)+p(xy^1)$ | 1.06 | 1.0 | 1.06 | c2 |
| 2019-10-08 | 190 | 612 | $p(t^3)+p(fwhm_x^1)+p(r^1)$ | 0.95 | 1.44 | 1.37 | c2 |
| 2019-10-13 | 180 | 614 | $p(fwhm_x^1)+p(fwhm_y^1)+p(xy^1)$ | 1.05 | 1.0 | 1.05 | c2 |
| 2019-10-20 | 188 | 617 | $p(t^2)+p(fwhm_x^1)+p(fwhm_y^1)+p(xy^1)+p(r^1)$ | 0.97 | 1.0 | 0.97 | c2 |
| **TRAPPIST-1d** | | | | | | | |
| 2016-09-22 | 134 | -4 | $p(fwhm_x^1)+p(fwhm_y^1)+p(xy^1)$ | 1.05 | 1.34 | 1.4 | c2 |
| 2016-09-26 | 114 | -3 | $p(fwhm_y^1)+p(xy^1)$ | 1.1 | 1.1 | 1.21 | c2 |
| 2016-09-30 | 154 | -2 | $p(xy^1)$ | 1.08 | 1.59 | 1.71 | c2 |
| 2016-10-04 | 145 | -1 | $p(fwhm_x^2)+p(xy^1)$ | 0.76 | 1.36 | 1.04 | c2 |
| 2016-10-08 | 133 | 0 | $p(xy^1)$ | 0.86 | 1.56 | 1.35 | c2 |
| 2017-02-19 | 122 | 33 | $p(xy^1)+p(r^1)$ | 0.94 | 1.06 | 0.97 | c2 |
| 2017-02-23 | 122 | 34 | $p(xy^1)+p(r^1)$ | 0.94 | 1.0 | 0.94 | c2 |
| 2017-02-27 | 134 | 35 | $p(fwhm_x^1)+p(fwhm_y^1)+p(xy^1)+p(r^1)$ | 0.96 | 1.04 | 1 | c2 |
| 2017-03-03 | 122 | 36 | $p(xy^1)$ | 0.89 | 1.0 | 0 ,89 | c2 |
| 2017-03-07 | 121 | 37 | $p(xy^1)$ | 1.01 | 1.0 | 1.01 | c2 |
| 2017-03-11 | 120 | 38 | $p(xy^1)+p(r^1)$ | 1.09 | 1.0 | 1.09 | c2 |
| 2017-03-15 | 142 | 39 | $p(t^2)+p(fwhm_y^1)+p(xy^1)$ | 1.01 | 1.0 | 1.01 | c2 |
| 2017-03-19 | 122 | 40 | $p(fwhm_x^1)+p(xy^1)$ | 0.99 | 1.0 | 0.99 | c2 |
| 2017-09-17 | 120 | 85 | $p(t^3)+p(xy^2)+p(r^1)$ | 1.03 | 1.4 | 1.44 | c1 |
| 2017-09-25 | 122 | 87 | $p(t^1)+p(fwhm_y^1)+p(xy^1)$ | 0.76 | 1.76 | 1.33 | c1 |

**Table 4.17** continued.

| Date | Number of Points | Epoch | Baseline | $\beta_w$ | $\beta_r$ | CF | Channel |
|---|---|---|---|---|---|---|---|
| 2017-10-08 | 122 | 90 | $p(t^3)+p(fwhm_y^2)+p(xy^2)$ | 0.75 | 1.32 | 0.98 | c1 |
| 2017-10-16 | 122 | 92 | $p(t^2)+p(xy^2)$ | 0.99 | 1.69 | 1.67 | c1 |
| 2017-10-20 | 129 | 93 | $p(xy^1)+p(r^1)$ | 0.98 | 1.0 | 0.98 | c2 |
| 2018-03-06 | 183 | 127 | $p(fwhm_x^1)+p(xy^1)+p(r^2)$ | 1.04 | 1.21 | 1.25 | c2 |
| 2018-03-31 | 106 | 133 | $p(xy^1)$ | 1.01 | 1.33 | 1.33 | c2 |
| **TRAPPIST-1e** | | | | | | | |
| 2016-09-22 | 97 | -1 | $p(xy^1)+p(fwhm_x^1)+p(fwhm_y^1)+p(r^1)$ | 1.00 | 1.12 | 1.12 | c2 |
| 2016-09-28 | 154 | 0 | $p(t^1)+p(xy^1)$ | 0.99 | 1.0 | 0.99 | c2 |
| 2017-02-22 | 106 | 24 | $p(fwhm_x^1)+p(xy^1)$ | 1.03 | 1.24 | 1.28 | c2 |
| 2017-02-28 | 99 | 25 | $p(xy^1)+p(r^1)$ | 0.85 | 1.02 | 0.87 | c2 |
| 2017-03-06 | 141 | 26 | $p(fwhm_x^1)+p(xy^1)$ | 1.06 | 1.09 | 1.15 | c2 |
| 2017-03-12 | 124 | 27 | $p(t^3)$ | 1.05 | 1.0 | 1.05 | c2 |
| 2017-03-18 | 134 | 28 | $p(t^1)+p(xy^1)+p(r^1)$ | 0.88 | 1.01 | 0.89 | c2 |
| 2017-03-24 | 127 | 29 | $p(xy^1)$ | 0.99 | 1.0 | 0.99 | c2 |
| 2017-09-17 | 88 | 58 | $p(t^2)+p(xy^1)$ | 1.01 | 1.02 | 1.03 | c1 |
| 2017-09-23 | 122 | 59 | $p(fwhm_x^1)+p(fwhm_y^1)+p(xy^1)+p(r^1)$ | 0.9 | 1.0 | 0.9 | c1 |
| 2017-10-12 | 113 | 62 | $p(xy^1)+p(r^2)$ | 0.93 | 1.07 | 1.01 | c1 |
| 2018-03-07 | 122 | 86 | $p(fwhm_y^1)+p(xy^1)+p(r^2)$ | 0.99 | 1.53 | 1.5 | c1 |
| 2018-03-13 | 71 | 87 | $p(fwhm_y^1)+p(xy^1)$ | 0.89 | 1.36 | 1.22 | c1 |
| 2018-03-19 | 161 | 88 | $p(fwhm_x^1)+p(xy^1)$ | 1.01 | 1.1 | 1.12 | c2 |
| 2018-03-25 | 113 | 89 | $p(xy^1)$ | 0.97 | 1.03 | 1.0 | c2 |
| 2019-10-01 | 122 | 180 | $p(t^1)+p(fwhm_x^1)+p(fwhm_y^1)+p(xy^1)$ | 1.04 | 1.42 | 1.48 | c2 |
| 2019-10-13 | 122 | 182 | $p(t^1)+p(fwhm_x^2)+p(fwhm_y^2)$ | 1.06 | 1.09 | 1.16 | c2 |
| **TRAPPIST-1f** | | | | | | | |
| 2016-09-30 | 170 | -1 | $p(xy^1)$ | 0.93 | 1.66 | 1.54 | c2 |
| 2016-10-09 | 200 | 0 | $p(fwhm_x^1)+p(fwhm_y^1)+p(xy^1)$ | 0.87 | 1.66 | 1.45 | c2 |
| 2017-02-24 | 150 | 15 | $p(t^1)+p(fwhm_x^1)+p(xy^1)$ | 1.04 | 1.74 | 1.81 | c2 |
| 2017-03-06 | 124 | 16 | $p(fwhm_x^1)+p(xy^1)+p(r^1)$ | 0.96 | 1.06 | 1.02 | c2 |
| 2017-03-15 | 173 | 17 | $p(t^1)+p(fwhm_y^1)+p(xy^1)+p(r^1)$ | 1.04 | 1.01 | 1.05 | c2 |
| 2017-03-24 | 138 | 18 | $p(fwhm_x^1)+p(xy^1)+p(r^1)$ | 0.96 | 1.48 | 1.42 | c2 |
| 2017-09-24 | 106 | 38 | $p(fwhm_x^1)+p(xy^1)+p(r^1)$ | 0.88 | 1.03 | 0.91 | c2 |
| 2018-03-09 | 160 | 56 | $p(fwhm_x^1)+p(xy^1)$ | 1.02 | 1.03 | 1.06 | c2 |
| 2018-03-18 | 150 | 57 | $p(fwhm_x^1)+p(xy^1)+p(r^2)$ | 0.85 | 1.23 | 1.04 | c1 |
| 2018-03-27 | 148 | 58 | $p(t^2)+p(fwhm_y^1)+p(xy^1)$ | 1.15 | 1.31 | 1.5 | c1 |
| 2019-10-01 | 182 | 118 | $p(fwhm_x^1)+p(fwhm_y^1)+p(xy^1)$ | 1.06 | 1.0 | 1.06 | c2 |
| 2019-10-10 | 150 | 119 | $p(t^2)+p(fwhm_x^1)+p(fwhm_y^1)+p(xy^1)+p(r^1)$ | 0.97 | 1.0 | 0.97 | c2 |
| 2019-10-28 | 150 | 121 | $p(t^1)+p(fwhm_x^1)+p(fwhm_y^1)+p(r^1)$ | 0.88 | 1.01 | 0.89 | c2 |
| **TRAPPIST-1g** | | | | | | | |
| 2016-10-03 | 147 | 30 | $p(fwhm_x^1)+p(fwhm_y^1)+p(xy^1)$ | 0.76 | 1.64 | 1.24 | c2 |
| 2017-03-01 | 86 | 12 | $p(fwhm_x^1)+p(fwhm_y^1)+p(xy^1)$ | 0.93 | 1.0 | 0.93 | c2 |
| 2017-03-13 | 150 | 13 | $p(t^2)+p(fwhm_y^1)+p(xy^1)$ | 0.98 | 1.0 | 0.98 | c2 |
| 2017-03-25 | 150 | 14 | $p(fwhm_x^1)+p(xy^2)$ | 1.08 | 1.0 | 1.08 | c2 |
| 2017-09-14 | 158 | 28 | $p(fwhm_y^2)+p(xy^2)+p(r^1)$ | 0.94 | 1.34 | 1.26 | c1 |
| 2018-03-06 | 156 | 42 | $p(t^2)+p(xy^1)$ | 1.09 | 1.01 | 1.1 | c2 |
| 2018-03-31 | 147 | 44 | $p(fwhm_x^1)+p(xy^1)+p(r^1)$ | 0.97 | 1.0 | 0.97 | c2 |
| 2019-10-08 | 190 | 89 | $p(t^3)+p(fwhm_x^1)+p(r^1)$ | 0.95 | 1.44 | 1.37 | c2 |
| 2019-10-20 | 188 | 90 | $p(t^2)+p(fwhm_x^1)+p(fwhm_y^1)+p(xy^1)+p(r^1)$ | 0.97 | 1.0 | 0.97 | c2 |
| **TRAPPIST-1h** | | | | | | | |
| 2016-10-01 | 174 | 0 | $p(fwhm_x^1)+p(fwhm_y^1)+p(xy^2)$ | 0.93 | 1.7 | 1.59 | c2 |
| 2017-03-18 | 139 | 9 | $p(fwhm_x^1)+p(xy^1)$ | 1.02 | 1.15 | 1.18 | c2 |
| 2017-09-22 | 136 | 19 | $p(xy^1)$ | 0.84 | 1.38 | 1.15 | c1 |
| 2017-10-11 | 156 | 20 | $p(t^1)+p(fwhm_x^1)+p(xy^1)$ | 0.98 | 1.02 | 1.01 | c2 |
| 2018-03-10 | 132 | 28 | $p(xy^1)+p(r^1)$ | 0.88 | 1.35 | 1.18 | c2 |
| 2018-03-29 | 150 | 29 | $p(fwhm_x^1)+p(fwhm_y^1)+p(xy^1)+p(r^1)$ | 0.95 | 1.31 | 1.24&c2 | |
| 2019-10-13 | 180 | 59 | $p(fwhm_x^1)+p(fwhm_y^1)+p(xy^1)$ | 1.05 | 1.0 | 1.05 | c2 |

**Table 4.18** Transit timings and depths obtained from individual analyses of each transit. Blended and partial transits are presented in a separate table 4.19.

| Epoch | Transit timing + 1$\sigma$ error [$BJD_{TDB} - 2450000$] | | Transit depth + 1$\sigma$ error (%) | | Channel |
|---|---|---|---|---|---|
| **TRAPPIST-1b** | | | | | |
| 78 | 7440.36499 | 0.00019 | 0.75 | 0.031 | c2 |
| 86 | 7452.45225 | 0.00017 | 0.759 | 0.028 | c2 |
| 93 | 7463.02846 | 0.00019 | 0.684 | 0.025 | c2 |
| 218 | 7651.88731 | 0.0002 | 0.759 | 0.035 | c2 |
| 219 | 7653.39799 | 0.00027 | 0.696 | 0.034 | c2 |
| 222 | 7657.93126 | 0.00023 | 0.728 | 0.034 | c2 |
| 224 | 7660.95216 | 0.00017 | 0.689 | 0.031 | c2 |
| 225 | 7662.46363 | 0.00027 | 0.717 | 0.038 | c2 |
| 228 | 7666.99561 | 0.00013 | 0.702 | 0.022 | c2 |
| 229 | 7668.50665 | 0.00018 | 0.725 | 0.027 | c2 |
| 230 | 7670.01776 | 0.00018 | 0.727 | 0.027 | c2 |
| 318 | 7802.9756 | 0.00015 | 0.753 | 0.025 | c2 |
| 320 | 7805.99698 | 0.00014 | 0.705 | 0.024 | c2 |
| 321 | 7807.50727 | 0.00017 | 0.714 | 0.029 | c2 |
| 322 | 7809.01832 | 0.0002 | 0.749 | 0.023 | c1 |
| 324 | 7812.04041 | 0.00019 | 0.695 | 0.028 | c2 |
| 325 | 7813.55125 | 0.00014 | 0.713 | 0.025 | c2 |
| 326 | 7815.06275 | 0.00019 | 0.726 | 0.025 | c1 |
| 327 | 7816.57335 | 0.00012 | 0.666 | 0.021 | c1 |
| 328 | 7818.08384 | 0.00015 | 0.715 | 0.026 | c2 |
| 329 | 7819.59477 | 0.00018 | 0.705 | 0.029 | c1 |
| 330 | 7821.10556 | 0.00015 | 0.72 | 0.026 | c1 |
| 332 | 7824.12734 | 0.00016 | 0.734 | 0.028 | c2 |
| 333 | 7825.63815 | 0.00014 | 0.731 | 0.027 | c1 |
| 334 | 7828.66083 | 0.00017 | 0.74 | 0.031 | c1 |
| 335 | 7828.66036 | 0.00023 | 0.728 | 0.03 | c1 |
| 338 | 7833.19286 | 0.00017 | 0.658 | 0.024 | c1 |
| 339 | 7834.70398 | 0.00014 | 0.694 | 0.018 | c1 |
| 341 | 7837.72528 | 0.00014 | 0.741 | 0.028 | c1 |
| 342 | 7839.23684 | 0.00022 | 0.792 | 0.033 | c1 |
| 455 | 8009.96629 | 0.00024 | 0.701 | 0.024 | c1 |
| 456 | 8011.47742 | 0.00024 | 0.695 | 0.031 | c1 |
| 457 | 8012.98805 | 0.00012 | 0.707 | 0.02 | c1 |
| 458 | 8014.49882 | 0.00017 | 0.68 | 0.028 | c1 |
| 459 | 8016.0104 | 0.00014 | 0.782 | 0.023 | c1 |
| 460 | 8017.52126 | 0.00023 | 0.712 | 0.029 | c1 |
| 462 | 8020.54237 | 0.00013 | 0.739 | 0.021 | c1 |
| 465 | 8025.0754 | 0.0002 | 0.711 | 0.027 | c1 |
| 467 | 8028.09738 | 0.0002 | 0.686 | 0.028 | c1 |
| 468 | 8029.60816 | 0.00016 | 0.703 | 0.029 | c1 |
| 472 | 8035.65155 | 0.00023 | 0.757 | 0.038 | c1 |
| 473 | 8037.16251 | 0.00023 | 0.71 | 0.03 | c1 |
| 475 | 8040.18429 | 0.00015 | 0.727 | 0.021 | c1 |
| 476 | 8041.69509 | 0.00014 | 0.709 | 0.021 | c1 |
| 477 | 8043.20589 | 0.00012 | 0.708 | 0.028 | c1 |
| 478 | 8044.71651 | 0.00015 | 0.754 | 0.027 | c1 |
| 479 | 8046.22749 | 0.00016 | 0.736 | 0.025 | c1 |
| 572 | 8186.74006 | 0.00018 | 0.782 | 0.028 | c2 |
| 573 | 8188.25135 | 0.00016 | 0.738 | 0.027 | c2 |
| 579 | 8197.31644 | 0.00021 | 0.699 | 0.03 | c2 |
| 583 | 8203.35999 | 0.00017 | 0.701 | 0.033 | c2 |
| 950 | 8757.85509 | 0.0002 | 0.784 | 0.028 | c2 |
| 956 | 8766.92066 | 0.00018 | 0.656 | 0.027 | c2 |
| 958 | 8769.94191 | 0.00016 | 0.786 | 0.026 | c2 |

**Table 4.18** continued.

| Epoch | Transit timing + 1$\sigma$ error [$BJD_{TDB} - 2450000$] | | Transit depth + 1$\sigma$ error (%) | | Channel |
|---|---|---|---|---|---|
| **TRAPPIST-1c** | | | | | |
| 70 | 7452.33467 | 0.00015 | 0.714 | 0.028 | c2 |
| 152 | 7650.92394 | 0.00024 | 0.698 | 0.029 | c2 |
| 153 | 7653.34548 | 0.00017 | 0.69 | 0.021 | c2 |
| 154 | 7655.768 | 0.00038 | 0.676 | 0.046 | c2 |
| 155 | 7658.18964 | 0.00022 | 0.685 | 0.03 | c2 |
| 157 | 7663.03331 | 0.00038 | 0.719 | 0.041 | c2 |
| 159 | 7667.87729 | 0.00017 | 0.69 | 0.023 | c2 |
| 160 | 7670.29871 | 0.00019 | 0.733 | 0.022 | c2 |
| 215 | 7803.49754 | 0.00017 | 0.675 | 0.025 | c2 |
| 216 | 7805.91881 | 0.00015 | 0.642 | 0.026 | c2 |
| 217 | 7808.3412 | 0.00026 | 0.689 | 0.03 | c2 |
| 218 | 7810.76281 | 0.00019 | 0.668 | 0.027 | c2 |
| 219 | 7813.18456 | 0.00024 | 0.669 | 0.024 | c2 |
| 220 | 7815.60585 | 0.00017 | 0.72 | 0.025 | c2 |
| 221 | 7818.02833 | 0.00018 | 0.75 | 0.028 | c2 |
| 222 | 7820.45018 | 0.00018 | 0.688 | 0.023 | c2 |
| 223 | 7822.87186 | 0.00021 | 0.757 | 0.028 | c2 |
| 224 | 7825.29382 | 0.0002 | 0.694 | 0.023 | c2 |
| 225 | 7827.71521 | 0.00015 | 0.73 | 0.021 | c2 |
| 227 | 7832.55892 | 0.00014 | 0.73 | 0.026 | c2 |
| 228 | 7834.98115 | 0.00023 | 0.689 | 0.028 | c2 |
| 229 | 7837.40276 | 0.00017 | 0.713 | 0.024 | c2 |
| 230 | 7839.8241 | 0.00025 | 0.686 | 0.043 | c2 |
| 301 | 8011.7715 | 0.00036 | 0.681 | 0.044 | c2 |
| 302 | 8014.19267 | 0.0002 | 0.735 | 0.027 | c1 |
| 305 | 8021.45847 | 0.00017 | 0.75 | 0.025 | c2 |
| 306 | 8023.87959 | 0.00021 | 0.715 | 0.028 | c1 |
| 310 | 8033.56753 | 0.00017 | 0.738 | 0.026 | c2 |
| 312 | 8038.41064 | 0.00028 | 0.712 | 0.035 | c1 |
| 313 | 8040.83258 | 0.00032 | 0.779 | 0.052 | c2 |
| 314 | 8043.25402 | 0.00017 | 0.739 | 0.024 | c1 |
| 315 | 8045.67653 | 0.00017 | 0.762 | 0.027 | c1 |
| 375 | 8190.98264 | 0.00022 | 0.675 | 0.023 | c1 |
| 380 | 8203.09199 | 0.0002 | 0.698 | 0.028 | c2 |
| 381 | 8205.51293 | 0.00021 | 0.748 | 0.027 | c1 |
| 609 | 8757.6834 | 0.00019 | 0.696 | 0.024 | c2 |
| 612 | 8764.94945 | 0.00024 | 0.719 | 0.032 | c2 |
| 614 | 8769.79254 | 0.00018 | 0.619 | 0.03 | c2 |
| 617 | 8777.0583 | 0.00021 | 0.699 | 0.024 | c2 |
| **TRAPPIST-1d** | | | | | |
| -4 | 7653.94267 | 0.00036 | 0.437 | 0.031 | c2 |
| -3 | 7657.99196 | 0.00054 | 0.324 | 0.025 | c2 |
| -2 | 7662.04263 | 0.00063 | 0.397 | 0.037 | c2 |
| -1 | 7666.09187 | 0.00048 | 0.35 | 0.03 | c2 |
| 0 | 7670.14194 | 0.00039 | 0.359 | 0.029 | c2 |
| 33 | 7803.79084 | 0.00046 | 0.367 | 0.019 | c2 |
| 34 | 7807.8403 | 0.0003 | 0.385 | 0.02 | c2 |
| 35 | 7811.89102 | 0.00039 | 0.388 | 0.021 | c2 |
| 36 | 7815.94061 | 0.00029 | 0.349 | 0.018 | c2 |
| 37 | 7819.99047 | 0.00054 | 0.313 | 0.02 | c2 |
| 38 | 7824.04153 | 0.00079 | 0.395 | 0.023 | c2 |
| 39 | 7828.0908 | 0.00034 | 0.375 | 0.028 | c2 |
| 40 | 7832.14042 | 0.00028 | 0.334 | 0.023 | c2 |
| 85 | 8014.37932 | 0.00095 | 0.329 | 0.031 | c1 |
| 87 | 8022.48021 | 0.00038 | 0.364 | 0.028 | c1 |

**Table 4.18** continued.

| Epoch | Transit timing + 1$\sigma$ error [$BJD_{TDB} - 2450000$] | | Transit depth + 1$\sigma$ error (%) | | Channel |
|---|---|---|---|---|---|
| 90 | 8022.47826 | 0.00033 | 0.354 | 0.025 | c1 |
| 92 | 8042.72676 | 0.00047 | 0.362 | 0.032 | c1 |
| 93 | 8046.77637 | 0.00028 | 0.376 | 0.023 | c2 |
| 127 | 8184.45805 | 0.00043 | 0.386 | 0.027 | c2 |
| 133 | 8208.75644 | 0.0005 | 0.333 | 0.029 | c2 |
| **TRAPPIST-1e** | | | | | |
| -1 | 7654.27853 | 0.00042 | 0.573 | 0.043 | c2 |
| 0 | 7660.3803 | 0.00026 | 0.507 | 0.018 | c2 |
| 24 | 7806.75764 | 0.00047 | 0.46 | 0.03 | c2 |
| 25 | 7812.85751 | 0.00032 | 0.447 | 0.018 | c2 |
| 26 | 7818.95509 | 0.0003 | 0.478 | 0.022 | c2 |
| 27 | 7825.05304 | 0.00035 | 0.439 | 0.025 | c2 |
| 28 | 7831.15206 | 0.00025 | 0.521 | 0.019 | c2 |
| 29 | 7837.2497 | 0.00027 | 0.503 | 0.019 | c2 |
| 58 | 8014.13087 | 0.0002 | 0.509 | 0.021 | c2 |
| 59 | 8020.23323 | 0.00023 | 0.485 | 0.019 | c1 |
| 62 | 8038.5351 | 0.00032 | 0.518 | 0.021 | c1 |
| 86 | 8184.94895 | 0.00036 | 0.415 | 0.028 | c1 |
| 87 | 8191.04813 | 0.00051 | 0.475 | 0.033 | c1 |
| 88 | 8197.14651 | 0.00034 | 0.52 | 0.022 | c1 |
| 89 | 8203.24763 | 0.00024 | 0.501 | 0.021 | c2 |
| 180 | 8758.28125 | 0.00053 | 0.498 | 0.034 | c2 |
| 182 | 8770.47845 | 0.00036 | 0.486 | 0.026 | c2 |
| **TRAPPIST-1f** | | | | | |
| -1 | 7662.18743 | 0.42 | 0.605 | 0.03 | c2 |
| 0 | 7671.39266 | 0.00045 | 0.622 | 0.046 | c2 |
| 15 | 7809.47541 | 0.0004 | 0.656 | 0.037 | c2 |
| 16 | 7818.68262 | 0.00028 | 0.633 | 0.021 | c2 |
| 17 | 7827.88676 | 0.00024 | 0.604 | 0.02 | c2 |
| 18 | 7837.10322 | 0.00049 | 0.577 | 0.03 | c2 |
| 38 | 8021.25068 | 0.00021 | 0.623 | 0.019 | c2 |
| 56 | 8186.91882 | 0.00026 | 0.623 | 0.022 | c2 |
| 57 | 8196.12561 | 0.00024 | 0.631 | 0.019 | c2 |
| 58 | 8205.32761 | 0.00027 | 0.668 | 0.029 | c1 |
| 118 | 8757.76211 | 0.00056 | 0.662 | 0.026 | c1 |
| 119 | 8766.96813 | 0.00024 | 0.626 | 0.025 | c2 |
| 121 | 8785.38901 | 0.00022 | 0.671 | 0.018 | c2 |
| **TRAPPIST-1g** | | | | | |
| 0 | 7665.35136 | 0.00048 | 0.602 | 0.036 | c2 |
| 12 | 7813.6068 | 0.00026 | 0.776 | 0.024 | c2 |
| 13 | 7825.96112 | 0.0002 | 0.8 | 0.02 | c2 |
| 14 | 7838.30652 | 0.00026 | 0.706 | 0.024 | c2 |
| 28 | 8011.24018 | 0.0003 | 0.705 | 0.029 | c2 |
| 42 | 8184.21905 | 0.00023 | 0.735 | 0.023 | c1 |
| 44 | 8208.93037 | 0.0002 | 0.716 | 0.019 | c2 |
| 89 | 8764.82751 | 0.00032 | 0.713 | 0.031 | c2 |
| 90 | 8777.17395 | 0.00026 | 0.75 | 0.021 | c2 |
| **TRAPPIST-1h** | | | | | |
| 0 | 7662.55449 | 0.0012 | 0.309 | 0.044 | c2 |
| 9 | 7831.46614 | 0.0006 | 0.342 | 0.02 | c2 |
| 19 | 8019.16844 | 0.0006 | 0.31 | 0.02 | c2 |
| 20 | 8037.93276 | 0.00051 | 0.377 | 0.019 | c1 |
| 28 | 8188.05067 | 0.00052 | 0.361 | 0.025 | c2 |
| 29 | 8206.81914 | 0.00071 | 0.334 | 0.023 | c2 |
| 59 | 8769.83809 | 0.00054 | 0.334 | 0.024 | c2 |

**Table 4.19** Transit timings and depths obtained from individual analyses of each blended or partial transit

| Epoch | **Transit timing + 1$\sigma$ error** [$BJD_{TDB} - 2450000$] | | **Transit depth + 1$\sigma$ error (%)** | | Channel |
|---|---|---|---|---|---|
| **TRAPPIST-1b** | | | | | |
| 226 | 7663.97530 | 0.00120 | 0.642 | 8.300 | c2 |
| 227 | 7665.48546 | 0.00030 | 0.761 | 0.036 | c2 |
| 231 | 7671.52791 | 0.00068 | 0.696 | 0.046 | c2 |
| 336 | 7830.17083 | 0.00020 | 0.729 | 0.035 | c2 |
| 340 | 7836.21439 | 0.00018 | 0.703 | 0.026 | c2 |
| 461 | 8019.03167 | 0.00027 | 0.662 | 0.067 | c1 |
| 464 | 8023.56458 | 0.00015 | 0.847 | 0.028 | c1 |
| 469 | 8031.11892 | 0.00012 | 0.796 | 1.100 | c1 |
| 474 | 8038.67292 | 0.00017 | 0.752 | 0.033 | c1 |
| 566 | 8177.67496 | 0.00027 | 0.707 | 0.027 | c2 |
| **TRAPPIST-1c** | | | | | |
| 71 | 7454.75685 | 0.00058 | 0.680 | 0.030 | c2 |
| 156 | 7660.611680 | 0.00051 | 0.698 | 0.036 | c2 |
| 158 | 7665.45539 | 0.00032 | 0.662 | 0.037 | c2 |
| 226 | 7830.13725 | 0.00024 | 0.733 | 0.034 | c2 |
| 304 | 8019.03635 | 0.00027 | 0.744 | 0.063 | c1 |
| 309 | 8031.14517 | 0.00015 | 0.755 | 0.024 | c1 |
| 311 | 8035.98910 | 0.00017 | 0.688 | 0.023 | c1 |
| 370 | 8178.87407 | 0.00015 | 0.729 | 0.020 | c1 |
| **TRAPPIST-1d** | | | | | |
| 41 | 7836.19171 | 0.00041 | 0.344 | 0.023 | c2 |
| 91 | 8038.67921 | 0.00033 | 0.330 | 0.030 | c1 |
| 130 | 8196.60651 | 0.00065 | 0.413 | 0.030 | c2 |
| **TRAPPIST-1e** | | | | | |
| 85 | 8178.84731 | 0.00019 | 0.536 | 0.017 | c1 |
| **TRAPPIST-1f** | | | | | |
| -2 | 7652.98592 | 0.00035 | 0.743 | 0.050 | c2 |
| 0 | 7671.39268 | 0.00041 | 0.621 | 0.043 | c2 |
| 55 | 8177.71567 | 0.00026 | 0.647 | 0.026 | c2 |
| **TRAPPIST-1g** | | | | | |
| -1 | 7652.99505 | 0.00037 | 0.734132 | 0.051 | c2 |
| 29 | 8023.59087 | 0.00023 | 0.778 | 0.021 | c1 |
| 30 | 8035.94551 | 0.00025 | 0.729 | 0.020 | c1 |
| 43 | 8196.57292 | 0.00031 | 0.750 | 0.026 | c2 |

**Table 4.20** Transit timings and depths obtained from global analyses of each transit with $ddf$ variations allowed for 3.6$\mu$m channel

| Epoch | **Transit timing + 1$\sigma$ error** [$BJD_{TDB} - 2450000$] | | **Transit depth + 1$\sigma$ error (%)** | |
|---|---|---|---|---|
| **TRAPPIST-1b** | | | | |
| 322 | 7809.01833 | 0.00022 | 0.730 | 0.025 |
| 326 | 7815.06277 | 0.00020 | 0.729 | 0.026 |
| 327 | 7816.57334 | 0.00012 | 0.658 | 0.021 |
| 329 | 7819.59475 | 0.00015 | 0.704 | 0.025 |
| 330 | 7821.10556 | 0.00016 | 0.719 | 0.026 |
| 333 | 7825.63814 | 0.00012 | 0.729 | 0.027 |
| 334 | 7827.14996 | 0.00014 | 0.723 | 0.027 |
| 335 | 7828.66039 | 0.00019 | 0.743 | 0.022 |
| 338 | 7833.19283 | 0.00021 | 0.657 | 0.026 |
| 339 | 7834.70397 | 0.00016 | 0.699 | 0.019 |

**Table 4.20** continued.

| Epoch | Transit timing + 1$\sigma$ error [$BJD_{TDB} - 2450000$] | | Transit depth + 1$\sigma$ error (%) | |
|---|---|---|---|---|
| 341 | 7837.72530 | 0.00018 | 0.735 | 0.032 |
| 342 | 7839.23688 | 0.00020 | 0.784 | 0.027 |
| 455 | 8009.96628 | 0.00023 | 0.724 | 0.023 |
| 456 | 8011.47739 | 0.00021 | 0.698 | 0.029 |
| 457 | 8012.98803 | 0.00013 | 0.706 | 0.023 |
| 458 | 8014.49878 | 0.00017 | 0.692 | 0.03 |
| 459 | 8016.01031 | 0.00014 | 0.761 | 0.024 |
| 460 | 8017.52126 | 0.00020 | 0.711 | 0.027 |
| 462 | 8020.54236 | 0.00014 | 0.739 | 0.022 |
| 465 | 8025.07537 | 0.00020 | 0.705 | 0.027 |
| 467 | 8028.09740 | 0.00023 | 0.679 | 0.027 |
| 468 | 8029.60819 | 0.00016 | 0.702 | 0.027 |
| 472 | 8035.65151 | 0.00025 | 0.759 | 0.039 |
| 473 | 8037.16249 | 0.00028 | 0.709 | 0.027 |
| 475 | 8040.18409 | 0.00018 | 0.740 | 0.027 |
| 476 | 8041.6951 | 00.00013 | 0.715 | 0.022 |
| 477 | 8043.20589 | 0.00016 | 0.762 | 0.027 |
| 478 | 8044.71646 | 0.00024 | 0.754 | 0.04 |
| 479 | 8046.22749 | 0.00013 | 0.735 | 0.021 |
| **TRAPPIST-1c** | | | | |
| 302 | 8014.19266 | 0.00021 | 0.734 | 0.024 |
| 306 | 8023.87966 | 0.00020 | 0.701 | 0.029 |
| 312 | 8038.41062 | 0.00024 | 0.707 | 0.034 |
| 314 | 8043.25404 | 0.00021 | 0.737 | 0.025 |
| 315 | 8045.67667 | 0.00037 | 0.762 | 0.049 |
| 375 | 8190.98265 | 0.00021 | 0.674 | 0.021 |
| 381 | 8205.51292 | 0.00023 | 0.731 | 0.027 |
| **TRAPPIST-1d** | | | | |
| 85 | 8014.37913 | 0.00040 | 0.333 | 0.0190 |
| 87 | 8022.48019 | 0.00031 | 0.362 | 0.0200 |
| 90 | 8034.62830 | 0.00031 | 0.323 | 0.0230 |
| 92 | 8042.72672 | 0.00033 | 0.353 | 0.0180 |
| **TRAPPIST-1e** | | | | |
| 58 | 8014.13087 | 0.00024 | 0.513 | 0.022 |
| 59 | 8020.23322 | 0.00024 | 0.463 | 0.016 |
| 62 | 8038.53515 | 0.00032 | 0.513 | 0.020 |
| 86 | 8184.94890 | 0.00032 | 0.439 | 0.025 |
| 87 | 8191.04817 | 0.00052 | 0.507 | 0.026 |
| **TRAPPIST-1f** | | | | |
| 57 | 8196.12562 | 0.00025 | 0.636 | 0.019 |
| 58 | 8205.32761 | 0.00029 | 0.665 | 0.030 |
| **TRAPPIST-1g** | | | | |
| 28 | 8011.24018 | 0.00034 | 0.710 | 0.033 |
| **TRAPPIST-1h** | | | | |
| 19 | 8019.16846 | 0.00064 | 0.312 | 0.021 |

**Table 4.21** Transit timings and depths obtained from global analyses of each transit with *ddf* variations allowed for 4.5$\mu$m channel

| Epoch | Transit timing + 1$\sigma$ error [$BJD_{TDB} - 2450000$] | | Transit depth + 1$\sigma$ error (%) | |
|---|---|---|---|---|
| **TRAPPIST-1b** | | | | |
| 78 | 7440.36517 | 0.00036 | 0.746 | 0.048 |

**Table 4.21** continued.

| Epoch | Transit timing + 1$\sigma$ error [$BJD_{TDB} - 2450000$] | | Transit depth + 1$\sigma$ error (%) | |
|---|---|---|---|---|
| 86 | 7452.45225 | 0.00017 | 0.751 | 0.027 |
| 93 | 7463.02843 | 0.00024 | 0.689 | 0.034 |
| 218 | 7651.88734 | 0.00022 | 0.755 | 0.036 |
| 219 | 7653.39799 | 0.00028 | 0.692 | 0.032 |
| 222 | 7657.93138 | 0.00022 | 0.736 | 0.034 |
| 224 | 7660.95209 | 0.00024 | 0.694 | 0.032 |
| 225 | 7662.46362 | 0.00036 | 0.726 | 0.046 |
| 228 | 7666.99560 | 0.00014 | 0.703 | 0.021 |
| 229 | 7668.50662 | 0.00018 | 0.726 | 0.027 |
| 230 | 7670.01772 | 0.00019 | 0.732 | 0.027 |
| 318 | 7802.97561 | 0.00015 | 0.749 | 0.025 |
| 320 | 7805.99698 | 0.00014 | 0.707 | 0.024 |
| 321 | 7807.50727 | 0.00020 | 0.708 | 0.031 |
| 324 | 7812.04032 | 0.00016 | 0.702 | 0.022 |
| 325 | 7813.55123 | 0.00013 | 0.710 | 0.025 |
| 328 | 7818.08384 | 0.00016 | 0.718 | 0.027 |
| 332 | 7824.12735 | 0.00018 | 0.734 | 0.032 |
| 572 | 8186.74003 | 0.00018 | 0.783 | 0.027 |
| 573 | 8188.25135 | 0.00015 | 0.741 | 0.027 |
| 579 | 8197.31644 | 0.00023 | 0.693 | 0.027 |
| 583 | 8203.36001 | 0.00018 | 0.697 | 0.033 |
| 950 | 8757.85493 | 0.00024 | 0.788 | 0.038 |
| 956 | 8766.92069 | 0.00020 | 0.778 | 0.039 |
| 958 | 8769.94187 | 0.00022 | 0.688 | 0.030 |
| **TRAPPIST-1c** | | | | |
| 70 | 7452.33466 | 0.00014 | 0.711 | 0.027 |
| 152 | 7650.92393 | 0.00027 | 0.699 | 0.033 |
| 153 | 7653.34547 | 0.00022 | 0.690 | 0.030 |
| 154 | 7655.76801 | 0.00051 | 0.673 | 0.047 |
| 155 | 7658.18964 | 0.00023 | 0.679 | 0.029 |
| 157 | 7663.03333 | 0.00040 | 0.709 | 0.039 |
| 159 | 7667.87731 | 0.00018 | 0.687 | 0.021 |
| 160 | 7670.29871 | 0.00019 | 0.727 | 0.023 |
| 215 | 7803.49753 | 0.00018 | 0.664 | 0.025 |
| 216 | 7805.91881 | 0.00017 | 0.636 | 0.030 |
| 217 | 7808.34117 | 0.00028 | 0.681 | 0.030 |
| 218 | 7810.76273 | 0.00019 | 0.673 | 0.031 |
| 219 | 7813.18463 | 0.00037 | 0.689 | 0.033 |
| 220 | 7815.60587 | 0.00019 | 0.721 | 0.029 |
| 221 | 7818.02836 | 0.00029 | 0.745 | 0.039 |
| 222 | 7820.45018 | 0.00018 | 0.681 | 0.022 |
| 223 | 7822.87187 | 0.00026 | 0.753 | 0.030 |
| 224 | 7825.29385 | 0.00035 | 0.707 | 0.039 |
| 225 | 7827.71522 | 0.00016 | 0.726 | 0.021 |
| 227 | 7832.55893 | 0.00019 | 0.733 | 0.036 |
| 228 | 7834.98112 | 0.00024 | 0.687 | 0.028 |
| 229 | 7837.40275 | 0.00019 | 0.704 | 0.025 |
| 230 | 7839.82416 | 0.00029 | 0.683 | 0.047 |
| 301 | 8011.77148 | 0.00032 | 0.668 | 0.040 |
| 305 | 8021.45848 | 0.00017 | 0.750 | 0.025 |
| 310 | 8033.56754 | 0.00018 | 0.732 | 0.029 |
| 313 | 8040.83258 | 0.00035 | 0.653 | 0.046 |
| 380 | 8203.09196 | 0.00021 | 0.696 | 0.029 |
| 609 | 8757.68343 | 0.00021 | 0.690 | 0.028 |
| 612 | 8764.94945 | 0.00023 | 0.615 | 0.042 |
| 614 | 8769.79242 | 0.00028 | 0.641 | 0.041 |

**Table 4.21** continued.

| Epoch | Transit timing + 1$\sigma$ error [$BJD_{TDB} - 2450000$] | | Transit depth + 1$\sigma$ error (%) | |
|---|---|---|---|---|
| 617 | 8777.05833 | 0.00022 | 0.707 | 0.028 |
| **TRAPPIST-1d** | | | | |
| -4 | 7653.94271 | 0.00032 | 0.432 | 0.022 |
| -3 | 7657.99205 | 0.00049 | 0.327 | 0.020 |
| -2 | 7662.04269 | 0.00028 | 0.412 | 0.021 |
| -1 | 7666.09182 | 0.00057 | 0.377 | 0.034 |
| 0 | 7670.14197 | 0.0003 | 0.357 | 0.021 |
| 33 | 7803.79079 | 0.00047 | 0.367 | 0.018 |
| 34 | 7807.84031 | 0.00033 | 0.385 | 0.020 |
| 35 | 7811.89086 | 0.00037 | 0.391 | 0.020 |
| 36 | 7815.94057 | 0.00030 | 0.352 | 0.020 |
| 37 | 7819.99084 | 0.00065 | 0.313 | 0.020 |
| 38 | 7824.04150 | 0.00038 | 0.383 | 0.022 |
| 39 | 7828.09075 | 0.00037 | 0.377 | 0.027 |
| 40 | 7832.14033 | 0.00032 | 0.330 | 0.022 |
| 93 | 8046.77628 | 0.00026 | 0.368 | 0.023 |
| 127 | 8184.45806 | 0.00034 | 0.388 | 0.021 |
| 133 | 8208.75641 | 0.00033 | 0.329 | 0.021 |
| **TRAPPIST-1e** | | | | |
| -1 | 7654.27828 | 0.00049 | 0.567 | 0.044 |
| 0 | 7660.3803 | 0.00027 | 0.504 | 0.018 |
| 24 | 7806.75787 | 0.00045 | 0.449 | 0.030 |
| 25 | 7812.85749 | 0.00033 | 0.445 | 0.019 |
| 26 | 7818.95509 | 0.00031 | 0.476 | 0.022 |
| 27 | 7825.05294 | 0.00053 | 0.452 | 0.032 |
| 28 | 7831.15205 | 0.00028 | 0.521 | 0.021 |
| 29 | 7837.24969 | 0.00027 | 0.500 | 0.019 |
| 88 | 8197.14652 | 0.00036 | 0.521 | 0.022 |
| 89 | 8203.24762 | 0.00025 | 0.498 | 0.020 |
| 180 | 8758.28132 | 0.00048 | 0.496 | 0.038 |
| 182 | 8770.47851 | 0.00032 | 0.486 | 0.025 |
| **TRAPPIST-1f** | | | | |
| -1 | 7662.18741 | 0.00044 | 0.606 | 0.030 |
| 0 | 7671.39267 | 0.00045 | 0.62 | 0.044 |
| 15 | 7809.47544 | 0.00039 | 0.662 | 0.034 |
| 16 | 7818.68262 | 0.00031 | 0.632 | 0.023 |
| 17 | 7827.88679 | 0.00027 | 0.598 | 0.021 |
| 18 | 7837.10323 | 0.00046 | 0.567 | 0.027 |
| 38 | 8021.25084 | 0.00030 | 0.627 | 0.027 |
| 56 | 8186.91882 | 0.00025 | 0.618 | 0.020 |
| 118 | 8757.76211 | 0.00026 | 0.645 | 0.022 |
| 119 | 8766.96815 | 0.00029 | 0.576 | 0.070 |
| 121 | 8785.38907 | 0.00021 | 0.673 | 0.018 |
| **TRAPPIST-1g** | | | | |
| 0 | 7665.35136 | 0.0005 | 0.696 | 0.024 |
| 12 | 7813.60685 | 0.00025 | 0.605 | 0.037 |
| 13 | 7825.96111 | 0.00021 | 0.772 | 0.024 |
| 14 | 7838.30656 | 0.00027 | 0.793 | 0.018 |
| 42 | 8184.21900 | 0.00037 | 0.784 | 0.032 |
| 44 | 8208.93034 | 0.00018 | 0.727 | 0.019 |
| 89 | 8764.82746 | 0.00035 | 0.701 | 0.038 |
| 90 | 8777.17382 | 0.00033 | 0.687 | 0.045 |
| **TRAPPIST-1h** | | | | |
| 0 | 7662.55444 | 0.0019 | 0.307 | 0.045 |
| 9 | 7831.46615 | 0.0006 | 0.343 | 0.021 |
| 20 | 8037.93277 | 0.00052 | 0.376 | 0.019 |

**Table 4.21** continued.

| Epoch | Transit timing + 1$\sigma$ error [$BJD_{TDB} - 2450000$] | | Transit depth + 1$\sigma$ error (%) | |
|---|---|---|---|---|
| 28 | 8188.05070 | 0.00059 | 0.360 | 0.024 |
| 29 | 8206.81913 | 0.00075 | 0.333 | 0.022 |
| 59 | 8769.83900 | 0.00077 | 0.313 | 0.059 |

**Table 4.22** Transit timings and transit timing variation calculated as the difference of the transit timing from the value given by the linear regression calculated with the reference timing, the period of the planet, and the epoch of the transit.

| Transit timing + 1$\sigma$ error [$BJD_{TDB} - 2450000$] | | TTV + 1$\sigma$ error (min) | | Channel |
|---|---|---|---|---|
| **TRAPPIST-1b** | | | | |
| 7440.36516 | 0.00037 | 0.37 | 0.53 | c2 |
| 7452.45228 | 0.00018 | 0.53 | 0.26 | c2 |
| 7463.02844 | 0.00023 | 0.58 | 0.33 | c2 |
| 7651.88733 | 0.00022 | -0.37 | 0.32 | c2 |
| 7653.39799 | 0.00034 | -0.68 | 0.49 | c2 |
| 7657.93137 | 0.00021 | 0.4 | 0.3 | c2 |
| 7660.95214 | 0.00022 | -1.02 | 0.32 | c2 |
| 7662.46368 | 0.00041 | -0.07 | 0.59 | c2 |
| 7666.99562 | 0.00013 | -1.06 | 0.19 | c2 |
| 7668.50666 | 0.00019 | -0.82 | 0.27 | c2 |
| 7670.01776 | 0.00019 | -0.5 | 0.27 | c2 |
| 7802.97561 | 0.00016 | 0.55 | 0.23 | c2 |
| 7805.99699 | 0.00015 | 0.02 | 0.22 | c2 |
| 7807.50726 | 0.00017 | -0.86 | 0.24 | c2 |
| 7809.01834 | 0.0002 | -0.56 | 0.29 | c1 |
| 7812.04034 | 0.00016 | -0.21 | 0.23 | c2 |
| 7813.55122 | 0.00015 | -0.2 | 0.22 | c2 |
| 7815.06274 | 0.0002 | 0.73 | 0.29 | c1 |
| 7816.57338 | 0.00019 | 0.38 | 0.27 | c1 |
| 7818.08384 | 0.00016 | -0.22 | 0.23 | c2 |
| 7819.59475 | 0.00021 | -0.17 | 0.3 | c1 |
| 7821.10555 | 0.00018 | -0.27 | 0.26 | c1 |
| 7824.12732 | 0.00017 | -0.25 | 0.24 | c2 |
| 7825.63815 | 0.00014 | -0.32 | 0.2 | c1 |
| 7827.14995 | 0.00012 | 1.01 | 0.17 | c1 |
| 7828.66035 | 0.00023 | 0.33 | 0.33 | c1 |
| 7833.19292 | 0.00024 | 0.24 | 0.35 | c1 |
| 7834.70398 | 0.00015 | 0.5 | 0.22 | c1 |
| 7837.72528 | 0.00017 | -0.15 | 0.24 | c1 |
| 7839.23687 | 0.00035 | 0.89 | 0.5 | c1 |
| 8009.96629 | 0.00021 | 1.44 | 0.3 | c1 |
| 8011.47739 | 0.00021 | 1.77 | 0.3 | c1 |
| 8012.98805 | 0.00012 | 1.46 | 0.17 | c1 |
| 8014.49881 | 0.00019 | 1.29 | 0.27 | c1 |
| 8016.01032 | 0.00016 | 2.2 | 0.23 | c1 |
| 8017.52125 | 0.0002 | 2.27 | 0.29 | c1 |
| 8020.54237 | 0.00015 | 1.36 | 0.22 | c1 |
| 8025.07536 | 0.0002 | 1.89 | 0.29 | c1 |
| 8028.09734 | 0.00029 | 2.21 | 0.42 | c1 |
| 8029.60817 | 0.00016 | 2.14 | 0.23 | c1 |
| 8035.65153 | 0.00029 | 1.93 | 0.42 | c1 |
| 8037.16248 | 0.00024 | 2.04 | 0.35 | c1 |

**Table 4.22** continued.

| **Transit timing + 1$\sigma$ error** [$BJD_{TDB} - 2450000$] | | **TTV + 1$\sigma$ error (min)** | | **Channel** |
|---|---|---|---|---|
| 8040.18409 | 0.00017 | 1.84 | 0.24 | c1 |
| 8041.6951 | 0.00013 | 2.03 | 0.19 | c1 |
| 8043.20589 | 0.00017 | 1.9 | 0.24 | c1 |
| 8044.71648 | 0.00016 | 1.5 | 0.23 | c1 |
| 8046.22747 | 0.00013 | 1.66 | 0.19 | c1 |
| 8186.74006 | 0.00031 | 3.22 | 0.45 | c2 |
| 8188.25135 | 0.00017 | 3.82 | 0.24 | c2 |
| 8197.31645 | 0.00021 | 3.58 | 0.3 | c2 |
| 8203.35999 | 0.00016 | 3.63 | 0.23 | c2 |
| 8757.85481 | 0.00032 | 8.23 | 0.46 | c2 |
| 8766.92065 | 0.00019 | 9.08 | 0.27 | c2 |
| 8769.94192 | 0.00017 | 8.38 | 0.24 | c2 |
| **TRAPPIST-1c** | | | | |
| 7452.33468 | 0.00014 | -3.24 | 0.2 | c2 |
| 7650.92393 | 0.00022 | -0.09 | 0.32 | c2 |
| 7653.3455 | 0.0002 | -0.41 | 0.29 | c2 |
| 7655.76806 | 0.00023 | 0.69 | 0.33 | c2 |
| 7658.18964 | 0.0002 | 0.38 | 0.29 | c2 |
| 7663.0333 | 0.00031 | 0.49 | 0.45 | c2 |
| 7667.8773 | 0.00017 | 1.08 | 0.24 | c2 |
| 7670.29872 | 0.00017 | 0.55 | 0.24 | c2 |
| 7803.49753 | 0.00017 | 0.79 | 0.24 | c2 |
| 7805.91883 | 0.00018 | 0.08 | 0.26 | c2 |
| 7808.34124 | 0.00022 | 0.97 | 0.32 | c2 |
| 7810.76274 | 0.00018 | 0.54 | 0.26 | c2 |
| 7813.18458 | 0.00026 | 0.61 | 0.37 | c2 |
| 7815.60585 | 0.00018 | -0.14 | 0.26 | c2 |
| 7818.02835 | 0.00018 | 0.88 | 0.26 | c2 |
| 7820.4502 | 0.00018 | 0.96 | 0.26 | c2 |
| 7822.87188 | 0.00021 | 0.79 | 0.3 | c2 |
| 7825.2938 | 0.0002 | 0.98 | 0.29 | c2 |
| 7827.71523 | 0.00018 | 0.45 | 0.26 | c2 |
| 7832.55892 | 0.00015 | 0.6 | 0.22 | c2 |
| 7834.98113 | 0.0002 | 1.2 | 0.29 | c2 |
| 7837.40274 | 0.00018 | 0.94 | 0.26 | c2 |
| 7839.8241 | 0.00018 | 0.31 | 0.26 | c2 |
| 8011.77142 | 0.00022 | 0.29 | 0.32 | c2 |
| 8014.19266 | 0.00016 | -0.51 | 0.23 | c1 |
| 8021.45845 | 0.00017 | 0.08 | 0.24 | c2 |
| 8023.87965 | 0.00018 | -0.77 | 0.26 | c1 |
| 8033.56754 | 0.00017 | 0.26 | 0.24 | c2 |
| 8038.41063 | 0.0002 | -0.46 | 0.29 | c1 |
| 8040.83248 | 0.00024 | -0.38 | 0.35 | c2 |
| 8043.25404 | 0.00016 | -0.71 | 0.23 | c1 |
| 8045.67663 | 0.00023 | 0.44 | 0.33 | c1 |
| 8190.98262 | 0.00024 | -1.9 | 0.35 | c1 |
| 8203.09199 | 0.00019 | -1.32 | 0.27 | c2 |
| 8205.51296 | 0.00019 | -2.5 | 0.27 | c1 |
| 8757.68344 | 0.00019 | -0.24 | 0.27 | c2 |
| 8764.94941 | 0.0002 | 0.61 | 0.29 | c2 |
| 8769.79241 | 0.00018 | -0.24 | 0.26 | c2 |
| 8777.05833 | 0.00019 | 0.54 | 0.27 | c2 |
| **TRAPPIST-1d** | | | | |
| 7653.9427 | 0.00042 | -6.45 | 0.6 | c2 |
| 7657.99196 | 0.00069 | -7.2 | 0.99 | c2 |
| 7662.04264 | 0.00076 | -5.9 | 1.09 | c2 |

**Table 4.22** continued.

| **Transit timing + 1$\sigma$ error** [$BJD_{TDB} - 2450000$] | | **TTV + 1$\sigma$ error (min)** | | **Channel** |
|---|---|---|---|---|
| 7666.09183 | 0.00054 | -6.76 | 0.78 | c2 |
| 7670.14193 | 0.00037 | -6.3 | 0.53 | c2 |
| 7803.79081 | 0.00045 | 2.53 | 0.65 | c2 |
| 7807.84029 | 0.00032 | 2.1 | 0.46 | c2 |
| 7811.891 | 0.00049 | 3.44 | 0.71 | c2 |
| 7815.94059 | 0.0003 | 3.16 | 0.43 | c2 |
| 7819.99043 | 0.00071 | 3.25 | 1.02 | c2 |
| 7824.0417 | 0.0011 | 5.39 | 1.58 | c2 |
| 7828.09082 | 0.00036 | 4.44 | 0.52 | c2 |
| 7832.1404 | 0.00034 | 4.15 | 0.49 | c2 |
| 8014.37954 | 0.00099 | 2.75 | 1.43 | c1 |
| 8022.48021 | 0.00044 | 4.35 | 0.63 | c1 |
| 8034.62828 | 0.00041 | 2.52 | 0.59 | c1 |
| 8042.72684 | 0.00049 | 1.08 | 0.71 | c1 |
| 8046.77634 | 0.00032 | 0.67 | 0.46 | c2 |
| 8184.45808 | 0.00056 | -14.87 | 0.81 | c2 |
| 8208.75643 | 0.00065 | -15.35 | 0.94 | c2 |
| **TRAPPIST-1e** | | | | |
| 7654.27839 | 0.00053 | 2.4 | 0.76 | c2 |
| 7660.3803 | 0.00037 | 18.2 | 0.53 | c2 |
| 7806.75784 | 0.00044 | 0.9 | 0.63 | c2 |
| 7812.85752 | 0.00044 | 1.06 | 0.63 | c2 |
| 7818.95511 | 0.00032 | -1.78 | 0.46 | c2 |
| 7825.05293 | 0.00048 | -4.29 | 0.69 | c2 |
| 7831.15209 | 0.0003 | -4.88 | 0.43 | c2 |
| 7837.24972 | 0.00028 | -7.66 | 0.4 | c2 |
| 8014.13085 | 0.00021 | -16.66 | 0.3 | c2 |
| 8020.23322 | 0.00024 | -12.62 | 0.35 | c2 |
| 8038.53517 | 0.00036 | -7.93 | 0.52 | c1 |
| 8184.94893 | 0.00032 | 26.92 | 0.46 | c1 |
| 8191.04818 | 0.00058 | 26.47 | 0.84 | c1 |
| 8197.14657 | 0.0004 | 24.78 | 0.58 | c1 |
| 8203.24765 | 0.00026 | 26.96 | 0.37 | c1 |
| 8758.28133 | 0.00047 | -11.51 | 0.68 | c2 |
| 8770.47849 | 0.00032 | -14.35 | 0.46 | c2 |
| **TRAPPIST-1f** | | | | |
| 7662.18742 | 0.00043 | 29.21 | 0.62 | c2 |
| 7671.39269 | 0.00044 | 27.3 | 0.63 | c2 |
| 7809.47546 | 0.00046 | 4.06 | 0.66 | c2 |
| 7818.68263 | 0.00027 | 4.89 | 0.39 | c2 |
| 7827.88681 | 0.00029 | 1.41 | 0.42 | c2 |
| 7837.10334 | 0.00053 | 15.72 | 0.76 | c2 |
| 8021.25083 | 0.00025 | 38.2 | 0.36 | c2 |
| 8186.91883 | 0.00025 | -34.8 | 0.36 | c2 |
| 8196.12562 | 0.00025 | -34.51 | 0.36 | c2 |
| 8205.32762 | 0.00028 | -41.13 | 0.4 | c2 |
| 8757.76211 | 0.00027 | 14.82 | 0.39 | c1 |
| 8766.96815 | 0.0003 | 14.02 | 0.43 | c1 |
| 8785.38907 | 0.00035 | 25.15 | 0.5 | c2 |
| **TRAPPIST-1g** | | | | |
| 7665.35141 | 0.00086 | -16.46 | 1.24 | c2 |
| 7813.60688 | 0.00026 | 1.97 | 0.37 | c2 |
| 7825.96111 | 0.00022 | 2.94 | 0.32 | c2 |
| 7838.30658 | 0.00028 | -8.7 | 0.4 | c2 |
| 8011.24017 | 0.00031 | -32.02 | 0.45 | c2 |
| 8184.219 | 0.00054 | 9.82 | 0.78 | c2 |

**Table 4.22** continued.

| Transit timing + 1$\sigma$ error [$BJD_{TDB} - 2450000$] | | TTV + 1$\sigma$ error (min) | | Channel |
|---|---|---|---|---|
| 8208.93033 | 0.00018 | 15.89 | 0.26 | c1 |
| 8764.82748 | 0.00031 | -2.63 | 0.45 | c2 |
| 8777.17377 | 0.00033 | -13.09 | 0.48 | c2 |
| **TRAPPIST-1h** | | | | |
| 7662.55448 | 0.0016 | -28.32 | 2.3 | c2 |
| 7831.46617 | 0.0006 | -19.37 | 0.86 | c2 |
| 8019.16844 | 0.00058 | 23.15 | 0.84 | c2 |
| 8037.93275 | 0.0006 | 18.88 | 0.86 | c2 |
| 8188.05076 | 0.00057 | -10.19 | 0.82 | c1 |
| 8206.81914 | 0.00073 | -8.59 | 1.05 | c2 |
| 8769.83907 | 0.00083 | -6.15 | 1.2 | c2 |

**Table 4.23** Median values ($median_{in}$, $median_{out}$) and median absolute deviations ($\sigma_{in}$ and $\sigma_{out}$) of the residuals in and out of transit, using the residuals from the global analyses planet-by-planet. The last column gives the significance of the difference between $median_{in}$ and $median_{out}$, computed as $\frac{|median_{in} - median_{out}|}{\sqrt{\sigma_{out}^2 + \sigma_{in}^2}}$

| Epoch | $median_{in}$ [ppm] | $\sigma_{in}$ [ppm] | $median_{out}$ [ppm] | $\sigma_{out}$ [ppm] | Significance | Channel |
|---|---|---|---|---|---|---|
| **TRAPPIST-1b** | | | | | | |
| 78 | 348 | 649 | 44 | 630 | 0.19 | c2 |
| 86 | 59 | 396 | 17 | 620 | 0.64 | c2 |
| 93 | -168 | 477 | 40 | 590 | 0.69 | c2 |
| 218 | -207 | 389 | 6 | 555 | 0.16 | c2 |
| 219 | 247 | 446 | 8 | 644 | 0.45 | c2 |
| 222 | -363 | 939 | 178 | 591 | 0.21 | c2 |
| 224 | -245 | 384 | -83 | 599 | 0.01 | c2 |
| 225 | 20 | 1076 | -8 | 535 | 0.4 | c2 |
| 228 | 199 | 367 | -4 | 565 | 0.28 | c2 |
| 229 | 308 | 646 | -49 | 513 | 0.18 | c2 |
| 230 | 11 | 596 | 41 | 574 | 0.11 | c2 |
| 318 | -99 | 478 | -22 | 560 | 0.01 | c2 |
| 320 | 185 | 696 | -121 | 428 | 0.02 | c2 |
| 321 | -122 | 549 | 12 | 577 | 0.45 | c2 |
| 322 | -31 | 347 | -154 | 545 | 0.45 | c1 |
| 324 | -14 | 526 | -62 | 458 | 0.55 | c2 |
| 325 | 158 | 406 | 12 | 562 | 0.03 | c2 |
| 326 | -379 | 504 | 75 | 502 | 0.65 | c1 |
| 327 | 337 | 393 | -180 | 632 | 0.12 | c1 |
| 328 | -256 | 515 | 73 | 516 | 0.07 | c2 |
| 329 | -59 | 656 | 80 | 542 | 0.29 | c1 |
| 330 | 214 | 504 | -130 | 574 | 0.21 | c1 |
| 332 | 90 | 550 | -158 | 814 | 0.04 | c2 |
| 333 | -6 | 416 | 117 | 424 | 0.2 | c1 |
| 334 | -15 | 535 | -5 | 484 | 0.5 | c1 |
| 335 | 103 | 478 | -196 | 563 | 0.26 | c1 |
| 338 | -178 | 386 | 14 | 555 | 0.38 | c1 |
| 339 | -72 | 269 | 17 | 428 | 0.23 | c1 |
| 341 | 45 | 426 | 113 | 436 | 0.28 | c1 |
| 342 | 118 | 558 | 126 | 356 | 0.34 | c1 |
| 455 | 49 | 480 | 36 | 410 | 0.06 | c1 |
| 456 | 278 | 401 | -22 | 528 | 0.27 | c1 |

**Table 4.23** continued.

| Epoch | $median_{in}$ [ppm] | $\sigma_{in}$ [ppm] | $median_{out}$ [ppm] | $\sigma_{out}$ [ppm] | Significance | Channel |
|---|---|---|---|---|---|---|
| 457 | 126 | 420 | -132 | 383 | 0.31 | c1 |
| 458 | -266 | 472 | 146 | 590 | 0.31 | c1 |
| 459 | -94 | 380 | -110 | 518 | 0.49 | c1 |
| 460 | -290 | 427 | 125 | 480 | 0.23 | c1 |
| 462 | 26 | 401 | -42 | 410 | 0.02 | c1 |
| 465 | -54 | 650 | -114 | 538 | 0.3 | c1 |
| 467 | 95 | 444 | -89 | 458 | 0.43 | c1 |
| 468 | 34 | 372 | 164 | 479 | 0.04 | c1 |
| 472 | 87 | 299 | 111 | 475 | 0.1 | c1 |
| 473 | -30 | 404 | 92 | 456 | 0.37 | c1 |
| 475 | 42 | 442 | -243 | 365 | 0.17 | c1 |
| 476 | 3 | 424 | -169 | 515 | 0.07 | c1 |
| 477 | -226 | 464 | 5 | 388 | 0.21 | c1 |
| 478 | 152 | 354 | 2 | 553 | 0.45 | c1 |
| 479 | 126 | 568 | -78 | 458 | 0.25 | c1 |
| 572 | 17 | 304 | 69 | 476 | 0.09 | c2 |
| 573 | 180 | 486 | -21 | 550 | 0.27 | c2 |
| 579 | -111 | 641 | 164 | 516 | 0.33 | c2 |
| 583 | 237 | 649 | -160 | 576 | 0.46 | c2 |
| 950 | -82 | 613 | 203 | 573 | 0.34 | c2 |
| 956 | -20 | 518 | 34 | 641 | 0.33 | c2 |
| 958 | 92 | 528 | -165 | 582 | 0.06 | c2 |
| **TRAPPIST-1c** | | | | | | |
| 70 | 111 | 344 | -26 | 718 | 0.02 | c2 |
| 152 | -243 | 418 | 62 | 586 | 0.27 | c2 |
| 153 | -223 | 420 | 112 | 475 | 0.07 | c2 |
| 154 | 220 | 561 | -76 | 645 | 0.45 | c2 |
| 155 | 107 | 563 | 22 | 644 | 0.04 | c2 |
| 157 | 701 | 782 | -124 | 761 | 0.41 | c2 |
| 159 | 376 | 659 | -21 | 501 | 0.07 | c2 |
| 160 | 14 | 395 | 75 | 531 | 0.17 | c2 |
| 215 | -51 | 660 | 35 | 563 | 0.42 | c2 |
| 216 | 11 | 539 | 99 | 471 | 0.53 | c2 |
| 217 | -185 | 428 | -59 | 831 | 0.35 | c2 |
| 218 | -212 | 393 | -7 | 652 | 0.1 | c2 |
| 219 | -268 | 738 | -14 | 622 | 0.76 | c2 |
| 220 | -15 | 401 | -137 | 697 | 0.48 | c2 |
| 221 | -9 | 552 | -16 | 388 | 0.09 | c2 |
| 222 | -70 | 564 | 24 | 471 | 0.1 | c2 |
| 223 | -98 | 545 | 92 | 666 | 0.12 | c2 |
| 224 | 232 | 556 | -3 | 661 | 0.13 | c2 |
| 225 | 20 | 602 | -78 | 468 | 0.27 | c2 |
| 227 | -16 | 452 | 118 | 690 | 0.26 | c2 |
| 228 | 106 | 594 | 64 | 598 | 0.15 | c2 |
| 229 | 96 | 511 | -82 | 468 | 0.01 | c2 |
| 230 | -30 | 644 | 8 | 586 | 0.13 | c2 |
| 301 | -198 | 721 | -38 | 579 | 0.22 | c2 |
| 302 | -22 | 494 | -37 | 486 | 0.27 | c1 |
| 305 | 124 | 605 | -14 | 726 | 0.13 | c2 |
| 306 | 128 | 395 | -60 | 561 | 0.16 | c1 |
| 310 | -1 | 790 | 6 | 598 | 0.05 | c2 |
| 312 | 20 | 547 | -30 | 425 | 0.26 | c1 |
| 313 | 367 | 676 | -2 | 521 | 0.04 | c2 |
| 314 | 260 | 356 | 3 | 454 | 0.17 | c1 |
| 315 | 44 | 516 | 24 | 283 | 0.15 | c1 |
| 375 | 86 | 274 | -128 | 438 | 0.01 | c1 |
| 380 | -142 | 570 | -3 | 652 | 0.43 | c2 |

**Table 4.23** continued.

| Epoch | $median_{in}$ [ppm] | $\sigma_{in}$ [ppm] | $median_{out}$ [ppm] | $\sigma_{out}$ [ppm] | Significance | Channel |
|---|---|---|---|---|---|---|
| 381 | -30 | 700 | 30 | 534 | 0.16 | c1 |
| 609 | 88 | 708 | -65 | 706 | 0.15 | c2 |
| 612 | -117 | 889 | 22 | 439 | 0.48 | c2 |
| 614 | 376 | 675 | -106 | 730 | 0.14 | c2 |
| 617 | 286 | 816 | -168 | 546 | 0.46 | c2 |
| **TRAPPIST-1d** | | | | | | |
| -4 | -73 | 594 | -24 | 699 | 0.07 | c2 |
| -3 | -14 | 501 | 128 | 565 | 0.29 | c2 |
| -2 | 76 | 824 | 60 | 584 | 0.17 | c2 |
| -1 | -57 | 698 | 56 | 709 | 0.01 | c2 |
| 0 | -96 | 450 | -13 | 519 | 0.05 | c2 |
| 33 | 85 | 647 | 14 | 468 | 0.19 | c2 |
| 34 | 124 | 332 | 61 | 606 | 0.02 | c2 |
| 35 | -105 | 800 | 91 | 532 | 0.11 | c2 |
| 36 | 143 | 490 | 49 | 582 | 0.12 | c2 |
| 37 | 93 | 610 | 33 | 576 | 0.09 | c2 |
| 38 | 196 | 582 | -111 | 653 | 0.09 | c2 |
| 39 | -44 | 510 | 68 | 617 | 0.2 | c2 |
| 40 | 99 | 576 | -60 | 563 | 0.12 | c2 |
| 85 | -144 | 675 | -84 | 516 | 0.07 | c1 |
| 87 | 62 | 326 | -95 | 439 | 0.35 | c1 |
| 90 | 89 | 280 | -3 | 445 | 0.14 | c1 |
| 92 | -24 | 508 | -17 | 483 | 0.2 | c1 |
| 93 | 124 | 632 | -34 | 560 | 0.19 | c2 |
| 127 | 94 | 728 | 26 | 630 | 0.07 | c2 |
| 133 | 344 | 661 | 81 | 586 | 0.3 | c2 |
| **TRAPPIST-1e** | | | | | | |
| -1 | -327 | 544 | 121 | 730 | 0.42 | c2 |
| 0 | -73 | 657 | 67 | 584 | 0.29 | c2 |
| 24 | 70 | 686 | 94 | 580 | 0.06 | c2 |
| 25 | 61 | 505 | 101 | 535 | 0.19 | c2 |
| 26 | 54 | 506 | -26 | 587 | 0.21 | c2 |
| 27 | 19 | 626 | 128 | 682 | 0.16 | c2 |
| 28 | 128 | 653 | 8 | 560 | 0.03 | c2 |
| 29 | -13 | 678 | 176 | 466 | 0.05 | c2 |
| 58 | 258 | 456 | -22 | 479 | 0.1 | c2 |
| 59 | 57 | 420 | -122 | 464 | 0.12 | c1 |
| 62 | 62 | 449 | 20 | 513 | 0.14 | c1 |
| 86 | 72 | 519 | -66 | 501 | 0.23 | c1 |
| 87 | 125 | 399 | -15 | 516 | 0.18 | c1 |
| 88 | -6 | 745 | 158 | 508 | 0.12 | c1 |
| 89 | -147 | 499 | -54 | 562 | 0.01 | c2 |
| 180 | 33 | 815 | 45 | 612 | 0.16 | c2 |
| 182 | -207 | 630 | -80 | 501 | 0.49 | c2 |
| **TRAPPIST-1f** | | | | | | |
| -1 | 37 | 558 | -23 | 559 | 0.1 | c2 |
| 0 | -220 | 824 | -15 | 738 | 0.23 | c2 |
| 15 | -220 | 552 | 12 | 689 | 0.08 | c2 |
| 16 | -75 | 552 | -18 | 558 | 0.19 | c2 |
| 17 | 92 | 536 | 30 | 570 | 0.26 | c2 |
| 18 | -68 | 390 | 38 | 533 | 0.07 | c2 |
| 38 | -36 | 482 | -102 | 438 | 0.08 | c2 |
| 56 | 205 | 555 | -66 | 450 | 0.16 | c2 |
| 57 | -78 | 590 | -8 | 407 | 0.1 | c2 |
| 58 | 82 | 545 | -86 | 502 | 0.38 | c1 |
| 118 | 89 | 386 | 287 | 746 | 0.24 | c1 |

**Table 4.23** continued.

| **Epoch** | $median_{in}$ **[ppm]** | $\sigma_{in}$ **[ppm]** | $median_{out}$ **[ppm]** | $\sigma_{out}$ **[ppm]** | **Significance** | **Channel** |
|---|---|---|---|---|---|---|
| 119 | -3 | 580 | 92 | 555 | 0.12 | c2 |
| 121 | 54 | 534 | -2 | 528 | 0.07 | c2 |
| **TRAPPIST-1g** | | | | | | |
| 0 | -123 | 429 | 75 | 737 | 0.04 | c2 |
| 12 | 46 | 391 | -24 | 597 | 0.23 | c2 |
| 13 | 7 | 590 | 146 | 469 | 0.1 | c2 |
| 14 | -129 | 588 | -7 | 622 | 0.18 | c2 |
| 28 | -74 | 554 | -42 | 480 | 0.14 | c2 |
| 42 | -200 | 569 | 105 | 705 | 0.34 | c1 |
| 44 | -130 | 606 | 6 | 575 | 0.16 | c2 |
| 89 | -59 | 548 | 117 | 643 | 0.21 | c2 |
| 90 | 21 | 358 | 30 | 583 | 0.01 | c2 |
| **TRAPPIST-1h** | | | | | | |
| 0 | -2 | 828 | 178 | 802 | 0.01 | c2 |
| 9 | 12 | 553 | 11 | 584 | 0.16 | c2 |
| 19 | 6 | 549 | -1 | 541 | 0.0 | c2 |
| 20 | 28 | 419 | 99 | 577 | 0.1 | c1 |
| 28 | 1 | 469 | 50 | 517 | 0.07 | c2 |
| 29 | -161 | 484 | -2 | 530 | 0.22 | c2 |
| 59 | 101 | 433 | 358 | 497 | 0.39 | c2 |

# Chapter 5

# Follow-up of the TRAPPIST-1 system with ground-based telescopes

Although the Spitzer campaign was unique and reached a photometric precision that could not be achieved with any other facilities, the current knowledge of the TRAPPIST-1 system also owes a lot to ground-based observations. In this chapter, I focus on multi-band photometric follow-up from the ground. In the first part of this chapter, I show how broad band photometry can be used to observationally constrained the effect of stellar contamination, and I present a related publication I led on TRAPPIST-1 in late 2018. In the second part of this chapter, I present some on-going work I am leading on SPECULOOS and Liverpool telescope data to (1) attempt to derive the photometric variability of TRAPPIST-1 in the I+z band; (2) to use multi-band photometric variability to constrain the nature of the putative active regions on the surface of the star; and (3) to compute transit timings for all seven planets and test how predictive the model by Agol et al. (2020a) is.

## 5.1 Stellar contamination

As mentioned in Chapter 4, TRAPPIST-1 planets are particularly promising candidates for the first thorough atmospheric characterisations of temperate terrestrial worlds with the upcoming James Webb Space Telescope (JWST) (Barstow et al. 2016; Fauchez et al. 2019; Lustig-Yaeger et al. 2019; Morley et al. 2017). However, some studies warned that an inhomogeneous stellar photosphere -as anticipated for red dwarfs like TRAPPIST-1- could strongly complicate the information content of the exoplanets' transmission spectra, limiting the deciphering of their properties (Apai et al. 2018; Rackham et al. 2018). In particular, Zhang et al. (2018) anticipate that the star should be almost entirely covered by spots ($\sim 30\%$)

and faculae (∼ 63%) -essentially a "two-component photosphere"- and predict dramatic (a few dozens of %) chromatic variations of the transit depths, especially in the optical. In the following, after a short introduction on stellar contamination, I present a study that I have led to verify these predictions with empirical results.

### 5.1.1 Introduction

High spatial resolution observations of the Sun enabled astronomers to confirm that the solar atmosphere is everything but homogeneous. The main sources of the heterogeneities in the solar photosphere and chromosphere are high contrast temperature regions that we refer as cool spots and faculae (hot spots). Those heterogeneities are caused by an interplay of plasma flows and the emergence of magnetic fields. Various studies suggest that such heterogeneities are also present in the atmospheres of cooler stars than the Sun, notably UCDS. However, as the fraction of heterogeneities present on the disk averaged stellar profile and their location on the stellar atmosphere varies with time, this creates a photometric and spectral time dependence. The presence of spots or faculae on a star therefore causes manifestations of stellar activity, e.g. brightness and spectral variability. In particular, when a planet transits a cool star, its light curves and/or spectra can be polluted by both occulted (spots or faculae present on the transit chord of the planet) and unocculted spots (spots or faculae located outside of the transit chord).

#### Occulted spots

When a planet passes in front of a starspot (faculae) during its transit, small bumps (deeps) will be detected in the star transit light curve, as illustrate on Figure 5.1. As a consequence, starspot (facula) occultations can decrease (increase) the apparent transit depth and have an impact on multiple transit parameters such as transit mid-time, the scaled orbital semi-major axis, and the orbital inclination. Hopefully, they are some solutions to deal with occulted spots that I briefly detail below:

- The most straightforward solution would be to simply remove the active region occultations from the transit profile but it is unclear what influence this drastic method will have on transit parameters determination. Furthermore, the problem can become more tricky if a multitude of active regions are present on the transit chord.
- Alternatively, one could rely on a transit-starspot model. A diversity of tools have been developed over the years to deal with such problem, among which (not a comprehensive

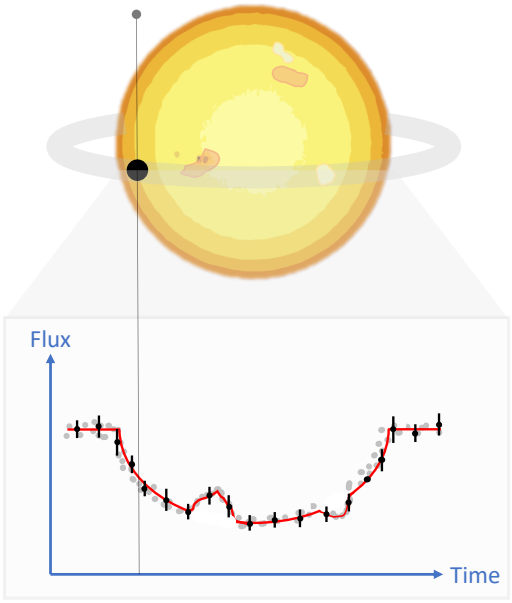


**Fig. 5.1** Illustration of the impact of occulted spots and fauclae on transit light curves. Credit: Elsa Ducrot

list): `PyTranSpot` (Juvan et al. 2018), `ellc` (Maxted 2016), `ECLIPSE` (Silva 2003), `SOAP-T` (Oshagh et al. 2013), `KSint` (Montalto et al. 2014), `STSP` (Morris et al. 2017). Such models usually require integration over a 2D grid of the stellar surface of a synthetic star with limb darkening, spots and/or faculae. The spots (or faculae) are usually simulated as dark (or bright) circles positioned along the transit chord according to their size and intensity. The temperature of the different regions of the stellar surface are generally estimated assuming blackbody emission for both the spots/plages and the stellar photosphere. Unfortunately, these models present several weaknesses. First the models are usually computationally expensively, with the computational time growing as the square of the grid resolution. Second, to simulated realistic spots/faculae, models of stellar magnetic activity should be used to inform priors on spot occultation parameters such as spot contrasts and temperatures. However, such stellar magnetic activity models are just begging to be available for our own Sun and can not be easily extrapolated to other types of stars as the effect of the magnetic field should strongly depend on the fundamental stellar parameters (e.g. mass, age, metallicity, rotation period). In particular, UCDS are clearly not smaller versions of the Sun but, instead, are a fundamentally different class of objects. To this date, still little is known on the nature (time-scales, sizes, temperature/intensity contrasts, shape) of the atmospheric heterogeneities that should be expected on UCDS.

- Finally, the most reliable solution might be to rely on long-term and/or simultaneous multiwavelength monitoring of the host stars during transit to constrain the properties of occulted active regions such as the spot coverage and temperature. In addition, using short-cadence observations to fully resolve the ingress and egress of the transit can also help constraining the planetary radius independently even when the transit is contaminated by significant spot/faculae occultation events, as described by Morris et al. (2018d).

Besides, as the effect of active regions is wavelength dependent, if left uncorrected we can expect them to impact the planetary transmission spectra and thus bias inferences of the properties of the exoplanetary atmosphere. The best example to illustrate this is the case of WASP-19b. Indeed, Sedaghati et al. (2017) reported the first detection of Titanium Oxyde, $TiO$, in the atmosphere of WASP-19b in 2017, whereas in 2019 Espinoza et al. (2019) did not detect any sign of $TiO$ absorption lines. A possible explanation for this inconsistency is that both occulted and unocculted stellar active regions on the stellar host have impacted the strength of such narrow-band features (Apai et al. 2018; Chachan et al. 2019; Rackham et al. 2018; 2019; Tinetti et al. 2018). In the next section, I thus discuss unocculted spots.

**Unocculted spots**

As stellar chromospheres and photospheres are not homogeneous the spectrum of any transit chord will differ slightly from the disk-integrated spectrum. When we construct the transmission spectrum of a transiting exoplanet, we assume the light source is the whole stellar disk whereas it should be the transited chord, which is unfortunately not directly observable. In reality, occulted and unocculted starspots, faculae and even flares will introduce slight spectral differences between the disk integrated and chord-integrated spectra, this is called the transit light source (TLS) effect. Figure 5.2, from Rackham et al. (2018), illustrate the TLS effect. The magnitude of the contamination is defined by the brightness contrast and the fractional area of magnetic features which is itself intrinsic to the nature of the host star. In that regard, Rackham et al. (2018) estimated the impact of unocculted active regions for FGKM stars with activity levels from empirical estimates. They found that spot covering fractions increase from $\simeq$0.1% for F dwarfs to 2%–4% for late-K dwarfs to $\simeq$10% for M dwarfs. Worryingly, their simulations predict that unocculted spots and faculae could alter the transit depths of planet transiting UCDS in the 0.3–5.5 $\mu m$ wavelength range by a few to tens of percent, depending on the assumptions made about spot/faculae sizes (giant spots or solar-like spots) and covering ratios. Different avenues are being explored to reveal and overcome this contamination:

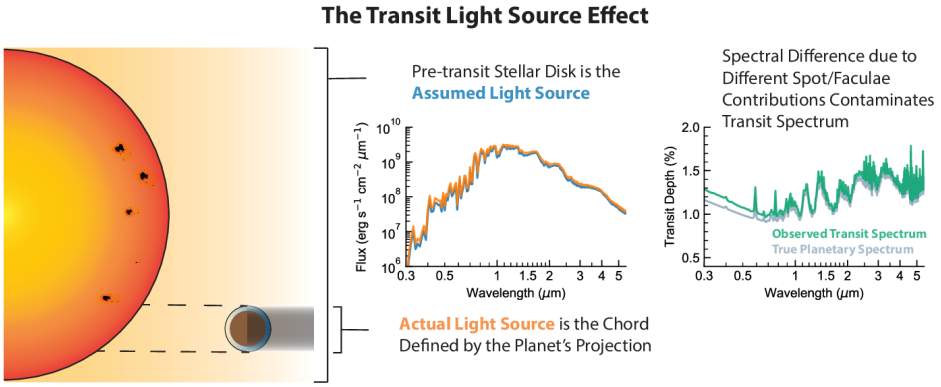


**Fig. 5.2** A Schematic of the Transit Light Source effect. During a transit, exoplanet atmospheres are illuminated by the portion of a stellar photosphere immediately behind the exoplanet from the point of view of the observer. Changes in transit depth must be measured relative to the spectrum of this light source. However, the light source is generally assumed to be the disk-integrated spectrum of the star. Any differences between the assumed and actual light sources will lead to apparent variations in transit depth. Figure from Rackham et al. (2018).

- High-precision transit photometry from space or the ground encodes information about the underlying stellar surfaces. The nature of stellar active regions can indeed by partly revealed with the observation of indirect photometric signatures:
  - First, we can monitor the variations of the transit depth of a given planet in a given bandpass with time. Transit depth variations result from a change in the relative brightness of the occulted stellar chord compared to the unocculted star light in the atmosphere. The reason for this change could be the result of dynamical interactions that make the transit chord shift and/or tilt (in a multiple planet system), or it could be the unocculted stellar surface that changes in brightness due to the growth or decay of active regions, and similarly for the occulted stellar surface. In the latter situation, we should be able to see spot crossing event in the transit light curve (back to occulted spot case discussed in section 5.1.1). If the depth variations are from dynamical origin, we expect them to be coupled with impact parameter variation and therefore transit duration variations (TDVs), according to equation 1.11). However, if no TDVs are observed simultaneously to the transit depth variations and there is not evidence for these variations to be predominantly caused by the growth of active regions along the transit chord, then it is plausible that this is the result of changes in an unocculted stellar surface.
  - Interestingly, Cauley et al. (2018) demonstrated that the amount of contamination depends strongly on the location of the active regions. The contamination therefore decreases dramatically as the angular separation between a planet transit

chord and an active region's latitude increases, with the most significant events occurring when the two are within five degrees from each other. With this in mind the planet can be used to scan the photosphere in order to recover the active regions' longitude and latitude and more generally learn about their distribution. In particular, the most promising configuration happens for multiple-planet systems with strong dynamical interactions. For example, the K2-146 system host two planets whose impact parameters can both change of $\simeq$10% over 10 years, leading to a $\simeq 10^{\circ}$ change in the projected latitude of the transit chord on the surface of the star, acting as a very useful natural scan of the stellar surface at a given time. Besides, systems with high stellar obliquities between their orbital axis and the stellar spin axis are also favourable, as illustrate in Figure 5.3. As a

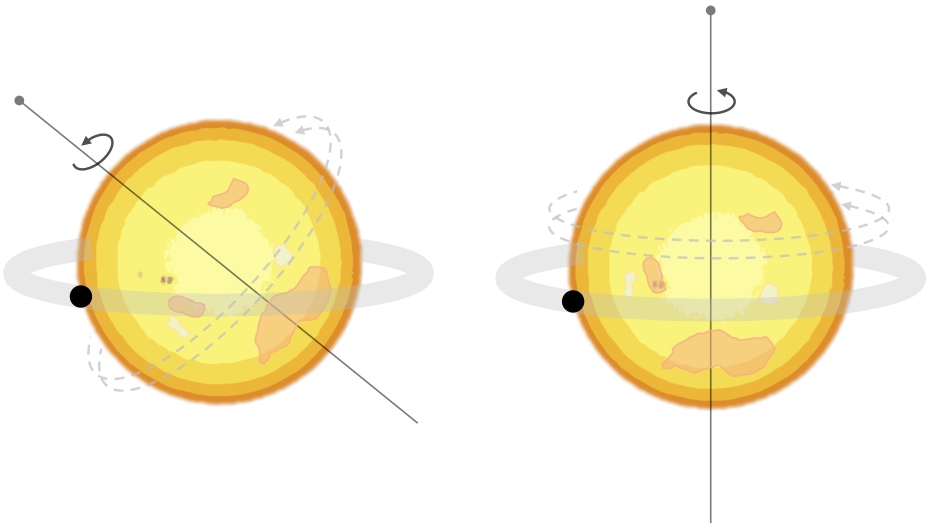

**Fig. 5.3** Illustration of the influence of stellar obliquity on the fraction of stellar surface covered by the transit chord over time. Credit: Elsa Ducrot

whole, monitoring occulted active regions over many years can bring a broader understanding of unocculted surfaces at the time of transmission spectroscopy observations, especially those surfaces within a few degrees of the transiting planet that are most critical for interpreting the transmission spectrum.

– Finally, unocculted spot could also be traced by the presence of stellar flares. Studies on the Sun (Mayfield et al. 1985) provided evidence that the energies of Solar flares are correlated with the magnetic energy in active regions (also demonstrated for solar-type stars in general (Notsu et al. 2013)). However, whether this is still true for stars that are different from the Sun is still unclear. From a sub-set of main sequence stars observed with *Kepler*, (Roettenbacher

et al. 2018) showed that low-amplitude flares display an increased occurrence rate close to the starspot groups, which is not the case for high-amplitude flares. However, for M dwarfs, neither Doyle et al. (2018) nor Feinstein et al. (2020) found any evidence for correlation between rotational phase due to starspots and flares on M dwarfs.

- Alternatively, we can use multi-band or other dataset than photometry to constraint the nature of spots and faculae:
  - Using simultaneous multi-band photometry, we can infer colour changes with time and determine spot/faculae temperatures and covering fractions on active stars. In particular, as faculae have much stronger spectral signatures than spots it can be particularly interesting to observe specific narrow bands where we expect this activity to be visible (such as *Ca*II, *H*, *K* lines). Unfortunately, there is still a degeneracy between covering fraction and temperature as a given amount of photometric modulation could be produced by a relatively small but very dark starspot or equally by a larger spot with a relatively small temperature contrast. As a whole, this technique is limited by our knowledge of the spectral profile and contrasts of faculae and spot for stars other than the sun.
  - High resolution spectroscopy can also be used to better estimate active region covering fractions. This owes to the fact that with high resolution spectroscopy, molecular bandpasses can be detected at high significance, and as the amplitude of these signatures is a strong function of the temperature, we can model the stellar surface as the sum of components at different temperatures. Additionally, as described by Afram et al. (2015), high-resolution spectropolarimetry can provide estimates of the overall magnetic fields of active stars using the traces of these same molecular features on the stellar magnetic field through their polarisation.

Now that I have introduced what is stellar contamination, and its impacts though occulted and unocculted active regions I will discuss it when applied to the TRAPPIST-1 system. More precisely, the rest of this section present the results of a study I led to construct the broadband transmission spectra of the TRAPPIST-1 planets. First, I introduce the context of this study, then I detail the observations and analysis that were carried out, and finally I discuss the results obtained.

### 5.1.2 Context, observations and analysis

#### Context

In 2018, from TRAPPIST-1's K2 variability, Rackham et al. (2018) estimated TRAPPIST-1's coverage to be $8^{+18}_{-7}$% of cold spots and $54^{+16}_{-46}$% of hot faculae, assuming Solar-type spots (which maximise the impact on the planets' transit spectra). They concluded that such a strong heterogeneous photosphere could alter the transit depth of the planets by roughly 1 to 15 times the strength of planetary features, dramatically complicating the follow-up observations with JWST. Later this year, Zhang et al. (2018) re-analysed the near-IR data obtained with HST/WFC3 (GO-14500 and GO-14873, PI: de Wit) for planets b to g, and compared their resulting transit spectra with stellar contamination model from Rackham et al. (2018). They concluded that the star should be almost entirely covered by spots ($\sim$ 30%) and faculae ($\sim$ 63%) and predicted strong chromatic variations of the transit depths, especially in the visible.

One way to validate or discard these predictions is to confront them with empirical measurements. In this context, my colleagues and I gathered as many transits as possible (at the time of the publication) in multiple band-passes to build the broadband transmission spectra of the TRAPPIST-1 planets over the 0.8-4.5 $\mu$m spectral range. We analysed 169 transit observed in the optical by the K2 (Luger et al. 2017a), SPECULOOS (Burdanov et al. 2017; Delrez et al. 2018b; Gillon 2018) and Liverpool (Steele et al. 2004) telescopes. We combined these measurements with the ones obtained in the near-IR by HST/WFC3 (De Wit et al. 2016; 2018) and by Spitzer/IRAC (Delrez et al. 2018a). Then, we confronted these spectra with stellar contamination models in order to assess the impact of the heterogeneity of the star's photosphere on the atmospheric characterisation of its planets.

#### Observations

The data analysed in this work consisted of transit light curves of the TRAPPIST-1 planets observed from the ground by the SPECULOOS (Delrez et al. 2018b; Gillon 2018; Sebastian et al. 2020) and Liverpool (Steele et al. 2004) telescopes and from space by the K2 mission (Howell et al. 2014).

We observed 37 different transits with 1 or 2 telescopes of the SPECULOOS-South Observatory (SSO) (Burdanov et al. 2017; Gillon 2018) at Cerro Paranal, Chile (see Table 1), in the context of the commissioning of the facility. This represents 52 transits in total as some were observed with two SSO telescopes simultaneously. These observations were carried out in an I+z filter for which we computed an effective wavelength of $\sim$0.9$\mu$m for a M8-type star like

TRAPPIST-1, taking into account the spectral response curve of the telescope+atmosphere. Exposure times of 23s were used for all observations. A standard calibration (bias, dark and flat-field corrections) was applied to each image, and fluxes were measured for the stars in the field with the DAOPHOT aperture photometry software (Stetson 1987). Differential photometry was then performed after a careful selection of comparison stars.

We also obtained 13 transits of the TRAPPIST-1 planets with the 2-m Liverpool Telescope (Steele et al. 2004) installed on the island of La Palma at the Roque de los Muchachos observatory. For those observations, we used the IO:O optical wide field camera which has 4k×4k deep-depletion CCD with 15 $\mu$m-sized pixels and 10×10 arcmin$^2$ field of view. We used 2×2 binning that resulted in 0.3 arcsec pixel$^{-1}$ image scale. All the observations were performed in Sloan z' band with 20 sec exposures. Data reduction and subsequent aperture photometry were carried out in the same manner as for the SSO data.

TRAPPIST-1 was observed with the K2 telescope in an overall bandpass ranging from 420 to 900 nm over a period of 79 days in Campaign 12, which represents a total of 104 transits. The short cadence Target Pixel File (TPF), with a cadence rate of 1-per-minute, was downloaded from the Mikulski Archive for Space Telescope (MAST). We used the same procedure to extract and detrend the lightcurve as in Luger et al. (2017a) and Grimm et al. (2018). We first applied a centroiding algorithm to find the (x,y) position of the PSF centre in each cadence frame. We summed the flux within a circular top-hat aperture, centred on the PSF centre in each frame. We used a Gaussian Process regression pipeline ((Luger et al. 2016), (Grimm et al. 2018)) to remove the instrumental systematics due to K2 telescope's periodic roll angle drift, and the stellar variability. The systematics were fitted using a kernel that contained additive terms for the time- and position-dependent variation, enabling us to separate and subtract them individually. To ensure that the transits were not fitted as stellar variability, we masked them out during the fitting and regression procedure. The stellar and long-term variability was then subtracted from the light curve.

We considered only well-isolated and complete transits in our analysis, discarding blended transits of different planets (9 transits discarded), partial transits (6 transits discarded), transits affected by flares (7 transits discarded), and transits affected by technical problems or bad weather conditions (3 transits discarded). In total 35 transits were discarded. Our final dataset was composed of 169 transit light curves, respectively 67 for TRAPPIST-1 b, 45 for -1 c, 21 for -1 d, 18 for -1 e, 8 for -1 f, 7 for -1 g, and 5 for -1 h. The number of transits kept for each planet is presented in Table 5.1 for K2, SSO, and LT.

| Planet | K2 | SSO | LT |
|---|---|---|---|
| TRAPPIST-1 b | 42 | 20 | 4 |
| TRAPPIST-1 c | 29 | 11 | 5 |
| TRAPPIST-1 d | 15 | 5 | 1 |
| TRAPPIST-1 e | 8 | 8 | 2 |
| TRAPPIST-1 f | 6 | 2 | / |
| TRAPPIST-1 g | 3 | 3 | / |
| TRAPPIST-1 h | 1 | 3 | 1 |

**Table 5.1** Number of transits observed by K2, SSO, and LT analysed in Ducrot et al. (2018).

### Data analysis

We chose to follow different approaches in our data analysis to ensure the robustness of our results. First, we analysed each transit individually to extract its individual properties and notably search for signs of short-timescale variability. Then, we proceeded to a global analysis of all transit light curves per planet to determine precisely the average transit depths in K2, SSO, and LT bandpasses. Finally, we performed an additional global analysis, this time enabling all transits to have different depths in order to assess their variability. For those two distincts global analyses, the transits observed by K2, SSO, and LT were analysed separately. All of our analyses were performed with the adaptive Markov Chain Monte-Carlo (MCMC) code introduced in Chapter 3 and described in details in Gillon et al. (2012a), 2014. In this work we assumed a quadratic limb-darkening law for all the analyses, using normal prior distributions for the limb-darkening coefficients $u_1$ and $u_2$ based on theoretical values and $1\sigma$ errors interpolated from the tables of Claret et al. (2012), 2013. The modes of the normal prior distributions for $u_1$ and $u_2$ for the non-conventional I+z filter used by SSO were chosen as the average of the values interpolated from the tables for the standard filters $I_c$ and $z'$.

#### *Individual analyses of the light curves*

First, we converted for each photometric measurement the mid-exposure time to the $BJD_{TDB}$ time system, as recommended by Eastman et al. (2010). We modelled each transit with the model from Mandel et al. (2002) multiplied by a baseline model accounting for the photometric variations of stellar, atmospheric, and instrumental origins (see Gillon et al. (2014)). For each light curve, the model selection was based on the minimisation of Bayesian Information Criterion (BIC) (Schwarz 1978). For a significant fraction of the light curves obtained by K2 and SSO, including a polynomial function of time in the model -to account

for the low-frequency signals like the rotational variability of the star- resulted in a significant decrease of the BIC. For some SSO and LT light curves, additional terms in the position or width of the stellar point-spread function were also favoured. A small fraction of the SSO's light curves' baselines also included an airmass and/or a background polynomial function.

For each transit light curve, the jump parameters of the MCMC analysis, i.e. the parameters perturbed at each step of the Markov chains, were:

- The transit depth (planet-to-star area ratio) $dF = (R_p/R_\star)^2$, the time of mid-transit (or inferior conjunction) $T_0$, and the transit impact parameter assuming a circular orbit $b{=}a\cos i/R_\star$, where $a$ is the semi major axis and $i$ the inclination of the orbit.
- The mass, radius, effective temperature, and metallicity of the star, for which we assumed the following normal prior distributions: $M_\star = 0.089 \pm 0.006 M_\odot$, $R_\star = 0.121 \pm 0.003 R_\odot$, $T_{eff} = 2516 \pm 41 K$, and $[Fe/H] = 0.04 \pm 0.08$ (Van Grootel et al. 2018), respectively.

We first assessed a Correction Factor $CF$ for each individual light curve via a short (10 000 steps) Markov chain. This correction factor was then used to re-scale the photometric error bars while accounting for a possible inadequate estimation of the white noise ($\beta w$) and the presence of red noise ($\beta r$) via $CF = \beta_w * \beta_r$ (as explained in Chapter 3). $\beta_r$ allows to account for possible correlated noise present in the light curve and is determined by following a procedure similar to the one presented by Winn (2008), i.e by comparing the standard deviations of the binned and unbinned residuals for different binning intervals ranging from 5 to 120min (the typical time scales of an eclipse light curve, e.g. the duration of ingress or egress). We then ran 2 chains of 100 000 steps for each light curve and successfully tested their convergence using the Gelman & Rubin statistical test of Gelman et al. (1992).

The results obtained from theses individual analyses are given in Table 5.7 for SSO, in Table 5.8 for K2, and in Table 5.9 for LT.

*Global analyses*

Our next step was to perform, for each planet and for each dataset (K2, SSO, and LT), a global analysis of all transit light curves, to better separate the actual transit signals from the correlated noise of similar frequencies, and thus to improve the accuracy of the derived transit depths. These global analyses were done in two steps: first, for each planet and each instrument, a general global analysis of all the transits with common transit shape parameters, followed by a global analysis allowing for transit depth variations.

We used the same priors on the stellar parameters as reported in Section. 5.1.2. However, in the first global analysis, we set the transit timing variation (TTV) of each transit as a jump parameter, fixing the planetary periods $P$ and reference transit timings $t_0$ to those reported in Delrez et al. (2018a). This global analysis includes 6 shared parameters across transits (the stellar parameters $M_*$, $T_{eff}$, $R_*$, [Fe/H] + limb darkening coefficients), the transita parameters are *df* and *b* for each planet and a TTV per transit.

For each transit, we assumed the baseline model derived from the individual analysis, followed the same procedure to re-scale the photometric error bars, and derived our parameter estimates from the posterior distributions obtained from two Markov chains of 100 000 steps, with 25% burn-in phase, whose convergence was checked using the Gelman & Rubin test. The median values and 1-$\sigma$ limits of the posterior probability distribution functions of the transit depths derived from these global MCMC analyses per planet are displayed in Table 5.2.

| Planet | $dF_{K2}$ (%) | $dF_{SSO}$ (%) | $dF_{LT}$(%) |
|---|---|---|---|
| TRAPPIST-1 b | 0.721 ± 0.021 | 0.760 ± 0.025 | 0.746 ± 0.036 |
| TRAPPIST-1 c | 0.684 ± 0.019 | 0.736 ± 0.029 | 0.724 ± 0.027 |
| TRAPPIST-1 d | 0.412 ± 0.028 | 0.354 ± 0.027 | 0.301 ± 0.071 |
| TRAPPIST-1 e | 0.449 ± 0.034 | 0.453 ± 0.025 | 0.475 ± 0.054 |
| TRAPPIST-1 f | 0.541 ± 0.034 | 0.672 ± 0.052 | / |
| TRAPPIST-1 g | 0.668 ± 0.070 | 0.755 ± 0.035 | / |
| TRAPPIST-1 h | 0.347 ± 0.058 | 0.321 ± 0.036 | 0.257 ± 0.035 |

**Table 5.2** Transit depths derived from the global analysis of all transits of each planet. Observations from K2, SSO, and LT were processed independently.

In a second step, we performed similar global MCMC analyses, but this time with the depths of all individual transits as jump parameters for all three instruments. The aim was to benefit from the constraint brought by a common transit shape (duration, impact parameter) to derive more accurate individual transit depths, and thus better assess their potential variability. This time the analysis included 4 shared parameters across transits (the stellar parameters $M_*$, $T_{eff}$, $R_*$, [Fe/H]), for each planet there were as many individual transit depths as transit plus the impact parameter (limb darkening coefficients were fixed), and same number of TTVs than number of transits.

The results can be found in Table 5.10, 5.11 and 5.12. The transit depth variations are shown for each planet in Figure 5.4 (we did not plot Liverpool data because of the small number of light curves, but the values can be found in Table 5.12). For further comparison, these figures

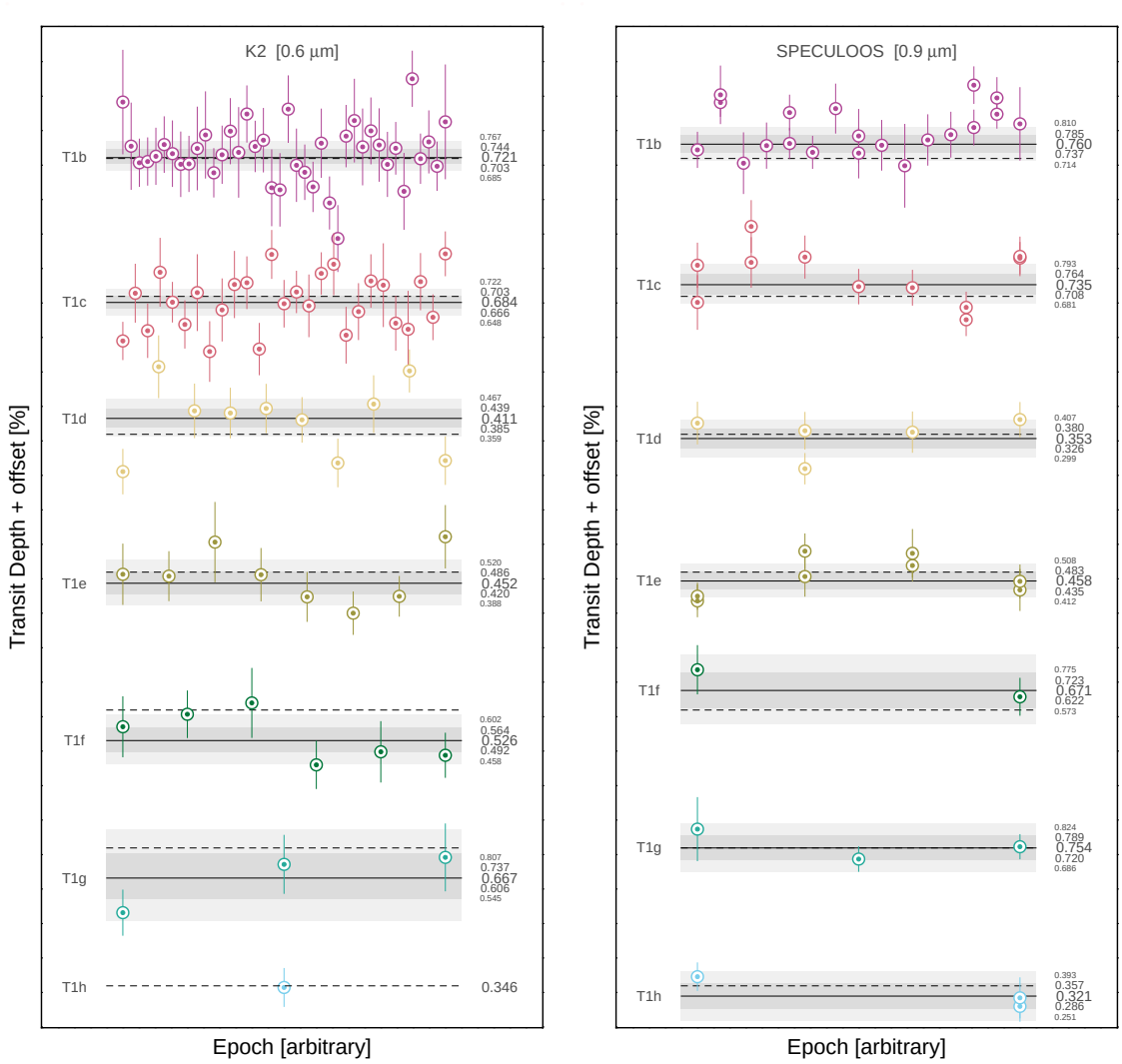


**Fig. 5.4** *Left:* Evolution of the measured transit depths from the global analysis of transit light curves gathered by K2 with time. The horizontal black lines show the medians of the global MCMC posteriors PDFs (with their 1 and 2$\sigma$ confidence intervals, in shades of grey), and dotted lines show the medians of the global MCMC posteriors PDFs for all transits of the same planet observed by *Spitzer*, as reported by Delrez et al. (2018a). Events are ranked in order of capture, left to right (but not linearly in time). *Right:* Similarly, but for transits observed with SSO. Neither SSO or K2 data show significant variability (less than 3$\sigma$).

also display the medians of the global MCMC posterior PDFs as measured with *Spitzer* at 4.5 $\mu$m by Delrez et al. (2018a), and the one derived from the first global MCMC analyses (assuming common transit depths).

We compared the results obtained from the individual and global analyses of the transits and found them to be fully consistent. Accurately constraining the transit shape through a global analysis slightly improves the errors on the depths or timings for several transits, while others

have larger errors due to the clearer separation between signal and red noise. For this reason, we adopt the results of our global analyses as our final ones.

### 5.1.3 Results and discussion

#### Temporal evolution of the transit depths

As introduced in section 5.1.1, monitoring variations in the transit depths measured for a planet in a given bandpass can be a way to track the presence of stellar heterogeneities on or outside the chord transited by the planet. Figure 5.4 shows the evolution of the transit depths derived from our global analyses of K2 and SSO light curves. These analyses assumed a common transit profile -except for the depths- for each planet and each instrument to better separate the correlated noise from the transit signals and thus guarantee robust results on the transit depths. From those results, we notice that for all planets the depths are consistent from one transit to another, with no discrepancy larger than $3\sigma$. We have computed the standard deviation of the measurements and compared it to the mean value of the measurement errors for each dataset. The values are presented in Table 5.3. We found that the standard deviation is consistent with the mean of the measurements errors for most of the planets/instruments associations. The exceptions are planet c (SSO, LT) and planet d (K2), where the scatter of the measurements is actually larger than the mean errors. These mild discrepancies could be genuine, but they could also originate from small-number statistics. Indeed, only 4 transits are used to compute the statistics for LT, 11 transits for SSO for planet c, and 10 transits for planet d for K2.

Looking at the few transits that were observed simultaneously with *Spitzer* (values from Delrez et al. (2018a)) and K2 (see Table 5.8) on one hand and with SPECULOOS (see Table 5.7) and LT (see Table 5.9) on the other hand, we see that the transit depths values are in agreement with one another (see Table 5.4), K2 error bars being significantly larger than *Spitzer* error bars. The depth derived for the transits of e and h observed simultaneously by two SPECULOOS telescopes and Liverpool are consistent as well. This achromaticity of the transit depth do not indicate the presence of occulted or unocculted spot on the surface of the star.

#### Transmission spectra of the TRAPPIST-1 planets

Combining the results of our analyses to the ones presented by Delrez et al. (2018a) for *Spitzer* measurements and by De Wit et al. (2016), 2018 for HST/WFC3 measurements, we

| Telescope | Planet | # transits | $\sigma$ (%) | Mean error (%) |
|---|---|---|---|---|
| K2 | -1b | 40 | 0.084 | 0.14 |
| | -1c | 27 | 0.080 | 0.081 |
| | -1d | 10 | 0.11 | 0.073 |
| | -1e | 8 | 0.077 | 0.080 |
| | -1f | 6 | 0.072 | 0.080 |
| | -1g | 3 | 0.087 | 0.085 |
| | -1h | 1 | / | / |
| SPECULOOS | -1b | 20 | 0.069 | 0.067 |
| | -1c | 11 | 0.080 | 0.059 |
| | -1d | 5 | 0.057 | 0.053 |
| | -1e | 8 | 0.055 | 0.053 |
| | -1f | 2 | 0.055 | 0.063 |
| | -1g | 3 | 0.044 | 0.055 |
| | -1h | 3 | 0.044 | 0.047 |
| Liverpool | -1b | 3 | 0.087 | 0.081 |
| | -1c | 4 | 0.102 | 0.062 |
| | -1e | 2 | 0.087 | 0.081 |

**Table 5.3** Standard deviation and mean errors of the measured transit depths. *Remark:* there are no values for planet h with K2 nor planets d, g, h with the Liverpool telescope because we had only one light curve for each of those planets.

construct the broadband 0.8-4.5 $\mu$m transit transmission spectra of TRAPPIST-1 planets, see Figure 5.5.

We first note that although the measurements obtained with the HST data do not show features over the WCF3 band (1.1 to 1.7 $\mu$m), the transit depths are significantly deeper than those obtained at other wavelengths for planets b and d. Although this is intriguing, these deeper transits could very well have an instrumental origin. Indeed, as HST is on a low-Earth orbit, it can monitor TRAPPIST-1 for an average of ~50 minutes per orbit out of the ~95 minute orbital duration. The observation of a transit during an HST visit is typically based on 4 or 5 orbits. Due to the small transit durations of the TRAPPIST-1 planets, only one window per visit covers a transit. Yet, although the transit durations of TRAPPIST-1 planets are short, they have roughly the same duration of HST's observation window leading to a small (and at times negligible) constraint on the baseline level from the in-transit orbit. As HST/WFC3 spectrophotometric observations are affected by orbit-dependent systematic effects, such

| Planet | Epoch | K2 | *Spitzer* |
|---|---|---|---|
| -1b | 318 | 0.830 ± 0.120 | 0.751 ± 0.027 |
| | 320 | 0.669 ± 0.160 | 0.699 ± 0.023 |
| | 321 | 0.988 ± 0.120 | 0.801 ± 0.028 |
| | 325 | 0.866 ± 0.130 | 0.732 ± 0.022 |
| | 326 | 0.693 ± 0.073 | 0.724 ± 0.023 |
| | 327 | 0.851 ± 0.086 | 0.663 ± 0.021 |
| -1c | 215 | 0.604 ± 0.090 | 0.672 ± 0.025 |
| | 216 | 0.686 ± 0.080 | 0.652 ± 0.020 |
| | 217 | 0.797 ± 0.120 | 0.735 ± 0.035 |
| | 218 | 0.809 ± 0.400 | 0.674 ± 0.029 |
| | 219 | 0.663 ± 0.071 | 0.668 ± 0.024 |
| | 220 | 0.830 ± 0.120 | 0.725 ± 0.024 |
| -1d | 34 | 0.304 ± 0.130 | 0.384 ± 0.020 |
| | 35 | 0.412 ± 0.210 | 0.382 ± 0.024 |
| | 36 | 0.361 ± 0.110 | 0.348± 0.019 |
| -1f | 15 | 0.494 ± 0.090 | 0.648 ± 0.025 |
| -1g | 12 | 0.867 ± 0.170 | 0.777 ± 0.020 |

| Planet | Epoch | SPECULOOS | Liverpool |
|---|---|---|---|
| -1e | 53 | 0.522 ± 0.055<br>0.590 ± 0.057 | 0.476 ± 0.069 |
| -1h | 17 | 0.316 ± 0.057<br>0.291 ± 0.044 | 0.257 ± 0.035 |

**Table 5.4** *Up:* Depth of transits observed simultaneously by K2 and *Spitzer*. *Down:* Same but for SPECULOOS and Liverpool telescope.

a limited constraint on the baseline level from the orbit constraining the transit depth can result in a diluted or amplified monochromatic transit depth. The current measurements are particularly limited in such joint "transit depth–baseline level" measurements for planet b see Figure 1 of De Wit et al. 2016 and planet d see Figure 1 of De Wit et al. 2018–and reduced for planets c and e–which is consistent with the level of discrepancies seen in Figure 5.5. We also note that the transit depth measured for planet f at 0.6$\mu$m (K2) is ~3-$\sigma$ shallower than the mean of the other measurements. This measurement could be explained by its low statistical significance (only 6 transits) or by the detrending of K2 systematic effects and significant stellar variability correction applied to the light curve before its modelling (see

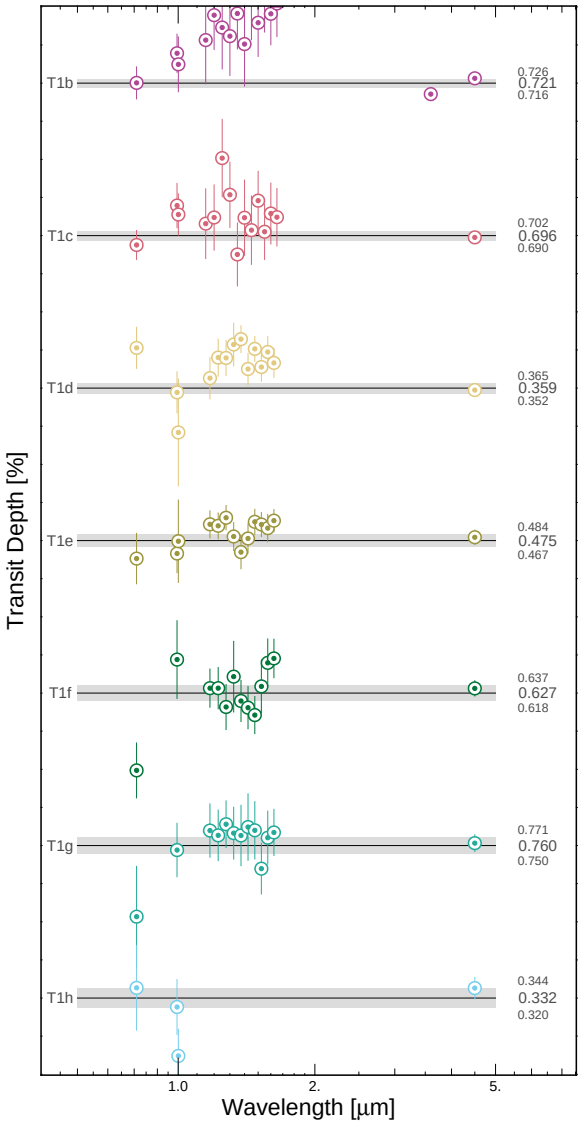


**Fig. 5.5** Transit transmission spectra of the seven TRAPPIST-1 planets (as it was at the time of publication in 2018). The continuous line is the weighted mean of all non-HST measurements for each planet (with its 1 $\sigma$ confidence, in shades of grey). Each point stands for the median of the global MCMC posterior PDF with error bars at the effective wavelength of the instrument (13 points (14 for T1b) per planet: one for K2, one for SSO, one for LT, 9 for HST/WFC3 and one (two for T1b, 3.6$\mu m$ and 4,5 $\mu m$) for *S pitzer*).

Section 2.1). Nevertheless, there seems to be no significant biases from detrending in the other planets measurements so we would better wait for the analyses of additional transits of planet f in this bandpass to confirm or discard this value. Such data will notably be obtained as part of JWST GTO ID 1201 with the NIRISS instrument [1]. For the other planets, no

[1] https://www.stsci.edu/jwst/science-execution/program-information?id=1201

significant (>3$\sigma$) chromatic variation is observed. Besides, we note that planet with similar transit impact parameters ({b,c,d}, {e,f} and {g,h}) do not show reproducible structures in their transit spectra while data where generally acquired at similar times for each planets (< 50 days). If we assume stellar heterogeneities present on the surface of the star are large enough to equally affect planets with similar impact parameters, the lack of reproducibility between spectral features on {b,c,d}, {e,f} and {g,h} does not favour stellar contamination origin.

Figure 5.6 shows the detrended period-folded photometry measured for each planet by K2 and SPECULOOS, as well as the corresponding best-fit transit model. We see that the measurements obtained in-transit do not reveal any transit shape asymmetry that could be related to recurrent spot/faculae crossing event. A visual inspection of all individual transit light curves did not reveal such crossing events neither.

### Confrontation with theoretical stellar contamination model

The strong stellar contamination inferred for TRAPPIST-1 planets by Zhang et al. (2018) is based on the model presented by Rackham et al. (2018), which assumes an heterogeneous photosphere composed of unocculted spots and faculae, and is described by the equation:

$$\epsilon_{\lambda,s+f} = \frac{1}{1 - f_{spot}(1 - \frac{F_{\lambda,spot}}{F_{\lambda,phot}}) - f_{fac}(1 - \frac{F_{\lambda,fac}}{F_{\lambda,phot}})}, \tag{5.1}$$

where $\epsilon_{\lambda,s+f}$ is the ratio of the observed transit depth $D_{\lambda,obs}$ by the nominal transit depth $D_\lambda$ (i.e., the square of the true wavelength-dependent planet-to-star radius ratio) and represents the stellar contamination at wavelength $\lambda$; $F_{\lambda,phot}$, $F_{\lambda,spot}$ and $F_{\lambda,fac}$ refer to the fluxes of the mean photosphere, spots and faculae respectively; and $f_{spot}$ and $f_{fac}$ refer to the unocculted spot- and faculae- covering fractions (Rackham et al. 2018).

The contamination spectrum $\epsilon_{\lambda,s+f}$ is then multiplied with an assumed wavelength-independent nominal planetary transit depth by Zhang et al. (2018) to obtain a transit spectrum whose wavelength-dependency is only due to the stellar contamination. Ultimately, a fit of the percentages of spots and faculae covering fractions is performed, combined with an estimation of their temperatures and that of the mean photosphere, to represent at best the transit spectra of the TRAPPIST-1 planets that they obtain from the re-analysis of the HST/WFC3 data presented in De Wit et al. (2016), 2018. The authors combine spectra of several planets, justifying their choice by the improved signal-to-noise ratio in detecting common spectral

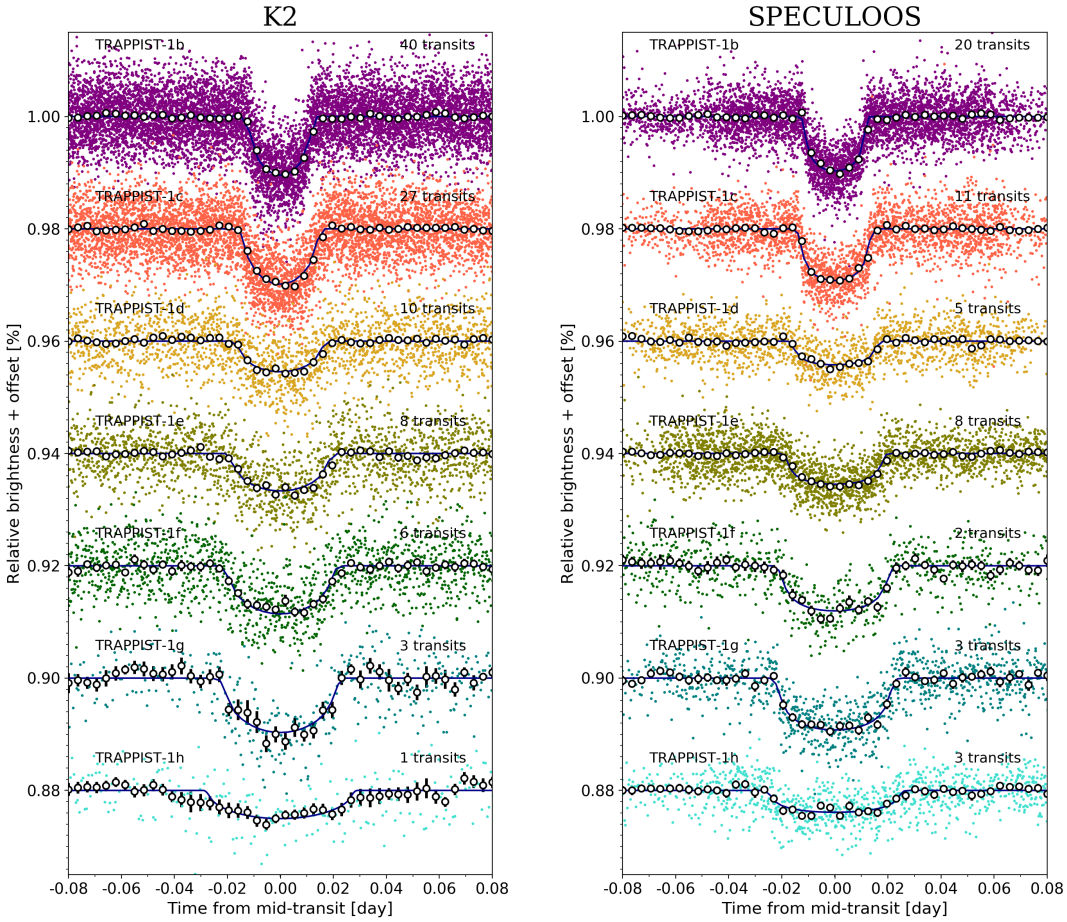


**Fig. 5.6** *Left:* Period-folded photometric measurements obtained by K2 near the transits of the seven planets, corrected for the measured TTVs. Colored dots show the unbinned measurements; open circles depict the 5minute-binned measurements for visual clarity. The best-fit transit models are shown as dark blue lines. The numbers of transits that were observed to produce these combined curves are written on the plot. *Right:* Similarly but for SSO.

features. To enable a straightforward comparison with theirs, we also performed the same combination ({b+c+d+e+f+g}, {b+c}, {d+e+f+g}).

Before I present the results I must precise some details about the timeline of the publication. In Feb 2018 a first version of Zhang et al. (2018) was submitted to the Astronomical Journal and posted on Arxiv. This work foresaw that TRAPPIST-1's photosphere should be highly heterogeneous, composed of $\sim 30\%$ of spots (with $T_{spot} \simeq$2100K) and $\sim 63\%$ of faculae (with $T_{fac} \simeq$2800K). In the following months, my colleagues and I analysed the data described

above and compared measurement to Zhang et al. (2018)'s predictions. We submitted our paper to the Astronomical Journal and posted a version of the paper on Arxiv in early July 2018 on the occasion of the Exoplanet II conference. As Zhang et al. (2018) paper was still in review at that time, the authors seize this opportunity to refine their predictions using the data that were presented in our paper, this time anticipating a photosphere composed of $\simeq$ 38% of spots (with $T_{spot}$ $\simeq$2000K) and $\simeq$ 48% of faculae (with $T_{fac}$ $\simeq$2950K). In the same time our paper was accepted for publication, such that our paper compares observations to an outdated version of Zhang et al. (2018). For the sake of consistency, a year latter, in the publication I led on the Spitzer dataset (see Chapter 4), I included a comparison of the most recent broadband spectra of the planets compared with the final best fit from Zhang et al. (2018).

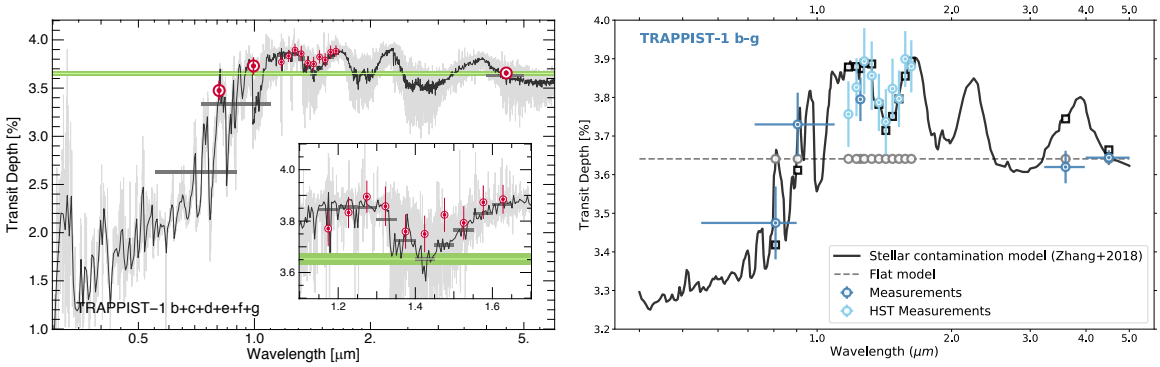


**Fig. 5.7** *Left:* Combined transmission spectrum for TRAPPIST-1 b+c+d+e+f+g. Red points show measurements from our 2018's paper (Ducrot et al. 2018). Continuous black and grey lines show the best-fitting contamination models at two different resolutions. The green line represents the weighted mean of all measurements except HST for the reasons outlined before. Finally, the grey horizontal bars are the band-integrated values for the model where the integrals are weighted uniformly in wavelength. Wavelength is in log scale. Figure from Ducrot et al. (2018). *Right:* Similarly, but with the most recent measurements (from 2020, (Ducrot et al. 2020)) in blue dots and updated best-fit stellar contamination model derived by Zhang et al. (2018) after review in continuous black line. The black squares are the integrated depth values as predicted by their final best-fit in each spectral band where observations were available. Grey dashed lines is the flat model at the weighted mean value of the transit depth. Figure from Ducrot et al. (2020).

The left panel of Figure 5.7 is the combined spectrum of planets b to g published in our 2018's paper with Zhang et al. (2018)'s initial best-fit over-plotted ($\sim$ 30% of spots and $\sim$ 63% of faculae). We see that the significant drop of the transit depth in the visible predicted by Zhang et al. (2018) model is not observed. Prediction for K2 bandpass are discrepant by more than 10$\sigma$ from the observations, at $\sim$ 6.5$\sigma$ for SSO, at $\sim$ 3.5$\sigma$ for *Liverpool*, and $\sim$ 1.4$\sigma$ for *Spitzer*. The contamination model initially presented by Zhang et al. (2018) is thus firmly discarded.

The right panel of Figure 5.7 shows the final best-fit model from Zhang et al. (2018) compared with the same measurements (K2, LT, and SPECULOOS) + one measurement at 1.2$\mu m$ (from UKIRT/AAT) (Burdanov et al. 2019) + two new Spitzer measurements at 3.6$\mu m$ and 4.5 $\mu m$ (updated value) from Ducrot et al. (2020). First, we note that the predicted impact of the TLS effect in the visible is significantly less severe in the revised version of Zhang et al. (2018) (drop of $dF_{K2}$ by ≃5% compared to ≃30% in their first version). Although the updated model fits perfectly our 2018 measurements (which is no surprise as the fit was selected on this criterion), it is not the case for the new observational points at 1.2$\mu m$ and 3.6$\mu m$ (discrepant at $\simeq 3\sigma$). Considering the large spot and faculae coverages associated to the final best-fit, the large number of transits analysed (169 + 25 + 188 = 382) and the fact that the planet transit chords cover ≃28% of projected stellar disk, we should expect several spot crossing events. Yet, as showed in section 5.1.3 for K2 and SPECULOOS data and in Chapter 4 section 4.1.3 for Spitzer, only one single transit seems to be clearly affected by a spot (see Figure 4.6). This finding does not favour Zhang et al. (2018)'s final best-fit model. Furthermore, it has been realised as posteriori to the publication that the model is inconsistent with the photometric brightness and Gaia distance to TRAPPIST-1 (i.e., the large coverage associated to the very hot component should make the star much brighter in the optical than it actually is).

While this model can be discarded, the presence of stellar contamination in the spectra of the TRAPPIST-1 planets remains a possibility. Indeed, the star's photosphere is definitely heterogeneous, as its K2 photometry shows a quasi-periodic variability of a couple % with a dominant period of 3.3d that is consistent with the rotation of an evolving inhomogeneous photosphere (Luger et al. 2017a), or with the characteristic timescale between flares followed by spot brightening (Morris et al. 2018c). Maybe we did not observe any spot/faculae crossing because heterogeneities appear at preferential latitudes, like the poles. One way to confirm this could be to use Doppler tomography with the upcoming E-ELT/HIRES instrument, as has already been done for a few brighter stars (J. R. Barnes et al. 2015), or to use spectral template fitting to constrain spot sizes and population through molecular band observations (Vogt 1979). While we wait for the ELT to be operational (currently announced for 2027), we can discuss alternative scenarios for the nature of TRAPPIST-1's surface.

#### On the possible photospheric structure of TRAPPIST-1

In their studies, Rackham et al. (2018) and Zhang et al. (2018) assumed that the active regions of TRAPPIST-1 are qualitatively similar to solar active regions in the spot and facular flux contrasts, and in the relative areas of each component. However, there is abundant evidence

that the Sun is a poor analogue for the starspot distributions of fully-convective stars (J. R. Barnes et al. 2015; Donati et al. 2003; Morin et al. 2008; 2010), which are likely driven by a different magnetic dynamo process (Donati 2010; Reiners 2012). In this paragraph we propose some alternative scenarios.

*Giant cold spots?*

Instead of solar-type spot + faculae we can wonder whether TRAPPIST-1 could be covered with giant cold polar spot + faculae, in a similar manner as the circumpolar spots observed for young (not older than 1 Gyr) mid- to late-type M-dwarfs see J. R. Barnes et al. 2015. In this case, according to the predictions of Rackham et al. (2018), for Earth-twin type planets, the stellar heterogeneity would not jeopardise the detection of planetary atmospheric features with JWST anymore. Considering a precision of 30ppm with JWST, Rackham et al. (2018) indicate that for a M8V type star like TRAPPIST-1 the depth variations due to atmospheric features should be of the order of 90ppm whereas the variations due to stellar heterogeneity should be of the order of ≈20ppm, consequently allowing detections of planetary features despite stellar contamination (although with decreased significance). Such high-latitude spots that never cross the planets' transit chords, could explain why no spot crossing events were observed except for a very large one caught during a transit of planet g (see section 4.1.3). This could also explain the variability detected in the K2 bandpass. Yet, as only one transit of g was affected and none of the other planet at the same period, the lifetime of this giant spot must have been short (which is not unexpected for giant spot) or its shape must be variable on short-time scale.

However, TRAPPIST-1 is not a young dwarf, its age having been estimated to be 7.6 ± 2.2 Gyr by Burgasser et al. (2017), and the out-of-transit rotational variability resulting from a giant dark polar spot does not match the small observed variability of 2ppm (Delrez et al. 2018a) seen in the infrared (Morris et al. 2018c). In addition, the giant spot model is disfavoured by the correlations between flares and spot brightening seen in the K2 dataset, which indicates that the brightening is not due to spots rotating out of view, but rather due to a temporary brightening of the star which follows each flare event (Morris et al. 2018c).

*Small hot faculae?*

Facular regions are particularly damaging in terms of TLS effect, as they have much stronger spectral signature and stronger UV contrasts than starspot regions. Therefore even a small percent of unocculted faculae on the stellar surface can induced some spectral contamination. Assuming a two component photosphere (quiescent and faculae only) we estimate in our 2018 paper that temperatures up to $T_{fac} = 4500$K are consistent at $\sim 2\sigma$ with the observed transit depths, excluding the HST data for the reasons discussed above, see Figure 5.8. These faculae produce a nearly-flat contamination spectrum for wavelengths $\gtrsim 0.7\mu$m, and

modest flux dilution (shallower transit depths) in the K2 bandpass. This scenario is based

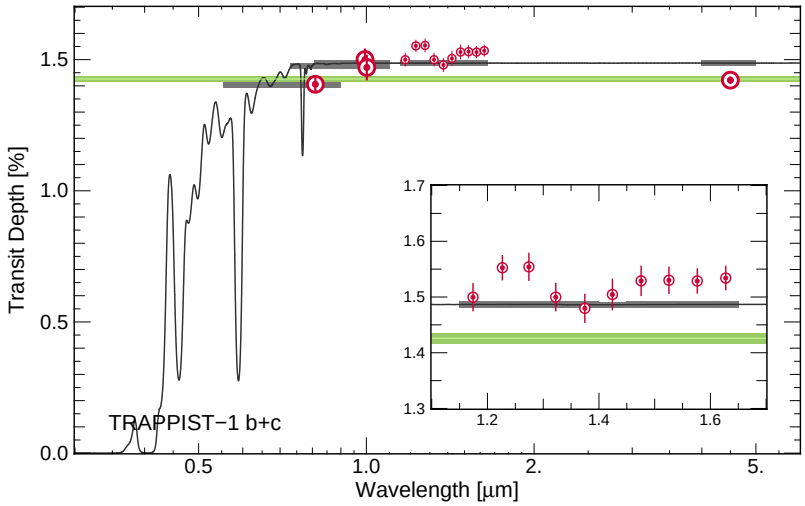


**Fig. 5.8** Comparison of the observed transit depths for K2, SPECULOOS, LT, HST WFC3 and Spitzer IRAC/Channel 2 (red points) with the predictions from stellar contamination due to the bright spots proposed by Morris et al. (2018c) at 4500K (grey continuous line). We used PHOENIX model atmospheres with photospheric temperature of 2511 K and the hot spot properties from Morris et al. (2018c). Figure from Ducrot et al. (2018).

on a study published in March 2018 and led by my co-author Dr Brett Morris (Morris et al. 2018c). This paper aims to constrain the heterogeneities present on the star's photosphere, using the photometric variability observed in two different bands, in the visible from K2 data and near infrared with Spitzer. The authors show that the star is best described as a heterogeneous mixture, consisting of a few small, bright spots (faculae) and a dimmer photospheric component. The proposed hot spots, which are correlated with the brightest flares, would drive the modulation with an 3.3 day period in the K2 bandpass without generating a corresponding signal in the *Spitzer* 4.5 $\mu$m band, in agreement with the observations. The maximum-likelihood model for such two-components photosphere has typical spot sizes of $R_{spot} \simeq 0.004 R_{\star}$ at temperature $T_{spot} \geq 5300 \pm 200K$. The very small size of the spots is consistent with the lack of spot crossing events.

In parallel, Wakeford et al. (2018) presents a method to separate the planetary transmission spectrum from stellar molecular features using the out-of-transit stellar spectra, planetary transit geometries, and planetary atmospheric models, and applies it to the spectrum of TRAPPIST-1g. After discarding several scenarios, the authors concludes that a three-components flux model composed of the photosphere, slightly hotter spots ($\simeq$ 35%, with $T_{spot} = 3000K$) and some faculae (<3%, with $T_{fac} > 4000K$)), with an additional small fraction of flux (1%) from magnetic activity would be the most likely scenario for TRAPPIST-1,

and that the planetary transmission spectra are likely not significantly contaminated by any stellar spectral features (Wakeford et al. 2018). These simulations anticipate a spot size of $\simeq$ 1220 kms, comparatively the smallest spots on the Sun are $\simeq$1750 kms (Solanki 2003). This is still potentially plausible for TRAPPIST-1 given that it is an M star and smallscale magnetic activity could be present to this level (Wakeford et al. 2018). We also note that such small size spots could explain why we do not see any evidence of spot crossings in any of the transits.

As a whole, it seems that a promising avenue to constrain photospheric hetegeneities is to used long multi-bands observations to derive the evolution of the photometric variability of the star as a function of the wavelength. This was done by Morris et al. (2018c) with K2 and Spitzer photometry, and in the next section I discuss my intention to add an intermediate bandpass: I+z ($0.7 - 1.0\ \mu m$). In theory, I could also include HST time series but as the programs were only focused on a couple of visits, the time spent on target is insufficient to thoroughly probe the variability of the star at each wavelength.

## 5.2 Follow-up with SPECULOOS

For the last three years, we (the SPECULOOS team) have been monitoring the TRAPPIST-1 system from the ground with the SPECULOOS telescopes and the Liverpool telescope, an effort that I led in the framework of my PhD. In the following, I present the objective of this extensive campaign, the dataset, and the status of the analysis as it is still on-going. I aim to present this work in a publication as soon as possible.

### 5.2.1 Objectives

Our objectives are three folded:

1. *Task 1:* to understand the origin of the existing inconsistency between K2 and Spitzer photometric variability. For this task, our aim is to derive, if possible, the photometric variability of the star in the I+z band ($0.7 - 1.0\ \mu m$). Then we wish to pursue the work done by Morris et al. (2018c) to propose a spot variability model that would agree with the observations in each band and at the same time provide insights on the nature of the photospheric heterogeneities of TRAPPIST-1. To do so, we have organised an intensive monitoring campaign during the summer 2018 (see description in 5.2.2) to get daily observations of TRAPPIST-1 in I+z band. A near-IR photometric monitoring is especially important, as the stellar SED peaks at $\simeq$1 microns and this is where the

photometric modulations due to the rotation of spots and/or faculae should have the highest amplitude, as shown on the right panel of Figure 5.9. In term of contrast, if the

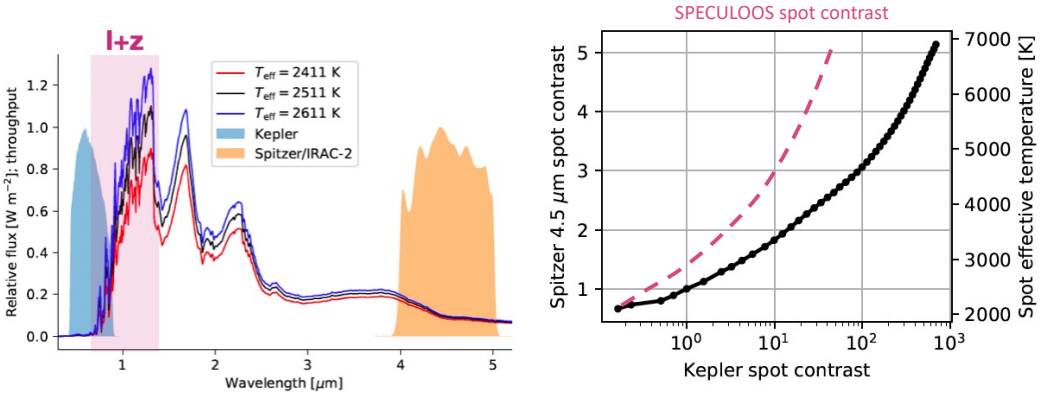


**Fig. 5.9** *Right:* Comparison of the K2, SPECULOOS (I+z) and Spitzer bandpasses with a PHOENIX model atmosphere with $T_{eff} = 2511K$. Figure adapted from Morris et al. (2018c). *Left:* Spot contrasts in the Spitzer vs Kepler bandpasses (black solid line), and the spot temperatures that produce those contrasts, for a star with $T_{eff} = 2500K$ using PHOENIX+BT Settl model spectra. The trend of the expected spot contrasts in the Spitzer vs SPECULOOS bandpasses is shown in dashed pink link for comparison. Figure adapted from Morris et al. (2018c).

scenarios proposed by Morris et al. (2018c) (few small very bright spots) is correct, we would expect the spot modulation in I+z to be larger than in the one in Spitzer and smaller that the one in K2. This owes to the fact that the contrast of bright spots increase more and more slowly at longer wavelengths, as shown on the left panel of Figure 5.9. Besides, if we do find a periodic photometric variability, we will look for any correlation with flaring events. Indeed, Morris et al. (2018c) observe that in the visible flares occur preferentially when TRAPPIST-1 is bright, and when the brightness is increasing most rapidly.

2. Task 2: to catch spot crossing events and flares. As we have explained in section 5.1.1 spot crossing events are handy to scan the stellar surface. Unfortunately, such spot crossing events are not predictable and quiet rare on TRAPPIST-1, so we maximise our chances by observing all visible transits. In parallel, we aim to observe as many flares as possible for the stake of task 1 on one hand, and to improve statistics for abiogenesis zone studies on the other hand (see section 4.1.3).

3. Task 3: to monitor the transit timings of the seven planets. As described extensively in Chapter 4, TTVs are extremely valuable to measure the masses and densities of the planets, constrain their orbital properties and dynamics, and possibly to reveal the existence of addition bodies (if present). Furthermore, the most up-to-date TTV

model is based on transits that have been monitored for only two times the super period $P_{TTV}$ = 491 days, such that it needs to be refined frequently with all available timings (particularly for the outer planets, whose transits are less frequent). Any significant outlier in the new timings compares to the predictions from Agol et al. (2020a) could be the sign that we have missed something in the system.

### 5.2.2 Description of the data

#### 2018 campaign

For almost three months in 2018, we have scheduled TRAPPIST-1 every night on one of the SSO telescopes (the only SPECULOOS observatory that was operational at this time) for a duration of at least 10min and relied on `spock` to ensure observations were performed at the same airmass each night to minimise its systematical impact. We chose 10 min not to impact SPECULOOS core program too much. The filter used was I+z and the exposure time was 23s. Accounting for technical and weather losses, we obtained data for 60 nights out of the 92 initially schedule, which represent 65% of completion. In parallel, we scheduled almost all visible transits of TRAPPIST-1 planets from Paranal from May to December 2018. For planet b and c not all windows were scheduled as transits are very frequent and, again, we did not want to impinge too much on SPECULOOS core program. A summary of the observations can be found on Table 5.5.

| Planet | b | c | d | e | f | g | h | **Total** |
|---|---|---|---|---|---|---|---|---|
| **SPECULOOS** | | | | | | | | |
| # transits 2018 | 19 | 7 | 6 | 4 | 3 | 4 | 2 | 45 |
| Flares | 3 | | | | | | | |
| Spot-crossing | 1 | | | | | | | |

**Table 5.5** Summary of the TRAPPIST-1 planets transits observed in 2018 on the SPECULOOS telescopes.

#### 2019 and 2020 campaigns

The next years, we continued scheduling observations of all transits of the outermost planets and one out of every two transits of the inner planets (b and c). From autumn 2019, the SNO and Saint-Ex telescopes reinforced this effort, opening more latitudes and transit windows.

In parallel, monitoring was also performed with the Liverpool telescope (Steele et al. 2004). Table 5.6 summarises the number of transits actually observed in 2019 and 2020. We note

| Planet | b | c | d | e | f | g | h | **Total** |
|---|---|---|---|---|---|---|---|---|
| **SPECULOOS** | | | | | | | | |
| # transits 2019 | 20 | 11 | 9 | 3 | 1 | 1 | 2 | 47 |
| # transits 2020 | 11 | 8 | 5 | 7 | 1 | 3 | 1 | 36 |
| Flares | 2 | | | | | | | |
| Spot-crossing | 0 | | | | | | | |
| **Liverpool** | | | | | | | | |
| # transits 2019 | 10 | 7 | 3 | 4 | 3 | 1 | 0 | 28 |
| # transits 2020 | 9 | 4 | 3 | 2 | 2 | 1 | 1 | 22 |
| Flares | 2 | | | | | | | |
| Spot-crossing | 2 | | | | | | | |

**Table 5.6** Summary of the TRAPPIST-1 planets transits observed in 2019 and 2020 on the SPECULOOS and Liverpool telescopes.

that the 2020 campaign was affected by the COVID-19 pandemic. From March to September 2019 the SSO and Saint-Ex observatories were closed. Due to a different a policy in the Canaries island SNO and Liverpool were less impacted.

In total, we gathered 178 transits over three years. A few of these transits were observed simultaneously by Liverpool and SPECULOOS, we count 14 duplicates.

### 5.2.3 Current status

#### Data analysis

In terms of analyses, I wish to carry out individual analyses to identify the most appropriate baseline model for each light curve. Then, using these baselines I will carry out global analyses per planet to derive the transit depth variations and transit duration variations and check for any correlation between those two variables. Finally, I will carry out additional per planet analyses with TTVs as jump parameters to compute the precise transit timings. Currently, all individual analysis and per-planet TTV global analyses have been performed for the four outer planets. The rest of the individual and global analyses are still on-going.

In parallel, I aim to identify the putative photometric variability of the star in the I+z band. To do so, I have reduced all data from summer 2018 night by night (applying bias, dark, and flat-field corrections individually) and then treated the reduced images as a single long observation night with gaps to ensure the same comparison stars we used for the aperture photometry. The resulting light curve is shown on Figure 5.10.

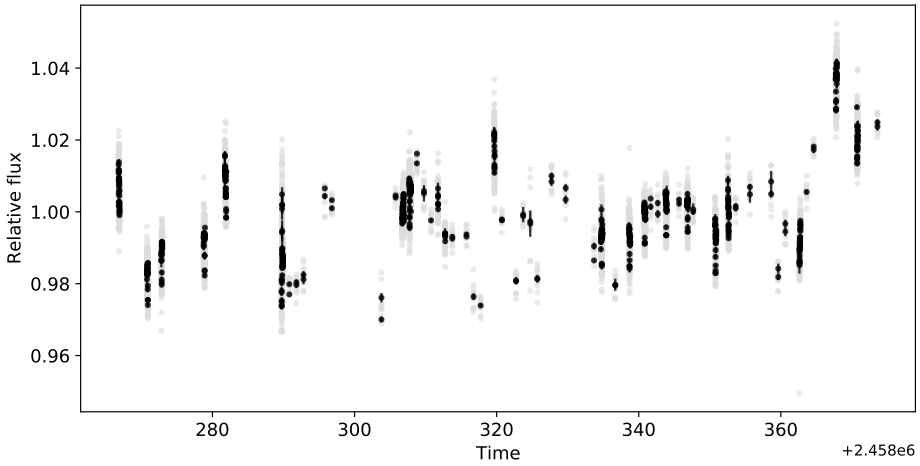


**Fig. 5.10** Global light curve of TRAPPIST-1 with observation spanning from June 2018 to September 2018. Gray dots stand for the raw light curve and black dots for the binned ones. Figure produced with the Python framework `prose` (Garcia et al. 2021b).

### Photometric variability

Using the results from the analyses described above, I will be able to precisely model or mask all transits in the global light curve shown on Figure 5.10. The correction of systematical effects is more complicated because of the effect of airmass and precipitable water vapour (PWV) which are night dependent. For the other systematics such as FWHM or dx, dy positions, we know that their evolution timescale is way shorter (of the order of the minute) than the kind of period we are looking for (of the order of the day), therefore I do not expect them to impact the recovery of the star's brightness variability period. I have planned to work with two distinct approaches: (1) model the variability with Gaussian processes and simultaneously correct all night from PWV and airmass using polynomials (2) model the variability with Gaussian processes and simultaneously correct for airmass only to avoid potential over-detrending that could hide the true variability. I have decided to work with Gaussian processes following the recommendation by Angus et al. (2018) who demonstrate that Gaussian process methods can identify periods that are more accurate than both a sine-fitting periodogram and an autocorrelation function method. This reasoning is based on the

fact that variability in the light curves of spotted, rotating stars is often non-sinusoidal and quasi-periodic.

Besides, I should note that Morris et al. (2018c) showed that, if present, hypothetical spot/faculae on the surface of TRAPPIST-1 would have a likely short evolution timescale as only few repeated patterns were identified in the K2 light curve. Indeed, as spots move on the stellar surface and have finite lifetimes, stellar flux variations slowly shift in phase. This implies that to catch one of those variability patterns, we must observe the star intensively over a relatively short duration (a few weeks). For this reason, I plan to split the search for periodic variability on subsets of the global lightcurve defined by a sliding window of variable length and starting point.

Finally, I will carry out a joint fit of the SPECULOOS, K2 and Spitzer light curves. First, I will use all data available and then I will focus on the K2 and Spitzer data that were taken with the least offset in time possible compared to the SPECULOOS ones. For Spitzer we have some observations in March 2018, so only two month before the SPECULOOS campaign began but for K2 the closest observations in time are from February 2017. The outcomes for these two approaches might be quiet different as empirical observation suggest that the length of the activity cycles of M stars is comprised between 50 to 100 days (Suárez Mascareño et al. 2017). For these joint multi-band fits, I intend to rely on an MCMC approach with the following jump parameters: number of spots, spot positions, spot radii, spot contrast.

### TTVs monitoring

So far, I have completed the global analyses per planet for planets f, g, and h. The resulting transit timings compared to the model from Agol et al. (2020a) are shown on Figure 5.11. A key initial step in computing such TTV time series is to assume a value for the average period of the planet. Otherwise the plot does not look 'flat' and the TTV signal can deviate from the initial values very quickly. To overcome this, I simply take the very first and very last transit times for each planet and the number of epochs between the first and the last transit times to get the slope $s$ and compute the TTVs as follow:

$$\begin{aligned} TTV &= t_{0,observed} - t_{0,predicted} \\ TTV &= t_{0,observed} - \left(t_{m,min} + e.s\right) \\ TTV &= t_{0,observed} - \left(t_{m,min} + e.\frac{t_{m,max} - t_{m,min}}{ne_{\{t_{m,max}-t_{m,min}\}}}\right) \end{aligned} \tag{5.2}$$

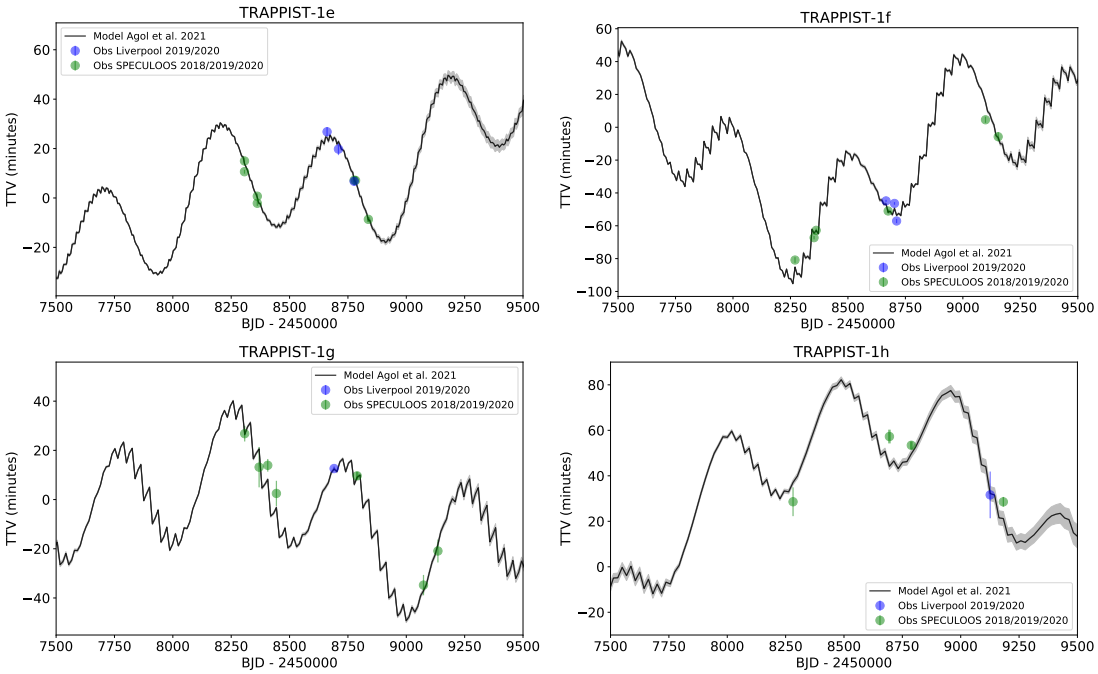


**Fig. 5.11** Transit time variation measurements from SPECULOOS and Liverppol observations (green and blue dots respectively) over-plotted with the best-fit transit-time model from Agol et al. (2020a) (black lines).

where $t_{m,min}$ ($t_{m,max}$) is the minimum (maximum) timing for which the model was computed, $e$ is the epoch of the transit, and $ne_{\{t_{m,max}-t_{m,min}\}}$ is the number of epochs between the first and the last transit times for which the model was computed.

Except for one TRAPPIST-1h timing (at 2458694.77706 $BJD_{TDB}$), the preliminary results show great agreement between the model and the new timings from the ground-based follow-up campaign for the four outer planets. Once all timings will be computed, the goal will be to run an updated transit timing analysis (as the one described in Chapter 4.2.1) to validate and/or refine the current model. In addition, the accumulation of timings allow to improve the timing predictions. At some point, these predictions could be precise enough to enable the detection of deviations originating from tidal effects (Bolmont et al. 2020). Indeed, depending on the vertical profile of the planet (parametrised by the love number $k_2$), we could expect some heterogeneity in the repartition of mass of the planets caused by one or more attractors to complicate the dynamics of the system and result in additional TTVs (of the order of the second). Tidal deformation is anticipated to be larger for the inner planets: b, c, and d. This is made possible by the very compact configuration of the system that induce deformations three orders of magnitude greater than what the Moon exerts on Earth (Zanazzi et al. 2019). In addition, very precise TTVs could help revealing whether the planets

are perfectly tidal locked (as expected) or not exactly (as a result of atmospheric tides for instance (Leconte et al. 2015), see section 1.3.2). Indeed, if a planet such as TRAPPIST-1b was to have a rotation period significantly different than its orbital period this would create a drift in the TTVs that could be detectable. For $P_{rot,b} = 1.05 P_{orb,b}$, we would have a 20s drift in the TTV, something that is not observed by Agol et al. (2020a). However, we need a large amount of transits to expect constraining such low level effects, and although transits are accumulating, we still have not reached the required precision.

As a whole, ground-based observations can bring a lot to exoplanet characterisation. Notably, the follow-up of the TRAPPIST-1 system during this last four years has allowed to:

1. obtain the first empirical constraints on the impact of stellar contamination on transmission spectroscopy. In particular we can notice that this issue has now become of general interest to the community as a NASA Study analysis Group (SAG), SAG21, has been created in 2020 and is dedicated to "The Effect of Stellar Contamination on Space-based Transmission Spectroscopy". SAG21 aims to bring together an interdisciplinary team of scientists from the heliophysics, stellar astrophysics, and exoplanet communities to study the impact of stellar contamination on transmission spectra. I have myself joined the SAG 21 effort in Sep 2020.

2. accumulate enough photometric time series for the detection of flares, spot crossing and variability studies.

3. monitor the timings of the transits of the seven planets, which will eventually help refining their masses, eccentricities and could even be used to constrain the impact of tides on their deformations and maybe one day reveal their vertical density profiles.

## 5.3 Appendix of Chapter 5

### 5.3.1 Results from the individual analyses

**Table 5.7** TRAPPIST-1 transit timings and depths obtained from the individual analyses of SPECULOOS light curves. Each row represents a transit, the first column gives the planet's name, the second the epoch of the transit, the third the measured mid-transit timing and the corresponding $1\sigma$ error, and the last column the measured transit depth and corresponding $1\sigma$ error resulting from the analysis.

| Planet | Epoch | Transit timing [$BJD_{TDB} - 2450000$] | | Transit depth (%) | |
|---|---|---|---|---|---|
| b | 398 | 7923.84586 | 0.00043 | 0.764 | 0.060 |
| | 406 | 7935.93284 | 0.00028 | 0.842 | 0.047 |
| | 406 | 7935.93316 | 0.00053 | 0.893 | 0.088 |

Continued on next page

**Table 5.7 – continued from previous page**

| | | | | | |
|---|---|---|---|---|---|
| | 427 | 7967.66254 | 0.00053 | 0.686 | 0.068 |
| | 431 | 7973.70588 | 0.00058 | 0.759 | 0.078 |
| | 435 | 7979.74899 | 0.00030 | 0.835 | 0.058 |
| | 435 | 7979.74864 | 0.00034 | 0.738 | 0.048 |
| | 439 | 7985.79209 | 0.00034 | 0.721 | 0.052 |
| | 443 | 7991.83579 | 0.00041 | 0.845 | 0.079 |
| | 460 | 8017.52106 | 0.00041 | 0.774 | 0.079 |
| | 462 | 8020.54219 | 0.00036 | 0.758 | 0.056 |
| | 472 | 8035.65192 | 0.00065 | 0.801 | 0.085 |
| | 480 | 8047.73788 | 0.00059 | 0.676 | 0.094 |
| | 507 | 8088.53228 | 0.00033 | 0.796 | 0.060 |
| | 507 | 8088.53206 | 0.00026 | 0.920 | 0.059 |
| | 509 | 8091.55411 | 0.00036 | 0.878 | 0.065 |
| | 509 | 8091.55364 | 0.00035 | 0.809 | 0.045 |
| | 511 | 8094.57595 | 0.00067 | 0.822 | 0.120 |
| | 445 | 7994.85842 | 0.00047 | 0.819 | 0.084 |
| | 445 | 7994.85833 | 0.00051 | 0.855 | 0.083 |
| c | 294 | 7994.81758 | 0.0004 | 0.835 | 0.068 |
| | 294 | 7994.81885 | 0.00065 | 0.695 | 0.082 |
| | 301 | 8011.77150 | 0.00046 | 0.826 | 0.066 |
| | 301 | 8011.77102 | 0.00036 | 0.878 | 0.078 |
| | 310 | 8033.56743 | 0.00041 | 0.801 | 0.060 |
| | 315 | 8045.67598 | 0.00035 | 0.738 | 0.055 |
| | 329 | 8079.58077 | 0.00042 | 0.649 | 0.055 |
| | 329 | 8079.58172 | 0.00050 | 0.679 | 0.055 |
| | 336 | 8096.53342 | 0.00037 | 0.789 | 0.055 |
| | 336 | 8096.53330 | 0.00051 | 0.819 | 0.062 |
| | 322 | 8062.62794 | 0.00039 | 0.727 | 0.160 |
| d | 72 | 7961.73755 | 0.00012 | 0.394 | 0.057 |
| | 74 | 7969.83771 | 0.00020 | 0.264 | 0.062 |
| | 74 | 7969.83665 | 0.00100 | 0.375 | 0.065 |
| | 75 | 7973.88834 | 0.00140 | 0.401 | 0.062 |
| | 90 | 8034.62829 | 0.00063 | 0.405 | 0.048 |
| e | 45 | 7934.83251 | 0.00088 | 0.442 | 0.046 |
| | 45 | 7934.82990 | 0.00092 | 0.417 | 0.044 |
| | 46 | 7940.93132 | 0.00049 | 0.547 | 0.048 |
| | 46 | 7940.92923 | 0.00061 | 0.454 | 0.055 |
| | 53 | 7983.62886 | 0.00095 | 0.522 | 0.055 |
| | 53 | 7983.62706 | 0.00053 | 0.590 | 0.057 |
| | 54 | 7989.73173 | 0.00210 | 0.449 | 0.065 |
| | 54 | 7989.72916 | 0.00067 | 0.458 | 0.045 |
| f | 35 | 7993.63410 | 0.00070 | 0.741 | 0.074 |
| | 40 | 8039.66021 | 0.00084 | 0.639 | 0.056 |
| g | 21 | 7924.76924 | 0.00055 | 0.791 | 0.051 |
| | 24 | 7961.82599 | 0.00075 | 0.723 | 0.059 |
| | 29 | 7813.60697 | 0.00200 | 0.867 | 0.17 |
| h | 16 | 7962.86330 | 0.0018 | 0.372 | 0.052 |
| | 17 | 7981.63159 | 0.0016 | 0.290 | 0.046 |
| | 17 | 7981.63059 | 0.0030 | 0.301 | 0.046 |

**Table 5.8** TRAPPIST-1 transit timings and depths obtained from the individual analyses of K2 light curves. Each row represents a transit, the first column gives the planet's name, the second the epoch of the transit, the third the measured mid-transit timing and the corresponding $1\sigma$ error, and the last column the measured transit depth and corresponding $1\sigma$ error resulting from the analysis.

| Planet | Epoch | Transit timing [$BJD_{TDB} - 2450000$] | | Transit depth (%) | |
|---|---|---|---|---|---|
| b | 277 | 7741.02841 | 0.0011 | 0.959 | 0.200 |
| | 278 | 7742.54031 | 0.00120 | 0.804 | 0.160 |
| | 279 | 7744.05191 | 0.00063 | 0.740 | 0.095 |
| | 280 | 7745.56254 | 0.00071 | 0.721 | 0.080 |
| | 282 | 7748.58511 | 0.00071 | 0.728 | 0.084 |
| | 283 | 7750.09533 | 0.00150 | 0.776 | 0.110 |
| | 284 | 7751.60539 | 0.00093 | 0.799 | 0.150 |
| | 285 | 7753.11716 | 0.00064 | 0.746 | 0.100 |
| | 286 | 7754.62846 | 0.00071 | 0.720 | 0.089 |
| | 287 | 7756.13952 | 0.00110 | 0.775 | 0.150 |
| | 288 | 7757.64925 | 0.00098 | 0.784 | 0.100 |
| | 289 | 7759.16120 | 0.00100 | 0.689 | 0.080 |
| | 290 | 7760.67229 | 0.00086 | 0.743 | 0.097 |
| | 291 | 7762.18295 | 0.00090 | 0.569 | 0.055 |
| | 292 | 7763.69272 | 0.00110 | 0.741 | 0.130 |
| | 293 | 7765.20352 | 0.00056 | 0.843 | 0.083 |
| | 294 | 7766.71525 | 0.00074 | 0.766 | 0.089 |
| | 295 | 7768.22451 | 0.00089 | 0.932 | 0.180 |
| | 296 | 7769.73779 | 0.00140 | 0.666 | 0.200 |
| | 297 | 7771.24857 | 0.00140 | 0.673 | 0.150 |
| | 298 | 7772.75851 | 0.00120 | 0.643 | 0.120 |
| | 299 | 7774.26913 | 0.00085 | 0.889 | 0.110 |
| | 300 | 7775.78022 | 0.00099 | 0.736 | 0.120 |
| | 301 | 7777.28984 | 0.00069 | 0.685 | 0.085 |
| | 302 | 7778.80191 | 0.00084 | 0.632 | 0.070 |
| | 303 | 7780.31394 | 0.00058 | 0.719 | 0.089 |
| | 305 | 7783.33438 | 0.00110 | 0.604 | 0.082 |
| | 306 | 7784.84448 | 0.00150 | 0.555 | 0.110 |
| | 311 | 7792.40048 | 0.00110 | 0.788 | 0.092 |
| | 313 | 7795.42062 | 0.00110 | 0.902 | 0.210 |
| | 314 | 7796.93214 | 0.00093 | 0.772 | 0.130 |
| | 315 | 7798.44260 | 0.00065 | 0.836 | 0.120 |
| | 316 | 7799.95368 | 0.00100 | 0.822 | 0.200 |
| | 317 | 7801.46362 | 0.00099 | 0.707 | 0.100 |
| | 318 | 7802.97696 | 0.00099 | 0.830 | 0.280 |
| | 319 | 7804.48723 | 0.00065 | 0.783 | 0.099 |
| | 320 | 7805.99725 | 0.00110 | 0.669 | 0.160 |
| | 322 | 7809.02001 | 0.00063 | 0.988 | 0.120 |
| | 323 | 7810.52858 | 0.00059 | 0.809 | 0.120 |
| | 325 | 7813.55299 | 0.00079 | 0.866 | 0.130 |
| | 326 | 7815.06305 | 0.00067 | 0.693 | 0.073 |
| | 327 | 7816.57407 | 0.00058 | 0.851 | 0.086 |
| c | 189 | 7740.53417 | 0.00083 | 0.589 | 0.091 |
| | 190 | 7742.95370 | 0.00100 | 0.737 | 0.091 |
| | 191 | 7745.37836 | 0.00200 | 0.656 | 0.150 |
| | 192 | 7747.79745 | 0.00100 | 0.864 | 0.150 |
| | 193 | 7750.21906 | 0.00092 | 0.699 | 0.065 |
| | 194 | 7752.64173 | 0.00100 | 0.652 | 0.079 |
| | 196 | 7757.48363 | 0.00150 | 0.770 | 0.160 |
| | 197 | 7759.90355 | 0.00081 | 0.552 | 0.077 |
| | 198 | 7762.32917 | 0.00098 | 0.697 | 0.100 |
| | 199 | 7764.74926 | 0.00120 | 0.818 | 0.120 |
| | 200 | 7767.17041 | 0.00120 | 0.791 | 0.160 |
| | 201 | 7769.59305 | 0.00082 | 0.579 | 0.090 |

Continued on next page

**Table 5.8 – continued from previous page**

| | | | | | |
|---|---|---|---|---|---|
| | 202 | 7772.01577 | 0.00110 | 0.846 | 0.081 |
| | 203 | 7774.43531 | 0.00084 | 0.732 | 0.090 |
| | 204 | 7776.85884 | 0.00084 | 0.789 | 0.130 |
| | 205 | 7779.27985 | 0.00150 | 0.713 | 0.110 |
| | 206 | 7781.70135 | 0.00081 | 0.785 | 0.081 |
| | 207 | 7784.12337 | 0.00080 | 0.837 | 0.100 |
| | 210 | 7791.38904 | 0.00080 | 0.588 | 0.086 |
| | 211 | 7793.81167 | 0.00085 | 0.674 | 0.082 |
| | 212 | 7796.23257 | 0.00072 | 0.771 | 0.085 |
| | 213 | 7798.65449 | 0.00110 | 0.798 | 0.140 |
| | 214 | 7801.07700 | 0.00084 | 0.771 | 0.140 |
| | 215 | 7803.49803 | 0.00100 | 0.604 | 0.090 |
| | 216 | 7805.91971 | 0.00068 | 0.686 | 0.080 |
| | 217 | 7808.34120 | 0.00120 | 0.797 | 0.120 |
| | 218 | 7810.76238 | 0.00210 | 0.809 | 0.400 |
| | 219 | 7813.18452 | 0.00110 | 0.663 | 0.071 |
| | 220 | 7815.60631 | 0.00070 | 0.856 | 0.074 |
| d | 17 | 7738.99254 | 0.00400 | 0.286 | 0.110 |
| | 18 | 7743.03818 | 0.00120 | 0.564 | 0.092 |
| | 20 | 7751.14013 | 0.00180 | 0.468 | 0.100 |
| | 21 | 7755.18855 | 0.00140 | 0.537 | 0.120 |
| | 22 | 7759.24739 | 0.00180 | 0.461 | 0.073 |
| | 23 | 7763.28944 | 0.00130 | 0.419 | 0.062 |
| | 24 | 7767.34079 | 0.00330 | 0.318 | 0.130 |
| | 25 | 7771.39074 | 0.00420 | 0.453 | 0.120 |
| | 26 | 7775.44035 | 0.00180 | 0.466 | 0.090 |
| | 27 | 7779.48982 | 0.00320 | 0.603 | 0.240 |
| | 30 | 7791.64154 | 0.00098 | 0.570 | 0.076 |
| | 34 | 7807.84073 | 0.00570 | 0.304 | 0.130 |
| | 35 | 7811.88917 | 0.00460 | 0.412 | 0.210 |
| | 36 | 7815.94153 | 0.00170 | 0.361 | 0.110 |
| e | 13 | 7739.67183 | 0.00160 | 0.509 | 0.100 |
| | 14 | 7745.77293 | 0.00180 | 0.514 | 0.110 |
| | 16 | 7757.96796 | 0.00310 | 0.587 | 0.110 |
| | 17 | 7764.07021 | 0.00150 | 0.521 | 0.120 |
| | 18 | 7770.17149 | 0.00240 | 0.447 | 0.130 |
| | 19 | 7776.26457 | 0.00190 | 0.383 | 0.075 |
| | 20 | 7782.36274 | 0.00190 | 0.430 | 0.070 |
| | 22 | 7794.56245 | 0.00180 | 0.599 | 0.089 |
| f | 8 | 7745.03067 | 0.00210 | 0.613 | 0.160 |
| | 9 | 7754.23474 | 0.00140 | 0.653 | 0.110 |
| | 10 | 7763.44545 | 0.00240 | 0.651 | 0.130 |
| | 11 | 7772.64854 | 0.00180 | 0.461 | 0.061 |
| | 14 | 7800.27394 | 0.00220 | 0.524 | 0.120 |
| | 15 | 7809.47737 | 0.00270 | 0.494 | 0.090 |
| g | 8 | 7764.19229 | 0.00180 | 0.559 | 0.071 |
| | 11 | 7801.25085 | 0.00120 | 0.727 | 0.100 |
| | 12 | 7813.60698 | 0.00200 | 0.867 | 0.170 |
| h | 5 | 7756.38806 | 0.00300 | 0.346 | 0.058 |

**Table 5.9** TRAPPIST-1 transit timings and depths obtained from the individual analyses of LT light curves. Each row represents a transit, the first column gives the planet's name, the second the epoch of the transit, the third the measured mid-transit timing and the corresponding $1\sigma$ error, and the last column the measured transit depth and corresponding $1\sigma$ error resulting from the analysis.

| Planet | Epoch | Transit timing [$BJD_{TDB} - 2450000$] | | Transit depth (%) | |
|---|---|---|---|---|---|
| b | 386 | 7905.71514 | 0.00088 | 0.848 | 0.130 |
| | 421 | 7958.59599 | 0.00038 | 0.696 | 0.062 |
| | 425 | 7964.63878 | 0.00043 | 0.830 | 0.063 |
| | 429 | 7970.68530 | 0.00051 | 0.706 | 0.063 |
| c | 270 | 7936.69651 | 0.00040 | 0.721 | 0.053 |
| | 298 | 8004.50488 | 0.00052 | 0.879 | 0.058 |
| | 303 | 8016.61384 | 0.00087 | 0.612 | 0.090 |
| | 319 | 8055.36295 | 0.00044 | 0.765 | 0.059 |
| | 284 | 7970.60046 | 0.00085 | 0.638 | 0.070 |
| d | 86 | 8018.43071 | 0.00096 | 0.353 | 0.027 |
| e | 53 | 7983.62882 | 0.00140 | 0.481 | 0.075 |
| | 56 | 8032.43398 | 0.00180 | 0.475 | 0.100 |
| h | 17 | 7981.63343 | 0.00110 | 0.257 | 0.035 |
| | | | | | |

## 5.3.2 Results from the global analyses

**Table 5.10** Median values and 1-$\sigma$ limits of the posterior PDFs deduced for the timings and depths from their global analyses for SPECULOOS observations. Each row represents a transit, the first column gives the planet's name, the second the epoch of the transit, the third the measured mid-transit timing and the corresponding $1\sigma$ error, and the last column the measured transit depth and corresponding $1\sigma$ error resulting from the analysis.

| Planet | Epoch | Transit timing [$BJD_{TDB} - 2450000$] | | Transit depth (%) | |
|---|---|---|---|---|---|
| b | 398 | 7923.84588 | 0.00043 | 0.744 | 0.053 |
| | 406 | 7935.93286 | 0.00023 | 0.882 | 0.040 |
| | 406 | 7935.93286 | 0.00023 | 0.904 | 0.084 |
| | 427 | 7967.66246 | 0.00054 | 0.706 | 0.090 |
| | 431 | 7973.70578 | 0.00053 | 0.756 | 0.066 |
| | 435 | 7979.74887 | 0.00022 | 0.852 | 0.052 |
| | 435 | 7979.74887 | 0.00022 | 0.763 | 0.044 |
| | 439 | 7985.79210 | 0.00031 | 0.737 | 0.047 |
| | 443 | 7991.83581 | 0.00042 | 0.864 | 0.073 |
| | 460 | 8017.52101 | 0.00061 | 0.758 | 0.072 |
| | 472 | 8035.65154 | 0.00062 | 0.773 | 0.073 |
| | 480 | 8047.73785 | 0.00061 | 0.788 | 0.065 |
| | 462 | 8020.54220 | 0.0004 | 0.698 | 0.120 |
| | 507 | 8088.53214 | 0.00022 | 0.809 | 0.051 |
| | 507 | 8088.53214 | 0.00022 | 0.932 | 0.054 |
| | 509 | 8091.55387 | 0.00026 | 0.895 | 0.059 |
| | 509 | 8091.55387 | 0.00026 | 0.848 | 0.041 |
| | 511 | 8094.57599 | 0.00059 | 0.82 | 0.110 |
| | 445 | 7994.85799 | 0.00055 | 0.735 | 0.073 |
| | 445 | 7994.85799 | 0.00055 | 0.784 | 0.078 |
| c | 294 | 7994.81840 | 0.00034 | 0.792 | 0.069 |
| | 294 | 7994.81840 | 0.00034 | 0.684 | 0.078 |
| | 301 | 8011.77116 | 0.00029 | 0.800 | 0.072 |
| | 301 | 8011.77116 | 0.00029 | 0.904 | 0.076 |
| | 310 | 8033.56743 | 0.00038 | 0.816 | 0.061 |
| | 315 | 8045.67601 | 0.00034 | 0.73 | 0.050 |

Continued on next page

**Table 5.10 – continued from previous page**

| | | | | | |
|---|---|---|---|---|---|
| | 329 | 8079.58130 | 0.00030 | 0.634 | 0.046 |
| | 329 | 8079.58130 | 0.00030 | 0.67 | 0.044 |
| | 336 | 8096.53332 | 0.00030 | 0.813 | 0.046 |
| | 336 | 8096.53332 | 0.00030 | 0.818 | 0.056 |
| | 322 | 8062.62799 | 0.00037 | 0.727 | 0.051 |
| d | 72 | 7961.73774 | 0.00130 | 0.398 | 0.061 |
| | 74 | 7969.83692 | 0.00070 | 0.266 | 0.044 |
| | 74 | 7969.83692 | 0.00070 | 0.376 | 0.053 |
| | 75 | 7973.88758 | 0.00150 | 0.372 | 0.059 |
| | 90 | 8034.62829 | 0.00069 | 0.409 | 0.050 |
| e | 45 | 7934.83078 | 0.00065 | 0.406 | 0.048 |
| | 45 | 7934.83078 | 0.00065 | 0.421 | 0.038 |
| | 46 | 7940.92999 | 0.00069 | 0.540 | 0.050 |
| | 46 | 7940.92999 | 0.00069 | 0.471 | 0.057 |
| | 53 | 7983.62772 | 0.00086 | 0.518 | 0.047 |
| | 53 | 7983.62772 | 0.00086 | 0.553 | 0.070 |
| | 54 | 7989.72944 | 0.00075 | 0.446 | 0.061 |
| | 54 | 7989.72944 | 0.00075 | 0.463 | 0.049 |
| f | 35 | 7993.63412 | 0.00084 | 0.732 | 0.071 |
| | 40 | 8039.66014 | 0.00091 | 0.653 | 0.055 |
| g | 21 | 7924.76918 | 0.00140 | 0.810 | 0.092 |
| | 24 | 7961.82610 | 0.00053 | 0.723 | 0.036 |
| | 29 | 8060.65579 | 0.00047 | 0.758 | 0.036 |
| h | 16 | 7962.86307 | 0.0016 | 0.377 | 0.050 |
| | 17 | 7981.63147 | 0.0012 | 0.291 | 0.044 |
| | 17 | 7981.63147 | 0.0012 | 0.316 | 0.057 |

**Table 5.11** Median values and 1-$\sigma$ limits of the posterior PDFs deduced for the timings and depths from their global analyses for K2 observations. Each row represents a transit, the first column gives the planet's name, the second the epoch of the transit, the third the measured mid-transit timing and the corresponding 1$\sigma$ error, and the last column the measured transit depth and corresponding 1$\sigma$ error resulting from the analysis.

| **Planet** | **Epoch** | **Transit timing** [$BJD_{TDB} - 2450000$] | | **Transit depth (%)** | |
|---|---|---|---|---|---|
| b | 277 | 7741.02854 | 0.00088 | 0.883 | 0.16 |
| | 278 | 7742.54031 | 0.00100 | 0.755 | 0.130 |
| | 279 | 7744.05189 | 0.00060 | 0.707 | 0.069 |
| | 280 | 7745.56251 | 0.00069 | 0.710 | 0.069 |
| | 282 | 7748.58503 | 0.00073 | 0.725 | 0.082 |
| | 283 | 7750.09517 | 0.00130 | 0.759 | 0.082 |
| | 284 | 7751.60547 | 0.00093 | 0.733 | 0.099 |
| | 285 | 7753.11697 | 0.00093 | 0.702 | 0.095 |
| | 286 | 7754.62839 | 0.00068 | 0.704 | 0.081 |
| | 287 | 7756.13946 | 0.00095 | 0.748 | 0.120 |
| | 288 | 7757.64914 | 0.00096 | 0.787 | 0.130 |
| | 289 | 7759.16115 | 0.00095 | 0.678 | 0.071 |
| | 290 | 7760.67223 | 0.00092 | 0.729 | 0.084 |
| | 291 | 7762.18186 | 0.00067 | 0.798 | 0.098 |
| | 292 | 7763.69279 | 0.00130 | 0.737 | 0.130 |
| | 293 | 7765.20350 | 0.00056 | 0.848 | 0.082 |
| | 294 | 7766.71535 | 0.00058 | 0.754 | 0.074 |
| | 295 | 7768.22554 | 0.00086 | 0.772 | 0.093 |
| | 297 | 7771.24824 | 0.00150 | 0.634 | 0.110 |
| | 298 | 7772.75842 | 0.00120 | 0.628 | 0.110 |
| | 299 | 7774.26926 | 0.00093 | 0.862 | 0.097 |
| | 300 | 7775.78035 | 0.00099 | 0.699 | 0.110 |

Continued on next page

**Table 5.11 – continued from previous page**

| | | | | | |
|---|---|---|---|---|---|
| | 301 | 7777.28988 | 0.00067 | 0.679 | 0.081 |
| | 302 | 7778.80210 | 0.00086 | 0.637 | 0.072 |
| | 303 | 7780.31392 | 0.00089 | 0.763 | 0.099 |
| | 305 | 7783.33449 | 0.00099 | 0.590 | 0.078 |
| | 306 | 7784.84429 | 0.00200 | 0.487 | 0.096 |
| | 311 | 7792.40048 | 0.00060 | 0.784 | 0.090 |
| | 313 | 7795.42063 | 0.00095 | 0.829 | 0.120 |
| | 314 | 7796.93209 | 0.00087 | 0.753 | 0.110 |
| | 315 | 7798.44265 | 0.00078 | 0.799 | 0.098 |
| | 316 | 7799.95390 | 0.00090 | 0.758 | 0.110 |
| | 317 | 7801.46367 | 0.00093 | 0.702 | 0.095 |
| | 319 | 7804.48731 | 0.00062 | 0.749 | 0.076 |
| | 320 | 7805.99734 | 0.00120 | 0.623 | 0.110 |
| | 322 | 7809.01987 | 0.00050 | 0.950 | 0.080 |
| | 323 | 7810.52885 | 0.00070 | 0.718 | 0.072 |
| | 325 | 7813.55233 | 0.00087 | 0.767 | 0.091 |
| | 326 | 7815.06311 | 0.00069 | 0.696 | 0.070 |
| | 327 | 7816.57415 | 0.00014 | 0.825 | 0.170 |
| c | 189 | 7740.53434 | 0.00071 | 0.572 | 0.057 |
| | 190 | 7742.95387 | 0.00096 | 0.711 | 0.085 |
| | 191 | 7745.37552 | 0.00130 | 0.602 | 0.079 |
| | 192 | 7747.79788 | 0.00100 | 0.772 | 0.099 |
| | 193 | 7750.21885 | 0.00077 | 0.685 | 0.058 |
| | 194 | 7752.64222 | 0.00130 | 0.620 | 0.069 |
| | 196 | 7757.48369 | 0.00120 | 0.713 | 0.110 |
| | 197 | 7759.90363 | 0.00091 | 0.542 | 0.087 |
| | 198 | 7762.32938 | 0.00099 | 0.662 | 0.091 |
| | 199 | 7764.74912 | 0.00160 | 0.736 | 0.096 |
| | 200 | 7767.17049 | 0.00110 | 0.741 | 0.076 |
| | 201 | 7769.59284 | 0.00079 | 0.549 | 0.075 |
| | 202 | 7772.01581 | 0.01000 | 0.823 | 0.072 |
| | 203 | 7774.43569 | 0.00092 | 0.681 | 0.068 |
| | 204 | 7776.85852 | 0.00081 | 0.715 | 0.060 |
| | 205 | 7779.27989 | 0.00120 | 0.674 | 0.090 |
| | 206 | 7781.70123 | 0.00058 | 0.768 | 0.060 |
| | 207 | 7784.12346 | 0.00092 | 0.795 | 0.089 |
| | 210 | 7791.38893 | 0.00084 | 0.589 | 0.081 |
| | 211 | 7793.81172 | 0.00086 | 0.657 | 0.081 |
| | 212 | 7796.23247 | 0.00074 | 0.746 | 0.078 |
| | 214 | 7801.07714 | 0.00150 | 0.734 | 0.120 |
| | 215 | 7803.49838 | 0.00085 | 0.624 | 0.078 |
| | 216 | 7805.91962 | 0.00110 | 0.606 | 0.110 |
| | 217 | 7808.34096 | 0.00140 | 0.744 | 0.082 |
| | 219 | 7813.18461 | 0.00096 | 0.641 | 0.065 |
| | 220 | 7815.60652 | 0.00072 | 0.825 | 0.064 |
| d | 17 | 7738.99218 | 0.00230 | 0.258 | 0.065 |
| | 18 | 7743.03815 | 0.00087 | 0.562 | 0.091 |
| | 20 | 7751.14085 | 0.00230 | 0.434 | 0.079 |
| | 21 | 7755.18922 | 0.00130 | 0.428 | 0.072 |
| | 22 | 7759.24736 | 0.00210 | 0.441 | 0.070 |
| | 23 | 7763.28937 | 0.00140 | 0.408 | 0.065 |
| | 24 | 7767.33969 | 0.00260 | 0.283 | 0.070 |
| | 26 | 7775.44044 | 0.00160 | 0.454 | 0.082 |
| | 30 | 7791.64168 | 0.00088 | 0.549 | 0.062 |
| | 36 | 7815.94088 | 0.00260 | 0.289 | 0.070 |
| e | 13 | 7739.67188 | 0.00610 | 0.478 | 0.089 |
| | 14 | 7745.77245 | 0.00430 | 0.473 | 0.072 |
| | 16 | 7757.96794 | 0.00340 | 0.572 | 0.120 |
| | 17 | 7764.06998 | 0.00120 | 0.477 | 0.077 |
| | 18 | 7770.17137 | 0.00270 | 0.413 | 0.071 |

Continued on next page

**Table 5.11 – continued from previous page**

| | | | | | |
|---|---|---|---|---|---|
| | 19 | 7776.26467 | 0.00190 | 0.365 | 0.063 |
| | 20 | 7782.36298 | 0.00170 | 0.414 | 0.059 |
| | 22 | 7794.56266 | 0.00210 | 0.587 | 0.092 |
| f | 8 | 7745.03110 | 0.00230 | 0.567 | 0.090 |
| | 9 | 7754.23467 | 0.00160 | 0.603 | 0.069 |
| | 10 | 7763.44538 | 0.00200 | 0.636 | 0.100 |
| | 11 | 7772.64872 | 0.00220 | 0.456 | 0.070 |
| | 14 | 7800.27402 | 0.00230 | 0.494 | 0.088 |
| | 15 | 7809.47707 | 0.00170 | 0.484 | 0.064 |
| g | 8 | 7764.19196 | 0.00160 | 0.567 | 0.068 |
| | 11 | 7801.25070 | 0.00120 | 0.707 | 0.087 |
| | 12 | 7813.60635 | 0.00140 | 0.728 | 0.100 |
| h | 5 | 7756.38806 | 0.00300 | 0.346 | 0.058 |

**Table 5.12** Median values and 1-$\sigma$ limits of the posterior PDFs deduced for the timings and depths from their global analyses for Liverpool telescope observations. Each row represents a transit, the first column gives the planet's name, the second the epoch of the transit, the third the measured mid-transit timing and the corresponding 1$\sigma$ error, and the last column the measured transit depth and corresponding 1$\sigma$ error resulting from the analysis.

| **Planet** | **Epoch** | **Transit timing** [$BJD_{TDB} - 245000$] | | **Transit depth (%)** | |
|---|---|---|---|---|---|
| b | 386 | 7905.71519 | 0.00088 | 0.834 | 0.120 |
| | 421 | 7958.59605 | 0.00036 | 0.687 | 0.061 |
| | 425 | 7964.63885 | 0.00044 | 0.838 | 0.053 |
| | 429 | 7970.68541 | 0.00041 | 0.707 | 0.062 |
| c | 270 | 7936.69651 | 0.00035 | 0.723 | 0.047 |
| | 298 | 8004.50488 | 0.00053 | 0.853 | 0.054 |
| | 303 | 8016.61367 | 0.00068 | 0.605 | 0.084 |
| | 319 | 8055.36297 | 0.00047 | 0.764 | 0.066 |
| | 284 | 7970.60044 | 0.00088 | 0.641 | 0.070 |
| d | 86 | 8018.43071 | 0.00096 | 0.353 | 0.027 |
| e | 53 | 7983.62906 | 0.00130 | 0.476 | 0.069 |
| | 56 | 8032.43405 | 0.00190 | 0.478 | 0.100 |
| h | 17 | 7981.63343 | 0.00110 | 0.257 | 0.035 |

### 5.3.3 Combined spectra

| Planets | **Effective bandpass** ($\mu$m) | Z18 (%) | Observations (%) |
|---|---|---|---|
| b+c | 4.5 | 1.44 ± 0.03 | 1.424 ± 0.008 |
| | 1.6 | 1.54 ± 0.03 | 1.539 ± 0.028 |
| | 1.55 | 1.52 ± 0.03 | 1.536 ± 0.033 |
| | 1.5 | 1.49 ± 0.03 | 1.542 ± 0.033 |
| | 1.45 | 1.45 ± 0.03 | 1.534 ± 0.040 |
| | 1.4 | 1.42± 0.03 | 1.494 ± 0.037 |
| | 1.35 | 1.46 ± 0.03 | 1.484 ± 0.034 |
| | 1.3 | 1.51 ± 0.03 | 1.534 ± 0.035 |
| | 1.25 | 1.54± 0.03 | 1.592 ± 0.033 |
| | 1.2 | 1.53± 0.03 | 1.531 ± 0.028 |
| | 1.15 | 1.53± 0.03 | 1.487 ± 0.039 |
| | 0.8-1.1 | **1.33 ± 0.03** | 1.470 ± **0.032** |
| | **0.73-1.1** | **1.27 ± 0.03** | 1.490 ± 0.027 |
| | **0.55-0.9** | **0.94 ± 0.03** | 1.400 ± 0.020 |
| b+c+d+e+f+g | 4.5 | 3.55 ± 0.06 | 3.646 ± 0.009 |
| | 1.63 | 3.91 ± 0.06 | 3.885 ± 0.027 |
| | 1.58 | 3.72 ± 0.06 | 3.873 ± 0.032 |
| | 1.53 | 3.75 ± 0.06 | 3.793 ± 0.032 |
| | 1.48 | 3.78 ± 0.06 | 3.824 ± 0.032 |
| | 1.43 | 3.47 ± 0.06 | 3.750 ± 0.035 |
| | 1.38 | 3.79 ± 0.06 | 3.759 ± 0.033 |
| | 1.33 | 3.86 ± 0.06 | 3.858 ± 0.038 |
| | 1.28 | 3.89 ± 0.06 | 3.895 ± 0.03 |
| | 1.23 | 3.89 ± 0.06 | 3.834 ± 0.029 |
| | 1.18 | 3.88 ± 0.06 | 3.771 ± 0.033 |
| | 0.8-1.1 | / | / |
| | **0.73-1.1** | **3.34 ± 0.06** | 4.370 ± 0.049 |
| | **0.55-0.9** | **2.62 ± 0.06** | 3.474 ± 0.038 |
| d+e+f+g | 4.5 | 2.19 ± 0.05 | 2.222 ± 0.010 |
| | 1.63 | 2.37 ± 0.05 | 2.345 ± 0.023 |
| | 1.58 | 2.27 ± 0.05 | 2.337 ± 0.027 |
| | 1.53 | 2.28 ± 0.05 | 2.251 ± 0.027 |
| | 1.48 | 2.29 ± 0.05 | 2.291 ± 0.025 |
| | 1.43 | 2.13 ± 0.05 | 2.257 ± 0.029 |
| | 1.38 | 2.30 ± 0.05 | 2.276 ± 0.028 |
| | 1.33 | 2.34 ± 0.05 | 2.324 ± 0.033 |
| | 1.28 | 2.35 ± 0.05 | 2.303 ± 0.025 |
| | 1.23 | 2.35 ± 0.05 | 2.303 ± 0.026 |
| | 1.18 | 2.35± 0.05 | 2.284 ± 0.027 |
| | 0.8-1.1 | / | / |
| | **0.73-1.1** | **2.05 ± 0.05** | 2.233 ± 0.037 |
| | **0.55-0.9** | **1.66 ± 0.05** | 2.074 ± 0.044 |

**Table 5.13** Combined transit depth values (in percent) for b+c, b+c+d+e+f+g, and d+e+f+g, as predicted from the best-fit stellar contamination model of Z18, and as measured from K2, SPECULOOS, HST/WFC3, and *Spitzer* observations in their effective bandpass relatively to an M8 star spectrum.

# Chapter 6

# Conclusion

In this chapter, I review the research I have been carrying out during my PhD and highlight the main results. Finally, I discuss some prospects for my future research.

## 6.1 Summary

The search for life elsewhere in the Universe is an extraordinary endeavour that needs extraordinary instrumental precisions and modelling capabilities. It requires that we ask ourselves "what are we looking for?" and thus implicitly : "what is life?". Astrobiologists have understood that the most appropriate way to address this question is through an interdisciplinary approach. In the last decades, astrobiology has bridged several domains including exoplanetology, the astronomical science field dedicated to the search for and study of extra-solar planets. For various reasons that I exposed in my introduction chapter, it is believed that our best shot to find life on an extra-solar planet is to aim for terrestrial planets residing in the HZ of their host star. However, with the current capabilities only very specific systems are in our reach: systems with potentially habitable planets orbiting (and transiting) low-mass red dwarfs, and especially the smallest / coolest / lowest-mass of them: UCDS. A consensus to seize this opportunity has emerged. For the last few years, ground- and space-based surveys, spatial missions, and theoretical studies of planets orbiting UCDS have been developed extensively. In particular, the James Webb Space Telescope (JWST), to be launched at the end of this year 2021, will be well suited to study such systems through transmission and/or emission spectroscopy given its infrared spectral coverage, sensitivity, and resolution. In that regard, the current effort that the community must undertake is twofold: (1) to identify the most amenable targets, i.e to detect more transiting rocky planets orbiting nearby UCDS, and (2) to understand the dynamical environment and characteristics of such planets, notably to

prepare their future characterisation with the JWST.
During my PhD, I have addressed both fronts, by participating to the deployment of the SPECULOOS project and by carrying out intensive follow-up campaigns and analyses to unravel the nature of the TRAPPIST-1 system.

In Chapter 2, I have presented the SPECULOOS project (Search for Planets EClipsing ULtra-cOOl Stars) which aims to detect terrestrial planets eclipsing UCDS that are suited for atmospheric characterisation, and set constraints on the structure and occurrence of planetary systems of UCDS (Delrez et al. 2018b; Sebastian et al. 2020). I was involved in several aspects of the SPECULOOS project, including:

- The technical monitoring of the telescopes. I participated to two technical on-site missions at the SSO observatory (Paranal, Chile) in July and October 2018. Those missions included the commissioning of the *Ganymede* telescope and the maintenance of the three other telescopes (changing cameras, cleaning filter wheels, testing the telescopes performances, etc). In addition, I have been operating SSO telescopes remotely one week per month for four years.

- The target selection and strategy. Considering the extensive number of targets in the SPECULOOS catalogue (1657), a crucial step to find as many planets as possible was the optimisation of the observational strategy. To this aim, I co-led a study focused on the optimisation of the target selection and observational strategy of the project (Sebastian et al. 2020). Furthermore, I developed an open source tool, named `spock`[1], to implement the chosen strategy and optimise the scheduling of the observations of the SPECULOOS targets on the telescopes. The aim of `spock` is to prepare observation plans each night for SSO, SNO and Saint-Ex observatories, while taking into account strategical, physical, and technical constraints. It also includes a short-term-scheduler module to plan the observations of external programs (which represent 20% of the SPECULOOS telescopes time). In addition, `spock` is versatile and can be adapted to handle the observations strategy and scheduling on other astronomical surveys/projects.

- The analysis of the data. I have been taking part in the daily inspection of the outputs of the SSO and PRINCE pipelines to report any transit-like structures, flares, and/or periodic photometric variability. For intriguing transit-like structures, I performed independent reduction/aperture photometry to estimate the effects of systematics and weight of comparisons stars. For the most convincing events, I carried out further analyses with the MCMC code presented in Chapter 3 to estimate the transit parameters

[1] https://github.com/educrot/spock

and eventually to validate/discard the planetary origin of the event. In parallel, for targets observed for a significant amount of hours (≥100 hours), I have performed phase coverage estimations and injection recovery tests to estimate the probability that we missed a transit as a function of the orbital period of an hypothetical planet. So far, since TRAPPIST-1 planets, no new exoplanets have been confirmed on any of the SPECULOOS targets observed, yet.

Besides, through the scheduling of external program targets with `spock`, I took part in every follow-up programs observations performed on the SPECULOOS telescopes. For each program, I planed all observations, and performed independent data reduction and analyses when needed to help in the determination of the systems characteristics. To that extent, I had the chance to take part in the discovery of a variety of new astronomical objects, such as: a double-line eclipsing sub-stellar binary (Triaud et al. 2020), the confirmation of a couple of new exoplanets (Bryant et al. 2021; Cooke et al. 2020; Kostov et al. 2019; Leleu et al. 2019; Nielsen et al. 2019; Quinn et al. 2019; Temple et al. 2019a; Turner et al. 2019; R. G. West et al. 2019), and the characterisation of a set of M-dwarf stars with complex, sharp-peaked, and strictly periodic photometric modulations (Günther et al. 2020a). Notably, I was particularly involved in the discovery of the exoplanet K2-315b that joined the exclusive group of terrestrial exoplanets amenable for atmospheric characterisation with the JWST, as I explained in Chapter 2.

The first (and only so far) planetary system discovered by the SPECULOOS core project was the TRAPPIST-1 system (Gillon et al. 2016; Gillon et al. 2017b). In that regards, a vast part of my PhD was dedicated to its characterisation. I was in charge of all TRAPPIST-1 follow up observations with SPECULOOS and involved in most of the follow-up carried out with other ground- (Liverpool telescope, Devasthal Optical telescope) and space-based (K2, NASA Spitzer space telescope) telescopes.

As I explained in Chapter 4, I was given the extraordinary opportunity to lead the analysis of the entire Spitzer Space Telescope's time-series photometry of the TRAPPIST-1 system (Ducrot et al. 2020). This represents more than 1000 hours of observations (188 transits) in channel 1 and 2 of Spitzer's Infrared Array Camera (IRAC). My analysis of this extensive dataset led to exquisitely precise measurements of the transit depths of the TRAPPIST-1 planets (precision as low as ≃70ppm). This study also brought tighter constraints on several system's parameters (planets and host) and allowed for the first attempts to characterise the planets' atmospheres and habitability. Notably, I combined the transmission spectra of the six inner planets to decrease the error bars down to ≃ 30ppm and showed that it is unlikely that most of the TRAPPIST-1 planets possess $CH_4$-dominated atmospheres. Furthermore, I

discussed the impact of flares on the habitability of TRAPPIST-1 habitable zone planets and showed that none of them currently lies in the abiogenesis zone of their star (a zone where flaring activity is strong enough to initiate prebiotic chemistry via the mechanisms detailed in Rimmer et al. (2018) and Xu et al. (2018)). Finally, I aimed at detecting the secondary eclipse of the two inner planets and, although no a significant signal was found, my analyses allowed to set the first constraints on the brightness temperature of planets b and c.

In continuation of my work on Spitzer, brought a significant contribution to a study that aimed at refining the masses, radii, densities, dynamics, and ephemerides of the seven TRAPPIST-1 planets from a N-body transit-timing analysis combined with a photodynamical analysis (Agol et al. 2020b). The inputs of both analyses were the timings and the detrended light curves derived from my previous work (Ducrot et al. 2020). The transit timing analysis allowed to derived masses for the TRAPPIST-1 planets with a precision of 3 to 5%, which is equivalent to a radial-velocity (RV) precision of 2.5 cm/sec (two orders of magnitude better than current RV capabilities on such target). Such tight constraints on the masses enabled to compute the planets' bulk densities and discuss potential planetary interior scenarios. Results suggested that all seven TRAPPIST-1 planets have a uniform planetary composition which result in lower densities than the Earth, Venus, and even Mars. However, possible interior composition scenarios to explain such observations are degenerated. Theoretically, the planets could either have a deficit of high-density material (e.g., less iron) relative to Earth, or an excess of low-density material (e.g., more water), or both. Only more precise measurements, in particular of the stellar parameters, could help disentangle between scenarios. Finally, the results from the TTV analysis put strong constraints on the orbital eccentricities of the planets and their inclinations, and allowed to conclude that all planets have eccentricity values below 0.01 and are co-planar to a few hundredth of degrees.

In parallel, as I described in Chapter 5, I also worked on leveraging the estimated impact of the *transit light source* (TLS) effect on the transit transmission spectra of the TRAPPIST-1 planets. The TLS effect is a kind of stellar contamination that arises from photospheric heterogeneities present on the host star, such as cold spots or bright faculae, that have spectral signatures that can imprint the transit transmission spectra of the planets and produce apparent transit depth variations that can mimic or mask exoplanetary atmospheric features. To quantify its impact, I gathered a large amount of space- and ground- based data and confront the observations with theoretical predictions from Zhang et al. (2018). My work consisted in the analysis of 169 transits observed in the optical from space with K2 and the near-IR from the ground with the SPECULOOS and the Liverpool telescope. Combining measured transit depths obtained from this extensive set of transits with literature results in the mid/near-IR with Spitzer/IRAC and HST/WFC3, I was able to construct broadband

transmission spectra of the TRAPPIST-1 planets over the 0.8-4.5 $\mu m$ spectral range (Ducrot et al. 2018). From the comparison of observations with contamination models, my work concluded that the impacts of the TLS effect on TRAPPIST-1 planets' spectra is less severe than predicted and that (Zhang et al. 2018)'s model could be discarded. Yet, I noticed that the spectra of the seven planets show some spectral variability (amplitude of hundreds of ppm) which could still be sign of stellar heterogeneity. In that regard, in Chapter 5, I discussed some alternative scenarios such as giant cold spots, or small hot faculae. I also outlined that one of the best avenue to address the stellar contamination issue with our current instrumental capabilities could be to rely on multi-band photometry to study the chromatic evolution of the stellar photometric variability.

Currently, I am leading this effort through a new analysis of ground-based observations of TRAPPIST-1 (Ducrot et al. 2021). My intention is now to study the variability of the host star - and derive its rotation period (if any) - in the I+z band ($0.7 - 1.0\ \mu m$). To achieve this goal, I have organised a daily monitoring of the star for three months with the SPECULOOS telescopes, in addition to the usual transit follow-up observations. The outcomes of these observations will prove extremely useful to solve the current puzzle that exists on the true value of the rotation period of TRAPPIST-1. Intriguingly, a rotation period of 3.3 days was derived from K2 observations (in the visible) (Luger et al. 2017a) but this variability was not observed in Spitzer's photometry (in the near-IR) (Delrez et al. 2018a). The identification of a rotational period in I+z (or the lack of) will hopefully provide insights on the proportion and temperature of spots on the star's photosphere, which will ultimately help constrain/model the impact of the TLS effect on planetary spectra.

## 6.2 Prospects

### 6.2.1 The future of SPECULOOS

SPECULOOS will continue its operation for at least 10 years (Delrez et al. 2018b) and will hopefully detect a lot more exoplanets orbiting UCDS. In the next future, two main upgrades of the facilities will be made that will likely open new horizons.

1. Firstly, SPECULOOS telescope's filter wheels will soon count a new filter called "z-cut". z-cut is an optimised filter design imagined by my collaborator Peter Pedersen to minimise the effect of precipitable water vapour (PWV) on a target's light curve while keeping reasonable flux, even for the faintest SPECULOOS targets (Pedersen et al.

2021a). Such z-cut filters have been manufactured by the company *Asashi Spectra*[2], installed on Artemis and SAINT-EX telescopes very recently (only a few weeks ago), and are currently under testing.

2. Secondly, for the last three years, the project SPIRIT (SPECULOOS InfraRed photometric Imager for Transits) has been in development. The first step of the SPIRIT project was to quantify the gain that could be made in terms of photometric precision for the faintest and latest SPECULOOS targets, by replacing one of our current Andor iKon-L camera with an infrared camera. This study was led by my colleague Peter Pedersen who proved the feasibility of the project and predicted improved photometric performances, notably for stars with spectral type later than M8V. These results will soon be presented in a corresponding paper (Pedersen et al. 2021b). The camera that ended to be chosen is currently being manufactured by the company *Princeton Infrared Technologies*[3] and should be sensitive up to 1.7$\mu m$. Yet, the filter chosen will only spans from 0.81 to 1.33$\mu m$ (combination of z', Y, and J bands). The decision was made to cut all wavelengths above 1.33$\mu m$ due to the presence of a strong water absorption band that can produce high PWV dependency, and below 0.81$\mu m$ because the faintest UCDS have almost no flux in this spectral region. Remarkably, with SPIRIT, the effect of PWV on a target light curve is expected to strongly decrease compared to what we currently obtain with the Andor Ikon-L camera equipped with I+z filter (the reddest band available). This owes to fact that the change of flux due to PWV weekly depends on the spectral type of the target at this wavelength range, such that it has almost no impact on the differential photometry. Furthermore, because of the larger flux in this band, exposure time expected with SPIRIT are way smaller than the one required in I+z for the same targets. This will result in improved samplings and duty cycles.

Besides, the SPECULOOS team has initiated several parallel efforts to carry out robust transit search on existing SPECULOOS data. Indeed, for the last four years, data have accumulated to the point where performances and detectability statistics can now provide significant insights on the planet-yield. To do so, tools developed by members of the SPECULOOS team have been developed (such as the Github package `Splash`[4] designed by my collaborator Prajwal Niraula) or under development (such as the Python framework `nuance` designed by my collaborator Lionel Garcia (Garcia et al. 2021a)). In parallel, population studies of UCDS including flares and/or rotational periods, such as the one led by my collaborator Catriona Murray in C. Murray et al. (2021), will be continued.

[2] https://www.asahi-spectra.com/
[3] https://www.princetonirtech.com/
[4] https://github.com/disruptiveplanets/splash

Although I am starting a new post doctoral position in September 2021, I intend to keep an active role in the SPECULOOS project. In particular, as I will be joining the team of the JWST/MIRI instrument, I hope that I could make the bridge between SPECULOOS and MIRI on various scientific cases, notably the TRAPPIST-1 planets.

### 6.2.2 The future of TRAPPIST-1

As outlined extensively in Chapter 4 and 5, TRAPPIST-1 is the most observationally favourable system of potentially habitable planets known to exist. Notably, JWST is ideally poised to conduct further reconnaissance of many TRAPPIST-1 planets via transmission and, for the hottest planets in the system, emission spectroscopy. As a matter of fact, several studies prospect very promising outcomes in terms of constraints on the TRAPPIST-1 planets' interiors and atmospheric composition from their observations with JWST (Agol et al. 2020b; Dobos et al. 2019; Fauchez et al. 2019; Grimm et al. 2018; Krissansen-Totton et al. 2018a; Lincowski et al. 2018; Lustig-Yaeger et al. 2019; Morley et al. 2017; Turbet et al. 2020a; Wunderlich et al. 2019). This enthusiasm around TRAPPSIT-1 is well illustrated by the fact that it is the only exoplanet target to be observed as part of four JWST GTO programs (GTO 1177, PI: Thomas Greene; GTO 1279, PI: Pierre-Olivier Lagage; GTO 1201, PI: David Lafreniere; and GTO 1331, PI: Nikole Lewis). In addition, it has recently been announced that it will also be observed as part of three GO programs (GO IDs: 2304, PI: Laura Kreidberg; GTO 2420, PI: Alexander Rathcke; GTO 2589, PI: Olivia Lim). I will myself take part in this effort, as I explain at the end on this section.

In terms of atmospheric characterisation, JWST instruments will allow to perform transmission spectroscopy during transits as well as emission and phase curve photometry. While waiting for the telescope to be launched (announced for Oct 2021), several detectability studies, for various atmospheric scenarios assuming the seven planets have been carried out. Either using 1-D radiative-convective model coupled with photochemistry modules or more sophisticated 3-D Global Climate Model (GCMs), simulations agrees on the inference that $CO_2$ could be detected in fewer than 10 transits, for all seven TRAPPIST-1 planets (Fauchez et al. 2019; Lustig-Yaeger et al. 2019; Morley et al. 2017), providing their atmospheres lack high-altitude aerosols. In particular, as outlined by Turbet et al. (2020a), the 4.3$\mu m$ $CO_2$ band appears to be the most promising absorption feature to look after in transmission, as it is weakly affected by clouds or hazes and its detectability is a small function of the concentration of $CO_2$ in the planet's atmosphere. Other molecular features could also be detected. For instance, $O_2$ could be detected via transmission spectroscopy through the $O_2$-$O_2$ infrared collision-induced absorption at 6.4$\mu m$ (Fauchez et al. 2020a). However, simulations

for TRAPPIST-1e showed that a $5\sigma$ detection would require several hundreds of transits (Fauchez et al. 2020b), which is not feasible. Alternatively, Lincowski et al. (2019) showed that the detection of isotopologue bands such as $HDO$ or $^{18}O^{12}C^{16}O$ could inform us on the abundance ratios of isotopes such as deuterium $D$ or Oxygen 18 $^{18}O$. Important isotopic fractions, as observed on Venus for instance, could then indicate an ocean-free surface, an extreme atmospheric loss, oxygen build-up, and thus inform us on the planet's habitability (Lincowski et al. 2019). In terms of detectability, such features should be detectable on the inner planets in $\simeq$10 transits, providing they have a clear-sky atmosphere not dominated by $CO_2$.

In parallel, observations of the infrared thermal emission of the TRAPPIST-1 planets with JWST/MIRI, through occultations and/or full-orbit phase curves, will offer a complementary approach to probe the planets atmospheric properties. Although inconclusive, the analyses I carry out on Spitzer photometry pave the way toward the first constraints on planet b and c's brightness temperature. Morley et al. (2017) foresees promising results with JWST/MIRI, with $\leq 9$ eclipse observations of planet b needed to detect the band-integrated thermal emission at a $25\sigma$ confidence (for a Venus-like atmosphere). In addition, simulations predict that tens of secondary eclipses with MIRI LRS should allow us to detect a 10 bar clear-sky $CO_2$ atmosphere and even disentangle it from a $H_2O$ dominated atmosphere (Koll et al. 2019; Lustig-Yaeger et al. 2019; Malik et al. 2019). Furthermore, it is important to note that secondary emission spectrophotometry presents the great advantage of being poorly impacted by stellar contamination.

In terms of TTVs, we expect the transit timing precision to be as good as 0.6 to 1.7 second per transit with JWST/NIRSpec (Agol et al. 2020a). Then combined with numerous (although less precised) transit timings from extensive ground-based follow up, we foresee a revisit of the N-body dynamical analysis mentioned in Chapter 4, and presumably a significant improvement of the planet mass uncertainties. In parallel, such precise timings, monitored on a significant timescale, might open the way towards the empirical estimation of the planets tidal deformation from TTVs as suggested by Bolmont et al. (2020).

Alternatively, we could also expect new mass measurements to be obtained from radial velocity measurements with the development of cutting-edge near-infrared (NIR) spectrographs mounted on large telescopes such as the SPectropolarimètre InfraROUge (SPIRou) (Donati et al. 2018), the Infrared Doppler (IRD) instrument (Akiyama et al. 2018; Kotani et al. 2014; Omiya et al. 2012), and the Near Infra-Red Planet Searcher (NIRPS) (Wildi et al. 2017).
However, despite new or more accurate mass measurements, it seems that the limiting factor in our estimation of the planet mass-radius relationships will anyway come from our precision on the stellar radius. Indeed, this value mainly depends on the uncertainty on the age of

TRAPPIST-1 (Burgasser et al. 2017) which propagates to stellar radius uncertainty in stellar evolution models such as those of Filippazzo et al. (2015). However, such models are not flawless, for instance they do not include the computation of potential biases induced by magnetic activity and/or tidal interactions with the planets (Burgasser et al. 2017; Gonzales et al. 2019). Besides, the stellar mass depends on mass-luminosity-metallicity relations such as the one derived by Mann et al. (2019), and are not perfectly exact either. As the stellar density is well constrained by the transits, if we manage to improve our measurement of the stellar radius, we could improve our precision on the stellar mass accordingly. Yet, it is not clear how such progress will be made.

High resolution NIR spectroscopy could also be used to infer the properties of the TRAPPIST-1 system via the detection of the Rossiter-McLaughlin effect (McLaughlin 1924; Rossiter 1924). Recently, Hirano et al. (2020) has announced in a letter that they had potentially detected the Rossiter-McLaughlin effect with the Subaru-IRD spectrograph and derived a projected rotation velocity for TRAPPIST-1 of $1.49^{+0.36}_{-0.37}$ $km/s$ which corresponds to a maximum stellar rotation period of $3.97^{+1.32}_{-0.77}$ days (Turbet et al. 2020a), consistent with the one observed in K2 photometry (Morris et al. 2018c).

Finally, very high spectral resolution could be used to individually resolved molecular absorption lines and then co-add their signals using cross-correlation methods (described by Snellen et al. (2013)) to probe the exoplanet's atmospheric composition (Serindag et al. 2019). Simulations predict that the detection of molecules such as $H_2O$ or $O_2$ (at $760nm$) could be attempted with the Extremely Large Telescope (ELT) (Rodler et al. 2014; Serindag et al. 2019; Snellen et al. 2013). However, such a detection would require 42 to 60 transits for HZ planets orbiting a late M dwarf like TRAPPIST-1, which makes it challenging to achieve in practice.

Back on the search for life, although TRAPPIST-1 system harbour the most promising targets for such a search with the JWST, detecting biosignatures on one of its planets in the next decade will likely be very challenging. For instance, for the significant detection of a biosignature such as ozone $O_3$ (considered as the photochemical byproduct of $O_2$) on an habitable zone planet such as TRAPPIST-1e, simulations predict that at least 100 transits would have to be observed with either JWST/NIRSpec or JWST/MIRI LRS. Considering the finite lifetime of the JWST mission, the restricted visibility of the star, the high demand for GO programs, and the significant amount of observing time required, it is very a priori unlikely that such intensive observations will be performed without tangible proof that the planet has an atmosphere and that it is likely to contain oxygen. Otherwise, Robinson (2018) suggest that detecting water in the atmosphere of one of the TRAPPIST-1 HZ planets could indirectly hint at surface habitability. However, even in the ideal case of clear sky and 1-bar

$O_2$◂$N_2$ atmosphere with $H_2O$, more than 30 transits of TRAPPIST-1e with JWST/NIRSpec are still required for such detection (Lustig-Yaeger et al. 2019). Furthermore, Lustig-Yaeger et al. (2019) outline that water vapour is expected to have a tendency to be concentrated in the lower atmosphere (because of stratospheric "cold traps") such that clouds should have a strong effect on its detectability via transmission spectroscopy. In a nut shell, because of those observational limitations, combined with the existence of several false positives (as I discussed in Chapter 1), even the detection of biosignatures with the JWST would likely not make a definitive claim for the existence of life of one of the TRAPPIST-1 HZ planets. As a whole, it appears that a robust assessment of an exoplanet's habitability will have to wait for future direct imaging telescope that can provide integrated emission (or reflection) spectra of rocky planets, which will allow us to probe the atmosphere's composition and structure, and thus to indirectly constrain the presence of liquid water on the surface. In that respect, future space-based direct imaging mission such as The Large UV/Optical/IR Surveyor (LUVOIR) (Team 2019) or the Habitable Exoplanet Observatory (HabEx) (Gaudi et al. 2020) could offer the first opportunity to image terrestrial planets in reflected light and characterise potentially habitable worlds (notably Earth-like planets orbiting truly Sun-like stars). However, these missions are still at the state of concepts and we will likely have to wait 2050 to see one of them fly.

As a whole, in just a few years, TRAPPIST-1 has become a prime target for comparative planetology. Although exoplanetologists are aware that they will not detect absolute evidence for life on its HZ planets in the next decade, this system offers an unprecedented richness of information on a very different kind of potentially habitable environment as the one we have on Earth. For these reasons, many efforts are initiated to strengthen our knowledge of the system both theoretically and observationally. These efforts are notably embodied by the creation of (1) the TRAPPIST-1 JWST initiative that arose from the collaboration of several teams to discuss/coordinate proposal submissions and ensure the scientific return of the study of the TRAPPIST-1 system with JWST is maximised (Gillon et al. 2020); (2) the TRAPPIST-1 Habitable Atmosphere Intercomparison (THAI) protocol created to compare a diversity of planetary GCMs on the study case of TRAPPIST-1e (Fauchez et al. 2020b); and (3) the NASA Study Analysis Group (SAG) 21 dedicated to the characterisation of the effect of stellar contamination on space-based transmission spectroscopy (report in preparation) to ensure the highest scientific return of the JWST transit transmission spectra. I am myself involved in the observational aspects of each of these efforts and I intent to intensify these ties during my post-doctorate.

From September 2021 on, I will be starting a postdoctoral fellowship at the *Commissariat à l'énergie atomique et aux énergies* (CEA) and simultaneously joining the JWST/MIRI instrument team to characterise TRAPPIST-1 inner planets via thermal infrared secondary eclipses observations. As a fellow, I will have a privileged access to GTO ID 1279 data (PI: Pierre-Olivier Lagage). GTO 1279 will look at the inner most planet of the TRAPPIST-1 system: TRAPPIST-1b, to detect its occultation by the host star. The reason that motivated this GTO lays in the fact that TRAPPIST-1 b is believed to have day-side thermal emission large enough to be detected through the observation of a few occultations with MIRI, which could bring key insights into the existence of an atmosphere. As part of GTO 1279, 5 eclipses of planet b will be observed with the MIRI instrument in imaging mode using the 12.8 microns filter. This program will be conducted in coordination with GTO 1177 that will observe 5 additional eclipses of planet b using MIRI as well (also in imaging mode) but in a different filter (15.0 microns). Different eclipse depths in these two channels will provide insights on the potential presence of $CO_2$ in the planet's atmosphere. Similarly, an achromatic and large eclipse depth could indicate the absence of a thick atmosphere on TRAPPIST-1b (as an airless rocky planet should have a very hot dayside). Those GTO observations will represent an important milestone in exoplanetology as no secondary eclipse of any known earth-sized temperate planets has ever been observed before. Besides, I intend to benefit from the key role of MIRI and privilege access to GTO observations to prepare even more challenging proposals such as phase curve observations of TRAPPIST-1b (if feasible). More generally, MIRI has been designated as one of the optimal instruments for the detection of individual molecular species in the atmosphere of terrestrial planet around UCDS (Barstow et al. 2016; Lustig-Yaeger et al. 2019). Therefore, beyond GTOs and TRAPPIST-1, any prior knowledge and experience with MIRI will prove essential for the characterisation of rocky planets.

In parallel, as I have a strong interest in astrobiology, I hope I will be able to significantly contribute to the PhOtotrophy on Rocky HAbiTAble PLanets (PORTAL) project led by the University of Liège. PORTAL is an on-going project that aims to address the potential habitability of temperate rocky planets in orbit around UCDS, and the possibility to detect life on such planets. The three research directions of the projects are: (1) to bring strong observational constraints on the physical and irradiative conditions at the surface of the planets orbiting in the habitable zone of the nearby dwarf star TRAPPIST-1; (2) to use those constraints to investigate the possibilities of phototrophy in the infra-red range and the detectability of their signatures in samples from the early Earth and modern extreme habitats; and (3) to simulate conditions of rocky exoplanets in orbit around TRAPPIST-1-like UCDS

in a biodome. Considering my astronomical background, my participation to this project will of course focus on the first task.

### 6.2.3 Last words

Remarkably, the field of exoplanetology is still in its youth. In only 26 years, we have gone from the first detection of an extra-solar Hot Jupiter planet orbiting a solar-type star (Mayor et al. 1995) to the deployment of space missions fully dedicated to the discovery of new transiting exoplanets and their characterisation (such as TESS or CHEOPS). And the future is even brighter, with multiple observatories, missions and instruments being under-development such as the ELT (Neichel et al. 2018), ARIEL (Pascale et al. 2018), PLATO (Rauer et al. 2014), the Nancy-Roman telescope (Kasdin et al. 2020), and even some conceptual missions such as LUVOIR (Team 2019), HabEx (Gaudi et al. 2020) or Origins (Arenberg et al. 2021). Not to mention all the exceptional theoretical advances in the planetary systems formation and evolution, planetary dynamics, stellar evolution, planetary atmospheres, planetary interiors, and even habitability.

I would like to end this thesis on a personal note by saying that, although I have always been attracted to astronomy, through the academics years my will to learn about life sciences has kept growing. With astrobiology I have found a domain where all my interests meet. I feel extremely lucky for all the opportunities I was given both on SPECULOOS and TRAPPIST-1, that paved me a way towards the study of potentially habitable planets around UCDS. I find it fascinating that today exoplanets studies can rime with climatology, biosignatures, photochemisty, geology, and many more. I believe the strength of astrobiology resides in this intrinsic multi-disciplinary nature, as it reveals all the best aspects of science. And I have hope that in the next decades, this approach will progressively brings us closer to an answer to the fascinating question "is there life elsewhere in the Universe?".

# Appendix A

# Publications

## A.1 First author publications

∗ **E. Ducrot** et al. “TRAPPIST-1:Global results of the Spitzer Exploration Science Program Red Worlds”, *Astronomy & Astrophysics*,vol. 640, p. A112, Aug. 2020. doi: 10.1051/0004-6361/201937392

∗ **E. Ducrot** et al., “The 0.8-4.5$\mu$m broadband transmission spectra of TRAPPIST-1 planets”, *The Astronomical Journal*, vol. 156, p. 218, Oct. 2018. doi: 10.3847/1538-3881/aade94

## A.2 Significant contribution publications

∗ E. Agol, C. Dorn, S. Grimm, M. Turbet, **E. Ducrot** et. al., “Refining the transit timing and photometric analysis of TRAPPIST-1: Masses, radii, densities, dynamics, and ephemerides.”, *The Planetary Science Journal*, Jan 2021. doi: 10.3847/PSJ/abd022

∗ D. Sebastian, M. Gillon, **E. Ducrot** et al., "SPECULOOS - Ultracool Dwarf Transit Survey, Target List and Strategy", *Astronomy & Astrophysics*, Sept. 2020. arXiv:2011.02069

∗ P. Niraula, J. de Wit, B. V. Rackham, **E. Ducrot** et al., “$\pi$ Earth: A 3.14 day Earth-sized Planet from K2’s Kitchen Served Warm by the SPECULOOS Team”, *The Astronomical Journal*, vol. 160, p. 172, Sept. 2020. doi: 10.3847/1538-3881/aba95f

∗ M. N. Günther, D. A. Berardo, **E. Ducrot** et al., "Complex Modulation of Rapidly Rotating Young M Dwarfs: Adding Pieces to the Puzzle", *Submitted to The Astronomical Journal*, Aug. 2020. arXiv: 2008.11681.

## A.3 Other co-authored publications

∗ E. Bryant, D. Bayliss, A. Santerne, P. Wheatley, V. Nascimbeni, Ducrot, **E. Ducrot** et al., "A transit timing variation observed for the long-period extremely low-density exoplanet HIP 41378 f", *Monthly Notices of the Royal Astronomical Society*, Jun. 2021. doi: 10.1093/mnrasl/slab037

∗ A. Leleu et al. incl. **E. Ducrot**, "Six transiting planets and a chain of Laplace resonances in TOI-178", *Astronomy & Astrophysics*, Dec. 2020. doi: 10.1051/0004-6361/202039767

∗ F. Lienhard, et al. incl. **E. Ducrot**, "Global Analysis of the TRAPPIST Ultra-Cool Dwarf Transit Survey", *Monthly Notices of the Royal Astronomical Society*, vol. 497, pp. 3790–3808, Sept. 2020. doi: 10.1093/mnras/staa2054

∗ B. F. Cooke, et al. incl. **E. Ducrot**, "Two Transiting Hot Jupiters from the WASP Survey: WASP-150band WASP-176b", *The Astronomical Journal*, vol. 159, p. 255, June 2020. doi: 10.3847/1538-3881/ab88db

∗ C. A. Murray, et al. incl. **E. Ducrot**, "Photometry and performance of SPECULOOS-South", *Monthly Notices of the Royal Astronomical*, vol. 495, pp. 2446–2457, May 2020. doi: 10.1093/mnras/staa1283

∗ A. H. M. J. Triaud, et al. incl. **E. Ducrot**, "An eclipsing substellar binary in a young triple system discovered by SPECULOOS", *Nature Astronomy*, Mar. 2020. doi: 10.1038/s41550-020-1018-2

∗ L. Y. Temple, et al. incl. **E. Ducrot**, "WASP-180Ab: Dopplertomography of a hot Jupiter orbiting the primary star in a visual binary", *Monthly Notices of the Royal Astronomical Society*, vol. 490, pp. 2467–2474, Dec. 2019. doi: 10.1093/mnras/stz2632

∗ S. N. Quinn, et al. incl. **E. Ducrot**, “Near-resonance in a System of Sub-Neptunes from TESS”, *The Astronomical Journal*, vol. 158, p. 177, Nov. 2019. doi: 10.3847/1538-3881/ab3f2b

∗ L. D. Nielsen, et al. incl. **E. Ducrot**, “WASP-169, WASP-171, WASP-175, and WASP-182: three hot Jupiters and one bloatedsub-Saturn mass planet discovered by WASP-South”, *Monthly Notices of the Royal Astronomical*, vol. 489, pp. 2478–2487, Oct. 2019. doi: 10.1093/mnras/stz2351

∗ A. Y. Burdanov, et al. incl. **E. Ducrot**, “Ground-based follow-up observations of TRAPPIST-1 transits in the near-infrared”, *Monthly Notices of the Royal Astronomical Society*, vol. 487, pp. 1634–1652, Aug. 2019. arXiv: 1905.06035. doi: 10.1093/mnras/stz1375

∗ V. B. Kostov, et al. incl. **E. Ducrot**, “The L 98-59 System: ThreeTransiting, Terrestrial-size Planets Orbiting a Nearby M Dwarf”, *The Astronomical Journal*, vol. 158, p. 32, July 2019. doi: 10.3847/1538-3881/ab2459

∗R. G. West, et al. incl. **E. Ducrot**, “NGTS-4b: A sub-Neptune transiting in thedesert”, *Monthly Notices of the Royal Astronomical Society*, vol. 486, pp. 5094–5103, July 2019. doi: 10.1093/mnras/stz1084

∗ O. D. Turner, et al. incl. **E. Ducrot**, “Three hot-Jupiters on the upper edge of the mass-radius distribution: WASP-177, WASP-181,and WASP-183”, *Monthly Notices of the Royal Astronomical Society*, vol. 485, pp. 5790–5799, June 2019. doi: 10.1093/mnras/stz742

∗ K. Barkhaoui, et al. incl. **E. Ducrot**, "Discovery of Three New Transiting Hot Jupiters: WASP-161 b, WASP-163 b, and WASP-170 b", *The Astronomical Journal*, vol. 157, pp 10, Feb 2019. 10.3847/1538-3881/aaf422

∗ E. Jehin, et al. incl. **E. Ducrot**, “The SPECULOOS Southern Observatory Begins itsHunt for Rocky Planets”, *The Messenger*, vol. 174, pp. 2–7, Dec. 2018. doi: 10.18727/0722-6691/5105

∗ M. Oshagh, et al. incl. **E. Ducrot**, “Activity induced variation in spin-orbit angles as derivedfrom Rossiter-McLaughlin measurements”, *Astronomy & Astrophysics*, vol. 619, p. A150, Nov. 2018. doi: 10.1051/0004-6361/201833709

∗ K. L. Heritier, et al. incl. **E. Ducrot**, “Plasma source and loss atcomet 67p during the rosetta mission”, *Astronomy & Astrophysics*, vol. 618, p. A77, Oct. 2018. doi: 10.1051/0004-6361/201832881

∗ M. N. Günther, et al. incl. **E. Ducrot** “Unmasking thehidden NGTS-3Ab: a hot Jupiter in an unresolved binary system”, *Monthly Notices of the Royal Astronomical Society*, vol. 478, pp. 4720–4737, Aug. 2018. doi: 10.1093/mnras/sty1193

∗ B. M. Morris, et al. incl. **E. Ducrot**, “Non-detection of Contamination by Stellar Activity in the Spitzer Transit Light Curves of TRAPPIST-1”, *The Astrophysical Journal*, vol. 863, p. L32, Aug. 2018. doi: 10.3847/2041-8213/aad8aa

∗ C. Buisset, et al. incl. **E. Ducrot**, “The evanescent wave coronagraph project: setup results and demonstrator preliminary design”, *Advances in Optical and Mechanical Technologies for Telescopes and Instrumentation III, Society of Photo-Optical Instrumentation Engineers (SPIE) Conference Series*, vol. 107062P, July 2018. doi: 10.1117/12.2311958

∗ L. Delrez, et al. incl. **E. Ducrot** et al., “SPECULOOS: a network of robotic telescopes to hunt for terrestrial planets around the nearest ultracool dwarfs”, *Proceedings of the SPIE*, Volume 10700, id. 107001I 21 pp. (2018), June 2018. doi: 10.1117/12.2312475

∗ C. Buisset, et al. incl. **E. Ducrot**, “Study of a coronagraphic mask using evanescent waves”, *Optics Express*, vol. 25, pp. 7273–7287, Apr. 2017. doi: 10.1364/OE.25.007273

## A.4 Proceedings

∗ D. Sebastian, P. P. Pedersen, C. A. Murray, **E. Ducrot** et al., "Development of the SPECULOOS exoplanet search project", *SPIE conference proceedings*, Dec. 2020. doi: 10.1117/12.2563563

∗ **E. Ducrot** and Gillon, M, "Latest news of SPECULOOS and TRAPPIST-1 ", *EPSC-DPS Joint Meeting*, Sep. 2019. EPSC-DPS2019-1974

# References


Afram, N. et al. (Apr. 2015). "Molecules as magnetic probes of starspots". In: *Astronomy and Astrophysics* 576, A34. DOI: 10.1051/0004-6361/201425314.

Aganze, C. et al. (Feb. 2016). "CHARACTERIZATION OF THE VERY-LOW-MASS SECONDARY IN THE GJ 660.1AB SYSTEM". en. In: *The Astronomical Journal* 151.2. Publisher: American Astronomical Society, p. 46. DOI: 10.3847/0004-6256/151/2/46.

Agol, E. et al. (May 2005). "On detecting terrestrial planets with timing of giant planet transits". en. In: *Monthly Notices of the Royal Astronomical Society* 359.2, pp. 567–579. DOI: 10.1111/j.1365-2966.2005.08922.x.

Agol, E. et al. (2018). "Transit Timing and Duration Variations for the Discovery and Characterization of Exoplanets". In: *arXiv:1706.09849 [astro-ph]*. arXiv: 1706.09849, pp. 797–816. DOI: 10.1007/978-3-319-55333-7_7.

Agol, E. et al. (Feb. 2020a). "Analytic Planetary Transit Light Curves and Derivatives for Stars with Polynomial Limb Darkening". en. In: *The Astronomical Journal* 159.3. Publisher: American Astronomical Society, p. 123. DOI: 10.3847/1538-3881/ab4fee.

Agol, E. et al. (Oct. 2020b). "Refining the transit timing and photometric analysis of TRAPPIST-1: Masses, radii, densities, dynamics, and ephemerides". In: *arXiv:2010.01074 [astro-ph]*. arXiv: 2010.01074.

Agol, E. et al. (June 2021). "A differentiable N-body code for transit timing and dynamical modeling. I. Algorithm and derivatives". In: *arXiv e-prints* 2106, arXiv:2106.02188.

Airapetian, V. S. et al. (June 2016). "Prebiotic chemistry and atmospheric warming of early Earth by an active young Sun". In: *Nature Geoscience* 9, pp. 452–455. DOI: 10.1038/ngeo2719.

Akiyama, E. et al. (2018). *Search for Planets like Earth around Late-M Dwarfs: Precise Radial Velocity Survey with IRD*. en.

Alencar, S. H. P. et al. (Sept. 2010). "Accretion dynamics and disk evolution in NGC 2264: a study based on CoRoT photometric observations". en. In: *Astronomy & Astrophysics* 519. Publisher: EDP Sciences, A88. DOI: 10.1051/0004-6361/201014184.

Allard, F. et al. (Sept. 2000). "TiO and H2O Absorption Lines in Cool Stellar Atmospheres". In: *The Astrophysical Journal* 540, pp. 1005–1015. DOI: 10.1086/309366.

Almenara, J. M. et al. (Nov. 2015). "Absolute masses and radii determination in multiplanetary systems without stellar models". In: *Monthly Notices of the Royal Astronomical Society* 453.3. arXiv: 1508.06596, pp. 2645–2653. DOI: 10.1093/mnras/stv1735.

Alonso, R. (2018). "Characterization of Exoplanets: Secondary Eclipses". In: *arXiv:1803.06204 [astro-ph]*. arXiv: 1803.06204, pp. 1441–1467. DOI: 10.1007/978-3-319-55333-7_40.

Anderson, D. R. et al. (Apr. 2010). "H-band thermal emission from the 19-h period planet WASP-19b". en. In: *Astronomy & Astrophysics* 513. Publisher: EDP Sciences, p. L3. DOI: 10.1051/0004-6361/201014226.

Anderson, D. R. et al. (Jan. 2011). "WASP-30b: A 61 M Jup Brown Dwarf Transiting a V = 12, F8 Star". In: *The Astrophysical Journal Letters* 726, p. L19. DOI: 10.1088/2041-8205/726/2/L19.

Angelo, I. et al. (Mar. 2017). "Kepler-1649b: An Exo-Venus in the Solar Neighborhood". en. In: *The Astronomical Journal* 153.4. Publisher: American Astronomical Society, p. 162. DOI: 10.3847/1538-3881/aa615f.

Angus, R. et al. (Feb. 2018). "Inferring probabilistic stellar rotation periods using Gaussian processes". In: *Monthly Notices of the Royal Astronomical Society* 474.2. arXiv: 1706.05459, pp. 2094–2108. DOI: 10.1093/mnras/stx2109.

Ansdell, M. et al. (Oct. 2016). "Dipper discs not inclined towards edge-on orbits". In: *Monthly Notices of the Royal Astronomical Society: Letters* 462.1, pp. L101–L105. DOI: 10.1093/mnrasl/slw140.

Apai, D. et al. (Mar. 2018). "Understanding Stellar Contamination in Exoplanet Transmission Spectra as an Essential Step in Small Planet Characterization". In: *arXiv:1803.08708 [astro-ph]*. arXiv: 1803.08708.

Arenberg, J. W. et al. (Feb. 2021). "Alternate architecture for the Origins Space Telescope". In: *Journal of Astronomical Telescopes, Instruments, and Systems* 7.1. Publisher: International Society for Optics and Photonics, p. 011006. DOI: 10.1117/1.JATIS.7.1.011006.

Armstrong, J. et al. (Apr. 2014). "Effects of Extreme Obliquity Variations on the Habitability of Exoplanets". In: *Astrobiology* 14.4, pp. 277–291. DOI: 10.1089/ast.2013.1129.

Arrhenius, T. et al. (Feb. 1994). "Archean geochemistry of formaldehyde and cyanide and the oligomerization of cyanohydrin". en. In: *Origins of life and evolution of the biosphere* 24.1, pp. 1–17. DOI: 10.1007/BF01582036.

Bailey, S. (Sept. 2012). "Principal Component Analysis with Noisy and/or Missing Data". en. In: *Publications of the Astronomical Society of the Pacific* 124.919. Publisher: IOP Publishing, p. 1015. DOI: 10.1086/668105.

Baraffe, I. et al. (Sept. 1998). "Evolutionary models for solar metallicity low-mass stars: mass-magnitude relationships and color-magnitude diagrams". In: *Astronomy and Astrophysics* 337, pp. 403–412.

Barkaoui, K. et al. (Feb. 2019). "Discovery of Three New Transiting Hot Jupiters: WASP-161 b, WASP-163 b, and WASP-170 b". In: *The Astronomical Journal* 157, p. 43. DOI: 10.3847/1538-3881/aaf422.

Barnes, J. R. et al. (Oct. 2015). "STARSPOT DISTRIBUTIONS ON FULLY CONVECTIVE M DWARFS: IMPLICATIONS FOR RADIAL VELOCITY PLANET SEARCHES". en. In: *The Astrophysical Journal* 812.1. Publisher: American Astronomical Society, p. 42. DOI: 10.1088/0004-637X/812/1/42.

Barnes, R. (Dec. 2017). "Tidal locking of habitable exoplanets". en. In: *Celestial Mechanics and Dynamical Astronomy* 129.4, pp. 509–536. DOI: 10.1007/s10569-017-9783-7.

Barnes, R. et al. (Dec. 2009a). "Tidal Constraints on Planetary Habitability". In: *arXiv:0912.2095 [astro-ph]*. arXiv: 0912.2095.

Barnes, R. et al. (June 2009b). "TIDAL LIMITS TO PLANETARY HABITABILITY". en. In: *The Astrophysical Journal* 700.1. Publisher: IOP Publishing, p. L30. DOI: 10.1088/0004-637X/700/1/L30.

Barstow, J. K. et al. (Sept. 2016). "Habitable worlds with *JWST* : transit spectroscopy of the TRAPPIST-1 system?" en. In: *Monthly Notices of the Royal Astronomical Society: Letters* 461.1, pp. L92–L96. DOI: 10.1093/mnrasl/slw109.

Bartlett, S. et al. (Apr. 2020). "Defining Lyfe in the Universe: From Three Privileged Functions to Four Pillars". en. In: *Life* 10.4. Number: 4 Publisher: Multidisciplinary Digital Publishing Institute, p. 42. DOI: 10.3390/life10040042.

Batalha, N. E. et al. (Apr. 2017). "PandExo: A Community Tool for Transiting Exoplanet Science withJWST&HST". en. In: *Publications of the Astronomical Society of the Pacific* 129.976. Publisher: IOP Publishing, p. 064501. DOI: 10.1088/1538-3873/aa65b0.

Batalha, N. E. et al. (Apr. 2018). "Strategies for Constraining the Atmospheres of Temperate Terrestrial Planets with JWST". In: *The Astrophysical Journal Letters* 856, p. L34. DOI: 10.3847/2041-8213/aab896.

Bayes, T. et al. (Jan. 1763). "LII. An essay towards solving a problem in the doctrine of chances. By the late Rev. Mr. Bayes, F. R. S. communicated by Mr. Price, in a letter to John Canton, A. M. F. R. S". In: *Philosophical Transactions of the Royal Society of London* 53. Publisher: Royal Society, pp. 370–418. DOI: 10.1098/rstl.1763.0053.

Becker, J. C. et al. (Sept. 2015). "WASP-47: A Hot Jupiter System with Two Additional Planets Discovered by K2". In: *arXiv:1508.02411 [astro-ph]*. arXiv: 1508.02411. DOI: 10.1088/2041-8205/812/2/L18.

Benneke, B. et al. (Jan. 2017). "SPITZEROBSERVATIONS CONFIRM AND RESCUE THE HABITABLE-ZONE SUPER-EARTH K2-18b FOR FUTURE CHARACTERIZATION". en. In: *The Astrophysical Journal* 834.2. Publisher: American Astronomical Society, p. 187. DOI: 10.3847/1538-4357/834/2/187.

Benz, A. O. et al. (2010). "Physical Processes in Magnetically Driven Flares on the Sun, Stars, and Young Stellar Objects". In: *Annual Review of Astronomy and Astrophysics* 48.1. _eprint: https://doi.org/10.1146/annurev-astro-082708-101757, pp. 241–287. DOI: 10.1146/annurev-astro-082708-101757.

Berner, R. (1999). *A New Look at the Long-term Carbon Cycle*. en.

Betancourt, M. (July 2018a). "A Conceptual Introduction to Hamiltonian Monte Carlo". In: *arXiv:1701.02434 [stat]*. arXiv: 1701.02434.

– (Jan. 2018b). "The Convergence of Markov chain Monte Carlo Methods: From the Metropolis method to Hamiltonian Monte Carlo". In: *arXiv:1706.01520 [physics, stat]*. arXiv: 1706.01520.

Bitsch, B. et al. (Apr. 2019). "Rocky super-Earths or waterworlds: the interplay of planet migration, pebble accretion, and disc evolution". In: *Astronomy and Astrophysics* 624, A109. DOI: 10.1051/0004-6361/201935007.

Bochanski, J. J. et al. (June 2010). "The Luminosity and Mass Functions of Low-Mass Stars in the Galactic Disk: II. The Field". In: *The Astronomical Journal* 139.6. arXiv: 1004.4002, pp. 2679–2699. DOI: 10.1088/0004-6256/139/6/2679.

Bodman, E. H. L. et al. (Sept. 2017). "Dippers and dusty disc edges: new diagnostics and comparison to model predictions". In: *Monthly Notices of the Royal Astronomical Society* 470.1, pp. 202–223. DOI: 10.1093/mnras/stx1034.

Bolmont, E. et al. (Jan. 2017). "Water loss from terrestrial planets orbiting ultracool dwarfs: implications for the planets of TRAPPIST-1". In: *Monthly Notices of the Royal Astronomical Society* 464, pp. 3728–3741. DOI: 10.1093/mnras/stw2578.

Bolmont, E. et al. (Nov. 2016). "Effect of the rotation and tidal dissipation history of stars on the evolution of close-in planets". In: *Celestial Mechanics and Dynamical Astronomy* 126.1-3. arXiv: 1603.06268, pp. 275–296. DOI: 10.1007/s10569-016-9690-3.

Bolmont, E. et al. (Mar. 2020). "On the impact of tides on the transit-timing fits to the TRAPPIST-1 system". In: *Astronomy & Astrophysics* 635. arXiv: 2002.02015, A117. DOI: 10.1051/0004-6361/202037546.

Bonfils, X. et al. (Nov. 2005). "Metallicity of M dwarfs: I. A photometric calibration and the impact on the mass-luminosity relation at the bottom of the main sequence". en. In: *Astronomy & Astrophysics* 442.2, pp. 635–642. DOI: 10.1051/0004-6361:20053046.

Bourrier, V. et al. (Aug. 2017). "Temporal Evolution of the High-energy Irradiation and Water Content of TRAPPIST-1 Exoplanets". en. In: *The Astronomical Journal* 154.3, p. 121. DOI: 10.3847/1538-3881/aa859c.

Braak, C. J. F. T. (Sept. 2006). "A Markov Chain Monte Carlo version of the genetic algorithm Differential Evolution: easy Bayesian computing for real parameter spaces". en. In: *Statistics and Computing* 16.3, pp. 239–249. DOI: 10.1007/s11222-006-8769-1.

Bradley, L. et al. (Dec. 2019). *astropy/photutils: v0.7.2*. DOI: 10.5281/zenodo.3568287.

Braun, K. von et al. (Mar. 2011). "Astrophysical Parameters and Habitable Zone of the Exoplanet Hosting Star GJ 581". In: *The Astrophysical Journal Letters* 729, p. L26. DOI: 10.1088/2041-8205/729/2/L26.

Braun, K. von et al. (July 2012). "The GJ 436 System: Directly Determined Astrophysical Parameters of an M Dwarf and Implications for the Transiting Hot Neptune". In: *The Astrophysical Journal* 753, p. 171. DOI: 10.1088/0004-637X/753/2/171.

Broeg, C. et al. (Feb. 2005). "A new algorithm for differential photometry: computing an optimum artificial comparison star". In: *Astronomische Nachrichten* 326, pp. 134–142. DOI: 10.1002/asna.200410350.

Brooks, S. P. et al. (Dec. 1998). "General Methods for Monitoring Convergence of Iterative Simulations". In: *Journal of Computational and Graphical Statistics* 7.4. Publisher: Taylor & Francis _eprint: https://www.tandfonline.com/doi/pdf/10.1080/10618600.1998.10474787, pp. 434–455. DOI: 10.1080/10618600.1998.10474787.

Brown, T. M. (June 2001). "Transmission Spectra as Diagnostics of Extrasolar Giant Planet Atmospheres". In: *The Astrophysical Journal* 553, pp. 1006–1026. DOI: 10.1086/320950.

Browning, M. K. (Apr. 2008). "Simulations of Dynamo Action in Fully Convective Stars". en. In: *The Astrophysical Journal* 676.2. Publisher: IOP Publishing, p. 1262. DOI: 10.1086/527432.

Bryant, E. M. et al. (June 2021). "A transit timing variation observed for the long-period extremely low-density exoplanet HIP 41378 f". In: *Monthly Notices of the Royal Astronomical Society* 504, pp. L45–L50. DOI: 10.1093/mnrasl/slab037.

Burdanov, A. et al. (Oct. 2017). "SPECULOOS exoplanet search and its prototype on TRAPPIST". In: *arXiv:1710.03775 [astro-ph]*. arXiv: 1710.03775. DOI: 10.1007/978-3-319-55333-7_130.

Burdanov, A. et al. (Aug. 2019). "Ground-based follow-up observations of TRAPPIST-1 transits in the near-infrared". In: *Monthly Notices of the Royal Astronomical Society* 487.2, pp. 1634–1652. DOI: 10.1093/mnras/stz1375.

Burgasser, A. J. et al. (Feb. 2015). "WISE J072003.20-084651.2: AN OLD AND ACTIVE M9.5 $\mathplus$ T5 SPECTRAL BINARY 6 pc FROM THE SUN". en. In: *The Astronomical Journal* 149.3. Publisher: American Astronomical Society, p. 104. DOI: 10.1088/0004-6256/149/3/104.

Burgasser, A. J. et al. (Aug. 2017). "On the Age of the TRAPPIST-1 System". In: *The Astrophysical Journal* 845, p. 110. DOI: 10.3847/1538-4357/aa7fea.

Burrows, A. S. (Sept. 2014). "Highlights in the study of exoplanet atmospheres". en. In: *Nature* 513.7518, pp. 345–352. DOI: 10.1038/nature13782.

Callahan, M. P. et al. (Aug. 2011). "Carbonaceous meteorites contain a wide range of extraterrestrial nucleobases". eng. In: *Proceedings of the National Academy of Sciences of the United States of America* 108.34, pp. 13995–13998. DOI: 10.1073/pnas.1106493108.

Carey, S. J. et al. (Oct. 2004). "Observing with the infrared array camera (IRAC) on the Spitzer Space Telescope". In: *Optical, Infrared, and Millimeter Space Telescopes*. Vol. 5487. International Society for Optics and Photonics, pp. 211–222. DOI: 10.1117/12.550968.

Carter, J. A. et al. (Dec. 2008). "Analytic Approximations for Transit Light-Curve Observables, Uncertainties, and Covariances". In: *The Astrophysical Journal* 689, pp. 499–512. DOI: 10.1086/592321.

Carter, J. A. et al. (Feb. 2011). "KOI-126: A Triply Eclipsing Hierarchical Triple with Two Low-Mass Stars". In: *Science* 331, p. 562. DOI: 10.1126/science.1201274.

Carter, J. A. et al. (Aug. 2012). "Kepler-36: A pair of planets with neighboring orbits and dissimilar densities". English (US). In: *Science* 337.6094. Publisher: American Association for the Advancement of Science, pp. 556–559. DOI: 10.1126/science.1223269.

Casali, M. et al. (May 2007). "The UKIRT wide-field camera". en. In: *Astronomy & Astrophysics* 467.2. Number: 2 Publisher: EDP Sciences, pp. 777–784. DOI: 10.1051/0004-6361:20066514.

Castro-Almazán, J. A. et al. (July 2016). "Precipitable Water Vapour at the Canarian Observatories (Teide and Roque de los Muchachos) from routine GPS". In: *Observatory Operations: Strategies, Processes, and Systems VI*. Vol. 9910. International Society for Optics and Photonics, 99100P. DOI: 10.1117/12.2232646.

Catling, D. (2013). *Astrobiology: a very short introduction*. en. First edition. Very short introductions. OCLC: ocn855703162. Oxford: Oxford University Press.

Catling, D. C. et al. (June 2018). "Exoplanet Biosignatures: A Framework for Their Assessment". In: *Astrobiology* 18.6, pp. 709–738. DOI: 10.1089/ast.2017.1737.

Cauley, P. W. et al. (Oct. 2018). "The Effects of Stellar Activity on Optical High-resolution Exoplanet Transmission Spectra". en. In: *The Astronomical Journal* 156.5. Publisher: American Astronomical Society, p. 189. DOI: 10.3847/1538-3881/aaddf9.

Chabrier, G. et al. (Nov. 1997). "Structure and evolution of low-mass stars". In: *Astronomy and Astrophysics* 327, pp. 1039–1053.

Chachan, Y. et al. (Nov. 2019). "A Hubble PanCET Study of HAT-P-11b: A Cloudy Neptune with a Low Atmospheric Metallicity". en. In: *The Astronomical Journal* 158.6. Publisher: American Astronomical Society, p. 244. DOI: 10.3847/1538-3881/ab4e9a.

Charbonneau, D. et al. (Dec. 1999). "Detection of Planetary Transits Across a Sun-like Star". en. In: *The Astrophysical Journal* 529.1. Publisher: IOP Publishing, p. L45. DOI: 10.1086/312457.

Charbonneau, D. et al. (June 2005). "Detection of Thermal Emission from an Extrasolar Planet". en. In: *The Astrophysical Journal* 626.1. arXiv: astro-ph/0503457, pp. 523–529. DOI: 10.1086/429991.

Charbonneau, D. et al. (June 2007). "The Dynamics-Based Approach to Studying Terrestrial Exoplanets". In: *arXiv:0706.1047 [astro-ph]*. arXiv: 0706.1047.

Chen, J. et al. (Dec. 2016). "PROBABILISTIC FORECASTING OF THE MASSES AND RADII OF OTHER WORLDS". en. In: *The Astrophysical Journal* 834.1. Publisher: American Astronomical Society, p. 17. DOI: 10.3847/1538-4357/834/1/17.

Chew, Y. G. M. et al. (Dec. 2014). "The EBLM project - II. A very hot, low-mass M dwarf in an eccentric and long-period, eclipsing binary system from the SuperWASP Survey". en. In: *Astronomy & Astrophysics* 572. Publisher: EDP Sciences, A50. DOI: 10.1051/0004-6361/201424265.

Claret, A. et al. (Oct. 2012). "New limb-darkening coefficients for PHOENIX/1D model atmospheres: I. Calculations for 1500 K $T_{\rm eff}$ 4800 K *Kepler* , CoRot, *Spitzer* , *uvby* ,

*UBVRIJHK* , Sloan, and 2MASS photometric systems". en. In: *Astronomy & Astrophysics* 546, A14. DOI: 10.1051/0004-6361/201219849.

Claret, A. et al. (Apr. 2013). "New limb-darkening coefficients for Phoenix/1d model atmospheres: II. Calculations for 5000 K $T_{\rm eff}$ 10 000 K *Kepler* , CoRot, *Spitzer* , *uvby* , *UBVRIJHK* , Sloan, and 2MASS photometric systems". en. In: *Astronomy & Astrophysics* 552, A16. DOI: 10.1051/0004-6361/201220942.

Clark, R. N. (1993). *The U. S. Geological Survey, Digital Spectral Library: Version 1 (0.2 to 3.0um)*. Tech. rep.

Cleaves, H. J. (Sept. 2012). "Prebiotic Chemistry: What We Know, What We Don't". en. In: *Evolution: Education and Outreach* 5.3. Number: 3 Publisher: BioMed Central, pp. 342–360. DOI: 10.1007/s12052-012-0443-9.

Cockell, C. S. (Dec. 2015). *Astrobiology: Understanding Life in the Universe*. en. Wiley-Blackwell.

– (June 2020). *Astrobiology: Understanding Life in the Universe, 2nd Edition | Wiley*. en-do.

Cody, A. M. et al. (Mar. 2014). "CSI 2264: SIMULTANEOUS OPTICAL AND INFRARED LIGHT CURVES OF YOUNG DISK-BEARING STARS IN NGC 2264 WITHCoRoTand-SPITZER—EVIDENCE FOR MULTIPLE ORIGINS OF VARIABILITY". en. In: *The Astronomical Journal* 147.4. Publisher: American Astronomical Society, p. 82. DOI: 10.1088/0004-6256/147/4/82.

Coleman, G. A. L. et al. (Nov. 2019). "Pebbles versus planetesimals: the case of Trappist-1". In: *Astronomy and Astrophysics* 631, A7. DOI: 10.1051/0004-6361/201935922.

Collaboration, G. et al. (Nov. 2016). "The Gaia mission". en. In: *Astronomy & Astrophysics, Volume 595, id.A1, <NUMPAGES>36</NUMPAGES> pp.* 595, A1. DOI: 10.1051/0004-6361/201629272.

Cooke, B. F. et al. (June 2020). "Two Transiting Hot Jupiters from the WASP Survey: WASP-150b and WASP-176b". In: *The Astronomical Journal* 159, p. 255. DOI: 10.3847/1538-3881/ab88db.

Correia, A. C. M. et al. (2010). "Tidal Evolution of Exoplanets". In: *Exoplanets*. Ed. by e. b. S. Seager. Tucson, AZ : University of Arizona Press, pp. 239–266.

Cottin, H. et al. (July 2017). "Astrobiology and the Possibility of Life on Earth and Elsewhere..." en. In: *Space Science Reviews* 209.1, pp. 1–42. DOI: 10.1007/s11214-015-0196-1.

Covey, K. R. et al. (Oct. 2008). "The ChaMP Extended Stellar Survey (ChESS): Photometric and Spectroscopic Properties of Serendipitously Detected Stellar X-Ray Sources". In: *The Astrophysical Journal Supplement Series* 178, pp. 339–358. DOI: 10.1086/590909.

Cowan, N. B. et al. (Jan. 2011). "A Model for Thermal Phase Variations of Circular and Eccentric Exoplanets". In: *The Astrophysical Journal* 726.2. arXiv: 1011.0428, p. 82. DOI: 10.1088/0004-637X/726/2/82.

Cowan, N. B. et al. (2018). "Mapping Exoplanets". In: *arXiv:1704.07832 [astro-ph]*. arXiv: 1704.07832, pp. 1469–1484. DOI: 10.1007/978-3-319-55333-7_147.

Cox, A. N. (2000). "Allen's astrophysical quantities". In: *Allen's Astrophysical Quantities*. ISBN: 9780387987460.

Crossfield, I. J. M. et al. (June 2019). "A super-Earth and sub-Neptune transiting the late-type M dwarf LP 791-18". In: *arXiv:1906.09267 [astro-ph]*. arXiv: 1906.09267. DOI: 10.3847/2041-8213/ab3d30.

Cruz, K. L. et al. (May 2002). "Meeting the Cool Neighbors. III. Spectroscopy of Northern NLTT Stars". en. In: *The Astronomical Journal* 123.5. Publisher: American Astronomical Society, pp. 2828–2840. DOI: 10.1086/339973.

Cunha, D. et al. (Apr. 2015). "Spin evolution of Earth-sized exoplanets, including atmospheric tides and core–mantle friction". en. In: *International Journal of Astrobiology* 14.2. Publisher: Cambridge University Press, pp. 233–254. DOI: 10.1017/S1473550414000226.
DasSarma, S. et al. (2021). "Early evolution of purple retinal pigments on Earth and implications for exoplanet biosignatures". fr. In: *International Journal of Astrobiology* (). Publisher: Cambridge University Press, pp. 1–10. DOI: 10.1017/S1473550418000423.
Davenport, J. R. A. (Jan. 2017). "ROTATING STARS FROM *KEPLER* OBSERVED WITH *GAIA* DR1". en. In: *The Astrophysical Journal* 835.1, p. 16. DOI: 10.3847/1538-4357/835/1/16.
Davenport, J. R. A. et al. (Feb. 2019). "The Evolution of Flare Activity with Stellar Age". en. In: *The Astrophysical Journal* 871.2, p. 241. DOI: 10.3847/1538-4357/aafb76.
Davenport, J. R. A. et al. (June 2020). "10 Years of Stellar Activity for GJ 1243". en. In: *The Astronomical Journal* 160.1. Publisher: American Astronomical Society, p. 36. DOI: 10.3847/1538-3881/ab9536.
Dawson, R. I. et al. (July 2014). "Large eccentricity, low mutual inclination: the three-dimensional architecture of a hierarchical system of giant planets". In: *The Astrophysical Journal* 791.2. arXiv: 1405.5229, p. 89. DOI: 10.1088/0004-637X/791/2/89.
De Wit, J. et al. (Dec. 2013). "Constraining Exoplanet Mass from Transmission Spectroscopy". en. In: *Science* 342.6165. arXiv: 1401.6181, pp. 1473–1477. DOI: 10.1126/science.1245450.
De Wit, J. et al. (Sept. 2016). "A combined transmission spectrum of the Earth-sized exoplanets TRAPPIST-1 b and c". en. In: *Nature* 537.7618. arXiv: 1606.01103, pp. 69–72. DOI: 10.1038/nature18641.
De Wit, J. et al. (Mar. 2018). "Atmospheric reconnaissance of the habitable-zone Earth-sized planets orbiting TRAPPIST-1". en. In: *Nature Astronomy* 2.3. arXiv: 1802.02250, pp. 214–219. DOI: 10.1038/s41550-017-0374-z.
Delrez, L. et al. (Apr. 2018a). "Early 2017 observations of TRAPPIST-1 with $\textit{Spitzer}$". In: *Monthly Notices of the Royal Astronomical Society* 475.3. arXiv: 1801.02554, pp. 3577–3597. DOI: 10.1093/mnras/sty051.
Delrez, L. et al. (June 2018b). "SPECULOOS: a network of robotic telescopes to hunt for terrestrial planets around the nearest ultracool dwarfs". In: *arXiv:1806.11205 [astro-ph]*. arXiv: 1806.11205.
Deming, D. et al. (Apr. 2005). "Infrared radiation from an extrasolar planet". en. In: *Nature* 434.7034. arXiv: astro-ph/0503554, pp. 740–743. DOI: 10.1038/nature03507.
Demory, B.-O. et al. (Oct. 2020). "A super-Earth and a sub-Neptune orbiting the bright, quiet M3 dwarf TOI-1266". In: *Astronomy and Astrophysics* 642, A49. DOI: 10.1051/0004-6361/202038616.
Denison, D. G. T. et al. (May 2002). *Bayesian Methods for Nonlinear Classification and Regression*. en. Google-Books-ID: SIlDWySNuXgC. John Wiley & Sons.
Des Marais, D. J. et al. (Aug. 2008). "The NASA Astrobiology Roadmap". eng. In: *Astrobiology* 8.4, pp. 715–730. DOI: 10.1089/ast.2008.0819.
Dieterich, S. B. et al. (Mar. 2014). "THE SOLAR NEIGHBORHOOD. XXXII. THE HYDROGEN BURNING LIMIT," en. In: *The Astronomical Journal* 147.5. Publisher: American Astronomical Society, p. 94. DOI: 10.1088/0004-6256/147/5/94.
Dittmann, J. A. et al. (Apr. 2017). "A temperate rocky super-Earth transiting a nearby cool star". eng. In: *Nature* 544.7650, pp. 333–336. DOI: 10.1038/nature22055.

Dittmann, J. A. et al. (Mar. 2014). "TRIGONOMETRIC PARALLAXES FOR 1507 NEARBY MID-TO-LATE M DWARFS". en. In: *The Astrophysical Journal* 784.2. Publisher: American Astronomical Society, p. 156. DOI: 10.1088/0004-637X/784/2/156.

Dobos, V. et al. (Apr. 2019). "Tidal Heating and the Habitability of the TRAPPIST-1 Exoplanets". en. In: *Astronomy & Astrophysics* 624. arXiv: 1902.03867, A2. DOI: 10.1051/0004-6361/201834254.

Dobrovolskis, A. R. (Sept. 2013). "Insolation on exoplanets with eccentricity and obliquity". en. In: *Icarus* 226.1, pp. 760–776. DOI: 10.1016/j.icarus.2013.06.026.

Domagal-Goldman, S. D. et al. (June 2011). "Using Biogenic Sulfur Gases as Remotely Detectable Biosignatures on Anoxic Planets". en. In: *Astrobiology* 11.5, pp. 419–441. DOI: 10.1089/ast.2010.0509.

Domagal-Goldman, S. D. et al. (Aug. 2016). "The Astrobiology Primer v2.0". In: *Astrobiology* 16.8. Publisher: Mary Ann Liebert, Inc., publishers, pp. 561–653. DOI: 10.1089/ast.2015.1460.

Donati, J.-F. (June 2010). "Large-scale magnetic fields of low-mass dwarfs: the many faces of dynamo". en. In: *Proceedings of the International Astronomical Union* 6.S271. Publisher: Cambridge University Press, pp. 23–31. DOI: 10.1017/S1743921311017431.

Donati, J.-F. et al. (Nov. 2003). "Dynamo processes and activity cycles of the active stars AB Doradus, LQ Hydrae and HR 1099". In: *Monthly Notices of the Royal Astronomical Society* 345, pp. 1145–1186. DOI: 10.1046/j.1365-2966.2003.07031.x.

Donati, J.-F. et al. (2018). "SPIRou: A NIR Spectropolarimeter/High-Precision Velocimeter for the CFHT". In: *Handbook of Exoplanets*, p. 107. DOI: 10.1007/978-3-319-55333-7_107.

Dong, C. et al. (Jan. 2018). "Atmospheric escape from the TRAPPIST-1 planets and implications for habitability". In: *Proceedings of the National Academy of Science* 115, pp. 260–265. DOI: 10.1073/pnas.1708010115.

Dorn, C. et al. (Jan. 2017). "A generalized Bayesian inference method for constraining the interiors of super Earths and sub-Neptunes". en. In: *Astronomy & Astrophysics* 597. Publisher: EDP Sciences, A37. DOI: 10.1051/0004-6361/201628708.

Doyle, L. et al. (Nov. 2018). "Searching for the Origin of Flares in M dwarfs". In: *arXiv:1811.06594 [astro-ph]*. arXiv: 1811.06594. DOI: 10.5281/zenodo.1489285.

Driscoll, P. E. et al. (Sept. 2015). "Tidal Heating of Earth-like Exoplanets around M Stars: Thermal, Magnetic, and Orbital Evolutions". In: *Astrobiology* 15, pp. 739–760. DOI: 10.1089/ast.2015.1325.

Duane, S. et al. (Sept. 1987). "Hybrid Monte Carlo". en. In: *Physics Letters B* 195.2, pp. 216–222. DOI: 10.1016/0370-2693(87)91197-X.

Ducrot, E. et al. (Oct. 2018). "The 0.8-4.5$\mu$m broadband transmission spectra of TRAPPIST-1 planets". en. In: *The Astronomical Journal* 156.5. arXiv: 1807.01402, p. 218. DOI: 10.3847/1538-3881/aade94.

Ducrot, E. et al. (Aug. 2020). "TRAPPIST-1: Global Results of the Spitzer Exploration Science Program {\it Red Worlds}". In: *Astronomy & Astrophysics* 640. arXiv: 2006.13826, A112. DOI: 10.1051/0004-6361/201937392.

Ducrot, E. et al. (2021). "Intensive photometric follow-up of TRAPPIST-1 with SPECULOOS". In: *in prep*.

Eastman, J. et al. (Aug. 2010). "Achieving better than 1 minute accuracy in the Heliocentric and Barycentric Julian Dates". In: *Publications of the Astronomical Society of the Pacific* 122.894. arXiv: 1005.4415, pp. 935–946. DOI: 10.1086/655938.

Elkins-Tanton, L. T. et al. (Nov. 2008). "Coreless Terrestrial Exoplanets". en. In: *The Astrophysical Journal* 688.1. Publisher: IOP Publishing, p. 628. DOI: 10.1086/592316.

Enoch, B. et al. (June 2010). "An improved method for estimating the masses of stars with transiting planets". en. In: *Astronomy & Astrophysics* 516. Publisher: EDP Sciences, A33. DOI: 10.1051/0004-6361/201014326.

Espinoza, N. et al. (Jan. 2019). "ACCESS: A featureless optical transmission spectrum for WASP-19b from Magellan/IMACS". en. In: *Monthly Notices of the Royal Astronomical Society* 482.2. arXiv: 1807.10652, pp. 2065–2087. DOI: 10.1093/mnras/sty2691.

Etiope, G. et al. (2013). "Abiotic Methane on Earth". en. In: *Reviews of Geophysics* 51.2. _eprint: https://agupubs.onlinelibrary.wiley.com/doi/pdf/10.1002/rog.20011, pp. 276–299. DOI: https://doi.org/10.1002/rog.20011.

Fabrycky, D. C. et al. (Apr. 2012). "TRANSIT TIMING OBSERVATIONS FROMKEPLER. IV. CONFIRMATION OF FOUR MULTIPLE-PLANET SYSTEMS BY SIMPLE PHYSICAL MODELS". en. In: *The Astrophysical Journal* 750.2. Publisher: IOP Publishing, p. 114. DOI: 10.1088/0004-637X/750/2/114.

Fang, J. et al. (Apr. 2013). "Are Planetary Systems Filled to Capacity? A Study Based on Kepler Results". In: *The Astrophysical Journal* 767.2. arXiv: 1302.7190, p. 115. DOI: 10.1088/0004-637X/767/2/115.

Fauchez, T. J. et al. (Dec. 2019). "Impact of Clouds and Hazes on the Simulated JWST Transmission Spectra of Habitable Zone Planets in the TRAPPIST-1 System". en. In: *The Astrophysical Journal* 887.2. arXiv: 1911.08596, p. 194. DOI: 10.3847/1538-4357/ab5862.

Fauchez, T. J. et al. (Apr. 2020a). "Sensitive Probing of Exoplanetary Oxygen via Mid Infrared Collisional Absorption". In: *Nature Astronomy* 4.4. arXiv: 2001.01361, pp. 372–376. DOI: 10.1038/s41550-019-0977-7.

Fauchez, T. J. et al. (Feb. 2020b). "TRAPPIST-1 Habitable Atmosphere Intercomparison (THAI): motivations and protocol version 1.0". English. In: *Geoscientific Model Development* 13.2. Publisher: Copernicus GmbH, pp. 707–716. DOI: 10.5194/gmd-13-707-2020.

Feinstein, A. D. et al. (Nov. 2020). "Flare Statistics for Young Stars from a Convolutional Neural Network Analysis of $\textit{TESS}$ Data". In: *The Astronomical Journal* 160.5. arXiv: 2005.07710, p. 219. DOI: 10.3847/1538-3881/abac0a.

Filippazzo, J. C. et al. (Sept. 2015). "FUNDAMENTAL PARAMETERS AND SPECTRAL ENERGY DISTRIBUTIONS OF YOUNG AND FIELD AGE OBJECTS WITH MASSES SPANNING THE STELLAR TO PLANETARY REGIME". en. In: *The Astrophysical Journal* 810.2, p. 158. DOI: 10.1088/0004-637X/810/2/158.

Fleming, D. P. et al. (Mar. 2020). "On The XUV Luminosity Evolution of TRAPPIST-1". In: *The Astrophysical Journal* 891.2. arXiv: 1906.05250, p. 155. DOI: 10.3847/1538-4357/ab77ad.

Ford, E. B. (2006). "IMPROVING THE EFFICIENCY OF MARKOV CHAIN MONTE CARLO FOR ANALYZING THE ORBITS OF EXTRASOLAR PLANETS". en. In: 642.1, p. 18.

Foreman-Mackey, D. (June 2016). "corner.py: Scatterplot matrices in Python". en. In: *Journal of Open Source Software* 1.2, p. 24. DOI: 10.21105/joss.00024.

Foreman-Mackey, D. et al. (Nov. 2013). "emcee: The MCMC Hammer". In: *arXiv:1202.3665 [astro-ph, physics:physics, stat]*. arXiv: 1202.3665. DOI: 10.1086/670067.

Fulton, B. J. et al. (Aug. 2017). "The California-KeplerSurvey. III. A Gap in the Radius Distribution of Small Planets". en. In: *The Astronomical Journal* 154.3. Publisher: American Astronomical Society, p. 109. DOI: 10.3847/1538-3881/aa80eb.

Gagliuffi, D. C. B. et al. (Oct. 2019). "The Ultracool SpeXtroscopic Survey. I. Volume-limited Spectroscopic Sample and Luminosity Function of M7-L5 Ultracool Dwarfs". en.

In: *The Astrophysical Journal* 883.2. Publisher: American Astronomical Society, p. 205. DOI: 10.3847/1538-4357/ab253d.

Gaia Collaboration et al. (Aug. 2018). "*Gaia* Data Release 2: Summary of the contents and survey properties". en. In: *Astronomy & Astrophysics* 616, A1. DOI: 10.1051/0004-6361/201833051.

Gao, P. et al. (May 2015). "Stability of CO2 Atmospheres on Desiccated M Dwarf Exoplanets". In: *arXiv:1501.06876 [astro-ph]*. arXiv: 1501.06876.

Garcia, L. et al. (2021a). "nuance: a Python framework for full fetched transit search". In: *in prep*.

Garcia, L. et al. (2021b). "prose: modular astronomy in python". In: in prep.

Garraffo, C. et al. (July 2017). "The Threatening Magnetic and Plasma Environment of the TRAPPIST-1 Planets". In: *The Astrophysical Journal Letters* 843, p. L33. DOI: 10.3847/2041-8213/aa79ed.

Gaudi, B. S. et al. (Jan. 2020). "The Habitable Exoplanet Observatory (HabEx) Mission Concept Study Final Report". In: *arXiv:2001.06683 [astro-ph]*. arXiv: 2001.06683.

Gelman, A. (2013). "Bayesian Data Analysis, Third Edition". en. In: p. 656.

Gelman, A. et al. (1992). "Inference from Iterative Simulation Using Multiple Sequences". In: *Statistical Science* 7.4. Publisher: Institute of Mathematical Statistics, pp. 457–472.

Gelman, A. et al. (2021). "Bayesian Data Analysis Third edition (with errors fixed as of 6 April 2021)". en. In: p. 677.

Gibbs, A. et al. (Mar. 2020). "EDEN: Sensitivity Analysis and Transiting Planet Detection Limits for Nearby Late Red Dwarfs". en. In: *The Astronomical Journal* 159.4. arXiv: 2002.10017, p. 169. DOI: 10.3847/1538-3881/ab7926.

Gibson, N. P. et al. (2012). "A Gaussian process framework for modelling instrumental systematics: application to transmission spectroscopy". en. In: *Monthly Notices of the Royal Astronomical Society* 419.3. _eprint: https://onlinelibrary.wiley.com/doi/pdf/10.1111/j.1365-2966.2011.19915.x, pp. 2683–2694. DOI: 10.1111/j.1365-2966.2011.19915.x.

Gilbert, W. (Feb. 1986). "Origin of life: The RNA world". en. In: *Nature* 319.6055. Number: 6055 Publisher: Nature Publishing Group, pp. 618–618. DOI: 10.1038/319618a0.

Gillon, M. et al. (2013). "TRAPPIST-UCDTS: A prototype search for habitable planets transiting ultra-cool stars". en. In: *EPJ Web of Conferences*, p. 4.

Gillon, M. et al. (July 2010). "The *Spitzer* search for the transits of HARPS low-mass planets: I. No transit for the super-Earth HD 40307b". en. In: *Astronomy and Astrophysics* 518, A25. DOI: 10.1051/0004-6361/201014144.

Gillon, M. et al. (2011). "TRAPPIST: a robotic telescope dedicated to the study of planetary systems". en. In: *EPJ Web of Conferences* 11. Publisher: EDP Sciences, p. 06002. DOI: 10.1051/epjconf/20101106002.

Gillon, M. et al. (Mar. 2012a). "Improved precision on the radius of the nearby super-Earth 55 Cnc e". en. In: *Astronomy & Astrophysics* 539. arXiv: 1110.4783, A28. DOI: 10.1051/0004-6361/201118309.

Gillon, M. et al. (June 2012b). "The TRAPPIST survey of southern transiting planets: I. Thirty eclipses of the ultra-short period planet WASP-43 b". en. In: *Astronomy & Astrophysics* 542, A4. DOI: 10.1051/0004-6361/201218817.

Gillon, M. et al. (Mar. 2014). "Search for a habitable terrestrial planet transiting the nearby red dwarf GJ 1214". en. In: *Astronomy & Astrophysics* 563, A21. DOI: 10.1051/0004-6361/201322362.

Gillon, M. et al. (May 2017a). "The Spitzer search for the transits of HARPS low-mass planets. II. Null results for 19 planets". In: *Astronomy and Astrophysics* 601, A117. DOI: 10.1051/0004-6361/201629270.

Gillon, M. (Apr. 2018). "Searching for red worlds". en. In: *Nature Astronomy* 2.4, pp. 344–344. DOI: 10.1038/s41550-018-0443-y.

Gillon, M. et al. (May 2016). "Temperate Earth-sized planets transiting a nearby ultracool dwarf star". In: *Nature* 533.7602. arXiv: 1605.07211, pp. 221–224. DOI: 10.1038/nature17448.

Gillon, M. et al. (Feb. 2017b). "Seven temperate terrestrial planets around the nearby ultracool dwarf star TRAPPIST-1". en. In: *Nature* 542.7642, pp. 456–460. DOI: 10.1038/nature21360.

Gillon, M. et al. (Feb. 2020). "The TRAPPIST-1 JWST Community Initiative". In: *arXiv:2002.04798 [astro-ph]*. arXiv: 2002.04798.

Gizis, J. E. et al. (Mar. 2017). "K2 Ultracool Dwarfs Survey I: Photometry of an L Dwarf Superflare". en. In: *The Astrophysical Journal* 838.1. arXiv: 1611.07080, p. 22. DOI: 10.3847/1538-4357/aa6197.

Glazier, A. L. et al. (June 2020). "Evryscope and K2 Constraints on TRAPPIST-1 Superflare Occurrence and Planetary Habitability". In: *arXiv:2006.14712 [astro-ph]*. arXiv: 2006.14712.

Gomes, R. et al. (May 2005). "Origin of the cataclysmic Late Heavy Bombardment period of the terrestrial planets". In: *Nature* 435, pp. 466–469. DOI: 10.1038/nature03676.

Gonzales, E. C. et al. (Nov. 2019). "A Reanalysis of the Fundamental Parameters and Age of TRAPPIST-1". en. In: *The Astrophysical Journal* 886.2. arXiv: 1909.13859, p. 131. DOI: 10.3847/1538-4357/ab48fc.

Goodman, J. et al. (2010). "Ensemble samplers with affine invariance". In: *Communications in Applied Mathematics and Computational Science, Vol. 5, No. 1, p. 65-80, 2010* 5, pp. 65–80. DOI: 10.2140/camcos.2010.5.65.

Gordon, I. E. et al. (Dec. 2017). "The HITRAN2016 molecular spectroscopic database". en. In: *Journal of Quantitative Spectroscopy and Radiative Transfer*. HITRAN2016 Special Issue 203, pp. 3–69. DOI: 10.1016/j.jqsrt.2017.06.038.

Gregory, P. C. (Apr. 2005). "Bayesian Logical Data Analysis for the Physical Sciences: A Comparative Approach with 'Mathematica' Support". In: *Bayesian Logical Data Analysis for the Physical Sciences: A Comparative Approach with 'Mathematica' Support. Edited by P. C. Gregory. ISBN 0 521 84150 X (hardback); QA279.5.G74 2005 519.5'42 – dc22; 200445930. Published by Cambridge University Press, Cambridge, UK, 2005.*

Grimm, S. L. et al. (Oct. 2014). "THE GENGA CODE: GRAVITATIONAL ENCOUNTERS INN-BODY SIMULATIONS WITH GPU ACCELERATION". en. In: *The Astrophysical Journal* 796.1. Publisher: American Astronomical Society, p. 23. DOI: 10.1088/0004-637X/796/1/23.

Grimm, S. L. et al. (May 2018). "The nature of the TRAPPIST-1 exoplanets". In: *Astronomy & Astrophysics* 613. arXiv: 1802.01377, A68. DOI: 10.1051/0004-6361/201732233.

Günther, M. N. et al. (Dec. 2019). "A super-Earth and two sub-Neptunes transiting the nearby and quiet M dwarf TOI-270". en. In: *Nature Astronomy* 3.12. Number: 12 Publisher: Nature Publishing Group, pp. 1099–1108. DOI: 10.1038/s41550-019-0845-5.

Günther, M. N. et al. (Aug. 2020a). "Complex Modulation of Rapidly Rotating Young M Dwarfs: Adding Pieces to the Puzzle". In: *arXiv:2008.11681 [astro-ph]*. arXiv: 2008.11681.

Günther, M. N. et al. (Jan. 2020b). "Stellar Flares from the First Tess Data Release: Exploring a New Sample of M-dwarfs". In: *The Astronomical Journal* 159.2. arXiv: 1901.00443, p. 60. DOI: 10.3847/1538-3881/ab5d3a.

Hamano, K. et al. (May 2015). "Lifetime and Spectral Evolution of a Magma Ocean with a Steam Atmosphere: Its Detectability by Future Direct Imaging". en. In: *arXiv:1505.03552 [astro-ph]*. arXiv: 1505.03552.

Harman, C. E. et al. (Oct. 2015). "Abiotic O$_{2}$ Levels on Planets around F, G, K, and M Stars: Possible False Positives for Life?" en. In: *The Astrophysical Journal* 812.2. arXiv: 1509.07863, p. 137. DOI: 10.1088/0004-637X/812/2/137.

Hastings, W. K. (Apr. 1970). "Monte Carlo sampling methods using Markov chains and their applications". In: *Biometrika* 57.1, pp. 97–109. DOI: 10.1093/biomet/57.1.97.

Hawley, S. L. et al. (Sept. 1991). "The great flare of 1985 April 12 on AD Leonis". en. In: *The Astrophysical Journal* 378, p. 725. DOI: 10.1086/170474.

Hawley, S. L. et al. (Dec. 2014). "*KEPLER* FLARES. I. ACTIVE AND INACTIVE M DWARFS". en. In: *The Astrophysical Journal* 797.2, p. 121. DOI: 10.1088/0004-637X/797/2/121.

He, M. Y. et al. (Jan. 2017). "First limits on the occurrence rate of short-period planets orbiting brown dwarfs". en. In: *Monthly Notices of the Royal Astronomical Society* 464.3, pp. 2687–2697. DOI: 10.1093/mnras/stw2391.

Henry, G. W. et al. (Dec. 1999). "A Transiting "51 Peg-like" Planet*". en. In: *The Astrophysical Journal* 529.1. Publisher: IOP Publishing, p. L41. DOI: 10.1086/312458.

Henry, T. J. et al. (Nov. 2004). "The Solar Neighborhood. X. New Nearby Stars in the Southern Sky and Accurate Photometric Distance Estimates for Red Dwarfs". en. In: *The Astronomical Journal* 128.5. Publisher: IOP Publishing, p. 2460. DOI: 10.1086/425052.

Henry, T. J. et al. (June 2018). "The Solar Neighborhood XLIV: RECONS Discoveries within 10 parsecs". en. In: *The Astronomical Journal* 155.6. Publisher: American Astronomical Society, p. 265. DOI: 10.3847/1538-3881/aac262.

Hernandez, D. M. et al. (Sept. 2015). "Symplectic integration for the collisional gravitational $N$-body problem". In: *Monthly Notices of the Royal Astronomical Society* 452.2. arXiv: 1503.02728, pp. 1934–1944. DOI: 10.1093/mnras/stv1439.

Hinse, T. C. et al. (Jan. 2015). "PREDICTING A THIRD PLANET IN THE KEPLER-47 CIRCUMBINARY SYSTEM". en. In: *The Astrophysical Journal* 799.1. Publisher: American Astronomical Society, p. 88. DOI: 10.1088/0004-637X/799/1/88.

Hippke, M. et al. (Mar. 2019a). "Optimized transit detection algorithm to search for periodic transits of small planets". en. In: *Astronomy & Astrophysics* 623, A39. DOI: 10.1051/0004-6361/201834672.

Hippke, M. et al. (Sept. 2019b). "Wōtan: Comprehensive Time-series Detrending in Python". en. In: *The Astronomical Journal* 158.4. Publisher: American Astronomical Society, p. 143. DOI: 10.3847/1538-3881/ab3984.

Hirano, T. et al. (Feb. 2020). "Evidence for Spin–Orbit Alignment in the TRAPPIST-1 System". en. In: *The Astrophysical Journal* 890.2. Publisher: American Astronomical Society, p. L27. DOI: 10.3847/2041-8213/ab74dc.

Holman, M. J. et al. (Dec. 2004). "The Use of Transit Timing to Detect Extrasolar Planets with Masses as Small as Earth". In: *arXiv:astro-ph/0412028*. arXiv: astro-ph/0412028. DOI: 10.1106/science.1107822.

Hori, Y. et al. (Jan. 2020). "Do the TRAPPIST-1 Planets Have Hydrogen-rich Atmospheres?" en. In: *The Astrophysical Journal* 889.2. arXiv: 1912.05749, p. 77. DOI: 10.3847/1538-4357/ab6168.

Howe, A. R. et al. (Sept. 2012). “Theoretical Transit Spectra for GJ 1214b and Other "Super-Earths"”. In: *The Astrophysical Journal* 756, p. 176. DOI: 10.1088/0004-637X/756/2/176.
Howell, S. B. et al. (Apr. 2014). “The K2 Mission: Characterization and Early Results”. In: *Publications of the Astronomical Society of the Pacific* 126, p. 398. DOI: 10.1086/676406.
Hu, Y. et al. (Jan. 2014). “Role of ocean heat transport in climates of tidally locked exoplanets around M dwarf stars”. en. In: *Proceedings of the National Academy of Sciences* 111.2. Publisher: National Academy of Sciences Section: Physical Sciences, pp. 629–634. DOI: 10.1073/pnas.1315215111.
Husser, T.-O. et al. (May 2013). “A new extensive library of PHOENIX stellar atmospheres and synthetic spectra”. en. In: *Astronomy & Astrophysics* 553. Publisher: EDP Sciences, A6. DOI: 10.1051/0004-6361/201219058.
Ingalls, J. G. et al. (Aug. 2016). “Repeatability and Accuracy of Exoplanet Eclipse Depths Measured with Post-Cryogenic Spitzer”. In: *The Astronomical Journal* 152.2. arXiv: 1601.05101, p. 44. DOI: 10.3847/0004-6256/152/2/44.
Irwin, M. J. et al. (Sept. 2004). “VISTA data flow system: pipeline processing for WFCAM and VISTA”. In: *Optimizing Scientific Return for Astronomy through Information Technologies*. Vol. 5493. International Society for Optics and Photonics, pp. 411–422. DOI: 10.1117/12.551449.
Izidoro, A. et al. (Apr. 2021). “Formation of planetary systems by pebble accretion and migration: Hot super-Earth systems from breaking compact resonant chains”. In: *Astronomy & Astrophysics*. arXiv: 1902.08772. DOI: 10.1051/0004-6361/201935336.
Jackson, B. et al. (July 2008). “Tidal Heating of Extra-Solar Planets”. In: *The Astrophysical Journal* 681.2. arXiv: 0803.0026, pp. 1631–1638. DOI: 10.1086/587641.
Jackson, R. J. et al. (Oct. 2009). “The radii of M-dwarfs in the young open cluster NGC 2516”. In: *Monthly Notices of the Royal Astronomical Society: Letters* 399.1, pp. L89–L93. DOI: 10.1111/j.1745-3933.2009.00729.x.
Jehin, E. et al. (2018). “The SPECULOOS Southern Observatory Begins its Hunt for Rocky Planets”. en. In: *Published in The Messenger vol. 174* pp. 2-7. Artwork Size: 6 pages Medium: PDF Publisher: European Southern Observatory (ESO), 6 pages. DOI: 10.18727/0722-6691/5105.
Jenkins, J. M. et al. (Aug. 2016). “The TESS science processing operations center”. In: *Software and Cyberinfrastructure for Astronomy IV*. Vol. 9913. International Society for Optics and Photonics, 99133E. DOI: 10.1117/12.2233418.
Jones, A. et al. (Dec. 2013). “An advanced scattered moonlight model for Cerro Paranal”. en. In: *Astronomy & Astrophysics* 560. Publisher: EDP Sciences, A91. DOI: 10.1051/0004-6361/201322433.
Joshi, M. (June 2003). “Climate Model Studies of Synchronously Rotating Planets”. In: *Astrobiology* 3.2. Publisher: Mary Ann Liebert, Inc., publishers, pp. 415–427. DOI: 10.1089/153110703769016488.
Juvan, I. G. et al. (Feb. 2018). “PyTranSpot: A tool for multiband light curve modeling of planetary transits and stellar spots”. en. In: *Astronomy & Astrophysics* 610. Publisher: EDP Sciences, A15. DOI: 10.1051/0004-6361/201731345.
Kaltenegger, L. et al. (Jan. 2010). “Deciphering Spectral Fingerprints of Habitable Extrasolar Planets”. In: *Astrobiology* 10.1. arXiv: 0906.2263, pp. 89–102. DOI: 10.1089/ast.2009.0381.
Kane, S. R. et al. (Sept. 2016). “A CATALOG OFKEPLERHABITABLE ZONE EXOPLANET CANDIDATES”. en. In: *The Astrophysical Journal* 830.1. Publisher: American Astronomical Society, p. 1. DOI: 10.3847/0004-637X/830/1/1.

Kasdin, N. J. et al. (Dec. 2020). "The Nancy Grace Roman Space Telescope Coronagraph Instrument (CGI) Technology Demonstration". In: *Space Telescopes and Instrumentation 2020: Optical, Infrared, and Millimeter Wave*. arXiv: 2103.01980, p. 194. DOI: 10.1117/12.2562997.

Kasting, J. F. et al. (Jan. 1993). "Habitable Zones around Main Sequence Stars". In: *Icarus* 101, pp. 108–128. DOI: 10.1006/icar.1993.1010.

Kataria, T. et al. (Apr. 2016). "The Atmospheric Circulation of a Nine-hot-Jupiter Sample: Probing Circulation and Chemistry over a Wide Phase Space". In: *The Astrophysical Journal* 821, p. 9. DOI: 10.3847/0004-637X/821/1/9.

Katyal, N. et al. (Apr. 2019). "Evolution and Spectral Response of a Steam Atmosphere for Early Earth with a Coupled Climate–Interior Model". en. In: *The Astrophysical Journal* 875.1. Publisher: American Astronomical Society, p. 31. DOI: 10.3847/1538-4357/ab0d85.

Kay, C. et al. (July 2016). "PROBABILITY OF CME IMPACT ON EXOPLANETS ORBITING M DWARFS AND SOLAR-LIKE STARS". en. In: *The Astrophysical Journal* 826.2. Publisher: IOP Publishing, p. 195. DOI: 10.3847/0004-637X/826/2/195.

Keeling, C. D. et al. (Jan. 1976). "Atmospheric carbon dioxide variations at Mauna Loa Observatory, Hawaii". en. In: *Tellus* 28.6, pp. 538–551. DOI: 10.3402/tellusa.v28i6.11322.

Kerber, F. et al. (Sept. 2012). "A water vapour monitor at Paranal Observatory". In: *Ground-based and Airborne Instrumentation for Astronomy IV*. Vol. 8446. International Society for Optics and Photonics, 84463N. DOI: 10.1117/12.924340.

Kiang, N. Y. et al. (Feb. 2007). "Spectral signatures of photosynthesis II: coevolution with other stars and the atmosphere on extrasolar worlds". In: *Astrobiology* 7.1. arXiv: astro-ph/0701391, pp. 252–274. DOI: 10.1089/ast.2006.0108.

Kiman, R. et al. (May 2019). "Exploring the Age-dependent Properties of M and L Dwarfs Using Gaia and SDSS". en. In: *The Astronomical Journal* 157.6. Publisher: American Astronomical Society, p. 231. DOI: 10.3847/1538-3881/ab1753.

Kipping, D. M. (Sept. 2010). "Investigations of approximate expressions for the transit duration". In: *Monthly Notices of the Royal Astronomical Society* 407.1. arXiv: 1004.3819, pp. 301–313. DOI: 10.1111/j.1365-2966.2010.16894.x.

Kirkpatrick, J. D. et al. (Feb. 1995). "The solar neighborhood. 2: The first list of dwarfs with spectral types of M7 and cooler". In: *The Astronomical Journal* 109, pp. 797–807. DOI: 10.1086/117323.

Kirkpatrick, J. D. et al. (Feb. 1997). "The Coolest Isolated M Dwarf and Other 2MASS Discoveries". In: *The Astrophysical Journal* 476, pp. 311–318. DOI: 10.1086/303613.

Kirkpatrick, J. D. et al. (June 2016). "THE ALLWISE MOTION SURVEY, PART 2". en. In: *The Astrophysical Journal Supplement Series* 224.2. Publisher: American Astronomical Society, p. 36. DOI: 10.3847/0067-0049/224/2/36.

Kitzmann, D. (Apr. 2017). "Clouds in the atmospheres of extrasolar planets. V. The impact of CO2 ice clouds on the outer boundary of the habitable zone". In: *Astronomy & Astrophysics* 600. arXiv: 1701.07513, A111. DOI: 10.1051/0004-6361/201630029.

Knutson, H. A. et al. (Jan. 2009). "Multi-Wavelength Constraints on the Day-Night Circulation Patterns of HD 189733b". In: *The Astrophysical Journal* 690.1. arXiv: 0802.1705, pp. 822–836. DOI: 10.1088/0004-637X/690/1/822.

Koll, D. D. B. (July 2019). "A Scaling Theory for Atmospheric Heat Redistribution on Rocky Exoplanets". In: *arXiv:1907.13145 [astro-ph]*. arXiv: 1907.13145.

Koll, D. D. B. et al. (Dec. 2019). "Identifying Candidate Atmospheres on Rocky M Dwarf Planets via Eclipse Photometry". en. In: *The Astrophysical Journal* 886.2. Publisher: American Astronomical Society, p. 140. DOI: 10.3847/1538-4357/ab4c91.

Kopparapu, R. K. (2018). "The Habitable Zone: The Climatic Limits of Habitability". en. In: *Handbook of Exoplanets*. Ed. by H. J. Deeg et al. Cham: Springer International Publishing, pp. 2981–2993. DOI: 10.1007/978-3-319-55333-7_58.

Kopparapu, R. K. et al. (Feb. 2013). "HABITABLE ZONES AROUND MAIN-SEQUENCE STARS: NEW ESTIMATES". en. In: *The Astrophysical Journal* 765.2. Publisher: IOP Publishing, p. 131. DOI: 10.1088/0004-637X/765/2/131.

Kopparapu, R. k. et al. (Aug. 2017). "Habitable Moist Atmospheres On Terrestrial Planets Near the Inner Edge Of the Habitable Zone Around M-dwarfs". In: *The Astrophysical Journal* 845.1. arXiv: 1705.10362, p. 5. DOI: 10.3847/1538-4357/aa7cf9.

Kopparapu, R. k. et al. (Nov. 2019). "Characterizing Exoplanet Habitability". In: *arXiv:1911.04441 [astro-ph]*. arXiv: 1911.04441.

Kostov, V. B. et al. (June 2019). "The L 98-59 System: Three Transiting, Terrestrial-Sized Planets Orbiting a Nearby M-dwarf". In: *The Astronomical Journal* 158.1. arXiv: 1903.08017, p. 32. DOI: 10.3847/1538-3881/ab2459.

Kotani, T. et al. (July 2014). "Infrared Doppler instrument (IRD) for the Subaru telescope to search for Earth-like planets around nearby M-dwarfs". In: *Ground-based and Airborne Instrumentation for Astronomy V*. Vol. 9147. International Society for Optics and Photonics, p. 914714. DOI: 10.1117/12.2055075.

Kovari, Z. et al. (July 1997). "Testing the stability and reliability of starspot modelling." In: *Astronomy and Astrophysics* 323, pp. 801–808.

Kowalski, A. F. et al. (May 2010). "A White Light Megaflare on the dM4.5e Star YZ CMi". In: *The Astrophysical Journal Letters* 714, pp. L98–L102. DOI: 10.1088/2041-8205/714/1/L98.

Krasnopolsky, V. A. et al. (Dec. 2004). "Detection of methane in the martian atmosphere: evidence for life?" en. In: *Icarus* 172.2, pp. 537–547. DOI: 10.1016/j.icarus.2004.07.004.

Kreidberg, L. (Nov. 2015). "batman: BAsic Transit Model cAlculatioN in Python". In: *Publications of the Astronomical Society of the Pacific* 127.957. arXiv: 1507.08285, pp. 1161–1165. DOI: 10.1086/683602.

Kreidberg, L. et al. (Sept. 2014a). "A Precise Water Abundance Measurement for the Hot Jupiter WASP-43b". In: *The Astrophysical Journal* 793.2. arXiv: 1410.2255, p. L27. DOI: 10.1088/2041-8205/793/2/L27.

Kreidberg, L. et al. (Jan. 2014b). "Clouds in the atmosphere of the super-Earth exoplanet GJ 1214b". In: *Nature* 505.7481. arXiv: 1401.0022, pp. 69–72. DOI: 10.1038/nature12888.

Kretzschmar, M. (June 2011). "Sun-as-a-star Observation of White-Light Flares". en. In: *Astronomy & Astrophysics* 530. arXiv: 1103.3125, A84. DOI: 10.1051/0004-6361/201015930.

Krissansen-Totton, J. et al. (Jan. 2016). "On detecting biospheres from chemical thermodynamic disequilibrium in planetary atmospheres". In: *Astrobiology* 16.1. arXiv: 1503.08249, pp. 39–67. DOI: 10.1089/ast.2015.1327.

Krissansen-Totton, J. et al. (Aug. 2018a). "Detectability of Biosignatures in Anoxic Atmospheres with the *James Webb Space Telescope* : A TRAPPIST-1e Case Study". en. In: *The Astronomical Journal* 156.3, p. 114. DOI: 10.3847/1538-3881/aad564.

Krissansen-Totton, J. et al. (Jan. 2018b). "Disequilibrium biosignatures over Earth history and implications for detecting exoplanet life". en. In: *Science Advances* 4.1, eaao5747. DOI: 10.1126/sciadv.aao5747.

Lammer, H. et al. (Feb. 2007). "Coronal Mass Ejection (CME) Activity of Low Mass M Stars as An Important Factor for The Habitability of Terrestrial Exoplanets. II. CME-Induced Ion Pick Up of Earth-like Exoplanets in Close-In Habitable Zones". In: *Astrobiology* 7.1. Publisher: Mary Ann Liebert, Inc., publishers, pp. 185–207. DOI: 10.1089/ast.2006.0128.

Lang, D. et al. (Mar. 2010). "ASTROMETRY.NET: BLIND ASTROMETRIC CALIBRATION OF ARBITRARY ASTRONOMICAL IMAGES". en. In: *The Astronomical Journal* 139.5. Publisher: American Astronomical Society, pp. 1782–1800. DOI: 10.1088/0004-6256/139/5/1782.

Laskar, J. (Nov. 2017). "Des premiers travaux de Le Verrier à la découverte de Neptune". fr. In: *Comptes Rendus Physique*. Science in the making: The Comptes rendus de l'Académie des sciences throughout history 18.9, pp. 504–519. DOI: 10.1016/j.crhy.2017.10.011.

Lecavelier Des Etangs, A. et al. (Apr. 2008). "Rayleigh scattering in the transit spectrum of HD 189733b". In: *Astronomy and Astrophysics* 481, pp. L83–L86. DOI: 10.1051/0004-6361:200809388.

Leconte, J. et al. (Feb. 2015). "Asynchronous rotation of Earth-mass planets in the habitable zone of lower-mass stars". In: *arXiv:1502.01952 [astro-ph, physics:physics]*. arXiv: 1502.01952. DOI: 10.1126/science.1258686.

Leleu, A. et al. (Jan. 2021). "Six transiting planets and a chain of Laplace resonances in TOI-178". In: *Astronomy & Astrophysics*. arXiv: 2101.09260. DOI: 10.1051/0004-6361/202039767.

Leleu, A. et al. (Apr. 2019). "Co-orbital exoplanets from close period candidates: The TOI-178 case". en. In: *Astronomy & Astrophysics* 624. arXiv: 1901.07250, A46. DOI: 10.1051/0004-6361/201834901.

Lienhard, F. et al. (2019). "Global Analysis of the TRAPPIST-South Ultra-Cool Dwarf Survey". en. In: p. 16.

Lincowski, A. P. et al. (Nov. 2018). "Evolved Climates and Observational Discriminants for the TRAPPIST-1 Planetary System". en. In: *The Astrophysical Journal* 867.1. Publisher: American Astronomical Society, p. 76. DOI: 10.3847/1538-4357/aae36a.

Lincowski, A. P. et al. (June 2019). "Observing Isotopologue Bands in Terrestrial Exoplanet Atmospheres with the James Webb Space Telescope—Implications for Identifying Past Atmospheric and Ocean Loss". en. In: *The Astronomical Journal* 158.1. arXiv: 1905.12821, p. 26. DOI: 10.3847/1538-3881/ab2385.

Lindegren, L. et al. (Aug. 2018). "Gaia Data Release 2. The astrometric solution". In: *Astronomy and Astrophysics* 616, A2. DOI: 10.1051/0004-6361/201832727.

Lissauer, J. J. et al. (Jan. 2012). "Almost All of Kepler's Multiple Planet Candidates are Planets". In: *arXiv:1201.5424 [astro-ph]*. arXiv: 1201.5424. DOI: 10.1088/0004-637X/750/2/112.

Lithwick, Y. et al. (Dec. 2012). "EXTRACTING PLANET MASS AND ECCENTRICITY FROM TTV DATA". en. In: *The Astrophysical Journal* 761.2, p. 122. DOI: 10.1088/0004-637X/761/2/122.

Liu, Z. et al. (Dec. 2019). "Harnessing Chemical Energy for the Activation and Joining of Prebiotic Building Blocks". en. In: Publisher: ChemRxiv. DOI: 10.26434/chemrxiv.11210867.v1.

Lovelock, J. E. (Aug. 1965). "A Physical Basis for Life Detection Experiments". en. In: *Nature* 207.4997. Number: 4997 Publisher: Nature Publishing Group, pp. 568–570. DOI: 10.1038/207568a0.

Luger, R. et al. (Feb. 2015). "Extreme Water Loss and Abiotic O$_2$ Buildup On Planets Throughout the Habitable Zones of M Dwarfs". en. In: *Astrobiology* 15.2. arXiv: 1411.7412, pp. 119–143. DOI: 10.1089/ast.2014.1231.

Luger, R. et al. (Oct. 2016). "EVEREST: Pixel Level Decorrelation of K2 Light curves". In: *The Astronomical Journal* 152.4. arXiv: 1607.00524, p. 100. DOI: 10.3847/0004-6256/152/4/100.

Luger, R. et al. (June 2017a). "A seven-planet resonant chain in TRAPPIST-1". en. In: *Nature Astronomy* 1.6. arXiv: 1703.04166, p. 0129. DOI: 10.1038/s41550-017-0129.

Luger, R. et al. (Dec. 2017b). "Planet-Planet Occultations in TRAPPIST-1 and Other Exoplanet Systems". en. In: *The Astrophysical Journal* 851.2. arXiv: 1711.05739, p. 94. DOI: 10.3847/1538-4357/aa9c43.

Luhman, K. L. (Mar. 2013). "DISCOVERY OF A BINARY BROWN DWARF AT 2 pc FROM THE SUN". en. In: *The Astrophysical Journal* 767.1. Publisher: American Astronomical Society, p. L1. DOI: 10.1088/2041-8205/767/1/L1.

Lustig-Yaeger, J. et al. (June 2019). "The Detectability and Characterization of the TRAPPIST-1 Exoplanet Atmospheres with JWST". en. In: *The Astronomical Journal* 158.1. arXiv: 1905.07070, p. 27. DOI: 10.3847/1538-3881/ab21e0.

MacKay, D. J. C. (2003). "Information Theory, Inference, and Learning Algorithms". en. In: p. 640.

Madhusudhan, N. (Aug. 2019). "Exoplanetary Atmospheres: Key Insights, Challenges and Prospects". en. In: *Annual Review of Astronomy and Astrophysics* 57.1. arXiv: 1904.03190, pp. 617–663. DOI: 10.1146/annurev-astro-081817-051846.

Makarov, V. V. et al. (Apr. 2018). "Spin-orbital Tidal Dynamics and Tidal Heating in the TRAPPIST-1 Multiplanet System". In: *The Astrophysical Journal* 857, p. 142. DOI: 10.3847/1538-4357/aab845.

Malik, M. et al. (Dec. 2019). "Analyzing Atmospheric Temperature Profiles and Spectra of M dwarf Rocky Planets". In: *arXiv:1907.13135 [astro-ph]*. arXiv: 1907.13135. DOI: 10.3847/1538-4357/ab4a05.

Mandel, K. et al. (Dec. 2002). "Analytic Lightcurves for Planetary Transit Searches". In: *The Astrophysical Journal* 580.2. arXiv: astro-ph/0210099, pp. L171–L175. DOI: 10.1086/345520.

Mann, A. W. et al. (2011). "Ground-Based Submillimagnitude CCD Photometry of Bright Stars Using Snapshot Observations". In: *Publications of the Astronomical Society of the Pacific* 123.909. Publisher: [The University of Chicago Press, Astronomical Society of the Pacific], pp. 1273–1289. DOI: 10.1086/662640.

Mann, A. W. et al. (May 2014). "Prospecting in Ultracool Dwarfs: Measuring the Metallicities of Mid- and Late-M Dwarfs". In: *The Astronomical Journal* 147.6. arXiv: 1403.5560, p. 160. DOI: 10.1088/0004-6256/147/6/160.

Mann, A. W. et al. (Jan. 2019). "How to Constrain Your M dwarf II: the mass-luminosity-metallicity relation from 0.075 to 0.70$M_\odot$". en. In: *The Astrophysical Journal* 871.1. arXiv: 1811.06938, p. 63. DOI: 10.3847/1538-4357/aaf3bc.

Marais, D. J. D. et al. (1999). "Astrobiology: Exploring the Origins, Evolution, and Distribution of Life in the Universe". In: *Annual Review of Ecology and Systematics* 30.1. _eprint: https://doi.org/10.1146/annurev.ecolsys.30.1.397, pp. 397–420. DOI: 10.1146/annurev.ecolsys.30.1.397.

Marcq, E. et al. (2017). "Thermal radiation of magma ocean planets using a 1-D radiative-convective model of H2O-CO2 atmospheres". en. In: *Journal of Geophysical Research: Planets* 122.7. _eprint: https://agupubs.onlinelibrary.wiley.com/doi/pdf/10.1002/2016JE005224, pp. 1539–1553. DOI: https://doi.org/10.1002/2016JE005224.

Maxted, P. F. L. (June 2016). "ellc: A fast, flexible light curve model for detached eclipsing binary stars and transiting exoplanets". In: *Astronomy and Astrophysics* 591, A111. DOI: 10.1051/0004-6361/201628579.

Mayfield, E. B. et al. (Apr. 1985). "The correlation of solar flare production with magnetic energy in active regions". en. In: *Solar Physics* 96.2, pp. 293–305. DOI: 10.1007/BF00149685.

Mayor, M. et al. (Nov. 1995). "A Jupiter-mass companion to a solar-type star". en. In: *Nature* 378.6555. Number: 6555 Publisher: Nature Publishing Group, pp. 355–359. DOI: 10.1038/378355a0.

McCormac, J. et al. (Apr. 2013). "DONUTS: A Science Frame Autoguiding Algorithm with Sub-Pixel Precision, Capable of Guiding on Defocused Stars". en. In: *Publications of the Astronomical Society of the Pacific* 125.927. Publisher: IOP Publishing, p. 548. DOI: 10.1086/670940.

McGinnis, P. et al. (Sept. 2020). "The magnetic obliquity of accreting T Tauri stars". In: *Monthly Notices of the Royal Astronomical Society* 497.2, pp. 2142–2162. DOI: 10.1093/mnras/staa2041.

McLaughlin, D. B. (July 1924). "Some results of a spectrographic study of the Algol system." In: *The Astrophysical Journal* 60, pp. 22–31. DOI: 10.1086/142826.

Meadows, V. S. (2008). "Planetary Environmental Signatures for Habitability and Life". en. In: *Exoplanets: Detection, Formation, Properties, Habitability*. Ed. by J. W. Mason. Springer Praxis Books. Berlin, Heidelberg: Springer, pp. 259–284. DOI: 10.1007/978-3-540-74008-7_10.

Meadows, V. S. et al. (June 2018a). "Exoplanet Biosignatures: Understanding Oxygen as a Biosignature in the Context of Its Environment". In: *Astrobiology* 18.6. arXiv: 1705.07560, pp. 630–662. DOI: 10.1089/ast.2017.1727.

Meadows, V. S. et al. (2018b). "Factors Affecting Exoplanet Habitability". en. In: *Handbook of Exoplanets*. Ed. by H. J. Deeg et al. Cham: Springer International Publishing, pp. 1–24. DOI: 10.1007/978-3-319-30648-3_57-1.

Méndez, A. et al. (Feb. 2017). "The Equilibrium Temperature of Planets in Elliptical Orbits". en. In: *The Astrophysical Journal Letters* 837.1. Publisher: IOP Publishing, p. L1. DOI: 10.3847/2041-8213/aa5f13.

Ment, K. et al. (Jan. 2019). "A Second Terrestrial Planet Orbiting the Nearby M Dwarf LHS 1140". en. In: *The Astronomical Journal* 157.1. Publisher: IOP Publishing, p. 32. DOI: 10.3847/1538-3881/aaf1b1.

Merline, W. J. et al. (Jan. 1995). "A realistic model for point-sources imaged on array detectors: The model and initial results". en. In: *Experimental Astronomy* 6.1, pp. 163–210. DOI: 10.1007/BF00421131.

Miller-Ricci, E. et al. (Oct. 2009a). "ON THE EMERGENT SPECTRA OF HOT PROTOPLANET COLLISION AFTERGLOWS". en. In: *The Astrophysical Journal* 704.1, pp. 770–780. DOI: 10.1088/0004-637X/704/1/770.

Miller-Ricci, E. et al. (Jan. 2009b). "THE ATMOSPHERIC SIGNATURES OF SUPER-EARTHS: HOW TO DISTINGUISH BETWEEN HYDROGEN-RICH AND HYDROGEN-POOR ATMOSPHERES". en. In: *The Astrophysical Journal* 690.2, pp. 1056–1067. DOI: 10.1088/0004-637X/690/2/1056.

Mills, S. M. et al. (May 2016). "A resonant chain of four transiting, sub-Neptune planets". In: *Nature* 533.7604. arXiv: 1612.07376, pp. 509–512. DOI: 10.1038/nature17445.

Mills, S. M. et al. (Jan. 2017). "KEPLER-108: A MUTUALLY INCLINED GIANT PLANET SYSTEM". en. In: *The Astronomical Journal* 153.1. Publisher: American Astronomical Society, p. 45. DOI: 10.3847/1538-3881/153/1/45.

Moffatt, H. K. (1978). "Magnetic field generation in electrically conducting fluids". In: *Cambridge, England, Cambridge University Press, 1978. 353 p.*

Monnahan, C. C. et al. (2017). "Faster estimation of Bayesian models in ecology using Hamiltonian Monte Carlo". en. In: *Methods in Ecology and Evolution* 8.3. _eprint:

https://besjournals.onlinelibrary.wiley.com/doi/pdf/10.1111/2041-210X.12681, pp. 339–348. DOI: https://doi.org/10.1111/2041-210X.12681.
Montalto, M. et al. (Oct. 2014). "Improvements on analytic modelling of stellar spots". In: *Monthly Notices of the Royal Astronomical Society* 444, pp. 1721–1728. DOI: 10.1093/mnras/stu1530.
Morales-Calderón, M. et al. (May 2011). "YSOVAR: THE FIRST SENSITIVE, WIDE-AREA, MID-INFRARED PHOTOMETRIC MONITORING OF THE ORION NEBULA CLUSTER". en. In: *The Astrophysical Journal* 733.1. Publisher: American Astronomical Society, p. 50. DOI: 10.1088/0004-637X/733/1/50.
Moran, S. E. et al. (Nov. 2018). "Limits on Clouds and Hazes for the TRAPPIST-1 Planets". en. In: *The Astronomical Journal* 156.6, p. 252. DOI: 10.3847/1538-3881/aae83a.
Morin, J. et al. (Feb. 2008). "The stable magnetic field of the fully convective star V374 Peg". In: *Monthly Notices of the Royal Astronomical Society* 384, pp. 77–86. DOI: 10.1111/j.1365-2966.2007.12709.x.
Morin, J. et al. (July 2010). "Large-scale magnetic topologies of late M dwarfs: Magnetic topologies of late M dwarfs". en. In: *Monthly Notices of the Royal Astronomical Society* 407.4, pp. 2269–2286. DOI: 10.1111/j.1365-2966.2010.17101.x.
Morley, C. V. et al. (Nov. 2017). "Observing the Atmospheres of Known Temperate Earth-sized Planets with JWST". en. In: *The Astrophysical Journal* 850.2. arXiv: 1708.04239, p. 121. DOI: 10.3847/1538-4357/aa927b.
Morris, B. M. et al. (Sept. 2017). "The Starspots of HAT-P-11: Evidence for a Solar-like Dynamo". In: *The Astrophysical Journal* 846, p. 99. DOI: 10.3847/1538-4357/aa8555.
Morris, B. M. et al. (Feb. 2018a). "astroplan: An Open Source Observation Planning Package in Python". In: *The Astronomical Journal* 155.3. arXiv: 1712.09631, p. 128. DOI: 10.3847/1538-3881/aaa47e.
Morris, B. M. et al. (Aug. 2018b). "Non-detection of Contamination by Stellar Activity in the Spitzer Transit Light Curves of TRAPPIST-1". In: *The Astrophysical Journal* 863.2. arXiv: 1808.02808, p. L32. DOI: 10.3847/2041-8213/aad8aa.
Morris, B. M. et al. (Apr. 2018c). "Possible Bright Starspots on TRAPPIST-1". In: *The Astrophysical Journal* 857.1. arXiv: 1803.04543, p. 39. DOI: 10.3847/1538-4357/aab6a5.
Morris, B. M. et al. (Aug. 2018d). "Robust Transiting Exoplanet Radii in the Presence of Starspots from Ingress and Egress Durations". en. In: *The Astronomical Journal* 156.3. arXiv: 1807.04886, p. 91. DOI: 10.3847/1538-3881/aad3b7.
Mortara, L. et al. (Jan. 1981). "Evaluations of Charge-Coupled Device / CCD / Performance for Astronomical Use". In: 290. Conference Name: Society of Photo-Optical Instrumentation Engineers (SPIE) Conference Series, p. 28. DOI: 10.1117/12.965833.
Morton, T. D. et al. (May 2016). "False positive probabilties for all Kepler Objects of Interest: 1284 newly validated planets and 428 likely false positives". In: *The Astrophysical Journal* 822.2. arXiv: 1605.02825, p. 86. DOI: 10.3847/0004-637X/822/2/86.
Moulane, Y. et al. (Aug. 2020). "Photometry and high-resolution spectroscopy of comet 21P/Giacobini-Zinner during its 2018 apparition". In: *Astronomy and Astrophysics* 640, A54. DOI: 10.1051/0004-6361/202037997.
Muirhead, P. S. et al. (Apr. 2018). "A Catalog of Cool Dwarf Targets for the Transiting Exoplanet Survey Satellite". en. In: *The Astronomical Journal* 155.4. Publisher: American Astronomical Society, p. 180. DOI: 10.3847/1538-3881/aab710.
Mulders, G. D. et al. (Jan. 2015). "A Stellar-mass-dependent Drop in Planet Occurrence Rates". In: *The Astrophysical Journal* 798, p. 112. DOI: 10.1088/0004-637X/798/2/112.

Mullan, D. J. et al. (July 2018). "Photosynthesis on a planet orbiting an M dwarf: enhanced effectiveness during flares". In: *arXiv:1807.05267 [astro-ph]*. arXiv: 1807.05267. DOI: 10.3847/1538-4357/aadfd1.

Murray, C. A. et al. (June 2020). "Photometry and Performance of SPECULOOS-South". en. In: *Monthly Notices of the Royal Astronomical Society* 495.2. arXiv: 2005.02423, pp. 2446–2457. DOI: 10.1093/mnras/staa1283.

Murray, C. D. et al. (Feb. 2011). "Keplerian Orbits and Dynamics of Exoplanets". In: *arXiv:1009.1738 [astro-ph]*. arXiv: 1009.1738.

Murray, C. et al. (2021). "Study of Flares in the Ultra-Cool Regime from SPECULOOS-South". In: *Monthly Notices of the Royal Astronomical Society* in prep.

Neal, R. (2011). *Handbook of Markov Chain Monte Carlo*. en.

Neichel, B. et al. (Dec. 2018). "Overview of the European Extremely Large Telescope and its instrument suite". In: *arXiv:1812.06639 [astro-ph]*. arXiv: 1812.06639.

Nelder, J. et al. (1965). "A Simplex Method for Function Minimization". In: *Comput. J.* DOI: 10.1093/COMJNL/7.4.308.

Nesvorny, D. et al. (2013). "KOI-142, THE KING OF TRANSIT VARIATIONS, IS A PAIR OF PLANETS NEAR THE 2:1 RESONANCE". en. In: *The Astrophysical Journal*, p. 9.

Nesvorný, D. et al. (May 2016). "DYNAMICS AND TRANSIT VARIATIONS OF RESONANT EXOPLANETS". en. In: *The Astrophysical Journal* 823.2, p. 72. DOI: 10.3847/0004-637X/823/2/72.

Neves, V. et al. (Aug. 2014). "Metallicity of M dwarfs IV. A high-precision [Fe/H] and Teff technique from high-resolution optical spectra for M dwarfs". In: *Astronomy & Astrophysics* 568. arXiv: 1406.6127, A121. DOI: 10.1051/0004-6361/201424139.

Newton, E. et al. (May 2017). "Age, rotation, and activity in M dwarfs and the implications for planet-hosting stars". In: Conference Name: Radio Exploration of Planetary Habitability (AASTCS5), p. 101.02.

Newton, E. R. et al. (Apr. 2016). "The rotation and Galactic kinematics of mid M dwarfs in the Solar Neighborhood". In: *The Astrophysical Journal* 821.2. arXiv: 1511.00957, p. 93. DOI: 10.3847/0004-637X/821/2/93.

Newville, M. et al. (2021). "LMFIT: Non-Linear Least-Square Minimization and Curve-Fitting for Python". en. In: *Zenodo* (). DOI: 10.5281/zenodo.11813.

Nielsen, L. D. et al. (Oct. 2019). "WASP-169, WASP-171, WASP-175, and WASP-182: three hot Jupiters and one bloated sub-Saturn mass planet discovered by WASP-South". In: *Monthly Notices of the Royal Astronomical Society* 489, pp. 2478–2487. DOI: 10.1093/mnras/stz2351.

Niraula, P. et al. (Aug. 2020). "pi Earth: a 3.14-day Earth-sized Planet from K2's Kitchen Served Warm by the SPECULOOS Team". In: *arXiv:2006.07308 [astro-ph]*. arXiv: 2006.07308.

Noll, S. et al. (July 2012). "An atmospheric radiation model for Cerro Paranal - I. The optical spectral range". en. In: *Astronomy & Astrophysics* 543. Publisher: EDP Sciences, A92. DOI: 10.1051/0004-6361/201219040.

Notsu, Y. et al. (June 2013). "SUPERFLARES ON SOLAR-TYPE STARS OBSERVED WITHKEPLERII. PHOTOMETRIC VARIABILITY OF SUPERFLARE-GENERATING STARS: A SIGNATURE OF SLAR ROTATION AND STARSPOTS". en. In: *The Astrophysical Journal* 771.2. Publisher: American Astronomical Society, p. 127. DOI: 10.1088/0004-637X/771/2/127.

Nutzman, P. et al. (Mar. 2008). "Design Considerations for a Ground-Based Transit Search for Habitable Planets Orbiting M Dwarfs". In: *Publications of the Astronomical Society of the Pacific* 120, p. 317. DOI: 10.1086/533420.

O'Malley-James, J. T. et al. (Dec. 2018). "Biofluorescent worlds: global biological fluorescence as a biosignature". en. In: *Monthly Notices of the Royal Astronomical Society* 481.2, pp. 2487–2496. DOI: 10.1093/mnras/sty2411.

– (July 2017). "UV surface habitability of the TRAPPIST-1 system". en. In: *Monthly Notices of the Royal Astronomical Society: Letters* 469.1, pp. L26–L30. DOI: 10.1093/mnrasl/slx047.

Omiya, M. et al. (Aug. 2012). "Search for Low-Mass Planets Around Late-M Dwarfs Using IRD". en. In: *Proceedings of the International Astronomical Union* 8.S293. Publisher: Cambridge University Press, pp. 201–203. DOI: 10.1017/S1743921313012830.

Ormel, C. et al. (Aug. 2017). "Formation of TRAPPIST-1 and other compact systems". en. In: *Astronomy & Astrophysics* 604. arXiv: 1703.06924, A1. DOI: 10.1051/0004-6361/201730826.

Osborn, J. et al. (Sept. 2015). "Atmospheric scintillation in astronomical photometry". In: *Monthly Notices of the Royal Astronomical Society* 452.2, pp. 1707–1716. DOI: 10.1093/mnras/stv1400.

Oshagh, M. et al. (Jan. 2013). "SOAP-T: a tool to study the light curve and radial velocity of a system with a transiting planet and a rotating spotted star". In: *Astronomy and Astrophysics* 549, A35. DOI: 10.1051/0004-6361/201220173.

Ourisson, G. et al. (Sept. 1994). "The terpenoid theory of the origin of cellular life: the evolution of terpenoids to cholesterol". en. In: *Chemistry & Biology* 1.1, pp. 11–23. DOI: 10.1016/1074-5521(94)90036-1.

Owen, J. E. et al. (July 2016). "Habitability of Terrestrial-Mass Planets in the HZ of M Dwarfs. I. H/He-Dominated Atmospheres". en. In: *Monthly Notices of the Royal Astronomical Society* 459.4. arXiv: 1601.05143, pp. 4088–4108. DOI: 10.1093/mnras/stw959.

Papaloizou, J. C. B. et al. (June 2018). "The TRAPPIST-1 system: Orbital evolution, tidal dissipation, formation and habitability". In: *Monthly Notices of the Royal Astronomical Society* 476.4. arXiv: 1711.07932, pp. 5032–5056. DOI: 10.1093/mnras/stx2980.

Paris, P. von et al. (Oct. 2013). "The Dependence of the Ice-Albedo Feedback on Atmospheric Properties". In: *Astrobiology* 13.10, pp. 899–909. DOI: 10.1089/ast.2013.0993.

Parker, E. N. (1979). "Cosmical magnetic fields: Their origin and their activity". In: *Oxford, Clarendon Press; New York, Oxford University Press, 1979, 858 p.*

Parmentier, V. et al. (2018). "Exoplanet phase curves: observations and theory". In: *arXiv:1711.07696 [astro-ph]*. arXiv: 1711.07696, pp. 1419–1440. DOI: 10.1007/978-3-319-55333-7_116.

Pascale, E. et al. (July 2018). "The ARIEL space mission". In: *Space Telescopes and Instrumentation 2018: Optical, Infrared, and Millimeter Wave*. Vol. 10698. International Society for Optics and Photonics, 106980H. DOI: 10.1117/12.2311838.

Patel, B. H. et al. (Apr. 2015). "Common origins of RNA, protein and lipid precursors in a cyanosulfidic protometabolism". eng. In: *Nature Chemistry* 7.4, pp. 301–307. DOI: 10.1038/nchem.2202.

Paudel, R. R. et al. (May 2018). "K2 Ultracool Dwarfs Survey. III. White Light Flares are Ubiquitous in M6-L0 Dwarfs". en. In: *The Astrophysical Journal* 858.1. arXiv: 1803.07708, p. 55. DOI: 10.3847/1538-4357/aab8fe.

Paudel, R. R. et al. (June 2019). "K2 Ultracool Dwarfs Survey. V. High superflare rates on rapidly rotating late-M dwarfs". en. In: *Monthly Notices of the Royal Astronomical Society* 486.1. arXiv: 1812.07631, pp. 1438–1447. DOI: 10.1093/mnras/stz886.

Pecaut, M. J. et al. (Sept. 2013). "Intrinsic Colors, Temperatures, and Bolometric Corrections of Pre-main-sequence Stars". In: *The Astrophysical Journal Supplement Series* 208, p. 9. DOI: 10.1088/0067-0049/208/1/9.

Pedersen, P. et al. (2021a). "A photometric correction for precipitable water vapour". In: *in prep*.

– (2021b). "SPIRIT: SPECULOOS InfraRed photometric Imager for Transits". In: *in prep*.

Perryman, M. (Aug. 2018). *The Exoplanet Handbook | Planetary systems and astrobiology 2nd edition*. en.

Peterson, M. et al. (2021). "A temperate Earth-sized planet transiting the M6 dwarf LP 791-18". In: in prep.

Pierrehumbert, R. et al. (Apr. 2011). "Hydrogen Greenhouse Planets Beyond the Habitable Zone". In: *arXiv:1105.0021 [astro-ph]*. arXiv: 1105.0021. DOI: 10.1088/2041-8205/734/1/L13.

Pont, F. et al. (Nov. 2006). "The effect of red noise on planetary transit detection". en. In: *Monthly Notices of the Royal Astronomical Society* 373.1, pp. 231–242. DOI: 10.1111/j.1365-2966.2006.11012.x.

Pope, B. J. S. et al. (Oct. 2016). "Transiting exoplanet candidates from *K2* Campaigns 5 and 6". en. In: *Monthly Notices of the Royal Astronomical Society* 461.4, pp. 3399–3409. DOI: 10.1093/mnras/stw1373.

Pozuelos, F. J. (2021). "A super-Earth and mini-Neptune near to 1:2 MMR straddling the radius valley limits". In: in prep.

Price-Whelan, a. A. M. et al. (Aug. 2018). "The Astropy Project: Building an Open-science Project and Status of the v2.0 Core Package". en. In: *The Astronomical Journal* 156.3. Publisher: American Astronomical Society, p. 123. DOI: 10.3847/1538-3881/aabc4f.

Prusti, T. et al. (Nov. 2016). "The Gaia mission". en. In: *Astronomy & Astrophysics* 595. Publisher: EDP Sciences, A1. DOI: 10.1051/0004-6361/201629272.

Quinn, S. N. et al. (Oct. 2019). "Near-resonance in a System of Sub-Neptunes from TESS". en. In: *The Astronomical Journal* 158.5. Publisher: American Astronomical Society, p. 177. DOI: 10.3847/1538-3881/ab3f2b.

Quirrenbach, A. et al. (July 2014). "CARMENES instrument overview". In: 9147. Conference Name: Ground-based and Airborne Instrumentation for Astronomy V, 91471F. DOI: 10.1117/12.2056453.

Rackham, B. V. et al. (Jan. 2018). "The Transit Light Source Effect: False Spectral Features and Incorrect Densities for M-dwarf Transiting Planets". en. In: *The Astrophysical Journal* 853.2. arXiv: 1711.05691, p. 122. DOI: 10.3847/1538-4357/aaa08c.

– (Feb. 2019). "The Transit Light Source Effect II: The Impact of Stellar Heterogeneity on Transmission Spectra of Planets Orbiting Broadly Sun-like Stars". In: *The Astronomical Journal* 157.3. arXiv: 1812.06184, p. 96. DOI: 10.3847/1538-3881/aaf892.

Ranjan, S. et al. (Jan. 2016). "Influence of the UV Environment on the Synthesis of Prebiotic Molecules". en. In: *Astrobiology* 16.1, pp. 68–88. DOI: 10.1089/ast.2015.1359.

Ranjan, S. et al. (Aug. 2017). "The Surface UV Environment on Planets Orbiting M-Dwarfs: Implications for Prebiotic Chemistry & Need for Experimental Follow-Up". In: *arXiv:1705.02350 [astro-ph]*. arXiv: 1705.02350. DOI: 10.3847/1538-4357/aa773e.

Rasmussen, R. A. (1974). "Emission of biogenic hydrogen sulfide". en. In: *Tellus* 26.1-2. _eprint: https://onlinelibrary.wiley.com/doi/pdf/10.1111/j.2153-3490.1974.tb01974.x, pp. 254–260. DOI: https://doi.org/10.1111/j.2153-3490.1974.tb01974.x.

Rasool, S. I. et al. (June 1970). "The Runaway Greenhouse and the Accumulation of CO 2 in the Venus Atmosphere". en. In: *Nature* 226.5250. Bandiera_abtest: a Cg_type: Nature

Research Journals Number: 5250 Primary_atype: Research Publisher: Nature Publishing Group, pp. 1037–1039. DOI: 10.1038/2261037a0.
Rauer, H. et al. (Nov. 2014). "The PLATO 2.0 mission". en. In: *Experimental Astronomy* 38.1, pp. 249–330. DOI: 10.1007/s10686-014-9383-4.
Raymond, S. N. et al. (Nov. 2007). "A Decreased Probability of Habitable Planet Formation around Low-Mass Stars". en. In: *The Astrophysical Journal* 669.1. Publisher: IOP Publishing, p. 606. DOI: 10.1086/521587.
Raymond, S. N. et al. (Sept. 2018). "Migration-driven diversity of super-Earth compositions". In: *Monthly Notices of the Royal Astronomical Society* 479, pp. L81–L85. DOI: 10.1093/mnrasl/sly100.
Reid, N. et al. (Feb. 1995). "Chromospheric and coronal activity in low-mass Hyades dwarfs". In: *Monthly Notices of the Royal Astronomical Society* 272, pp. 828–842. DOI: 10.1093/mnras/272.4.828.
Reiners, A. (Feb. 2012). "Observations of Cool-Star Magnetic Fields". en. In: *Living Reviews in Solar Physics* 9.1, p. 1. DOI: 10.12942/lrsp-2012-1.
Reinhard, C. T. et al. (Apr. 2017). "False negatives for remote life detection on ocean-bearing planets: Lessons from the early Earth". In: *Astrobiology* 17.4. arXiv: 1702.01137, pp. 287–297. DOI: 10.1089/ast.2016.1598.
Reylé, C. (Nov. 2018). "New ultra-cool and brown dwarf candidates in Gaia DR2". en. In: *Astronomy & Astrophysics* 619. Publisher: EDP Sciences, p. L8. DOI: 10.1051/0004-6361/201834082.
Ricker, G. R. et al. (Oct. 2014). "The Transiting Exoplanet Survey Satellite". In: *arXiv:1406.0151 [astro-ph]*. arXiv: 1406.0151. DOI: 10.1117/1.JATIS.1.1.014003.
Rimmer, P. B. et al. (Aug. 2018). "The origin of RNA precursors on exoplanets". en. In: *Science Advances* 4.8, eaar3302. DOI: 10.1126/sciadv.aar3302.
Rimmer, P. B. et al. (Jan. 2019). "Origin of Life's Building Blocks in Carbon- and Nitrogen-Rich Surface Hydrothermal Vents". In: *Life* 9.1. DOI: 10.3390/life9010012.
Robinson, T. D. (2018). "Characterizing Exoplanet Habitability". en. In: *Handbook of Exoplanets*. Ed. by H. J. Deeg et al. Cham: Springer International Publishing, pp. 3137–3157. DOI: 10.1007/978-3-319-55333-7_67.
Robitaille, T. P. et al. (Oct. 2013). "Astropy: A community Python package for astronomy". en. In: *Astronomy & Astrophysics* 558. Publisher: EDP Sciences, A33. DOI: 10.1051/0004-6361/201322068.
Rodler, F. et al. (Jan. 2014). "FEASIBILITY STUDIES FOR THE DETECTION OF O2IN AN EARTH-LIKE EXOPLANET". en. In: *The Astrophysical Journal* 781.1. Publisher: American Astronomical Society, p. 54. DOI: 10.1088/0004-637X/781/1/54.
Roettenbacher, R. M. et al. (Dec. 2017). "The Stellar Activity of TRAPPIST-1 and Consequences for the Planetary Atmospheres". en. In: *The Astrophysical Journal* 851.2. arXiv: 1711.02676, p. 77. DOI: 10.3847/1538-4357/aa991e.
Roettenbacher, R. M. et al. (Nov. 2018). "The Connection between Starspots and Flares on Main-Sequence Kepler Stars". In: *The Astrophysical Journal* 868.1. arXiv: 1810.04762, p. 3. DOI: 10.3847/1538-4357/aae77e.
Rogers, L. A. (Mar. 2015). "MOST1.6 EARTH-RADIUS PLANETS ARE NOT ROCKY". en. In: *The Astrophysical Journal* 801.1. Publisher: American Astronomical Society, p. 41. DOI: 10.1088/0004-637X/801/1/41.
Rosotti, G. P. et al. (July 2014). "Protoplanetary disc evolution affected by star–disc interactions in young stellar clusters". In: *Monthly Notices of the Royal Astronomical Society* 441.3, pp. 2094–2110. DOI: 10.1093/mnras/stu679.

Rossiter, R. A. (July 1924). "On the detection of an effect of rotation during eclipse in the velocity of the brigher component of beta Lyrae, and on the constancy of velocity of this system." In: *The Astrophysical Journal* 60, pp. 15–21. DOI: 10.1086/142825.

Rugheimer, S. et al. (Aug. 2015). "Effect of UV Radiation on the Spectral Fingerprints of Earth-like Planets Orbiting M dwarfs". In: *The Astrophysical Journal* 809.1. arXiv: 1506.07202, p. 57. DOI: 10.1088/0004-637X/809/1/57.

Sagan, C. et al. (Oct. 1993). "A search for life on Earth from the Galileo spacecraft". en. In: *Nature* 365.6448. Number: 6448 Publisher: Nature Publishing Group, pp. 715–721. DOI: 10.1038/365715a0.

Salese, F. et al. (May 2020). "Sustained fluvial deposition recorded in Mars' Noachian stratigraphic record". en. In: *Nature Communications* 11.1. Bandiera_abtest: a Cc_license_type: cc_by Cg_type: Nature Research Journals Number: 1 Primary_atype: Research Publisher: Nature Publishing Group Subject_term: Geomorphology;Inner planets Subject_term_id: geomorphology;inner-planets, p. 2067. DOI: 10.1038/s41467-020-15622-0.

Saltzman, E. S. et al., eds. (Apr. 1989). *Biogenic Sulfur in the Environment*. en. Vol. 393. ACS Symposium Series. Washington, DC: American Chemical Society. DOI: 10.1021/bk-1989-0393.

Sanchis-Ojeda, R. et al. (July 2012). "Alignment of the stellar spin with the orbits of a three-planet system". In: *Nature* 487.7408. arXiv: 1207.5804, pp. 449–453. DOI: 10.1038/nature11301.

Scargle, J. D. (Dec. 1982). "Studies in astronomical time series analysis. II. Statistical aspects of spectral analysis of unevenly spaced data." In: *The Astrophysical Journal* 263, pp. 835–853. DOI: 10.1086/160554.

Scholz, R.-D. (May 2020). "New ultracool dwarf neighbours within 20pc from Gaia DR2". In: *Astronomy & Astrophysics* 637. arXiv: 2003.10949, A45. DOI: 10.1051/0004-6361/201937373.

Schoonenberg, D. et al. (July 2019). "Pebble-driven planet formation for TRAPPIST-1 and other compact systems". en. In: *Astronomy & Astrophysics* 627. arXiv: 1906.00669, A149. DOI: 10.1051/0004-6361/201935607.

Schwartz, J. C. et al. (June 2015). "Balancing the Energy Budget of Short-Period Giant Planets: Evidence for Reflective Clouds and Optical Absorbers". In: *Monthly Notices of the Royal Astronomical Society* 449.4. arXiv: 1502.06970, pp. 4192–4203. DOI: 10.1093/mnras/stv470.

Schwarz, G. (1978). "Estimating the Dimension of a Model". In: *The Annals of Statistics* 6.2. Publisher: Institute of Mathematical Statistics, pp. 461–464.

Schwieterman, E. (2016). "Exploring Habitability Markers, Biosignatures, and Their False Positives Using Spectral Models of Terrestrial Exoplanets". en. In: *undefined*.

Schwieterman, E. W. et al. (June 2018). "Exoplanet Biosignatures: A Review of Remotely Detectable Signs of Life". en. In: *Astrobiology* 18.6, pp. 663–708. DOI: 10.1089/ast.2017.1729.

Seager, S. (May 2013). "Exoplanet Habitability". en. In: *Science* 340.6132, pp. 577–581. DOI: 10.1126/science.1232226.

Seager, S. et al. (Mar. 2003). "A Unique Solution of Planet and Star Parameters from an Extrasolar Planet Transit Light Curve". en. In: *The Astrophysical Journal* 585.2, pp. 1038–1055. DOI: 10.1086/346105.

Seager, S. et al. (June 2005). "Vegetation's Red Edge: A Possible Spectroscopic Biosignature of Extraterrestrial Plants". en. In: *Astrobiology* 5.3, pp. 372–390. DOI: 10.1089/ast.2005.5.372.

Sebastian, D. et al. (Nov. 2020). "SPECULOOS – Ultracool Dwarf Transit Survey: Target List and Strategy". In: *arXiv:2011.02069 [astro-ph]*. arXiv: 2011.02069.
Sedaghati, E. et al. (Sept. 2017). "Detection of titanium oxide in the atmosphere of a hot Jupiter". In: *Nature* 549.7671. arXiv: 1709.04118, pp. 238–241. DOI: 10.1038/nature23651.
Segura, A. et al. (Sept. 2010). "The Effect of a Strong Stellar Flare on the Atmospheric Chemistry of an Earth-like Planet Orbiting an M Dwarf". en. In: *Astrobiology* 10.7, pp. 751–771. DOI: 10.1089/ast.2009.0376.
Selsis, F. et al. (Dec. 2007). "Habitable planets around the star Gliese 581?" In: *Astronomy and Astrophysics* 476, pp. 1373–1387. DOI: 10.1051/0004-6361:20078091.
Serindag, D. B. et al. (Jan. 2019). "Testing the Detectability of Extraterrestrial $\mathrm{O}_2$ with the ELTs using Real Data with Real Noise". In: *The Astrophysical Journal* 871.1. arXiv: 1901.02469, p. L7. DOI: 10.3847/2041-8213/aafa1f.
Sheppard, K. et al. (Nov. 2017). "Evidence for a Dayside Thermal Inversion and High Metallicity for the Hot Jupiter WASP-18b". In: *The Astrophysical Journal* 850.2. arXiv: 1711.10491, p. L32. DOI: 10.3847/2041-8213/aa9ae9.
Shibayama, T. et al. (Oct. 2013). "Superflares on Solar Type Stars Observed with Kepler I. Statistical Properties of Superflares". en. In: *The Astrophysical Journal Supplement Series* 209.1. arXiv: 1308.1480, p. 5. DOI: 10.1088/0067-0049/209/1/5.
Shields, A. L. et al. (July 2013). "The Effect of Host Star Spectral Energy Distribution and Ice-Albedo Feedback on the Climate of Extrasolar Planets". In: *Astrobiology* 13.8. Publisher: Mary Ann Liebert, Inc., publishers, pp. 715–739. DOI: 10.1089/ast.2012.0961.
Shields, A. L. et al. (Feb. 2017). "The Habitability of Planets Orbiting M-dwarf Stars". In: *arXiv:1610.05765 [astro-ph]*. arXiv: 1610.05765. DOI: 10.1016/j.physrep.2016.10.003.
Showman, A. P. et al. (July 2009). "ATMOSPHERIC CIRCULATION OF HOT JUPITERS: COUPLED RADIATIVE-DYNAMICAL GENERAL CIRCULATION MODEL SIMULATIONS OF HD 189733b and HD 209458b". en. In: *The Astrophysical Journal* 699.1, pp. 564–584. DOI: 10.1088/0004-637X/699/1/564.
Siebenmorgen, R. et al. (June 2011). "The Science Impact of HAWK-I". In: *The Messenger* 144, pp. 9–12.
Silva, A. V. R. (Mar. 2003). "Method for Spot Detection on Solar-like Stars". In: *The Astrophysical Journal* 585, pp. L147–L150. DOI: 10.1086/374324.
Sing, D. K. et al. (Jan. 2016). "A continuum from clear to cloudy hot-Jupiter exoplanets without primordial water depletion". en. In: *Nature* 529.7584. Number: 7584 Publisher: Nature Publishing Group, pp. 59–62. DOI: 10.1038/nature16068.
Skrutskie, M. F. et al. (Feb. 2006). "The Two Micron All Sky Survey (2MASS)". en. In: *The Astronomical Journal* 131.2. Publisher: IOP Publishing, p. 1163. DOI: 10.1086/498708.
Smart, R. L. et al. (May 2019). "The Gaia Ultra-Cool Dwarf Sample – II: Structure at the end of the main sequence". In: *Monthly Notices of the Royal Astronomical Society* 485.3. arXiv: 1902.07571, pp. 4423–4440. DOI: 10.1093/mnras/stz678.
Snellen, I. A. G. et al. (Feb. 2013). "FINDING EXTRATERRESTRIAL LIFE USING GROUND-BASED HIGH-DISPERSION SPECTROSCOPY". en. In: *The Astrophysical Journal* 764.2. Publisher: American Astronomical Society, p. 182. DOI: 10.1088/0004-637X/764/2/182.
Snellen, I. A. G. et al. (May 2009). "The changing phases of extrasolar planet CoRoT-1b". In: *Nature* 459, pp. 543–545. DOI: 10.1038/nature08045.
Sojo, V. et al. (Dec. 2016). "The origin of life in alkaline hydrothermal vents". In: *AGU Fall Meeting Abstracts* 33.

Solanki, S. K. (Jan. 2003). "Sunspots: An overview". In: *Astronomy and Astrophysics Review* 11, pp. 153–286. DOI: 10.1007/s00159-003-0018-4.

Stassun, K. G. et al. (July 2018). "Evidence for a Systematic Offset of -80 as in the Gaia DR2 Parallaxes". In: *The Astrophysical Journal* 862, p. 61. DOI: 10.3847/1538-4357/aacafc.

Stauffer, J. et al. (Mar. 2017). "Orbiting Clouds of Material at the Keplerian Co-rotation Radius of Rapidly Rotating Low-mass WTTs in Upper Sco". en. In: *The Astronomical Journal* 153.4. Publisher: American Astronomical Society, p. 152. DOI: 10.3847/1538-3881/aa5eb9.

Stauffer, J. et al. (Jan. 2018). "More Rapidly Rotating PMS M Dwarfs with Light Curves Suggestive of Orbiting Clouds of Material". en. In: *The Astronomical Journal* 155.2. Publisher: American Astronomical Society, p. 63. DOI: 10.3847/1538-3881/aaa19d.

Steele, I. A. et al. (Sept. 2004). "The Liverpool Telescope: performance and first results". In: *Ground-based Telescopes*. Vol. 5489. International Society for Optics and Photonics, pp. 679–692. DOI: 10.1117/12.551456.

Steffen, J. H. et al. (Aug. 2012). "TRANSIT TIMING OBSERVATIONS FROM KEPLER. VI. POTENTIALLY INTERESTING CANDIDATE SYSTEMS FROM FOURIER-BASED STATISTICAL TESTS". en. In: *The Astrophysical Journal* 756.2. Publisher: IOP Publishing, p. 186. DOI: 10.1088/0004-637X/756/2/186.

Stetson, P. B. (Mar. 1987). "DAOPHOT - A computer program for crowded-field stellar photometry". en. In: *Publications of the Astronomical Society of the Pacific* 99, p. 191. DOI: 10.1086/131977.

Stevenson, K. B. et al. (Aug. 2012). "TRANSIT AND ECLIPSE ANALYSES OF THE EXOPLANET HD 149026b USING BLISS MAPPING". en. In: *The Astrophysical Journal* 754.2, p. 136. DOI: 10.1088/0004-637X/754/2/136.

Suárez Mascareño, A. et al. (July 2017). "Characterization of the radial velocity signal induced by rotation in late-type dwarfs". In: *Monthly Notices of the Royal Astronomical Society* 468.4, pp. 4772–4781. DOI: 10.1093/mnras/stx771.

Sullivan, P. W. et al. (Aug. 2015). "THE TRANSITING EXOPLANET SURVEY SALITE: SIMULATIONS OF PLANET DETECTIONS AND ASTROPHYSICAL FALSE POSITIVES". en. In: *The Astrophysical Journal* 809.1. Publisher: American Astronomical Society, p. 77. DOI: 10.1088/0004-637X/809/1/77.

Szabó, G. M. et al. (Mar. 2012). "Spin-orbit resonance, transit duration variation and possible secular perturbations in KOI-13". In: *Monthly Notices of the Royal Astronomical Society* 421, pp. L122–L126. DOI: 10.1111/j.1745-3933.2012.01219.x.

Tamayo, D. et al. (May 2017). "Convergent Migration Renders TRAPPIST-1 Long-lived". In: *The Astrophysical Journal* 840.2. arXiv: 1704.02957, p. L19. DOI: 10.3847/2041-8213/aa70ea.

Tamburo, P. et al. (Oct. 2019). "Design Considerations for a Ground-based Search for Transiting Planets around L and T Dwarfs". en. In: *Publications of the Astronomical Society of the Pacific* 131.1005. Publisher: IOP Publishing, p. 114401. DOI: 10.1088/1538-3873/ab3a1e.

Team, T. L. (Dec. 2019). "The LUVOIR Mission Concept Study Final Report". In: *arXiv:1912.06219 [astro-ph]*. arXiv: 1912.06219.

Temple, L. Y. et al. (Dec. 2019a). "WASP-180Ab: Doppler tomography of a hot Jupiter orbiting the primary star in a visual binary". In: *Monthly Notices of the Royal Astronomical Society* 490.2, pp. 2467–2474. DOI: 10.1093/mnras/stz2632.

Temple, L. Y. et al. (Mar. 2019b). "WASP-190b: Tomographic Discovery of a Transiting Hot Jupiter". en. In: *The Astronomical Journal* 157.4, p. 141. DOI: 10.3847/1538-3881/ab095a.

Tennyson, J. et al. (Sept. 2012). "ExoMol: molecular line lists for exoplanet and other atmospheres". In: *Monthly Notices of the Royal Astronomical Society* 425.1, pp. 21–33. DOI: 10.1111/j.1365-2966.2012.21440.x.

Tilley, M. A. et al. (Jan. 2019). "Modeling Repeated M-dwarf Flaring at an Earth-like Planet in the Habitable Zone: I. Atmospheric Effects for an Unmagnetized Planet". In: *Astrobiology* 19.1. arXiv: 1711.08484, pp. 64–86. DOI: 10.1089/ast.2017.1794.

Tinetti, G. et al. (Nov. 2018). "A chemical survey of exoplanets with ARIEL". en. In: *Experimental Astronomy* 46.1, pp. 135–209. DOI: 10.1007/s10686-018-9598-x.

Torres, G. et al. (Feb. 2010). "Accurate masses and radii of normal stars: modern results and applications". In: *Astronomy and Astrophysics Review* 18, pp. 67–126. DOI: 10.1007/s00159-009-0025-1.

Trail, D. et al. (Dec. 2011). "The oxidation state of Hadean magmas and implications for early Earth's atmosphere". en. In: *Nature* 480.7375. Bandiera_abtest: a Cg_type: Nature Research Journals Number: 7375 Primary_atype: Research Publisher: Nature Publishing Group Subject_term: Atmospheric chemistry;Geodynamics;Geology Subject_term_id: atmospheric-chemistry;geodynamics;geology, pp. 79–82. DOI: 10.1038/nature10655.

Trauger, J. T. et al. (Apr. 2007). "A laboratory demonstration of the capability to image an Earth-like extrasolar planet". en. In: *Nature* 446.7137. Bandiera_abtest: a Cg_type: Nature Research Journals Number: 7137 Primary_atype: Research Publisher: Nature Publishing Group, pp. 771–773. DOI: 10.1038/nature05729.

Triaud, A. H. M. J. et al. (Apr. 2013). "A search for rocky planets transiting brown dwarfs". In: *arXiv:1304.7248 [astro-ph]*. arXiv: 1304.7248.

Triaud, A. H. M. J. et al. (Mar. 2020). "An eclipsing substellar binary in a young triple system discovered by SPECULOOS". en. In: *Nature Astronomy*. DOI: 10.1038/s41550-020-1018-2.

Turbet, M. et al. (Apr. 2018). "Modeling climate diversity, tidal dynamics and the fate of volatiles on TRAPPIST-1 planets". en. In: *Astronomy & Astrophysics* 612, A86. DOI: 10.1051/0004-6361/201731620.

Turbet, M. et al. (July 2020a). "A review of possible planetary atmospheres in the TRAPPIST-1 system". In: *arXiv:2007.03334 [astro-ph, physics:physics]*. arXiv: 2007.03334.

Turbet, M. et al. (June 2020b). "Revised mass-radius relationships for water-rich rocky planets more irradiated than the runaway greenhouse limit". en. In: *Astronomy & Astrophysics* 638. Publisher: EDP Sciences, A41. DOI: 10.1051/0004-6361/201937151.

Turner, O. D. et al. (June 2019). "Three hot-Jupiters on the upper edge of the mass–radius distribution: WASP-177, WASP-181, and WASP-183". In: *Monthly Notices of the Royal Astronomical Society* 485.4, pp. 5790–5799. DOI: 10.1093/mnras/stz742.

Unterborn, C. T. et al. (Apr. 2018). "Inward migration of the TRAPPIST-1 planets as inferred from their water-rich compositions". English (US). In: *Nature Astronomy* 2.4. Publisher: Nature Publishing Group, pp. 297–302. DOI: 10.1038/s41550-018-0411-6.

Valio, A. et al. (Aug. 2018). "The biological impact of superflares on planets in the Habitable Zone". en. In: *Proceedings of the International Astronomical Union* 14.S345. Publisher: Cambridge University Press, pp. 176–180. DOI: 10.1017/S1743921319002035.

Van Grootel, V. et al. (Jan. 2018). "Stellar parameters for TRAPPIST-1". en. In: *The Astrophysical Journal* 853.1. arXiv: 1712.01911, p. 30. DOI: 10.3847/1538-4357/aaa023.

Vida, K. et al. (June 2017). "Frequent Flaring in the TRAPPIST-1 System—Unsuited for Life?" en. In: *The Astrophysical Journal* 841.2, p. 124. DOI: 10.3847/1538-4357/aa6f05.

Vogt, S. S. (Oct. 1979). "A spectroscopic and photometric study of the star spot on HD 224085." In: *Publications of the Astronomical Society of the Pacific* 91, p. 616. DOI: 10.1086/130549.

Wakeford, H. R. et al. (Dec. 2018). "Disentangling the Planet from the Star in Late-Type M Dwarfs: A Case Study of TRAPPIST-1g". en. In: *The Astronomical Journal* 157.1. Publisher: American Astronomical Society, p. 11. DOI: 10.3847/1538-3881/aaf04d.
Walker, S. I. et al. (June 2018). "Exoplanet Biosignatures: Future Directions". In: *Astrobiology* 18.6. arXiv: 1705.08071, pp. 779–824. DOI: 10.1089/ast.2017.1738.
Wells, R. et al. (Jan. 2018). "Transit visibility zones of the Solar system planets". en. In: *Monthly Notices of the Royal Astronomical Society* 473.1, pp. 345–354. DOI: 10.1093/mnras/stx2077.
Wells, R. (2021). "A Large Sub-Neptune Orbiting the Thick Disk M4V TOI-2406". In: *Astronomy & Astrophysics* in prep.
Wenger, M. et al. (Apr. 2000). "The SIMBAD astronomical database - The CDS reference database for astronomical objects". en. In: *Astronomy and Astrophysics Supplement Series* 143.1. Number: 1 Publisher: EDP Sciences, pp. 9–22. DOI: 10.1051/aas:2000332.
West, A. A. et al. (Dec. 2006). "Using the Galactic Dynamics of M7 Dwarfs to Infer the Evolution of Their Magnetic Activity". In: *The Astronomical Journal* 132, pp. 2507–2512. DOI: 10.1086/508652.
West, A. A. et al. (Mar. 2008). "Constraining the Age-Activity Relation for Cool Stars: The Sloan Digital Sky Survey Data Release 5 Low-Mass Star Spectroscopic Sample". In: *The Astronomical Journal* 135, pp. 785–795. DOI: 10.1088/0004-6256/135/3/785.
West, A. A. et al. (Mar. 2011). "The Sloan Digital Sky Survey Data Release 7 Spectroscopic M Dwarf Catalog I: Data". In: *The Astronomical Journal* 141.3. arXiv: 1101.1082, p. 97. DOI: 10.1088/0004-6256/141/3/97.
West, A. A. et al. (Oct. 2015). "AN ACTIVITY–ROTATION RELATIONSHIP AND KINEMATIC ANALYSIS OF NEARBY MID-TO-LATE-TYPE M DWARFS". en. In: *The Astrophysical Journal* 812.1. Publisher: American Astronomical Society, p. 3. DOI: 10.1088/0004-637X/812/1/3.
West, R. G. et al. (July 2019). "NGTS-4b: A sub-Neptune transiting in the desert". In: *Monthly Notices of the Royal Astronomical Society* 486.4, pp. 5094–5103. DOI: 10.1093/mnras/stz1084.
Wheatley, P. J. et al. (Apr. 2018). "The Next Generation Transit Survey (NGTS)". In: *Monthly Notices of the Royal Astronomical Society* 475.4, pp. 4476–4493. DOI: 10.1093/mnras/stx2836.
Wheatley, P. J. et al. (Feb. 2017). "Strong XUV irradiation of the Earth-sized exoplanets orbiting the ultracool dwarf TRAPPIST-1". In: *Monthly Notices of the Royal Astronomical Society: Letters* 465.1. arXiv: 1605.01564, pp. L74–L78. DOI: 10.1093/mnrasl/slw192.
Wildi, F. et al. (Sept. 2017). "NIRPS: an adaptive-optics assisted radial velocity spectrograph to chase exoplanets around M-stars". In: *Techniques and Instrumentation for Detection of Exoplanets VIII*. Vol. 10400. International Society for Optics and Photonics, p. 1040018. DOI: 10.1117/12.2275660.
Williams, D. M. et al. (Jan. 2002). "Earth-like worlds on eccentric orbits: excursions beyond the habitable zone". en. In: *International Journal of Astrobiology* 1.1. Publisher: Cambridge University Press, pp. 61–69. DOI: 10.1017/S1473550402001064.
Winn, J. N. (May 2008). "Measuring accurate transit parameters". en. In: *Proceedings of the International Astronomical Union* 4.S253. arXiv: 0807.4929, pp. 99–109. DOI: 10.1017/S174392130802629X.
– (Sept. 2014). "Transits and Occultations". In: *arXiv:1001.2010 [astro-ph]*. arXiv: 1001.2010.

Winn, J. N. et al. (Mar. 2009). "The Transit Light Curve Project. X. A Christmas Transit of HD 17156b". en. In: *The Astrophysical Journal* 693.1. arXiv: 0810.4725, pp. 794–803. DOI: 10.1088/0004-637X/693/1/794.

Winn, J. N. et al. (July 2010). "HOT STARS WITH HOT JUPITERS HAVE HIGH OBLIQUITIES". en. In: *The Astrophysical Journal Letters* 718.2. Publisher: IOP Publishing, p. L145. DOI: 10.1088/2041-8205/718/2/L145.

Wittenmyer, R. A. et al. (Jan. 2017). "The Anglo-Australian Planet Search Legacy". In: 229. Conference Name: American Astronomical Society Meeting Abstracts #229, p. 320.07.

Wolf, E. T. (Apr. 2017). "Assessing the Habitability of the TRAPPIST-1 System Using a 3D Climate Model". In: *The Astrophysical Journal* 839.1. arXiv: 1703.05815, p. L1. DOI: 10.3847/2041-8213/aa693a.

Wolf, E. T. et al. (Mar. 2017). "Constraints on Climate and Habitability for Earth-like Exoplanets Determined from a General Circulation Model". In: *The Astrophysical Journal* 837.2. arXiv: 1702.03315, p. 107. DOI: 10.3847/1538-4357/aa5ffc.

Wolfgang, A. et al. (June 2015). "How Rocky Are They? The Composition Distribution of Kepler's Sub-Neptune Planet Candidates within 0.15 AU". In: *The Astrophysical Journal* 806, p. 183. DOI: 10.1088/0004-637X/806/2/183.

Wolszczan, A. et al. (Jan. 1992). "A planetary system around the millisecond pulsar PSR1257 + 12". en. In: *Nature* 355.6356. Number: 6356 Publisher: Nature Publishing Group, pp. 145–147. DOI: 10.1038/355145a0.

Wordsworth, R. (June 2015). "Atmospheric Heat Redistribution and Collapse on Tidally Locked Rocky Planets". In: *The Astrophysical Journal* 806, p. 180. DOI: 10.1088/0004-637X/806/2/180.

Wright, N. J. et al. (Sept. 2018). "The stellar rotation–activity relationship in fully convective M dwarfs". In: *Monthly Notices of the Royal Astronomical Society* 479.2, pp. 2351–2360. DOI: 10.1093/mnras/sty1670.

Wunderlich, F. et al. (Apr. 2019). "Detectability of atmospheric features of Earth-like planets in the habitable zone around M dwarfs". en. In: *Astronomy & Astrophysics* 624. arXiv: 1905.02560, A49. DOI: 10.1051/0004-6361/201834504.

Xu, J. et al. (2018). "Photochemical reductive homologation of hydrogen cyanide using sulfite and ferrocyanide". en. In: *Chemical Communications* 54.44, pp. 5566–5569. DOI: 10.1039/C8CC01499J.

Yang, J. et al. (Apr. 2014). "Strong Dependence of the Inner Edge of the Habitable Zone on Planetary Rotation Rate". In: *The Astrophysical Journal* 787.1. arXiv: 1404.4992, p. L2. DOI: 10.1088/2041-8205/787/1/L2.

Zanazzi, J. J. et al. (June 2019). "The ability of significant tidal stress to initiate plate tectonics". en. In: *Icarus* 325, pp. 55–66. DOI: 10.1016/j.icarus.2019.01.029.

Zhan, Z. et al. (May 2019). "Complex Rotational Modulation of Rapidly Rotating M Stars Observed with TESS". en. In: *The Astrophysical Journal* 876.2. Publisher: American Astronomical Society, p. 127. DOI: 10.3847/1538-4357/ab158c.

Zhang, Z. et al. (Oct. 2018). "The Near-Infrared Transmission Spectra of TRAPPIST-1 Planets b, c, d, e, f, and g and Stellar Contamination in Multi-Epoch Transit Spectra". In: *The Astronomical Journal* 156.4. arXiv: 1802.02086 version: 3, p. 178. DOI: 10.3847/1538-3881/aade4f.

Zsom, A. et al. (Nov. 2013). "Towards the Minimum Inner Edge Distance of the Habitable Zone". In: *The Astrophysical Journal* 778.2. arXiv: 1304.3714, p. 109. DOI: 10.1088/0004-637X/778/2/109.